

MECHANISTIC CONSIDERATIONS IN RETROGRADE REACTION

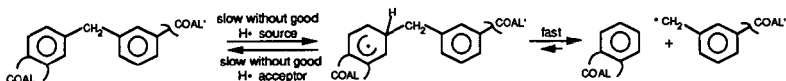
Donald F. McMillen, and Ripudaman Malhotra
Chemistry and Chemical Engineering Laboratories, SRI International
333 Ravenswood Ave., Menlo Park, California, 94025

Key Words: Retrograde reaction, Coal liquefaction, Hydrogen transfer.

INTRODUCTION

The importance of retrogressive reactions has become obvious through the study of liquefaction kinetics and products, but the fundamental chemical reactions and their kinetics have remained more obscure. For instance, researchers such as Neavel recognized some time ago that soluble products could be generated and consumed very rapidly under coal liquefaction conditions.¹ Similar observations have been made for pyridine solubles under pyrolysis conditions, where there is no added solvent². In a sense the whole technology of heavy oil conversion is bound up with retrograde reactions, in that thermal treatment of petroleum asphaltenes under a variety of conditions can produce similar amounts of distillate, but the amount of retrograde product (coke) generated in conjunction with these volatiles is critically dependent on conditions of catalyst, medium, and hydrogen pressure.^{3,4} Thus the impact of retrograde processes has been quite obvious, but the detailed nature of the responsible bond forming reactions has remained unclear.

Similarly, hydrogen transfer has been acknowledged for many years to play a key role in coal liquefaction, though not until more recently was it recognized as a prerequisite to the cleavage of strong bonds in both liquefaction and pyrolysis.^{5,6} The extension of the induced strong-bond scission picture and the consideration of its microscopic reverse provides new insights for bond-forming processes. Thus, the reverse of H-atom displacement of C-C or O-C linkages to aromatic clusters is the addition of a C-centered or O-centered radical to an aromatic ring system, to displace an H-atom. When the adding radical is resonance stabilized, the addition is highly reversible. Just as the key step in the de-substitution (cleavage) reaction is H-atom transfer to the coal linkage, the key step in the microscopic reverse (the substitution reaction) is H-atom transfer from the substitution adduct.



In this paper we extend some earlier qualitative discussion⁷ of these aspects of bond formation with the quantitative results of a numerical model. This model was originally assembled to fit and help interpret experimental data for bond cleavage in model systems;⁸ however, since it includes the reverse of essentially all of the fundamental reaction steps incorporated, it is equally suitable for exploring bond formation, or retrograde reaction. We use it here to illustrate limits on the ability to scavenge radicals, the relative importance of recombination and addition, and the key role of H-atom removal from retrograde intermediates.

MODELING CONSIDERATIONS AND PROCEDURES

Chemical Constituents. We chose the addition of stabilized radicals, as indicated in Scheme 1 above, as the major retrograde reaction type on which to focus, not because we believe it to necessarily be always the most important class of retrograde reaction, but as a highly reversible reaction, its outcome is quite sensitive to changing hydrogen-transfer conditions. However, since for completeness the model necessarily incorporates the possibility of recombination of resonance stabilized radicals, that route to retrograde products is also examined. Retrograde reaction by recombination of course also depends on H-transfer to "lock in" a stable product, since otherwise the weak bond formed by recombination will not represent a permanent retrograde linkage.

The mechanistic numerical model we have used incorporates a single surrogate "coal" structure [1,2-(1,1'-dinaphthyl)ethane] in a reaction medium consisting of aromatic/hydroaromatic mixture (phenanthrene/dihydrophenanthrene) of various compositions, with and without H₂ overpressure. This four starting-component reaction system provides for both weak-bond- and strong-bond scission, H-transfer by H-atom abstraction, free H-atom addition, reverse radical-disproportionation, and RHT, retrograde reaction by radical addition, radical recombination, and radical displacement. When limited to only the more important reactions, including virtually all of the reverse reactions, this provides a set of more than 40 species and 150 reactions. Thus the model is very detailed in that it incorporates all relevant fundamental chemical reactions (non-ionic) of essentially all species, both closed shell and free radical, in the reaction system. Because of this mechanistic detail, the model, of necessity, is very simple in that it includes only a very limited set of starting structures. To limit the complexity, we have confined the model to a pure hydrocarbon system, though the same general considerations will also apply to systems containing phenolics, where the presence of the -OH groups will in all likelihood further promote radical addition (as well as promoting attack of electrophilic fragments and the subsequent loss of hydrogen as a proton).

Mechanistic Considerations. The model is homogeneous; it consists of relatively low-molecular-weight species assumed to be miscible in all proportions. We have made the simplifying assumptions that the system is free of concentration gradients and requires no mass- or heat-transport.* The activity of H_2 in solution is taken to equal that provided by presumed equilibrium with the gas-phase H_2 pressure.

We emphasize that this model was *not* intended in any way to actually simulate the conversion of a real coal, or even, in the present case, to match exactly the experimental retrograde behavior of model systems, but to provide a general illustration of how chemical factors influence certain classes of retrograde reactions under different circumstances. However, because the strength of the weak central bond in 1,2-dinaphthylethane (55 kcal/mol) leads to a 400°C-half-life of about 12 minutes at 400°C, it was previously chosen by other researchers⁹ as a prototypical linkage type that would give coal linkages lifetimes similar to those observed for actual coals during liquefaction, *assuming* the dominant bond cleavage reaction is weak-bond scission. We subsequently subjected a polymeric version of 1,2-dinaphthylethane to donor solvent liquefaction conditions, and observed a product mixture that strikingly revealed some of the shortcomings of the then-accepted weak-bond scission picture of coal liquefaction.¹⁰ As it happens, the numerical modeling results presented here reproduce some of the experimental observations on bond scission, notwithstanding the fact that nothing has been done to force such a correspondence, except to use the best available experimental or estimated rate parameters for each of the individual reactions included in the numerical model. We therefore expect the model to provide valid illustrations, in general terms, of the relative importance of retrograde reaction types under various circumstances.**

As reflected by the total number of reactions, the scheme that follows from even the limited set of starting structures used here appears rather complex, but is based on relatively few reaction types. These reaction types and the products in which they result are shown below in Scheme 2. In the figures that follow, we generally have grouped together all of a common product that follows from several different examples of a given reaction type, and have identified them by a generic heading, rather than individual acronyms used in the integration program.

Scheme 1. Categories of Bond Cleavage and Bond Formation

"Strong-bond cleavage-1"

This category includes all H-atom displacements, or hydrogenolyses, from 1,2-dinaphthylethane (producing naphthalene and ethylnaphthalene), from all sources of H-atoms: free $H\cdot$, RRD, and RHT, coming from either solvent or substrate species.

"Strong bond cleavage-2"

This category also generates ethylnaphthalene, but results instead from displacement (i.e., addition-elimination) by radical species other than H-atom. "Strong-bond cleavage-2" is not a *net* cleavage, in that whenever the displacing radical is a naphthylmethyl radical, one aryl-aryl coupling is simply being traded for another.

"True retrograde product"

In the present work, dinaphthylmethane is the dominant coupling product that, as indicated above, is companion to the cleavage product generated in strong-bond cleavage-2. This coupling product is formed from attack of a naphthylmethyl radical on the starting substrate 1,2-dinaphthylethane, or on the other products naphthylmethane or naphthyl ethane. It is also formed in a "net" retrograde reaction by addition of naphthylmethyl radical to naphthalene, followed by successful removal of the ipso hydrogen from the initial adduct. The term "true retrograde product" is used here because the bond is about 87 kcal/mol, with a homolytic half-life of more than 10 years even at 500°C.

"Weak bond cleavage"

The "weak-bond cleavage" product is of course the naphthylmethane that results from scavenging of the naphthylmethyl radicals that are generated by homolysis of the weak (ca. 55 kcal/mol) central bond in dinaphthylethane.

* Limits on miscibility are of course very important in retrograde reactions, as evidenced by the importance of micelle formation during coke formation in heavy-oil upgrading. However, covalent bond formation is both a *cause* of, and a *result* of, phase separation. Therefore it is probably not possible to find a simple *partisan* answer to the question of which of these most controls coke formation and other retrograde processes.

** Since this model was originally used with a more limited set of reactions to address the competition in cleavage processes between H-transfer by free H-atoms, the reverse of radical-disproportionation (RRD), and radical hydrogen-transfer (RHT), and since the outcome of such attempts at deconvolution of parallel, competing H-transfer processes is still a matter of dispute, it is reasonable to ask whether that dispute should cast doubt on the illustrations and conclusions provided below. The answer to this question is no. Just as the functional form of overall cleavage dependence does not allow one to easily assign exact proportions of the transferred H to free $H\cdot$, RRD, and RHT, when they are in competition, so also any error that may exist in the assigned parameters for RHT will not result in any gross miss-statement of bond formation outcomes that we are addressing here.

"Recombination product"

The "recombination product" is simply the dinaphthylmethane that results from recombination of the initial weak-bond scission product, naphthylmethyl radical. In reality it is indistinguishable from the starting material itself, but in the numerical integration simulations is distinguished by nomenclature from the original molecules of the starting material. The recombination product undergoes all of the reactions that the original starting material does. Since this recombination product is itself just as fragile as the starting material, in the area graphs that follow, the amount of the recombination product that survives is so small that it cannot be seen on the scale of the figures.

"Stilbene product"

The fragility of the recombination product of course does not apply to the "stilbene product," which is the naphthalene analog of stilbene resulting from loss by various processes of 2(H) from either the original dinaphthylethane substrate or the recombination product that comes from the reversal of the weak-bond cleavage. The central double bond of this stilbene analog is very strong, and represents one of the ways that weakly bonded recombination products can be converted to more refractory retrograde products.*

Integration Procedure. The conversion simulations using this model were performed on a VAX 11/750 computer using a numerical integration routine based on the Gear algorithm. Some of the results are shown below using area graphs to depict the evolution of various products as a function of time, or bar graphs to show product distributions at a fixed time for different starting compositions. The time-steps used in the integration were very much smaller than the time steps output by the program and used to construct the area graphs shown here.

RESULTS AND DISCUSSION

Figure 1 shows the evolution of the computed product distribution for the "bibenzyl" starting material in a system of minimal H-donor content. There is of course rapid loss of substrate, but not all to desired products: about 2/3 of the mass after 2 hours, consists of uncleaved or retrograde products. The recombination product itself is not visible on the scale of the figure: it has either rehomolyzed, or lost 2(H) to form the "stilbene" product. The weak-bond cleavage product is substantial, but accounts for slightly less than 15% of the mass of starting material. The two strong-bond cleavage products (displacement by H• and by R•) are almost as prominent as the weak-bond cleavage product, even though the original donor content of the system was quite low (ca. 15 m% of substrate). In an actual coal, the stilbene retrograde product would not persist, owing to the thermodynamic driving force for unsaturation to be grouped in aromatic systems.

For comparison, Figure 2 shows the effects of added H₂ at 400°C. Strong-bond cleavage product 1 (displacement by free H• and solvent-mediated H•) has increased about five-fold, and is now more important than strong-bond cleavage product 2, which has actually declined. Weak-bond cleavage product has increased substantially, and the stilbene product has declined. Interestingly, the "true retrograde" product (dinaphthylmethane from H• and R• displacement reactions) has increased substantially, so that the sum of stilbene and true retrograde product is essentially unchanged by the addition of H₂. The important observation here is that while the presence of 1000 psi H₂ has markedly increased the strong-bond cleavage that results from displacement by H•, there has been essentially *no* suppression of the true retrograde products. That is, H₂ in a purely thermal system clearly does indeed react with resonance stabilized radicals in the system (as Vernon showed experimentally some years ago¹¹) to substantially increase strong-bond cleavage, but the "scavenging" aspect of this reaction has essentially no effect retrograde reaction by addition-elimination reactions of resonance-stabilized radicals. Clearly, there is a large increase in H-atom activity, but no significant fractional decrease in resonance-stabilized radical concentration.

The result of the inability to fully scavenge stabilized radicals, is that at long reaction times such radicals will continue to form retrograde products through addition-elimination reactions, particularly in the present case, through displacement of methyl radical from the weak-bond cleavage product, methyl naphthalene. The consequence of this factor is that long reaction times or higher temperatures tend to be beneficial *only* in the presence of H₂ or a H-donor, as illustrated in Figure 3, which shows the sum of cleavage products with and without H₂ at several different sets time/temperature conditions.

Comparisons of the effectiveness of two different H-donors, dihydrophenanthrene and 9,10-dihydroanthracene leads to additional interesting observations of short-term vs long-term behavior. At short reaction times, where there is a large generation of fragment radicals from homolysis of the weakly bonded coal surrogate, modeling indicates that dihydroanthracene, as the better scavenger, indeed maximizes the yield of capped fragment radicals, and minimizes the yield of recombination products and radical displacement retrograde products.

* Although the double bond in stilbene is "very strong," this refers to the enthalpy input required to break the double bond directly, forming two naphthylcarbene moieties. As a non-aromatic double bond, there will be a great tendency for any stilbene-like double bond to undergo rearrangements such that all unsaturation comes to reside in aromatic structures. Such "tertiary" reactions are not included in the present model.

However, at long reaction times, the "better" scavenger actually *enhances* the yield of retrograde product. This is because, at longer reaction times when the burst of radicals from the decomposing coal has largely died away, the principal source of fragment radicals is abstraction of hydrogen atoms from the previously capped fragment species by the pool of scavenger radicals generated by the scavenger itself. Thus, the model appears to further explain a trend which has been noted previously, namely that coal conversion tends to be better in the presence of hydroaromatics that are *not* the best scavengers, and is evidently better because these latter scavengers tend to be better hydrogenolysis reagents, while being poorer radical initiators.

The origin of the effects of H_2 can be seen more clearly with the help of Figures 4 and 5. Figure 4 shows that hydrogen pressure (at a somewhat higher temperature where they occur more strongly in these uncatalyzed systems) serves, as expected, to partially maintain the H-donor (dihydrophenanthrene) level in the reaction medium. Figure 5 shows that the percent increase in hydrogenolysis rates is much higher than the percent increase in donor concentration. In other words, the total new H-atom activity resulting from the presence of H_2 is much larger than the increase in H-donor. Thus, in the short term, the steady-state concentration of $H\cdot$ and $ArH\cdot$ has increased more than the steady-state concentration of ArH_2 .

Returning to the observation that scavenging increases hydrogenolysis, but does not, through its "scavenging" action, decrease the rate of formation of retrograde products, Figure 6 shows the computed ratios of scavenger concentration ($[H_2]/[PhenH_2]$), the ratios of scavenging by these two components, and the percent of recombination that occurs (for $H_2 = 0$ and 1000 psi.) for the naphthylmethyl radicals produced by homolysis of the original weak bond. Clearly, not only is the scavenging ability of H_2 inconsequential, compared even to a small concentration of H-donor (as expected because of their greatly different bond strengths), but the ability of H_2 to limit recombination is barely observable, even at 600°C.

Perhaps more surprising are the computed effects of H_2 or added H-donor on stabilization of the "true retrograde" intermediate (the removal of H-atom from the ipso-substituted radical addition intermediate). Figure 7 shows the instantaneous net rate of stabilization at by each of the major H-transfer processes for three different starting conditions: no added H_2 and 0.1 M $PhenH_2$, 1000 psi H_2 and 0.1 M $Phen_2$, and 0 H_2 and 0.5 M $PhenH_2$. In all three cases, H-removal by radical disproportionation with 9-hydrophenanthryl-, naphthylmethyl-, and dinaphthylethyl-ethyl radicals gives a net formation rate for the dinaphthylmethane retrograde product. Either added H_2 or increased starting H-donor actually serve to *increase* the net rate of formation of the true retrograde product by radical addition and H-atom removal in disproportionation processes. This increased formation by the first three categories is more than compensated for by large negative rates of retrograde product formation by free H-atoms and RHT. That is, free H-atoms transfer much more H to dinaphthylmethane than they take away from ipso-H-substituted dinaphthylmethane, and are net destroyers, not net formers, of retrograde product. Thus, addition of H_2 or H-donor does *not* actually prevent retrograde product formation (it in fact increases it), but serves to cleave such products more effectively *after* they are formed!

This finding makes somewhat moot earlier discussions of whether coal linkages are dominated by strong or by weak bonds: Even if coal starts out with many of most of its linkages connected by weak bonds, there will very shortly be many strong bonds formed, whose subsequent cleavage will likely be critical to the ultimate conversion yield from the coal. The findings here also serve to articulate and explain our earlier experimental observations with a polymeric version of the dinaphthylethane substrate¹⁰ we have computationally studied here: even when a substrate has a weak bond between every pair of aromatic clusters, as in 1,2-diarylethane linkages, there will be much cleavage not only of the weak bond between the two aliphatic carbons in the linkage but also of the strong aryl-alkyl bonds at either side. This cleavage will result not only from hydrogenolysis, but also from displacement by carbon-centered radicals to form retrograde products with new, strong linkages that can only be cleaved by hydrogenolysis. Thus in many cases, coal liquefaction may be as much about cleaving retrograde bonds as it is about cleaving linkages that are original to the coal structure.

SUMMARY AND CONCLUSIONS

In some cases the results presented here are a quantitative illustration of what can be qualitatively anticipated from thermochemical considerations, while in other cases the results were qualitatively surprising. The major conclusions and points to be emphasized from the modeling results are the following.

- All scavengers that operate via a radical capping process have a dual role—they also act as initiators.
- Higher temperatures provide more reaction, but if there is not something to mitigate retrograde reactions, higher temperatures tend to cause the retrograde reactions to increase as fast or faster than the bond-cleavage reactions. This modeling result appears to be completely in accord with the common observation that increasing liquefaction temperature beyond about 440°C tends to lower coal conversion, and similarly in pyrolysis, that higher heating rates tend

to decrease char yields, *primarily* when the higher heating rates are associated with more rapid removal of volatile products.

- The presence of H_2 does *not* inhibit retrograde product formation as much as it hydrogenolyzes retrograde products faster after they are formed. In fact, modeling indicates that H_2 can, at certain reactions times, *increase* the yield of retrograde products.
- The impact of added H_2 on hydrogenolysis (at least in the short term) does *not* come primarily through its maintenance of a useful hydroaromatic content, as has often been postulated in coal liquefaction, but through a higher steady state concentration of $H\cdot$ that is established long before the hydroaromatic content can be substantially affected.

ACKNOWLEDGMENT

The authors wish to acknowledge the Support of the U.S. Department of Energy in various projects whose goals have included an improved understanding of the chemistry responsible for coal liquefaction.

REFERENCES

1. McMillen, D. F.; Malhotra, R.; Nigenda, S. E. *Fuel*, **1989**, *68*, 380.
1. Neavel, R. C. *Fuel*, **1976**, *55*, 237.
2. Fong, W. S.; Peters, W. A.; Howard, J. B. *Fuel*, **1986**, *65*, 251.
3. Savage, P. E.; Klein, M. T.; Kukes, S. G. *Fuel*, **1988**, *2*, 619.
4. Khorasheh, F.; Rangwala, H. A.; Gray, M. R.; Dalla Lana, I. G. *Energy & Fuels*, **1989**, *3*, 716.
5. McMillen, D. F.; Malhotra, R.; Chang, S.-J.; Ogier, W. C.; Nigenda, S. E.; Fleming, R. H. *Fuel*, **1987**, *66*, 1611.
6. Malhotra, R.; McMillen, D. F. *Energy & Fuels*, **1993**, *7*, 227.
7. McMillen, D. F.; Malhotra, R. *Am. Chem. Soc. Div Fuel Chem. Preprints* **1992**, *37*(1), 385.
8. Malhotra, R.; McMillen, D. F. *Energy & Fuels*, **1990**, *4*, 184.
9. Squire, K. R.; Solomon, P. R.; Carangelo, R. M.; DiTaranto, M. B. *Fuel* **1986**, *65*, 833.
10. Malhotra, R.; McMillen, D. F.; Tse, D. S.; StJohn, G. A. *Energy & Fuels* **1989**, *3*, 465.
11. Vernon, L. W. *Fuel*, **1980**, *59*, 102.

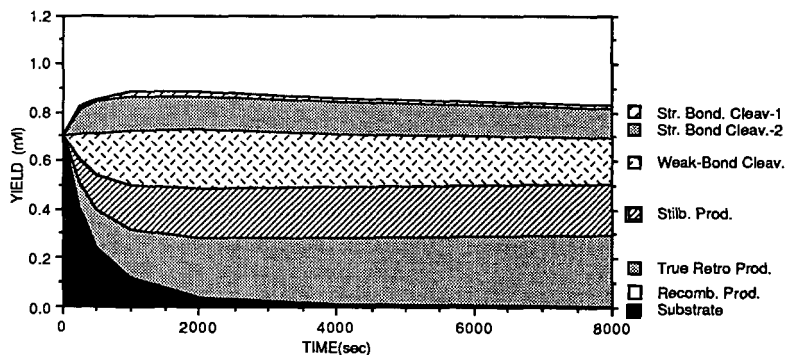


Figure 1. Computed product distribution at 400°C with minimal H-donor content. $[PhenH_2] = 0.1M$, $P(H_2) = 0$.

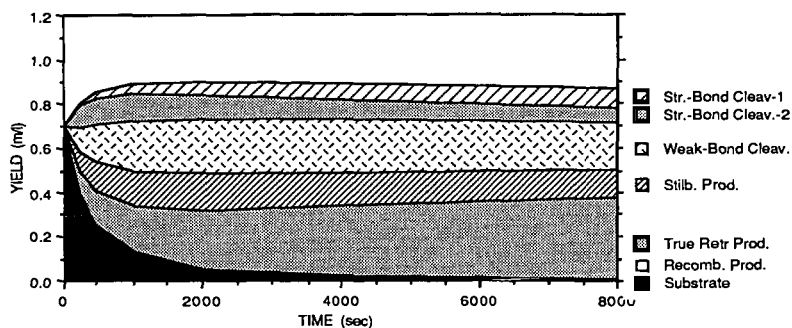


Figure 2. Computed product distribution at 400°C with minimal donor content but added H₂. [PhenH₂] = 0.1M, P (H₂) = 1000 psi.

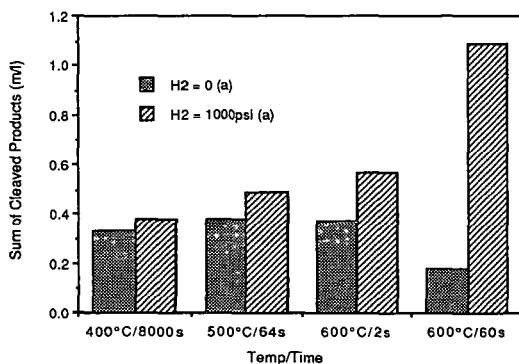


Figure 3. Sum of cleavage products for different time and temperature conditions. [PhenH₂] = 0.1M.

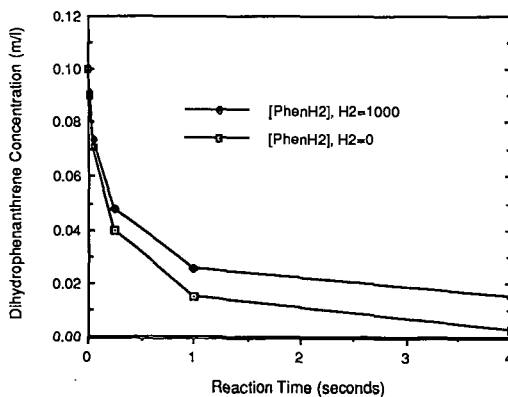


Figure 4. Computed H-donor concentration at 500°C as a function of time with and without 1000 psi added H₂. [PhenH₂] = 0.1M.

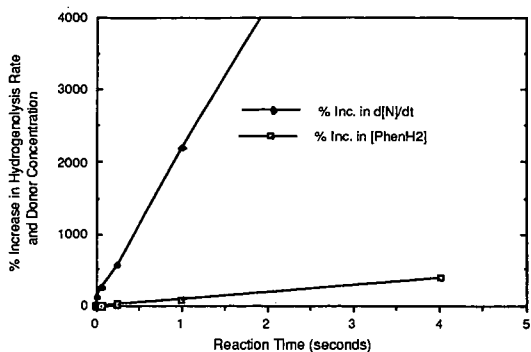


Figure 5. Comparison of percent increase in hydrogenolysis rate and donor concentration as a result of 1000 psi added H_2 . $500^\circ C$; $[PhenH_2] = 0.1M$.

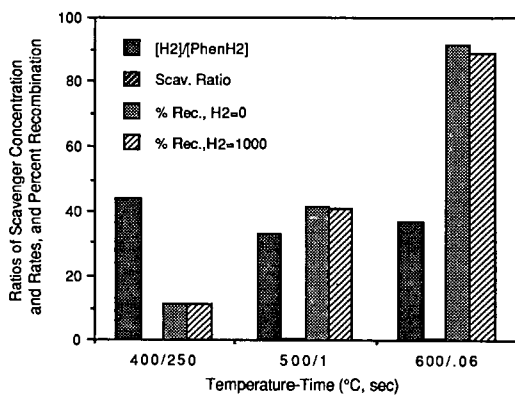


Figure 6. Computed ratios of scavenger concentration, scavenging rates for H_2 and H-donor, and the percent recombination of homolysis fragments with and without 1000 psi H_2 . $[PhenH_2] = 0.1 M$.

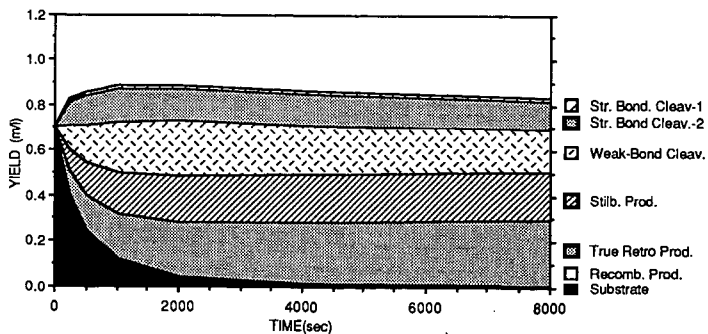


Figure 7. Computed net rates of H-removal from diarylmethane retrograde intermediate for various H-tran

PYROLYSIS KINETICS AND MECHANISMS FOR POLYCYCLIC PERHYDROARENES BEARING LONG N-ALKYL CHAINS

Phillip E. Savage
University of Michigan
Department of Chemical Engineering
Ann Arbor, MI 48109-2136

keywords: hydrocarbons, pyrolysis, mechanisms

ABSTRACT

A set of long-chain polycyclic n-alkylperhydroarenes was pyrolyzed neat at temperatures between 400 and 475°C. The disappearance of these compounds typically followed first-order kinetics. The pyrolysis of a perhydroarene with an n-carbon containing n-alkyl chain generated numerous primary products. The primary products with the highest initial selectivities were generally the perhydroarene plus an α -olefin with n carbon atoms, the methylene perhydroarene plus an n-alkane with n-1 carbon atoms, and a polycyclic mono-olefin plus an n-alkane with n carbon atoms. The kinetics data from this investigation were used to test a structure-reactivity correlation in the literature for the pyrolysis of saturated cyclic compounds and to update it so that it becomes consistent with the kinetics of long-chain n-alkylperhydroarenes.

INTRODUCTION

Naphthenic (perhydroarene) moieties decorated with n-alkyl substituents exist in heavy hydrocarbon resources such as coal, heavy oils, and asphaltenes. Additionally, these types of chemical structures are present in the endothermic jet fuels being developed for the next generation of high-performance jet aircraft. Given the presence of these structures in these materials, which experience elevated temperatures of around 400°C during their processing or use, it is clear that information about the thermal decomposition of saturated cyclic compounds with alkyl substituents at temperatures around 400°C would be useful.

Until very recently, the literature was limited to kinetics data at a single temperature (700K) for 28 saturated cyclic compounds (six were polycyclic), most of which bore short chains (Fabuss et al., 1964) and more extensive kinetics data and mechanistic information for a single one-ring compound, tridecylcyclohexane (Savage and Klein, 1988; Mushrush and Hazlett, 1984). Indeed, prior to the publication of our group's recent work (Humburg and Savage, 1996; Mizan et al., 1997), the literature provided no information about the pyrolysis kinetics, pathways, or mechanisms for any polycyclic perhydroarenes bearing a long (> C₄) n-alkyl chain. This lack of information about the behavior of polycyclic n-alkylperhydroarenes and previous results showing that the pyrolysis of other polycyclic hydrocarbons led to products that differed from those of their single ring analogs (Savage et al., 1989; Virk et al., 1979) motivated the investigations with n-alkyl-substituted polycyclic perhydroarenes.

EXPERIMENTAL

The model compounds were obtained from the Thermodynamics Research Center at Texas A & M University, Pfaltz and Bauer, TCI Organics, and Wiley Organics. All chemicals were used as received. All pyrolyses were conducted neat in batch microreactors fashioned from a nominal 1/4 inch stainless steel Swagelok port connector and two caps. We loaded between 10 and 40 mg of the reactant and about 10-15 mg of biphenyl (an internal standard) into each reactor, and these quantities were weighed to within ± 0.1 mg. The loaded reactors were placed in a fluidized sand bath maintained at the desired pyrolysis temperature. When the desired batch holding time had elapsed, the reactors were removed from the sand bath, and the reaction was quenched by immersing the reactors in water at room temperature. The reactors were then opened and their contents retrieved by repeated additions of methylene chloride. The reaction products were identified and quantified via capillary-column gas chromatography with either a mass spectrometric or flame-ionization detector. Product molar yields, calculated as the number of moles of product formed divided by the number of moles of reactant initially loaded into the reactor, were obtained from the chromatographic analysis using experimentally determined detector response factors. Additional details about the experimental methods appear in the literature (Humburg and Savage, 1996; Mizan et al., 1997).

RESULTS AND DISCUSSION

This section summarizes the experimental results obtained from n-alkylperhydroarene pyrolysis. These results were used to determine the reaction rate law and to develop the reaction network for neat pyrolysis.

Pyrolysis Kinetics

The objectives of the kinetics analysis were to determine the global reaction order (m) and Arrhenius parameters (A, E) for the power-law rate expression in Equation 1 that best describes n-alkylperhydroarene disappearance.

$$\text{rate} = kC^m = A \exp\left(\frac{-E}{RT}\right) C^m \quad (1)$$

The parameters in the rate law were determined by examining the results of numerous experiments at different temperatures, holding times, and initial concentrations. First order kinetics

gave an adequate description of the kinetics for each compound examined in detail. Our previous reports (Humburg and Savage, 1996; Mizan et al., 1997) provide the experimental data and the details of the kinetics analysis for 9-dodecylperhydroanthracene (DDPA) and 1-undecylperhydronaphthalene (UPN). Additionally, Table 1 provides new kinetics data for the pyrolysis of nine other n-alkylperhydroarenes.

Structure-Reactivity Relations

The reaction kinetics for compounds in a single family can often be correlated using a structure-based reactivity index. Such structure-reactivity correlations are useful in computer models of the reactions of complex materials such as fossil fuels and for predicting the reactivity of compounds that have not been investigated experimentally. One needs a large set of reliable kinetics data to develop structure-reactivity correlations. Fabuss et al. (1964) provide data for the pyrolysis kinetics at 800°F (700K) of 28 saturated cyclic compounds that were either unsubstituted or bore short ($\leq C_4$) alkyl substituents. They correlated the disappearance kinetics using a "characterization number", n , as the reactivity index. The Fabuss et al. (1964) correlation is

$$k \text{ (hr}^{-1}\text{)} = 0.044 - 0.0114n + 0.0008n^2 \quad (2)$$

The characterization number can be determined by inspection of the structure of the compound, and it is based on group-additivity. The characterization number for decylcyclohexane, for example, is 49 (12 for the cyclohexane ring, plus 4 for each of the nine CH_2 group in the alkyl chain, plus 2 for the terminal methyl group in the chain, and minus 1 for the one C-H bond in the ring structure replaced by an alkyl substituent). We note that the equation above shows 0.0114 as the coefficient for the second term, whereas the equation that appears in Fabuss et al. shows 0.114. We believe the equation in Fabuss et al. contains a typographical error because using 0.114 in Equation 2 leads to negative values for the rate constants.

In this report, we expand the existing database by providing new kinetics data (see Table 1) for the pyrolysis of long-chain and polycyclic perhydroarenes at 427°C. We can use the data in Table 1, along with that previously reported for tridecylcyclohexane, TDC, (Savage and Klein, 1988; Mushrush and Hazlett, 1984), undecylperhydronaphthalene, UPN (Mizan et al., 1997), and dodecylperhydroanthracene, DDPA, (Humburg and Savage, 1996) to assess the predictive ability of the Fabuss et al. (1964) structure-reactivity relation.

Figure 1 shows the correlation of Fabuss et al. along with our experimental data for 11 different long-chain n-alkylperhydroarenes. It is clear that the correlation fails to predict the kinetics for these compounds. Fabuss et al., to their credit, anticipated that the performance of their correlation would deteriorate as the length of the alkyl substituent exceeded four carbon atoms. Indeed, none of the compounds they pyrolyzed had characterization numbers that exceeded 40, and Figure 1 shows that the correlation performs poorly when extrapolated to these higher characterization numbers.

We next combined the kinetics data provided by Fabuss et al. with our more recent data for long-chain compounds to develop a new structure-reactivity relation that uses the characterization number as the sole correlating parameter. We fit the experimental kinetics data in Fabuss et al. along with our data for long-chain perhydroarenes to a quadratic equation of the form originally used by Fabuss et al. (Equation 2). The results from the non-linear regression showed that the uncertainty in the second parameter exceeded the value of the parameter itself. In fact, a value of zero was contained within the 95% confidence interval for this parameter. Consequently, we repeated the non-linear regression of the kinetics data, but with the statistically insignificant term set equal to zero. The resulting correlation is

$$k \text{ (hr}^{-1}\text{)} = -0.041 + 0.00035n^2 \quad (3)$$

The level of agreement between the new correlation and the experimental data is apparent upon inspection of Figure 2. We expect that the correlation of Equation 3 will provide reasonable estimates of the rate constants for long-chain alkylperhydroarenes. The only compound for which the correlation performs poorly is decylperhydropyrene. The reason for this failure is not clear, and additional experiments with other polycyclic compounds are required to address this issue.

The structure-reactivity relation of Fabuss et al. qualitatively incorporates some fundamental aspects of hydrocarbon pyrolysis kinetics in their characterization number. For example, a CH_2 group adds more to the characterization number than does a CH_3 group, which is consistent with secondary C-H bonds being weaker and hence more reactive than primary C-H bonds. This correlation is empirical, however, because the relative contributions of the different structural groups were determined by fitting data rather than by building squarely upon the foundation of the governing reaction mechanism. The mechanism for the pyrolysis of saturated cyclic hydrocarbons is reasonably well established, and closed-form analytical rate expressions are available (Savage, 1990). A mechanism-based structure-reactivity relation has already appeared for n-alkylbenzenes (Savage and Korotney, 1990). Thus, the stage is now set for progress toward a mechanism-based structure-reactivity relation for long-chain n-alkylperhydroarenes.

Pyrolysis Products, Network, and Mechanism

The neat pyrolysis of n-alkylperhydroarenes led to numerous reaction products, and the product spectrum comprised n-alkanes, 1-alkenes, perhydroarenes substituted with alkyl or alkenyl chains, and partially hydrogenated arenes. Our work with these compounds showed that a perhydroarene with an n-carbon-containing alkyl substituent pyrolyzed to form three pairs of major

primary products and numerous minor primary products. This network is illustrated in Figure 3 for UPN. The major primary product pairs are the perhydroarene plus a C_n olefin (decalin plus undecene for UPN), the methylene perhydroarene plus a C_{n-1} alkane (methylene decalin plus decane for UPN), and a cyclic olefin plus a C_n alkane (octahydronaphthalene plus undecane for UPN).

Although the identities of the three major primary product pairs are analogous for the different n-alkylperhydroarenes, the relative abundances of these products differ for the different compounds. The ring-containing products from the neat pyrolysis of the 2- and the 3-ring compounds were, in order of decreasing selectivity, the cyclic olefin, the methylene perhydroarene, and the perhydroarene. The pyrolysis of DPP, a 4-ring compound, on the other hand, led to the perhydroarene being the most abundant product, followed by the methylene perhydroarene and the cyclic olefin. The product spectrum from DPP more closely resembled that of an alkylcyclohexane, wherein the major primary pyrolysis products are cyclohexane, methylene cyclohexane, and lesser amounts of cyclohexene and methylcyclohexane. This comparison of the major primary products from neat pyrolysis of 1-, 2-, 3-, and 4-ring n-alkylperhydroarenes shows that an analogous set of three major product pairs forms in all cases. The compound-to-compound differences involve only the relative abundance of these different product pairs. This similarity in the reaction network suggests a corresponding similarity in the underlying reaction mechanism. Thus, the free-radical reaction steps advanced previously for 1-, 2-, and 3-ring alkylperhydroarenes (Savage and Klein, 1988; Humburg and Savage, 1996; Mizan et al., 1997) appear to be general.

SUMMARY AND CONCLUSIONS

This paper provides a summary of results from the pyrolysis of long-chain polycyclic n-alkylperhydroarenes. The neat pyrolysis typically follows first-order kinetics. The reaction network for n-alkylperhydroarenes includes parallel primary reactions to form an α -olefin plus the perhydroarene, an n-alkane plus the methylene perhydroarene, and an n-alkane plus a polycyclic mono-olefin. The numerous minor primary products were other n-alkanes, α -olefins, alkylperhydroarenes, and alkenylperhydroarenes. The arene and methylarene appeared as products at the more severe reaction conditions.

Kinetics data for the pyrolysis of n-alkylperhydroarenes revealed that the correlation of Fabuss et al. (1964) cannot be extrapolated to predict the reactivity of long-chain and polycyclic perhydroarenes. Equation 3 provides a new correlation, based on the Fabuss et al. characterization number, that is consistent with both their data and that reported herein. This correlation can be used to predict the kinetics of a wide variety of saturated cyclic compounds.

REFERENCES

- Fabuss, B. M.; Kafesjian, R.; Smith, J. O.; Satterfield, C. N. Thermal Decomposition Rates of Saturated Cyclic Hydrocarbons. *Ind. Eng. Chem. Proc. Des. Dev.* **1964**, *3*, 248.
- Humburg, R. E.; Savage, P. E. Pyrolysis of Polycyclic Perhydroarenes 1. 9-n-Dodecylperhydroanthracene. *Ind. Eng. Chem. Res.* **1996**, *35*, 2096.
- Mizan, T. I.; Savage, P. E.; Perry, B. Pyrolysis of Polycyclic Perhydroarenes 1. 1-n-Undecylperhydronaphthalene. *Energy Fuels* **1997**, *11*, in press.
- Mushrush, G. W.; Hazlett, R. N. Pyrolysis of Organic Compounds Containing Long Unbranched Alkyl Groups. *Ind. Eng. Chem. Fundam.* **1984**, *23*, 288.
- Savage, P. E. Pyrolysis of a Binary Mixture of Complex Hydrocarbons: Reaction Modeling. *Chem. Eng. Sci.* **1990**, *45*, 859.
- Savage, P. E.; Jacobs, G. E.; Javanmardian, M. Autocatalysis and Aryl-Alkyl Bond Cleavage in 1-Dodecylpyrene Pyrolysis. *Ind. Eng. Chem. Res.* **1989**, *28*, 645.
- Savage, P. E.; Klein, M. T. Asphaltene Reaction Pathways: 4. Pyrolysis of Tridecylcyclohexane and 2-Ethyltetralin. *Ind. Eng. Chem. Res.*, **1988**, *27*, 1348.
- Savage, P. E.; Klein, M. T. Asphaltene Reaction Pathways: 5. Chemical and Mathematical Modeling. *Chem. Eng. Sci.* **1989**, *44*, 393.
- Savage, P. E.; Korotney, D. J. Pyrolysis Kinetics for Long-Chain n-Alkylbenzenes: Experimental and Mechanistic Modeling Results. *Ind. Eng. Chem. Res.* **1990**, *29*, 499.
- Virk, P. S.; Korosi, A.; Woebcke, H. N. Pyrolysis of Unsubstituted Mono-, Di-, and Tricycloalkanes. In ACS Advances in Chemistry Series; Oblad, A. G., Davis, H. G., Eddinger, R. T., Eds.; American Chemical Society: Washington, DC, 1979; Vol. 183, p. 67.

Table 1: Rate Constants (in sec^{-1}) for Neat Pyrolysis of Long-Chain n-Alkyl naphthenes at 427°C

Compound	$k \times 10^4$	95% C.I.
2-Octylperhydrochrysene (OPC)	2.97	1.64
9-Dodecylperhydrophenanthrene (9DPPh)	4.22	0.38
1-Dodecylperhydrophenanthrene (1DPPh)	3.73	0.78
1-Decylperhydropyrene (DPP)	1.28	0.56
Tridecylcyclohexane (TDC)	2.90	0.86
Dodecylcyclohexane (DDC)	2.75	0.70
Decylcyclohexane (DC)	2.57	0.96
Heptylcyclohexane (HPC)	1.63	0.30
Hexylcyclohexane (HXC)	1.01	0.49

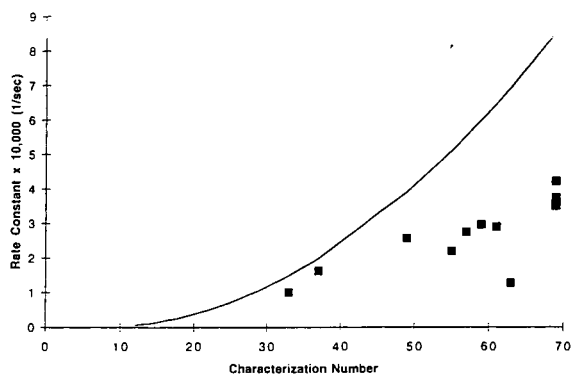


Figure 1: Structure-reactivity relation of Fabuss et al. (solid curve) and experimental data for long-chain n-alkylperhydroarenes (discrete points).

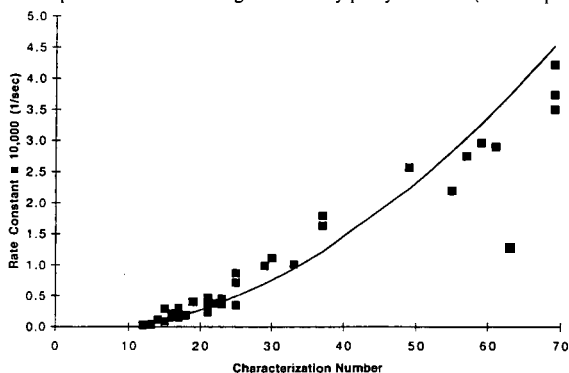


Figure 2: Updated structure-reactivity relation for saturated cyclic compounds.

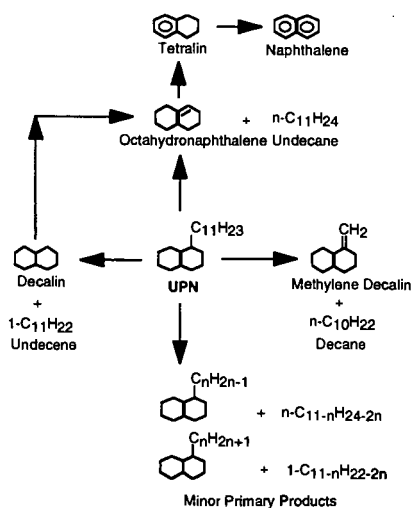


Figure 3: General reaction network for alkylperhydroarene neat pyrolysis.

RAPID CLEAVAGE OF DIARYL ETHERS IN FUEL PROCESSING INDUCED BY *ortho*-BENZYLIC RADICAL FORMATION: KINETICS OF REARRANGEMENT OF THE 2-PHENOXYBENZYL RADICAL

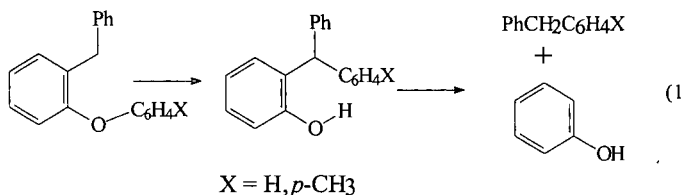
James A. Franz, John C. Linehan, Anne E. Crump, Lauren Kaune, Mikhail S. Alnajjar, Donald M. Camaioni, and Tom Autrey

Pacific Northwest National Laboratory
P.O. Box 999
Richland, WA 99352

Keywords: Kinetics, Radical Rearrangements, Aryl Ether Cleavage

INTRODUCTION

Recently we reported the cleavage of the aryl ether bond of 2-benzylidiphenyl ether in reactions with an iron sulfide nanocatalyst in dihydrophenanthrene at 400 °C (1). In that work, the rearrangement of 2-benzylidiphenylether to 2-(diphenylmethyl)phenol and the subsequent rapid scission of 2-diphenylmethylphenol to give diphenylmethane and phenol (eq. 1, X = H) was found to occur not



by a direct ether C-O bond scission pathway, but rather by stepwise formation of a benzylic radical followed by phenyl migration from oxygen to the carbon radical center (Scheme 1). Substitution of a methyl group on the phenyl ether ring confirmed that diphenylmethane was formed in a rearrangement reaction (eq. 1, X = *p*-CH₃). Thus, alkyl substituents adjacent to aromatic ether linkages provide a pathway for enhanced thermal cleavage of the relatively inert ether C-O bond. Note that the alternate pathway to eq. 1 is cleavage of the benzyl group to form a diphenyl ether. As shown by the first two entries in Table 1, direct benzyl cleavage is the slow, but favored pathway for the 4-benzyl-substituted diphenylethers. To further explore and quantitate this pathway for strong bond scission in fuels processing, we have determined rate constants for the rearrangement of the 2-phenoxybenzyl radical to the 2-benzylphenoxy radical. We present global rate constants for conversion of substituted diphenyl ethers by nanophase FeS catalysts that illustrate that *ortho* alkyl substitution of a diaryl ether leads to an enhanced rate of scission of the aryl ether bond under hydrocarbon processing conditions.

EXPERIMENTAL

Kinetics of Rearrangement of the 2-Phenoxybenzyl Radical. 2-Phenoxybenzyl radical (2, Scheme 1) was formed either by the reaction of 2-phenoxybenzyl chloride and Bu₃SnH or by the photolysis of ketone 1, Scheme 1, which was prepared by the method of Sasaki and Kitagawa(2). The rearrangement kinetics were performed by photolysis of reagents sealed in quartz tubes in a specially modified GC oven equipped with a quartz photolysis window. The tubes were placed in an aluminum block in the GC oven at reaction temperature through a hole on top of the oven and allowed to equilibrate for 5 minutes prior to photolysis. Solutions containing the ketone 1 (10⁻² M), tributyltin hydride (1 × 10⁻⁴ to 5 × 10⁻³ M), and eicosane (an internal GC standard) in dodecane were made up in an inert atmosphere box. The solutions were syringed in 100 ul portions into 4 mm o.d. quartz tubes. The tubes were placed on a vacuum line and degassed in three freeze-pump-thaw cycles prior to sealing. Analysis by GC of tubes sealed in this manner showed no evidence of reaction during preparation and sealing. The samples were photolyzed, through a quartz window in the GC oven door, with a 150-watt deuterium/mercury lamp. The reactions were run between 190 °C and 270 °C to 20% or less consumption of Bu₃SnH. GC analyses were performed on a J&W Scientific 15-m DB-5 column using a Hewlett-Packard model 5890 GC with FID detection. The rate constants were calculated by computer solution of the integrated rate expression relating unrearranged product (4), rearranged product (5), initial tributyl tin hydride concentration (B₀), and the relative rate $r = k_{re}/k_{abs}$:

$$[4 + 5] = (B_0 + r) \cdot (1 - \exp(-[5]/r)) \quad (2)$$

The relative rate constants (r) were combined with an absolute rate expression for abstraction of hydrogen from Bu_3SnH by benzyl radical (3): $\log(k_{\text{abs}}/\text{M}^{-1}\text{s}^{-1}) = 8.65 - 5.58/\theta$, $\theta = 2.3\text{RT kcal/mol}$, to yield the rearrangement rate constants k_{re} .

Kinetics of Reactions of Diaryl Ethers With FeS Catalysts. Samples of diaryl ethers (15-20 mg) were sealed in glass ampules in the presence of dihydrophenanthrene (100 mg), FeS catalyst precursor (3 mg), and sulfur (3 mg), and heated in a fluidized sand bath at 390°C . Products were analyzed by GC using authentic products. Detailed procedures for FeS/substrate reactions have been published (4-6).

RESULTS AND DISCUSSION

The 1,4-aryl migration of 2-phenoxybenzyl radical, **2**, to form the 2-benzylphenoxy radical, **3**, follows the Arrhenius rate expression $\log(k_{\text{re}}/\text{s}^{-1}) = (10.8 \pm .8) - (20.2 \pm 1.8)/\theta$, $\theta = 2.3 \text{ RT kcal/mol}$. These Arrhenius parameters suggest that the rearrangement occurs efficiently at coal liquefaction temperatures ($k_{\text{re}} = 3 \times 10^4 \text{ s}^{-1}$ at 700K). The controlling factor for this category of rearrangement will be the efficiency of radical formation and the unimolecular lifetime of the radical relative to bimolecular reaction with available hydrogen donors. With efficient radical initiation, such as in the presence of sulfur-derived thiyl radicals, regeneration of benzylic radicals will occur through many cycles. Once the radical has undergone rearrangement, subsequent trapping by available hydrogen donors produces an ortho-hydroxydiphenylmethane, which undergoes rapid unimolecular homolysis (7).

Rate constants for the disappearance of methyl substituted 2- and 4-benzylidiphenylethers (Table 1) reveal that benzyl substitution at the 2-position enhances the rate of "uncatalyzed" ether conversion by a factor of 30 compared to substitution at the 4-position. For the catalyzed cases, the 2-benzyl-substituted diphenyl ether is about 10 times more reactive than the 4-benzyl-substituted diphenyl ether. Table 1 shows that for the cases of 4-benzyl-substituted diphenylmethanes, catalyzed cleavage of the benzyl-aromatic ring C-C bond occurs exclusively, illustrating the regiochemical requirements for C-O cleavage leading to diphenylmethane formation. These results demonstrate a pattern of enhancement of cleavage of diaryl ethers consistent with the participation of the 1,4- oxygen-to-carbon aryl migration reaction.

ACKNOWLEDGMENT

This work was supported by the U. S. Department of Energy, Office of Energy Research, Office of Basic Energy Sciences, Chemical Sciences Division, Process and Techniques Branch. This work was conducted at Pacific Northwest National Laboratory, which is operated by Battelle Memorial Institute for the U. S. DOE under contract DE-AC06-76-RLO 1830. Support for LK was provided through AWU-NW under grant DE-FG06-89ER-75522 from the U. S. Department of Energy.

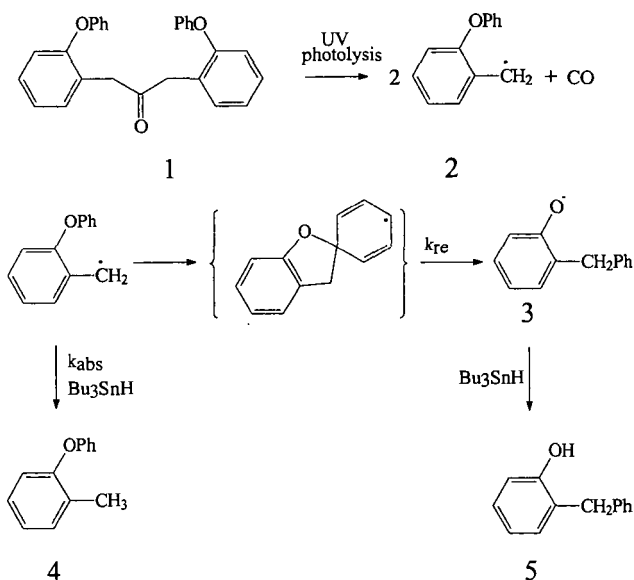
REFERENCES

- (1) Autrey, T.; Linehan, J.C.; Camaioni, D. M.; Powers, T. R.; McMillan, E. F. And Franz, J. A. *Fuel Preprints*, **1995**, 973-977.
- (2) Sasaki, H. And Kitagawa, T. *Chem. Pharm. Bull.* **1983**, *31*, 2868.
- (3) Franz, J.A.; Suleman, N.K.; and Alnajjar, M.S. *J. Org. Chem.* **1986**, *51*, 19-25.
- (4) Autrey, T.; Linehan, J.C.; Camaioni, D.M.; Kaune, L.E.; Watrob, H.M.; and Franz, J.A *Catalysis Today*, **1996** *31*, 105-111.
- (5) Matson, D.W., J.C. Linehan, J.G. Darab, D.C. Camaioni, S.T. Autrey, and E. Lui. **1995**, "New Nanophase Iron-Based Catalysts for Hydrocracking Applications" MRS Symposium Proceedings #368, Synthesis and Properties of Advanced Catalytic Materials, E. Iglesia, P.W. Lednor, D.A. Nagaki, L.T. Thompson, eds. pp.243-248.
- (6) Linehan, J. C.; Matson, D. W.; and Darab, J. G. *Energy & Fuels* **1994**, *56*.
- (7) McMillen, D.F; Ogier, W. C.; and Ross, D. S. *J. Org. Chem.* **1981**, *46*, 3322.

Table I
Rate Constants for the Disappearance of Benzyldiphenyl Ethers
with Iron-Sulfide Catalysts

Substrate ^a DPM/DPE	Catalyst Precursor ^b	Rxn Temp	k (l x 10 ⁴ s ⁻¹)	% Consumed ^c	
(4'Me)-4-BzDPE	none	390°C	0.04 ± .005	3	d
(4'Me)-4-BzDPE	6-line	390°C	0.40 ± .08	25	0.02 ^e
(4'Me)-2-BzDPE	none	390°C	1.3 ± .2	50	70 ^f
(4'Me)-2-BzDPE	6-line	390°C	3.8 ± .3	90	23 ^f

a) DPM = diphenylmethane, DPE = diphenylether, 4-BzDPE = 4-benzyldiphenylether, 2-BzDPE = 2-benzyldiphenylether, (4'Me)-2-BzDPE = 4'-methyl-2-benzyldiphenylether, (4'Me)-4-BzDPE = 4'-methyl-4-diphenylether. b) 6-line = 6-line ferrihydrite, see refs. 4-6. c) Percent consumed in 90 minutes. d) No DPM observed. e) MeDPM/MeDPE. f) 4-methyldiphenyl -methane and 4-methyldiphenylether.



Scheme 1. Photolysis of Ketone 1 provides radical 2, which undergoes irreversible rearrangement, k_{re}, in competition with hydrogen abstraction, k_{abs}, from Bu₃SnH.

CONTRASTING RETROGRESSIVE REARRANGEMENT PATHWAYS DURING THERMOLYSIS OF SILICA-IMMOBILIZED BENZYL PHENYL ETHER

A. C. Buchanan, III, Phillip F. Britt, and J. Todd Skeen

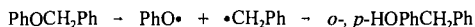
Chemical & Analytical Sciences Division
Oak Ridge National Laboratory
P.O. Box 2008, MS-6197
Oak Ridge, Tennessee 37831-6197

Keywords: Retrogressive reactions, rearrangements, restricted diffusion, ether linkages

INTRODUCTION

Many coal model compound studies have focused on the mechanisms of bond *cleavage* reactions, and the means to alter reaction conditions to promote such reactions. However, there has become increasing interest in elucidating mechanisms associated with retrogressive or retrograde reactions in coal processing, which involve the *formation* of refractory bonds.⁽¹⁻³⁾ Retrograde reactions inhibit efficient thermochemical processing of coals into liquid fuels, which has been particularly well-documented for low rank coals where abundant oxygen-containing functional groups are thought to play a key role in the chemistry. For example, the decarboxylation mechanism of carboxylic acids is being investigated because of the correlation between CO₂ evolution and cross-linking in low rank coals.^(4,5) In addition, phenols have been investigated because of their ability to undergo condensation reactions.^(6,7)

Much less is known about retrogressive reactions for ether-containing model compounds. Radical recombination through ring coupling of phenoxy radicals in benzyl phenyl ether (BPE) is known to lead to more refractory diphenylmethane linkages to a limited extent.^(2,8-11)



Since this chemistry may be attributed at least in part to cage recombination, it could be promoted in a diffusionally constrained environment such as in the coal macromolecule. Using silica-immobilization to simulate restricted diffusion in coal, we have found that retrogressive reactions can be promoted for certain hydrocarbon model compounds.^(12,13) We have now begun an examination of the thermolysis behavior of silica-immobilized benzyl phenyl ether (=BPE, where = represents the Si-O-C linkage to the surface as shown in Table I) at 275-325 °C. Our initial results indicate that *two retrogressive reaction pathways*, radical recombination as shown above and molecular rearrangement through $\approx\text{PhOCH}\cdot\text{Ph}$, are promoted by restricted diffusion. Remarkably, the retrograde products typically account for 50 mol % of the thermolysis products.

EXPERIMENTAL

The precursor phenol, *m*-HOC₆H₄OCH₂C₆H₅ (HOBPE), was synthesized by the reaction of benzyl bromide with the sodium salt of resorcinol (NaH in DMF). Following addition of water and acidification, the organics were extracted into toluene. Ether was added to the toluene solution, and the desired phenol was separated from the dibenzylated byproduct by extraction with 2 M NaOH. The basic layer was acidified and extracted with diethyl ether, which was then washed with brine, dried over Na₂SO₄, filtered, and the solvent removed under reduced pressure to produce a brown oil. The product was eluted twice from silica gel columns, once with toluene and then with toluene:hexane (75:25). Multiple recrystallizations from hot toluene:hexane (1:1) gave the desired phenol in 99.9 % purity by GC.

Chemical attachment of the precursor phenol to the surface of a nonporous silica (Cabosil M-5, Cabot Corp.; 200 m²g⁻¹; ca. 1.5 mmol SiOH per g) was accomplished as described below. HOBPE (2.715g; 13.6 mmol) was dissolved in dry benzene (distilled from LiAlH₄) and added to a benzene slurry of silica (9.00g; 13.5 mmol SiOH) that had been dried at 225 °C for 4 h under vacuum. Following stirring and benzene removal on a rotovap, the solid was added to a Pyrex tube which was evacuated to 2 x 10⁻⁶ torr and flame sealed. The attachment reaction was performed at 200 °C for 1 h. Unattached HOBPE was removed by Soxhlet extraction (6h) with dry benzene under argon. The silica-attached BPE (=BPE) was then dried under vacuum.

Surface coverage analysis was accomplished by dissolution of the solid (ca. 130 mg) in 30 mL of 1N NaOH over night. 3,4-Dimethylphenol and 4-phenylphenol in 1N NaOH were added as internal standards. The solution was acidified with HCl (pH ~ 4) and extracted with diethyl ether (3x). The ether layer was washed with 20 mL of brine, and the emulsion separated by centrifugation. The ether phase was dried over MgSO_4 , filtered, and the solvent was removed under reduced pressure. Silylation with *N,O*-bis-(trimethylsilyl)trifluoroacetamide (BSTFA) in pyridine (2.5 M) produced the corresponding trimethylsilyl ether, which was analyzed by GC (HP 5890) on a J&W Scientific 30 m x 0.25 mm i.d. (0.25 μm film thickness) methyl silicone column with flame ionization detection. GC analysis of multiple assays gave a surface coverage of $0.245 (\pm 1\%) \text{ mmol g}^{-1}$ with a purity of 98.3 %.

Thermolyses were conducted at $275\text{--}325^\circ\text{C}$ ($\pm 1^\circ\text{C}$) in sealed, evacuated (2×10^{-6} torr), T-shaped Pyrex tubes in a temperature controlled tube furnace. Volatile products were trapped as they were produced in liquid nitrogen, and subsequently analyzed by GC and GC-MS (HP 5972A/5890 Series II) with the use of internal calibration standards. Surface-attached products were similarly analyzed after separation by digestion of the silica in aqueous base and silylation of the resulting phenols to the corresponding trimethylsilyl ethers as described above for the surface coverage analysis procedure. Independent recovery studies show that resorcinol, a major product from the thermolysis, is quantitatively recovered by this work-up procedure. The identities of nearly all the products in Table 1 were confirmed with authentic commercial materials. Two isomers of benzyl resorcinol were identified by GC-MS, and the 4-benzyl- isomer was confirmed with a commercial sample. 3-Hydroxybenzhydrol was synthesized from 3-hydroxybenzophenone by reduction with LiAlH_4 in ether. The benzylated $\approx\text{BPE}$ isomers were identified solely by GC-MS.

RESULTS AND DISCUSSION

Thermolysis of $\approx\text{BPE}$ proceeds readily at 275°C to afford a complex array of products. A linear plot of conversion (%) vs. reaction time (6-runs from 2.5–13.3 % conversion) yields a rate for $\approx\text{BPE}$ conversion of $17 \times 10^{-4} \% \text{ s}^{-1}$ or $6.1 \% \text{ h}^{-1}$ ($r=0.998$). The principal products are shown in Table 1, and typically account for 98–99% of the products at 275°C . Small amounts ($\leq 0.2 \text{ mol \%}$ each) of bibenzyl, stilbene, and 3-hydroxydiphenylmethane are also detected. As observed from the data in Table 1, the product distributions do not exhibit a marked dependence on conversion or temperature. Mass balances are typically $\geq 97\%$ at 275°C .

Typically, thermolysis of BPE in fluid phases has been reported to yield phenol, toluene, and benzylphenols as major products along with minor amounts of bibenzyl, diphenylmethane, and benzylated aromatics.^(6,11) Clearly, for surface-immobilized BPE, a much more rich chemistry exists that produces numerous new thermolysis products. A plausible reaction scheme for the formation of these products is shown in Figure 1. Homolysis of the weak O-C bond (ca. 54 kcal mol^{-1}) generates phenoxy and benzyl radicals (Eq. 1), which can abstract hydrogen from $\approx\text{BPE}$ to generate the $\approx\text{PhOH}$ and PhCH_3 products (Eqs. 3–4). However, these radicals can also recouple prior to hydrogen abstraction at the ring carbons of the phenoxy radical to produce, following tautomerization, isomers of benzylphenol (Eq. 2). Benzyl radicals are also lost through addition to aromatic rings to form higher molecular weight products as illustrated in Eq. 7 for addition to $\approx\text{BPE}$ (addition to only one ring is shown in the table and figure for convenience). In fluid phases, the retrograde radical coupling reaction analogous to Eq. 2, which generates a more refractory diphenylmethane linkage as well as a reactive phenol functionality, can account for as much as 15 mol % of the thermolysis products. However, the restricted mass transport experienced by $\approx\text{BPE}$ (and $\approx\text{PhO}\cdot$) apparently results in a substantially enhanced probability of recoupling, and the isomeric benzylphenols (analyzed as benzylresorcinols after cleavage from the surface) account for 27–31 mol % of the products.

In addition to enhanced benzylphenol production, two major new products, surface-attached benzophenone and benzhydrol, were formed in comparable amounts and totaled 21–24 % of the products. Although there are numerous studies of BPE thermolysis in fluid phases, we have found only one report of analogous compounds identified in trace amounts amongst the products.⁽⁹⁾ Formation of these products under restricted diffusion can be explained by reactions of the $\approx\text{PhOCH}\cdot\text{Ph}$ radical intermediate (Eq. 5), which is formed in Eqs. 3–4 by hydrogen abstraction. This radical can undergo a 1,2-phenyl shift to form $\approx\text{PhCH(Ph)O}\cdot$ followed by loss of hydrogen (Eq. 5a) to form the benzophenone, or hydrogen abstraction (Eq. 5b) to form the benzhydrol. The 1,2-phenyl migration from oxygen to carbon proposed in Eq. 5 has been detected previously in the thermolysis of other aryl alkyl ethers.⁽¹⁴⁾ The retrograde molecular rearrangement process shown in Eq. 5 is clearly promoted by the restrictions on molecular diffusion, and a similar rearrangement pathway was observed previously to be the dominant reaction in the thermolysis of surface-immobilized

bibenzyl [$\approx \text{PhCH}_2\text{CH}_2\text{Ph} \rightarrow \approx \text{PhCH}(\text{Ph})\text{CH}_3$].⁽¹²⁾ For $\approx \text{BPE}$, the benzophenone and benzhydrol products also contain reactive functional groups that can also become involved in additional retrograde reactions (reduction to diphenylmethane linkages, addition to aromatics, formation of complex cyclic ethers, etc.) under coal processing conditions.^(6,7,15) Finally, the hydrogen required for formation of the unexpected hydrocracked products (Eq. 6) likely arises from the formation of the aldehyde and ketone products (principally the benzophenone (Eq. 5a)) and the benzylation of aromatics such as $\approx \text{BPE}$ (Eq. 7).

CONCLUSIONS

Thermolysis of benzyl phenyl ether under conditions of restricted mass transport has been found to produce a dramatically different product distribution compared with fluid phases. Two significant retrograde, free-radical reaction pathways are found to be promoted for $\approx \text{BPE}$ under these conditions. Radical coupling at phenolic ring positions is observed to be substantially enhanced as a consequence of restricted diffusion for $\approx \text{PhO}^\bullet$ radicals compared with fluid phases. A second, kinetically competitive retrograde reaction not observed in fluid phases involves rearrangement via $\approx \text{PhOCH}^\bullet\text{Ph}$ intermediates to form benzophenone and benzhydrol products in significant yields. The sum of these two retrograde processes accounts for a remarkable 50-54 mol % of the products at 275 °C. In addition to forming more stable diphenylmethyl-type bridges, these two processes also generate reactive hydroxyl and keto functionalities that can be involved in secondary retrograde reactions. Current research is exploring the effect of surface coverage and reaction temperature on the rate of $\approx \text{BPE}$ thermolysis and on the selectivity for these two retrograde pathways.

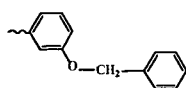
ACKNOWLEDGEMENTS

Research sponsored by the Division of Chemical Sciences, Office of Basic Energy Sciences, U.S. Department of Energy under contract DE-AC05-96OR22464 with Oak Ridge National Laboratory, managed by Lockheed Martin Energy Research Corp.

REFERENCES

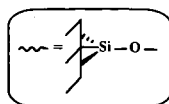
1. Buchanan, III, A. C.; Britt, P. F. *Prepr. Pap., Am. Chem. Soc., Div. Fuel Chem.* **1994**, 39, 22.
2. Malhotra, R.; McMillen, D. F. *Energy Fuels* **1993**, 7, 227.
3. McMillen, D. F.; Malhotra, R. *Prepr. Pap., Am. Chem. Soc., Div. Fuel Chem.* **1992**, 37, 385.
4. Eskay, T. P.; Britt, P. F.; Buchanan, III, A. C. *Energy Fuels* **1996**, 10, 1257.
5. Manion, J. A.; McMillen, D. F.; Malhotra, R. *Energy Fuels* **1996**, 10, 776.
6. Poutsma, M. L.; Dyer, C. W. *J. Org. Chem.* **1982**, 47, 3367.
7. McMillen, D. F.; Chang, S.-J.; Nigenda, S. E.; Malhotra, R. *Prepr. Pap., Am. Chem. Soc., Div. Fuel Chem.* **1985**, 30, 414.
8. Meyer, D.; Nicole, D.; Delpuech, J. J. *Fuel Proc. Technol.* **1986**, 12, 255.
9. Sato, Y.; Yamakawa, T. *Ind. Eng. Chem. Fundam.* **1985**, 24, 12.
10. King, H.-H.; Stock, L. M. *Fuel* **1984**, 63, 810.
11. Korobkov, V. Y.; Grigorieva, E. N.; Bykov, V. I.; Senko, O. V.; Kalechitz, I. V. *Fuel* **1988**, 67, 657.
12. Buchanan, III, A. C.; Dunstan, T. D. J.; Douglas, E. C.; Poutsma, M. L. *J. Am. Chem. Soc.* **1986**, 108, 7703.
13. Britt, P. F.; Buchanan, III, A. C.; Malcolm, E. A.; Biggs, C. A. *J. Anal. Appl. Pyrol.* **1993**, 25, 407.
14. Britt, P. F.; Buchanan, III, A. C.; Malcolm, E. A. *J. Org. Chem.* **1995**, 60, 6523.
15. Choi, C.-Y.; Stock, L. M. *J. Org. Chem.* **1984**, 49, 2871.

Products From Pyrolysis of Silica-Immobilized Benzyl Phenyl Ether



(0.25 mmol/g)

where



PRODUCT (mol %)	275 °C, 90 min 9.7 % convn. 99.4 % mass bal.	275 °C, 360 min 25.5 % convn. 97.8 % mass bal.	300 °C, 30 min 17.9 % convn. 101.1 % mass bal.	325 °C, 10 min 22.7 % convn. 92.6 % mass bal.
	21.6	24.3	24.0	25.6
	11.0	11.1	11.0	11.9
	29.0	26.7	28.5	27.7
	12.5	12.2	10.0	10.4
	11.6	12.4	10.2	9.6
	2.6	2.4	3.0	4.0
	3.6	3.4	3.1	2.5
	1.9	1.5	1.8	2.1
	1.8	1.5	2.0	2.5
	1.5	1.3	2.0	2.5
	1.6	0.9	1.5	0.6

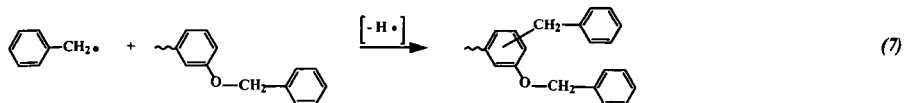
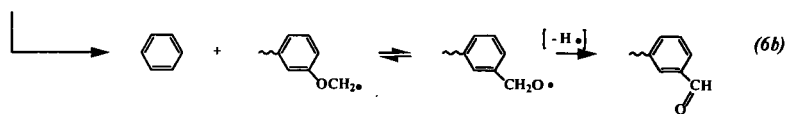
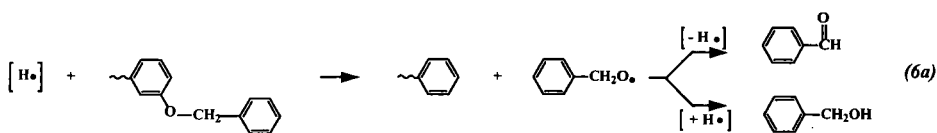
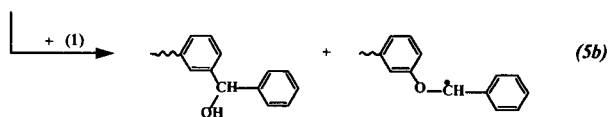
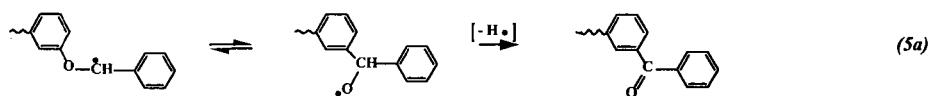
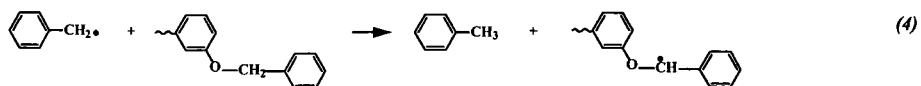
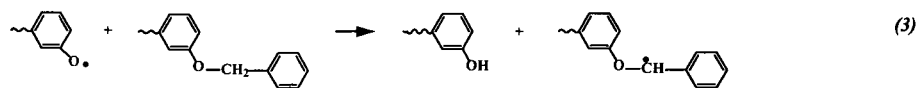
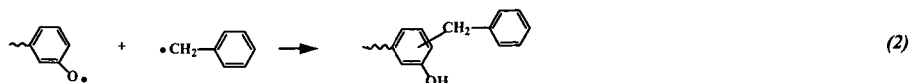
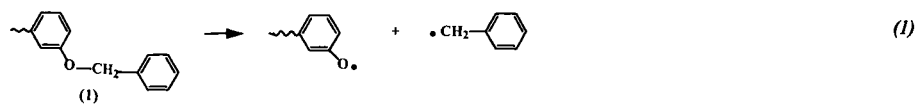


Figure 1. Proposed Reaction Mechanism For Principal Product Formation

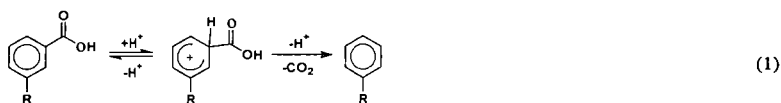
INVESTIGATION OF THE ROLE OF AROMATIC CARBOXYLIC ACIDS IN CROSS-LINKING PROCESSES IN LOW-RANK COALS.*

Thomas P. Eskay, Phillip F. Britt, and A. C. Buchanan, III
Chemical and Analytical Sciences Division, Oak Ridge National Laboratory
P.O. Box 2008, MS-6197, Oak Ridge, Tennessee 37831-6197

Keywords: Carboxylic acids, Cross-Linking, Decarboxylation

INTRODUCTION

In recent years, oxygen functional groups in low-rank coals have clearly been shown to be the major actors in retrograde reactions that inhibit efficient thermochemical processing of low-rank coals. In the pyrolysis and liquefaction of low-rank coals, low-temperature cross-linking reactions have been correlated with the loss of carboxyl groups and the evolution of CO₂ and H₂O [1,2]. Pretreatments such as methylation, demineralization, or ion-exchange of the inorganic cations reduce cross-linking and CO₂ evolution in pyrolysis [2a,3a]. In pyrolysis and liquefaction, the exchange of Na⁺, K⁺, Ca⁺⁺, or Ba⁺⁺ into demineralized coal increases cross-linking and CO₂ evolution [3,4]. Solomon et al. has modeled cross-linking in coals by including one cross-link for every CO₂ evolved [2a], while Niksa has modeled the evolution rates and yields of oxygen-containing species by including char links when non-condensable gases are expelled [5]. These results suggest that decarboxylation may occur by a pathway that initiates retrograde (cross-linking) reactions in the coal polymer. However, the mechanism by which decarboxylation occurs in low-rank coals is not known. Hence, it is not clearly understood how decarboxylation leads to cross-linking beyond the suggestion that decarboxylation could be a radical process that involves radical recombination or radical addition reactions. However, the role of decarboxylation in cross-linking processes has been brought into question by Manion et al. by their observation that the decarboxylation of benzoic acid derivatives in tetralin yielded only small amounts of aryl-aryl coupling products [6]. Further, we have recently conducted a study of the pyrolysis of 1,2-(3,3'-dicarboxyphenyl)ethane (1) and 1,2-(4,4'-dicarboxyphenyl)ethane (2) and found that decarboxylation occurs readily between 350-425 °C with no evidence of coupling products or products representative of cross-links [7]. We proposed that decarboxylation occurred primarily by an acid-promoted cationic pathway, and the source of acid was a second carboxylic acid (eq 1). The possible involvement of decarboxylation by a free-radical pathway was ruled out with our finding that no deuterium (<5 mol %) was incorporated into the aryl ring following decarboxylation of 1,1,2,2-tetradeuterio-1,2-(3,3'-



dicarboxyphenyl)ethane at 400 °C [7a,b]. The decarboxylation of 1 and 2 was also investigated in diphenyl ether and naphthalene as inert diluents. In each solvent, the rate of decarboxylation dropped by roughly a factor of 2 upon dilution from the neat liquid to ca. 0.4 mole fraction of acid, but further dilution had no effect on the rate, which is contrary to a bimolecular reaction mechanism. This could be a consequence of hydrogen bonding or an intramolecular protonation. Molecular mechanics calculations indicated that 1 and 2 can adopt an appropriate conformation for internal proton transfer from a carboxy group on one ring to the second aryl ring without a significant energy penalty. In addition, the dicarboxylic acid could internally hydrogen bond, which may further complicate the reaction mechanism. Therefore, we have conducted a study of the pyrolysis of a monocarboxybiphenyl, 1-(3-carboxyphenyl)-2-(4-biphenyl)ethane (3), to determine if decarboxylation occurs by an ionic pathway in the absence of intramolecular pathways.

* Research sponsored by the Division of Chemical Sciences, Office of Basic Energy Sciences, U.S. Department of Energy, under Contract DE-AC05-96OR22464 with Oak Ridge National Laboratory, managed by Lockheed Martin Energy Research Corp. T.P.E. was supported in part by an appointment to ORNL Postdoctoral Research Associate program administered jointly by Oak Ridge Institute for Science and Education and ORNL.

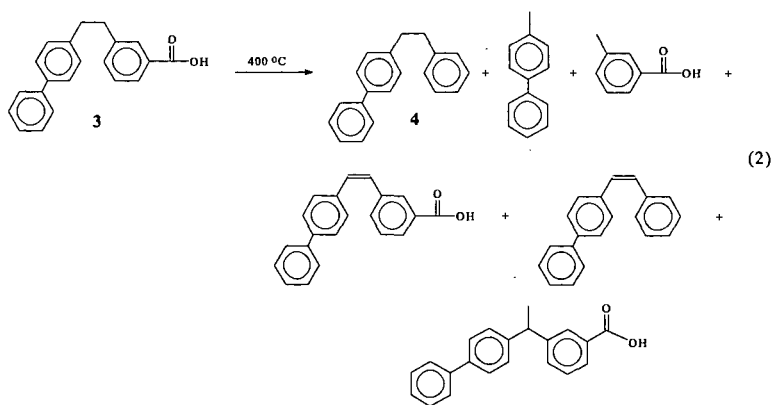
EXPERIMENTAL

1-(3-carboxyphenyl)-2-(4-biphenyl)ethane (**3**) was synthesized as described previously [7d]. The anhydride of **3** was synthesized via dicyclohexylcarbodiimide (DCC) coupling of **3** in THF. 1-(3-carboxaldehydephenyl)-2-(4-biphenyl)ethane (**7**) was synthesized by reduction of **3** to the benzyl alcohol with LiAlH_4 , followed by oxidation to the aldehyde with pyridinium chlorochromate (PCC). 1-(3-(1-naphthyl)phenyl)-2-(4-biphenyl)ethane (**5**) was synthesized by $\text{Pd(PPh}_3)_4$ coupling of 1-naphthylboronic acid and 1-(3-bromophenyl)-2-(4-biphenyl)ethene followed by hydrogenation to the bibenzyl with Pd/C . Full details of these syntheses will be reported later. Naphthalene (Aldrich, 99.9 %) was used without further purification. Gas chromatography analysis was performed using a Hewlett-Packard 5890 Series II gas chromatograph equipped with a J&W Scientific 30 m x 0.25 mm id, 0.25 μm film thickness DB-1 column and a flame ionization detector. Mass spectra were obtained at 70 eV on a Hewlett-Packard 5972 GC/MS equipped with a capillary column identical to that used for GC analysis. Reverse phase HPLC was obtained using a Water's 600E System equipped with a Nova-Pak C18 3.9 mm x 150 mm column (4 μm particle size), and a Water's 996 Diode Array detector using a solvent mixture of 50:50 $\text{CH}_3\text{CN:H}_2\text{O}$ for 10 min then a linear gradient to 90:10 $\text{CH}_3\text{CN:H}_2\text{O}$ at 25 min. Analysis of HPLC data was performed using Water's Millenium software.

Pyrolyses. Pyrolyses in naphthalene were performed by loading pyrex tubes with the appropriate amounts of carboxylic acid and naphthalene and conducting 3 freeze-pump-thaw cycles prior to sealing the tube at 10^{-5} Torr. Neat pyrolyses were performed in an analogous manner with the omission of naphthalene. The pyrolyses were performed in a Carbolite tube furnace, which maintained a temperature of $400 \pm 1^\circ\text{C}$. Following the pyrolysis, the samples were quickly removed from the furnace and cooled in liquid N_2 . The tubes were cracked open, and the solid products were removed with a 2:1 mixture of pyridine: N,O -bis(trimethylsilyl)trifluoroacetamide (BSTFA). Internal standards (2-phenylbenzoic acid and 3,5-dimethylbenzoic acid) were added and the reaction mixtures analyzed by GC and GC-MS. The identities of products from the thermolysis of **3** were determined by GC-MS analysis and were further confirmed by comparison with commercially available or synthesized authentic materials.

RESULTS AND DISCUSSION

Thermolyses of **3** were conducted in sealed, evacuated pyrex tubes at 400°C . The products identities were determined by GC-MS and comparison with authentic materials, either commercially available or independently synthesized, and the reaction products were quantitated by GC. The major products from the thermolysis of neat **3** are shown in equation 2, and a typical

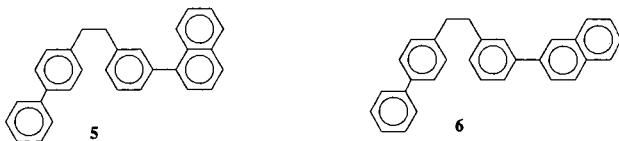


product distribution for a 1 h pyrolysis is given in Table 1, entry 1. Product distributions were similar at higher conversions and mass balances were good (97 % at 40 % conversion). Several other products are formed in the pyrolysis that have not been identified, but based upon the GC

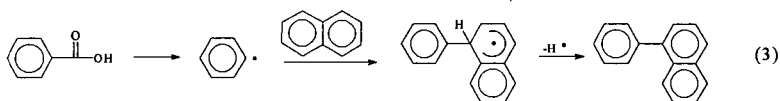
peak area and the good mass balance, the amount of these products are small (<2 mol %).

As observed with diacids **1** and **2** (see Introduction [7]), decarboxylation is the dominant process in the pyrolysis of **3**. The excellent mass balances establish that the decarboxylation pathway does not lead to any significant amounts of coupling or cross-linking products not detected by our analysis. The apparent first-order rate constant for decarboxylation of **3** to 1-(phenyl)-2-(4-biphenyl)ethane (**4**) at 400 °C was $2.8 \pm 0.7 \times 10^{-5} \text{ s}^{-1}$, which is similar to the rate constant for decarboxylation of **1** ($3.7 \pm 0.2 \times 10^{-5} \text{ s}^{-1}$). Based on the similar rate constants for decarboxylation and the similar products distributions of the monoacid and diacids, we propose that the decarboxylation of neat **3** is occurring primarily by the acid-promoted cationic mechanism as previously proposed for the decarboxylation of **1** and **2** (eq 1).

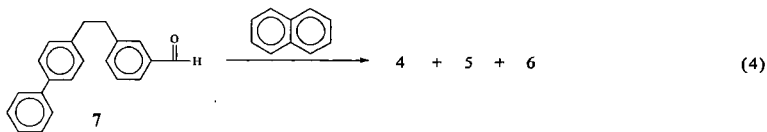
The study of the thermolysis of **3** was extended to dilution (10-fold) in a non-donor solvent, naphthalene, to better mimic the environment of carboxylic acids in coal. The major products from the thermolysis at 400 °C were the same as in the neat pyrolysis (see Table 1, entries 2 and 3), and the mass balances were excellent indicating that we are not missing any significant amount of unidentified products. In naphthalene, there is a small shift in the product distribution as a consequence of a decrease in the rate for the bimolecular decarboxylation reaction while the rate of C-C homolysis remained roughly constant. In addition, two new minor products (< 3 mol %), **5** and **6**, were identified in which naphthalene was grafted onto **4**. The identity of these new products was determined from MS, and the point of attachment to the



aromatic ring was confirmed by independent synthesis of **5**. Similar arylated products were also observed in the thermolysis of **1** diluted in naphthalene (10-fold). Specifically, the major product from the thermolysis of **1** at 400 °C for 45 min was monoacid (59 %), but a small amount of naphthylated products was found (2.7 %). The yield of **5** and **6** was reduced 2-fold by the thermolysis of **3** in a mixture of naphthalene:tetralin (1:1), when compared to a pyrolysis in naphthalene:biphenyl (1:1), indicating the pathway for arylation may involve the formation of an aryl radical as shown in equation 3. Stein has studied the free-radical reaction of aryl radicals, formed from the decomposition of aromatic aldehydes, with aromatic rings in the gas phase at

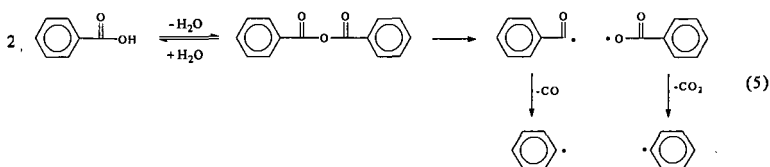


400 and 450 °C [8]. To investigate if **5** and **6** could arise from a free-radical pathway, we studied the pyrolysis of 1-(3-carboxaldehydephenyl)-2-(4-biphenyl)ethane, (**7**). The aryl radical can be produced by homolysis of the benzylic C-C bond of **7** to form benzyl radicals, hydrogen abstraction from the aldehydic hydrogen, followed by rapid decarbonylation. Pyrolysis of **7** under the same dilution conditions used for the acid (10:1, naphthalene:7) produced **4**:**5**:**6**, as the major products in a ratio of 1.0:1.1:1.0, respectively (eq 4), showing that **5** and **6** can arise via a



free-radical pathway. On the basis of the product distribution, the ratio of arylation to hydrogen abstraction by the aryl radical is 2:1. However, in the pyrolysis of **3** in naphthalene, >8 times more **4** is produced than arylated products (**5** and **6**) indicating that the majority of the decarboxylation (>80%) can not be produced by a radical pathway, which is consistent with our proposal that an ionic decarboxylation mechanism is dominant.

Formation of 5 and 6 from pyrolysis of 3 suggests that aryl radicals are formed during the pyrolysis. On the basis of bond strengths, it is unlikely that abstraction of hydrogen from the carboxylic acid (O-H 101 kcal/mol [9]) by benzylic radicals (from C-C homolysis of 3) would be competitive with hydrogen abstraction from the benzylic hydrogens of 3 (86 kcal/mol [10]). At this point, it was unclear how aryl radicals could arise in the pyrolysis of 3. However, it was later shown that water could affect the yields of 5 and 6. The results of two runs in which 1.6 and 3.5 eq of H₂O:3 were added are shown in Table 1, entries 4 and 5. These results show that there is ca. 2-3-fold reduction in the rate of formation of these coupled products with H₂O present. Water did not have any influence on the ratio of 4:5:6 in the pyrolysis of 7:naphthalene:H₂O (1:10:1.5 molar ratio), indicating that the water does not inhibit the arylation reaction. Therefore, the reduction of products 5 and 6 with the addition of H₂O demands that their formation must come from a pathway that is inhibited by H₂O. One possible route to the formation of an aryl radical that would be sensitive to water is through the decomposition of an anhydride formed from the coupling of two carboxylic acids. Anhydrides are known to be formed if carboxylic acids (such as benzoic acid) are heated under conditions that remove H₂O [11]. As shown in equation 5, homolysis of the C-O bond of the anhydride would produce fragments that could decarboxylate and decarbonylate to form two aryl radicals. Although thermochemical estimates predict that



benzoic anhydride should not decompose by this pathway to any significant extent at 400 °C, we investigated the pyrolysis of benzoic anhydride diluted in naphthalene to determine if the reaction pathway outlined in equation 5 can occur at a reasonable rate at 400 °C (Table 2). Surprisingly, benzoic anhydride decomposed at an average rate of 12 %/h to benzene and 1-and 2-phenylnaphthalene, which is consistent with the formation of aryl radicals from the anhydride decomposition. Furthermore, the radical nature of the anhydride decomposition is supported by the formation of small amounts of binaphthyls in the pyrolysis: i.e. naphthyl radicals are formed by abstraction of hydrogen by an aryl radical or hydrogen atom, followed by coupling with a second naphthalene. Hence, if an anhydride could be formed in the pyrolysis of the acids, it appears it could produce phenyl radicals by its decomposition under these reaction conditions.

Because it is unlikely that the anhydride would be detectable by GC, we investigated whether the anhydride of 3 was formed during the pyrolysis of 3 in naphthalene by HPLC. In the pyrolysis of 3:naphthalene (1:4), at 400 °C for 1.5 h, a small amount of anhydride was found. The amount of anhydride is currently unquantified but most likely its formation is ~1% of the starting amount of 3 based on peak area. This is supported by the excellent mass balances obtained in these pyrolyses (Table 1), which do not include the anhydride. The identity of the anhydride was confirmed by comparison of the HPLC retention time of the product formed in the pyrolysis with an authentic sample of the anhydride prepared by independent synthesis. While the anhydride was detected without H₂O added, the addition of H₂O (1.5 eq to 3), inhibited the formation of the anhydride. These results show that the anhydride can be formed in the pyrolysis of 3, its formation is inhibited by H₂O, and benzoic anhydride decomposes at a reasonable rate to produce arylated products. More importantly, if we estimate that the conversion of the anhydride of 3 will be the same as benzoic anhydride, only ~1-3 % of the starting acid needs to be converted to the anhydride to produce the amount of coupling products observed in the pyrolysis as shown in Table 1. This calculation does not take into account any chain chemistry that may also be operating as a result of anhydride decomposition in the presence of carboxylic acids that could potentially lower the amount of anhydride needed to produce the coupling products.

SUMMARY AND CONCLUSION

The pyrolysis of 3 was studied both neat and diluted in naphthalene to determine the role of thermal decarboxylation in the thermal processing of low-rank coal. The mechanism of decarboxylation proceeds primarily by an acid-promoted ionic pathway that does not lead to cross-linking or coupling products. However, with a 10-fold dilution in naphthalene, 10-15 % of

the carboxylic acid lost can result in a cross-link by a pathway involving the formation of an aryl radical at the ring position of the carboxylic acid. The radical pathway can be reduced by a factor of 2 either by tetralin (in 1:1 mixtures with naphthalene) or H_2O . These preliminary results indicate that the radical pathway, in part, arises as a result of the formation and decomposition of the anhydride of 3. Further studies on the mechanism of the anhydride decomposition pathway and the influence of the anhydride decomposition in the presence of aromatic carboxylic acids are currently in progress. In addition, we are investigating further why the cross-linking is not evident in the pyrolysis of neat 3.

In reference to the behavior of low-rank coals, the results of this study suggest that carboxylic acids may lead to a small amount of cross-linking; however, it appears unlikely that the majority of acid decarboxylations produce a cross-link. If it is true that a cross-link is made in coal for every CO_2 evolved, there must be additional chemistry other than decarboxylation involved in cross-link formation. In addition, it is likely that the aromatic carboxylic acids in low-rank coals are contained on rings that contain electron donating groups, such as methoxy groups. The presence of these electron-donating substituents should increase the rate of decarboxylation by the ionic pathway, which could further minimize the amount of cross-linking observed from carboxy groups. However, while the results of this paper and our previous papers have established a framework for understanding the thermal chemistry of carboxylic acids, it should be realized that the results from our model compounds do not consider the restricted mass transport that would exist in coal. In addition, the carboxylic acids in low-rank coal may be present as carboxy salts and not as free carboxylic acids. These features need to be further explored before the role of decarboxylation and cross-linking can be fully evaluated.

REFERENCES

1. Suuberg, E.M.; Lee, D.; Larsen, J.W. *Fuel* **1985**, *64*, 1668.
2. (a) Solomon, P.R.; Serio, M.A.; Despande, G.V.; Kroo, E. *Energy Fuels* **1990**, *4*, 42. (b) Ibarra, J.V.; Moliner, R.; Gavilan, M.P. *Fuel* **1991**, *70*, 408.
3. (a) Serio, M.A.; Kroo, E.; Chapernay, S.; Solomon, P.R. *Prepr. Pap.-Am. Chem. Soc. Div., Fuel Chem.* **1993**, *38(3)*, 1021. (b) Serio, M.A.; Kroo, E.; Teng, H.; Solomon, P.R. *Prepr. Pap.-Am. Chem. Soc., Div. Fuel Chem.* **1993**, *38(2)*, 577.
4. Joseph, J.T.; Forria, T.R. *Fuel* **1992**, *71*, 75.
5. Niksa, S. *Energy Fuels* **1996**, *10*, 173.
6. (a) Manion, J.A.; McMillen, D.F.; Malhotra, R. *Prepr. Pap.-Am. Chem. Soc., Div. Fuel Chem.* **1992**, *37(4)*, 1720. (b) Manion, J.A.; McMillen, D.F.; Malhotra, R. *Energy Fuels* **1996**, *10*, 776.
7. (a) Eskay, T.P.; Britt, P.F.; Buchanan, III, A.C. *Prepr. Pap.-Am. Chem. Soc., Div. Fuel Chem.* **1996**, *41(2)*, 739. (b) Eskay, T.P.; Britt, P.F.; Buchanan, III, A.C. *Energy Fuels* **1996**, *10*, 1257. (c) Britt, P.F.; Buchanan, III, A.C.; Hoenigman, R.L. *Coal Science* Pajares, J.A. and Tascon, J. M. D. Eds.; Coal Science and Technology 24; Elsevier Science B.V.: Amsterdam, Netherlands, 1995, 437. (d) Eskay, T.P.; Britt, P.F.; Buchanan, III, A.C. *Prepr. Pap.-Am. Chem. Soc., Div. Fuel Chem.* **1996**, *41(3)*, 1084.
8. (a) Fahr, A.; Stein, S.E. *J. Phys. Chem.* **1988**, *92*, 495. (b) Chen, R.H.; Kafafi, S.A.; Stein, S.E. *J. Am. Chem. Soc.* **1989**, *111*, 1418.
9. The bond strength for the O-H bond was calculated using additivity Tables in Benson, S. *Thermochemical Kinetics, Second Edition*, John Wiley and Sons, New York, 1976 and heat of formation of $PhCO_2$ (-21 ± 2 kcal/mol) in Mortimer, C.T., *Reaction Heats and Bond Strengths*, Pergamon Press, New York, 1962, p. 142.
10. McMillen, D.F.; Golden, D.M. *Ann. Rev. Phys. Chem.* **1982**, *33*, 493.
11. Davison, D.; Newman, P. *J. Am. Chem. Soc.* **1952**, *74*, 1515.

Table 1. Product Distributions from the Pyrolysis of 1-(3-carboxyphenyl)-2-(4-biphenyl)ethane (3) at 400 °C for One Hour Under Various Conditions.

Entry	1	2	3	4	5
Product (mole %) ^a	Neat	10:1 Naph:3	10:1 Naph:3	10:1:1.6 Naph:3: H ₂ O	10:1:3.5 Naph:3: H ₂ O
PhCO ₂ H	0.3	0.2	0.2	0.2	nd
3-CH ₃ PhCO ₂ H	13.6	24.6	27.0	26.5	26.0
3-CH ₃ CH ₂ PhCO ₂ H	0.6	0.9	1.0	0.9	0.6
4-Ph-PhCH ₃	14.9	25.7	28.0	27.4	27.2
4-Ph-PhCH ₂ CH ₃	0.5	0.8	0.9	0.7	0.4
4-Ph-PhCH(CH ₃)Ph	0.2	0.2	nd	0.1	Nd
4-Ph-PhCH ₂ CH ₂ Ph (4)	44.9	27.0	20.2	21.9	25.2
4-Ph-PhCH=CHPh	1.1	0.5	0.5	0.4	0.7
4-Ph-PhCH ₂ PhCO ₂ H	0.8	0.4	0.4	0.5	nd
4-Ph-PhCH(CH ₃)PhCO ₂ H	7.8	4.7	5.0	5.0	3.6
4-Ph-PhCH=CHPhCO ₂ H	15.0	12.3	14.0	15.0	15.2
4-Ph-PhCH ₂ CH ₂ Ph-3-(1-naphthyl) (5)	nd	1.4	1.4	0.6	0.5
4-Ph-PhCH ₂ CH ₂ Ph-3-(2-naphthyl) (6)	nd	1.5	1.4	0.7	0.4
Conversion ^b	12.6	10.8	9.5	10.35	10.0
Mass Balance	98.1 %	100.1	99.7	99.8	100.0

a-Based on products detected and quantified.

b-Conversion based on products recovered.

Naph=naphthalene

nd-not detected

Table 2. Product Distributions from the Pyrolysis of Benzoic Anhydride in Naphthalene (1:10 molar ratio) at 400 °C for 50 min.

Product ^a	Run # 1	Run # 2
Benzene	31 %	30 %
1-Phenylnaphthalene	43 %	39 %
2-Phenylnaphthalene	26 %	31 %
Conversion ^b	14 %	9 %

a-Small amounts of phenyl benzoate and 1- and 2-naphthylphenyl ketone were also formed.

b-Conversion based on products detected.

THERMOLYSIS OF A POLYMER MODEL OF AROMATIC CARBOXYLIC ACIDS IN LOW-RANK COAL

William S. Mungall¹, Phillip F. Britt², A. C. Buchanan, III²

¹Department of Chemistry, Hope College, Holland, Michigan 49423

²Chemical and Analytical Sciences Division, Oak Ridge National Laboratory
P. O. Box 2008, Oak Ridge, Tennessee 37831-6197

Keywords: cross-linking reactions, pyrolysis mechanisms, polymer pyrolysis

ABSTRACT

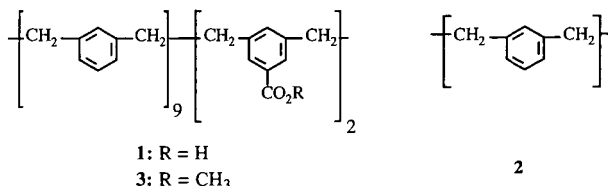
To compliment our current investigation into the role that decarboxylation of aromatic carboxylic acids plays in the low-temperature cross-linking of low-rank coals, we are investigating the thermolysis of a polymeric coal model compound to determine if the polymeric network structure of coal can alter the decarboxylation pathways. In this investigation, a bibenzyl polymer, poly-(*m*-xylylene-co-5-carboxy-*m*-xylylene), **1**, was synthesized containing 2.3 carboxylic acids per 100 carbons, which is similar to that found in Zapp lignite. The pyrolysis of **1** was compared to poly-*m*-xylylene, **2**, and the methyl ester of **1**, **3**, to determine if the carboxy group enhances cross-linking reactions. The major product from the pyrolysis of **1** at 375 °C or 400 °C for 1 h was a THF insoluble residue (60-75 wt%), while pyrolysis of **2** or the methyl ester of **1** produced only a THF soluble product. The mechanistic pathways leading to cross-linking will be discussed.

INTRODUCTION

In recent years, it has been proposed that oxygen functional groups (i.e. carboxylic acids, phenols, and ethers), prevalent in low rank coals, are major contributors to retrograde reactions that inhibit the efficient conversion of low-rank coals to liquid fuels and chemicals. In the pyrolysis and liquefaction of low rank coals, low-temperature ($T \leq 400$ °C) cross-linking reactions (measured by the solvent swelling technique) have been correlated with the loss of carboxyl groups in the char and the evolution of CO₂ and H₂O [1,2]. The pyrolytic loss of solvent swelling in coal has also been modeled by including one cross-link for every CO₂ evolved [1]. Cross-linking can be reduced by methylation, demineralization, or a hydrogen donor solvent and increased by oxidation or ion-exchanging Na⁺, K⁺, or Ca²⁺ into a demineralized coal [1]. These results suggest that the reaction pathways that lead to decarboxylation may play an important role in cross-linking. However, the reaction pathways for decarboxylation and cross-linking in low-rank coals are not known. Therefore, to gain a better understanding of the reaction pathways that lead to decarboxylation at temperatures relevant to coal processing, we have studied the pyrolysis of 1,2-(3,3'-dicarboxyphenyl)ethane (HO₂CC₆H₄CH₂CH₂C₆H₄CO₂H) neat and diluted in naphthalene or tetralin at 400 °C as a model of free carboxylic acids in low rank coal [3]. In these studies, decarboxylation did not produce any significant amount of coupling or other high molecular weight products that might be indicative of cross-linking reactions. However, recent pyrolysis studies of a monoacid, 1-(3-carboxyphenyl)-2-(4-biphenyl)ethane, diluted in naphthalene have shown the formation of small amounts (<3 mol %) of coupled products. It was proposed that decarboxylation occurred predominantly by an acid promoted ionic pathway. However, it is realized that simple model compounds may not be able to completely portray the complex chemistry and physical environment found in coal. Moreover, a small amount of cross-linking chemistry (1-5%) could go undetected in a simple model compound study (showing up as mass balances slightly less than 100% or a series of small unidentified peaks in a GC or GC-MS trace), but a small amount of cross-linking could have a profound impact on the solvent swelling properties of a complex macromolecule. For example, polystyrene (an organic polymer highly soluble in organic solvents) can be made insoluble by cross-linking with only 1-2 mol % divinylbenzene. Therefore, to determine if a polymeric network can alter the reaction pathways, we have incorporated aromatic carboxylic acids into a polymeric network and studied the pyrolysis of the polymer under a variety of conditions.

In this investigation, we have synthesized poly(*m*-xylylene-co-5-carboxy-1,3-xylylene), **1**, as a polymeric model for aromatic carboxylic acids in low-rank coal. The density of carboxylic acid in the polymer, 2.3 carboxylic acids per 100 carbons, is similar to that reported for Beulah-Zap coal, 2.2 acids per 100 carbons [4]. To determine if the carboxy functional group enhances cross-linking reactions, the pyrolysis of **1** will be compared to the unsubstituted homopolymer,

2. Our previous studies on the pyrolysis of carboxy-substituted bibenzyls will also provide useful insights into interpreting the pyrolysis results for **1** [3].



EXPERIMENTAL

The synthesis of **1** and **2** has been previously described [5]. The methyl ester of the carboxy polymer, **3**, was prepared by methylation of **1** with an excess of diazomethane. Molecular weight distributions were determined by gel permeation chromatography (GPC) using a Waters chromatography system consisting of a 600E system controller and pump, 717 autosampler, and 410 differential refractometer interfaced to a computer running Waters Millennium 2010 software for GPC analysis. A bank of three columns (Waters Styragel HR1, HR3 and HR5E) were calibrated using six narrow molecular weight standards (polystyrene, Mw 89,300; 25,400; 12,600; 4,000; 687 and bibenzyl, Mw 182) at 32 °C in THF at a flow rate of 1.00 mL/min. The molecular weight, M_N , and polydispersity (M_w/M_N) of **1** and **2** were 11,300 (2.8) and 9900 (2.5), respectively. A similar molecular weight was obtained for the methyl ester **3**. The polymers were characterized by ^{13}C -NMR, FTIR, and elemental analysis. By CP/MAS ^{13}C -NMR, there is one acid per 5.4 ± 0.5 aromatic rings or 2.3 acids per 100 carbons. Similar results were obtained by elemental analysis.

In a typical pyrolysis experiment, the polymer (ca. 45 mg) and a small plug of glass wool was loaded into a T-shaped tube (8 mm), the tube was pumped down, and sealed under vacuum ($<10^{-5}$ Torr). One end of the tube was placed in a liquid nitrogen trap and the polymer was placed in a Carbolite three zone tube furnace (38 mm ID). The pyrolysis temperature was measured by a RTD thermocouple placed beside the sample, and the temperature was held ± 1.0 °C over the sample length. After the reaction, the tube was opened, the glass wool plug was rinsed with THF, and THF (2.0 mL) was added to the pyrolysis residue. The tube was capped and heated to 60–70 °C for 18–24 h. The THF layer was removed and the insoluble residue was washed with THF (2x). The combined washings were concentrated, dried under vacuum, weighed, redissolved in THF, filtered, and analyzed by GPC, GC, and GC-MS. The insoluble residue was dried under vacuum and weighed. The volatile products that collected in the cold trap were dissolved in CH_2Cl_2 (1.0 mL) containing an internal standard (pentamethylbenzene), and analyzed by GC and GC-MS.

Infrared spectra were recorded on a Bio-Rad FTS-60 FT-IR in a KBr matrix or as a thin film formed by pressing the polymer melt between Teflon sheets. TGA was performed on a Sinku-Riko differential thermal-galvanometric analyzer TGD 7000 and TGA-MS was performed on a TGD 7000 interfaced to a VG mass spectrometer. The heating rate for the TGA and TGA-MS experiments was 5 °C min $^{-1}$ and the experiments were run under argon. Samples sizes were typically 10–25 mg for these experiments.

RESULTS AND DISCUSSION

Figure 1 show the weight loss curves for **1**, **2**, and **3** at a heating rate of 5 °C min $^{-1}$ under argon. The thermograms for the three polymers are very similar: weight loss starts at ca. 400 °C with the major degradation occurring between 425 – 500 °C. However, the carboxylated polymer forms ca. 2.5 times more char than the unsubstituted polymer. Methylation of the carboxylic acid decreases char formation. A similar trend has been observed in the pyrolysis of lignite coal in which methylation increased tar yield and reduce cross-linking [1]. Figure 2a shows the evolution of volatile materials from the depolymerization of the homopolymer, **2**, by monitoring the benzyl fragment m/e 91 (C_7H_7^+) from the fragmentation of the pyrolysis products in the mass spectrometer. From the sealed tube pyrolysis of **2** and **1** (see below), the major volatile products identified by GC-MS were monomer (*m*-xylene), dimer, trimer, and tetramer (which contain m/e 91 in their mass spectral fragmentation patterns). A similar TGA-MS evolution profile was found for **2** by monitoring the xylylene fragment (m/e 105). Figure 2b shows that the evolution of CO_2 (m/e 44) from **1** precedes depolymerization of the polymer backbone (by monitoring the benzyl fragment, m/e 91). For low-rank coals, a similar trend in gas evolution,

measured by TGA-FTIR, has been reported [1] in which CO₂ evolution precedes tar evolution. To our delight, these simple bibenzyl polymers reproduce many of the qualitative trends found in the pyrolysis of low-rank coals, but in a much simpler matrix such that it may be possible to gain mechanistic insight into specific reaction pathways that lead to cross-linking.

Much of the experimental data on the cross-linking behavior of low-rank coals has been obtained in pyrolysis experiments in which the volatile materials are swept away (sometimes for additional analysis) from the char by an inert gas. To investigate the pyrolysis of **1**, **2**, and **3** under conditions in which the volatile products are removed, the pyrolysis was performed in sealed T-shaped tubes (see experimental) under vacuum in which one leg of the tube was placed in a liquid nitrogen trap to remove the volatile products. After pyrolysis, the tubes were broken, THF was added, and the solutions were heated to 60-70 °C overnight (16 h). The soluble and insoluble fractions were separated (if present) and the molecular weight distribution of the soluble fraction was determined by GPC. The results from the pyrolysis of the polymers are summarized in Table 1. Pyrolysis of **1**, **2**, and **3** at 375 °C for 1 h produced very small amounts of volatile products (as anticipated from the TG analysis and the low reactivity of bibenzyl at 375 °C). Analysis by GC and GC-MS found monomer, dimer, trimer, and tetramer as the major products. The residue from the pyrolysis of **2** and **3** was soluble in THF, but a large fraction of the residue from the pyrolysis of **1** was still insoluble in THF. As shown in entries 1, 2, 5-8 in Table 1, pyrolysis of **1** for <60 min at 375 or 400 °C typically produced 60-75 wt% of an insoluble polymer. The reactions that lead to a loss of solubility occur quickly at 400 °C because the yield of insoluble polymer is established after 15 min and does not change significantly except for long reaction times. However, the molecular weight of the THF soluble fraction decreases as the longer reaction times increase as a consequence of C-C homolysis. At very longer reaction times (60 h) at 400 °C, the yield of volatile products increased and some of the insoluble residue was converted to lower molecular weight products, but a significant fraction of the polymer still remained insoluble in THF. In contrast, no insoluble residue was found in the pyrolysis of **2** or **3** at 375 °C or 400 °C even at long reaction times (60 h, see entry 9 Table 1).

These results indicate that cross-linking reactions can occur in the bibenzyl polymer as a consequence of the carboxyl group to produce an insoluble polymer. This is in stark contrast to the results previously obtained in the pyrolysis of simple model compound (1,2-(3,3'-dicarboxyphenyl)ethane) in which no cross-linking was observed [3]. This highlights the importance of the polymeric network in influencing reaction chemistry. When the carboxylic acid is removed or methylated, the pyrolysis residue is completely soluble in THF and the yield of char decreases. The reaction pathways leading to the cross-linking reaction are currently under investigation and the results will be discussed in the presentation.

ACKNOWLEDGMENTS

Research sponsored by the Division of Chemical Sciences, Office of Basic Energy Sciences, U.S. Department of Energy, under contract DE-AC05-96OR22464 with Oak Ridge National Laboratory, managed by Lockheed Martin Energy Research Corp.

REFERENCES

1. (a) Solomon, P. R.; Serio, M. A.; Deshpande, G. V.; Kroo, E. *Energy Fuels* **1990**, *4*, 42 and references therein. (b) Serio, M. A.; Kroo, E.; Chapernay, S.; Solomon, P. R. *Prep. Pap.-Am. Chem. Soc., Div. Fuel Chem.* **1993**, *38*(3), 1021.
2. Suuberg, E. M.; Lee, D.; Larsen, J. W. *Fuel* **1985**, *64*, 1668.
3. (a) Eskay, T. P.; Britt, P. F.; Buchanan, III, A. C. *Energy Fuels* **1996**, *10*, 1257. (b) Eskay, T. P.; Britt, P. F.; Buchanan, III, A. C. *Prep. Pap.-Am. Chem. Soc., Div. Fuel Chem.* **1996**, *41*(2), 739. (c) Eskay, T. P.; Britt, P. F.; Buchanan, A. C. III *Prep. Pap.-Am. Chem. Soc., Div. Fuel Chem.* **1996**, *41*(3), 1084.
4. Jung, B.; Stachel, S. J.; Calkins, W. H. *Prep. Pap.-Am. Chem. Soc., Div. Fuel Chem.* **1991**, *36*(3), 869.
5. (a) Britt, P. F.; Buchanan, III, A. C.; Hoenigman, R. L. *Coal Science* Pajares, J. A.; Tascon, J. M. D. Eds.; Coal Science and Technology 24; Elsevier; Amsterdam, Netherlands, 1995, 437. (b) Mungall, W. S.; Britt, P. F.; Buchanan, III, A. C. manuscript in preparation.

Table 1. Thermolysis of 1, 2, and 3 in sealed tubes under vacuum.

Entry	Polymer ^a	Temp °C	Time min	Volatile Products	THF Soluble	M _w x10 ³ ^b	THF Insoluble	Mass Balance
1	1	375	60	1 %	41 %	10.8	60 %	102 %
2	1	375	60	1 %	31 %	23.2	67 %	99 %
3	3	375	60	1 %	93 %	74.7	— ^c	94 %
4	2	375	60	1 %	95 %	19.0	— ^c	96 %
5	1	400	15	2 %	24 %	7.3	73 %	99 %
6	1	400	30	4 %	18 %	4.4	76 %	98 %
7	1	400	60	7 %	21 %	3.5	73 %	101 %
8	1	400	3600	49 %	7 %	1.3	39 %	95 %
9	2	400	3600	26 %	70 %	7.6	— ^c	97 %

^a M_w of 1, 2, and 3 is 31,500, 24,700, and 33,100, respectively. ^b Weight averaged molecular weights determined by GPC vs. polystyrene standards. ^c No insoluble material was detected.

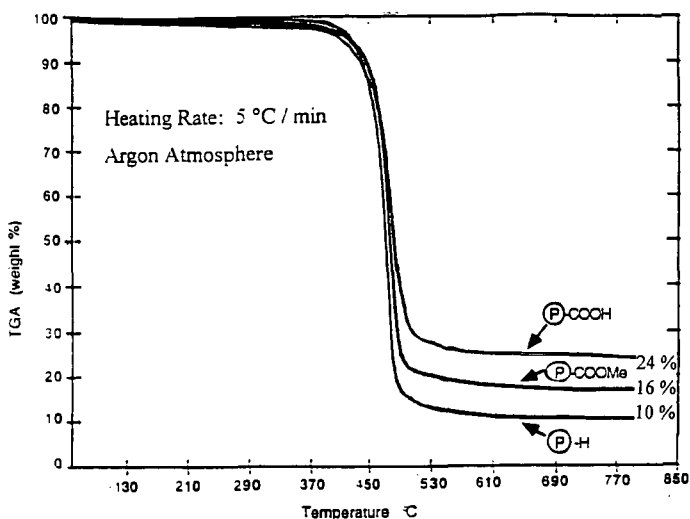


Figure 1. TG curves for polymers 1 (P-COOH), 2 (P-H), and 3 (P-COOMe).

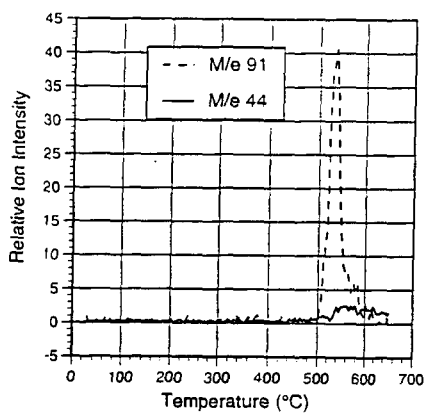


Figure 2a. TG-MS of 2 (P-H) monitoring *m/e* 91 (benzyl fragment) and *m/e* 44 (CO₂).

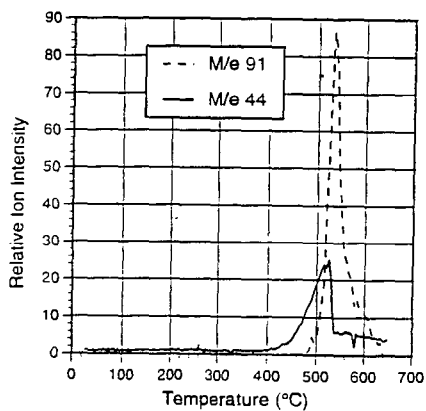


Figure 2b. TG-MS of 1 (P-COOH) monitoring *m/e* 91 (benzyl fragment) and *m/e* 44 (CO₂).

DECARBOXYLATION AND COUPLING REACTIONS OF PHENYLACETIC ACID UNDER COAL-LIQUEFACTION CONDITIONS

Jeffrey A. Manion, Donald E. McMillen, and Ripudaman Malhotra
Molecular Physics Laboratory, SRI International
333 Ravenswood Ave., Menlo Park, California, 94025

INTRODUCTION

The conversion of low-rank coals to liquids or volatile hydrocarbons is known to be substantially hindered by retrograde reaction, and oxygen functional groups in the coal structure are strongly correlated with these retrograde reactions. Carboxyl functions have been implicated in the crosslinking of coals during heating at relatively low temperatures,^{1,2} and Solomon et al.³ have been able to model the pyrolytic loss of solvent swelling by including one additional crosslink in the network for every CO₂ evolved. However, carboxyl groups are not the dominant oxygen-containing moieties, even in low-rank coals, and we suspected hydroxyl functions may play just as large a role, particularly since phenolic -OH in polyhydroxy systems are known to lead to furanic systems under coal liquefaction conditions.⁴ Therefore we have examined the rates of decarboxylation some prototypical carboxylic acids to see if crosslinking results directly from decarboxylation, as well as how crosslinking is affected by H-donors, electron transfer reagents, the addition of water, and other conditions relevant to pretreatment and liquefaction of coals.

We have previously reported the decarboxylation and coupling reactions of aromatic carboxylic acids and their calcium salts,⁵ and found that little coupling generally followed from these decarboxylations. Generally, fewer than one in ten decarboxylations led to a crosslinking reaction, except in the presence of 1-electron oxidants where, under some non-reducing conditions, one coupling reaction occurred for every two decarboxylations of benzoic acid. Recently Eskay, et al. prepared and studied polymers containing unactivated aromatic carboxylic acids to test whether the presence of a polymeric structure would significantly enhance crosslinking reactions, but they also observed little coupling resulted from decarboxylation of unactivated benzoic acid structures.⁶

For activated aromatic acids, we found that coupling by direct reactions of radical fragments is very low, but coupling as an indirect result of decarboxylation can be very substantial. Loss of the electron-withdrawing carboxyl group from, for example, 2-hydroxybenzoic acid, allows the hydroxy group to exert its full activating effect toward any subsequent substitution by electrophiles. Thus we showed that by this route, decarboxylation of activated aromatic acids can lead to ring coupling and even to subsequent ring-closure, though not by the radical-coupling routes that are often cited.

Because it is likely that some carboxyl groups in low-rank coals are not attached directly to an aromatic ring, we have extended our examination to the thermal behavior of phenylacetic acid, a prototypical structure with an aliphatic acid side chain. In addition to a very early report on the thermolysis of the neat liquid,⁷ there are more recent gas phase studies at high temperature.⁸ A recent study of PAA decomposition at 250°C reported that a major pathway for phenylacetic acid decomposition at 250°C involves net elimination of H₂O and CO₂ to form the coupling product dibenzyl ketone (DBK) and proposed a four-membered ring rearrangement of the anhydride to the unstable β -keto acid, which then easily decarboxylates.⁹ The presence of water completely inhibits the ketone formation.

EXPERIMENTAL

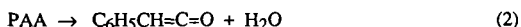
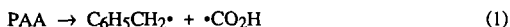
Reactions were performed in fused silica ampoules, heated inside a stainless steel pressure jacket, as described previously.⁵ Products were analyzed by GC (FID) and GC-MS. The estimated overall accuracy was $\pm 2\%$ in most cases, $\pm 5\%$ for some polar products, and $\pm 12\%$ for phenylacetic acid itself. Phenylacetic acid (99+% by GC analysis), naphthalene (Aldrich 99+%), tetralin (Aldrich, 99%), pyridine (Mallinckrodt, AR grade, 99+% by GC analysis), and Fe₃O₄ powder (particle size $\sim 0.2 \mu\text{m}$) were used without further purification.

RESULTS AND DISCUSSION

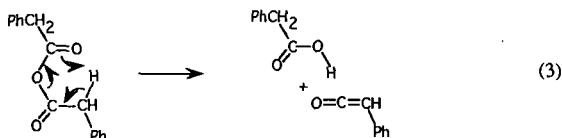
Decarboxylation Rates and Major Products. Table 1 shows the major thermal decomposition products of PAA in naphthalene/tetralin mixtures. In 1 hour at 400°C, 28 to 43% decarboxylation is observed. The primary products were toluene and dibenzyl ketone (DBK), as described in the literature,⁷⁻⁹ along with one isomer of tetralylbenzyl ketone (TBK), bibenzyl, and trans-stilbene. Also found were small quantities of benzylnaphthalenes, dihydrobenzylnaphthalenes, phenylnaphthalenes, and an isomer of benzyltetralin. Benzene accounted for less than 0.5% of the PAA that was consumed. We also found coupling products formed entirely from solvent: binaphthyls, bi-tetralyls, their cross products, and partially hydrogenated versions of these compounds. Together, these solvent coupling products accounted for less than 0.5% of the starting acid. Mass balances were generally $>97\%$, except in the two experiments with naphthalene-only solvent, where only 91% of the PAA was accounted for.

Figure 1 shows the changes in the distribution of the main products as the solvent was shifted from naphthalene to tetralin. Decarboxylation of PAA, as measured by toluene formation, decreased by about 25%, but the proportions of toluene and total ketones were not changed significantly.

Mechanism of Decarboxylation. Although the mechanism of the condensed phase thermal decarboxylation of phenylacetic or other aliphatic acids has not, to our knowledge, been fully elucidated, the thermal reaction in the gas phase has been reported to proceed via reactions (1) and (2) at temperatures between 587 and 722°C.⁸ Reaction 1 would give toluene in two steps, but its parameters, as selected in a critical review of the work,¹⁰ would dictate a half-life for PAA of about 10,000 h at 400°C.

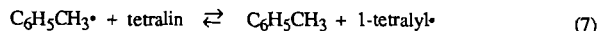
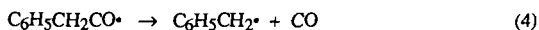


This projected half-life is orders of magnitude longer than that actually observed here, and therefore the liquid phase reaction must proceed via another mechanism. Similarly, four-center elimination of water from the phenylacetic acid, as implied by Reaction 2 as written, is unlikely under our conditions because the analogous elimination from acetic acid, for instance, has a very high activation energy (68 kcal/mol¹¹). It is more likely that reaction proceeds through an anhydride intermediate, which can eliminate PAA and generate phenyl ketene in a favorable 6-center transition-state (Reaction 3). Radical addition to ketene could then give the observed ketone products. The parameters reported¹² for acetic acid anhydride decomposition, $k/s^{-1} = 10^{12.0} - 7540/T$, would lead to a half-life of only about a tenth of a second at 400°C, easily fast enough to give the required ketene, provided that the formation of the anhydride is itself facile.



The anhydride could be formed via either a concerted or an acid- or base-catalyzed elimination of water. While the formation of toluene is consistent with reaction via $\text{PhCH}_2\cdot$, as previously suggested,⁹ the observation of small amounts of 1,2-diphenylethane (1,2-DPE), trans-stilbene, benzylnaphthalenes, and dibenzyl ketone (see below) appear more consistent with the presence of benzyl radicals. Similarly, decomposition of the anhydride to ketene is not limited to a concerted reaction. Since H-atom chain reactions are often, at high temperatures, close competitors to electrocyclic eliminations, the ketene could also be formed from the anhydride by an H-abstraction, β -scission process to yield phenylacetoxyl radical as the companion product. This radical would decarboxylate extremely rapidly, possibly leading to some reaction of its product benzyl radical with ketene before they left the solvent cage. If benzyl radical and ketene are formed exclusively by an H-abstraction, β -scission process chain process, then the presence of substantial cross products indicates escape from the cage is competitive with cage addition of benzyl radical.

Effect of Donor Solvent on Ketone Formation. As the reaction medium was shifted from naphthalene to tetralin, a gradual four-fold drop in formation of dibenzyl ketone was observed, while a new species, tetralylbenzyl ketone, became a prominent product. This result, shown graphically in Figure 2, suggests that benzyl radicals are increasingly scavenged by tetralin. The formation of cross-products certainly means that DBK does not form exclusively by the sequence of concerted rearrangement to a β -keto acid, followed by facile decarboxylation, as has been suggested previously.⁹ Cross products also mean that radical reaction is not limited to recombination within a cage. Therefore, we suggest instead that dibenzyl ketone is formed in reactions (5) and (6). No rate parameters for (5) have been reported, but the reaction would be expected to be rapid.



As tetralin is added to the system, benzyl radicals will be partly scavenged by tetralin, and tetralyl radicals will replace benzyl radicals in Reaction 5 to give tetralyl benzyl ketone, as reflected in the data in Figure 2. Because the 1-tetralyl radical is ~12 kcal/mol more stable than the 2-isomer,¹³ the TBK product should be almost entirely 1-tetralyl benzyl ketone, as observed. However, even in pure tetralin, only about 2/3 of the dibenzyl ketone was replaced with tetralylbenzyl ketone. The inability of tetralyl radicals to intercept a greater proportion of the presumed intermediate phenyl ketene needs to be considered carefully because it bears on the hypothesis that this radical addition is the route to benzyphenyl ketene.

Because the equilibrium constant¹⁴ for Reaction 7 is ≥ 10 , and because the tetralin was in substantial excess over toluene, it is apparent from the ratio of DBK/TBK (Table 1), that either Equilibrium 7 has not been established, or k_5/k_7 is very large. Estimation of the rates of reactions 5 and 7, based on measured rates of analogous reactions and thermochemical data, suggests that indeed, scavenging of benzyl radical is simply not fast enough to completely outpace its addition to ketene.

The Effect of Added Water. A rationale involving reaction through the anhydride and the corresponding ketene suggests that the addition of water to the reaction mixture should slow the formation of ketenes, both through hydrolysis of the proposed anhydride intermediate and by the rapid reaction of phenylketene with water¹⁵ to re-form phenylacetic acid (Reaction -2, above). In partial accord with this expectation, and as Katritzky et al. have reported⁹ for lower temperatures, we found that the addition of 34 mol% of water to a mixture of naphthalene and PAA led to more than a seven-fold drop in dibenzyl ketone formation (Table 1). Curiously, however, there is *no* decrease in the rate of decarboxylation: the decrease in ketone formation corresponds almost exactly to the increase in toluene formation. Added water does *not* simply send anhydride or ketene back to acid. Since water with its very strong HO-H bond is a terrible radical scavenger but a good acid, the diversion of ketone to toluene suggests an anhydride-like intermediate whose benzyl fragment can act as a carbanionic species. This reaction would be similar to hydrolysis of the anhydride, except that the CO-CH₂ bond would act as the electrophile, rather than the C=O double bond, as occurs in a normal hydrolysis.

Water also caused a three-fold decrease in benzylnaphthalenes and a six-fold decrease in the sum of bibenzyl and stilbene. The system containing water had the lowest coupling/(total reaction) ratio at 0.024. Because bibenzyl and stilbene can plausibly result only from benzyl radical recombination, and because water is a poor radical scavenger, this observation provides additional evidence that water shifts decomposition of PAA more towards ionic pathways, so that fewer radicals are generated in the first place. This explanation would require an intermediate X that decomposes either via radical production or via an ionic pathway: by increasing the rate of the ionic pathway, the steady state concentration of X (and the consequent generation of radicals) is reduced, though the overall decarboxylation rate remains unchanged. Water, acting as an acid, captures an anionic benzyl fragment from the intermediate, increasing the toluene yield and decreasing those products that result from radical reactions.

Non-Ketone Coupling Products. In pure naphthalene solvent, traces of benzylnaphthalenes were observed. When tetralin was added to the naphthalene, we observed increased levels of benzylnaphthalenes, as well as dihydrobenzylnaphthalenes and a single isomer of benzyltetralin [identified by mass spectrometry as α -benzyltetralin (1,2,3,4-tetrahydro-1-benzylnaphthalene)]. The absence of significant amounts of benzylnaphthalenes in pure naphthalene presumably reflects the fact that addition of benzylic radicals to aromatic systems forms an initial cyclohexadienyl adduct radical having a very weak C-C bond, and is therefore a highly reversible process. The initial adduct cannot be stabilized unless the ipso-hydrogen is rapidly removed, in a bimolecular fashion, by some H-acceptor species. However, when tetralin is present, α -tetralyl radicals will constitute a significant part of the radical population and can provide additional routes to benzylnaphthalenes.

The marked increase in benzylnaphthalene formation with added tetralin is accompanied by a similar increase in the ratio of 1-benzylnaphthalene/2-benzylnaphthalene. As the reaction medium is shifted from naphthalene to pure tetralin, the yield of benzylnaphthalenes increases by 20X, and the ratio of the 1-isomer to the 2-isomer increases from near 1 to almost 40 (Figure 3). This predominance of 1-benzylnaphthalene, together with the observation that only the α -isomer of benzyltetralin was observed, suggests that in tetralin, 1-benzylnaphthalene is formed predominantly by recombination of benzyl radical with the dominant α -tetralyl radical, followed by dehydrogenation of the α -benzyltetralin. In pure naphthalene, on the other hand, the benzylnaphthalenes are evidently formed only by radical addition to naphthalene, which should show more limited selectivity, though still favoring the 1- position of naphthalene.

The Effect of an Amine Base. The addition of 10 mol% of pyridine to the naphthalene/PAA mixture (Table 1) did *not* increase decarboxylation, but did increase toluene yield by about 20%. The effect is thus different than that observed with benzoic acid, where 10% pyridine increased decarboxylation fourfold.⁵ The effect of base on ketone formation was minor, decreasing formation of dibenzylketone by about 10%. More surprising was its effect on the other coupling products. The sum of 12DPE and trans-stilbene was increased a factor of 2.5, and new products appeared, including diphenylmethane (DPM, 0.47%), an isomer of phenylpyridinylethane (0.17%), phenylnaphthalenes (0.12%), pyridinylnaphthalenes (0.13%), and various unidentified coupling products of higher molecular weight. The precise sources of these products are unclear: DPM has been identified by Miller and Stein¹⁶ as a significant product in the *later* stages of neat 1,2-DPE pyrolysis, but they were unable to identify the route to this product. It is not likely to arise from addition of benzyl radicals to benzene, since the formation of the initial adduct would be even more readily reversed than in the benzylnaphthalene case discussed above. Similarly, the formation of phenylnaphthalenes and pyridinylnaphthalenes suggests that the generation of aryl radicals from the solvent components is somehow being promoted by pyridine. Although we

observed similar coupling products in the case of decarboxylation of aromatic acids,⁵ in that case the addition of pyridine actually resulted in a *lower* total yield of products most easily attributable to radicals.

The Effect of Fe_3O_4 . In the previous study of aromatic acids, we had found that under some conditions the addition of electron transfer agents, which may be present in coals as inorganic components, increased the rates of decarboxylation and coupling. Fe_3O_4 was the most effective of these agents at promoting coupling, and therefore we examined its effect on the decarboxylation and coupling of PAA. The effects of iron oxide on the course of the reaction were somewhat different, depending on whether the solvent was pure naphthalene, or contained a donor component. When the solvent was naphthalene only, addition of 10 mol% Fe_3O_4 doubled the total conversion of PAA, but resulted in little or no increase in the "major" products: dibenzyl ketone was unchanged, and toluene increased only 25%. Most of the additional conversion resulted in various "minor" coupling products, which were increased to the point where they constituted, in total, about half of the coupling products. The sum of bibenzyl and t-stilbene was increased by a factor of nearly 25 when compared to the case without added Fe_3O_4 . Benzylnaphthalenes were increased by a factor of 45, with both isomers now found in similar quantities. Perhaps most surprising was the presence of phenylnaphthalenes, not formed at all without added Fe_3O_4 , but now found at about 75% of the level of the benzylnaphthalenes. A new ketone, benzylphenyl ketone, was found at about 10% of the level of dibenzyl ketone.

When the solvent contained tetralin, Fe_3O_4 roughly doubled the fractional conversion of PAA, as it had in pure naphthalene solvent, but with the donor present, dibenzyl ketone was increased by 300%! Toluene and most of the minor coupling products, such as benzylnaphthalene and phenylnaphthalene, decreased significantly. This effect can also be stated in terms of tetralin addition: in the absence of Fe_3O_4 , tetralin addition suppresses dibenzyl ketone by ~70% (essentially replacing it with tetralylbenzyl ketone), but when Fe_3O_4 is present, tetralin addition increases dibenzyl ketone by 300%.

Evidently, Fe_3O_4 increases the number of decomposition intermediates, or complexes, regardless of whether tetralin is present. If tetralin isn't present, then most of these decomposition intermediates go on to generate radicals that are distributed in the bulk of the solvent, and therefore primarily give coupling products that involve one or two solvent molecules. However, when tetralin is present, it evidently can prevent escape of benzyl radicals from the "cage" of decomposition intermediates, and send most of the intermediates to dibenzylketone. If the last step in ketone formation from PAA is indeed radical addition to phenyl ketene, then stabilization of the adduct requires transfer of a hydrogen to that adduct; tetralin would clearly help to provide this hydrogen. This case is in curious contrast to the "normal" case of retrograde reaction, where addition to an aromatic ring system requires H-removal from the initial adduct in order to achieve a stable, aromatic coupling product. In that case, formation of a stable adduct is most facilitated by a hydrogen *acceptor*, rather than a hydrogen *donor*.

Implications for Coal Liquefaction and Gasification. Because of its ca. 1-h half life at 400°C, phenylacetic acid, and by extension, other short chain fatty acids, are probably not related to the coal species that undergo rapid decarboxylation below ca. 400°C. Thus, barring substantial promotion of decarboxylation rates by indigenous coal substances, these aliphatic acids appear unlikely to account for the crosslinking at mild conditions that has been observed for low-rank coals. Such decarboxylation would appear to be limited to aromatic acids activated by hydroxy substitution. On the other hand, the primary coupling reactions of PAA, which lead to ketones, and the secondary coupling reactions, which lead to alkyl-aryl and aryl-aryl coupling products through addition of substrate- and solvent-derived radicals, could well contribute to retrograde reactions that occur between 400 and 450°C. Such ketone formation is expected to be quite general for other fatty acids possessing α -hydrogens. In coal structures, these reactions that require two acid groups may be restricted by limited availability of other acid functionalities in the nearby coal matrix. In fact, the opportunity to form retrograde products via anhydride intermediates could help to explain how such products are enhanced when divalent metal cations are ion-exchanged into low-rank coals, forming di-acid salts. The observed diversion by water of dibenzyl-ketone-forming intermediates to toluene could also help to explain some of the reported benefits^{17,18} of added water on coal liquefaction.

Decarboxylation to generate radical species which then undergo simple recombination reactions or addition to aromatic rings appears to be directly responsible for only a limited amount of coupling, with generally less than one crosslink for every ten decarboxylations of PAA. These radical-recombination or addition routes can be partially controlled through the use of H-donors. As the solvent composition is shifted from pure aromatic to hydroaromatic, the dominant route to alkyl-aryl coupling products can be seen to shift from radical addition to radical recombination, where the bulk of initial recombination products survive at 400°C only because aromatization enormously increases adduct bond strength.

The electron transfer agent Fe_3O_4 caused a two-fold enhancement of decarboxylation, but because it seems to primarily enhance radical pathways, resulted in a four-fold enhancement of coupling products. In the presence of Fe_3O_4 , added tetralin caused a dramatic enhancement of dibenzyl

ketone formation rates. This unexpected effect, presumably a result of enhanced trapping of a cage addition product, provides yet another illustration of fact that "hydrogen transfer" is not always good for liquefaction, in that it is equally necessary for both the formation and the scission of strong bonds.

SUMMARY AND CONCLUSIONS

Phenylacetic acid in naphthalene at 400°C undergoes about 25% decarboxylation in one hour, intermediate to the rates of the activated and unactivated aromatic acids. The rate decreases about 25% as the solvent medium is switched to tetralin, but is essentially unchanged by the addition of amine base or water. The major coupling products of PAA are dibenzylketone (DBK) and, when tetralin was present, tetralylbenzyl ketone (TBK), probably formed from reaction of phenylketene with benzyl and tetralyl radicals, respectively. Smaller amounts of 1,2-diphenylethane, trans-stilbene, benzyl naphthalenes, and benzyl tetralins are also formed. Total coupling is between 14-23% of reaction except in the presence of added water, where the coupling was reduced to about 2%. The ketones account for 40-90% of the coupling products, with the percentage decreasing as tetralin is added. Only ~2 to 15% of the total retrograde products result from actual recombination of the parent benzyl radicals, the commonly invoked retrograde reaction.

Water inhibits the formation of the ketones without decreasing the extent of decarboxylation, presumably by diverting intermediates that could have led to anhydride or ketene formation. Other coupling products evidently result from radical recombination or addition/elimination reactions. The one-electron oxidant Fe_3O_4 caused a two-fold increase in decarboxylation and a more substantial increase in products expected from radical reactions. Fe_3O_4 added to naphthalene had little effect on DBK formation, but Fe_3O_4 added in the presence of tetralin markedly increased the formation of DBK and increased the ratio of coupling/(total reaction) to about 0.5, independent of the amount of tetralin present (at tetralin > 10%). In the presence of tetralin and Fe_3O_4 , about 80% of the total coupling was due to formation of DBK.

REFERENCES

1. Suuberg, E. M.; Lee, D.; Larsen, J. W., *Fuel* **1985**, *64*, 1668.
2. Serio, M. A.; Hamblen, D. A.; Markham, J. R.; Solomon, P. R. *Energy Fuels* **1987**, *1*, 138.
3. Solomon, P. R.; Serio, M. A.; Deshpande, G. V.; Kroo, E., *Energy Fuels* **1990**, *4*, 42.
4. McMillen, D.F.; Chang, S.-J.; Nigenda, S. E.; Malhotra, R. *Am. Chem. Soc. Div Fuel Chem. Preprints* **1985**, *30(4)*, 414.
5. Manion, J. A.; McMillen, D. F.; Malhotra, R. *Energy & Fuels*, **1996**, *10*, 776.
6. Eskay, T. P.; Britt, P. F.; Buchanan, A. C., III *Am. Chem. Soc. Div Fuel Chem. Preprints* **1996**, *41(2)*, 739.
7. C. Engler and Ed. Low, *Ber.*, **1893**, *26*, 1436.
8. Back, M. H.; Sehon, A.H., *Can. J. Chem.*, **1960**, *38*, 1261.
9. Katritzky; Luxem, F. J.; Siskin, M. *Energy & Fuels*, **1990**, *4*, 514.
10. Benson, S.W.; O'Neil, H.E., *Kinetic Data on Gas Phase Unimolecular Reactions*, National Bureau of Standards, NSRDS-NBS 21, Washington, 1970.
11. Bamford, C.H.; Dewar, M.J. S. *J. Chem. Soc.* **1949**, 2877.
12. Murawski, J.; Szwarc, M. *Trans. Faraday Soc.* **1951**, *47*, 269.
13. Berkowitz, J.; Ellison, G. B.; Gutman, D. *J. Phys. Chem.* **1994**, *98*, 2744.
14. Benson, S. W., *Thermochemical Kinetics*, 2nd ed; John Wiley and Sons: New York, **1976**.
15. Allen, A.D.; Kresge, J.A.; Schepp, N.P.; Tidwell, T.T. *Can. J. Chem.* **1987**, *65*, 1719.
16. Miller, R. E.; Stein, S. E. *J. Phys. Chem.* **1981**, *85*, 580.
17. Serio, M. A.; Kroo, E.; Charpenay, S.; Solomon, P. R. *Am. Chem. Soc. Div Fuel Chem. Preprints* **1993**, *38(3)*, 1021.
18. Song, C.; Saini, A. K.; Schobert, H. H. *Energy & Fuels*, **1994**, *8*, 301.

Table 1
MAJOR REACTION PRODUCTS OF PHENYLACETIC ACID IN
NAPHTHALENE/TETRALIN MIXTURES^a

REACTANTS ^b	J40	J75	J39	J67	J71	J70	J72	J25
% Tetralin	0.0	0.0	0.0	12.38	47.90	66.38	77.23	100.00
Ph-Acetic Acid	9.83	6.59	10.92 ^m	11.07	10.04	9.97	9.90	10.29 ^m
Naphthalene	79.01	59.12	89.08 ^m	77.92	46.87	30.27	20.52	—
Tetralin	—	—	—	11.01	43.09	59.76	69.58	89.71
Pyridine	11.16	—	—	—	—	—	—	—
H ₂ O	—	34.17	—	—	—	—	—	—
PRODUCTS ^b								
Pyridine	77.4	—	—	—	—	—	—	—
Ph-Acetic Acid	61.3	57.5	57.1	64.8	65.9	70.4	71.9	67.2
Naphthalene	99.2	102.8	99.2	87.7	52.6	34.7	24.2	2.7
Tetralin	—	—	—	11.9	46.3	64.6	75.1	94.1
Benzene ^c								
Toluene	31.6	32.9	27.2	27.4	25.4	22.2	22.4	19.7
Bibenzyl	0.36	0.028	0.24	0.071	0.056	0.067	0.069	0.026
t-Stilbene	0.46	0.026	0.071	0.11	0.086	0.060	0.061	0.037
Benzylphenyl ketone	< 0.01	< 0.01	< 0.01	< 0.01	< 0.01	< 0.01	< 0.01	< 0.01
Dibenzyl ketone	5.10	0.75	5.57	5.75	3.87	2.71	2.92	1.40
Benzyltetralyl ketone	< 0.01	< 0.01	< 0.01	0.68	1.76	1.33	1.60	1.32
Bz-Naph(H) ₂ ^d	< 0.01	< 0.01	< 0.01	0.11	0.13	0.15	0.16	0.14
1234H-5-BzNaph ^e	< 0.01	< 0.01	< 0.01	0.049	0.098	0.23	0.21	0.26
Unk. 20,20	< 0.01	< 0.01	< 0.01	< 0.01	0.21		0.053	0.0
Bz-Naph(H) ₂ ^d	< 0.01	< 0.01	< 0.01	0.043	0.078	0.14	0.17	0.23
Bz-Naph(H) ₂ ^d	< 0.01	< 0.01	< 0.01	0.011	0.024	0.047	0.053	0.081
1-Ph-Naphthalene	0.053	< 0.05	< 0.05	< 0.05	< 0.05	< 0.05	< 0.05	< 0.05
2-Ph-Naphthalene	0.067	< 0.05	< 0.05	< 0.05	< 0.05	< 0.05	< 0.05	< 0.05
1-Bz-Naphthalene	0.025	0.0084	0.023	0.21	0.37	0.42	0.49	0.48
2-Bz-Naphthalene	0.028	0.0054	0.024	0.016	0.020	0.014	0.015	0.012
Sum Bz-Naph(H) ₂ ^f	0.053	0.014	0.047	0.43	0.72	1.01	1.10	1.19
Sum coupling	7.93	0.82	6.09	7.04	6.73	5.24	5.86	4.53
coupling/Rxn ^g	0.21	0.024	0.14	0.200	0.23	0.18	0.20	0.14
Sum PAA products ^h	98.9	91.2	90.8	99.3	97.8	97.9	100.0	93.6
Sum Bz-Naph(H) ₂	< 0.01	< 0.01	< 0.01	0.15	0.22	0.34	0.38	0.45
1/2 Bz-Naph ⁱ	0.90	1.56	0.95	13.0	18.5	29.4	32.6	38.3
Sum Ketones	5.10	0.75	5.57	6.43	5.63	4.05	4.52	2.72

- Reaction time 1 hr @ 400°C.
- Reactants are shown in mole % of reaction mixture; products of phenylacetic acid are shown as a mole % of the starting acid, naphthalene and tetralin are shown as mole % of the sum of starting naphthalene and tetralin, and coupling products are shown as a mole % of the starting acid that they contain.
- Benzene not determined because of interference by GC solvent.
- An unspecified dihydro-benzyl-naphthalene isomer.
- 1,2,3,4-tetrahydro-5-benzyl-naphthalene.
- The sum of various partially hydrogenated benzyl-naphthalenes.
- The ratio of phenylacetic acid incorporated in coupling products to the sum of that which has undergone reaction of any kind.
- The sum of phenylacetic acid and all identified phenylacetic acid products, as a mole % of the starting acid.
- The ratio of 1-benzyl-naphthalene to 2-benzyl-naphthalene.

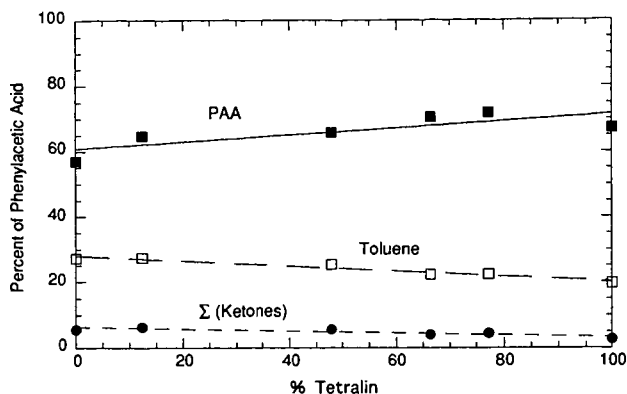


Figure 1. Formation of major products as a function of the H-donor content of the solvent.

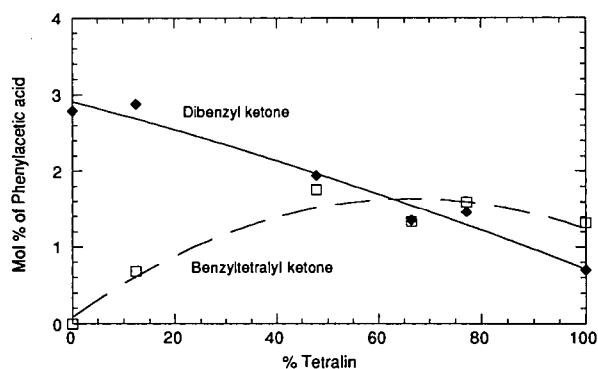


Figure 2. Ketone formation as a function of the H-donor content of the solvent.

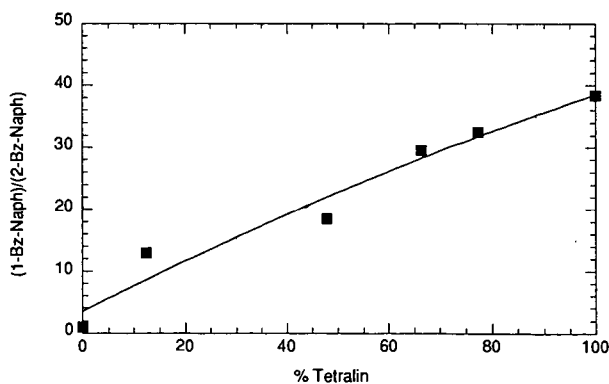


Figure 3. Ratio of 1-benzyl-naphthalene/2-benzyl-naphthalene as a function of the donor content of the solvent.

COPROCESSING OF POLYMERIC WASTE WITH COAL: REACTION OF POLYETHYLENE AND COAL MODEL COMPOUNDS

Mathew J. De Witt and Linda J. Broadbelt
Department of Chemical Engineering
Northwestern University
Evanston, Illinois 60208

Keywords: Coprocessing, Coal, Polymeric Waste

ABSTRACT

Environmental and economical concerns over diminishing landfill space and the growing abundance of mixed plastic waste mandate development of viable strategies for recovering high-valued resources from waste polymers. Co-processing of waste polymer mixtures with coal allows for the simultaneous conversion of coal and plastics into high-valued fuels. However, there is limited information about the underlying reaction pathways, kinetics, and mechanisms controlling coal liquefaction in the presence of polymeric materials.

A series of model compound experiments has been conducted, providing a starting point for unraveling the complex, underlying chemistry. Neat pyrolysis studies of model compounds of polyethylene and coal were conducted in batch reactors. Tetradecane ($C_{14}H_{30}$) was used as a polyethylene mimic, and 4-(naphthylmethyl)biphenyl was used as a coal model compound. Reaction temperatures were 420 and 500°C, and batch reaction times ranged from 5-150 minutes. Detailed product analysis using gas chromatography and mass spectrometry enabled the reactant conversion and product selectivities to be determined. Reaction of single components and binary mixtures allowed the kinetic coupling between feedstocks to be examined.

INTRODUCTION

Recently, concerns over the inadequacy of current treatment and disposal methods for mixed plastic wastes have driven the exploration of new strategies for viable plastics resource recovery. The emphasis of the recovery is to obtain high-valued, useful products from the waste polymers. Post-consumer waste plastics are a major contributor to the municipal solid waste (MSW) stream, constituting approximately 11% by weight and 21% by volume of waste in landfills¹. Over 40% of the landfills in the United States were closed in the past decade, and it is estimated that over half of the remaining ones will be full by the end of the century². This poses a significant dilemma since there appears to be no immediate decrease in the usage of plastic products; in fact, due to their versatility, the usage will most likely increase.

The current motivation for the recovery of plastics is due to government mandates, rather than to industrial initiatives. Some states, such as California, Oregon, and Wisconsin, have passed laws which specify that plastic bottles must be manufactured from a minimum of 25% recycled plastics. Germany has dictated that over 80% of all plastic packaging must be recycled by methods other than combustion by 1996³⁻⁵. Conventional plastics recycling technologies encounter a number of difficulties which range from costly separation to removal of impurities and contaminants. A consequence of these problems is that products manufactured from recycled polymers are of lower quality and higher cost (approximately 10% higher for high-density polyethylene (HDPE)) than those from the corresponding virgin polymer⁴. As a result, in the United States, only about 4% of 30 million tons of total plastics produced each year is recycled⁶.

Coprocessing of polymeric waste with other materials may provide potential solutions to the deficiencies of current resource recovery processes, including unfavorable process economics. By incorporating polymeric waste as a minor feed into an existing process, variations in plastic supply and composition could be mediated and as a result, allow for continuous operation. One option for coprocessing is to react polymeric waste with coal under direct liquefaction conditions^{2,7,8}. Coprocessing of polymeric waste with coal provides for simultaneous conversion of both feedstocks into high-valued fuels and chemicals.

EXPERIMENTAL

In order to obtain information about underlying reaction pathways, kinetics, and mechanisms without the complicating effects of the macrostructure, experiments were performed using model compounds for both coal and polyethylene, a voluminous component of mixed plastic waste. To mimic the structure of coal, 4-(naphthylmethyl)biphenyl (NBBM) was used. NBBM contains both condensed and isolated aromatic species connected by short alkyl chains. An added feature is that it contains five different aromatic-aliphatic or aliphatic-aliphatic carbon-carbon bonds. Successful predictions of the relevant primary products for real systems using NBBM confirmed the adequacy of this model compound, and thus, it will be employed in this study⁹⁻¹². The structure of NBBM is depicted in Figure 1. Although numerous hydrocarbons may serve as appropriate model compounds for high density and low density polyethylene, tetradecane, $C_{14}H_{30}$, was chosen as an appropriate compromise in reactant size.

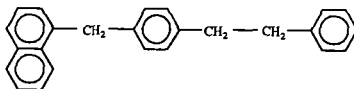


Figure 1: Structure of coal model compound 4-(naphthylmethyl)biphenyl.

Batch pyrolyses were carried out in an isothermal ($\pm 1^\circ\text{C}$) fluidized sand bath. The experiments were conducted in 2 ml glass cryovials charged with ca. 20 mg of reactant for the neat reactions. Equimolar ratios of tetradecane/NBBM were used for the binary experiments, with loadings based on ca. 10 mg of NBBM. After filling, the ampoules were purged with argon, and then sealed using an oxygen/propane flame. Pyrolysis was conducted at both 420 and 500°C, and reaction times ranged from 5-150 minutes. Upon completion of the reaction period, the ampoules were removed from the sand bath and permitted to cool at room temperature. The experiments were replicated a minimum of two times, and conversions and selectivities were reproducible with an error of less than 1%.

Soluble reaction products were extracted from the ampoules using 5 ml of methylene chloride, and an external standard (biphenyl) was added. Product identification and quantification, which enabled reactant conversions and product selectivities to be determined, was achieved using an HP 6890 GC/MS and HP 5890 GC equipped with a flame ionization detector, respectively, each employing a Hewlett Packard 30 m crosslinked 5% Ph Me Silicone capillary column.

RESULTS AND DISCUSSION

The reactant conversions for pyrolysis of tetradecane and NBBM at 500°C were very high, as almost complete conversion was achieved at a reaction time of 10 minutes for all the systems studied. As evidenced by the product spectra and the temporal variations of the major products, secondary and tertiary reactions occurred, making it difficult to deconvolute reaction pathways. Therefore, the reaction temperature was lowered to 420°C, a value still within the range of relevant liquefaction conditions, to achieve lower conversions and isolate primary decomposition pathways. It was noted from the data at 500°C, however, that the conversion of tetradecane was enhanced slightly in the presence of NBBM as compared to the neat reaction.

Reactions carried out at 420°C facilitated identification of the underlying reaction pathways and kinetics. As illustrated in Figure 2, the conversion was significantly lower at a given reaction time as compared to that observed at 500°C. For example, only 37 % of the tetradecane was converted after 150 minutes of reaction time.

The major products observed from the pyrolysis of tetradecane were α -olefins, with minor selectivity to n-alkanes. The highest selectivity, 0.13, was obtained for 1-heptene, and α -olefins with carbon numbers of 6 to 11 were also observed in significant quantities. As reaction time increased, the selectivity to α -olefins decreased, while that of n-alkanes slightly increased, as observed in Figure 3. This behavior can be explained by noting that hydrogenation of olefins and continued thermal cracking can occur as reaction time increases.

The product distribution was rationalized in terms of the typical free radical Rice-Herzfeld and Rice-Kossiakoff mechanisms¹³⁻¹⁶. The mechanism is initiated by carbon-carbon bond fission along the main chain to form two primary radicals. These primary radicals form secondary radicals through hydrogen abstraction from a secondary carbon or an intramolecular hydrogen rearrangement. These secondary radicals then undergo β -scission to form α -olefins and primary radicals. Termination occurs by recombination of radicals.

Two of the major products from pyrolysis of NBBM, which are formed by carbon-carbon bond fission and subsequent hydrogen abstraction, were toluene and 1-methyl-4-(naphthylmethyl) benzene, each observed with a selectivity of greater than 0.28 at all reaction times studied. The other major product was 1-(2-phenylethenyl)-4-(naphthylmethyl) benzene, with an initial selectivity of approximately 0.35 which decreased linearly with reaction time to 0.11 at 150 minutes. Minor selectivities were observed for a number of products from NBBM pyrolysis. Methyl bibenzyl and 1-(4-(4-methyl)phenylmethyl)benzyl naphthalene were observed with initial selectivities of 0.055 and 0.070, respectively. Other minor products included 1,4-(binaphthylmethyl) benzene, phenyl methyl naphthalene, naphthalene, methyl naphthalene, 1-(phenylmethyl)-4-(naphthylmethyl) benzene, 1-methyl-4-(2-phenylethenyl) benzene and p-xylene.

Mechanistic interpretation using the ideas put forth by Walter et al. (1994) successfully accounted for the observed product spectra. The products anticipated from scission of the five main bonds of NBBM, labeled A-E, and subsequent hydrogen abstraction and β -scission, are depicted in Figure 4. The formation of high yields of toluene and 1-methyl-4-(naphthylmethyl) benzene is consistent with the proposed mechanism involving bond D fission. This is the weakest bond in the molecule, since the radicals which are formed can be stabilized by the adjacent benzyl substituents. Similarly, the C₁ linkage in NBBM possesses the most easily abstractable hydrogens. Once a secondary radical is formed, it can undergo β -scission to form 1-(2-phenylethenyl)-4-(naphthylmethyl) benzene. This compound could then undergo degradation reactions similar to those observed for NBBM, leading to a reduction in selectivity as reaction time increases.

A comparison of the selectivities of products associated with cleavage of bond A as a function of conversion is shown in Figure 5. If these products were solely formed by bond A scission, it would be expected that the selectivities would be equal for naphthalene and the sum of methyl bibenzyl and its corresponding derivatives. This is clearly not the case. Therefore, another reaction pathway for the formation of these products must exist. Upon examination of other bond scission pairs, a discrepancy between bond C products, phenyl methyl naphthalene, which was observed, and ethylbenzene, which was not, was noted. Also, as stated, other products which can not be explained by one of the five bond scissions were observed, which leads to investigation of secondary pathways. These observations are consistent with a free radical ipso-substitution scheme for the formation of the various products as proposed by Walter et al. (1994). For example, attack by a benzyl radical of the NBBM molecule at the 1-naphthyl position would afford phenyl methyl naphthalene. This scheme would involve the formation of a mole of naphthalene and phenyl methyl naphthalene for every mole formed of methyl bibenzyl and its derivatives. This

comparison is presented in the plot of Figure 6. Likewise, various radical attack at bond C can explain the appearance of 1-(4-(4-methylphenylmethyl)benzyl) naphthalene, 1,4-(binaphthylmethyl) benzene, and 1-(phenylmethyl)-4-(naphthylmethyl) benzene. Overall, the main reaction families for NBBM pyrolysis are therefore bond thermolysis, hydrogen abstraction, radical ipso-substitution, β -scission, and radical recombination¹².

Reactions of binary mixtures of tetradecane and NBBM revealed interactions between the reactants and synergistic effects. As observed in Figure 2, tetradecane conversion was increased in the presence of NBBM, which can be rationalized in terms of kinetic coupling¹⁷. The internal carbon-carbon bonds of tetradecane have a higher bond dissociation energy (90 kcal mol⁻¹) than that of bond D in NBBM (60 kcal mol⁻¹)¹⁸. This has the potential to increase the quantity of radicals in the system with respect to the neat tetradecane experiments at a particular reaction time. The NBBM-derived radicals can easily abstract hydrogen from the secondary carbons of tetradecane, forming a tetradecane-derived radical and converting a tetradecane molecule, enhancing its conversion. Once formed, these tetradecane-derived radicals undergo their own decomposition reactions as observed for neat pyrolysis, and similar product yields are observed.

The interactions between NBBM and tetradecane can be further supported by examining the products derived from NBBM. Since abstraction of hydrogen from tetradecane is facile and has a high reaction path degeneracy of 24, NBBM radicals are capped and stabilized through this abstraction step before undergoing secondary reactions. This effect on the overall product yields can be discerned from Figure 7. The radicals formed from bond D thermolysis abstract hydrogen with higher selectivity and afford higher yields of toluene. Correspondingly, the selectivity to the radical ipso-substitution pathway and formation of phenyl methyl naphthalene is diminished. Therefore, it can be seen that during low pressure pyrolysis, favorable interactions between the two reactants exist. The effective tetradecane conversion is increased, and primary product selectivities are enhanced.

CONCLUSIONS

Recent investigations have demonstrated the feasibility coprocessing of coal with polymers. In this study, feedstock interactions were observed using model compound mimics of both coal and polyethylene. In binary mixtures, the conversion of tetradecane increased while the selectivity to primary products of NBBM pyrolysis was enhanced. These observations were attributed to the stabilization of NBBM-derived radicals through hydrogen abstraction from tetradecane which in turn, increases the rate of tetradecane conversion. In order to optimize the interaction between reactants, further experimental and theoretical studies will be conducted at high pressures and in the presence of catalysts in order to delineate the underlying kinetics, pathways, and mechanism controlling coal/polymer coprocessing.

ACKNOWLEDGMENTS

This work was supported by the United States Department of Energy Grant DE-FG22-96-PC96204.

REFERENCES

- 1-Rowatt, R.J., *Chemtech*, 1993, **23**, 56-60.
- 2-Taghei, M., Feng, Z., Huggins, F., and Huffman, G.R., *Energy & Fuels*, 1994, **8**, 1228-1232.
- 3-Menges, G., Emminger, H., and Lackner, G., *International Journal of Materials and Product Technology*, 1991, **6**, 307-330.
- 4-Graff, G., *Modern Plastics*, 1992, **69**, 45.
- 5-Fouhy, K., Kim, I., Moore, S., and Culp, E., *Chemical Engineering*, 1993, **100**, 30-33.
- 6-EPA, U.S. Environmental Protection Agency, 1992.
- 7-Anderson, L.L. and Tuntawiroon, W., *American Chemical Society, Division of Fuel Chemistry-Preprints*, 1993, **38**, 816-822.
- 8-Joo, H.K. and Curtis, C.W., *Energy & Fuels*, 1996, **10**, 603-611.
- 9-Farcasiu, M. and Smith, C., *Energy & Fuels*, 1991, **5**, 83-87.
- 10-Matson, D.W., Linahan, J.C., Darab, J. G., and Buehler, M. F., *Energy & Fuels*, 1994, **8**, 10-18.
- 11-Tang, Y. and Curtis, C.W., *Energy & Fuels*, 1994, **8**, 63.
- 12-Walter, T.D., Casey, S.M., Klein, M.T., and Foley, H.C., *Catalysis Today*, 1994, **19**, 367-380.
- 13-Rice, F.O., *Journal of the American Chemical Society*, 1933, **55**, 3035-3040.
- 14-Kossiakoff, A. and Rice, F.O., *Journal of American Chemical Society*, 1943, **65**, 590-595.
- 15-Voge, H.H. and Good, G.M., *Journal of American Chemical Society*, 1949, **71**, 593-597.
- 16-Mushrush, G. W. and Hazlett, R.N., *Industrial & Engineering Chemistry Fundamentals*, 1984, **23**, 288-294.
- 17-LaMarca, C., Libanati, C., and Klein, M.T., *Chemical Engineering Science*, 1990, **45**, 2059-2065.
- 18-Poutsma, M.L., *Energy & Fuels*, 1990, **4**, 113-131.

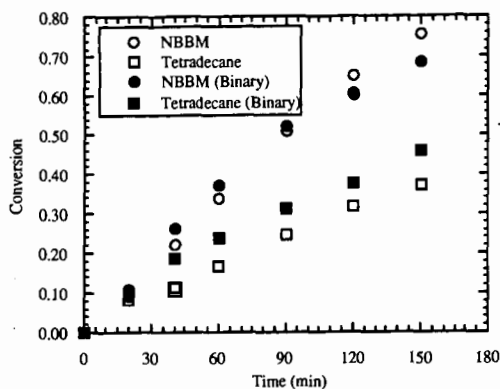


Figure 2: Conversion of tetradecane and NBBM, neat and in binary mixtures, at 420 °C.

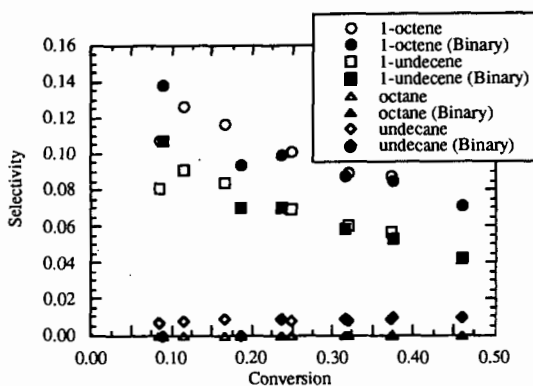


Figure 3: Comparison of alkane/alkene selectivities during neat and binary mixture reactions.

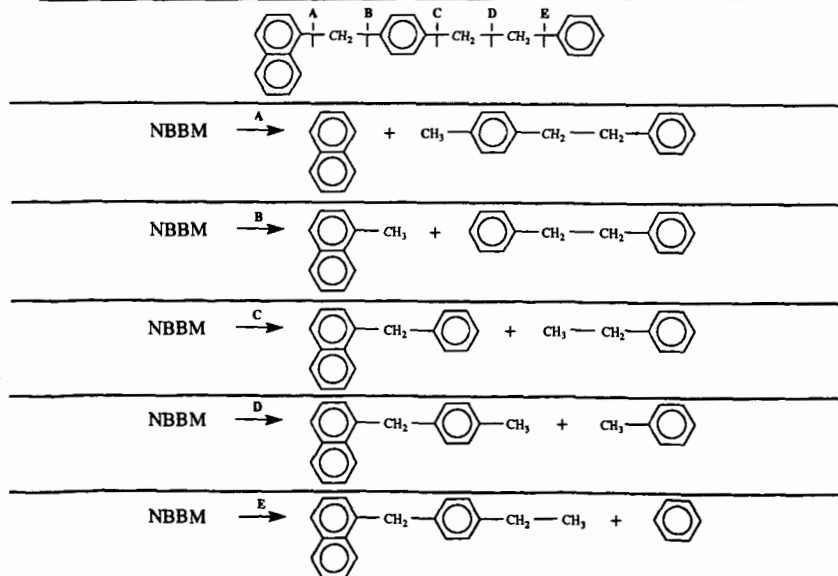


Figure 4: Bond assignment and corresponding products of NBBM pyrolysis, allowing for only bond fission, hydrogen abstraction, and β -scission.

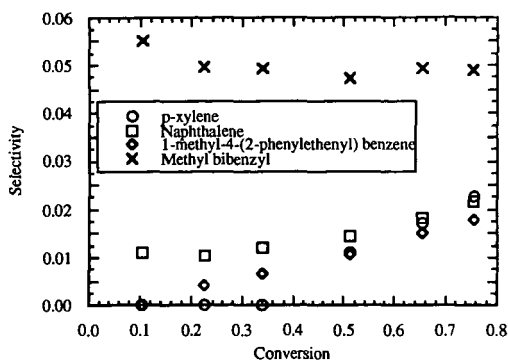


Figure 5: Comparison of selectivities of products associated with cleavage of bond A as a function of conversion.

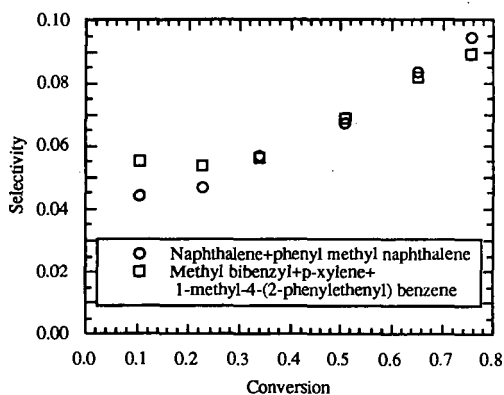


Figure 6: Comparison of products from free radical ipso-substitution reaction which accounts for cleavage of bond A.

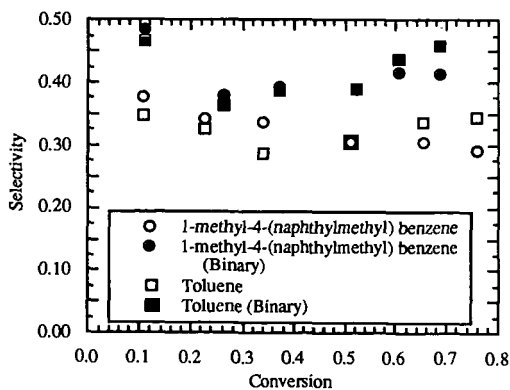


Figure 7: Comparison of products from bond D cleavage during neat NBBM and binary mixture reactions.

Catalysis of Arene Hydrogenation by Thermally Activated Silica

Todd Fields
Robert D. Guthrie
Venkatasubramanian K. Rajagopal
Department of Chemistry
University of Kentucky
Lexington, KY 40506

Burton H. Davis
Kentucky Center for Applied Energy Research
3572 Iron Works Pike, Lexington, KY 40511

Keywords: Hydrogen, Deuterium, Tetramethyl Orthosilicate, Diphenylmethane

INTRODUCTION

Silica has been used as a support material for a variety of catalysts, usually noble metals or transition metal oxides, for many years. Recent articles attest to its continued popularity.¹ For the most part, discussions of catalytic mechanisms have focussed on the metals and ignored the support.² Its role in these catalytic processes has usually been considered to be passive. It is often coated with various organic compounds for use as a chromatographic stationary phase, but even when the organic ligand is attached chemically, the silica itself is regarded essentially as an anchor.³ This has also been true for studies of thermolysis mechanisms where it was desired to immobilize organic substrates for comparison with naturally occurring nonvolatile materials such as coal.⁴ Studies in which silica-immobilized substrates have been heated under pressure of H₂ and D₂ have shown no special effects that might be attributed to catalytic involvement of the support.⁵

However, recent work by Bittner, Bockrath and Solar⁶ showed that fumed silica, after thermal activation above 330 °C under argon flow, will catalyze the reaction, H₂ + D₂ → 2 HD, at temperatures as low as 120 °C in a pulse-flow microreactor and will also catalyze the hydrogenation of ethene to ethane at 150 °C, producing ethane-d₄ when D₂ is used as a flow gas. This suggested that silica, by itself, could serve as a catalyst for hydrogenation reactions. Accordingly, we studied the reaction of thermally-activated, fumed silica and H₂ with selected alkenes in a static reactor and showed that it could function as a hydrogenation catalyst,⁷ allowing stilbene and other alkenes to be hydrogenated at temperatures at least 100 °C below those required for a purely thermal reaction. As part of that study, we also showed that hydrogenation of diphenylacetylene gave predominantly the thermodynamically less stable *cis* isomer of stilbene, demonstrating *syn* hydrogenation in a manner reminiscent of that observed with metal catalysts.⁸

We also reported our preliminary observation that under some circumstances aromatic ring reduction was catalyzed by thermally-activated, fumed silica, but noted that this behavior varied with the source of the particular fumed silica employed. We now wish to report experiments intended to probe this phenomenon and to offer possible explanations.

EXPERIMENTAL

Materials. Hydrogenation substrates were the best available commercial grade. Fumed silica was obtained both from Cabot Corporation (Cab-O-Sil grade M-5) or from Aldrich Chemical Co. (both 0.014 and 0.007 micron size were employed.) Several different lot numbers of Cabot silica were tried some were activatable for carrying out aromatic hydrogenations, others were not. The Aldrich silicas proved inactive unless treated with HCl as described below. Tetramethyl orthosilicate was purchased from Aldrich Chemical Co. It produced an activatable silica after hydrolysis as described below.

HCl Treatment of Fumed Silica. Approximately 800 to 900 mg of commercial fumed silica was allowed to stir for approximately 15 min in 50 mL of concentrated HCl. The resulting slurry was then separated by vacuum filtration through a 50 M fritted glass filter. This produced a dull white filter cake which was allowed to dry by passing a stream of air over the cake for roughly two hours, breaking the caked silica periodically with a glass rod. The cake was allowed to dry to a point where it could be transferred conveniently, usually weighing approximately 2 g at this point. This damp silica (ca. 1 g) was then transferred into the glass reactor tube, initially open at both ends. It was activated by passing argon over the material at 430 °C for 10 to 16 h. Following the thermal activation, the non-capillary end of the reactor was sealed. Solid substrates were introduced through the wide opening in the reaction tube before sealing. Liquid substrates were introduced by syringe after sealing.

Preparation of Silica by Hydrolysis of Tetramethyl Orthosilicate. Tetramethyl orthosilicate (2 mL) was added to approximately 50 mL of deionized water. The mixture was allowed to stand at approximately 25 °C for 10 to 16 h. The resultant brittle cake was broken up with a glass stirring rod and dried in a stream of air as described for hydrolyzed fumed silica. This produced approximately 1 g of silica which was reduced to 800 mg after activation. In some experiments, the tetramethyl orthosilicate was treated with aqueous HCl prepared by passing gaseous HCl into deionized water. Treatment with aqueous HCl produced a solid gel immediately.

Hydrogenation Procedure. Reactions were carried out in glass bulbs of approximately 12 mL volume with a 16 cm section of 1 - 2 mm capillary attached to one end. The procedures for activating the catalyst, loading the reactors and carrying out the reactions have been described in earlier publications.⁷

Workup Procedures. In some cases, reaction vessels were cracked open and the silica hydrolyzed as described earlier. In others, products were removed by distillation at pressures of less than 0.1 Torr into a liquid nitrogen-cooled trap. Reaction products were combined with a measured volume of standardized biphenyl or naphthalene solution in CH_2Cl_2 then analyzed by gas chromatography (GC) and gas chromatography-mass spectrometry (GC/MS). Recoveries were generally greater than 90 % based on response factors estimated from carbon numbers or standard mixtures when available.

RESULTS AND DISCUSSION

In our previous papers⁷ we reported that fumed silica which was activated by heating under argon flow at 350 °C promoted the hydrogenation of diphenylethane (DPE) to a mixture of cyclohexylphenylethane (CPE) and dicyclohexylethane (DCE). When the reaction was carried out using D_2 the products were highly deuterated, with the CPE showing ions of mass d_6 to d_{18} with maximum intensity at d_{11} , and the DCE showing ions of mass d_{12} to d_{26} with maximum intensity at d_{19} . Using the same silica samples, naphthalene was hydrogenated to less than 2% conversion. Moreover, inclusion of naphthalene along with DPE prevented hydrogenation of DPE. During the course of these experiments, we exhausted our bottle of fumed silica and found that a new sample, obtained from the same supplier, but displaying a different lot number, used in the same procedure, failed to promote hydrogenation of DPE. Subsequent experiments showed that some fumed silica samples worked and some did not. Samples obtained from a second supplier in two different particle sizes also failed to promote the reaction. For reasons which may or may not explain the effect of the procedure, we tried treating the ineffective samples with concentrated HCl prior to thermal activation. This procedure had the desired effect in that the resultant samples promoted hydrogenation of DPE.

We then determined the effect of the various silicas on the reaction of H_2 with diphenylmethane. The products of this reaction are shown in Figure 1 and yields are listed in Table I. It will be noted that the variability observed for DPE with different silica sources is also observed with DPM. In an attempt to rule out trace metal contamination as a source of the differing catalytic activities, some of the silicas were subjected to ICP (inductively coupled plasma) analysis. The results are listed in Table II. We would suggest that the values determined, which generally border on the limits of experimental detection, are not sufficiently different for these samples to explain their differing effectiveness in promoting the hydrogenation of DPM. Data for the two ineffective silicas (C2 and A1) do not differ in any systematic way from the data for C1 and C3.

In the absence of a catalytic contaminant, we must tentatively conclude that structural differences within the silica matrix are responsible for differing catalytic effectiveness. As in the DPE reaction, treatment of inactivatable silica with concentrated HCl prior to the thermal activation process has the effect of producing an activatable catalyst (compare entries 5 and 6 in Table I). No chlorinated products were detected when HCl-treated silica was used for hydrogenations and it is therefore hypothesized that the effect of the HCl treatment is to disrupt the silica matrix such that subsequent thermal dehydration can produce sites which are catalytic for the hydrogenation. Thermal dehydration of fumed silica has been recently studied by NMR which showed that hydrogen bonded surface silanols are gradually reduced in number.⁹ In our case, it is suspected that the disruption and dehydration is promoted by HCl during the thermal activation stage rather than during the HCl treatment itself because thorough water washing of the HCl-treated material prior to heating precludes activation as shown by entry 7 in Table I.

To provide further evidence that silica itself is responsible for promotion of arene hydrogenation, silica samples were prepared by hydrolysis of tetramethyl orthosilicate ($\text{Si}(\text{OCH}_3)_4$) using deionized water alone and with deionized water containing HCl (see Experimental). Both treatments produced thermally activatable silicas as shown by entries 8 and 9 in Table I. Having established that treatment of 0.014 micron fumed silica with aqueous HCl followed by thermal

Table I. Yields of Products from Treatment of Diphenylmethane DPM with H₂ (14 MPa) in the Presence of Various Thermally-Activated Fumed Silicas.

Silica Type	Products (%)				
	CPM	DCM	PhMe	CMe	PhH
C1 ^a	39	12	n.d. ^f	n.d. ^f	n.d. ^f
C2 ^a	3	0.3	n.d. ^f	n.d. ^f	n.d. ^f
C3 ^a	31	11	0.24	<0.1	0.24
A1 ^b	1.1	0.2	0.15	0.14	0.14
A2 ^b	2.7	0.4	0.16	<0.1	0.16
A2 (HCl) ^c	25	54	0.2	0.2	0.4
A2 (HCl/H ₂ O) ^d	4.7	<0.1	0.3	<0.1	0.1
TMS (H ₂ O) ^e	12	62	0.25	0.6	0.7
TMS (HCl) ^e	28	60	0.3	1.0	1.0

Notes for Table I: ^a C1, C2 and C3 are Cabot Grade M5 (0.014 micron) fumed silicas having different lot numbers. ^b A1 is Aldrich 0.007 micron fumed silica; A2 is Aldrich 0.014 micron fumed silica. ^c A2 (HCl) is Aldrich 0.014 micron fumed silica treated with concentrated HCl as described in the experimental section. ^d A2 (HCl/H₂O) is the same as A2 (HCl) except for being washed with water to neutral pH before thermal activation. ^e TMS (H₂O) is silica produced by hydrolysis of tetramethyl orthosilicate with deionized water. TMS (HCl) is the same with HCl added. ^f Not determined.

Table II. Trace Metal Content of Silicas used for the Hydrogenation of DPM in Table I.

Silica Type ^a	Metal Content (ppm)						
	Ca	Cr	Co	Cu	Fe	Mn	Ni
C1	<30	5	<4	16	30	<2	15
C2	200	3	<4	28	68	<2	38
C3	60	<2	<4	20	67	<2	15
A1	<30	<2	6	20	40	<2	<3

^a See notes for Table I.

activation produces an active catalyst for the hydrogenation of DPE and DPM, we reexamined the reaction of naphthalene. Results for this and other substrates are shown in Figure II. As before, only a small conversion (4%) to tetralin could be accomplished either with A2 (HCl) or with TMS (H₂O). Biphenyl was also resistant but toluene showed substantial reaction. Chloronaphthalene gave a 22% yield of naphthalene with silica A2 under the same conditions.

CONCLUSIONS

The pattern which is emerging from these studies shows that when silica possesses the proper structural characteristics, the nature of which are unknown at the present time, it can then be converted by heating at 350 °C to a form which will catalyze the hydrogenation of certain arenes. Some commercial fumed silicas work, others do not. Those that do not work benefit from treatment with aqueous HCl prior to thermal activation. One commercial sample which was ineffective in the DPM reaction also refused activation to promote the H₂ + D₂ - HD reaction in a pulsed microreactor. HCl treatment remedied this situation. Silica prepared from hydrolysis of Si(OMe)₄ with pure water proved an effective catalyst after heating. We have found that arenes which are most extensively hydrogenated are those with benzylic C-H groups, DPE, DPM, or PhMe. Naphthalene, which should be easier to hydrogenate in the thermodynamic sense, gave only a few percent conversion under the same conditions and seemed to poison the surface toward reactions with arenes which could be hydrogenated in its absence. As a working hypothesis, we suggest that silicas with appropriate structural features, promote isomerization of alkyl arenes to cyclic polyenes

which are then rapidly reduced. This scheme is shown in Figure I. With DPM, a small but significant amount of hydrocracking is also observed. We suggest that this is a high-temperature, alternate route for partially hydrogenated intermediates as shown in Figure I. Preliminary results indicate that hydrocracking is the major reaction outcome when DPM is treated with H_2 and silica at 450 °C.

ACKNOWLEDGMENTS

T. F. thanks Kentucky DOE EPSCoR for a traineeship as part of DE-FCO2-91ER75661. We thank Drs. B. C. Bockrath and E. W. Bittner for assistance in pulse microreactor experiments.

REFERENCES

1. (a) Kiviaho, J.; Hanaoka, T.; Kubota, Y.; Sugi, Y. *J. Mol. Catal.* **1995**, *101*, 25-31. (b) Tsubokawa, N.; Kimoto, T.; Endo, T. *ibid.* **1995**, *101*, 45-50. © Drelinkiewicz, A. *ibid.* **1995**, *101*, 61-74. (d) Startsev, A. *Cat. Rev. -Sci. Eng.* **1995**, *37*, 353-424. (g) Morys, P.; Schlieper, T. *J. Mol. Catal., A* **1995**, *95*, 27-34. (h) Voyatzis, R.; Mofat, J. B. *Energy and Fuels* **1995**, *9*, 240-247.
2. See for example, Bond, G. C. *Accts. Chem. Res.* **1993**, *26*, 490-495 and references therein.
3. (a) Vranken, K. C.; VanDerVroot, P.; Posseiers, K.; Bansant, E. F. *J. Coll. Interfac. Sci.* **1995**, *174*, 86-91. (b) Piers, A. S.; Rochester, C. H. *ibid.* **1995**, *174*, 97-103. © Kamagawa, K.; Yoshica, H. *ibid.* **1995**, *172*, 94-97.
4. (a) Buchanan, A. C., III; Dunstan, T. D. J.; Douglas, E. C.; Poutsma, M. L. *J. Am. Chem. Soc.* **1986**, *108*, 7703-7715. (b) Buchanan, A. C., III; Britt, P. F.; Biggs, C. A. *Energy and Fuels* **1990**, *4*, 415-417. © Buchanan, A. C., III.; Biggs, C. A. *J. Org. Chem.* **1989**, *54*, 517-525. © Britt, P. F.; Buchanan, A. C., III *J. Org. Chem.* **1991**, *56*, 6132-6140.
5. Guthrie, R. D.; Ramakrishnan, S.; Britt, P. F.; Buchannan, A. C. III; Davis, B. H. *Energy and Fuels* **1995**, *9*, 1097-1103.
6. Bittner, E. W.; Bockrath, B. C.; Solar, J. M. *J. Catal.* **1994**, *149*, 206
7. (a) Rajagopal, V. K.; Guthrie, R. D.; Fields, T.; Davis, B. H. *Catalysis Today* **1996**, *31*, 57-63. (b) Rajagopal, V. K.; Guthrie, R. D.; Davis, B. H. *Prep. Pap. - Am. Chem. Soc. Div. Fuel Chem.* **1995**, *40*, 945-949.
8. (a) Campbell, K. N.; Campbell, B. K. *Chem. Rev.* **1942**, *31*, 77. (b) Farkas, A.; Farkas, L. *Trans. Faraday Soc.* **1937**, *33*, 837. © Ott, E.; Behr, A.; Schroter, R. *Chem. Ber.* **1928**, *61*, 2124. (d) Wessely, F. V.; Welleba, H. *Chem. Ber.* **1941**, *74*, 777.
9. Liu, C. C.; Maciel, G. E. *J. Am. Chem. Soc.* **1996**, *118*, 5103-5119.

Figure I

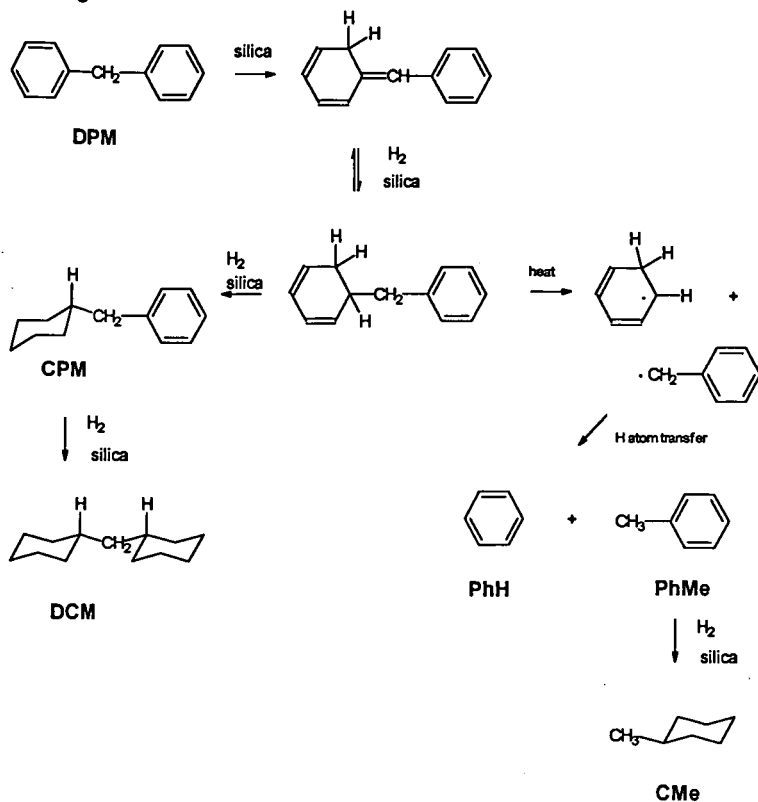
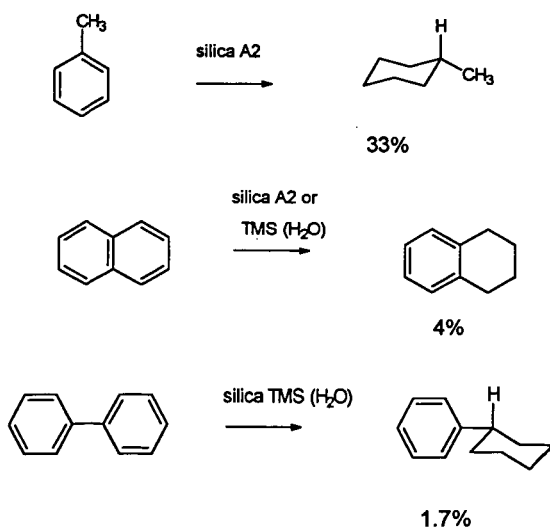


Figure II



HYDRODESULFURIZATION OF THIOPHENIC COMPOUNDS ON MoS₂: A COMPUTATIONAL STUDY USING ZINDO

Xiaoliang Ma and Harold H. Schobert
Fuel Science Program, Department of Materials Science and Engineering
The Pennsylvania State University, 209 Academic Projects Building,
University Park, PA 16802-2303

Keywords: hydrodesulfurization, MoS₂ catalyst, computation

INTRODUCTION

To meet environmental regulations on reduction of sulfur content in fuels there has been a growing need to develop new catalysts that can carry out deep hydrodesulfurization (HDS). MoS₂ and sulfided Co (or Ni) promoted molybdenum catalysts have been used extensively in HDS, both in basic investigations and in petroleum refineries. However, the nature of the active sites, even on a single slab of MoS₂, as well as how they interact with sulfur species are still unclear. Considerable effort has been devoted to understanding the active sites of MoS₂ crystal and their HDS mechanisms. Some excellent reviews have been published in this regard (1-3). Since it is still difficult technically to characterize the chemical properties of the MoS₂ surface, some researchers have done chemical simulations or calculations in order to understand the active sites on the surface of MoS₂ catalyst and their interaction with sulfur species. Most of them used smaller clusters as a model, the classical Newtonian physics method (molecular mechanics) or the extended Hückel molecular orbital method which is an empirical approximation (4-9). The nature of the active sites and mechanisms of reaction suggested by the results were very different among these various studies.

In this study, we used a semi-empirical quantum chemical method, ZINDO (Zerner's Intermediate Neglect of Differential Overlap program), and chose a single slab of regular hexagonal Mo₁₂S₃₈ as a basic model to examine possible active sites or active edges by removing the sulfur atoms from the periphery of Mo₁₂S₃₈ cluster on the basis of their bond orders and required energy. Furthermore, the interaction of inferred active sites with the sulfur species was explored by comparison of the total energies of different adsorption states. We attempt to answer 1) which positions at MoS₂ crystal are easier to form the sulfur vacancies, or which edge in a single slab of MoS₂ is easier to form a sulfur poor edge; and 2) how such sulfur vacancies or sulfur poor edge interact with thiophenic compounds.

MODELING AND COMPUTATION

In order to make the cluster of MoS₂ be a more realistic mimic of highly dispersed MoS₂ particles, we designed a single slab of regular hexagonal Mo₁₂S₃₈ as a basic model cluster, which contains 12 Mo and 38 S atoms as shown in Figure 1. There are two types of edge plane, as noted by I (1010) and II (1010) respectively. Each S atom in the edge I plane bonds with only one Mo atom, and each S atom in the edge II plane bonds with two neighboring Mo atoms. In this cluster, the S/Mo ratio is not stoichiometric. To keep the S/Mo ratio around 2 and to form the sulfur vacancies, the sulfur atoms at the periphery of the cluster should be removed. Reasonable positions of the sulfur vacancies and the sulfur-poor edge were determined by comparison of the charge distribution, bond indexes in the Mo₁₂S₃₈ cluster, and the total energy of the clusters with sulfur vacancies. The adsorption configuration of sulfur species on the formed sulfur vacancies was examined by locating the sulfur atom of a sulfur species at an appointed sulfur vacancy. The adsorption state was explored by comparison in the total energy of compound-cluster system.

The Mo—Mo, Mo—S and S—S bond lengths were determined according to MoS₂ crystal size from the literature (4, 6). The geometries of the sulfur species were optimized by using ZINDO before locating them at the sulfur vacancies. The calculation of charge distribution, bond order and the total energy of the clusters and compound-cluster was done without geometry optimization.

All quantum chemical calculation in this study was done by using ZINDO, which was developed by the University of Florida Quantum Theory Project. ZINDO uses the theoretically based INDO parameterization and therefore can use d orbitals, and then can be used for many transition series metals (10).

RESULTS AND DISCUSSION

1) Electronic properties of Mo₁₂S₃₈ cluster. According to their different positions, the sulfur atoms in Mo₁₂S₃₈ cluster can be classified into five types which are labeled with a, b, c, d and e, respectively, as shown in Figure 1. Each sulfur atom on the corner (position b) and in the edge plane I (position a) is bonded to one Mo atom, and each sulfur atom in the edge plane II (position c) is bonded to two Mo atoms. All sulfur atoms in the basal plane are connected with three Mo atoms. The Mo atoms sandwiched between the top and bottom basal planes in the cluster can also

be classified into three types on the basis of their positions, which are labeled with α , β and γ , respectively.

The calculated results of charge distribution and bond index of $\text{Mo}_{12}\text{S}_{36}$ cluster are listed in Table 1 and 2, respectively. The results show that the charge distribution is strongly dependent on the atomic position in the cluster. S(b), the sulfur located at the position *b*, has the least negative charge in all of S atoms, being -0.486. S(a) located in the position *a* has the second least negative charge. As connected with two Mo atoms, S(c) has larger negative charge although it is located in a edge plane. The sulfur atoms in the two basal planes, S(d) and S(e), have the largest negative charge among the five types of the sulfur atoms, due to their bonding with three Mo atoms. Such charge distribution suggests that S(b) and S(a) atoms have less interaction with the cluster whole than that of S(c) atoms.

With the bond indexes listed in Table 2, it was found that all bond indexes between neighboring S and Mo atoms are higher than 0.8, indicating that there is a strong interaction between neighboring S and Mo atoms, and the atoms in MoS_2 lattice are held together dominantly through such bonding. There is also considerable interaction between two neighboring Mo atoms, their bond indexes being in the range 0.18–0.31. Most pairs of two neighboring S atoms show weak interactions, with the exception of S(a)—S(a') and S(b)—S(b') bonds. In this study, our interest is focused on the sulfur atoms at the periphery of the cluster. The S(c)—Mo(β) bond index is 1.023, lower than those of S(a)—Mo(α) (1.248) and S(b)—Mo(β) (1.158). However, the S(c) atom is connected simultaneously with two Mo(β) atoms, and the sum of the two bond indexes is as high as 2.046. The results indicate that S(a) and S(b) atoms are the easier to be removed than an S(c) atom during the formation of the sulfur vacancies, which is in agreement with the charge distribution as stated above. The calculation of the total energy of the cluster with a sulfur vacancy at the position *a*, *b* and *c*, respectively, was also done, and the results show that the cluster with S(b) vacancy has the lowest energy, while the cluster with S(c) vacancy has the highest energy in three types of the sulfur atoms. These results further support the point that the sulfur vacancies formed should be on the corner and the edge plane 1.

2) *Adsorption of sulfur species on sulfur vacancies.* In order to examine the interaction of sulfur species with the sulfur vacancies, we chose Mo(α) in the $\text{Mo}_{12}\text{S}_{36}$ cluster with six sulfur vacancies at the edge plane 1 as an active adsorption site, and assume that the sulfur atom of sulfur species is adsorbed at the position *a*. Considering atom limit and CPU in the calculation, a smaller cluster Mo_6S_{24} as shown in Figure 2A was designed to replace the $\text{Mo}_{12}\text{S}_{36}$ cluster used above for the compound-cluster adsorption model. The reasonableness for such replacement is based on the consideration that 1) the edge in Mo_6S_{24} cluster has the same structure as the edge plane 1 in $\text{Mo}_{12}\text{S}_{36}$ cluster; and 2) the calculated charge distribution in the edge plane of Mo_6S_{24} cluster shows it is similar to that in the edge plane 1 of $\text{Mo}_{12}\text{S}_{36}$ cluster. The structure of Mo_6S_{18} cluster, which is derived from Mo_6S_{24} cluster by removing six sulfur atoms in an edge plane, and the thiophene- Mo_6S_{18} adsorption are shown respectively in Figure 2B and 2C. The change in the total energy of the thiophene- Mo_6S_{18} with the angle included between thiophenic plane and the edge plane are listed in Table 3. It was found that the thiophene- Mo_6S_{18} has the least energy at 0° angle, meaning that a parallel adsorption as shown in Figure 3A is the most stable. The same results were also observed when replacing the adsorbate on Mo_6S_{18} cluster with dibenzothiophene. Two other adsorption configurations, as shown in Figure 3B and 3C, respectively, were also calculated, and both have higher total energy than that of the parallel adsorption. The calculated results suggest that thiophene and dibenzothiophene are adsorbed on the exposed Mo(α) atom not only through a S—Mo(α) bond but also through a bond between π electrons on the thiophenic ring and Mo(α) atom. The parallel adsorption of such sulfur compounds on the exposed Mo(α) atom is the most stable in the all adsorption cases addressed in this study.

REFERENCES

1. Startsev, A. N. *Catal. Rev. Sci. Eng.* **1995**, 37, 353-423.
2. Portela, L.; Grange, P. and Delmon, B. *Catal. Rev. Sci. Eng.* **1995**, 34, 699-731.
3. Vasudevan, P. T. and Fierro, J. L. G. *Catal. Rev. Sci. Eng.* **1996**, 38, 161-188.
4. Joffer, J.; Geneste, P. and Lerner, D. A. *J. Catal.* **1986**, 97, 543-548.
5. Pis Diez, R. and Jubert A. H. *J. Mol. Structure (Theochem)* **1990**, 210, 329-336.
6. Chen, R. and Xin, Q. *J. Mol. Catal.* **1991**, 64, 321-335.
7. Daage, M. and Murray, H. H. Preprints, Symposium on the Mechanism of HDS/HDN Reactions, 206th National Meeting, Am. Chem. Soc. Chicago, IL, August, **1993**, 660-664.
8. Smit, T. S. and Johnson, K. H. *Chem. Phys.* **1993**, 212, 525-533.
9. Diemann, E.; Weber, Th. and Müller, A. *J. Catal.* **1994**, 148, 288-303.
10. Pople, J. A. and Beveridge, D. L. *Approximate Molecular Orbital Theory*, McGraw-Hill, New York, 1970.

Table 1 Charge distribution in $\text{Mo}_{12}\text{S}_{38}$ cluster

Atom	Charge
Sulfur	
a	-0.550
b	-0.486
c	-0.733
d	-0.748
e	-0.808
Molybdenum	
α	+2.095
β	+2.173
γ	+1.609

Table 3 Total energy of compound- Mo_6S_{18} at different included angle θ

Included angle θ°	Total energy (a.u.*)	
	thiophene	dibenzothiophene
0	-275.53	-330.49
45	-273.65	-325.89
90	-273.00	
135	-272.90	

* atomic units

Table 2 Bond index in $\text{Mo}_{12}\text{S}_{38}$ cluster

S-Mo bond	bond index	Mo-Mo bond	bond index	S-S bond	bond index
S(a)-Mo(α)	1.248	Mo(α)-Mo(β)	0.185	S(a)-S(b)	0.153
S(b)-Mo(β)	1.158	Mo(α)-Mo(γ)	0.296	S(a)-S(d)	0.060
S(c)-Mo(β)	1.023	Mo(β)-Mo(β)	0.232	S(b)-S(c)	0.068
S(d)-Mo(α)	0.815	Mo(β)-Mo(γ)	0.302	S(b)-S(d)	0.057
S(d)-Mo(β)	0.844	Mo(γ)-Mo(γ)	0.308	S(a)-S(a')	0.206
S(d)-Mo(γ)	0.826			S(b)-S(b')	0.738
S(e)-Mo(γ)	0.836			S(c)-S(c')	0.094

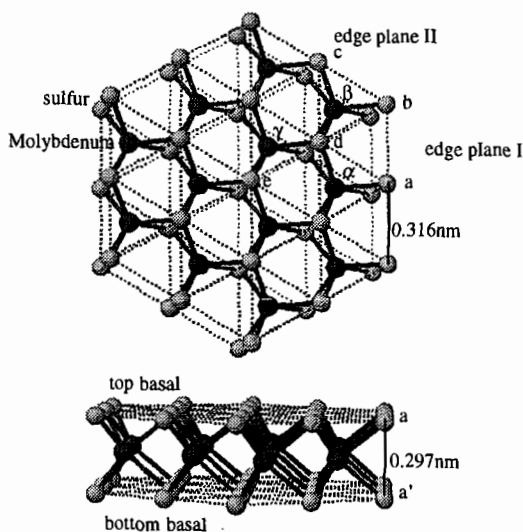


Figure 1 Schematic diagram of $\text{Mo}_{12}\text{S}_{38}$ cluster

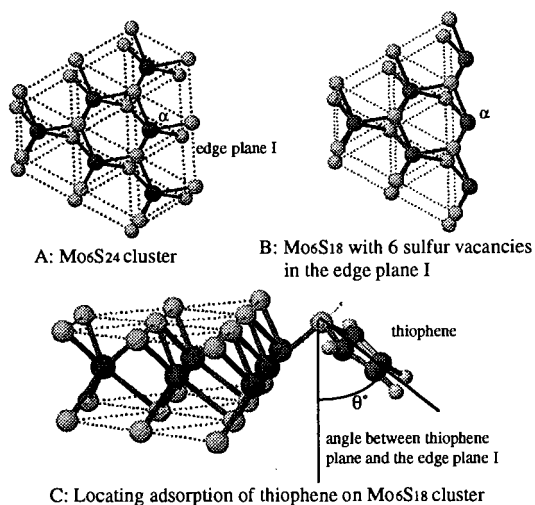


Figure 2 Schematic diagrams of Mo₆S₂₄ and thiophene-Mo₆S₁₈

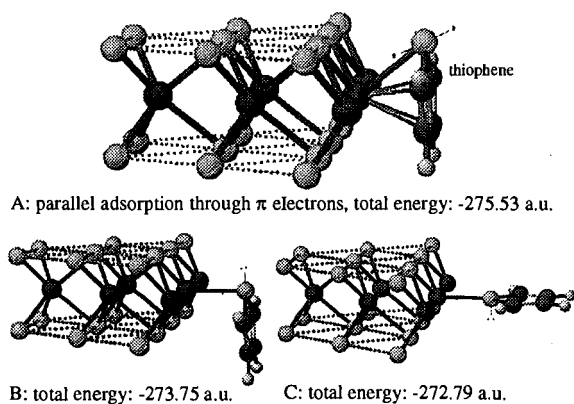


Figure 3 Different adsorption states of thiophene on sulfur poor edge of Mo₆S₁₈

PROMOTING EFFECT OF WATER ON IN-SITU GENERATED MoS₂ CATALYST FOR HYDROGENATION AND C-O BOND CLEAVAGE OF DINAPHTHYL ETHER

Yoshiharu Yoneyama and Chunshan Song*
Fuel Science Program and Laboratory for Hydrogenation Process Chemistry,
The Pennsylvania State University,
209 Academic Projects Building, University Park, PA 16802

Keywords: hydrogenation, MoS₂ dispersed catalyst, water

INTRODUCTION

In our recent work, we found a strong promoting effect of water on low-severity catalytic coal liquefaction using molybdenum sulfide catalyst in-situ generated from ammonium tetrathiomolybdate (ATTM): addition of H₂O to the run using ATTM as a catalyst precursor increased the conversion of Wyodak coal at 350 °C from 29.5 to 66.5 wt% [1]. Initially, this strong promoting effect of water was surprising to us, because it has been shown that better drying method for moisture removal results in higher coal conversion in catalytic liquefaction using molybdenum sulfide catalyst [2]. It was also observed that addition of water to catalytic coal hydroliquefaction has negative effect [3-5]. On the other hand, water addition to non-catalytic coal conversion reactions and some model reactions has been shown to have positive impacts [6-10]. More recently, it has been reported that ether compounds such as 1-phenoxy-naphthalene and 9-phenoxyphenanthrene cleave in water at 315 °C, and this cleavage is enhanced at higher temperature; since water becomes a stronger acid as temperature increased, this cleavage reaction was shown to proceed through ionic process [9,10].

In the present study, in order to clarify the role of water in catalytic hydroliquefaction of coal, we carried out hydrogenation and hydrogenolysis of 2,2'-dinaphthyl ether (DNE) using ATTM as a catalyst precursor in the absence and presence of H₂O or D₂O. There are many connecting linkages in coal structures; the aromatic C-O and aromatic-aliphatic C-C bonds are believed to be important linkages between aromatic moieties of coal structures. Therefore, in order to increase the conversion of coal to liquids, it is necessary to cleave these connecting linkages. Coal structures have not been clarified at the molecular level. The use of coal-related model compounds is suitable for understanding fundamental chemistry. The products from the hydrogenation of model compounds can be easily identified by GC/MS. DNE has been shown to be thermally unreactive in the absence of catalyst, but its conversion is enhanced by some metal sulfide catalyst [11]. Here we used DNE to investigate the effect of the addition of water on cleavage of ether-linkages and on hydrogenation of aromatic rings using ATTM under the conditions of coal liquefaction.

EXPERIMENTAL

Catalyst Precursor

Ammonium tetrathiomolybdate (ATTM) was purchased from Aldrich, and 2,2'-dinaphthyl ether (DNE) from TCI America. ATTM and DNE were used without further purification. It was noted in previous work in this laboratory that long-time storage of ATTM in reagent vials in air may lead to degradation of the reagent, which results in deviations in the observed activity of in-situ generated MoS₂ catalyst from different bottles of ATTM reagent. In this work, a bottle of newly purchased ATTM was used in all the experiments on DNE runs, and the reagent bottle was stored in a refrigerator in order to minimize oxidative degradation.

Model Compound Reactions

A horizontal tubing bomb microautoclave reactor with a capacity of 25 mL was loaded with ca. 0.216 g DNE, 1 wt% catalyst precursor (1 wt% Mo based on DNE) and 1.47 g solvent (n-tridecane). When water was added, the weight ratio of H₂O to DNE was 0.56, unless otherwise mentioned. The reactor was purged four times with H₂ and then pressurized with 6.9 MPa H₂ at room temperature for all experiments. A preheated fluidized sand bath was used as the heating source, and the horizontal tubing bomb reactor was vertically agitated to provide mixing (about 240 strokes/min). After the reaction the hot tubing bomb was quenched in a cold water bath. The contents were washed out with 30-40 mL acetone, and filtered through a low speed filter paper for subsequent GC analysis of the filtrate. Two-step reaction was also carried out in a similar manner as described above, except that the active MoS₂ catalyst was prepared first using ATTM with and without H₂O in the first-step reaction, and subsequently, the reactor was opened, and DNE was then added into the reactor. DNE was treated with and without H₂O in the second-step reaction.

The products were identified by GC-MS using a Hewlett-Packard 5890 II GC coupled with a HP 5971 A mass-selective detector operating at electron impact mode (EI, 70 eV). The column used for GC-MS was a J&W DB-17 column; 30-m x 0.25-mm, coated with 50% phenyl 50% methylpolysiloxane with a coating film thickness of 0.25 µm. For quantification, a Perkin Elmer 8500 GC with flame ionization detector and the same type of column (DB-17) was used. Both GC

* Corresponding author. E-mail: csong@psu.edu; Fax: 814-865-3075; Tel: 814-863-4466

and GC-MS were programmed from 80 to 280 °C at a heating rate of 4 °C/min and a final holding time of 8 min. The response factors for 5 of the products were determined using pure compounds.

RESULTS AND DISCUSSION

One-Step Reaction

Table 1 shows the results of non-catalytic and catalytic runs of DNE with in-situ generated dispersed MoS₂ catalyst at 350, 375 and 400 °C. Without ATTM, the conversions of DNE are very low, even at 400 °C. Adding water alone seems to inhibit the conversion of DNE completely. However, in the presence of ATTM conversions are significant. An addition of water to the runs with ATTM substantially increases the conversion of DNE. Upon addition of water to the catalytic runs, the conversion of DNE increases from 46.0 % to 83.8 % at 350 °C. The principal products are tetralin, naphthalene, 2-naphthol, 5, 6, 7, 8-tetrahydro-2-naphthol, octahydroDNE, and tetrahydroDNE. Formation of these products suggests that both the ether linkage cleavage reaction and hydrogenation of aromatic rings occur simultaneously. Because the yields of tetralin are higher for the runs with added water than for those without water, the hydrogenation of aromatic ring prevails in the run with water and ATTM.

In order to clarify the role of water, DNE was hydrogenated with ATTM and D₂O. Because some aryl ethers cleave in H₂O at high temperature above 315 °C through ionic mechanism [9,10], this ionic effect of H₂O on the cleavage of C-O bond in DNE is investigated. Even though water alone has inhibition effect on conversion of DNE as described above. Table 2 represents the results of catalyst run of DNE with dispersed catalysts and H₂O or D₂O at 350, 375 and 400 °C. Comparing the results using H₂O and D₂O, the conversions of DNE are almost the same in each pair of corresponding runs. There are no apparent isotopic effect on the conversion of DNE and the yields of the products. The results of GC/MS analysis indicate that the products and recovered DNE contain a few deuterium atom, and the fragmentation of mass spectra of the products indicate that deuterium atoms are introduced into the products unselectively. These results show that the hydrogen from water has a little effect on the conversion of DNE. In other words, we have found no clear evidence that H₂O enhanced ether bond cleavage: the ionic effect of water on cleavage of ether-linkage in DNE is not significant, under the conditions employed.

Two-Step Reaction

As shown in Tables 1 and 2, the conversion of DNE increases with an addition of water. In order to further clarify the role of addition of water on the hydrogenation of DNE, two-step reaction was carried out. In the first-step, the Mo sulfide catalyst was prepared from decomposition of ATTM in the presence and the absence of water at 350, 375 and 400 °C under hydrogen pressure for 30 min. Subsequently the reactor was quenched, vented, and opened to allow the loading of DNE followed by purge and repressurization with H₂. The hydrogenation of DNE, as the second-step, was carried out with and without H₂O at 350 °C under hydrogen pressure for 30 min. Table 3 shows the results of the two-step reactions. Using the catalyst prepared from ATTM alone at 350, 375 and 400 °C, the conversions of DNE are almost the same at 64-67 %: the activities of the catalysts are very similar. However, highly active catalysts are generated from ATTM with added H₂O, the conversion of DNE is the largest at 375 °C: the catalyst prepared at 375 °C is most active. This finding corroborates with our previous results on coal liquefaction [12]. After the preparation of catalyst, the addition of water decreases the conversion of DNE. For example the conversion of DNE decreased from 64.4 % to 32.9 % at 350 °C (first-step) after the addition of water to the second-step run. In addition, after the preparation of catalyst from ATTM and water at 350 °C complete removal of water caused about 100 % conversion of DNE at 350 °C at the second-step. These results suggest that water itself does not have promoting effect on hydrogenation of DNE, but that it is effective for the preparation of active catalyst for hydrogenation and bond cleavage of DNE.

Effect of H₂O/DNE Ratio

In the test discussed above, the weight ratio of H₂O/DNE was maintained at 0.56 for the determination of role of water addition on hydrogenation of DNE. We have also attempted to determine the optimum amount of added water. This was done by examining the relationship between the conversion of DNE and amount of added D₂O. Figure 1 shows the relationship between the amount of D₂O added and the conversion of DNE from the runs at 350 °C for 30 min. The conversions of DNE gradually increase from 46 % to 100% with increasing water amount from 0 to 0.2 g corresponding to a D₂O/DNE weight ratio of about 0.93, and they decrease from 100% to 60 % with further addition of water. These results also clearly indicate that 0.026 of the ratio of ATTM to D₂O is optimum for conversion of DNE under the conditions employed. It seems that since water is used for the preparation of effective catalyst from ATTM for hydrogenation and bond cleavage of DNE, the conversion of DNE is large up to 0.235 g of D₂O. However water itself has a negative effect for the hydrogenation of DNE, further additions of D₂O over 0.235 g seem to cause the decrease of the conversion of DNE.

CONCLUSION

A proper amount of added water has a strong promoting effect on hydrogenation and hydrogenolysis of DNE using molybdenum sulfide catalyst in-situ generated from ATTM. We have found that the addition of water is not effective for DNE conversion, but is effective for the preparation of active catalyst from ATTM for hydrogenation and hydrogenolysis of DNE.

ACKNOWLEDGMENTS

We are most grateful to Prof. Harold H. Schobert for his encouragement, support, and many helpful discussion. This work was supported partially by the U. S. Department of Energy, Pittsburgh Energy Technology Center under contract No. DE-AC22-92PC92122.

REFERENCES

- 1 C. Song and A. K. Saini, *Energy Fuels*, **9**, 188 (1995)
- 2 F. J. Derbyshire, A. Davis, R. Lin, P. G. Stansberry, and M. -T. Terror, *Fuel Process. Technol.*, **12**, 127 (1986)
- 3 Y. Kamiya, T. Nobusawa and S. Futamura, *Fuel Process. Technol.*, **18**, 1(1988)
- 4 B. C. Bockrath, D. H. Finseth and E. G. Illig, *Fuel Process. Technol.*, **12**, 175 (1986)
- 5 J. A. Ruether, J. A. Mima, R. M. Kornosky, and B. C. Ha, *Energy Fuels*, **1**, 198(1987)
- 6 R. A. Graff and S. D. Brandes, *Energy Fuels*, **1**, 84 (1987)
- 7 S. H. Townsend and M. T. Klein, *Fuel*, **64**, 635 (1985)
- 8 D. S. Ross, B. H. Loo, S. Tse, and A. S. Hirshon, *Fuel*, **70**, 289 (1991)
- 9 A. R. Katritzky and S. M. Allin, *Acc. Chem. Res.*, **29**, 399 (1996)
- 10 M. Siskin, A. R. Katritzky and M. Balasubramanian, *Fuel*, **72**, 1435 (1993)
- 11 L. Artok, O. Erbatur, and H. H. Schobert, *Fuel Process. Technol.*, **47**, 153 (1996)
- 12 C. Song, A. K. Saini, and J. McConnie, *Coal Science*, **1995**, 1391; C. Song, *Energeia*, **6**, 1 (1995)

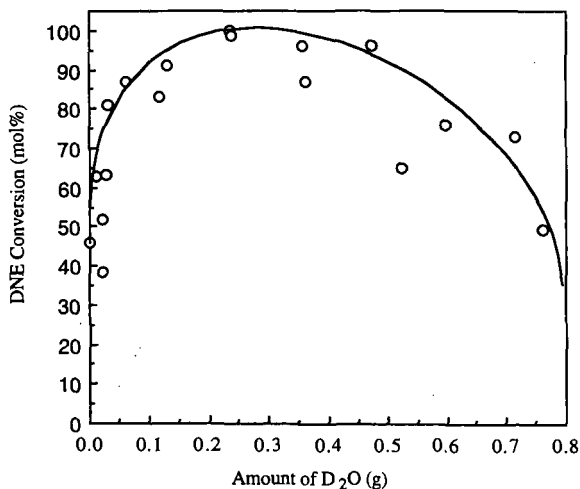


Fig. 1 Effect of addition of D₂O on conversion of 2,2'-dinaphthyl ether (DNE) at 350 °C for 30 min in 25 mL reactor. DNE: 0.216g; ATTM: 0.006g; n-C₁₃: 1.47g

Table 1 Effect of addition of H₂O on reactions of DNE at 350-400 °C under 6.9 MPa H₂.

Run No.	16	17	15	19	18	20	7	6	8	5	3	4
Catalyst Precursors	None	None	None	H ₂ O	H ₂ O	H ₂ O	ATTM	ATTM	ATTM	ATTM + H ₂ O	ATTM + H ₂ O	ATTM + H ₂ O
Temperature (°C)	350	375	400	350	375	400	350	375	400	350	375	400
DNE Conversion (mol %)	0.7	0.5	4.6	0.0	0.0	0.0	46.0	86.4	82.4	83.8	95.2	94.2
Products (mol %)												
Tetralin		0.7	5.4				31.4	70.9	66.7	72.7	106.1	109.1
Naphthalene		0.3	2.0				33.1	74.1	73.4	57.1	66.2	70.8
5,6,7,8-Tetrahydro-2-naphthol							8.0	6.2	3.6	8.1	9.5	6.0
2-Naphthol							2.2	4.7	12.6	3.4		
OctahydroDNE			0.3				1.3	2.0	1.0	2.5	2.2	
TetrahydroDNE	0.6		0.6				7.4	6.5	3.2	10.6	2.1	1.2

Table 2 Catalytic reactions of DNE using ATTM and D₂O at 350-400 °C under 6.9 MPa H₂

Rnu No.	29	5	32	3	27	4
Catalyst Precursor	ATTM + D ₂ O	ATTM + H ₂ O	ATTM + D ₂ O	ATTM + H ₂ O	ATTM + D ₂ O	ATTM + H ₂ O
Temperature(°C)	350	350	375	375	400	400
DNE Conversion (mol%)	82.9	83.8	95.5	95.2	95.6	94.2
Products (mol%)						
Tetralin	68.8	72.3	106.5	106.1	106.5	109.1
Naphthalene	59.7	57.2	71.2	66.2	64.7	70.8
5,6,7,8-Tetrahydro-2-naphthol	7.9	8.0	9.0	9.5	6.6	6.0
2-naphthol	2.2	3.2			1.1	
OctahydroDNE	2.4	3.1	0.7	2.2	1.1	
TetrahydroDNE	11.2	11.3	1.5	2.1	1.2	1.2

Table 3 Two-step reactions of DNE under 6.9 MPa H₂.

Run No.	44	48	49	41	42	51	68	67	50	96*
1st-step Catalyst	ATTM	ATTM	ATTM	ATTM + H ₂ O	ATTM + H ₂ O	ATTM + H ₂ O	ATTM	ATTM	ATTM	ATTM + H ₂ O
1st-Step Temperature(°C)	350	375	400	350	375	400	350	375	400	350
2nd-step Addition	None	None	None	None	None	None	H ₂ O	H ₂ O	H ₂ O	None
2nd-Step Temperature(°C)	350	350	350	350	350	350	350	350	350	350
Conversion (mol %)	64.4	66.7	66.0	82.7	96.0	76.9	32.9	29.7	41.2	97.0
Products (mol%)										
Tetralin	49.1	46.9	44.7	58.6	76.5	53.1	26.8	22.9	31.9	89.6
Naphthalene	67.5	72.6	72.6	79.5	85.1	75.9	26.6	25.5	39.5	104.4
Tetrahydronaphthol	0.8	0.6	1.0	1.4	1.6	4.2	1.2	0.6	0.7	
2-naphthol	0.8	0.6	1.0	0.4	0.1	2.2	1.6	0.8	1.0	
OctahydroDNE	0.3	0.3	0.4	0.8	2.1	0.7	0.2	0.2	0.2	
TetrahydroDNE	5.1	6.1	6.0	12.0	12.2	8.5	4.6	4.6	4.4	

* After the first-step reaction, water was completely removed by hot venting at 200 °C for 35 min., prior to the addition of DNE for second-step reaction.

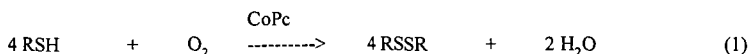
MECHANISM OF THE COBALT PHTHALOCYANINE-CATALYZED AUTOXIDATION OF ALIPHATIC THIOLS

E. I. Kozliak, A. Navid, Chemistry Dept., University of North Dakota, Grand Forks, ND 58202.

Keywords: cobalt phthalocyanines, autoxidation of thiols, Merox process

INTRODUCTION

Cobalt phthalocyanine (CoPc)-catalyzed autoxidation of thiols to disulfides has been used for the deodorization of oil distillates and exhaust gases in the fuel industry (1):



The mechanism of this reaction is known to include the formation of a ternary complex of CoPc with both substrates: the thiolate-ion (RS^-) and molecular oxygen (1-5). Based on the results of our kinetic studies of cobalt tetrasulfophthalocyanine (CoTSPc)-catalyzed autoxidation of cysteine, we suggested that two thiolates and one oxygen may be bound by one molecule of CoPc to comprise the intermediate ternary complex (5). This hypothesis may be summarized by the kinetic scheme presented on Fig. 1.

In this paper we address the elucidation of the nature of the second thiolate binding to CoTSPc as well as the oxidation state of cobalt in the proposed intermediates. Association of CoTSPc occurring in the aqueous media (6) is not considered here since we have presented evidence that this phenomenon does not appear to affect the mechanism of reaction (1) (5).

EXPERIMENTAL

CoTSPc was synthesized as described by Weber and Busch (7), with minor modifications in purification. Initial reaction rates were measured by the oxygen consumption, which was monitored by one of two methods: amperometrically at a fixed potential of -0.6 V using a self-made Clark oxygen electrode, and also using an Intech oxygen monitoring system connected to a Gateway computer. The catalytic reaction rate was calculated as a difference between the rates of oxygen consumption with and without CoTSPc. All experiments were carried out at 25°C in 0.1 M sodium borate (for pH 9.0-12.2) or phosphate buffer (for pH 7.8-9.5); the reaction rates in different buffers for overlapping values of pH were similar within the margin of the experimental error. 0.5 M sodium perchlorate was added to all solutions to assure the constancy of the ionic strength. Spectral studies were conducted using a self-made evacuated cuvet on two spectrophotometers: Beckman-3600 and Shimatsu-260; the two devices gave comparable results. Before mixing, solutions of reagents (CoTSPc and a thiol) were frozen a few times by liquid nitrogen followed by the removal of the air and thawing the samples. Reactive grade reagents were used without purification.

RESULTS AND DISCUSSION

Binding of thiolate-ions by CoTSPc. Reaction of CoTSPc with low concentrations of cysteine (10^{-4} - 10^{-2} M) in anaerobic conditions results in the appearance of new bands at 450 and 643 nm. Previously this spectrum was believed to be that of the plain reduced Co(II)TSPc (8). Now we report that this is not quite true. Whereas the band at 450 nm is, indeed, characteristic for any reduced complex of Co(II)TSPc , regardless of the reducing agent used, the band at 640-650 nm turned out to be specific only for thiols (cysteine, mercaptoethanol, sodium hydrosulfide, and ethyl mercaptan have been tested). The spectra of CoTSPc with different concentrations of cysteine are provided on Fig. 2, curves 1-5). CoTSPc reduced by other reducing agents [hydrazine at pH 13, NaBH_4 , or Cr(II)] adsorbs light at 680 nm (Fig. 2, curve 8). Upon increasing the cysteine concentration to $5 \cdot 10^{-1}$ M at pH 9.5, the difference in spectra for different reduced forms of CoTSPc disappears (Fig. 2, curves 6-8). This points to a successive binding of two thiolate molecules to CoTSPc. The stability constants found from the data of Fig. 2 are $1.7 \cdot 10^4 \text{ M}^{-1}$ and 52 M^{-1} ; they correspond, respectively, to K_1 and K_2 from the suggested kinetic scheme [Fig. 1, equations (1') and (3')].

Analysis of the adsorption at 450 nm shows that binding of the first thiolate is accompanied only by a partial reduction of Co(II)TSPc , whereas the second thiolate binding

results in its quantitative reduction to Co(I)TSPc (see Fig. 2). Perhaps, this is related to an increase of the electron density on the cobalt ion upon the binding of the second basic thiolate ligand. It is logical to suggest that even more basic hydroxyl anion would cause the same effect. Indeed, at pH 12.2 the absorbance at 450 nm, reflecting the reduction of Co(II) to Co(I), is much higher than at pH 9-11.5 (Fig. 3) for any non-saturating concentration of cysteine. Actually, at pH 12.2 even as low as 10^{-2} M cysteine reduces Co(II) as efficiently as 10^{-1} M cysteine at lower pH, and at $5 \cdot 10^{-2}$ M cysteine at pH 12.2 the reduction is complete (not shown). This phenomenon cannot be ascribed to the deprotonation of the amino group of cysteine since the threshold pH value 12.2 is much higher than the pK_a of the amino group [10.36 (2)]. We assumed that pH 12 appears to be the pK_a of deprotonation of the water molecule coordinated to cobalt in the monothiolate complex, $(RS^-)Co(II)TSPc(H_2O)$.

There are other indications that pH 12 is a threshold value for the reduction of Co(II)TSPc. It is known that hydrazine and hydroxylamine reduce Co(II)TSPc only at $pH > 11.7$, and their autoxidation occurs only at those high values of pH (9,10). In the absence of reducers in aerobic conditions, the binuclear adducts of CoTSPc with hydroxyl anion and oxygen are formed only at $pH > 12$ (6). It was also shown that in the water-DMF system the coordination of hydroxyl anion to CoTSPc in anaerobic conditions results in the reduction of Co(II) to Co(I); in aerobic conditions the labile oxygen adduct is formed (11). In aqueous solutions, hydroxyl anion itself does not reduce Co(II)TSPc. Perhaps, the association of CoTSPc in aqueous solutions (6) interferes with the reduction of Co(II). However, despite this association, hydroxyl anion appears to reduce the monothiolate complex of Co(II)TSPc or other CoTSPc complexes with basic reducing ligands (hydrazine, hydroxylamine).

Kinetics of reaction (1) at different pH. The kinetic constants of CoTSPc-catalyzed autoxidation of cysteine at different pH are shown in Table 1. Comparison of binding constants of cysteine to CoTSPc obtained by kinetic and spectroscopic methods appears to confirm our hypothesis suggested in (5) that binding the first substrate molecule (K_1) does not show up in the kinetics because the concentration of thiolate is too high for any free CoTSPc to exist in the solution. Therefore, only the binding of the second thiol molecule shows up kinetically as K_S , see Table 1 and Fig. 1.

Kinetic data also appear to confirm the presence of a critical point at $pH > 12$ for reaction (1) (Table 1). The value of K_S is virtually not changed at pH 9-10 when the deprotonation of the amino group of cysteine occurs, but it drops at pH 12.2 along with the reaction rate. Leung and Hoffmann (4) and Shirai *et al.* (13) observed the drop of the rate of reaction (1) for other aliphatic mercaptans, such as mercaptoethanol, aminoethanol, and ethane thiol. Therefore, this drop seems to be an inherent feature of reaction (1) and does not depend on the presence of other functional groups in cysteine. This occurs at the same value of pH 12 as the reduction of the monothiolate Co(II)TSPc complex discussed above (see Fig. 3). Hydroxyl anion, therefore, may be considered a competitive inhibitor of this reaction. The word "competitive", however, does not necessarily mean the literal competition of the hydroxyl ion and thiol for the same binding site; it merely reflects the fact that binding of the hydroxyl anion results in a decrease of the second thiolate binding constant, K_S . Apparently, the observed reduction of the monocysteinate CoTSPc complex by OH^- makes binding of the second electronodonor ligand, such as a thiol or thiolate, unfavorable.

In turn, the drop of K_S would result in the first kinetic order with respect to a thiol in alkaline solutions ($pH > 12$) even for higher concentrations of the substrate (see kinetic equation (7') on Fig. 1). This indeed has been observed by Fomin *et al.* (14). In contrast, at lower pH, the order of reaction (1) with respect to the mercaptan should be 1 and 0 at low and high concentrations of the thiol, respectively, which has been observed in (4,5,15).

As mentioned above, the rate of reaction (1) drops at higher pH (Table 1). It may be explained in two ways: either the k_{cat} or binding constants of thiols drop above that pH, see kinetic equation (7') on Fig. 1. Both effects have been observed for the CoTSPc-catalyzed autoxidation of cysteine (Table 1). However, there are indications that the drop of k_{cat} at $pH > 9.5$ is specific for cysteine, whereas the decrease of the thiolate binding to CoTSPc at $pH > 12$ is a more general feature of the CoTSPc-catalyzed autoxidation of all aliphatic thiols. The drop of k_{cat} takes place at pH about 10, which is way below 12, and thus appears to be caused by the deprotonation of the amino group of cysteine [$pK_a = 10.36$ (2)]. This deprotonation may result in a non-productive binding of some cysteine (by the amino group), thus causing the observed drop of k_{cat} . Indeed, Skorobogaty and Smith (15) did not observe any drop of the rate of reaction (1) for mercaptoethanol (no amino group) while increasing pH up to 11.5 at saturation by the thiol (zero kinetic order), when the value of k_{cat} determines the rate of the reaction.

It is interesting that the values of the constant of cysteine binding to CoTSPc, K_S , obtained from kinetic data, slightly increase while pH is decreased in the interval of pH 7.8-10.0, see Table 1. It apparently means that the complex $(RS^-)CoTSPc(RSH)$ may be a little more stable than $(RS^-)_2CoTSPc$. That makes sense, because thiolates are much stronger electron donors than thiols, and the second thiolate binding to the electron-rich partially reduced monothiolate complex of CoTSPc may be slightly hindered even if this binding, as suggested below, takes place on the ligand.

Besides changes of K_S , there is one more kinetic parameter which is greatly affected by pH: parameter α . This parameter is actually the ratio of the oxygen binding constants of bis- and monocysteinate complexes (see equations 2' and 4' on Fig. 1). The question is: why the biscysteinate complex of CoTSPc is able to efficiently bind oxygen, especially at pH>12? It should have very low affinity to oxygen if the latter competes with the second cysteine for the second axial position of cobalt.

The most plausible explanation is the second thiolate binding is at least in part not coordinative and involves some weak interactions with the phthalocyanine ligand rather than with cobalt. Since the binding of the second thiolate results in the complete reduction of Co(II), one may assume that the RS radical formed may be shifted from cobalt into the ligand. A similar migration of the alkyl and acyl radicals was observed for alkyl- or acylcobalt(III) porphyrins by Dolphin *et al.* (12). The suggested non-axial binding of the second thiolate molecule may explain why the value of parameter α is not much less than 1 at all studied values of pH (Table 1); in other words, the second thiolate does not appear to be much in the way of the oxygen.

Let us consider the pH-dependence of α . Binding of the thiol should not contribute in the oxygen binding as much as that of the thiolate; perhaps, this is why α gets slightly lower when pH decreases within the range 7.8-10. One question remains to be answered: why the value of α sharply increases at pH 12.2? It appears to be related to the above suggested deprotonation of the water molecule coordinated to cobalt. Unfortunately, in contrast to the binding of cysteine, we have no spectral data to discuss the binding of oxygen to CoTSPc; ternary thiolate-oxygen complexes of CoTSPc are unstable in aqueous media. We may only speculate that at pH>12 the monocysteinate complex appears to have hydroxyl anion as the second axial ligand, and it may result in a poorer oxygen binding by this complex than at lower pH. So, perhaps, the axially bound hydroxyl ion slightly hinders the oxygen binding by the monothiolate CoTSPc complex (although it is not a big obstacle, the value of K_O at pH 12.2 is only slightly lower, see Table 1). However, the binding of the second thiolate increases the electron density on cobalt, thus forcing the OH⁻ out and facilitating the binding of the electron-acceptor oxygen molecule. The combination of those effects may result in the observed increase of α at pH 12.2, although this effect needs to be further studied.

Evidence of the hydrophobic binding of thiols to CoPc. Thus far we have considered the binding of the thiolates or thiols to CoTSPc only through coordination by their sulfur atoms. However, it is possible that hydrophobic interactions of the phthalocyanine ligand with the R group of a thiol may play some role in the substrate binding. Fomin *et al.* (14) studied the cobalt disulfophthalocyanine (CoDSPc)-catalyzed autoxidation of aliphatic thiols in very alkaline solutions (0.1 M sodium hydroxide). They found that longer-chain mercaptans are oxidized much faster, and tried to explain it by the electronic and steric effects. However, both of these effects appear to be insufficient to account for the significant increase of reaction (1) rates observed with the elongation of the carbon chain. The switch of the methyl group in the RSH to the ethyl group would result in the biggest inductive effect, and the subsequent addition of each methylene group would result in much less prominent changes. However, the observed effect is just the opposite (Table 2). This phenomenon may alternatively be explained by the binding of the R groups of thiols (RSH) or thiolates (RS⁻) to the hydrophobic region of the phthalocyanine ligand. In contrast with electron effects, the hydrophobic binding would become more tenacious with addition of each methylene group, as it was observed in (14), see Table 2. We obtained a good correlation between the values of the observed first-order reaction rate constants for RSH from (14) and the distribution coefficients of the corresponding alcohols (ROH) in the system octanol-water [(16), Table 2]. Since at pH above 12 the first-order kinetics with respect to the thiol have been observed (14), the effective first-order kinetic constant should include K_S and be proportional to any factor affecting binding of the thiol, including its hydrophobicity. This is one more indication that the binding of one of the thiol molecules to CoTSPc appears to be non-coordinative.

PRACTICAL CONCLUSION

The Merox process of the removal of mercaptans from oil fractions consists of the extraction of mercaptans by alkaline solutions followed by the CoPc-catalyzed autoxidation of the mercaptides in the aqueous phase (1). For both processes the high concentrations of NaOH were considered optimal (1,17). However, we assumed that the increase of the rate of reaction (1) upon the addition of the extra sodium hydroxide observed in (17) may be irrelevant to the change of pH and may be accounted for by an unusually high salt effect in reaction (1) (5). Since the increase of pH above 12 appears to result in a decrease of the reaction rate, it would make sense to actually decrease the pH after extraction, at the same time adding some salt, such as NaCl, instead of NaOH, in order to increase the efficiency of catalysis. Obviously, this assumption takes into account only the rate of reaction (1) and disregards possible negative consequences of lowering the pH, such as an increase of thiol volatility and a decrease of its solubility in water.

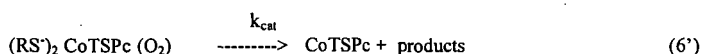
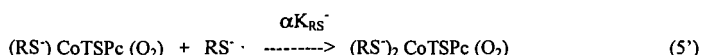
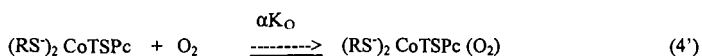
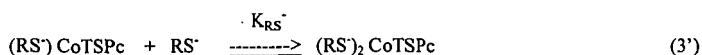
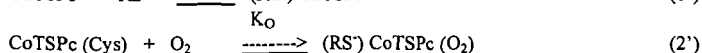
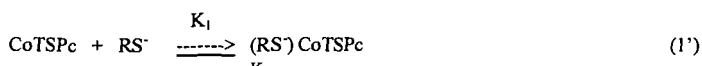
ACKNOWLEDGEMENTS

The authors thank Dr. A. K. Yatsimirsky (UNAM, Mexico) for valuable suggestions. The work was supported by NSF-EPSCoR through NSF grant # OSR-9452892.

REFERENCES

1. Basu, B.; Satapathy, S.; Bhatnagar A. K. *Catalysis Reviews*, **1993**, 35, 571-609.
2. Dolinsky, J.; Wagnerova, D. M.; Veprek-Siska, J. *Coll. Czechoslovak. Chem. Commun.*, **1976**, 41, 2326-2334.
3. Brouwer, W. M.; Piet, P.; German, A. L. *Journal of Molecular Catalysis*, **1984**, 22, 297-308.
4. Leung, P.-S. K.; Hoffmann, M. R. *J. Phys. Chem.*, **1989**, 93, 434-441.
5. Kozliak, E. I. *Preprints of ACS Division of Petroleum Chemistry*, **1996**, 41, 628-631.
6. Gruen, L. C.; Blagrove, J. *Austral. J. Chem.*, **1973**, 26, 319-325.
7. Weber, J. H.; Busch, D. H. *Inorganic Chemistry*, **1965**, 4, 469-471.
8. Simonov, A. D.; Keyer, N. P.; Kundo, N. N.; Mamaeva, E. K.; Glazneva, E. V. *Kinetics and Catalysis (USSR)*, **1973**, 14, 864-868.
9. Wagnerova, D. M.; Schwertnerova, E.; Veprek-Siska, J. *Coll. Czechoslovak. Chem. Commun.*, **1974**, 39, 1980-1988.
10. Hong, A. P.; Chen, T.-C. *Environ. Sci. Technol.*, **1993**, 27, 2404-2411.
11. Dubrovina, A. S.; Malkova, A. I.; Tupikov, V. I. *Coordination Chemistry (USSR)*, **1984**, 10, 1207-1210.
12. Dolphin, D.; Halko, D. J.; Johnson, E. *Inorganic Chemistry*, **1981**, 20, 4348-4351.
13. Shirai, H.; Tsiuki, H.; Masuda, E.; Koyama, T.; Hanabusa, K.; Kobayashi, N. *J. Phys. Chem.*, **1991**, 95, 417-423.
14. Fomin, V. A.; Mazgarov, A. M.; Lebedev, N. N. *Petroleum Chemistry (USSR)*, **1979**, 18, 298-306.
15. Skorobogaty, A.; Smith, T. D. *J. Mol. Catal.*, **1982**, 16, 131-146.
16. Leo, A.; Hunch, C.; Elkins, D. *Chem. Rev.*, **1971**, 71, 525-548.
17. Fomin, V. A.; Mazgarov, A. M. *Petroleum Chemistry (USSR)*, **1981**, 21, 265-273.

Fig. 1. Suggested kinetic scheme of reaction (1).



Observed kinetic equation [obtained in (5)]:

$$v_0 = \frac{d[\text{O}_2]}{dt} = \frac{\alpha k_{\text{cat}} K_O K_{\text{Cys}} [\text{CoTSPc}] [\text{Cys}] [\text{O}_2]}{1 + K_O [\text{O}_2] + K_{\text{Cys}} [\text{Cys}] + \alpha K_O K_{\text{Cys}} [\text{Cys}] [\text{O}_2]} \quad (7')$$

Table 1. Kinetic parameters of reaction (1) at different pH

pH	K_O, M^{-1}	K_S, M^{-1}	α	$k_{\text{cat}}, \text{s}^{-1}$
7.8	$5.2 \cdot 10^4$	120	0.15	4.8
9.0	$2.7 \cdot 10^4$	90	0.33	9.4
9.5	$2.0 \cdot 10^4$	60	0.5	10.5
10.0	$3.5 \cdot 10^4$	80	0.6	4.6
12.2	$1.3 \cdot 10^4$	9	5.3	3.0

Table 2. Observed rate constants of CoDSPc-catalyzed autoxidation of alkyl mercaptides in 0.1 M aqueous solution at saturation with oxygen [k_{obs} (14)] vs. the distribution coefficient of the corresponding alcohol, ROH, between n-octanol and water, P_{ROH} (16).

Mercaptan	$k_{\text{obs}} \cdot 10^{-4}, \text{s}^{-1}$	P_{ROH}
Methyl thiol	0.9	0.2
Ethyl thiol	1.0	0.5
1-Propyl thiol	2.3	2.2
1-Butyl thiol	4.5	7.6
1-Pentyl thiol	11.7	29

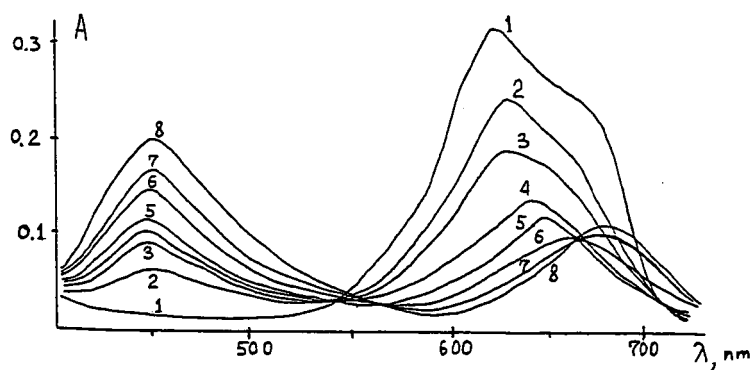


Fig. 2. Spectral changes occurring upon addition of the increased amounts of cysteine to the aqueous $8 \cdot 10^{-6}$ M solution of Co(II)TSPc in anaerobic conditions (pH 9.5, 0.1 M borate buffer, 0.5 M NaClO_4). 1. CoTSPc, no cysteine added; 2-7. Same solution with 10^{-4} , $2 \cdot 10^{-4}$, $5 \cdot 10^{-4}$, $5 \cdot 10^{-3}$, $5 \cdot 10^{-2}$, $5 \cdot 10^{-1}$ M cysteine, respectively; 8. Solution 1 with 10^{-2} M hydrazine, pH 13.

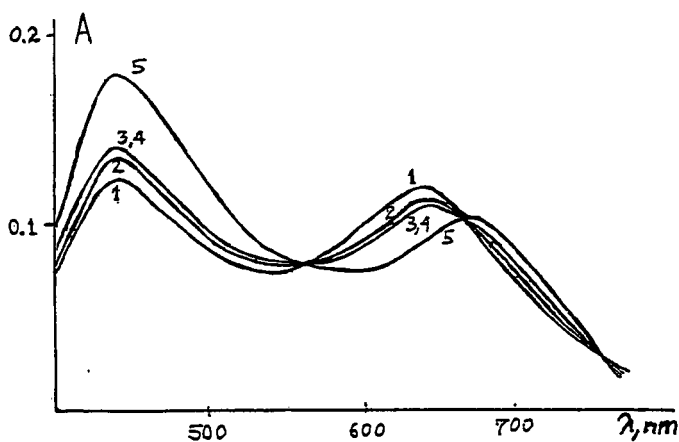


Fig. 3. Spectra of the complex of CoTSPc ($8 \cdot 10^{-6}$ M) with cysteine (10^{-2} M) at different pH: 1. 9.0; 2. 9.5; 3. 10.0; 4. 11.0; 5. 12.0, respectively.

A MECHANISTIC STUDY OF THE CHAIN PROPAGATION STEP IN THE FISCHER-TROPSCH SYNTHESIS

Ruhksana Quyoum, Helen C. Long, Michael L. Turner, Peter M. Maitlis

Department of Chemistry, The University of Sheffield, Sheffield S3 7HF, U.K.

KEY WORDS: Fischer-Tropsch synthesis, methylene, labelling studies

INTRODUCTION

The reductive polymerization of carbon monoxide to hydrocarbon mixtures (the Fischer-Tropsch synthesis) is a reaction that has attracted considerable interest ever since it was first discovered.^{1,2} Typically, syn gas (CO/H_2) is passed over a heated, supported metal catalyst at atmospheric pressure or above which leads to the formation of a complex product mixture composed mainly of linear alkenes and alkanes.

The mechanism of the polymerization has long been the subject of debate. Early proposals by Fischer and Tropsch were that surface methylene, formed by the hydrogenation of dissociated CO, polymerized on the surface. Experiments by Brady and Pettit³ confirmed the importance of methylene in hydrocarbon formation. They, and others⁴ proposed that chain growth was initiated by surface alkyl/hydride groups thus giving surface alkyls as the chain carriers. This mechanism, however, is not without limitations; for example, low levels of C_2 hydrocarbons are formed which are not accounted for by this mechanism. Consequently, there has been renewed interest in the mechanism of C-C bond formation in the Fischer-Tropsch synthesis. One approach, used by us and others⁵ involved studies of the reactions of well-defined metal complexes as model systems.

Early studies in this field were initiated by the decomposition reactions of organometallic complexes such as $[(\eta^5\text{-C}_5\text{Me}_5)\text{Rh}(\text{CH}_2)]_2(\text{Me})(\text{MeCN})]^+$ which modelled a portion of a rhodium catalyst during carbon monoxide hydrogenation.⁶ ^{13}C and D labelling studies indicated that C-C coupling proceeded by an unexpected route where vinyl ($-\text{CH}=\text{CH}_2$), rather than alkyl, was implicated as the key intermediate which coupled further with surface methylene to give the products.⁷ Such alkenyl + methylene couplings may well represent lower energy processes than the couplings of the corresponding of alkyl + methylene groups.⁸ These findings prompted further interest in the mechanism of C-C bond formation, and the nature of the intermediate species in the heterogeneously metal catalyzed hydrogenation of CO.

Our studies have further investigated the mechanism of the Fischer-Tropsch reaction, and in particular, evaluated the roles played by vinyl and methylene groups in hydrocarbon formation. This approach utilizes probe reactions which other workers,⁹ have been found to be successful in providing mechanistic information during CO hydrogenation and extends earlier work involving the co-reaction of model reactants, including vinyl and methylene precursors, with CO and H_2 under Fischer-Tropsch reaction conditions.¹⁰ For this study, ^{13}C probe molecules were used since unambiguous mechanistic information could be gained if they were incorporated into the products. Furthermore, other reactions of the probes could be investigated.

EXPERIMENTAL

Equipment

Quantitative analysis of the reaction products was carried out by gas chromatography on a Supelco SPB-1 (60 m x 0.53 mm x 5 mm) capillary column. The level of ^{13}C incorporation was analysed by GC-MS (HP 5890 - 5171 A).

Catalyst preparation

The catalysts were prepared by impregnation of the support (Davisil grade 645 silica gel) to incipient wetness to give metal loadings of 4%. $\text{Rh}(\text{NO}_3)_3$, $\text{RuCl}_3 \cdot x\text{H}_2\text{O}$ and $\text{Co}(\text{NO}_3)_2 \cdot 6\text{H}_2\text{O}$ were added to the support and slowly heated to 373 K with frequent stirring at which temperature the catalysts were fully dried. A solution of $\text{Ce}(\text{NO}_3)_3$ was added to the rhodium catalyst in order to increase the activity.

Reaction conditions and catalyst activation

The catalyst was reduced under a steady stream of hydrogen (1 atm, 700 cm³ h⁻¹), with programmed heating (4 K min⁻¹) from room temperature to 673 K. The catalyst was then cooled to the reaction temperature under hydrogen and the gas flow was switched to syn gas (1 atm, flow rate 500 cm³ h⁻¹). The products of the reaction were either sampled directly from the gas stream and analyzed by gas chromatography or collected in a liquid nitrogen trap and analyzed by GC-MS. For the runs with probes, the products were analyzed by GC and GC-MS before, during and after probe additions. A background GC was initially obtained to show the distribution of the products. After a period of 1.5 h, the probe molecule was added to the syn gas feed stream. Nitromethane and ethene were directly injected into the gas mixture through a septum and diazomethane gas was introduced by diverting the syn gas flow through the vessel which contained the diazomethane gas, prepared *in situ*. A GC analysis was performed after the probe had been added. After a further 1.5 h period, a final GC was carried out to determine the activity of the catalyst after addition of probe. Products were identified by comparison of their mass spectra with Wiley library spectra, stored in the HP ChemStation software.

RESULTS

Vinyl and methylene probes were individually reacted with CO-H₂ over Co/SiO₂, Ru/SiO₂, Rh/Ce/SiO₂ catalysts under Fischer-Tropsch reaction conditions (CO:H₂ = 1:2, 1 atm over 1 g catalyst). Diazomethane and nitromethane were used as sources of methylene (C₁) and vinyl species (C₂) were derived from ethene. Prior to any probe addition, the products of CO hydrogenation were typical for those obtained for the polymerization, containing mainly linear alkenes and alkanes together with some oxygenates. The product distribution followed modified Anderson-Schulz-Flory kinetics, with high C₁ and low C₂ fractions and a stepwise linear decrease beyond C₃.¹¹

Vinyl probe addition

The effect of adding ethene as a source of vinyl to the CO hydrogenation was to increase the formation rate of the C₂ to C₇ hydrocarbons. During addition of the probe, the probability of chain growth, α , decreased for the various catalysts studied. Selected data of ¹³C_x incorporation into the C_n hydrocarbons when ¹³C₂-ethene was used as a probe over cobalt for example, (= 0, 1, 2,...n) are given in Table 1.

Methylene probe addition

Diazomethane and nitromethane were used as sources of methylene since it was expected that under the experimental conditions those probes would decompose to give methylene intermediates, as previously reported.^{12,3} Probe addition to the syn gas feed caused significant changes to the product distributions; in particular, there was an increase in the formation rate of C₃ to higher products and an increase in the probability of chain growth. The results of ¹³C_x incorporation into the hydrocarbon products when ¹³CH₂N₂ or ¹³CH₃NO₂ was added to the CO hydrogenation over cobalt are summarized in Table 2.

DISCUSSION

Effect of probe molecule addition

The addition of the methylene (C₁) and vinyl (C₂) probe molecules to each of the experiments increased the amounts of higher hydrocarbons produced. Ethene addition caused an increase in C₂ to C₇ products; the effect was largest, as might be expected, for the formation of ethane by hydrogenation/hydrogenolysis. Addition of nitromethane and diazomethane probes to the CO hydrogenation increased the formation rate of C₃ to higher products. The changes in the hydrocarbon production during probe addition are marked by changes in the chain growth probabilities for each of the experiments; addition of ethene had the effect of decreasing α while methylene probe addition caused an increase in α . The latter is consistent with an increase in the rate of propagation during methylene probe addition.

¹³C labelling studies

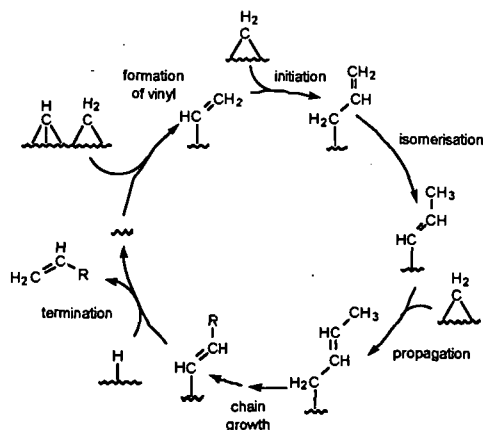
Addition of ¹³C₂-ethene to the ¹²CO/H₂ stream over all the catalysts studied clearly showed incorporation of ¹³C₂ units into the hydrocarbon products (Table 1). The levels of ¹³C₂ obtained are highly significant since they are many orders of magnitude greater than natural abundance. Incorporation of ¹³C₁ and ¹³C₃ units into the products are slightly higher than expected over cobalt. Thus, it is apparent that ethene undergoes some hydrogenolysis leading to the incorporation of ¹³C₁ units into the reaction products. Furthermore, there is little incorporation

of ^{13}C above natural abundance into the oxygenates indicating that they are not formed from vinyl groups. Similar patterns of ^{13}C labelling in the reaction products are obtained for the various catalysts studied.

The effect of adding $^{13}\text{CH}_2\text{N}_2$ or $^{13}\text{CH}_3\text{NO}_2$ to the ^{12}CO hydrogenation over cobalt gave results consistent with the incorporation of $^{13}\text{C}_1$ units into the hydrocarbon products (see Table 2). For both probes, the levels of $^{13}\text{C}_1$ incorporation are significant since they exceed those expected on the basis of natural abundance. In fact, the extent of ^{13}C incorporation in the products of the reaction is consistent with the mixing of methylene groups derived from the syn gas reaction ($^{12}\text{CH}_2$) with those derived from the probe ($^{13}\text{CH}_2$). It is clear from Table 2 that the arrangement of $^{13}\text{C}_x$ atoms in the products is close to that expected on the basis of random mixing of the methylene groups for the ratio of ^{12}C to ^{13}C used in these experiments. Furthermore, similar ^{13}C levels are obtained irrespective of whether $^{13}\text{CH}_2\text{N}_2$ or $^{13}\text{CH}_3\text{NO}_2$ is used as the methylene source suggesting that both probes react on the surface to yield a common intermediate. By contrast, identical experiments over rhodium catalysts showed quite different behaviour giving two parallel chain growth pathways each of which forms hydrocarbons. One is the hydrogenation of CO and the other is an oligomerization of the probe derived intermediates. Thus, over rhodium, there is very little crossover between the two routes and the hydrocarbon products effectively contain either only ^{12}C atoms with ^{13}C at natural abundance only, or fully ^{13}C -labelled hydrocarbons which contain little or no ^{12}C .

The alkenyl mechanism for Fischer-Tropsch homologation

The results show that there is most incorporation of $^{13}\text{C}_2$ units when $^{13}\text{C}_2$ -ethene is added to the $^{12}\text{CO}/\text{H}_2$ mixture. The degree of $^{13}\text{C}_2$ incorporation decreases with increasing number of carbons in the hydrocarbon products which is consistent with the C_2 species being involved in chain initiation. Addition of other probes such as ethyl bromide, vinyl bromide and tetravinylsilane indicate that the initiating species is the unsaturated vinyl group. The addition of methylene probes to the ^{12}CO hydrogenation result in the incorporation of $^{13}\text{C}_1$ units in the reaction products according to the alkenyl mechanism. The pattern of $^{13}\text{C}_1$ distribution in the products is determined by the nature of the metal. Thus, over cobalt, the degree of $^{13}\text{C}_1$ incorporation is consistent with a distribution based on random mixing of the methylenes derived from the probe and those from the syn gas. By contrast, similar reactions over rhodium lead to parallel chain growth pathways. One is CO hydrogenation, which forms products derived exclusively from ^{12}C , the other is a homopolymerization of methylene intermediates derived from the probe giving fully ^{13}C labelled products and there is very little crossover between the two routes. It is proposed that over rhodium, alternative methylene intermediates, possibly CH_2N , may form which lead to independent polymerization pathways.



The alkenyl mechanism for Fischer-Tropsch homologation. Hydrocarbon formation is initiated by vinyl and propagated by methylene groups.

Table 1. Incorporation of $^{13}\text{C}_x$ from $^{13}\text{C}_2\text{H}_4$ over Co/SiO_2

x	0	1	2	3	4	5	6
1-butene	50	8 (2)	32	7	3		
1-pentene	55	9 (3)	27	8	2	1	
1-hexene	62	9 (4)	19	6	3	1	0

Figures in parentheses correspond to the expected % $^{13}\text{C}_1$ at natural abundance.

Table 2. Incorporation of $^{13}\text{C}_x$ from $^{13}\text{CH}_3\text{NO}_2$ and $^{13}\text{CH}_2\text{N}_2$ over Co/SiO_2

x	$^{13}\text{CH}_2\text{N}_2$							$^{13}\text{CH}_3\text{NO}_2$						
	0	1	2	3	4	5	6	0	1	2	3	4	5	6
1-butene	66	18	10	2	4			70	17	6	3	5		
1-pentene	75	15	7	2	1	0		73	15	7	2	1	0	
1-hexene	76	18	4	1	0	0	0	76	18	4	1	0	0	0

REFERENCES

1. Fischer, F.; Tropsch, H. *Brennst.-Chem.* **1926**, *7*, 97; *Chem. Ber.* **1926**, *59*, 830.
2. Anderson, R. B. *The Fischer-Tropsch Reaction*; Academic Press: London, 1984.
3. Brady, R. C.; Pettit, R. *J. Am. Chem. Soc.* **1980**, *102*, 6181; **1981**, *103*, 1297.
4. Biloen, P.; Helle, J. N.; Sachtler, W. M. H. *J. Catal.* **1979**, *58*, 95.
5. Knox, S. A. R. *J. Cluster Sci.* **1992**, *3*, 385.
6. Maitlis, P. M. *J. Organomet. Chem.* **1995**, *500*, 239.
7. Saez, I. M.; Meanwell, N. J.; Nutton, A.; Isobe, K.; Vázquez de Miguel, A.; Bruce, D. W.; Okeya, S.; Andrews, D. G.; Ashton, P. R.; Johnstone, I. R.; Maitlis, P. M. *J. Chem. Soc., Dalton Trans.* **1986**, 1565. Martinez, J.; Gill, J. B.; Adams, H.; Bailey, N. A.; Maitlis, P. M. *J. Chem. Soc., Chem. Commun.* **1989**, 286.
8. Calhorda, M. J.; Brown, J. M.; Cooley, N. A. *Organometallics* **1991**, *10*, 1431. Evitt, E. R.; Bergman, R. G. *J. Am. Chem. Soc.* **1980**, *102*, 7003.
9. Hall, W. K.; Kokes, R. J.; Emmett, P. H. *J. Am. Chem. Soc.* **1959**, *82*, 1027. Hutchings, G. J.; Gottschalk, F. M.; Hall, M. V. M.; Hunter, R. *J. Chem. Soc., Faraday Trans. 1* **1987**, *83*, 571.
10. Turner, M. L.; Long, H. C.; Shenton, A.; Byers, P. K.; Maitlis, P. M. *Chem. Eur. J.* **1995**, *1*, 549. Maitlis, P. M.; Long, H. C.; Quyoum, R.; Turner, M. L.; Wang, Z.-Q. *J. Chem. Soc., Chem. Commun.* **1996**, 1. Quyoum, R.; Turner, M. L.; Long, H. C.; Maitlis, P. M. *J. Am. Chem. Soc.* **1996**, *118*, 10888. Quyoum, R.; Maitlis, P. M. unpublished work.
11. Biloen, P.; Sachtler, W. M. H. *Adv. Catal.* **1981**, *30*, 165.
12. Cavalcanti, F. A. P.; Oukaci, R.; Wender, I.; Blackmond, D. G. *J. Catal.* **1990**, *123*, 260.

MECHANISTIC INVESTIGATIONS OF THE IRON-SULFUR CATALYZED REDUCTION OF HYDROXYL-CONTAINING MODEL COMPOUNDS.

Tom Autrey, John C Linehan, Carrie J Stearns, Donald M Camaioni,
Lauren Kaune and James A Franz.

Pacific Northwest Laboratory, P.O. Box 999, Richland, WA 99352 USA

Key Words. Catalysis, mechanism, hydrogen transfer

INTRODUCTION.

The goal of our research has been to focus on the mechanisms of hydrogen transfer from donor solvents to coal model compounds in the presence and absence of iron/sulfur (FeS) catalysts. Previous work showed that hydrogen transfer from dihydroaromatic donor solvents occurs predominately by reverse radical disproportionation (RRD) and by free hydrogen atoms (HA) generated from the solvent derived cyclohexadienyl radicals.¹⁻⁶ Initially, our catalytic studies examined the efficiency of strong bond scission using a variety of FeS catalyst precursors.⁷⁻⁹ Those studies showed that 6-line ferrihydrite (FeOOH) is an efficient precursor to highly active catalysts. A hydrogen donor solvent, 9,10-dihydrophenanthrene, promoted facile scission of strong carbon-carbon bonds (Ar-CH₂Ar) in those studies. Recent mechanistic studies have used structure reactivity arguments to show that hydrogen transfer from the FeS catalysts is consistent with selective and reversible hydrogen atom transfer from the reduced catalyst by a radical-like mechanism.¹⁰⁻¹¹

In the present work we report our most recent results regarding the mechanistic pathways of hydrogen transfer from FeS catalysts to coal model compounds. The present study examines the effect of hydroxylic groups in the catalytic hydroliquefaction of coal. We report the results of our investigations of three different types of model compound structures, (1) *arylmethanols*; benzylalcohol, diphenylmethanol, 1-naphthalenemethanol, 1,2-diphenyl ethanol and (2) *alkyl alcohols*; 2-phenethylalcohol and octadecanol (3) *aryl alcohols*; phenol, naphthol and anisole. We show that reduction of these model compounds, by an apparent ionic pathway, competes with hydrogen transfer to the ipso-position of the substituted arenes.

EXPERIMENTAL.

Materials. All catalytic experiments used 6-line ferrihydrite, prepared by the Rapid Thermal Decomposition of Precursors (RTDS), as the catalyst precursor.⁷ The 9,10-dihydrophenanthrene (DHP), 1 and 2-naphthol, phenol, 1-naphthalenemethanol, benzyl alcohol, 2-phenethyl alcohol, and octadecanol were used as purchased from Aldrich except for DHP. The DHP was distilled and recrystallized from methanol/dichloromethane. The 1,2-ditolyethanol was available from a previous study.¹³

Thermolysis Studies. Model compound (15 mg), 6-line ferrihydrite (3 mg), sulfur (3 mg), and DHP solvent (100 mg) were loaded into 5-mm o.d. borosilicate glass tubes and sealed under vacuum. Thermolysis was carried out in a fluidized sand bath regulated at the specified temperature for various times. The GC and GC/MS analyses of the products were carried out as described previously.⁷

RESULTS AND DISCUSSION.

Aryl Methanols. Thermolysis of benzyl alcohol at 270 °C in DHP containing 6-line ferrihydrite and sulfur produced toluene as the major observable product. However, the mass balance was less than 50% (Table I). Some higher molecular weight products, assigned by GC/MS analysis as benzylated phenanthrenes, were also observed, suggesting an ionic intermediate. Since benzyl alcohols readily undergo dehydration in the presence of trace amounts of acid to yield a cationic intermediate, it is reasonable to assume that the catalyst protonates the alcohol to generate a benzyl cation. Subsequent addition of the benzyl cation to the solvent, phenanthrene, is likely to provide the major pathway under the conditions used (Scheme I). This mechanistic scheme is consistent with the low mass balance observed for the catalytic reduction of benzyl alcohol.

Similarly, thermolysis of 1-naphthalenemethanol at 265°C for 60 minutes yielded 1-methylnaphthalene as the major product. Again, the mass balance for products detected by GC was low, 40-60%, based upon consumption of the starting material. Consequently it appears that the initial catalytic reduction of aryl methanols leads to retrogressive reaction products. However, at a higher temperatures of 325°C, the observed mass balance improved to 70% for the same reaction time. We believe this is a result of secondary catalytic thermolysis pathways, a reasonable assumption since we have shown that benzylated arenes are efficiently consumed in the presence of the FeS catalyst.⁷

Alkyl Alcohols. Thermolysis of 2-phenethyl alcohol led to the eventual formation of ethylbenzene (Table I). However, we observed the transient formation of phenethylthiol. The thiol concentration grew slowly during the reaction and subsequently decreased after long reaction times. This observation is consistent with dehydration of the alcohol to form styrene, an intermediate product leading to sulfur incorporation or reduction to ethylbenzene. It is reasonable to assume that the thiol is also converted to the styrene and H₂S by a similar mechanism (Scheme II).

Thermolysis of octadecanol yielded similar results. The concentration of octadecathiol was observed to grow in over a period of ca. 30 minutes and then to disappear. Analogous to the catalytic thermolysis of phenethylalcohol, aliphatic alcohols are reduced in the presence of the

catalyst.

Catalytic reduction of the methyl ester of 1,2-diphenylethanol yielded bibenzyl as the major product. This is noteworthy because if electron transfer from the arene to the catalyst were an important pathway, carbon-carbon bond scission of the 1,2-diphenylethanol radical cation is expected to yield toluene derived products.¹⁴

Aryl Alcohols. Thermolysis of 1- and 2-naphthol in DHP in the presence of the FeS catalyst precursor led to the formation of two major products, naphthalene and tetralin (Table I). After 60 minutes at temperatures between 320 - 330 °C, about 30% of the naphthol was consumed to yield roughly a 1 to 1.1 ratio of naphthalene to tetralin. For comparison, note that the thermolysis of phenol, even at higher temperatures (390 °C) yielded no observable chemistry. This is an interesting observation, given that in a control experiment, anisole, the methyl ether of phenol, was consumed at a comparable rate to naphthol, to yield phenol.

The observations of this study are consistent with our previously proposed mechanism involving reversible hydrogen atom transfer from the catalyst to the arene.¹⁰ Ipso addition of a hydrogen atom is more endothermic than non-ipso addition and therefore not apt to be observed. The hydroxy group on naphthol stabilizes the radical adduct formed by transfer of a hydrogen from the catalyst. Hydrogen atoms likely transfer back and forth between the catalyst and the arene. Eventually the adduct is reduced by the transfer of a second hydrogen atom to yield dihydronaphthol. Subsequent reduction of the diene yields hydroxytetralin, followed by dehydration to dihydronaphthalene. Thermal pathways may also contribute to the observed products. (Scheme III).

As expected from our mechanistic proposal, aryl alcohols are reduced at a slower rate than either the alkyl or benzyl alcohols examined in this present work. Acid catalyzed reduction of aryl alcohols is expected to be extremely slow. Reduction of naphthol by a sequence of hydrogen atom transfer steps to yield an alkynol is the major route for the deoxygenation of 1 and 2-naphthol.

CONCLUSION

Several pathways for the deoxygenation of the hydroxylic functional groups in model compounds are likely operating under iron/sulfur catalytic conditions. The initial step appears to be catalytic dehydration. Unfortunately, dehydration products may yield retrogressive reaction products. Catalytic dehydration of aliphatic alcohols yields intermediate olefins which incorporates sulfur under the reaction conditions. Reactions of benzylic alcohols leads to formation of benzylated solvent products. Fortunately, the formation of the thiol is reversible with the intermediate olefin being reduced to the corresponding hydrocarbon and the strong carbon-carbon bonds of benzylated arenes are efficiently cleaved in the presence of FeS catalysts in DHP. In summary: although the hydroxylic function in our model compounds are consumed at a rapid rate, they lead to products that must be 'treated' by further reactions with the catalyst to yield the desired products. The net result is a slight increase in hydrogen demand to bring about liquefaction of hydroxylated structures in coal model compounds.

ACKNOWLEDGMENT

This work was supported by the U.S. Department of Energy, Office of Basic Energy Research, Chemical Sciences Division, Process and Techniques Branch. The work was conducted at Pacific Northwest Laboratory, which is operated by Battelle Memorial Institute for the U. S. Department of Energy under Contract DE-AC06-76RL0 1830. We thank Dean Matson for our supply of the catalyst precursors. Support for CJS and LK was provided through AWU-NW under grant DE-FG06-89ER-75522 with the U.S. Department of Energy.

REFERENCES

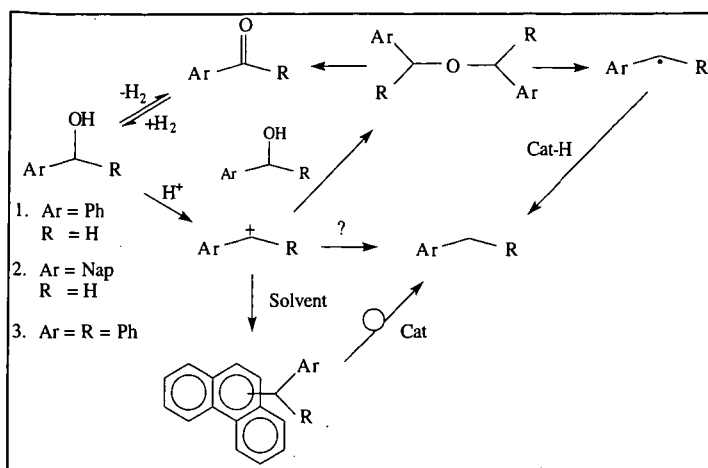
- (1) Autrey, T.; Cleveland, E. A.; Franz, J. A.; and Camaioni, D. M. *Energy and Fuels*, 1995, 9, 420-428.
- (2) Camaioni, D. M.; Autrey, T.; Salinas, T. B.; and JA Franz. *J. Am. Chem. Soc.* 1996, 118, 2013-2022.
- (3) Autrey, T.; Powers, T.; Cleveland, E. A.; Franz, J. A.; and Camaioni, D. M. Proceedings, 8th International Conference on Coal Science. 1995, pp1431-1434.
- (4) Camaioni, D. M.; Autrey, T.; and Franz, J. A. *J Phys. Chem.* 1993, 97, 5791.
- (5) Franz, J. A.; Ferris, K. F.; Camaioni, D. M.; and Autrey S. T. *Energy and Fuels*, 1994, 8, 1016-1019.
- (6) Watts, J. D.; Bartlett, R. J.; and Franz, J. A. *Chem. Phys. Letters*, 1996, 249, 496.
- (7) Matson, D. W.; Linehan, J. C.; Darab, J. G.; and Buehler, M. F. *Energy and Fuels*, 1994, 8, 10.
- (8) Matson, D.W.; Linehan, J. C.; Darab, J.G.; Camaioni, D.C.; Autrey, S.T.; and E. Lui. 1995 MRS Symposium Proceedings #368, Synthesis and Properties of Advanced Catalytic Materials, E. Iglesia, P.W. Lednor, D.A. Nagaki, L.T. Thompson, eds. pp.243-248.
- (9) Linehan, J. C.; Matson, D. W.; Darab, J. G. *Energy & Fuels* 1994, 56.
- (11) Autrey, T.; Linehan, J. C.; Camaioni, D. M.; Kaune, L.; Wartob, H.; and Franz, J. A. *Catalysis Today* 1996, 31, 105-111.
- (12) Autrey, T.; Linehan, J. C.; Camaioni, D. M.; Powers, T.; McMillan, E. F.; and Franz, J. A. *Fuel Preprints* 1995, 40(4) 973-977.
- (13) Camaioni, D. M. and Franz, J. A. *J. Org Chem.* 1984, 49, 1607.

Table I
Reaction Rates and Products of Model Compounds with "Iron-Sulfide" (FeS)
Catalysts in Sealed Tube Reactions with 9,10-Dihydrophenanthrene

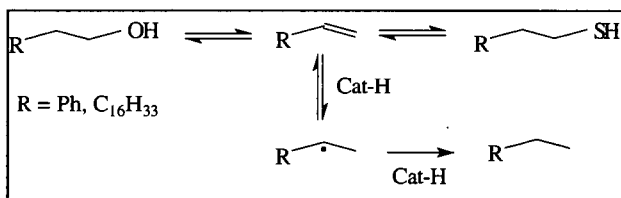
Model Compound	Reaction Temp. (°C)	Mass Balance	Disappearance Rate ($\times 10^{-4} \text{ s}^{-1}$)	Major Products
Benzyl Alcohol	270	40-50% ^a	33 ± 4	Toluene ^b
1-Naphthalene Methanol	265	40-60% ^c	80 ± 10	Naphthaldehyde 1-Methylnaphthalene
2-Phenethyl Alcohol	315	80%	$4.7 \pm .6$	Ethyl Benzene ^d
Octadecanol	340	60-70%	5 ± 1	Octadecane ^e
Phenol	390	95%	No Reaction	None
1-Naphthol	320	90%	$0.7 \pm .1$	Naphthalene, Tetralin ^f
2-Naphthol	330	95%	$1.1 \pm .1$	Naphthalene, Tetralin ^f

a) Slightly higher mass balance was obtained for reactions at higher temperatures. b) Other products identified were benzaldehyde, and various isomers of benzylphenanthrene. c) Again higher mass balance was obtained for reactions at higher temperatures. d) Phenylethylthiol was identified by GC/MS. e) Octadecathiol identified by GC/MS. f) Close to a 1:1 ratio of the two major products was obtained.

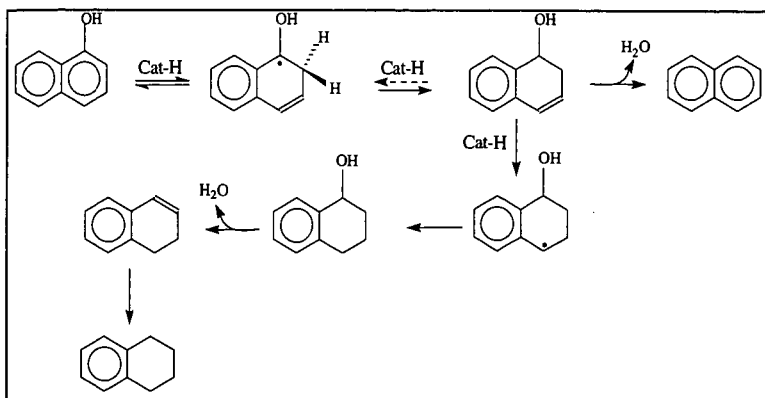
Scheme I



Scheme II



Scheme III



CONSIDERATION ON BOND CLEAVAGE REACTIONS OF BRIDGE STRUCTURE IN COAL MODELS AND COAL WITH TWO DIFFERENT HYDROGEN DONATING COMPOUNDS

Koh Kidena, Nobuo Bandoh, Satoru Murata, and Masakatsu Nomura
Department of Applied Chemistry, Faculty of Engineering, Osaka University
Suita, Osaka 565, JAPAN

Key words: bond cleavage, coal models, hydrogen donating compounds

INTRODUCTION

Coal organic material (COM) is believed to be an amorphous polymer consisting aromatic clusters with aliphatic side chains or bridges including naphthenic portion. Accordingly, COM should be described by certain chemical formula as other polymers are. Using various analytical methods coal chemical structure had been investigated in detail, however, COM is essentially far from the ordinal polymer. It does not contain any repeated units but many moieties and shows different behavior in its conversion reaction depending on its rank or its mining region. From these complexities, information concerning its chemical structure and reactivity is now still limited.

In coal utilization processes such as liquefaction, gasification or carbonization, decomposition of COM should be important. Judging from the accepted chemical structures for COM, the bond cleavage reaction of the bridge structure plays an important role in its decomposition. Now, we focus on this bond cleavage reaction in coal because this is one of the important reactions during heat-treatment of coal. There are many investigations which consider the coal models having the bridge structures as contained in coal and pursue the fashion of the reaction using the model compounds. Autrey et al.[1], Futamura et al.[2] and Nomura et al.[3] had mentioned the pyrolysis or hydrogenolysis of diarylmethane, while Korobkov et al.[4] reported the rate constants of thermolysis of diaryl or alkylethers in detail and discussed about their mechanisms. As to the behavior of side chains, Savage et al.[5] examined 1-alkylpyrene pyrolysis, and Nomura et al.[6] and Freund et al.[7] picked up the aromatic compounds having longer bridges or alkyl side chains. As to the mechanisms of the bond cleavage reactions occurred in coal, McMillen et al. proposed radical hydrogen transfer (RHT), which was also discussed by other researchers[1,8,9].

In a previous paper[10], we investigated the chemical structure change of coal during its carbonization process and pointed out the importance of the amount of the transferable hydrogen for development of coal plasticity. This seems to be parallel with many researcher's intentions. Here, by using DHA and DHP as the hydroaromatics, we considered two types of the bond cleavage reactions, the homolytic cleavage and the ipso position cleavage.

EXPERIMENTAL SECTION

Samples.

Coal samples employed in this work are the six kinds of bituminous coals, provided by the Iron and Steel Institute of Japan. The characteristics are summarized in Table 1. These coal samples were pulverized (-100 mesh) and dried at 100 °C for 6 h in vacuo prior to use. The substrates of model compounds 1,2-di(1-naphthyl)ethane (DNE) and 1,5-dibenzyl-naphthalene (DBN), were synthesized as follows: DNE was prepared by reduction of (1-chloromethyl)naphthalene with iron powder in water and DBN was obtained by $\text{Et}_3\text{SiH}/\text{CF}_3\text{COOH}$ reduction of 1,5-dibenzoylnaphthalene according to the method reported[3]. The other reagents or coal model compounds were commercially available and purified by recrystallization before use.

The heat-treatment of coal or its model compounds in the presence of hydrogen donating compounds.

A coal sample and 9,10-dihydroanthracene (abbreviated as DHA) or 9,10-dihydrophenanthrene (DHP) were put in a sealed tube (Pyrex, 6 mm inner diameter x 100 mm long) at the weight ratio of 1:1 (100 mg each), the tube being inserted into the electric furnace preheated at determined temperature (380 or 420 °C), and kept for 5 min. The temperature of the inside of the sealed tube was found to raise to the desired temperature within 2 min, the heating rate being about 200 K/min. After 5 min passed, the sealed tube was taken out and the products were recovered by breaking the tube and washing the inside of the tube with dichloromethane. After the addition of an appropriate internal standard, the amounts of DHA or DHP consumed were determined.

In the case of the model compounds [1,2-diphenylethane (DPE), benzylphenylether (BPE), 1,2-di(1-naphthyl)ethane (DNE) and 1,5-dibenzyl-naphthalene (DBN)], 0.25 mmol of the hydrogen donating compounds and each model compound were heated under the similar conditions to those mentioned above. Qualitative and quantitative analyses of the products were undertaken by a Shimadzu QP-2000A GC/MS and a Shimadzu GC-14APSFSC gas chromatograph with CBP-1 column (0.25 mm diameter x 25 m long), respectively. Duplicate runs, at least three times, were made for each set of the reaction to insure reproducibility.

RESULTS AND DISCUSSION

The reaction of coal with hydrogen donating compound.

The heat-treatment of the six sample coals with the hydrogen donating compounds, DHA or DHP was carried out at 380 or 420 °C for 5 min. The reaction gave the corresponding dehydrogenated compound, anthracene or phenanthrene, as the major product along with minor amounts of tetrahydro-derivatives (mainly 1,2,3,4-tetrahydro isomer). When either DHA or DHP was treated in a sealed tube without coal (blank runs), there observed negligible amounts of tetrahydro-derivatives. These results suggest tetrahydro-derivatives to be derived from coal-catalyzed disproportionation of DHA or DHP.

We evaluated the amounts of hydrogen transferred from DHA or DHP to coal according to the following equation:

$$\frac{\text{The amount of hydrogen transferred (mg H}_2\text{/g daf coal)}}{(\text{mg}) \times 2/178 - \text{wt. of tetrahydro-derivatives (mg)} \times 2/182} \times 1000/\text{wt. of daf coal (mg)}$$

The results of the reaction of coal with the hydrogen donating compounds are shown in Figure 1. The lower the rank of the coals was, the more amounts of hydrogen were consumed. As we had already reported, the chemistry in the reaction at around 400 °C was considered as the bond cleavage reactions of bridge structures contained in coal, this hypothesis being supported partially by the fact that lower rank coals have rich amount of easily cleavable bonds such as ether bonds due to their higher contents of oxygen.

It is interesting to note that in the reaction at 420 °C, the amounts of hydrogen transferred from DHP were larger than those from DHA, while at 380 °C, DHA tended to donate more amounts of hydrogen to coal than DHP did. It is reasonable, at first, that at 420 °C amounts of hydrogen transferred are larger than that at 380 °C because cleavage reactions took place extensively at higher temperature. As for interesting behavior of DHP and DHA, we can say that the bond cleavage reaction occurred during the heat-treatment is dependent on the type of the hydrogen donating compounds. Therefore, in order to compare the reactivity of the hydrogen donating compounds, DHA and DHP, we conducted the reaction of the coal model compounds which have the bridges between the aromatic moieties, such as 1,2-diphenylethane and so on with the hydrogen donating compounds under the similar conditions to the reaction with coal

Homolytic cleavage reaction of dimethylene and methylene-ether bonds.

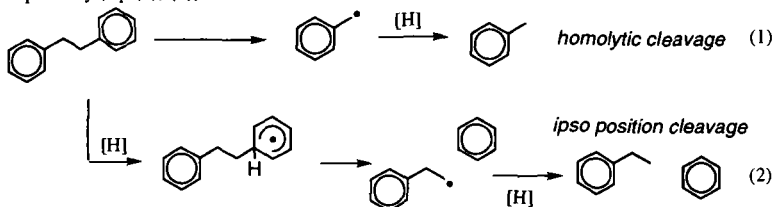
Generally, coal macromolecule is considered to consist of aromatic cluster and alkyl bridges or side chains including naphthenic portion, being regarded as cross-linking polymers as a whole. In the proposed coal chemical structure models, there observed the bridge structures between two aromatic rings, such as $-\text{CH}_2-\text{CH}_2-$, $-\text{CH}_2-\text{O}-$ or $-\text{CH}_2-$ and so on, these seeming to be important in the thermochemical reaction. On the basis of this background, we employed 1,2-diphenylethane (DPE), benzylphenylether (BPE), and 1,2-di(1-naphthyl)ethane (DNE) as coal model compounds having the bridge structures.

The heat-treatment of these compounds in the presence of DHA or DHP was conducted under the similar conditions to that of coal. It was found that the conversion of BPE was rather high (> 95 %) while those of DPE and DNE were low (< 6 %). The bridge structure in coal is thought to be cleaved more easily than those in DPE or DNE were because of the relatively large size and many substituents of coal aromatic rings which can assist, in general, the cleavage reactions. On the other hand, rather high reactivity of BPE with homolytic fission of bridge bond can be easily understood because bond dissociation energy of carbon-oxygen is low. Here, in order to observe much more difference of the reactivities of DPE and DNE in either DHA or DHP, the reaction time was prolonged as 60 min. The reaction temperature of BPE was set to 380 °C for 5 min because BPE was found to be more reactive than DPE or DNE.

Figure 2 shows the results of the reactions in the presence of two different hydrogen donors. Under these conditions, considerable amounts of DHA or DHP were converted in each blank run so that the yield of anthracene or phenanthrene would not properly reflect the exact amount of DHA or DHP consumed for hydrogen transfer. Therefore, we evaluate the degree of the bond cleavage reaction on the basis of the yields of the cleaved products. The conversion of the model compounds reflects the strength of cleavable bonds (order of bond dissociation energy is $\text{PhCH}_2-\text{OPh} \ll \text{NapCH}_2-\text{CH}_2\text{Nap} < \text{PhCH}_2-\text{CH}_2\text{Ph}$). DPE showed less reactivity even under these conditions (420 °C, 60 min), and slightly higher yield of toluene when DHP was used as the hydrogen donor than in the case of DHA. Actually, the same trend was observed with the reaction of DNE at 420 °C for 5 min. It is thought that the less reactivity of DPE might be caused by the small size of aromatic rings and the absence of substituents like $-\text{OH}$ or alkyl groups, however, much more reactivity would be expected with bridge bonds contained in the structure of coal. On the other hand, it should be noted that yields of the homolytic cleavage products from DNE or BPE, 1-methylnaphthalene or toluene and phenol, respectively, were higher when DHA was used than in the case of DHP. These results remind us that DHA has the higher potential to scavenge the radical generated.

Ipsso position cleavage reaction of the bridge structure in model compounds.

In the reactions of DPE and DNE, there also observed the formation of the ipso position cleavage products like benzene and ethylbenzene, and naphthalene and ethylnaphthalene, respectively (eq. (1), (2)).



The reaction of DPE or DNE with two different hydrogen donors at 420 °C for 60 min gave the ipso position cleavage products in 0.1-6.6% yield (Figure 3). These yields from the reaction using DHP were considerably higher than the case of DHA. In the case of BPE, only homolytic

cleavage reaction occurred. However, the yields of the ipso position cleavage products were relatively low in comparison with those of the homolytic cleavage products. Here we would like to refer to the reports concerning bridge bonds contained in coal[11]. RuO₄ oxidation reaction confirmed that, in coal, dimethylene bridge connecting two aromatic moieties exists because the formation of succinic acid was observed in the oxidized products of COM. The presence of succinic acid shows the presence of dimethylene bridge. However, as for monomethylene bridge this oxidation could not confirm its presence in COM because under these oxidation conditions, the malonic acid is unstable. In generally speaking, the prevailing presence of monomethylene bridge bond in COM is supported by many coal researchers. Then, we employed 1,5-dibenzyl-naphthalene (DBN) as the possible substrate of coal model compounds. It does not have homolytic cleavable linkages like -CH₂-CH₂- or -CH₂-O-, so only the ipso position cleavage is expected to take place. Its reaction afforded benzene, toluene, benzylnaphthalene and benzyl-methylnaphthalene. However, only small amount of naphthalene derivatives was obtained and the recovery of the substrate was not so high. This could be explained by assuming that some oligomerization or very complicated reaction might occur under the reaction conditions as we had pointed out in a previous paper[3]. Therefore, we judged the degree of cleavage on the basis of the sum of the yield of benzene and toluene. Also from this result, the ipso position cleavage by using DHP could proceed more efficiently than in the case of DHA. In this system, strong C_{alkyl}-C_{aryl} bond must be cleaved by solvent induced scission. It could be suggested that introduction of hydrogen atom as a result of radical hydrogen transfer or free hydrogen transfer occurred in heat-treatment of coal, and Malhotra et al. also mentioned the effectiveness of ipso position cleavage in liquefaction reaction[12].

Consideration about the bond cleavage reaction of the bridge structures in coal.

In the reactions of coal with DHA or DHP, at 420 °C, DHP had been consumed at larger amounts and at 380 °C, DHA was the case as shown in Figure 1. As we had already mentioned, we thought that these consumption of hydrogen donor could correlate to the degree of bond cleavage reaction occurred in coal. Although we know that the reactions during heat-treatment would be so complex that they could not be described simply, the bond cleavage reactions of the bridge structures in coal proceeded mainly under our conditions.

If we here assume that with higher rank coal in the present study, monomethylene bridge prevails, we can easily understand the results shown in this paper. At 420 °C for 5 min, DHP shows higher extent of hydrogen transfer than that of DHA, and DHP is favorable to DHA as for ipso position cleavage and above observation is readily understood by referring to the assumption that methylene bridge is prevailing bridge bond than more longer methylene bridges. At 380 °C, carbon-oxygen related bond is cleaved so that DHA is effective hydrogen transfer reagent than DHP. Therefore, we can say that there is a possibility to use DHP or DHA as the probe to understand the reactivity and structure of coal.

ACKNOWLEDGMENT

This work was partially supported by a Grant-in-aid provided by the Iron and Steel Institute of Japan, and the authors acknowledge the support of Sumitomo Metal Industries Ltd. for useful discussion.

REFERENCES

- 1 Autrey, T.; Albom, E. A.; Franz, J. A.; Camaioni, D. M. *Energy Fuels* **1995**, *9*, 420.
- 2 Futamura, S.; Koyanagi, S.; Kamiya, Y. *Fuel* **1988**, *67*, 436; *Fuel* **1989**, *68*, 130.
- 3 Murata, S.; Nakamura, M.; Miura, M.; Nomura, M. *Energy Fuels* **1995**, *9*, 849.
- 4 Korobkov, V. Y.; Grigorieva, E. N.; Bykov, V. I.; Senko, O. V.; Kalechitz, I. V. *Fuel* **1988**, *67*, 657; *Fuel* **1988**, *67*, 663; *Fuel* **1989**, *68*, 262; *Fuel* **1989**, *68*, 264.
- 5 Smith, C. M.; Savage, P. E. *Energy Fuels* **1994**, *8*, 545.
- 6 Murata, S.; Mori, T.; Murakami, A.; Nomura, M. *Energy Fuels* **1995**, *9*, 119.
- 7 Freund, H.; Matturro, M. G.; Olmstead, W. N.; Reynolds, R. P.; Upton, T. H. *Energy Fuels* **1991**, *5*, 840.
- 8 McMillen, D. F.; Malhotra, R.; Hum, G. P.; Chang, S.-J. *Energy Fuels* **1987**, *1*, 193.
- 9 Savage, P. E. *Energy Fuels* **1995**, *9*, 590.
- 10 Kidena, K.; Murata, S.; Nomura, M. *Energy Fuels* **1996**, *10*, 672.
- 11 Murata, S.; Uesaka, K.; Inoue, H.; Nomura, M. *Energy Fuels* **1994**, *8*, 1379.
- 12 Malhotra, R.; McMillen, D. F. *Energy Fuels* **1993**, *7*, 227.

Table 1. Ultimate and proximate analyses of the sample coals

Coal	Proximate analyses (wt%, db)			Ultimate analyses (wt%, daf)				
	Ash	VM	FC	C	H	N	S	O ^a
Lusca	9.5	23.5	67.0	88.3	4.6	1.5	0.3	5.3
Goonyella	9.8	23.4	66.8	88.1	5.1	1.9	0.6	4.3
Pittstone-M	7.3	34.3	58.4	85.7	5.5	1.7	1.0	6.1
Workworth	13.8	34.2	52.0	84.7	5.9	1.8	0.6	7.0
Witbank	8.0	32.9	59.1	82.7	4.5	2.2	0.6	10.0
K-Prima	3.8	43.4	52.8	81.2	5.9	1.3	0.4	11.2

^a By difference

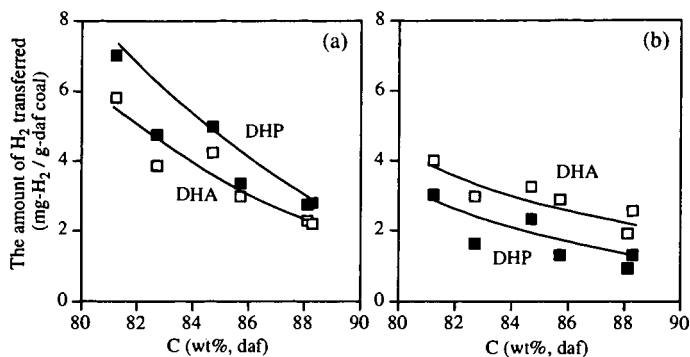


Figure 1. Evaluated amount of hydrogen transferred from DHA (□) or DHP (■) to coal at (a) 420 °C and (b) 380 °C

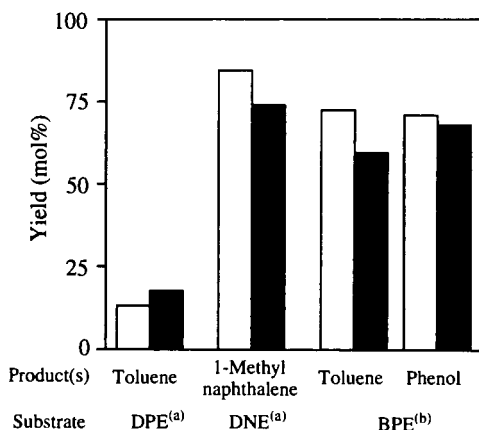


Figure 2. The yields of the homolytic cleavage products in the reaction of Ar-CH₂-X-Ar (X=CH₂, O) in the presence of hydrogen donor, DHA (□) or DHP (■): (a) 420 °C, 60 min, [Substrate]:[donor]=0.25:0.25 (in mmol), (b) 380 °C, 5 min, [Substrate]:[donor]=0.25:0.25 (in mmol)

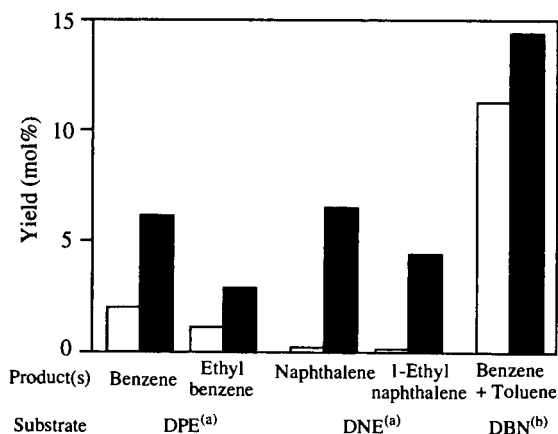


Figure 3. The yields of the ipso position cleavage products in the reaction of DPE, DNE and DBN in the presence of DHA (□) or DHP (■): (a) 420 °C, 60 min, [Substrate]:[donor]=0.25:0.25 (in mmol), (b) 430 °C, 60 min, [Substrate]:[donor]=0.25:0.25 (in mmol)

LIQUEFACTION OF MICRO ALGAE WITH IRON CATALYST

Toshimitsu Suzuki, Taka-o Matsui, Chiyo Ueda, and Na-oki Ikenaga
Department of Chemical Engineering, Kansai University
Suita, Osaka Japan 564

Keywords : Liquefaction, Micro algae, Dispersed iron catalyst

INTRODUCTION

Recently, carbon dioxide fixation by cultivating micro algae is being investigated. Since cultivated micro algae would be degraded into carbon dioxide, methane, and water by micro biological process, effective utilization of micro algae produced are highly required.

Production of liquid fuels from biomass have been extensively studied. Effects of hydrogen donor solvents¹ or alkali metal carbonate catalysts² on biomass conversion were reported under a hydrogen or a carbon monoxide atmosphere. Yokoyama *et al.* summarized techniques concerning the liquefaction of wood, and reported that sodium carbonate is effective catalyst for increasing the oil yield in water in the absence of reducing gas.³ More lighter oil was obtained in a high yield by the addition of organic solvents such as propanol, butanol and ethyl acetate.⁴ Dote *et al.* reported that sodium carbonate was effective catalyst for the liquefaction of *Botryococcus braunii* in water under nitrogen.⁵

In this work, we have investigated liquefaction of *Spirulina* in various organic solvents or water under a hydrogen, a nitrogen or a carbon monoxide atmosphere in the temperature range of 300-425 °C using Fe(CO)₅-S catalyst developed for the liquefaction of coal⁶ and discussed the effects of reaction conditions and catalysts on the product distribution and properties of oil.

EXPERIMENTAL SECTION

Spirulina (C 46.1; H 7.4; N 4.8; S 0.4; O 41.4 %, protein 57.5; fat 12.0; fatty acid 1.0; carbohydrate <0.5 %) was used as a micro alga. A 2.0 g of dried *Spirulina*, 8.0 g of tetralin, 1-methylnaphthalene, toluene or water and the prescribed amount of catalyst were put into a 50 mL magnetically stirred autoclave. The autoclave was pressurized to 5 MPa with hydrogen, nitrogen or carbon monoxide, and then the autoclave was heated up to a certain reaction temperature. After the reaction, products were separated by extraction with THF. THF soluble fraction was further separated into hexane-insoluble and hexane soluble (oil fraction). Gaseous products were analyzed by gas chromatography. As a catalyst, Fe(CO)₅-S (Fe 1.0 mmol, S/Fe=2) was used. Oil fractions obtained in toluene and water were analyzed by FT-IR and gel permeation chromatography. C, H, and N elemental analyses were carried out at Osaka university.

Heating values of oil fractions were estimated by equation (1). Where C, H, N, S and O are normalized to weight fractions of respective elements in oil.⁷

$$H_g = 8400C + 27765H + 1500N + 2500S - 2650O \quad [\text{cal/g}] \quad (1)$$

RESULTS AND DISCUSSION

Effect of reaction conditions in the liquefaction of *Spirulina*. Table 1 shows results of liquefaction of *Spirulina* at 350 °C for 60 min in tetralin or 1-methylnaphthalene under a hydrogen or a nitrogen atmosphere with or without a catalyst. More than 90 % of conversions and 50 % of oil yields were obtained under all the reaction conditions employed (runs 1-6). Gaseous products were mainly composed of methane (50-80 %) and carbon dioxide (10-30 %). Liquefaction of *Spirulina* under a nitrogen atmosphere without a catalyst gave 54.0 % of oil yield in 1-methylnaphthalene and 52.3 % in tetralin. Addition of Fe(CO)₅-S increased the oil yield to 63.7 and 66.9 % under a hydrogen atmosphere in 1-methylnaphthalene and tetralin, respectively. In the liquefaction under hydrogen without the catalyst (run 5), 0.28 wt% of hydrogen was absorbed from gas phase, whereas hydrogen consumption in the liquefaction increased to 1.2 wt% with the catalyst. Hydrogen activated on the dispersed catalyst might have contributed to increase the oil yield. Liquefaction of *Spirulina* in tetralin, a more efficient solvent for the liquefaction of woody biomass,¹ afforded similar conversion and product distribution as compare to those obtained in 1-methylnaphthalene. It is reported that tetralin is effective for the liquefaction of lignocellulose.⁸ However, *Spirulina* is mainly composed of proteins, thus fragment from *Spirulina* is considered to be stabilized easily even without a hydrogen donor. This is one of the characteristic differences between the liquefaction of micro algae and coal or woody biomass. Much smaller increases in the amount of hydrogen transferred to *Spirulina* would be accounted for the different mechanisms in the liquefaction of these two substances.

Effects of reaction temperature and reaction time in the liquefaction of *Spirulina*. Effects of reaction temperature on the product distribution in the liquefaction of *Spirulina* in tetralin is shown in Fig. 1 with or without catalyst. More than 90 % of conversions were obtained in the temperature range of 300-425 °C even without catalyst. Total yield of oil and gas increased from 46.8 to 80.4 % with increasing reaction temperature from 300 to 425 °C. Oil yield including water was 42.4 % at 300 °C and increased to 62.2 % at 400°C, but oil yield did not increase above 400 °C as compared to that at 400 °C, due to a large increase in the gas yields from 9.8 % at 400 °C to 13.9 % at 425 °C. Oil yield in the presence of catalyst showed similar tendencies, but effect of the catalyst was pronouncedly observed at 350 °C. Again remarkable increases in gas yields were observed above 400 °C. At a lower or a higher temperature, an addition of catalyst only slightly affected product distribution in the liquefaction of *Spirulina*.

Fig. 2 shows effects of reaction time on the product distribution in the liquefaction of *Spirulina* at 350 °C in tetralin without catalyst and with Fe(CO)₅-S. More than 90 % of conversions were obtained irrespective of reaction time and in the presence or absence of catalyst. Oil yield without

catalyst slightly increased from 46.8 to 53.6 % with increasing reaction time from 0 to 30 min. However, product distributions were almost constant for prolonged runs in the absence of catalyst. Oil yield with $\text{Fe}(\text{CO})_5\text{-S}$ increased from 52.3 to 66.9 % with increasing reaction time 0 to 60 min, further increase in the reaction time did not change product distribution. Slower reaction producing oil was promoted with the addition of a highly dispersed catalyst under hydrogen atmosphere.

Liquefaction in water. In practical process, drying wet *Spirulina* required a large quantity of energy. Thus liquefaction of *Spirulina* in wet form is desirable.

Spirulina was liquefied in 1-methylnaphthalene under carbon monoxide atmosphere with 0.5-2.0 g of water in the presence of $\text{Fe}(\text{CO})_5\text{-S}$ catalyst. The results are shown in Table 1 (runs 8-10). Gas yields were not measured, because major gaseous products from *Spirulina* are carbon monoxide and carbon dioxide, and they were masked with the charged carbon monoxide and the carbon dioxide produced according to the water gas shift reaction.

Addition of 0.5 g of water in the liquefaction of *Spirulina* with $\text{Fe}(\text{CO})_5\text{-S}$ under carbon monoxide afforded 74.5 % of oil yield (run 8). Oil plus gas yield of 75.5 % was obtained under hydrogen (run 6) with the same catalyst. Further increases in the amount of H_2O to 2.0 g (run 10) increased the oil plus gas yield to 83.1 %. Hydrogen produced was amounted to 2.1, 4.7, and 6.3 mmol after the reaction in the presence of 0.5, 1.0, and 2.0 g of water, respectively. Oil plus gas yields obtained with H_2O exceeded those obtained under hydrogen in 1-methylnaphthalene. The result that high oil yield of 64.3 % was obtained in 1-methylnaphthalene- H_2O mixed solvent (run 7) indicates that hydrolysis of *Spirulina* possibly occurred. Such behavior is quite different from coal and woody biomass liquefaction.

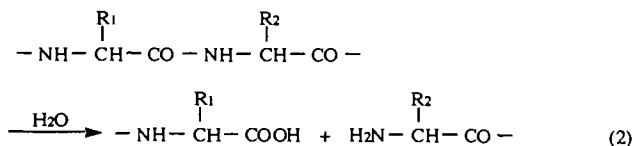
Spirulina was liquefied in water under nitrogen without catalyst in the temperature range of 200-350 °C (Fig. 3). Conversion increased from 71.8 to 93.5 % with increasing the reaction temperature from 200 to 350 °C. Gas yields were almost constant (6-8 %) in these temperature ranges. Oil yield increased from 48.4 to 78.3 % with increasing reaction temperature to 350 °C. However, conversion was slightly smaller than that obtained in 1-methylnaphthalene- H_2O mixed system under carbon monoxide with the catalyst.

Characterization of oil fractions. In order to eliminate contamination of the solvent, for the characterization of oil fractions, a more volatile solvent toluene was used in the liquefaction of *Spirulina*. The results are shown in Table 1 (runs 11-13). Similar tendencies in the liquefaction behavior were observed in toluene as compared to those obtained in 1-methylnaphthalene.

Elemental compositions of feed and oil fractions are shown in Table 2. Carbon contents of oil fractions obtained in toluene are 64.2-69.0 % and these values are higher than that of feed (46.1 %). Oxygen contents (by differences) of products were lowered to 14.0-19.9 % as compared to 41.4 % of feed. Oil fractions obtained in water showed lower carbon content of 57.3 % and consequently higher oxygen content of 28.5 %. Ratio of H/C in oil was almost constant irrespective of reaction conditions and decreased to 1.50-1.55 from 1.93 in the feed and ratio of O/C decreased to 0.15-0.37 from 0.67 in feed. These findings indicate that deoxygenation through dehydration or decarboxylation proceeded in the liquefaction of *Spirulina*.

Heating values of oil fractions were calculated according to the formula proposed by Ringen *et al.*⁷, using elemental composition. Heating values of oil fractions were higher than that of feed. Liquefaction of *Spirulina* in toluene gave oil fractions having heating values as high as 7700-7900 cal/g. Assuming water yield by the differences in the oxygen balance, 75.8 % and 71.1 % of heating values could be recovered as oil from the charged *Spirulina* having heating value of 4900 cal/g, in the liquefaction with or without $\text{Fe}(\text{CO})_5\text{-S}$ catalyst, respectively. Heating value of oil fraction obtained in water was 6200 cal/g and lower than that obtained in toluene, although a higher yield was obtained. Liquefaction in toluene with 1.0 g of water gave oil fraction not only in a high yield of 69.8 %, but also had a high heating value of 7300 cal/g. A presence of moderate amount of water is considered to be effective for the production of oil fraction having a high heating value in a high yield.

Fig. 4 shows FT-IR spectra of feed and oil fractions obtained in toluene and water with or without the Fe catalyst. Absorption at around 1652, 1545, and broad band 500-600 cm^{-1} ascribed to polypeptide in feed (a) are not seen in the spectrum of liquefied oil. This suggests that liquefaction of *Spirulina* proceeded by mainly scission of peptide linkages. Hydroxy or amine (3300 cm^{-1}), methyl and methylene (2800-3000, 1456, and 1389 cm^{-1}), and carbonyl (1705 and 1670 cm^{-1}) groups were confirmed by FT-IR spectra (b, c, and d). In the oil fraction obtained in water without the Fe catalyst (d), absorption peaks ascribed to carboxyl acid (3000-3300, 1705, and 1270 cm^{-1}) and amine (3300 and 1590 cm^{-1}) were more strongly observed as compared to the oil fraction obtained in toluene (b). This fact indicates that liquefaction of *Spirulina* proceeded via mainly hydrolyses of peptide linkages with water as shown in equation (2).



According to gel permeation chromatograms of the oil fractions prepared under different reaction conditions, molecular weights of oil fractions were distributed in broad range from 200 to 2000, showing peaks at 780 and 830. Since the evaporative light scattering detector was employed, detection of the low molecular weight component was limited to 200, possibility of the presence of lower molecular weight fraction can not be ruled out. Peaks at lower molecular weights region 400

and 490 were observed in the oil fractions obtained in toluene under hydrogen. Further increase in lower molecular weight product was observed in the liquefaction with the Fe catalyst. Thus the reactions to lower molecular weight product progressed through hydrocracking of C-C bonds with the catalyst under a hydrogen atmosphere.

These findings suggested that production of oil from *Spirulina* proceeded via mainly thermal decomposition or hydrolyses of peptide linkages with water fed or produced during liquefaction and hydrocracking of C-C bonds is promoted in the presence of a catalyst under hydrogen.

CONCLUSION

Liquefaction of *Spirulina* at 300-425 °C under hydrogen gave more than 90 % of conversions and 60 % of oil yields. Addition of Fe(CO)₅ catalyst increased oil yield from 52.3 to 66.9 % at 350 °C for 60 min in tetralin. Liquefaction in water gave oil yield as high as 78.3 % at 350 °C even under nitrogen atmosphere without the catalyst. Liquefaction in toluene gave oil fractions having high heating value of 7700-7900 cal/g, but the products containing large amount of oxygen estimated to have lower heating value of 6200 cal/g.

FT-IR and gel permeation chromatograph suggested that production of oil fractions mainly proceeded via thermal scission of polypeptide and hydrolysis with water, and further hydrocracking of C-C bond is promoted in the presence of Fe(CO)₅-S catalyst under hydrogen.

REFERENCES

- (1) Thring, R.W., Chornet, E. Can. J. Chem. Eng. 1993, **71**, 107.
- (2) Beckman, D., Boocock, D.G.B. Can. J. Chem. Eng. 1983, **61**, 80.
- (3) Yokoyama, S., Ogi, T., Koguchi, K., Murakami, M., Suzuki, A. Sekiyu Gakkaishi 1986, **29**, 262.
- (4) Ogi, T., Yokoyama, S., Minowa, T., Dote, Y. Sekiyu Gakkaishi 1990, **33**, 383.
- (5) Dote, Y., Sawayama, S., Inoue, S., Minowa, T., Yokoyama, S. Fuel 1994, **73**, 1855.
- (6) Watanabe, Y., Yamada, O., Fujita, K., Takegami, Y., Suzuki, T. Fuel 1984, **63**, 752.
- (7) Ringen, S., Llanum, J., Miknis, M.P. Fuel 1979, **58**, 69.
- (8) Vasilakos, N.P., Augstgen, D.M. Ind. Eng. Chem. Process. Des. Dev. 1985, **24**, 304.

Table 1 Results of the Liquefaction of *Spirulina* under Various Conditions

run	Solvent	H ₂ O (g)	Atmosphere	Catalyst	Conv.	Oil (%)	Gas	H ₂ -trans ^a (mmol)
1	TL		N ₂	none	91.9	52.3	5.2	0.3 ^b
2	TL		H ₂	none	92.2	54.2	7.2	4.5
3	TL		H ₂	Fe(CO) ₅ -S	92.0	66.9	6.2	5.6
4	1-MN		N ₂	none	88.1	54.0	5.2	0.1 ^b
5	1-MN		H ₂	none	91.8	54.4	8.9	2.8
6	1-MN		H ₂	Fe(CO) ₅ -S	94.9	63.7	11.8	11.7
7	1-MN	1.0	N ₂	none	95.4	64.3	9.7	0.6 ^b
8	1-MN	0.5	CO	Fe(CO) ₅ -S	96.1	74.5		2.1 ^b
9	1-MN	1.0	CO	Fe(CO) ₅ -S	96.6	79.0		4.7 ^b
10	1-MN	2.0	CO	Fe(CO) ₅ -S	97.8	83.1		6.3 ^b
11	TOL		H ₂	none	82.6	57.0	6.9	2.7
12	TOL		H ₂	Fe(CO) ₅ -S	90.1	63.3	4.1	3.6
13	TOL	1.0	N ₂	none	92.5	69.8	8.9	0.8 ^b
14	H ₂ O		N ₂	none	93.4	78.3	6.8	0.5 ^b

Reaction temperature 350 °C, reaction time 60 min, *Spirulina* 2.0 g, solvent 8.0 g, initial pressure 5 MPa, Fe(CO)₅ 1.0 mmol, S 2.0 mmol.

a) Amount of hydrogen transferred to products from gas phase and tetralin.

b) Amount of hydrogen produced after reaction.

Table 2 Elemental Analyses of Oil Fraction Products

run	C	H	N	O ^a	H/C	N/C	Heating Value (cal/g)
	46.1	7.4	4.8	41.4	1.93	0.09	4902
11	69.0	8.6	8.4	14.0	1.50	0.10	7939
12	66.7	8.6	7.5	16.2	1.55	0.10	7674
13	64.2	8.3	7.6	19.9	1.55	0.10	7284
14	57.3	7.4	6.8	28.5	1.55	0.10	6215

Reaction temperature 350 °C, reaction time 60 min, *Spirulina* 2.0 g, solvent 8.0 g, initial pressure 5 MPa, Fe(CO)₅ 1.0 mmol, S 2.0 mmol.

a) by differences

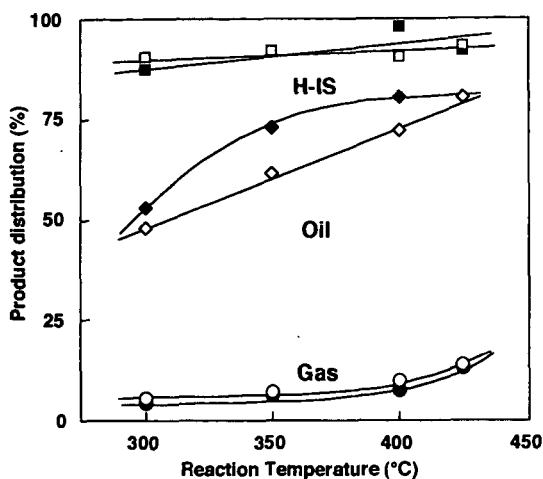


Fig.1 Effect of Reaction Temperature on the Product Distribution in the Liquefaction of Spirulina

Reaction time 60 min, Spirulina 2.0 g, TL 8.0 g,

PH₂ 5.0 MPa, Fe(CO)₅ 1.0 mmol, S 2.0 mmol

□ ◇ ○ without catalyst, ■ ◆ ● with Fe(CO)₅-S

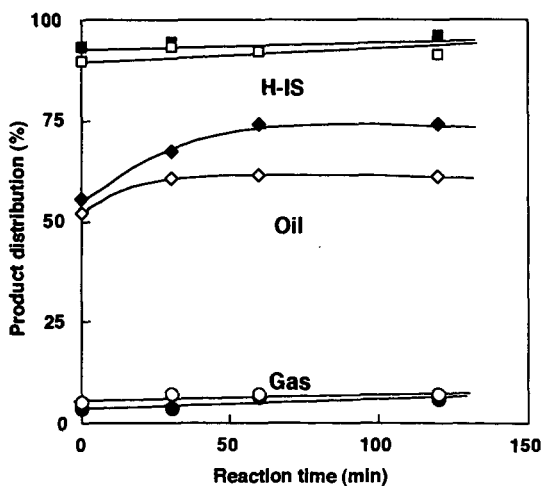


Fig.2 Effect of Reaction Time on the Product Distribution in the Liquefaction of Spirulina

Reaction temperature 350 °C, Spirulina 2.0 g, TL 8.0 g,

PH₂ 5.0 MPa, Fe(CO)₅ 1.0 mmol, S 2.0 mmol

□ ◇ ○ without catalyst, ■ ◆ ● with Fe(CO)₅-S

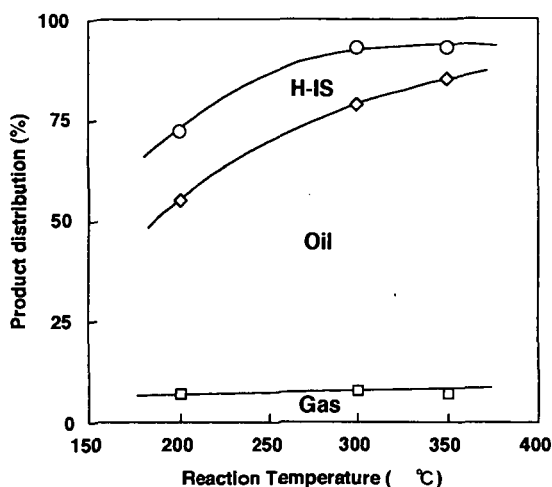


Fig.3 Effect of Reaction Temperature on the Product Distribution in the Liquefaction of Spirulina in water

Reaction time 60 min, Spirulina 2.0 g, H₂O 8.0 g, PN₂ 5.0 MPa

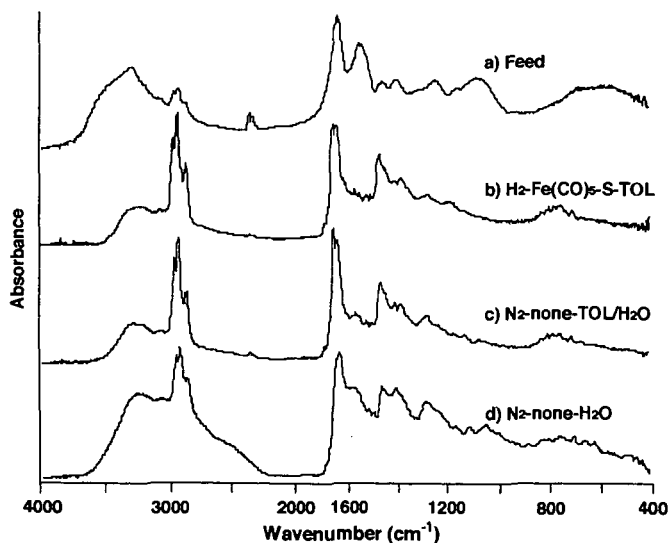


Fig.4 FT-IR Spectra of Spirulina and Liquefaction Products

Reaction temperature 350 °C, reaction time 60 min, Spirulina 2.0 g.
a) feed, b) PH₂ 5.0 MPa, toluene 8.0 g, Fe(CO)₅ 1.0 mmol, S 1.0 mmol,
c) PN₂ 5.0 MPa, toluene 8.0 g, H₂O 1.0 g, d) PN₂ 5.0 MPa, H₂O 1.0 g

MECHANISTIC MODELLING OF 9-METHYLANTHRACENE THERMOLYSIS

P.S. Virk and V.J. Vlastnik
Department of Chemical Engineering
M. I. T., Cambridge, MA 02139

KEYWORDS: Thermolysis, Mechanism, Kinetics, Numerical Simulation, Modelling.

INTRODUCTION

Motivation. This work on modelling thermolysis of 9-methylanthracene, abbr 9MA, continues our studies of methylated acenes, that mimic the chemical moieties found in complex fossil materials of engineering interest. Too, since 9MA is a primary product of 9,10-dimethylanthracene, abbr 910DMA, thermolyses [1, 2], it was hoped that the present work might buttress our understanding of 910DMA thermolyses at high conversions.

Previous Work. Detailed mechanistic modelling of 9MA thermolysis has not hitherto been attempted. However, the literature does contain some experimental information regarding 9MA thermolysis, which we have earlier summarized [3, 4, 5, 6].

Outline. Our modelling of 9MA thermolysis is based upon a 19-step mechanism, valid at low conversions, that was recently formulated to describe experimental observations [3]. Thermochemical parameters for all stable and radical species occurring in the mechanism were estimated from first principles. Next, enthalpies of reaction were calculated for each elementary step and used to infer Arrhenius parameters in both forward and reverse directions. Rate constants were then calculated for each reaction at a selected temperature, and these were used in conjunction with the differential conservation relations for each species to effect a full numerical solution of the model system, starting from an initial condition of pure substrate. The numerical simulation of 9MA thermolysis kinetics and product selectivities was directly compared with experimental observations at the same conditions. A sensitivity analysis was performed to discern how errors in the estimated Arrhenius parameters affected the model results. Finally, the Arrhenius parameters of certain elementary steps were adjusted, within their error limits, to provide an optimized model that best-fit the experimental observations.

REACTION PATHWAYS & MECHANISM

Pathways. Earlier experiments have identified three primary parallel pathways for thermolysis of 9MA, namely: (P1) hydrogenation to 9,10-dihydro-9-methylanthracene, abbr. DHMA, (P2) demethylation to anthracene, abbr. ANT, and (P3) methylation to 9,10-dimethylanthracene, abbr. 910DMA. The primary demethylation product ANT is associated with formation of methane gas CH₄; heavy products are also formed, including both pure- and cross-termination types of dimeric species related to 9MA and DHMA, most notably a bibenzyl dimer called 9MAD.

Mechanism. A possible mechanism for 9MA thermolysis is presented in Fig. 1. This elementary step "graph" is constructed with substrate and all stable molecular products arrayed in the bottom row and unstable radical intermediates arrayed in the top row. Reaction "nodes", arrayed in the middle row, connect the individual species in the bottom and top rows with arrows indicating the initial direction of reaction (all reactions are, of course, reversible). Initiation reactions are denoted by solid interconnecting lines, propagation reactions by various kinds of dashed lines and termination reactions by dotted lines. Arrow weights qualitatively depict relative elementary reaction traffic, to be discussed in the next section.

The 9MA substrate is in the middle of the bottom row, with light (propagation) products to its right and heavy (termination) products to its left. The free-radical cycle is initiated by the bimolecular disproportionation of substrate (R1), an intermolecular hydrogen transfer reaction, to form the respectively dehydrogenated and hydrogenated radical species 9MA* and HMA10*. Of these, the latter can either abstract hydrogen from 9MA by (R2), to form DHMA product, or undergo a β -scission type of radical decomposition by (R3), forming ANT product and a methyl radical CH₃*. The CH₃* can either abstract H from 9MA by (R4), to form methane product, or add to 9MA by (R5), to form the dimethyl radical HDMA*. The latter can then abstract H from 9MA via (R6) to form the observed 910DMA product. The cycle is terminated by the species 9MA* and HMA10* engaging in both pure- and cross-combinations, (R7-R9), to form various dimeric products. HMA10* radical can also terminate by disproportionation, (R10), to form 9MA and DHMA. The foregoing portion of the full 9MA thermolysis mechanism is analogous to a 910DMA thermolysis mechanism devised earlier [1, 2]. However, the 9MA substrate can also form the HMA9* radical, which can engage in all the reactions shown for HMA10* except for C-C bond scission, giving rise to steps (R11-R22) of the full mechanism. Thus substrate disproportionation by (R11) forms 9MA* and HMA9*, of which the latter can abstract hydrogen from 9MA by (R12), to form DHMA product. HMA9* can also form from H-transfer reactions (R16), between HDMA* and 9MA, and (R17), between HMA10* and 9MA, the latter causing radical isomerization. Finally, HMA9* can engage in a variety of termination reactions, including combinations (R18, R19, R21) that form dimeric products, and disproportionations (R20, R22) that form 9MA and DHMA.

The proposed mechanism accounts for the major products, ANT, DMAs, DHMA, CH₄ and heavies, observed during the initial stages of 9MA thermolysis. Each of the observed triad of primary pathways, namely, P1 hydrogenation, P2 demethylation and P3 methylation, also arise naturally as limiting cases of the elementary step graph, with P1 comprising the sets [R1, R2, R7] and [R11, R12, R7], P2 the set [R1, R3, R4, R7] and P3 the set [R1, R3, R5, R6, R7]. The stoichiometry of these sets restricts the maximum selectivity of each major product to 1/3, which is of the magnitude of the highest selectivities observed experimentally. The mechanism also offers some theoretical insights. It suggests that the relative kinetics of hydrogenation to demethylation, (P1)/(P2), are controlled by the HMA9* and HMA10* radicals. The HMA10* radical propagates both hydrogenation (R2) and demethylation (R3), but HMA9* propagates

only hydrogenation (R12), leading to the pathway ratio $(P1)/(P2) = [(R2)+(R12)]/(R3)$. Further, the methylation to demethylation ratio, $(P3)/(P2)$, is essentially governed by competition between methyl radical reactions (R4) and (R5), in which CH_3^{\bullet} either abstracts H from or adds to the 9MA substrate, the latter favoured by the presence of a potent unsubstituted 10-position.

MODELLING

Thermochemistry. Enthalpies of formation, ΔH_f^0 , for all chemical species participating in our 9MA thermolysis model were estimated by a "macro" group-additivity technique, using a basis set of bond strengths, D^0 kcal/mol, steric corrections, C^0 kcal/mol, and stable species enthalpies of formation, ΔH_f^0 , assembled from a variety of sources cited previously [2, 7]. Fig. 2 illustrates the estimation procedures. For the stable species 9MA in (a), we started with the largest, most structurally similar basis species available, namely ANT; other basis species and steric corrections, in this case 1MN, NAP and an alkene gauche interaction, were then either added or subtracted to bridge the structural differences between the starting and the desired species. The method provided both ΔH_f^0 , kcal/mol, and its rms error, kcal/mol. Calculations for a radical species, HDMA $^{\bullet}$, are shown in Fig. 2(b).

Arrhenius Parameters. Table 1 summarizes Arrhenius expressions, of the form $\log_{10} k = \log_{10} A - E^{\ddagger}/\Theta$, with rate constant k (l, mol, s units), pre-exponential factor A (same units as k), activation energy E^{\ddagger} (kcal/mol), and scaled temperature $\Theta = 0.004573 \cdot (T \text{ C} + 273.2)$, that were generated for each step of the 9MA thermolysis mechanism. An elementary reaction was first classified (column 2) according to standard free-radical reaction notation and then kinetic data for that type of reaction were analyzed to ascertain its activation parameters. Of these, $\log_{10} A = \log_{10} A_{\text{int}} + \log_{10}(\text{rpd})$ comprised an intrinsic portion, $\log_{10} A_{\text{int}}$ (column 3) and a reaction path degeneracy, rpd (column 4). Activation energy E^{\ddagger} was determined by an Evans-Polanyi expression (column 5), of form $E^{\ddagger} = E_0 + \alpha \cdot \Delta H_f^0$, with $\alpha = 0$ (combinations), 0.5 (H-abstraction and transfer) or 1 (homolysis, beta-scission). Values of the enthalpy of reaction ΔH_r^0 (column 6), derived from thermochemical estimates of the previous section, then led to E^{\ddagger} (column 7) and the final Arrhenius expression (column 8).

Numerical Solution. The model 9MA thermolysis reaction system was solved by a computer code called ACUCHEM [8]. This program numerically solves a system of differential equations that describe the temporal behavior of a spatially homogeneous, isothermal, multicomponent chemical reaction system. Integrations are performed by the method of Gear [9], appropriate for the stiff differential equations encountered in the present case. Two types of tests were performed to ensure reliable results. First, in regard to stability, it was verified that the program generated the same concentration profiles, regardless of the time step size. Second, in regard to fidelity, the concentrations of all species, both radical and stable, calculated by the numerical solution at low conversions $X < 0.1$ were found to agree with the corresponding concentrations obtained from pseudo-steady-state algebraic solutions at similar conditions.

RESULTS & DISCUSSION

Original Model. Numerical solutions of the 9MA thermolysis model were obtained at selected conditions covering the entire experimental grid, $315 < T \text{ C} < 409$ and $0.082 < [9\text{MA}]_0 \text{ mol/l} < 2.06$. The complete concentration histories of all radical and stable species obtained from each simulation are used in Figs. 1, 3 and 4.

Reaction Traffic. The arrows in Fig. 1 graphically depict the elementary reaction traffic calculated at $T = 370 \text{ C}$, $[9\text{MA}]_0 = 0.82 \text{ mol/l}$, and very low conversion $X \sim 0$, the thicker arrows denoting reactions with the greater net (forward - reverse) rates. The 910DMA substrate decomposes mainly, but not exclusively, by (R1) and (R11). The rates of hydrogenation (R2) and of demethylation (R3) are of comparable magnitudes, and the rate of methyl radical quenching by H-abstraction from substrate (R4) is appreciably less than that of its addition to the substrate (R5). Among termination reactions, 9MA $^{\bullet}$ combinations, (R7) and (R18), are dominant.

Kinetics. Fig. 3 compares substrate decay half-lives t^{\ddagger} calculated from the model (hollow points and dashed lines) with those observed experimentally, (solid points and lines). Fig. 3(a), a semi-logarithmic Arrhenius-type plot of t^{\ddagger} vs. $1/\Theta$, shows that, at constant $[9\text{MA}]_0 = 0.82 \text{ mol/l}$, the calculated t^{\ddagger} are about 2-fold higher than experimental and exhibit a lower apparent activation energy. Fig. 3(b), a log-log plot of t^{\ddagger} vs. $[9\text{MA}]_0$ at constant $T = 370 \text{ C}$, shows that the calculated t^{\ddagger} are 2- to 8-fold higher than experimental, the more so at the lowest $[910\text{DMA}]_0$, with the model predicting an apparent decomposition reaction order ~ 1.75 , somewhat greater than the experimentally observed order ~ 1.5 .

Product Selectivities. Fig. 4 compares (a) the selectivity to ANT product and (b) the ratio of 910DMA/ANT products, as calculated from the model, with those observed experimentally, using semi-logarithmic Arrhenius-type coordinates of either $S(\text{ANT})$ or $R(910\text{DMA}/\text{ANT})$ vs. $1/\Theta$ at constant $[9\text{MA}]_0 = 0.82 \text{ mol/l}$. In Fig. 4(a) the model is seen to predict an ANT selectivity $S(\text{ANT})$ from 0.2 to 0.5 orders of magnitude below experimental, while in Fig. 4(b) model predictions of the major product ratio $R(910\text{DMA}/\text{ANT})$ lie within ± 0.2 orders of magnitude of the experimental observations.

Sensitivity Analyses. The significance of the differences between model predictions and experimental observations was sought from sensitivity analyses at $T = 370 \text{ C}$ and $[9\text{MA}]_0 = 0.82 \text{ mol/l}$, the central point of the experimental grid, by separately perturbing the kinetics of selected elementary steps. The effects of these perturbations on the predicted decay half-life t^{\ddagger} , ANT selectivity $S(\text{ANT})$, and the primary product ratio $R(910\text{DMA}/\text{ANT})$, are shown by the vertical dashed lines in Figs. 3 and 4. In Figs. 3(a) and (b), for example, the uncertainty in t^{\ddagger} was estimated by perturbing the activation energies E^{\ddagger}_{11} and E^{\ddagger}_{11} by ± 3.4 and ± 4.0 kcal/mol respectively (the inherent errors in ΔH_{f1}^0 and ΔH_{f11}^0), since the elementary reactions R1 and R11 contribute most heavily to the destruction of 9MA substrate in our model. The upper and lower ends of the vertical dashed lines in each portion of Fig. 3 represent values of t^{\ddagger} obtained by joint negative and positive perturbations, respectively, of E^{\ddagger}_{11} and E^{\ddagger}_{11} . This sensitivity analysis shows that the inherent uncertainties of ± 1.1 orders of magnitude in values of t^{\ddagger} calculated by the model considerably exceed the 0.1 to 0.5 order of magnitude differences between the model results and experimental

observations. That is, within its (large) error limits, the model yields half-lives in agreement with experiments. Similar sensitivity analyses provided the vertical dashed lines in each of Figs. 4(a) and (b), showing that, within its error limits, the model also yielded 9MA selectivities and TMA/9MA ratios in accord with experiment.

Optimized Model. The preceding comparisons between model and experimental results are noteworthy because all the kinetic parameters employed in the original model were derived from first principles and used without adjustments. However, these comparisons also revealed the empirical alterations that might permit a best-fit of experimental results for engineering purposes, termed the "optimized" model. Specifically, the best-fit of all experimental data for 9MA thermolysis at $T = 370^\circ\text{C}$ with $[9\text{MA}]_0 = 0.82$ mol/l arose by altering the original activation energies ($E^*_1, E^*_2, E^*_3, E^*_{11}, E^*_{12}, E^*_{17}, E^*_{17}$) by respective amounts of $(-0.4, +2.2, -2.2, -0.4, +2.2, -2.2, +2.0, -2.0)$ kcal/mol, all of these changes being well within the inherent uncertainties of these parameters, respectively, $(\pm 3.4, \pm 3.5, \pm 3.5, \pm 2.4, \pm 4.0, \pm 4.1, \pm 4.1, \pm 3.9, \pm 3.9)$ kcal/mol. Figs. 5 (a) and (b) compare substrate and product histories obtained from the optimized model (lines) to the experimental data (points) for 9MA, ANT, 910DMA, CH₄, and DHDMA. Fig. 5(a) shows the optimized model to well predict the observed 9MA decay, with decay half-lives $t^* = 22000$ s from the model versus 23500 s experimental. The absolute amounts of ANT and of 910DMA formed by the model are respectively about 1.5-fold lower and higher than experimental in Fig. 5(a), and the model well predicts the relatively small amounts of DHMA, and its qualitative variation with time, in Fig. 5(b). Finally, Figs. 6(a) and (b) show that the optimized model provides the correct magnitudes of the major product ratios $R[\text{DHMA}/\text{ANT}]$ and $R[910\text{DMA}/\text{ANT}]$ at low conversions, $X \rightarrow 0$; at higher conversions the model qualitatively follows the variation of the former ratio but not the latter.

Modelling Perspective. In regard to both thermolysis kinetics and the selectivities of major products, the predictions of the optimized model are appreciably closer to the experimental observations than those of the original model. However, the differences between the activation parameters of the optimized and original models, of order 2 kcal/mol, are small relative to the inherent uncertainties in these parameters, of order 4 kcal/mol. Thus, although the optimized model effects an appealing cosmetic improvement over the original model, the two models remain statistically indistinguishable. Substantive scientific improvements in modelling 9MA thermolyses must await better methods, and more reliable data, for deriving the kinetics of the underlying elementary reactions.

ACKNOWLEDGEMENT: This work was supported in part by Cabot Corporation, Boston, MA.

REFERENCES

- [1] Virk, P.S.; Vlastnik, V.J.: PREPRINTS, Div. of Petrol. Chem., ACS, **38**(2), 422 (1993).
- [2] Virk, P.S.; Vlastnik, V.J.: PREPRINTS, Div. of Fuel Chem., ACS, **39**(3), 643 (1994).
- [3] Virk, P.S.; Vlastnik, V.J.: PREPRINTS, Div. of Fuel Chem., ACS, **40**(2), 239 (1995).
- [4] Pomerantz, M.; Combs Jr., G.L.; Fink, R.: J. Org. Chem., **45**, 143 (1980).
- [5] Pope, J.M.: Ph.D. Thesis, Dept. of Chem. Eng., MIT, Cambridge, MA (1987).
- [6] Smith, C.M.; Savage, P.E.: A.I.Ch.E. J., **39**, 1355 (1993).
- [7] Vlastnik, V.J.: Sc.D. Thesis, Dept. of Chem. Eng., MIT, Cambridge, MA (1993).
- [8] Braun, W.; Herron, J.T. and Kahaner, D.K.: *Int. J. Chem. Kinet.*, **20**, 51 (1988).
- [9] Gear, C.W.: *Numerical Initial Value Problems in Ordinary Differential Equations*, Prentice-Hall, N.J., 1971.

Table 1. Evans-Polanyi Relations and Arrhenius Parameters for Model Elementary Reactions.

Type of Reaction	$\ln A, \text{ s}^{-1}$	E^*	Radical Initiator Reaction $E^* =$	ΔH^\ddagger	E^\ddagger	Activation Dependence $\ln A, \text{ s}^{-1}$	Type of Reaction	$\ln A, \text{ s}^{-1}$	E^*	Radical Initiator Reaction $E^* =$	ΔH^\ddagger	E^\ddagger	Activation Dependence $\ln A, \text{ s}^{-1}$
R1 molecular decomposition	8.3	6	AB_2^*	43.7	43.7	1.3 - 0.70	R11 molecular decomposition	8.3	6	AB_2^*	43.5	43.5	1.3 - 0.50
R2 radical decomposition	8.3	1	0	-43.7	0	0	R41 radical decomposition	8.3	1	0	-43.5	0	0
R3 isomerization	8.1	3	$17.5 + AB_2/2$	-6.3	17.6	6.6 - 17.6	R12 isomerization	8.1	3	$17.5 + AB_2/2$	1.8	18.0	6.6 - 18.0
R4 isomerization	8.1	2	$17.5 + AB_2/2$	-6.3	17.6	6.6 - 17.6	R42 isomerization	8.1	1	$17.5 + AB_2/2$	-6.8	17.0	6.3 - 17.0
R5 methyl addition	13.3	1	$8.1 + AB_2^*$	39.3	38.9	13.3 - 13.3	R43 radical II transfer	8.1	1	$17.5 + AB_2/2$	-6.9	17.0	6.1 - 17.0
R6 CH ₄ addition	8.3	2	3.1	-39.3	3.1	6.6 - 3.1	R44 radical III transfer	8.1	3	$17.5 + AB_2/2$	0.9	17.0	6.6 - 18.0
R7 isomerization	8.1	3	$17.5 + AB_2/2$	-6.3	6.6	6.6 - 6.6	R45 radical II transfer	8.1	1	$17.5 + AB_2/2$	-1.3	16.9	6.1 - 16.0
R8 isomerization	8.1	4	$17.5 + AB_2/2$	-24.7	26.9	6.7 - 24.0	R46 radical II transfer	8.1	3	$17.5 + AB_2/2$	1.3	16.1	6.6 - 16.0
R9 CH ₄ addition	8.3	1	3.1	-39.3	3.1	6.6 - 3.1	R47 radical addition	8.3	1	0	-43.8	0	0
R10 methyl addition	13.3	1	$3.1 + AB_2^*$	39.3	32.6	13.3 - 13.3	R48 isomerization	13.3	1	AB_2^*	32.8	32.8	13.3 - 13.3
R11 radical II transfer	8.1	1	$17.5 + AB_2/2$	9.3	17.6	6.1 - 17.1	R49 radical decomposition	8.3	1	0	-43.5	0	0
R12 radical II transfer	8.1	1	$17.5 + AB_2/2$	9.3	17.0	6.3 - 17.6	R50 molecular decomposition	8.3	1	0	-43.5	0	0
R13 radical combination	8.3	1	0	-43.7	0	0	R51 molecular decomposition	8.3	1	0	-43.5	0	0
R14 isomerization	13.3	1	AB_2^*	36.7	36.7	13.3 - 13.3	R52 radical decomposition	8.3	1	0	-43.5	0	0
R15 radical combination	8.3	1	0	-43.6	0	0	R53 molecular decomposition	8.3	1	0	-43.5	0	0
R16 radical addition	13.3	1	AB_2^*	32.6	32.6	13.3 - 13.3	R54 radical decomposition	8.3	1	0	-43.5	0	0
R17 radical addition	13.3	1	0	-43.1	0	0	R55 isomerization	13.3	1	AB_2^*	32.8	32.8	13.3 - 13.3
R18 radical decomposition	8.3	1	0	-43.9	0	0	R56 radical decomposition	8.3	1	0	-43.7	0	0
R19 molecular decomposition	8.3	2	AB_2^*	43.9	43.7	6.6 - 43.0	R57 molecular decomposition	8.3	2	AB_2^*	43.7	43.7	6.6 - 43.0

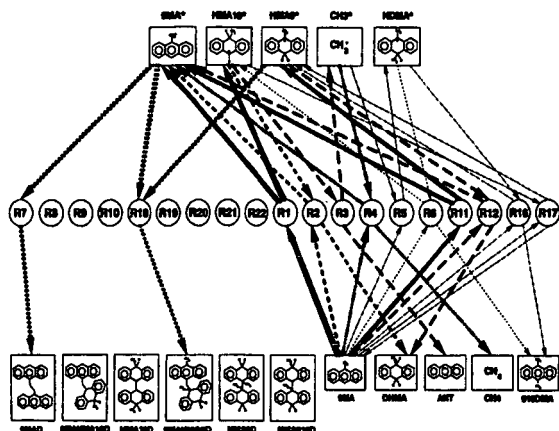


Figure 1. Elementary Step Graph of 9MA Thermolysis Mechanism. Arrow weights depict relative reaction traffic at $T = 370\text{ C}$, $[9MA]_0 = 0.82\text{ mol/l}$, and low conversion $X \sim 0$, as calculated from the original model (see text).

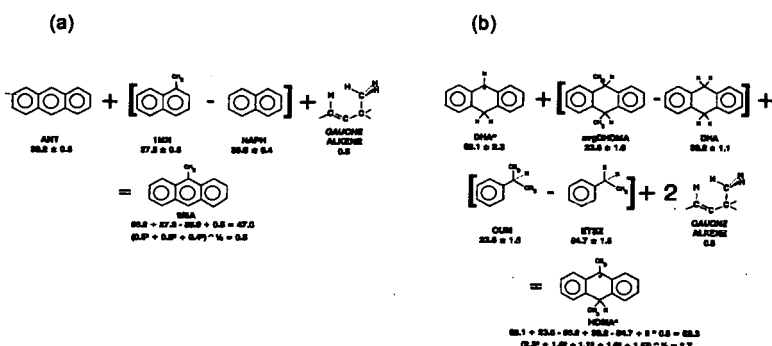


Figure 2. Illustration of Macro-Group Additivity Scheme for Estimation of Thermochemical Properties of (a) Stable and (b) Radical Species.

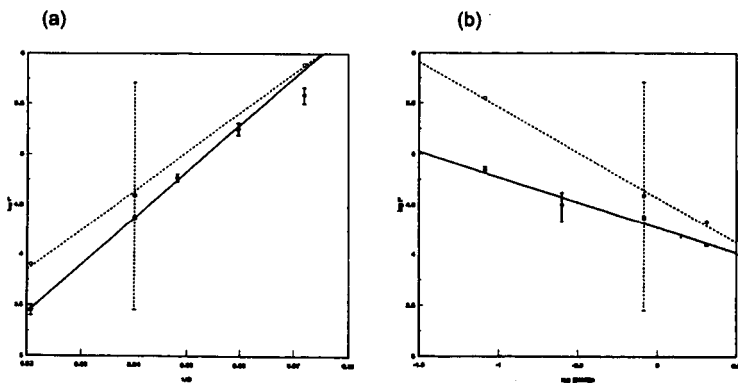


Figure 3. Decay Half-Lives t^* Experimental (solid circles and lines) Versus Calculated From Original Model (hollow circles, dashed lines) at (a) constant $[9MA]_0 = 0.82\text{ mol/l}$ and (b) constant $T = 370\text{ C}$.

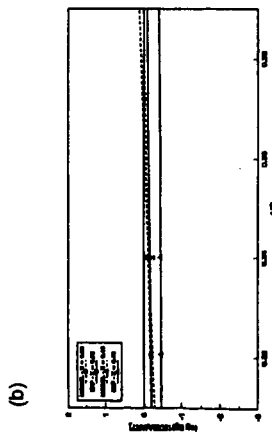
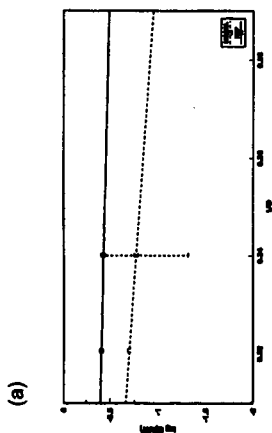


Figure 4. Original Model Results (hollow points, dashed lines) vs. Experiments (solid points, solid lines). (a) Selectivity to ANT, (b) Ratio [910DMA]/[ANT].

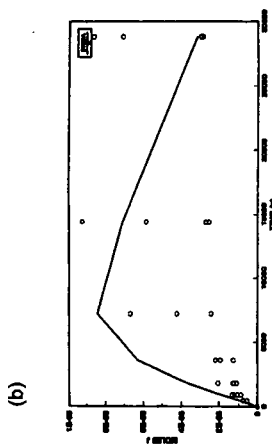
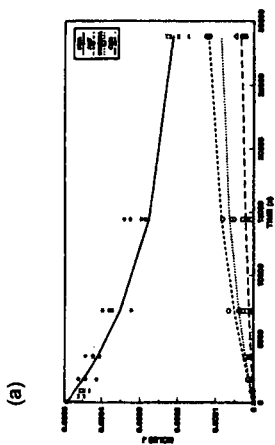


Figure 5. Optimized Model Results (lines) vs. Experiments (points) at $T = 370^\circ\text{C}$ with $[\text{GMA}]_0 = 1.82 \text{ mol/l}$. (a) 9MA, ANT, CH_4 , 910DMA, (b) DHMA.

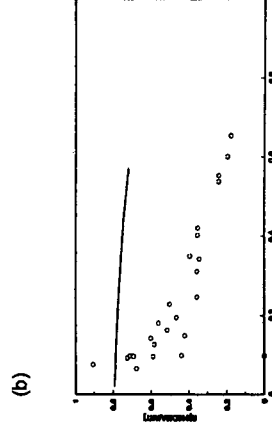
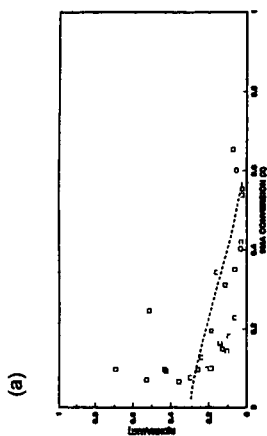


Figure 6. Optimized Model Results (lines) vs. Experiments (points) at $T = 370^\circ\text{C}$ with $[\text{GMA}]_0 = 1.82 \text{ mol/l}$. (a) Ratio DHMA/ANT, (b) Ratio 910DMA/ANT.

A Mechanistic Model for the Uncatalyzed Reaction of Stilbene with H₂

Venkatasubramanian K. Rajagopal
Robert D. Guthrie
Department of Chemistry
University of Kentucky
Lexington, KY 40506

Burtron H. Davis
Kentucky Center for Applied Energy Research
3572 Iron Works Pike, Lexington, KY 40511

Keywords: Hydrogenation, Kinetics, ACUCHEM, Glass Catalysis

INTRODUCTION

During the past few years, we have studied the thermolysis of a number of different substrates in the presence of H₂ or D₂ as models for the hydrothermolysis of coal.¹ To avoid catalysis by metal surfaces our reactions are carried out in glass reaction vessels with a length of capillary tubing separating the reaction mixture from the steel containment chamber. In our initial study of the hydrothermolysis of diphenylethane (DPE) we noted that the concentration of stilbene (STB), diphenylethene, formed in this reaction goes through a maximum value as the reaction proceeds.¹⁷ It was also noted that reactions carried out with lower starting concentrations of DPE generated less STB during the course of the reaction. There were few,² if any, examples of the uncatalyzed reactions of alkenes with H₂ in the literature, so we undertook to study the viability of such processes with selected substrates. Our initial survey used STB, 1-methylstyrene (2-phenylpropene), anthracene and phenanthrene.¹⁸ We found that the first three compounds could be hydrogenated at 410 °C and 14 MPa of D₂. In the case of STB, we observed an inverse concentration effect in that the yield of DPE was greater with lower starting STB concentrations under otherwise identical conditions. The reverse seemed to be true for 1-methylstyrene. Anthracene was hydrogenated with no significant concentration effect and phenanthrene refused to give hydrogenation products under conditions which were effective for the other three compounds. Of the two compounds that showed unusual concentration effects, STB seemed the best behaved in that it gave mainly DPE as a reaction product, whereas 1-methylstyrene gave higher molecular weight byproducts. For this reason and because of its relevance to our earlier study of the hydrothermolysis of DPE, STB was chosen for a more detailed investigation of its kinetic behavior.

EXPERIMENTAL

Substrate. The best grades of commercially available *trans*-stilbene (*trans*-STB) contained small amounts of diphenylethane (ca. 0.7 %). Some runs were carried out with STB synthesized by a modified Wittig procedure.³ No significant differences were observed for reactions carried out with this pure substrate. Diphenylethane was recrystallized commercial samples and showed no gas chromatographically detectable impurities. *cis*-STB for preparation of GC/MS standard was a commercially available product.

Reaction Procedure. The reaction vessel and general procedure for hydrogenations has been described previously.¹⁸ For the experiments described in this paper, greater attention was given to control of reaction temperature. Figure I shows differences in the temperatures registered by thermocouples placed (1) in the fluidized sandbath, (2) inside the glass reaction vessel and (3) between the glass vessel and its steel container. It will be noted that both internal temperatures lag behind that of the sandbath and remain substantially below it for a period in excess of ten minutes. The temperature inside and outside of the glass reactor become equal roughly four minutes after the reactor assembly is placed in the bath. These relationships varied somewhat depending on the particular steel reaction container employed, conditions in the sandbath, the shaking rate for the reactor, the depth of immersion of the reactor assembly, etc. As a result it was very difficult to reproduce exactly the reaction temperature from run to run as evidenced by variations in yield for reactions carried out for nominally equal times and temperatures. To avoid these problems, we adopted the approach of placing a small sealed capillary ampule containing DPE between the glass vessel and its steel housing. The arrangement is shown in Figure II. We then used the degree of thermolysis of DPE within this ampule to calculate an effective reaction time based on a separately-determined rate constant for the thermolysis of DPE placed in similar ampules emersed directly in the sandbath at 405 °C. The plot for DPE conversion is shown in Figure III. In essence, if 20% of DPE had been converted to products in the ampule, we read the effective time at 405 °C from Figure III (corresponds to approximately 150 min at 405 °C). This calculated time was then substituted for the

actually measured reaction time for the purpose of kinetic plotting of the STB conversion data.

Analysis of Reaction Mixture. *trans*-STB was converted to an equilibrium mixture of *cis*- and *trans*-isomers at temperatures well below that required for hydrogenation. Thus the product mixture consisted of an equilibrium mixture of *cis*- and *trans*-STB, DPE and, at longer times, products of the thermolysis of reduction-generated DPE. Unfortunately, the retention time of *cis*-stilbene was almost identical to that of DPE requiring that a secondary analysis of the gc peak by gas chromatography/mass spectrometry (GC/MS) be performed. Figure IV shows a plot of composition versus ion intensity ratios for synthetic mixtures of *cis*-STB and DPE integrated over the entire GC peak. This standard curve was used to calculate compositions of reaction mixtures.

Calculation of Theoretical Kinetic Plots. The ACUCHEM⁴ program was used to calculate theoretical curves of composition vs. time based on assumed rate constants as listed below.

RESULTS AND DISCUSSION

Although our earlier work attempted in several instances^{12,13} to follow the progress of hydrothermolysis reactions as a function of time, great difficulty was encountered in reproducing reaction temperatures with sufficient precision to provide data suitable for kinetic analysis. To circumnavigate this uncertainty we arranged to carry out a second, monitoring reaction inside the metal housing, but outside of the glass reactor. A small sample of DPE was sealed in a glass capillary tube and inserted in the reactor as shown in Figure II. The progress of this secondary reaction served as an internal clock by which we could determine an "effective" time for the reaction at 405 °C. Composition of the reaction mixture vs. effective time at 405 °C is given in Table I for runs carried out with 50 mg starting DPE. It is clear from perusal of this data that we have not eliminated as much scatter as we might have wished but a reasonable relationship between effective time and conversion may be adduced. Moreover, it is clear that we are far from the sort of pseudo first-order kinetics which might be expected for any simple bimolecular reaction between STB and H₂.

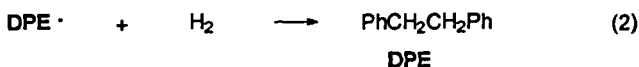
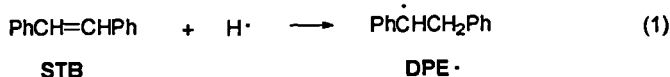
Table I. Composition of Reaction Mixtures for *trans*-STB with H₂ at 14 MPa vs. Effective Time at 405 °C.

Effective Time at 405 °C (min)	Reaction Composition					
	<i>t</i> -STB	<i>c</i> -STB	DPE	PhMe	PhEt	PhH
35.4	75.9	7.2	12.1	0.5	0.4	0.3
42.4	79.4	7.5	11.1	0.1	<0.2	<0.2
42.7	80.4	7.6	9.6	0.2	<0.1	<0.1
90.4	59.9	5.7	28.7	0.9	0.2	0.1
121	61.5	5.8	30.1	0.8	<0.4	<0.4
147	57.7	5.4	33.3	0.5	0.1	<0.1
214	26.2	2.5	60.4	4.6	1.3	0.6
264	18.4	1.8	62.7	7.3	2.0	1.1
388	0.6	<0.6	63.2	14.5	8.4	5.6

A log plot for disappearance of STB is shown in Figure V. The solid points represent experimental data with 50 mg and with 20 mg STB in the reaction bulb. Runs carried out with larger starting weights gave unmanageably slow conversion under these conditions.

The mechanistic model suggested earlier for this process¹⁴ consists most essentially of a kinetic chain process with H atoms and 1,2-diphenylethyl radicals, DPE[•], as chain carriers, eqs 1 and 2. The sequence generates DPE which can be expected to undergo its well-characterized dissociation to benzyl radicals, eq 3, followed by reaction of these both with H₂ and with DPE, eq 4 and eq 5, each process generating a chain carrier for the propagation cycle. The termination of the chain seems likely to be disproportionation of two DPE[•] to give DPE and STB, eq 6. There are a number of other processes known to be involved in the hydrothermolysis of DPE which might be considered, for example, the rearrangement of DPE[•] to give 1,1-diphenylethyl radicals. However, these would react to regenerate radicals and should not alter the kinetic pattern. Also, earlier work has shown that

the presence of H atoms can also lead to hydrocracking products, PhH and PhEt.¹⁷ However, Table I suggests that such processes become important only after the majority of the STB has been converted. This might be expected, as STB should be a effective trap for H atoms via eq 1.



Thus, a reasonable match of the kinetic data might be expected using only the sequence of eqs 1 through 6. It will be observed, however, that unless DPE is present initially, there is no initiation step for the chain. We found that commercially available STB invariably contained small amounts of DPE. Therefore, we went to some effort to synthesize DPE-free STB for selected experiments. As there was no significant difference in the kinetic data for these samples, we must assume that some other initiating process is involved. Temporarily avoiding the problem by arbitrarily imposing an unspecified process to generate H atoms from H₂ (with a rate constant, $k = 1 \times 10^{-7} \text{ s}^{-1}$) leads to the calculated plot in Figure V. The other rate constants used in its generation were as follows:

$k_1 = 5.7 \times 10^9 \text{ M}^{-1} \text{ s}^{-1}$ (Calculated from Benson's expression for the reaction of H· with ethylene.⁷)

$k_4 = 50 \text{ M}^{-1} \text{ s}^{-1}$ (This value is suggested by McMillen, Malhotra and Nigenda⁸ at 400 °C.)

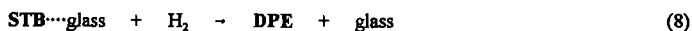
$k_2 = 9.3 \text{ M}^{-1} \text{ s}^{-1}$ (There was no guidance for this number but it could reasonably be expected to be somewhat smaller than k_4 .)

$k_3 = 2.4 \times 10^{-5} \text{ s}^{-1}$ (This is the first order rate constant from Figure III. It is in good agreement with literature values.⁷)

$k_5 = 1.7 \times 10^4 \text{ M}^{-1} \text{ s}^{-1}$ (Calculated from the expression $\log k = 8.8 - 14.2/\phi$ (per hydrogen) estimated by Poutsma.⁹)

$k_6 = 1 \times 10^6 \text{ M}^{-1} \text{ s}^{-1}$ (Suggested by Poutsma⁸ to be $\log k = 8.5$, based on studies by various groups of the rate constant for disproportionation of 1-phenylethyl radical to give styrene and ethylbenzene.⁹)

Of course it is thermochemically unreasonable to assume that H₂ dissociates with a rate constant as large as 10^{-7} . It is apparent that initiation occurs via some unknown catalytic process. As recent information indicates that silica can serve as a catalyst for the hydrogenation of alkenes,¹⁸ it seemed worth considering that the surface of the glass container was serving as a catalyst. Based on an estimate of the concentration equivalent of catalytic sites in our glass reactor being 3.2×10^{-11} , and the following reaction sequence, eqs 7 and 8 (with $k_7 = 5 \times 10^{10} \text{ M}^{-1} \text{ s}^{-1}$ and $k_8 = 4 \times 10^3 \text{ M}^{-1} \text{ s}^{-1}$):



the theoretical curves in Figure VI were calculated. While the match to experimental data is not as good as that of Figure V, the pattern and concentration dependence are preserved.

CONCLUSIONS

The scheme presented explains the inverse concentration effect noted earlier. At high concentrations of STB, the chain-carrying DPE· undergo disproportionation, terminating the chain.

At lower concentrations, they stand a better chance of reacting with H_2 . The rate increase with conversion is mainly due to the generation of DPE which serves as an initiator. We believe that this scheme is a reasonable mechanism for the hydrogenation of alkenes in the absence of metal catalysts, provided that some radical-generating initiator is present. We have also found that the hydrogen-transfer rate constants used in this scheme can be incorporated in a calculation to predict the pattern of D incorporation when DPE undergoes thermolysis under D_2 .^{1f} The proposed initiation by glass surface in the absence of a radical-generating species is, at present, purely speculative.

REFERENCES

1. (a) Guthrie, R. D.; Shi, B.; Sharipov, R.; Davis, B. *Prep. Pap.- Am. Chem. Soc. Div. Fuel Chem.* **1993**, *38*, 526-533. (b) Rajagopal, V.; Guthrie, R. D.; Shi, B.; Davis, B. H. *Prep. Pap.- Am. Chem. Soc. Div. Fuel Chem.* **1993**, *38*, 1114. © Ramakrishnan, S.; Guthrie, R. D.; Shi, B.; Davis, B. H. *Prep. Pap.- Am. Chem. Soc. Div. Fuel Chem.* **1993**, *38*, 1122. (d) Sharipov, R.; Guthrie, R. D.; Shi, B.; Davis, B. H. *Prep. Pap.- Am. Chem. Soc. Div. Fuel Chem.* **1993**, *38*, 1129. (e) Shi, B.; Ji, Y.; Guthrie, R. D.; Davis, B. H. *Energy and Fuels* **1994**, *8*, 1268-1275. (f) Guthrie, R. D.; Shi, B.; Rajagopal, V.; Ramakrishnan, S.; Davis, B. H. *J. Org. Chem.* **1994**, *59*, 7426-7432. (g) Rajagopal, V.; Guthrie, R. D.; Shi, B.; Davis, B. H. *Prep. Pap.- Am. Chem. Soc. Div. Fuel Chem.* **1994**, *39*, 673. (h) Guthrie, R. D.; Ramakrishnan, S.; Britt, P. F.; Buchanan, III., A. C.; Davis, B. H. *Prep. Pap.- Am. Chem. Soc. Div. Fuel Chem.* **1994**, *39*, 668. (i) Guthrie, R. D.; Sharipov, R. V.; Ramakrishnan, S.; Shi, B.; Davis, B. H. *J. Org. Chem.*, **1995**, *60*, 4504-4509. (j) Ramakrishnan, S.; Guthrie, R. D.; Britt, P. F.; Buchanan, A. C., III. *Prep. Pap.- Am. Chem. Soc. Div. Fuel Chem.* **1995**, *40*, 555-559. (k) Rajagopal, V.; Guthrie, R. D.; Davis, B. H. *Prep. Pap.- Am. Chem. Soc. Div. Fuel Chem.* **1995**, *40*, 945-949. (l) Guthrie, R. D.; Ramakrishnan, S.; Britt, P. F.; Buchanan, A. C. III.; Davis, B. H. *Energy and Fuels*, **1995**, *9*, 1097-1103. (m) Rajagopal, V. K.; Guthrie, R. D.; Fields, T.; Davis, B. H. *Catalysis Today* **1996**, *31*, 57-63.
2. There are some indications that early hydrogenation studies by V. N. Ipatieff were carried out in the absence of catalysts. See V. N. Ipatieff "Catalytic Reactions at High Temperatures and Pressures," The Macmillan Co., New York, 1937. However, it seems likely that metal reaction vessels were used.
3. Daniel, H.; LeCorre, M. *Tetrahedron Letters* **1987**, *28*, 1165-1168.
4. Available from: Braun, W.; Herron, J. T.; Kahaner, D. K., NIST, Gaithersburg, MD 20899. See *Int J. Chem. Kinet.* **1988**, *29*, 51.
5. S. W. Benson, "Thermochemical Kinetics", 2nd Ed. Wiley, New York, N. Y. 1976, p. 168.
6. McMillen, D. F.; Malhotra, R.; Nigenda, S.E. *Prepr. Pap.- Am. Chem. Soc. Div. Fuel Chem.* **1987** *32*(3), 180.
7. Poutsma, M. L. *Energy Fuels* **1990**, *4*, 113.
8. Poutsma, M. L.; Dyer, C. W. *J. Org. Chem.* **1982**, *47*, 4903 and ref. 6.
9. (a) Gibian, M. J.; Corley, R. C. *J. Am. Chem. Soc.* **1972**, *94*, 4178. (b) Manka, M. J.; Brown, R. L.; Stein, S. E. *Int. J. Chem. Kin.* **1987**, *19*, 943. © Manka, M. J.; Stein, S. E. *J. Phys. Chem.* **1984**, *88*, 5919. (d) Glexner, G.; Olaj, O. F.; Breitenbach, J. W. *Makromol. Chem.* **1979**, *180*, 258.

Figure I. Temperature Profile for Glass Reactor and Containment Vessel

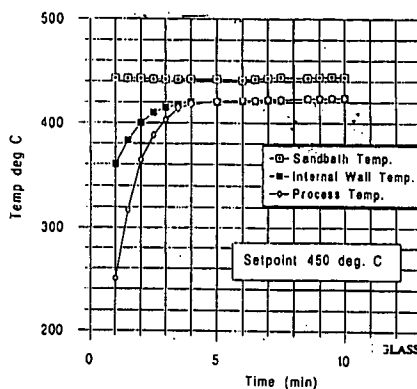


Figure II. Reactor Setup for Kinetics Experiments

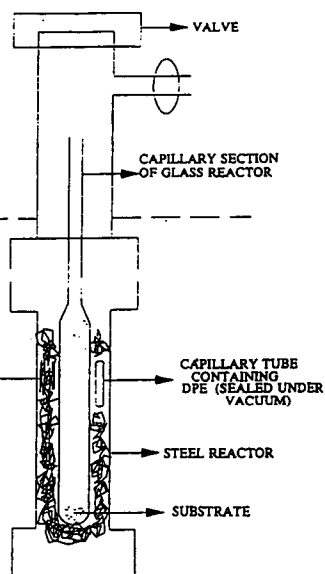


Figure III. Plot of DPE Loss Used for Calculation of Effective Time

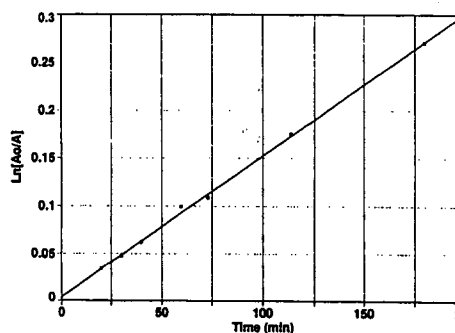


Figure IV. Calibration Curve Used to Determine DPE in the Presence of cis-STB

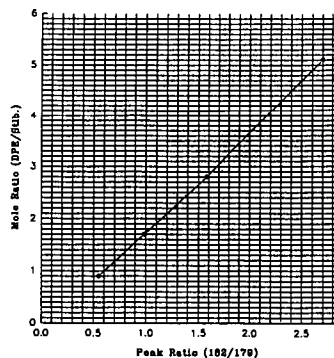


Figure V. Theoretical Matching of STB Loss (Unspecified H Atom Production)

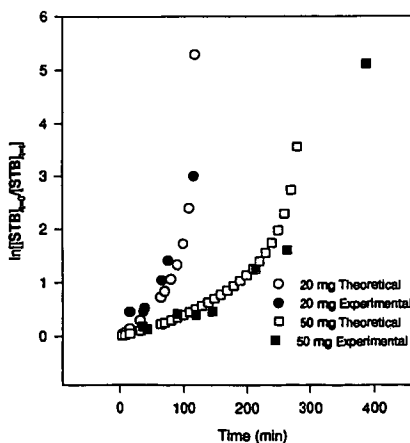
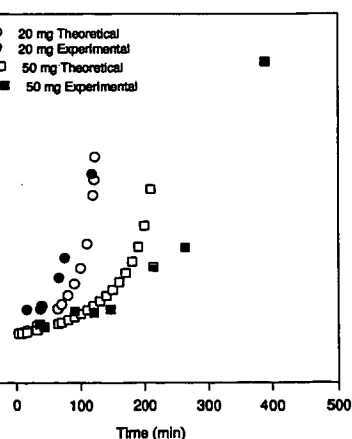


Figure VI. Theoretical Matching of STB Loss (Catalysis by Glass Reactor)



FLASH VACUUM PYROLYSIS OF LIGNIN MODEL COMPOUNDS

Mark J. Cooney, Phillip F. Britt, and A. C. Buchanan, III
Chemical and Analytical Sciences Division, Oak Ridge National Laboratory
P. O. Box 2008, Oak Ridge, Tennessee 37831-6197

Keywords: pyrolysis mechanisms, lignin pyrolysis, model compounds

ABSTRACT

Despite the extensive research into the pyrolysis of lignin, the underlying chemical reactions that lead to product formation are poorly understood. Detailed mechanistic studies on the pyrolysis of biomass and lignin under conditions relevant to current process conditions could provide insight into utilizing this renewable resource for the production of chemicals and fuel. Currently, flash or fast pyrolysis is the most promising process to maximize the yields of liquid products (up to 80 wt %) from biomass by rapidly heating the substrate to moderate temperatures, typically 500 °C, for short residence times, typically less than two seconds. To provide mechanistic insight into the primary reaction pathways under process relevant conditions, we are investigating the flash vacuum pyrolysis (FVP) of lignin model compounds that contain a β -ether linkage and α - or γ -alcohol, which are key structural elements in lignin. The dominant products from the FVP of $\text{PhCH}_2\text{CH}_2\text{OPh}$ (PPE), $\text{PhC(OH)HCH}_2\text{OPh}$, and $\text{PhCH}_2\text{CH}(\text{CH}_2\text{OH})\text{OPh}$ at 500 °C can be attributed to homolysis of the weakest bond in the molecule (C-O bond) or 1,2-elimination. Surprisingly, the hydroxy-substituent dramatically increases the decomposition of PPE. It is proposed that internal hydrogen bonding is accelerating the reaction.

INTRODUCTION

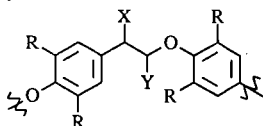
Over the past two decades, a good deal of attention has focused on the thermochemical conversion of renewable resources into higher value products [1]. Lignin, the second-most abundant naturally occurring biopolymer and a by-product of the pulping process, has received an enormous amount of attention as a consequence of its availability and its potential to produce higher value products. However, in spite of the extensive research to expand the use of lignin, the efforts have been only moderately successful [2]. This can be attributed to the structural diversity of lignin and the dependence of the chemical structure of lignin on the method of isolation [3]. To enhance the economic production of higher value products from lignin, it is necessary to understand those factors that maximize product yields and promote product selectivity. Over the past two decades, significant advances have been made in maximizing the yields of solid (charcoal) [4], liquid and gaseous products from biomass by pyrolysis [1,5,6]. While slow pyrolysis at low temperatures and long residence times produces charcoal, fast or flash pyrolysis produces high yields of liquid products (up to 60 wt% moisture-free organic liquids on a dry feed) by rapidly heating biomass to moderate temperatures (typically 500 °C, but ranging from 400-650 °C) for short periods of time (typically less than 2 s). At temperatures above 700 °C, fast pyrolysis maximizes gas yields (up to 80 wt%). However, despite the extensive research into the pyrolysis of biomass and lignin, the fundamental chemical reactions that lead to the complex array of products remains poorly understood, and as a result, there is little insight into how to control the product selectivity [7]. Currently, the most detailed mechanistic insights on lignin pyrolysis have been obtained from model compound studies [7,8]. However, most of these studies have been done at relatively low temperature (less than 450 °C) with long residence times (greater than 5 min) or slow heating rates. This makes it difficult to extrapolate these results to the moderate temperature, short contact-time reaction condition found in fast pyrolysis. Therefore, additional model compound studies are needed under conditions relevant to current process conditions (i.e., fast pyrolysis) to provide insight into controlling the reaction chemistry and product distribution to enhance the utilization of lignin.

There are many methods to rapidly heat compounds to high temperature, each with their own set of advantages and disadvantages. This paper investigates the flash vacuum pyrolysis of lignin model compounds at 500 °C. Flash vacuum pyrolysis (FVP) or flash vacuum thermolysis (FVT) has been used for decades by organic chemists for the preparation of highly reactive intermediates, for mechanistic investigations, and for preparative organic synthesis [9]. There are many different designs of flash vacuum pyrolysis apparatus operating at pressures from 1 atmosphere to $<10^{-4}$ mm Hg depending on the specific application and method of detection of the products [9]. However, all flash pyrolysis experiments are characterized by short contact times (sample typically remains in the hot zone for 0.001 - 1 s), low steady-state concentrations of the reactants and products in the hot zone, and rapid quenching of the products to low temperatures, typically 77 K. This method has been used to study thermally labile intermediates by a variety

of spectroscopic methods (for example, NMR, UV-Vis, FTIR, Raman, and photoelectron spectroscopy). A special variation of this experiment, very low-pressure pyrolysis (VLPP), was developed to directly measure the reactive intermediates (i.e., free-radicals) from unimolecular reactions and very fast bimolecular reactions (i.e., $10^{11} \text{ L mol}^{-1} \text{ s}^{-1} \geq k \geq 10^6 \text{ L mol}^{-1} \text{ s}^{-1}$) by mass spectrometry [10].

Flash vacuum pyrolysis seems ideally suited for the mechanistic investigation of the pyrolysis of lignin model compounds under conditions relevant to large scale fast pyrolysis reactors. Initial experiments can be run at low pressure ($<10^{-3} \text{ mm Hg}$) to characterize the primary reaction pathways and reactive intermediates that occur at moderate temperatures (500°C) with a minimum of interference from bimolecular reactions. Next, the pyrolysis can be investigated at higher pressures (0.1 mm Hg to 1 atmosphere) under a flow of inert gas (N_2) to determine the more complex secondary reactions. A focus of this project is to characterize and quantitate the products, and to determine the origin and efficiency of their production. With the reaction pathways defined for the production of the products, we can focus on changing the experimental conditions to promote product selectivity.

Lignin is a complex, heterogeneous, three-dimensional polymer formed from the enzyme-initiated, dehydrogenative, free-radical polymerization of three *p*-hydroxycinnamyl alcohol precursors that differ by the number of methoxy groups on the aromatic ring [1a,11]. Softwood lignin is formed from *trans*-coniferyl alcohol (4-hydroxy-3-methoxycinnamyl alcohol), hardwood lignin is formed from coniferyl and *trans*-sinapyl alcohol (4-hydroxy-3,5-dimethoxycinnamyl alcohol), and grass lignin is formed from coniferyl, sinapyl and *trans*-*p*-coumaryl alcohol (4-hydroxycinnamyl alcohol). As opposed to other biopolymers such as cellulose, lignin has many different types of linkages between monomer units. This arises from the distribution of the π -electron density throughout the phenylpropene monomer unit and the thermodynamic principles governing radical addition reactions [1a]. The dominant interunit linkage in lignin is the arylglycerol- β -aryl ether linkage, commonly referred to as the β -O-4 linkage, and the arylglycerol- α -aryl ether linkage, referred to as the α -O-4 linkage, which accounts for approximately 48-60 % and 6-8 %, respectively, of the total interunit linkages [1a,11], exemplified by the structure below. If this structure is stripped for all its substituents, the



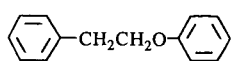
$\text{R} = \text{H}$ or OCH_3

$\text{X} = \text{OH}$, OAr or $=\text{O}$

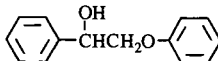
$\text{Y} = \text{CH}_2\text{OH}$ or CH_2OR

skeletal remnant would be phenethyl phenyl ether, the simplest model of the β -O-4 linkage, and the starting point for this mechanistic investigation.

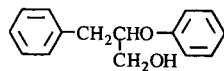
In this paper, the flash vacuum pyrolysis of lignin model compounds will be studied to determine the primary reaction that occurs at 500°C and low pressures ($<10^{-3} \text{ Torr}$) and the impact of substituents on the reaction pathways. As a consequence of the complexity of the pyrolysis reactions and the thermal sensitivity of the products, a graded approach is used to solve this problem in which simple model compounds are thoroughly studied to provide a solid foundation to assist in the interpretation of more complex model compounds and lignin. This investigation will focus on FVP of the β -O-4 linkage, and the impact of hydroxy functional groups on the reaction pathways. To our knowledge, this is the first investigation of the reaction pathways of the γ -alcohol (i.e. β - CH_2OH -PPE).



PPE



α -HO-PPE



β - CH_2OH -PPE

EXPERIMENTAL

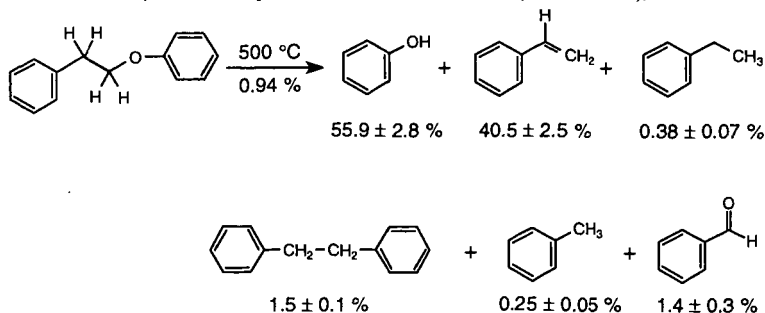
The synthesis of PPE and $\text{PhCD}_2\text{CH}_2\text{OPh}$ has been previously described [12]. The preparation of α -HO-PPE was accomplished by alkylation of α -bromoacetophenone with phenol (K_2CO_3 in DMF), reduction with lithium aluminum hydride, and recrystallization with hexanes/toluene. The preparation of β - CH_2OH -PPE was accomplished by alkylation of the enolate of ethyl

phenoxyacetate (by the reaction of lithium hexamethyldisilazide with ethyl phenoxyacetate in THF at -78 °C) with benzyl bromide, reduction with lithium aluminum hydride, and purification by reverse phase flash chromatography. All compounds were >99.5 % pure by GC analysis.

The FVP apparatus was based on the design reported by Trahanovsky [13, 14] and available from Kontes. The pyrolysis tube consisted of a quartz tube (62.5 cm x 2.5 cm) with a 34/45 male joint on one end and a 90° bend with a size 40 o-ring joint on the other end. The tube was packed with short pieces (1/4" x 6 mm OD) of quartz tubing to a length of ca. 40 cm and held in place by a small plug of quartz wool. The quartz chips prevent streaming of the substrate and increase residence time in the hot zone. The quartz tube was heated with a Carbolite three zone furnace (45 x 3.8 cm (ID)) and the temperature was maintained within ± 1 °C of the setpoint (500 °C) over a length of 30 cm (out of total heated zone of 40 cm). The sample (typically 100-200 mg) was weighed into a sublimation tube made from a 34/45 female joint and connected to the horizontal quartz pyrolysis tube. The pyrolysis tube was connected by a size 40 o-ring joint to a trap which is cooled with liquid nitrogen. To prevent products from condensing in the tube before the cold trap, the pyrolysis tube was warmed with a heating tape at the exit of the furnace. At the start of a pyrolysis experiment, the system was pumped down to $<10^{-4}$ mm Hg (measured after the cold trap), the furnace was equilibrated at 500 °C, and the sublimation chamber was enclosed in an aluminum cylinder wrapped with a heating tape. The temperature of the sublimation tube (monitored by a thermocouple in the aluminum cylinder) was increased to provide a throughput of 50 - 100 mg h⁻¹. Under these conditions, the residence time (i.e., contact time) is estimated to be ca. 10 ms and the steady state concentration of materials in the hot zone is 10^{-8} - 10^{-9} mol L⁻¹ such that only fast bimolecular reactions can occur in the hot zone, such as radical-radical couplings [9]. After the reaction, the trap was opened, products were washed out with a high purity acetone containing internal standards (cumene, dimethylphenol, and diphenyl ether), and the samples are analyzed by GC-MS at 70 eV and quantitated by GC with measured response factors. Products were identified by comparison of GC retention time and mass spectral fragmentation patterns with authentic samples or based on MS fragmentation patterns and comparison with the NIST spectral library. After each run, the tube was "burned out", by blowing air through the tube at 600 °C for 1 h, to remove any carbonaceous deposits (which were visible in the pyrolysis of phenethyl 2,6-dimethoxyphenyl ether). Duplicate pyrolyses were remarkably reproducible with similar mol % of products, mass balances (typically >95 %), and conversions ($\pm 15\%$). Changing the injection rate by a factor of two (50 to 100 mg h⁻¹) did not change the product distributions. To check the long term reproducibility of the pyrolysis runs to ensure that the relative reactivity of the substituted phenethyl phenyl ethers could be compared over time, the pyrolysis of phenethyl *o*-methoxyphenyl ether was run after every 3-5 pyrolyses and compared to previous pyrolyses. Currently, similar pyrolysis results (% conversion, mass balances, and product yields) have been obtained over the span of a six week period (over 30 pyrolyses).

RESULTS AND DISCUSSION

FVP of PPE. The major products from the FVP of PPE at 500 °C are shown below (average mol % from three runs). As a consequence of the low % conversions ($0.94 \pm 0.16\%$), the

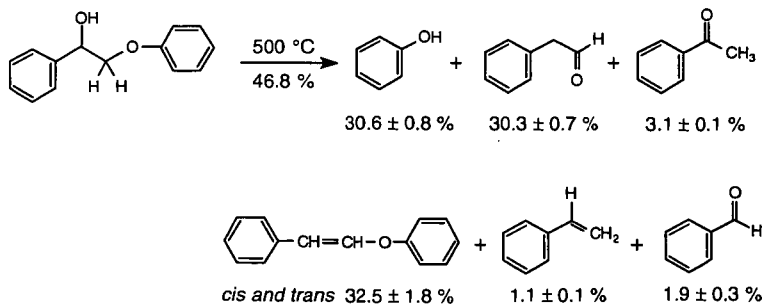


reproducibility and the mass balances were not as good as that found at higher conversions. In addition to the products shown below, a small amount (typically, $\leq 1\%$ of the starting material) of rearranged PPE, *o*-(2-phenylethyl)phenol and *p*-(2-phenylethyl)phenol, was also found. At higher temperatures (550 and 600 °C), the conversion of PPE increased to form the products shown above, but the yield of the rearranged products did not increase (ca. 1 % of the starting

material). Recombination of the phenoxy and phenethyl radicals (see below) to form the rearranged products seems unlikely on the basis that no cross-coupling products, phenoxyphenol or 1,4-diphenylbutane, were observed. Trahanovsky has shown that FVP (650 °C and 0.05 mm Hg) of an unsymmetrical oxalate, benzyl *p*-chlorobenzyl oxalate, lead to statistical scrambling of the benzyl group indicating intermolecular coupling of benzyl radicals [14]. Therefore, the rearranged products were attributed to a small amount of acid catalysis from the quartz chips. In the decomposition of an analogous alkyl phenyl ether, *n*-butyl phenyl ether, it was proposed that products were formed by C-O homolysis ($\log k \text{ (s}^{-1}) = 16.0 - 65.5 / 2.303 \text{ RT (kcal mol}^{-1})$) and by 1,2-elimination ($\log k \text{ (s}^{-1}) = 13.6 - 57.4 / 2.303 \text{ RT (kcal mol}^{-1})$) [15]. At 500 °C, the ratio of homolysis to 1,2-elimination is 1.3. Therefore, in the pyrolysis of PPE, the major products, styrene and phenol, could be produced by two competing pathways: a) homolytic cleavage of the weakest bond in the molecule ($D^{\circ}_{\text{C-O}}$ estimated as 63 kcal mol⁻¹) to give PhO• and PhCH₂CH₂• which can gain and lose a hydrogen atom, respectively, or b) 1,2-elimination to produce the phenol and styrene products directly. Unfortunately, it is very difficult to deconvolute these two pathways in the decomposition of PPE since both routes lead to the same products. However, if PPE were substituted with deuterium in the benzylic position (PhCD₂CH₂OPh, PPE-*d*₂), the rate of 1,2-elimination would be slower, as a consequence of the deuterium isotope effect in breaking the C-D bond, while the homolytic cleavage should not be influenced by the substitution (since β-scission of PhCD₂CH₂• is fast compared to C-O homolysis). At 500 °C, a maximum rate difference (in the absence of tunneling) of $k_{\text{H}}/k_{\text{D}} = 2.1$ is predicted. In the pyrolytic 1,2-elimination of hydrogen halide from ethyl chloride, ethyl bromide, and their deuterated analogues, the measured isotope effect was ($k_{\text{H}}/k_{\text{D}}$) 2.0 - 2.2 at 500 °C [16]. Comparison of the % conversion from three FVP runs of PPE-*d*₂ and PPE under similar conditions found that the deuterated PPE reacted approximately 20 % slower than PPE indicating that the 1,2-elimination contributes to the decomposition of PPE at low pressures. At higher pressures, radicals produced from C-O homolysis can start a chain reaction and the contribution of 1,2-elimination will most likely be small.

The small amounts of toluene, bibenzyl, and benzaldehyde that are observed can be formed from the homolysis of the C-C bond ($D^{\circ}_{\text{C-C}}$ estimated as 72 kcal mol⁻¹). Under the low pressure reaction conditions, a majority of the benzyl radicals couple to form bibenzyl. The phenoxyethyl radical (PhOCH₂•) produces benzaldehyde by a 1,2-phenyl shift, to form the benzyloxy radical (PhCH₂O•), followed by loss of a hydrogen atom. In support of this mechanism, the benzaldehyde formed in the FVP of PPE-*d*₂ contained no deuterium.

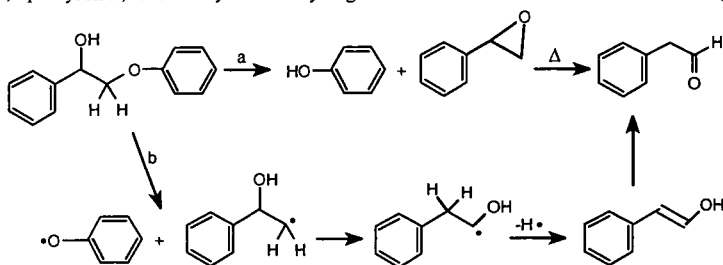
FVP of α-HO-PPE. The major products from the FVP of α-HO-PPE at 500 °C are shown below (average mol % from three runs). The reproducibility and mass balances ($98.5 \pm 1.5 \%$) of these runs are excellent. Surprisingly, the α-hydroxy group dramatically accelerates the rate of decomposition ($46.8 \pm 0.4 \%$ conversion, $23.4 \pm 0.9 \%$ without dehydration) of PPE. The major reaction is the 1,2-elimination of the α-hydroxy group to form the more refractory vinyl ether. The most studied 1,2-eliminations involve loss of hydrogen halide from alkyl halides to form alkenes, although loss of water, alcohol, ammonia, and hydrogen sulfide from alcohols, ethers, amines, and mercaptans have also been reported [15-17]. The transition state is proposed to be highly polar and electron donating species at the α-carbon dramatically accelerate the reaction



while electron donating substituents at the β-carbon have only a small effect [17]. Since the aromatic ring is typically substituted with a *p*-hydroxy or *p*-alkoxy group in lignin, it is predicted that 1,2-elimination will be an dominant reaction pathway in lignin pyrolysis. It would be

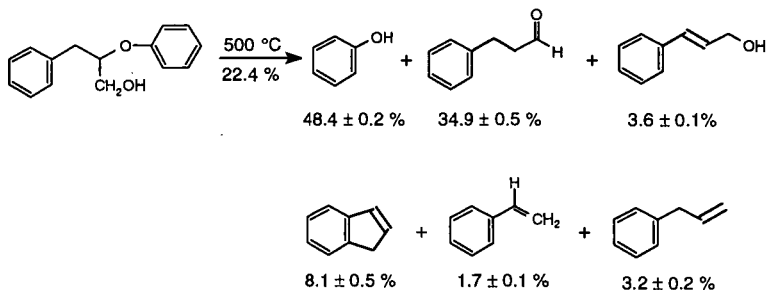
beneficial to find reaction conditions to minimize the dehydration reaction since it produces a more refractory product with the ejection of hydrogen (as water) from a carbon rich material.

On the basis of the FVP results of PPE, we would predict that the dominant products from the FVP of α -HO-PPE would be phenol and acetophenone (PhCOCH_3) by the C-O homolysis or 1,2-elimination pathway. Surprisingly, acetophenone is a minor product indicating that 1,2-elimination is not a significant pathway in the decomposition of α -HO-PPE. The formation of phenol and phenylacetaldehyde could arise from two different pathways as shown below: a) intramolecular attack of the hydroxyl group on the β -carbon to eliminate phenol and styrene oxide which can undergo additional decomposition by pyrolysis; or b) homolysis of C-O bond, 1,2-phenyl shift, followed by loss of a hydrogen atom and tautomerization. Alkaline cleavage of



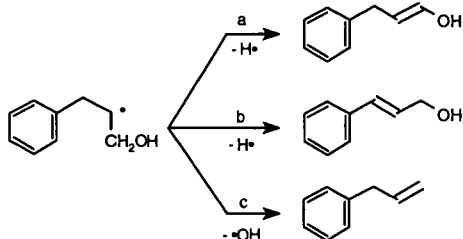
lignin model compounds at low temperatures (220-300 °C) was shown to proceed through an epoxide intermediate by an internal displacement reaction [18]. Pyrolysis of substituted styrene oxides have been shown to produce alkyl benzyl ketones (or aldehydes). For example, pyrolysis of 3,4-dimethoxyphenyloxirane at 500 °C produces 3,4-dimethoxyphenylacetaldehyde as the major product [19]. To determine the contribution between these two possible pathways, we are currently synthesizing α -hydroxy- α -deuteriophenethyl phenyl ether ($\text{PhC(OH)DCH}_2\text{OPh}$). Pathway (a) will provide phenylacetaldehyde labeled with deuterium in the benzylic position (PhCHDCHO) while pathway (b) will produce phenylacetaldehyde labeled in the aldehydic position (PhCH_2CDO). The contribution from the two pathways will be deduced from the mass spectrum fragmentation pattern of the phenylacetaldehyde produced in the FVP of $\text{PhC(OH)DCH}_2\text{OPh}$.

FVP of β -CH₂OH-PPE. The major products from the FVP of β -HOCH₂-PPE at 500 °C are shown below (average mol % from three runs). The reproducibility of the % conversion (22.4 ± 0.7 %) and mass balances (100.4 ± 0.4 %) of these runs are excellent. As observed for α -HO-



PPE, the rate is dramatically accelerated by the addition of the hydroxy group to the β -ether linkage. As predicted from the documented substituent effects on 1,2-elimination reactions, dehydration of the primary alcohol is a minor pathway for β -HOCH₂-PPE, since there are no electron donating substituents to stabilize the polar transition state as found in α -HO-PPE [17]. The dominant pyrolysis products can be rationalized by C-O homolysis, followed by β -scission of a hydrogen or a hydroxyl radical (see below). Thermochemical estimates predict that pathway (a) should be favored over (b) and (c) by 5-6 kcal mol⁻¹ [20] and $\text{PhCH}_2\text{CH}_2\text{CHO}$ is found to be the dominant product. However, it is impossible to rule out a contribution of a 1,2-elimination in the formations of $\text{PhCH}_2\text{CH}_2\text{CHO}$ and $\text{PhCH=CHCH}_2\text{OH}$. The origin of the indene is unclear,

but it has been shown that $\text{PhCH}=\text{CHCH}_2^\bullet$ can cyclize to indene [21]. However, under the low pressure conditions, hydrogen abstraction from $\text{PhCH}_2\text{CH}=\text{CH}_2$ is unlikely and thermochemical



estimates indicate that the homolysis of the C-O bond in $\text{PhCH}=\text{CHCH}_2\text{OH}$ would be slow at 500 °C [20]. Nevertheless, the indene most likely arises from decomposition of $\text{PhCH}=\text{CHCH}_2\text{OH}$.

Impact of the hydroxy group on the decomposition of the β -ether linkage. One surprising outcome of this investigation was the dramatic increase in the decomposition of PPE by the addition of a hydroxy-substituent. The average % conversion without dehydration for the FVP of PPE, α -HO-PPE, and β -HOCH₂-PPE at 500 °C was 0.96 %, 23.4 %, and 22.4 %. Thermochemical estimates, assuming C-O homolysis is the rate determining step, predict a β -hydroxy substituent might enhance the decomposition by a factor of 1-4 [22]. However, we observe rate enhancements greater than a factor of 20. One possible explanation for the similar rate enhancement for an α - and γ -hydroxy group is that internal hydrogen bonding is accelerating the C-O homolysis. Suryan, Kafafi, and Stein have measured the C-O bond dissociation energy of a series of substituted anisoles and found that the bond weakening caused by the *o*-hydroxy group was 4.7 kcal mol⁻¹ greater than that for the *p*-hydroxy group [23]. This additional stabilization was attributed to internal hydrogen bonding and not a destabilizing interaction in the guaiacol molecule. In α -HO-PPE and β -HOCH₂-PPE, molecular mechanics calculations indicate that the hydroxy group can interact with the ether oxygen without a significant energy penalty. The 20 fold rate enhancement in the decomposition of hydroxy-substituted PPE's at 500 °C corresponds to a difference of ca. 4.5 kcal mol⁻¹ in C-O bond strengths (assuming all products arise from C-O homolysis). Additionally, King and Stock have reported that hydrogen bonding by phenols or benzoic acid enhance the rate of decomposition of benzyl phenyl ether and dibenzyl ether [24]. However, it is still remarkable for weak hydrogen bonding interactions to have such a dramatic influence on the reaction chemistry at high temperatures. Therefore, to further investigate the potential role of hydrogen bonding in the decomposition of hydroxy-substituted PPE's, the methyl ether of α -HO-PPE and β -HOCH₂-PPE will be synthesized and subjected to FVP. This will remove the hydrogen bonding interactions and the conversions should be more similar to that found for PPE if hydrogen bonding is important.

ACKNOWLEDGMENTS

Research sponsored by the Division of Chemical Sciences, Office of Basic Energy Sciences, U.S. Department of Energy, under contract DE-AC05-96OR22464 with Oak Ridge National Laboratory, managed by Lockheed Martin Energy Research Corp. M. J. Cooney was supported by an appointment to ORNL Postdoctoral Research Associate program administered jointly by Oak Ridge Institute for Science and Education and ORNL.

REFERENCES

1. (a) A. V. Bridgwater (Ed.), *Thermochemical Processing of Biomass*, Butterworths, London, 1984. (b) E. J. Soltes and T. A. Milne (Eds.), *Pyrolysis Oils from Biomass-Producing, Analyzing, and Upgrading*, ACS Symposium Series No 376, American Chemical Society, Washington, DC 1988. (c) I. S. Goldstein (Ed.), *Organic Chemical from Biomass*, CRC Press, Boca Raton, FL 1981, Chapters 5 and 8.
2. Glasser, W. G.; Sarkanen, S. (Eds.), *Lignin Properties and Materials*, ACS Symposium Series No. 397, American Chemical Society, Washington, DC, 1989.
3. van der Hage, E. R. E.; Mulder, M. M.; Boon, J. J. *J. Anal. Appl. Pyrolysis* 1993, 25, 149.
4. Antal, Jr., M. J.; Croiset, E.; Dai, X.; DeAlmeida, C.; Mok, W. S-L.; Norberg, N.; Richard, J-R.; Majthoub, M. A. *Energy Fuels* 1996, 10, 652.
5. Elliott, D. C.; Beckman, D.; Bridgwater, A. V.; Diebold, J. P.; Gevert, S. B.; Solantausta, Y. *Energy Fuels* 1991, 5, 399.

6. Bridgwater, A. V.; Cottam, M-L. *Energy Fuels* **1992**, *6*, 113.
7. a) Antal, Jr., M. J. in Boer, K. W. and Duffie, J. A. (Eds.), *Advances in Solar Energy*, Vol 2, ASES Publication, New Toyk, 1985, p.175 and references therein. (b) Evans, R. J.; Milne, T. A.; Soltys, M. N. *J. Anal. Appl. Pyrolysis* **1986**, *9*, 207.
8. Klein, M. T.; Virk, P. S. *Ind. Eng. Chem. Fundam.* **1983**, *22*, 35.
9. (a) Brown, R. F. C. *Pyrolytic Methods in Organic Chemistry*, Academic Press, New York, 1980. (b) Seybold, G. *Angew. Chem. Int. Ed. Engl.* **1977**, *16*, 365. (c) Schaden, G. *J. Anal. Appl. Pyrolysis* **1985**, *8*, 135. (d) Wiersum, U. E. *Rec. Trav. Chim. Pays-Bas* **1982**, *101*, 317 and 365. (e) Hedaya, E. *Acc. Chem. Res.* **1969**, *2*, 367.
10. Golden, D. M.; Spokes, G. N.; Benson, S. W. *Angew. Chem. Int. Ed. Engl.* **1973**, *12*, 534.
11. Glasser, W. G.; Glasser, H. R.; Morohoshi, N. *Macromolecules* **1981**, *14*, 253. (b) Nimz, H. *Angew. Chem. Int. Ed. Engl.* **1974**, *13*, 313.
12. Britt, P. F.; Buchanan, III, A. C.; Malcolm, E. A. *J. Org. Chem.* **1995**, *60*, 6523.
13. Trahanovsky, W. S.; Ong, C. C.; Pataky, J. G.; Weilt, F. L.; Mullen, P. W.; Clardy, J. C.; Hansen, R. S. *J. Org. Chem.* **1971**, *36*, 3575.
14. Trahanovsky, W. S.; Ong, C. C.; Lawson, J. A. *J. Am. Chem. Soc.* **1968**, *90*, 2839.
15. Walker, J. A.; Tsang, W. *J. Phys. Chem.* **1990**, *94*, 3324.
16. Maccoll, A. *Chem. Rev.* **1969**, *69*, 33.
17. Maccoll, A.; Thomas, P. J. *Progress in Reaction Kinetics* **1967**, *4*, 119.
18. Nelson, D. A.; Samuels, W. D.; Hallen, R. T. *Energy Fuels* **1987**, *1*, 239.
19. Kuroda, K. *J. Anal. Appl. Pyrolysis* **1995**, *35*, 53.
20. (a) Benson, S. W. *Thermochemical Kinetics*, Wiley, New York, 1978. (b) Benson, S. W. *Chem. Rev.* **1993**, *93*, 2419 (c) NIST Structure and Properties Database and Estimation Program Version 2.02, S. E. Stein, J. M. Rukkers, and R. L. Brown NIST Reference Database 25 1994.
21. Trahanovsky, W. S.; Ong, C. C. *J. Am. Chem. Soc.* **1970**, *92*, 7174.
22. The D°_{C-H} of $\text{PhCH(OH)CH}_2\text{-H}$ is set equal to $\text{CH}_3\text{CH(OH)CH}_2\text{-H}$. Holmes, J. L.; Lossing, F. P.; Mayer, P. M. *J. Am. Chem. Soc.* **1991**, *113*, 9723.
23. Suryan, M. M.; Kafafi, S. A.; Stein, S. E. *J. Am. Chem. Soc.* **1989**, *111*, 1423.
24. King, H.-H.; Stock, L. M. *Fuel* **1984**, *63*, 810.

MODELING BIOMASS PYROLYSIS KINETICS AND MECHANISMS

Yonggang Chen, Sylvie Charpenay, Anker Jensen*, Michael A. Serio, and Marek A. Wójtowicz

Advanced Fuel Research, Inc., 87 Church Street, East Hartford, CT 06108-3742

*Department of Chemical Engineering, Technical University of Denmark, 2800 Lyngby, Denmark

Keywords: Biomass, Pyrolysis, Modeling

ABSTRACT

Over the next decade there will be a renewed emphasis on the production of chemicals and liquid fuels from biomass, the use of agricultural wastes as feedstocks, and the co-firing of coal and biomass materials. In view of the tremendous diversity of biomass feedstocks, a great need exists for a robust, comprehensive model that could be utilized to predict the composition and properties of pyrolysis products as a function of feedstock characteristics and process conditions. The objective of this work is to adapt an existing coal pyrolysis model and make it suitable for the pyrolysis of biomass. The soundness of this approach is based on numerous similarities between biomass and coal. There are important differences, however, which preclude direct application of the coal model. This work involved: 1) selection of a set of materials representing the main types of biomass; 2) development of a biomass classification scheme; 3) development of a modeling approach based on modifications of a coal pyrolysis model; 4) calibration of the model for a set of standard materials against pyrolysis data taken over a range of heating rates; 5) validation of the model against pyrolysis data taken under other (higher) heating rate conditions.

INTRODUCTION

The future outlook for biomass pyrolysis is quite promising, despite the fact that petroleum prices should remain low for at least the next decade [1]. The political and environmental benefits of using biomass will continue to provide impetus to the development of biomass pyrolysis processes (indigenous supply, low sulfur, no net CO₂, biodegradable, etc.). The current level of activity is high (about 650 activities were identified in a recent study [2]), and international in scope. Over the next several years there will be a renewed emphasis on the production of chemicals from biomass with minimal upgrading, and on the use of agricultural wastes as feedstocks. Research and development activities will also continue on the production of liquid fuels and chemicals from biomass, and on the development of crops and farming techniques optimized for fuel or chemical production.

In view of the anticipated rapid development of pyrolysis-based processes, and because of the tremendous diversity of biomass feedstocks, a great need exists for a robust, comprehensive model that could be utilized to predict yields, composition and properties of pyrolysis products. Such a model would constitute a valuable tool in process development and scale-up. No such model is currently available. The specific problem addressed in this study was related to the inability to predict *a priori* gas, liquid, and solid products on the basis of known feedstock characteristics and process conditions (temperature, pressure, heating rate, residence time, etc.). This makes it difficult, of course, to design a process where the most desirable slate of products is produced. This, in turn, leads to appreciable, and often unnecessary, costs of product upgrading.

This work involved modifying the currently available FG-DVC coal devolatilization model [3,4], and making it suitable for modeling pyrolysis of agricultural and forestry feedstocks. The soundness of this approach was based on numerous similarities between biomass and coal, such as the fact that coal was formed from biomass, and that it can actually be viewed as petrified biomass. There are important differences, however, which preclude direct application of the coal model to pyrolysis of biomass, and which make it necessary to create a separate model dedicated to biomass conversion.

The FG-DVC model for coal pyrolysis combines a functional group (FG) model for gas evolution and a statistical depolymerization, vaporization, and cross-linking (DVC) model for tar and char formation [3,4]. The FG model currently predicts gas yields from the functional group sources in the coal using rank-dependent kinetics. The DVC model simulates coal as a macromolecular network and includes the processes of depolymerization, cross-linking, and transport. The model accurately predicts volatile yields, extract yields, cross-link densities, fluidity, and tar (oil) molecular weight distributions. The variations of the variables with pressure, devolatilization temperature, rank, and heating rate are also accurately reproduced.

A version of the FG-DVC model has been developed for lignin [5], which is similar to coal in being a cross-linked aromatic structure. However, in the case of whole biomass, the lignin component is a relatively minor constituent and the modeling approach must be adjusted to account for the dominant components (cellulose and hemicellulose).

BACKGROUND

The pyrolysis of biomass has been the subject of numerous studies, as summarized in several reviews and collected papers [6-12]. Biomass pyrolysis is similar to coal pyrolysis with respect to pyrolysis products, which are char, tar and gases. Analogies are often drawn between pyrolysis of biomass and low-rank coals, but this should be done with caution. One of the principal differences is the fact that coal is predominantly an aromatic material, whereas the aromatic component of biomass (lignin) is a relatively minor constituent (~20%). In addition, because of the fossil nature

of coal, the mineral matter which has been incorporated into its structure influences the pyrolysis behavior in a different way than in the case of biomass. Biomass also has a much higher oxygen content as compared with coal. The oxygen is present as ether, hydroxyl, carboxyl, aldehyde, and ketone functionalities, which decompose during pyrolysis to produce oxygenated gases (CO , CO_2 , H_2O). The yields of these species are similar to those produced by pyrolysis of low-rank coals (5–10 dry wt.% for CO_2 and H_2O , 5–15 dry wt.% for CO). Biomass pyrolysis, however, produces much higher tar (liquid) yields as compared with low-rank coals (40–50% versus 10–20% on a dry basis). The increased tar yield comes primarily at the expense of char, the yield of which is much lower for biomass than for low-rank coals (<10% versus 40–50%). Apparently, the depolymerization of biomass is the predominant pyrolytic reaction, whereas, in the case of coal, depolymerization reactions compete with cross-linking events, which enhances char formation. Most of the char formed from biomass is derived from the lignin component, which is closest to low-rank coal in its chemical composition. As in the case of coal, the yield and distribution of products from pyrolysis of biomass depend on other variables in addition to the final temperature and holding time. These include heating rate, total pressure, ambient gas composition, and the presence of catalysts. An overview of these is given by Shafizadeh (in reference [10]). The trends are similar to those observed in coal, i.e., higher yields of volatiles are usually observed at higher heating rates, lower pressures, and in the presence of hydrogen. However, the data are quite scattered.

Historically, the quantitative modeling of biomass pyrolysis has proceeded along similar lines as for coal [1]. One approach is based on the approximation that the three main components of biomass (cellulose, hemicellulose, and lignin) behave independently during pyrolysis (see, e.g. Nunn *et al.* in ref. [10]). Consequently, yields can be predicted based on a knowledge of the pure component behavior. The shortcoming of this technique is that it cannot account for possible interactions between the biomass components. A more phenomenological approach was successfully used by Serio *et al.* [5] in modeling the pyrolysis of lignin. Their model was focused on observed evolution rates of major products rather than on the many individual reactions leading to the evolution of each product. The model of Serio *et al.* [5] and that of Petrocelli and Klein (discussed in reference [10]) involve a statistical treatment of lignin pyrolysis reactions. For the reasons discussed above, the network features of the FG-DVC model and similar models (such as the one proposed by Petrocelli and Klein) will be de-emphasized in favor of the original functional group (FG) description of gas and tar evolution [13,14]. While this is a more empirical approach, there is flexibility in the model to add more details of the whole biomass pyrolysis chemistry as these become known and can be represented in a tractable mathematical expression. A detailed review of modeling chemical and physical processes occurring during whole biomass pyrolysis can be found in reference [15]. Unlike in the case of coal, no comprehensive model of whole biomass pyrolysis has yet been developed.

EXPERIMENTAL

Sample Selection - A number of biomass samples were first recommended based on the abundance and availability of agricultural and forestry feedstocks in the United States. The initial recommendations included softwood, hardwood, corn stalk, wheat straw, copy paper and newspaper. Cellulose, lignin, and hemicellulose were also recommended in order to individually study the three main components of biomass independently. This initial list was modified due to the limited ability to acquire standardized materials. Six samples were obtained from the National Institute of Standards and Technology's Standard Reference Materials Program which included microcrystalline cellulose (C), sugar cane bagasse (B), wheat straw (WS), corn stalk (CS), softwood *Pinus radiata* (PR), and hardwood *Populus deltoides* (PD). These six samples were supplemented with two samples of the pure component materials: lignin (L) and hemicellulose (HC). The identification and elemental composition of all nine samples is given in Table 1. To understand the chemical structure of these feedstocks, the starting materials were characterized by several methods including trace elemental analysis, ultimate analysis, proximate analysis, Field Ionization Mass Spectrometry (FIMS), solvent extraction and solvent swelling. This was complemented by a compilation of relevant literature data. FIMS and solvent extraction/swelling data will be reported in a separate publication.

Ultimate and Proximate Analysis - This work was done by Huffman Laboratories (Golden, Colorado). In addition, the samples were subjected to trace element analysis. Trace elements have often been implicated in influencing the pyrolysis behavior of whole biomass ([16]; also Shafizadeh in reference [10]).

TG-FTIR Method - Details of the TG-FTIR method can be found in references [17] and [18]. The apparatus, consists of a sample suspended from a balance in a gas stream within a furnace. As the sample is heated, the evolving volatile products are carried out of the furnace directly into a 5 cm diameter gas cell (heated to 150 °C) where the gases are analyzed by FT-IR spectroscopy. The FT-IR spectrometer obtains spectra to determine quantitatively the evolution rate and composition of several hydrocarbon compounds. Coal tars can also be quantified but biomass tars are appreciably different and for the lack of calibration data are determined from the mass balance. The system allows the sample to be heated on a pre-programmed temperature profile, at rates 3–100 °C min⁻¹, up to a temperature between 20 °C and 1100 °C. Isothermal steps with a specified hold time are also possible.

RESULTS AND DISCUSSIONS

Biomass Classification Scheme - The first step in modeling was to develop a classification scheme for whole biomass samples. Several researchers have taken the approach of modeling the pyrolysis of whole biomass using a linear superposition of the results for the three main components, i.e., cellulose, hemicellulose, and lignin ([19-21]; also Nunn *et al.* in reference [10]). However, a problem with this approach is that input information is not always known or easily obtained, and the amounts determined are not always consistent from one laboratory to another. In addition, Nunn *et al.* reported that modeling the evolution of individual species in high-heating-rate experiments was unsuccessful, although the modeling of the char yield produced good results [10]. The above scheme was also tested at Advanced Fuel Research (AFR) by trying to reproduce the TG-FTIR results for a whole biomass sample using a superposition of the TG-FTIR evolution profiles obtained for pure components. In general, this approach was unsuccessful for the evolution of individual species, and this is thought to be due to variations in the component compositions depending on their source, the effect of trace components on the pyrolysis behavior, and the problem in isolating unaltered pure components.

For this reason, it was decided that an alternative approach would be pursued, in which the samples are classified based on a van Krevelen diagram (plot of H/C versus O/C atomic ratios). A similar classification scheme has been successfully used for coal pyrolysis [22]. A plot of the six samples and the pure component samples are shown in Figure 1, along with literature results for other biomass samples. In general, the H/C ratio correlates with the O/C ratio, especially for the data collected at AFR. Variations in moisture content and errors in elemental analysis results are believed to be responsible for part of the scatter.

Model Calibration - The classification scheme lends itself to a linear interpolation of the total yields of pyrolysis products as well as the kinetic files based on the known elemental composition. However, since most of the whole biomass samples are closely clustered to either one of the woody (PD, PR) or herbaceous samples (CS, WS), it was decided to use a close-neighbor approximation. In this case, the input files are obtained from the nearest neighbor of the standard set of samples which were chosen to be L, CS, PD, and C. These samples were subjected to a more detailed characterization in order to calibrate the kinetic and composition files. In future work, some refinement of this scheme will be developed which allows for discrimination of small differences in composition.

The close-neighbor approximation is also confirmed by the TG-FTIR data as shown in Figures 2 and 3, where the evolution profiles for PR, PD, and B, and WS and CS are compared. The TG-FTIR data shows that PR, PD and B behave similarly, which is in agreement with the van Krevelen data from Figure 1. The same can be said about WS and CS. In addition, the following general observations concerning the TG-FTIR data can be made: (1) for each biomass sample, all gas-evolution peaks (except for methane) occur at approximately the same temperature; (2) the methane evolution peak of woody samples is bimodal, whereas only a single peak is present in the case of herbaceous biomass; (3) all the herbaceous-samples peaks occur at temperatures approximately 30 °C lower than the corresponding peaks for the woody samples; and (4) a small low-temperature peak can be seen in the evolution patterns of the herbaceous samples.

Kinetics and Yields Determination - In what follows, the determination of the kinetic parameters and total yields of individual species is described in some detail. In general, the approach is similar to that applied to coal, i.e., the evolution of each functional group is described by a first-order reaction with a distributed activation energy of width σ [4]. In the case of biomass pyrolysis, a smaller number of functional groups is required to describe the process as the evolution of each species can usually be represented by the decomposition of a single functional group. In other words, each gas species released during biomass pyrolysis evolves in the form of a single peak, which is in contrast to coal pyrolysis where several peaks can be observed for an individual species. Methane is an exception, in the sense that it requires two functional groups in the case of coals and woody biomass, but only a single peak for herbaceous biomass.

Since the TG-FTIR biomass data show that, for each sample, the tar and other gas species evolve at the same temperature (Figs. 2 and 3), the same value of the activation energy was used for all species. This activation energy was derived from the overall weight-loss curve, and a non-isothermal T_{max} method was used for this purpose [23]. T_{max} is the temperature at which the rate of volatile evolution is maximum. Typically, T_{max} is measured at several heating rates, and the activation energy E and the pre-exponential factor A can be extracted from the equation: $\ln(M/T_{max}^2) = \ln(A/E) - E/(RT_{max})$ [23].

Although the value of E was kept identical for the biomass tar and all the gas species, slight adjustments in the value of σ were performed in order to match more closely the width of the evolution peak of each species. The amounts of the functional groups, and the corresponding yields of the volatiles, were obtained by fitting the model to the TG-FTIR data. The results from this analysis are given in Table 2. The values for the activation energies obtained are consistent with previous literature results [24]. The apparent discrepancy between our kinetic parameters and those reported for cellulose by Antal and Varhegyi [25] can be explained by the differences in the processing of raw experimental data. A detailed discussion of this topic will be included in a future publication.

Model Validation - Model predictions were compared with the yields and composition of pyrolysis products obtained under different conditions from those used to determine model

parameters (e.g., different heating rates). An example is shown in Fig. 4 for the high heating rate data of Nunn *et al.* (1000 K/sec) [26]. Experimental data for sweet gum hardwood are compared with model predictions generated using the kinetic input files for PD. The results are reasonable for the overall weight loss (Fig. 4) and CO₂ (not shown), but they are less good for the other gas species. In addition to the simplifications inherent in the predictive model, and the differences in the composition of the two materials, the observed discrepancies could also result from uncertainties in the time-temperature history and/or secondary reactions which alter the product distribution. Future work will involve refinement of the model to include secondary reactions, mineral effects, heating-rate effects, and an improved classification scheme to account for composition differences.

CONCLUSIONS

The FG-DVC coal pyrolysis model has been successfully applied to biomass. Preliminary data show that it may be possible to model the pyrolysis behavior of different biomass feedstocks using kinetic parameters and product yields interpolated among selected data-base materials (standards). The linear interpolation scheme is based on the feedstock elemental composition. Refinements of the proposed scheme and further validation of the model are under way.

ACKNOWLEDGMENTS

The support for this work came from the U.S. Department of Agriculture under Research Agreement No. 96-33610-2675. A research scholarship for Anker Jensen was provided by the Technical University of Denmark. The authors also acknowledge helpful discussions with Professor Eric M. Suuberg of Brown University.

REFERENCES

- 1 Serio, M. A., Wójtowicz, M. A. and Charpenay, S., "Pyrolysis," *Encyclopedia of Energy Technology and the Environment* (A. Bisio and S. G. Boots, Eds.), John Wiley & Sons, New York, 1995.
- 2 Bridgwater, A. V., *Biomass*, **22** (1-4), 279 (1990).
- 3 Solomon, P. R., Hamblen, D. G., Carangelo, R. M., Serio, M. A., and Deshpande, G. V., *Combustion and Flame*, **1988**, **71**, 137.
- 4 Solomon, P. R., Hamblen, D. G., Serio, M. A., Yu, Z. Z., and Charpenay, S., "A Characterization Method & Model for Predicting Coal Conversion Behavior," *Fuel*, **72**, (4), 489 (1993).
- 5 Serio, M. A., Charpenay, S., Bassilakis, R., and Solomon, P. R., "Measurement and Modeling of Lignin Pyrolysis", *Journal of Biomass & Bioenergy*, Vol. 7, Nos. 1-6, 107 (1994).
- 6 Antal, M. J., Jr., in *Adv. in Solar Energy* (Boer, K. W., Duffie, J. W., Eds.), American Solar Energy Society, Boulder, CO, **1**, 61 (1984); **2**, 175 (1985).
- 7 Shafizadeh, F., in *Proc. Specialists' Workshop on Fast Pyrolysis of Biomass* (J. Diebold, Ed.), SERI/CP-622-1096, Solar Energy Research Institute, Golden, CO, 79 (1980).
- 8 Shafizadeh, F., in *The Chemistry of Solid Wood* (R. M. Rowell, Ed.), *Advances in Chemistry Series No. 207*, American Chemical Society, Washington, DC (1984).
- 9 Bridgwater, A. V., and Cottam, M.-L., *Energy and Fuels*, **6**, (2), 113 (1992).
- 10 Overend, R. P., Milne, T. A., and Mudge, L. K., Eds., *Fundamentals of Thermochemical Biomass Conversion*, Elsevier, (1985).
- 11 Soltes, E. J., and Milne, T. A., Eds., *Pyrolysis Oils from Biomass: Producing, Analyzing and Upgrading*, ACS Symposium Series No. 376, American Chemical Society, Washington, DC (1988).
- 12 Chum, H. L., and Powers, A. J., in *Emerging Technologies for Materials and Chemicals from Biomass* (R. M. Rowell, T. P. Schultz, and R. Narayan, Eds.), ACS Symposium Series No. 476, ACS, Washington, DC, pp. 339-353 (1993).
- 13 Solomon, P. R. and Hamblen, D. G., Ch. 5 in *Chemistry of Coal Conversion* (R. H. Schlosberg, Ed.), Plenum, New York, 1985, pp. 121-251.
- 14 Serio, M. A., Hamblen, D. G., Markham, J. R. and Solomon, P. R., *Energy & Fuels*, **1**, 138 (1987).
- 15 Di Blasi, C., *Prog. Energy Combust. Sci.*, **19**, 71 (1993).
- 16 Varhegyi, G., Antal, M. J., Jr., Szekeley, T., Till, F., Jakab, E. and Szabo, P., *Energy & Fuels*, **2**, 273 (1988).
- 17 Carangelo, R. M., Solomon, P. R. and Gerson, D. J., *Fuel*, **66**, 960 (1987).
- 18 Whelan, J. K., Solomon, P. R., Deshpande, G. V., Carangelo, R. M., *Energy and Fuels*, **2**, 65, (1988).
- 19 Koufopoulos, C. A., Maschio, G. and Lucchesi, A., *Can. J. Chem. Eng.*, **67**, 75 (1989).
- 20 Ward, S. M. and Breslaw, J., *Comb. Flame*, **61**, 261 (1985).
- 21 Miller, R. S. and Bellan, J., submitted to *Combust. Sci. Tech.* (1996).
- 22 Zhao, Y., Serio, M. A., Bassilakis, R. and Solomon, P. R., *Twenty-Fifth Symposium (International) on Combustion*, The Combustion Institute, Pittsburgh, PA, 1994, pp. 553-560.
- 23 Van Heek, K. H. and Juentgen, H., *Ber. Bunsenges. Phys. Chem.*, **72**, 1223 (1968).

- 24 Milosavljevic, I. and Suuberg, E. M., *Ind. Eng. Chem. Res.*, **34**, 1081 (1995).
 25 Antal, M. J., Jr. and Varhegyi, G., *Ind. Eng. Chem. Res.*, **34**, 703 (1995).
 26 Nunn, T. R., Howard, J. B., Longwell, J. P. and Peters, W. A., *Ind. Eng. Chem. Process Des. Dev.*, **24**, 836 (1985).

Table 1. Proximate, ultimate, and trace-element analyses of the biomass samples used in this study (wt.%). Dry loss is on an as-received basis, while all other results are reported on a dried-sample basis. Legend: CS = Corn Stalk; WS = Wheat Straw; B = Sugar Cane Bagasse; PR = *Pinus radiata*; PD = *Populus deltoides*; C = Cellulose; ALC = ALC Lignin

	CS	WS	B	PR	PD	C	ALC
Dry Loss	5.0	7.9	7.1	6.6	6.6	4.8	N/A
Carbon	45.6	43.7	47.3	49.9	49.1	44.0	67.4
Hydrogen	5.9	5.6	5.8	6.1	6.0	6.4	6.2
Oxygen	44.0	40.9	42.8	43.6	43.8	49.5	26.3
Nitrogen	0.72	0.62	0.17	0.05	0.09	0.03	0.20
Sulfur	0.10	0.19	0.04	0.02	0.06	< 0.01	N/A
Ash	3.8	9.0	3.9	0.25	0.91	< 0.05	< 0.05
Vol. Matter	89.8	72.8	79.3	82.8	83.5	92.7	N/A
Fixed Carbon	6.4	18.2	16.8	17.0	15.6	7.3	N/A
Al	N/A	N/A	0.2%	L	L	N/A	N/A
Si	N/A	N/A	0.3%	L	L	N/A	N/A
Na	N/A	N/A	L	L	L	N/A	N/A
K	N/A	N/A	0.03%	0.02	0.02%	N/A	N/A
Fe	N/A	N/A	0.1%	N	N	N/A	N/A
Mg	N/A	N/A	L	N	N	N/A	N/A
Ca	N/A	N/A	0.05%	L	0.1	N/A	N/A
Ti	N/A	N/A	0.05%	N	N	N/A	N/A
Mn	N/A	N/A	50 ppm	N	N	N/A	N/A
B	N/A	N/A	L	N	N	N/A	N/A
Ba	N/A	N/A	L	N	N	N/A	N/A
Be	N/A	N/A	L	N	N	N/A	N/A
Cr	N/A	N/A	L	N	N	N/A	N/A
Ni	N/A	N/A	L	N	N	N/A	N/A
V	N/A	N/A	10 ppm	N	N	N/A	N/A

L = Detected but below detection limit, N = Not detected, N/A = Not Available

Table 2. Kinetic parameters and yields for the pyrolysis of corn stalk and *Populus deltoides*.

Sample	Species	A (s ⁻¹)	E/R (K)	σ/R (K)	Yield (wt.% daf)
Corn Stalk	CO ₂	8.3×10^{13}	22500	700	5.1
	CO	8.3×10^{13}	22500	700	2.2
	H ₂ O	8.3×10^{13}	22500	700	7.4
	CH ₄ Tight	N/A	N/A	N/A	N/A
	CH ₄ Loose	5.2×10^{12}	27500	2000	0.8
	Tar	8.3×10^{13}	22500	100	63.5
Populus Deltoides	CO ₂	2.8×10^9	17000	700	5.2
	CO	2.8×10^9	17000	700	3.4
	H ₂ O	2.8×10^9	17000	700	10.4
	CH ₄ Tight	6.0×10^{13}	31000	2500	0.54
	CH ₄ Loose	3.0×10^{13}	25000	1500	0.36
	Tar	2.8×10^9	17000	100	55.2

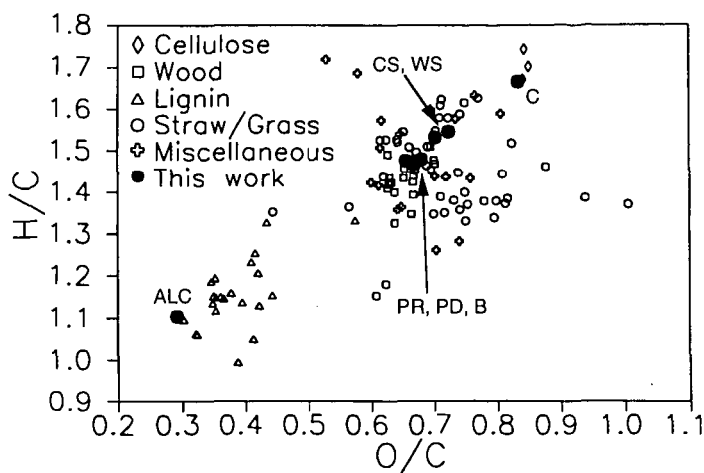


Figure 1. The van Krevelen diagram for biomass samples. H/C and O/C are atomic hydrogen-to-carbon and oxygen-to-carbon ratios.

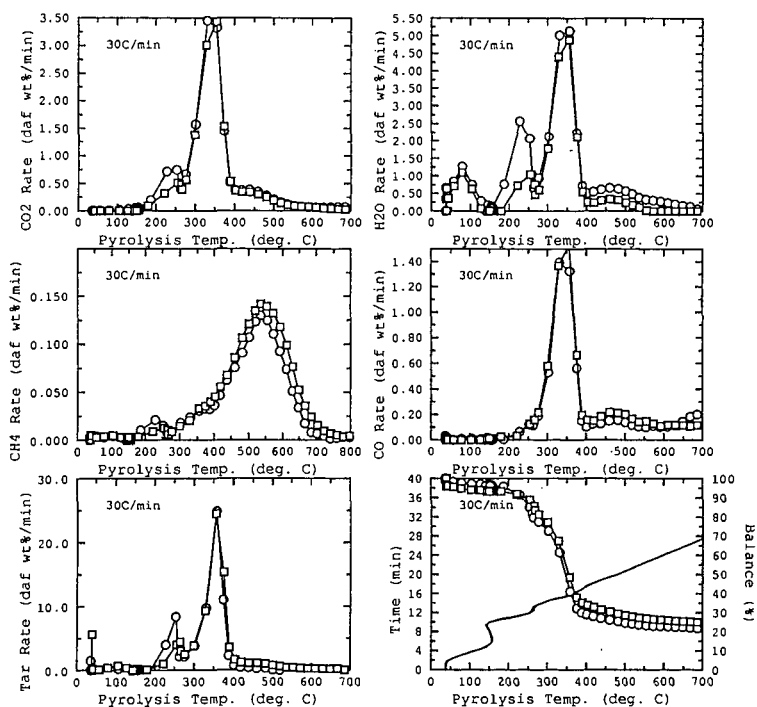


Figure 2. The TG-FTIR data for two herbaceous samples: corn stalk (circles) and wheat straw (squares).

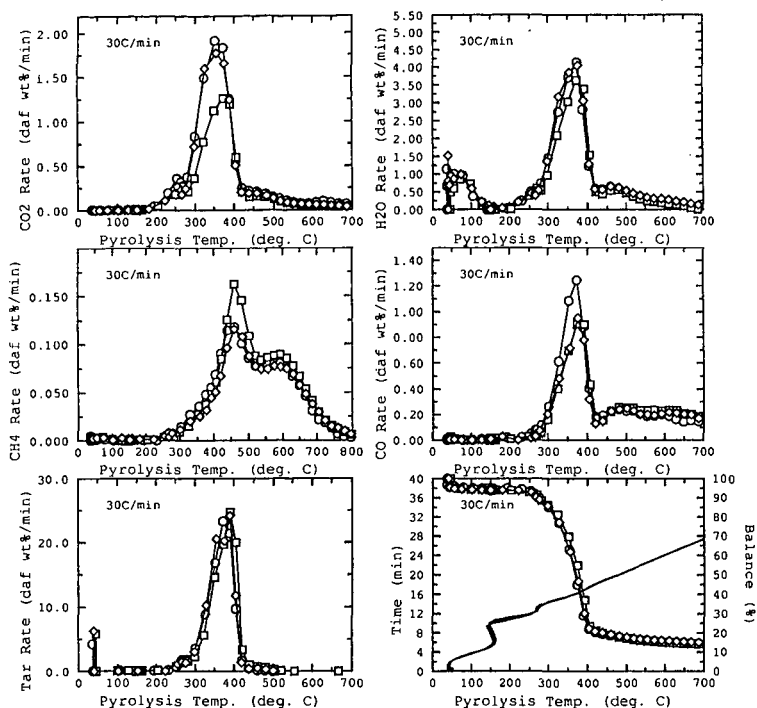


Figure 3. The TG-FTIR data for two woody samples: *Populus deltoides* (circles) and *Pinus radiata* (squares). The position of sugar cane bagasse on the van Krevelen diagram is in close proximity to the above two samples, and the TG-FTIR data for bagasse (diamonds) exhibit gas-evolution patterns similar to those of *Populus deltoides* and *Pinus radiata*.

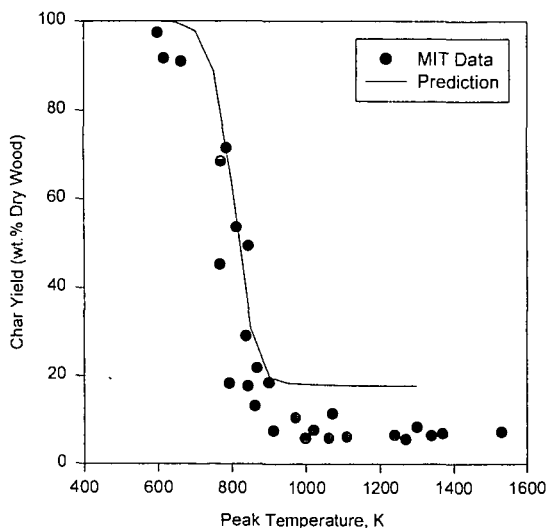


Figure 4. The comparison of char-yield experimental data (Nunn *et al.* [26]) and model predictions using the kinetic input files and product yields for *Populus deltoides*. The heating rate is 1000 K/s.

MECHANISM OF SILICA-IMMOBILIZED THIOANISOLE CONVERSION DURING AN AP-TPR-EXPERIMENT

H. Van den Rul, J. Yperman, A. C. Buchanan III^{*}, P. F. Britt^{*}, I. I. Maes, D. V. Franco, J. Mullens and L. C. Van Poucke, Laboratory of Inorganic and Physical Chemistry, Limburgs Universitair Centrum, B-3590 Diepenbeek, Belgium, ^{*} Chemical and Analytical Sciences Division, Oak Ridge National Laboratory, P. O. Box 2008, Oak Ridge, TN 37831-6197, USA

Keywords: Non-Isothermal Kinetics, AP-TPR, Model Compounds

ABSTRACT

A kinetic study of the AP-TPR-profile of silica-immobilized thioanisole was carried out, resulting in a better understanding of the mechanistic behaviour of this model compound under the specified conditions. AP-TPR (Atmospheric Pressure - Temperature-Programmed Reduction) with potentiometric sulfur detection is a thermoanalytical method used to differentiate between sulfur forms in solids like coals. In this respect, silica-immobilized thioanisole was recorded as a nonmelting calibrant. Several kinetic methods exist to analyze a heterogeneous process involving a solid that is heated by a linear temperature programme. The isoconversional method can be considered as one of the most accurate. It was applied to the AP-TPR-profile of thioanisole, showing the reduction of this compound very quickly becomes a diffusion-controlled reaction. Kinetic parameters are reported for this process under the AP-TPR-conditions.

INTRODUCTION

Temperature-Programmed Reduction (TPR) of sulfur-containing solid samples under atmospheric pressure (AP), is a method to study different sulfur functionalities in the sample [1]. Knowledge of the distribution of sulfur functional groups in materials is of practical importance. For example, the ease with which sulfur is released from coal is determined by the functional form of the sulfur present. Thiols and sulfides are labile sulfur compounds and undesirable because of environmental consequences. Thiophenes on the other hand are more stable. Recording of model compounds for sulfur functionality (in coal for example) is a key step in AP-TPR to evaluate characteristic temperature intervals where reduction of the specific sulfur group occurs.

A study of the AP-TPR-profiles of model compounds can also provide information about the mechanistic pathway of the occurring reactions that involve sulfur. In combination with other techniques a more detailed description can be given [2].

Also, a non-isothermal kinetic analysis of the AP-TPR-curves can be performed to get a better insight into the mechanism. A kinetic investigation of an AP-TPR-profile is different from conventional kinetics: the reaction studied is heterogeneous, a solid is involved and the temperature is raised during the experiment. Kinetic laws for homogeneous processes under isothermal conditions have been accurately determined. They can be considered as component parts of more complex kinetic models applied to heterogeneous processes [3].

For AP-TPR experiments, calibrants must neither melt nor evaporate before they are reduced in order that they remain in the reaction zone of the reactor. In this respect, nonmelting silica-immobilized (SI) substrates can be employed. It has been demonstrated the Si-O-C_{aryl} linkage is stable up to 500°C, even in reducing atmospheres [4].

In this work, AP-TPR-profiles of silica-immobilized thioanisole (\approx Ph-S-CH₃) are analyzed by non-isothermal kinetics, and more specifically by the isoconversional method [7].

EXPERIMENTAL

The AP-TPR-set-up is shown in figure 1. During an AP-TPR-experiment, the sample is located at the bottom of a quartz reactor, while H₂ gas is constantly flowing through it (fluidized bed system) at a rate of 50 ml/min. The oven is heated by a constant linear temperature programme, and the different sulfur functional groups are reduced in a characteristic temperature interval. The released H₂S is detected potentiometrically, resulting in a spectrum of H₂S evolution.

Silica-immobilized thioanisole was prepared from the sulfur-containing phenol (4-hydroxy-thioanisole, Aldrich Chemical Co.) and Cabosil fumed silica on a gram scale, as described previously for the synthesis of silica-immobilized diphenylalkanes [5].

For the AP-TPR-experiments, 20.0 mg SI thioanisole was used.

RESULTS AND DISCUSSION

Kinetic methods

Generally a simplified rate equation is used to describe reactions in solids [3]:

$$\frac{d\alpha}{dt} = k(T) \cdot f(\alpha) \quad (1)$$

where $\alpha = \frac{X_b - X}{X_b - X_a}$ is the degree of conversion (X is the measured quantity, e.g. mass sulphur in AP-TPR), normalised from 0 to 1, $k(T)$ is the Arrhenius rate constant, T is the temperature, t is the time and $f(\alpha)$ is a mathematical description of the reaction model. The form of $f(\alpha)$ is related to physico-geometric assumptions on the development of the reaction boundary between the initial solid substance and the product.

For non-isothermal conditions, when a constant heating rate $\beta = \frac{dT}{dt}$ is applied, eq. (1) is transformed:

$$\frac{d\alpha}{dT} = \frac{A}{\beta} \exp\left(-\frac{E}{RT}\right) f(\alpha) \quad (2)$$

where E is the Arrhenius activation energy, A the pre-exponential factor and R the gas constant. In integral form:

$$\int_0^\alpha \frac{d\alpha}{f(\alpha)} \equiv g(\alpha) = \frac{A}{\beta} \int_0^T \exp\left(-\frac{E}{RT}\right) dT \equiv \frac{A}{\beta} I(E, T) \quad (3)$$

Equation (2) as well as numerous approximations of its integral form (3) underlie most of the methods of kinetic processing [3].

Most frequently, those methods are utilized that employ data obtained at one heating rate. Different reaction models are fitted to the dataset, the best $f(\alpha)$ is discriminated using some criterion, and the Arrhenius parameters are evaluated based on this choice. The problem [6] is that usually quite different reaction models fit the data equally well (from a statistical point of view), whereas the values of the corresponding Arrhenius parameters markedly differ. The ambiguity of the kinetic parameters obtained by these "discriminating" methods implies that their physical meaning is doubtful. Moreover [6] this type of analysis yields a single kinetic triplet (A , E and $f(\alpha)$) for the overall process of thermal transformation and doesn't allow the detection of a possible change of rate-limiting step (and associated Arrhenius parameters).

Overcoming these problems can be done by using methods that employ data at different heating rates, like isoconversional methods [7]. Without having to discriminate a reaction model, values of E are obtained at each given conversion α . The isoconversional method used in this work can be described as follows [7]:

assuming the reaction model is independent of the heating rate, eq. (3) can be written for a given conversion and a set of data obtained at different heating rates β_i ($i=1, \dots, n$):

$$\frac{A_\alpha}{\beta_1} I(E_\alpha, T_{\alpha,1}) = \frac{A_\alpha}{\beta_2} I(E_\alpha, T_{\alpha,2}) = \dots = \frac{A_\alpha}{\beta_n} I(E_\alpha, T_{\alpha,n}) \quad (4)$$

Strict fulfilment of eq. (4) results in:

$$\sum_{i=1}^n \sum_{j=1}^n \frac{I(E_\alpha, T_{\alpha,i}) \beta_j}{I(E_\alpha, T_{\alpha,j}) \beta_i} = n(n-1) \quad (5)$$

where $j = 1, \dots, n$. Because the T_α values are measured with some experimental error, eq. (4) can only be satisfied as an approximate equality, in other words: eq. (5) can be met as a condition of minimum value:

$$n(n-1) - \sum_{i=1}^n \sum_{j=1}^n \frac{I(E_\alpha, T_{\alpha,i}) \beta_j}{I(E_\alpha, T_{\alpha,j}) \beta_i} = \min \quad (6)$$

Substituting experimental values of T_α and β into eq. (6) and varying E_α to reach the minimum gives the value of the activation energy at a given conversion. The values of $I(E, T)$ are approximated.

Applying the isoconversional method to a multi-step process shows the dependence of E_α on α . This dependence can be used as a criterion for a multi-step process [8]. Moreover, the shape of the dependence can help to elucidate the mechanism of the occurring reactions [8].

Kinetic analysis of the AP-TPR profiles of silica-immobilized thioanisole

Several AP-TPR experiments for silica-immobilized thioanisole were performed at four different heating rates (3.5, 5, 8 and 12 °C/min). All profiles were normalised and converted to (α, T) dependences: see figure 2. Before 400 °C no reaction was detected. When the heating rate is increased, a shift of the profile is observed to higher temperatures [3].

Several combinations of curves at different heating rates were selected, and analyzed by the isoconversional method, resulting in a typical $E-\alpha$ dependence: see figure 3. At the very beginning of the process, values of E higher than 100 kJ/mol are observed, but immediately the activation energy reduces to values lower than 45 kJ/mol. These low values are typical for the diffusion of a gas in a solid [6, 9].

This $E-\alpha$ dependence can be interpreted as follows. The values of E (>100 kJ/mol) in the beginning refer to a chemical reaction that controls the rate. To determine what reaction is occurring, a comparison could be made with bond dissociation energies for the thioanisole compound. However, at very low values of α , the calculation of E is less accurate and an exact value of E can not be given. It can only be proven E -values typical for chemical reaction are seen here. Moreover, even at the beginning diffusion could influence the reaction rate, thus lowering the calculated E -values. Subsequently, the dependence shows a decrease of E to values lower than 45 kJ/mol. This means there is a transition from a reaction-controlled process to a regime that is completely controlled by diffusion of a gas in a solid. A possible explanation for this transition can be as follows. The sulfur-containing particles that can easily be reached by the H_2 gas react quickly to release H_2S with an activation energy $E > 100$ kJ/mol. The rate of the process is controlled by this hydrogenation. The rest of the particles that are not in direct contact with the H_2 gas, react next. But at this point, diffusion of H_2 or H_2S gas through the bulk of firstly reacted particles becomes the rate-limiting step. Another explanation for the transition to a diffusion regime involves reaction of the evolved H_2S with the siloxanes of the silica support to generate $OSi-SH$ species that are then released slowly out of the solid.

A comment can be made here on the use of this model compound (SI thioanisole) for AP-TPR calibration. Since the hydrogenation is only rate-determining at the beginning of the process under AP-TPR-conditions, only the rate at the beginning is reproducible. The rest of the AP-TPR-rate-profile (differential form) is diffusion controlled, and can vary according to the specific conditions inside the AP-TPR-reactor. Because the sample amount used is very small (20 mg), and the experimental AP-TPR conditions are almost invariant, the differential profiles of thioanisole are very similar. Still, the diffusion-control has to be taken into account. This means that only the onset temperature can be used as a calibrant temperature for this thioanisole model compound. Additional studies have to be done to see if this conclusion also holds for other model compounds.

CONCLUSIONS

Application of the AP-TPR-technique in combination with non-isothermal kinetic analysis, is an efficient tool to study mechanistic pathways of reduction of sulfur in model compounds. The term "mechanism" indicates a kinetic scheme in this context, and not a sequence of elementary steps, because only those reactions can be seen in AP-TPR that induce the change in the measured quantity.

The results for silica-immobilized thioanisole show a transition from a (chemical) reaction-controlled process to a regime that is completely controlled by diffusion of a gas in a solid. Kinetic analyses of other model compounds like cysteine and silica-immobilized phenylbenzyl-sulphide will be discussed later.

ACKNOWLEDGEMENTS

This work is financed with a specialization grant of the 'Vlaams Instituut voor de bevordering van het wetenschappelijk-technologisch onderzoek in de industrie (IWT)'.

REFERENCES

1. Maes, I. I.; Yperman, J.; Van den Rul, H.; Franco, D. V.; Mullens, J.; Van Poucke, L. C.; Gryglewicz, G.; Wilk, P. *Energy & Fuels* **1995**, 9, 950
2. Ismail, K.; Mitchell, S. C.; Brown, S. D.; Snape, C. E.; Buchanan III, A. C.; Britt, P. F.; Franco, D. V.; Maes, I. I.; Yperman, J. *Energy & Fuels* **1995**, 9(4), 707
3. Sestak, J.; Thermal Analysis. Part D. Thermophysical Properties of Solids, Elsevier, New York, 1984
4. Lafferty, C. J.; Mitchell, S. C.; Garcia, R.; Snape, C. E.; Buchanan III, A. C.; Britt, P. F.; Klavetter, E. *Energy & Fuels* **1993**, 7, 331
5. Britt, P. F.; Buchanan III, A. C. *J. Org. Chem.* **1991**, 56, 6132
6. Vyazovkin, S. *Int. J. Chem. Kin.* **1996**, 28, 95
7. Vyazovkin, S.; Dollimore, D. *J. Chem. Inf. Comp. Sci.* **1996**, 36, 42
8. Vyazovkin, S. V.; Lesnikovich, A. I. *Thermochim. Acta* **1990**, 165, 273
9. Attar, A.; Dupuis, F. *Ind. Eng. Chem. Process Des. Dev.* **1979**, 18(4), 607

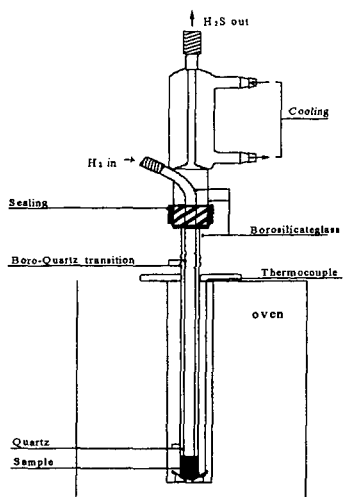


Figure 1: AP-TPR set-up

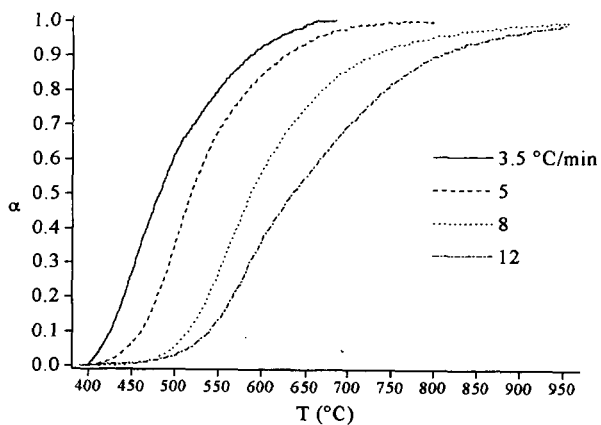


Figure 2: AP-TPR profiles of SI thioanisole shown as α , T dependences for 4 heating rates

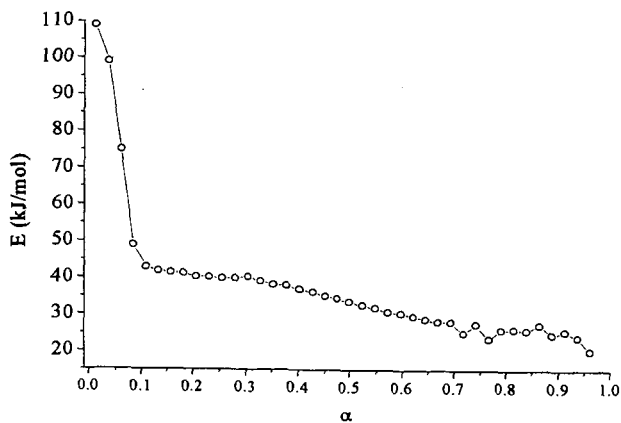


Figure 3: Typical E , α dependence for AP-TPR profiles of SI thioanisole

THE USE OF PHENOLIC RESINS CONTAINING POLYNUCLEAR AROMATIC MOIETIES TO MODEL ASPECTS OF COAL PYROLYSIS

C. McRae, O. Sirkecioglu and C. E. Snape

Department of Pure & Applied Chemistry, University of Strathclyde, Thomas Graham Building, 295 Cathedral St., Glasgow G1 1XL, Scotland, UK

Keywords: Phenolic resins, polycyclic aromatic hydrocarbons, carbonisation

INTRODUCTION

Coals and oil shales have highly complex, macromolecular organic structures¹⁻³ and, in order to obtain insights into the multitude of reactions which occur during their thermal breakdown, detailed compositional information on the aromatic, aliphatic and heteroatomic groups present and an understanding of how these different functionalities behave under processing conditions are required. To achieve the latter goal, model compound studies performed in both vapour and liquid phases have been used extensively⁴. However, a major drawback with such studies is that radical species generated by bond homolysis are mobile and free to diffuse independently prior to further reaction. In contrast, for highly cross-linked macromolecular solids such as coals and oil shales, many of the reactive intermediates remain covalently attached to the matrix of the solid and thus their reactivity is subject to diffusional constraints. Further, for thermal studies in open systems the use of non-softening substrates that neither melt nor vaporise and hence remain in the reactor is essential.

In order to probe the effects of restricted mobility in free radical reaction pathways during coal liquefaction, Buchanan and co-workers studied the thermal decomposition of model compounds immobilised on silica^{5,6}. It was recognised that these substrates also have considerable potential for modelling many aspects of solid fuel behaviour, including the release of sulphur and nitrogen species during coal conversion processes and the cleavage of diphenylalkane bridging groups during pyrolysis. Preliminary work establish that the SiO-C bond linking the substrate to the surface is reasonably stable and does not cleave below 500°C⁷. Immobilised sulphur moieties, typical of those found in solid fuels were subsequently prepared and used as calibrants in temperature programmed reduction (TPR)⁸, a thermal technique used to specify organic sulphur forms from their characteristic reduction temperatures^{9,10}.

Cured phenol-formaldehyde (PF) resins were identified as another flexible class of materials that could be used for investigating thermochemical phenomena in the solid state since a wide spectrum of hydrocarbon and heteroatomic moieties can readily be introduced into their macromolecular framework. A series of sulphur and nitrogen containing co-resoles and resites have been prepared and their characterisation has been reported previously¹¹. These resites have been used to study the release of sulphur dioxide during coal combustion¹² and as an alternative calibrant to the silica immobilised substrates for TPR^{13,14}.

Polycyclic aromatic hydrocarbons (PAH) are a series of ubiquitous environmental pollutants containing two or more fused benzene rings that are widely produced by the incomplete combustion of fossil fuels and other organic materials¹⁵⁻¹⁷. Due to the lack of mechanistic information concerning their formation during solid fuel conversion processes, there is a need for suitable model substrates and, in this investigation, a suite of PAH-containing resites have been prepared, with, as the second component, diphenylmethane, benzylnaphthalene, benzylanthracene, benzylphenanthrene and 2-naphthol. To illustrate the potential of the resites to study the formation of PAH in the utilisation of solid fuels, the carbonisation of the 9-(4-hydroxybenzyl)anthracene-containing resite has been investigated in a fluidised-bed reactor.

EXPERIMENTAL

Synthesis of precursors

The mono- or dihydroxydiphenylalkane and monohydroxy-phenyl PAHs used to prepare the resins were 4-hydroxy-diphenylmethane, 4,4'-dihydroxydiphenylethane, 2-naphthol, 4-naphthobenzylphenol, 9-(4-hydroxybenzyl)anthracene and 9-(4-hydroxybenzyl)phenanthrene. Of these, only 4-hydroxydiphenylmethane and 2-naphthol were commercially available.

To prepare 4,4'-dihydroxydiphenylethane, a Wolff-Kishner reduction was conducted on 4'-methoxy-2-(p-methoxyphenyl)acetophenone (deoxyanisoin) to yield 4,4'-

dimethoxydiphenylethane. This compound was then subjected to demethylation by refluxing for 20 minutes in 20 g of redistilled pyridine hydrochloride. This yielded the crude product which was recrystallised from hexane-ethylacetate to yield white shiny prismatic crystallites (M.Pt. 198-199°C).

To prepare 1-(4-hydroxybenzyl)naphthalene, naphthalene was first acylated with p-anisoylchloride to yield 1-(4-methoxybenzoyl)naphthalene. A Wolff-Kishner reduction was conducted on this compound to produce 1-(4-methoxybenzyl)naphthalene. This compound was then demethylated as described above. After cooling, the reaction product was extracted in diethylether and purified by vacuum distillation (180-182°C, 3-4 mmHg). The product was recrystallised from benzene-acetone (3:1 v/v) to yield yellow shiny needle crystallites (M.Pt. 166-167°C).

9-(4-hydroxybenzyl)anthracene was prepared by first reacting 9-anthracenecarboxylic acid with oxalylchloride to yield 9-anthracene carbonyl chloride. This was then acylated with anisole to produce 9-(4-methoxybenzoyl)anthracene which was then subjected to a Wolff-Kishner reduction. The resultant 9-(4-methoxybenzyl)anthracene was then demethylated as described above and the crude product was recrystallised from toluene to yield yellow shiny needle crystallites (M.Pt. 187-188°C).

To prepare 9-(4-hydroxybenzyl)phenanthrene, phenanthrene was first acylated with p-anisoylchloride to yield 9-(4-methoxybenzoyl)phenanthrene. A Wolff-Kishner reduction was conducted on this compound to yield 9-(4-methoxybenzyl)phenanthrene which was then demethylated as described earlier. The crude product was purified by vacuum distillation (200-201°C, 3-4 mmHg) and recrystallisation from hexane which yielded yellow shiny needle crystallites (M.Pt. 85-86°C).

Synthesis of resins

The co-resoles were prepared using a total phenol to formaldehyde mole ratio of 1:2.5 following established procedures^{18,19}. The mole ratio of phenol to the monohydroxydiphenylalkanes or monohydroxybenzyl PAHs was 3:1 to ensure that a reasonably high degree of crosslinking was achieved in the initial resoles. Sodium hydroxide was used as catalyst in the condensation reaction with mole ratio of 0.1 with respect to phenol. Phenol, the monohydroxydiphenylalkane or monohydroxybenzyl PAHs and formaldehyde (37% formaldehyde) were mixed in 250 cm³ 3-neck round bottom flask and stirred until all the phenol was in solution. The mixture was then cooled in an ice-bath for about 10 minutes before sodium hydroxide (0.006 mol, 20 M) was added dropwise to the reaction mixture. This was then refluxed at 70°C for 30 min., acidified with 85% lactic acid to a pH of 4-5 (indicated by universal indicator paper) before excess water was removed by vacuum distillation. The thick resinous material was poured into a capped container for curing in an oven purged with nitrogen gas that was initially set at 70°C for 4 days. The oven temperature was then raised to 130 and 200°C for additional 24 hour periods. For purposes of comparison, a normal PF resite and resole were prepared by the same procedure.

Pyrolysis

An all-silica fluidised-bed reactor system (5 cm dia.), based on the design used by Tyler and coworkers²⁰, was used to pyrolyse a normal PF resite and the 9-(4-hydroxybenzyl)anthracene - containing resite at a temperature of 900°C in a bed containing ca. 100g of acid-washed sand (200-300 μ). This was fluidised using a flow of 2-3 dm³ min⁻¹ of nitrogen. Approximately 4 g of resite (75-212 μ) was fed at a constant rate from a hopper, which was also fluidised with a flow of nitrogen (1 dm³ min⁻¹), over 20-30 minute period into the fluidised-bed at 900°C. Two 500 cm³ Dreschel bottles in series cooled with dry ice were used to trap the tars with virtually no carry over into the gas.

After the tests, the tars were recovered in toluene for analysis. The char and tar yield were calculated from the weight gains of the bed and the traps during each run with the weight gains of the traps being corrected for any water present determined via the Dean-Stark method. After the water had been removed from the toluene solutions of the tars, these were concentrated to facilitate fractionation of the tars by preparative-scale open-column alumina chromatography to provide aromatic fractions for high performance liquid chromatography (HPLC) analysis. The alkanes, aromatics and polars were eluted successively from the column containing activated alumina (500°C for 16 hr.) with n-hexane, toluene and methanol. For HPLC separation of the aromatic fractions by ring size, an electron-deficient, nitroaromatic-bonded silica column manufactured by Shandon (Hypersil CTA) was used in conjunction with an

Applied Chromatography Systems gradient elution pump, a Waters UV detector at 254 nm and a PC-based software package for peak integration. The volumetric flowrate was set at $0.6 \text{ cm}^3 \text{ min}^{-1}$ and a standard mixture of 16 PAHs (supplied by Supelco) was used to optimise the separation achieved with n-hexane and dichloromethane (DCM) mixtures, the most satisfactory gradient elution scheme being 10 % v/v DCM in hexane for 20 min., followed by 10 to 100 % v/v DCM in 60 min. and, finally, 100 % v/v DCM.

RESULTS AND DISCUSSION

The total yields of tar and aromatics and the yield of anthracene obtained from the fluidised-bed pyrolysis experiments on the normal PF and the 9-(4-hydroxybenzyl) anthracene-containing resite are listed in Table 1, together with the HPLC-determined distribution of ring size in the aromatics. Figure 1 compares the HPLC traces for the aromatics obtained from the two resites. The high pyrolysis temperature of 900°C ensures that parent PAH dominate over the alkyl-substituted counterparts (most alkyl and parent PAH co-elute in the HPLC separation). As expected from the volatile matter contents also shown in Table 1, a much higher tar yield has been obtained from the 9-(4-hydroxybenzyl)anthracene-containing resite. Indeed, the higher tar yield is accounted for completely by the additional aromatic material obtained (ca. 10% w/w resite).

As anticipated, anthracene dominates the HPLC trace of the aromatics for the 9-(4-hydroxybenzyl)anthracene-containing resite (Figure 1, phenanthrene being the major peak in the trace for the normal resite). However, the increase in anthracene yield of ca. 5% w/w resite only accounts for about half that in the total tar yield. Further, when this fact is taken with the estimated anthracene content of ca. 30% in the initial resite, strong evidence emerges for the anthracene becoming involved in many other reaction pathways other than simple homolytic cleavage of the anthracylbenzyl methane linkage. Since the total tar yield is only 34%, it can be inferred that a substantial portion of the anthracene is incorporated into the char. Further, the following HPLC results provide evidence that some of the anthracene present rearranges to form other low molecular mass PAH, particularly phenanthrene and acenaphthene, during pyrolysis.

Table 2 compares the mass ratios of phenanthrene (the major constituent in the aromatics from the normal resite, Figure 1) to a number of other PAH present. With the exception of acenaphthene, the ratios increase considerably indicating that the yields of phenanthrene and acenaphthene are both considerably greater for the 9-(4-hydroxybenzyl)anthracene-containing resite with the implication that they have been formed by rearrangement of the anthracene present. Indeed, it is estimated from the data in Table 2 that the phenanthrene yield increases from 2.2% (w/w) for the normal resite to 5.5% for the 9-(4-hydroxybenzyl)anthracene-containing resite.

The fact that the yield of aromatic material is significant from the normal PF resites provides direct evidence that phenolic moieties can transform directly into PAH during devolatilisation. The first step in this complex reaction pathway probably involves dehydration to form diphenyl ether and furan moieties, which then undergo subsequent ring growth with further dehydration. Since phenolic moieties are the major building blocks of both low-rank and high volatile bituminous coals¹, these are likely to be the prime source of PAH rather than the much smaller concentrations of large aromatic ring systems in these coals.

CONCLUSIONS

Although van Krevelen was the first to use PF resins in coal science to account for the plasticity behaviour of different coals¹, the approach adopted here for PAH represents a new direction in fuel science for investigating, in a macromolecular environment, the behaviour of the individual functional groups present during conversion processes. Non-softening PF co-resites are ideal substrates for probing the reaction pathways leading to PAH formation during devolatilisation since they facilitate the incorporation of individual PAHs into a highly cross-linked matrix. The volatile matter contents of the PAH-containing resites were higher than the corresponding normal PF resins due to the lability of the single diarylmethane linkage anchoring the PAHs into the macromolecular structure. The carbonisation of the normal PF and 9-(4-hydroxybenzyl)anthracene-containing resite in a fluidised-bed reactor served to illustrate the complexity of the reaction pathways undergone by the anthracene moiety, with evidence of rearrangement of the anthracene structure to form other PAH, primarily phenanthrene and acenaphthene.

REFERENCES

1. W. Van Krevelen, *Coal: Typology-Physics-Chemistry-Constitution*, 3rd ed., Elsevier (1993).
2. J. G. Speight, Ed., *Fuel Science & Technology Handbook*, M. Dekker, New York (1992).
3. C. E. Snape, Ed., *Geochemistry, Characterisation and Conversion of Oil Shales*, NATO ASI series Vol. C455, Kluwer (1995).
4. M. L. Poutsma, *Energy & Fuels*, **4**(2), 113, (1990) and references therein.
5. A. C. Buchanan III and C. A. Biggs, *J. Org. Chem.* **54**, 517, (1989).
6. P. F. Britt and A. C. Buchanan III, *J. Org. Chem.* **56**, 6132, (1991).
7. S. C. Mitchell, C. J. Lafferty, R. Garcia, K. Ismail, C. E. Snape, A. C. Buchanan III, P. F. Britt and E. Klavetter, *Energy & Fuels*, **7**, 331, (1993).
8. K. Ismail, S. C. Mitchell, S. D. Brown, C. E. Snape, A. C. Buchanan III, P. F. Britt D. Franco and J. Yperman, *Energy & Fuels*, **9**, 707, (1995).
9. S. C. Mitchell, C. E. Snape and K. D. Bartle, *Fuel*, **73**, 1159, (1994).
10. C. E. Snape, S. C. Mitchell, K. Ismail and R. Garcia, *Euroanalysis VII: Reviews on Analytical Chemistry*, Royal Society Chemistry, (1994), p. 103.
11. K. Ismail, O. Sirkecioglu, J. M. Andersen, S. D. Brown, P. J. Hall, C. E. Snape and W. Steedman, *Polymer*, accepted for publication.
12. S. D. Brown, K. Ismail, C. E. Snape, A. Harding and K. M. Thomas, *Energy & Fuels*, **9**, 1104, (1995).
13. K. Ismail, G. D. Love, S. C. Mitchell, S. D. Brown and C. E. Snape, *Prepr. Am. Chem. Soc. Div. Fuel Chem.*, **39**(2), 551, (1994).
14. K. Ismail, S. D. Brown, O. Sirkecioglu, C. E. Snape, D. V. Franco, I. I. Maes and J. Yperman, *Proc. 8th Int. Conf. Coal Science*, Vol. 1, (1995). p.351, Elsevier Science Amsterdam.
15. I. M. Smith, PAH from coal utilisation - emissions and effects, *IEA Coal Research Report No. ICTIS/TR29*, London, UK, 1984.
16. C.V. Knight, M. S. Graham and B. S. Neal, in *Polynuclear Aromatic Hydrocarbons : formation, metabolism and measurement, Seventh International Symposium on Polynuclear Aromatic Hydrocarbons*, Columbus, OH, USA, Batelle, 1983, pp 689-710.
17. A. R. Collier, M. M. Rhead, C. J. Trier, and M. A. Bell, *Fuel*, **74**, 362 (1995)
18. Y. Zaks, J. Lo, D. Raucher and E. M. Pearce, *J. Appl. Polymer Sci.*, **27**, 913, (1982).
19. H. Bar and Z. Aizenshtat, *J. Anal. Appl. Pyrolysis*, **265**, (1991).
20. P. F. Nelson, I. W. Smith, R. J. Tyler and J. C. Mackie, *Energy & Fuels*, **2**, 391 (1988)
21. P.J. Hall, M.M. Antxustegi and J.M.Calo, *Proc. Carbon '94*, p.442, Granada, Spain.
22. G.E. Maciel, I.S. Chuang, and L. Gollob, *Macromolecules*, **17**, 1081, (1984).
23. K. Hultsch, *Chem. Ber.*, **74**, 1539, (1941).
24. A.B. Turner, *Quart. Rev.*, **18**, 347, (1964).
25. A.J. Mackinnon, P.J. Hall and M.M. Antxustegi, *Fuel*, **73**, 113, (1994).
26. A.J. Mackinnon, P.J. Hall, C.E. Snape and P. Burchill, *Fuel*, **74**, 136, (1995).
27. O. Sirkecioglu, P. McQueen, W. Steedman and C. E. Snape, *Fuel*, submitted.

	Normal PF	Anthracene-containing resite
Volatile Matter (% w/w)	40	58
Tar (% w/w resin)	25	34
Aromatics (% w/w resin)	10	20
Anthracene (% w/w resin)	1.8	7.0
Anthracene (% aromatics)	18	34
2-ring (% aromatics)	25	9
3-ring (% aromatics)	64	85
4-ring (% aromatics)	9	5
5-ring (% aromatics)	2	1

Table 1 : Yields from fluidised-bed pyrolysis of resites

	Normal PF	Anthracene-containing resite
Naphthalene	6	9
Acenaphthene	4	3
Acenaphthylene	10	27
Fluorene	6	16
Anthracene	1.2	0.8
Fluoranthene	16	40
Pyrene	12	34
Benzantracene	9	28
Chrysene	8	15

Table 2 : Mass ratios of phenanthrene to other PAH in fluidised-bed pyrolysis tars

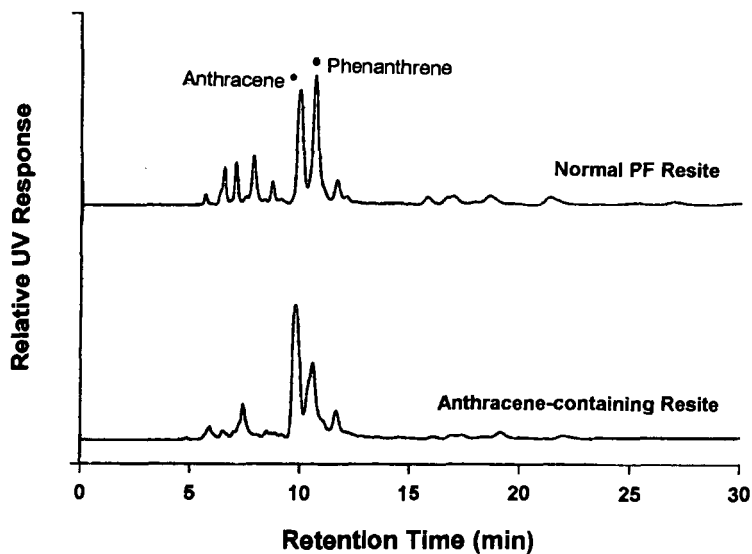


Figure 1 : HPLC traces of the aromatic fractions obtained from fluidised-bed pyrolysis of normal PF resite (top) and 9-(4-hydroxybenzyl)anthracene-containing resite (bottom)

LOCATION OF THE HYDROCARBON POTENTIAL DURING COAL PYROLYSIS: IMPLICATIONS ON THE CHEMICAL MODELLING

E. Langlois, R. Michels, M. Elie, L. Mansuy, O. Ruau and P. Landais

CNRS-CREGU, BP 23, 54501 Vandoeuvre Cedex, France.

Key words: artificial maturation, asphaltenes, resins, hydrocarbon generation.

INTRODUCTION

The modelling of hydrocarbon generation and the understanding of the compounds distributions (i.e. correlations on the basis of geochemical fingerprints) necessitate to establish genetic relationships between the kerogen and the corresponding rock extracts and oils (containing free hydrocarbons, but also the polars). These genetic relationships imply that the fate of the hydrocarbons in the organic system during maturation is known qualitatively (hydrocarbons distribution) and quantitatively (hydrocarbons potential). Hydrocarbons distributions and potential must therefore be defined for each organic fraction: the kerogen, the asphaltenes and resins as well as the free hydrocarbons. This implies a careful study of the composition of each fraction in regards to the degree of maturation and their respective behavior in the chemical maturation processes involved.

A precise study on the geochemical fingerprint and hydrocarbon potential of each organic fraction has been performed on an artificially matured coal. The combination of GC-MS and Py-GC-MS accompanied by semi-quantitation calculations allowed to identify the hydrocarbons distribution in each phase, to relate it to the respective hydrocarbon potential, and this for each maturation level.

EXPERIMENTAL

Sample. The sample used in this study is an immature homogeneous vitrinite-rich coal from the Mahakam delta (Indonesia) of low ash content (H/C=0.97; O/C=0.21; HI=335 mg/g) This sample has been widely studied and numerous data on both natural and artificial maturation are available^{1,2}.

Artificial maturation. 1 gram aliquots of the coal were loaded in gold cells (L=5cm; I.D.=1cm) under inert atmosphere. Isothermal confined pyrolysis runs were conducted at temperatures ranging from 250°C to 400°C by 10°C steps during 72h at 700bars pressure. The procedure and the pyrolysis apparatus are described elsewhere³. Detailed geochemical data on this series of maturation are available².

Collection of the different fractions. After pyrolysis, bitumen were extracted with chloroform at 60°C during 45 minutes. Asphaltenes were precipitated with 40 volumes of n-heptane at 40°C during 15 minutes. The maltene fraction, soluble in the n-heptane was fractionated into saturates, aromatics and resins using microcolumn liquid chromatography. Mass balance allowed quantitation of each fraction.

Gas Chromatography-Mass spectrometry (GC-MS). Saturates and aromatics were analyzed by gas chromatography-mass spectrometry (HP 5890 Serie II GC coupled to a HP 5971 mass spectrometer), using an on-column injector, a 60 m DB-5 J&W, 0.25 mm i.d., 0.1mm film fused silica column. The temperature program was 40 to 300°C at 3°C/min followed by an isothermal stage at 300°C for 15 min (constant helium flow of 25 cm/s)

Flash pyrolysis-Gas Chromatography-Mass Spectroscopy(Py-GC-MS). Py-GCMS of asphaltenes, resins and extracted residual kerogen were performed with a CDS 2000 pyroprobe. Samples were loaded in quartz tubes and heated at 620°C for 15s. The GCMS characteristics and temperature program were the same as described above. Flash pyrolysis yields were estimated by mass balance.

Semi-quantitation of the Pyrograms. The comparison of the absolute hydrocarbon potential of the asphaltenes, resins and residual kerogen in relation to the free hydrocarbons is very difficult because any quantitation technique has its limits and the actual quantitation of the source in the initial sample is impossible (it would require the quantitation of each functional group suspected to be the source of free hydrocarbons). However, the combination of the different techniques used in this work allows a relative mass balance to be calculated. The saturates potential has been assessed using a semi-quantitative approach combining Py-GC-MS yields, chromatogram integration, confined pyrolysis yields, the final value being expressed in mg of coal before pyrolysis. This method allows a relative comparison of the saturates potential of each fraction standardized to the initial coal potential.

RESULTS AND DISCUSSION

Table 1 gives the yields of hydrocarbons, asphaltenes, resins obtained after confined pyrolysis of Mahakam coal. The maximum of resins generation is reached at 320°C, while that of the asphaltenes occurs at 330°C. The maximum of C15+ saturates is reached at far higher temperature (360°C) while the C15+ aromatics are released over a large range of temperatures.

As far as the C15+ saturates are abundant in this sample and have a very characteristic pattern, the n-alkanes distribution will be used as tracer of hydrocarbons release in this study. Figure 1 gives an example of the m/z=57 chromatograms obtained for the free C15+ saturates (GC-MS), the resins, asphaltenes and residual kerogen (Py-GC-MS) obtained after confined pyrolysis at 260 and 350°C.

At a given maturation temperature, the aliphatic chain distribution in the resins pyrograms is quite similar to the free saturates chromatograms. The same odd-alkanes predominance is characteristic. On the contrary, the aliphatic distribution is different in the asphaltenes as well as in the residual solid: the odd alkanes predominance is less pronounced, and the maximum of the distribution is shifted towards the lower molecular weight hydrocarbons for the residual kerogen. An increased apparent maturity is therefore observed in the following order: the free saturates and resins look less mature than the asphaltenes which look less mature than the residual kerogen. These results show that although the coal has experienced the same thermal history, the compounds distribution in each organic phase does not reflect the degree of maturation in the same manner.

The flash pyrolysis yields of the Mahakam extracted residual kerogen, asphaltenes and resins have very different values and evolutions with maturation. Solid yields decrease from 40% (initial sample) to about 10% at 390°C, the main cause being the decrease of the oil potential. For asphaltenes and resins the pyrolyzate yields are

more important (about 60 and 80% respectively), and increase of about 10 to 15% with maturity, a behavior quite different from that of the resid.

Figure 2 shows the evolution of the saturates potential of each fraction (as defined in the experimental section) as a function of maturation. At the beginning of the maturation process the kerogen, of course, contains the most important amount of aliphatic hydrocarbons. In the mean time, the generation of polars is dominant. Consequently, the saturates potential of the kerogen decreases, while that of the polars increases. The decrease of the saturates content in the kerogen cannot be totally explained by the fairly low increase of the amount of free saturates (neither by the generation of the aromatic fraction that does not contain high amounts of long-chain alkyl-aromatics). A great part of the saturates potential is therefore transferred to the polars.

After the maximum of polars generation has been reached (330°C), the saturates potential calculated for the polars and the residual kerogen is fairly similar, and both contribute to the generation of the increasing amounts of free saturates. However, a look at the n-alkanes distribution within each of these fractions shows major differences between the polars and free saturates on one side and the residual kerogen on the other. This latter is highly dominated by lighter molecular weight n-alkanes, while the others still display a strong contribution of n-paraffins with a marked CPI. This feature suggests that the polars are mainly a source of C15+ n-alkanes at T>330°C, while the residual kerogen rather contributes to the generation of the C7-C14 n-alkanes. This picture is still valid at temperatures up to 360°C. From 360°C and higher, secondary cracking of the generated alkanes occurs, and the n-alkanes distribution in the various fractions is tending to homogenize (i.e. getting lighter), thus increasing the difficulty to properly identify the various sources of n-alkanes.

It has been shown earlier that the asphaltenes, resins and residual kerogen do not bear the same geochemical signature (i.e. alkanes and biomarkers distributions) at a given maturation step, the signature being the "most mature" for the solid and the "less mature" for the resins. Correlatively, their respective contribution to the generation of the free saturates, in terms of quality (hydrocarbon distribution) and timing (dominant hydrocarbon source) are different.

Thus, at the beginning of maturation (stages 250-330°C), a part of the kerogen (and its corresponding alkanes potential) is converted into the polar fraction in relation to the removal of low energy bonds (such as oxygen bonds). In a following maturation stage (330-360°C), the residual kerogen and the polars are thermally degraded and do not generate the same hydrocarbons.

CONCLUSIONS

The use of artificial maturation allows to compare the yields and composition of the free hydrocarbons, asphaltenes, resins and residual kerogen obtained from the pyrolysis of an immature coal. An integrated study of the various fractions gives interesting information concerning the evolution of the hydrocarbon potential of each phase and of the compounds distribution. The sample being characterized by a high n-paraffin content with a very typical distribution, the alkanes were used to discuss this aspect. It could be shown that:

- a great part of the hydrocarbon potential initially present in the kerogen, is progressively transferred into the polars (bitumen generation phase). At the mean time, low amounts of saturates are generated. Once the thermal degradation of asphaltenes and resins has been reached, both phases together with the residual kerogen contribute to the generation of free hydrocarbons.

- however, the distribution of the hydrocarbons released are different between the residual kerogen, asphaltenes, resins and free hydrocarbons. As a consequence, the relative maturity indicated by geochemical markers (biomarkers, compounds distribution) are different in each fraction.

It has been shown elsewhere^{4,5,6} that the polars have a different reactivity from the residual kerogen. Especially their interaction capabilities with the surrounding medium and their interaction with water imply that they play a specific role in the maturation process. This study shows that polars have also specific structural characteristics compared to the residual kerogen. As a consequence, the hydrocarbon release depends on a great part from the chemical reactivity of the polars, both quantitatively and qualitatively (the free hydrocarbons distribution mainly derives from the resins). This work suggests that the modellisation of hydrocarbons generation needs to take into account the specific behavior of the polars.

REFERENCES.

- (1) Monthieux M., Landais P., Monin J. C. *Org. Geochem.*, **1985**, *8*, 275-292.
- (2) Landais P. and Gérard L. *Coal geology*, **1996**, *30*, 285-301.
- (3) Landais P., Michels R. and Poty B. *Journal of Anal. and Appl. Pyrolysis*, **1989**, *16*, 103-115.
- (4) Mansuy L., Landais P. and Ruau O. *Energy Fuels*, **1995**, *9*, 691-703.
- (5) Mansuy L. and Landais P. *Energy Fuels*, **1995**, *9*, 809-821.
- (6) Michels R., Langlois E., Ruau O., Mansuy L., Elie M., and Landais P. *Energy Fuels*, **1996**, *10*, 39-48.

FIGURES AND TABLES

T(°C)	Asphaltenes	Resins	Saturates
250	1.7	3.2	0.3
260	1.9	3.1	0.4
270	2.1	4.1	0.5
280	2.0	4.1	0.4
290	2.1	5.6	0.8
300	2.7	6.4	1.0
310	3.1	8.6	1.5
320	3.8	9.0	1.8
330	4.8	8.7	2.5
340	2.2	7.3	3.1
350	1.6	6.2	4.6
360	1.0	6.2	5.8
370	1.0	3.2	3.3
380	0.6	1.9	2.5
390	0.5	1.1	1.8
400	0.3	0.8	1.0

Table 1: Asphaltenes, resins and saturates yields (in mass percent of initial coal) obtained after confined pyrolysis of Mahakam coal.

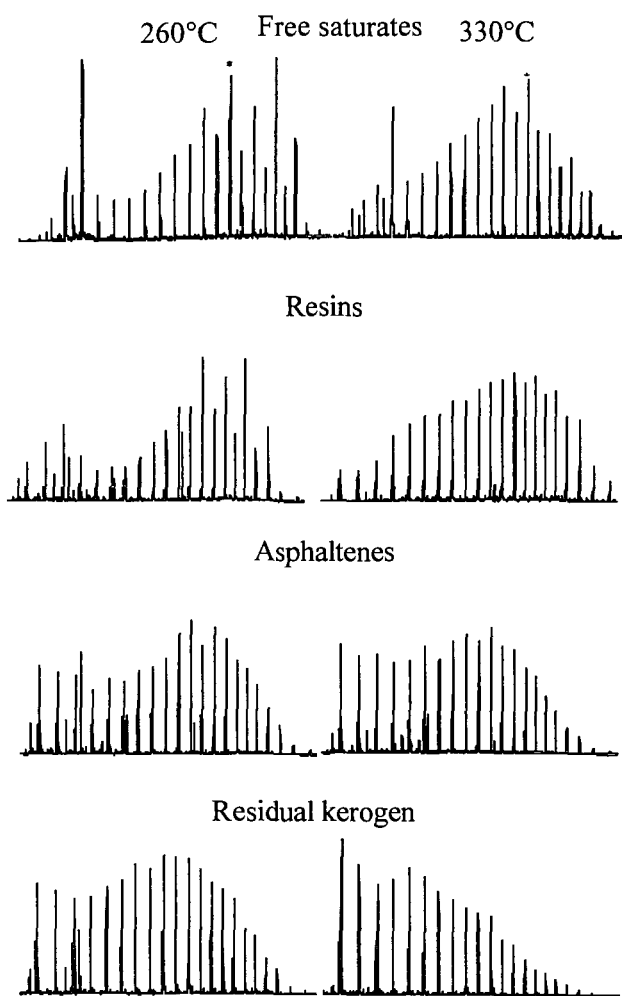


Figure 1: Comparison of the n-alkanes distributions ($m/z=57$; C17-C35 range, the star indicating nC27) observed in the free hydrocarbons (GC-MS) the resins, asphaltenes and residual kerogen (Py-GC-MS) generated from the Mahakam coal during confined pyrolysis at 260 and 330°C.

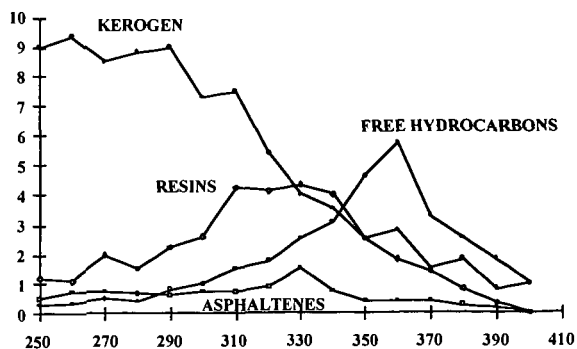


Figure 2: Evolution of n-alkanes yields (in weight percent of immature coal) obtained after semi-quantitative calculations based on Py-GC-MS yields, chromatogram integrations as well as confined pyrolysis yields of asphaltenes, resins and residual kerogen. These values represent the relative hydrocarbon potential for each phase. Are also plotted the free saturates yields obtained after confined pyrolysis (values also normalized to immature coal mass).

REACTIONS OF SOME ORGANIC CHLORINE AND SULFUR COMPOUNDS IN SUPERCRITICAL WATER

Thomas J. Houser and Xu Liu

Department of Chemistry
Western Michigan University
Kalamazoo, MI 49008-3842

Keywords: supercritical water, organic chloride and sulfur removal, reactor corrosion

INTRODUCTION

Because of the possible use of supercritical water (SW) for fuels processing and coal extraction to obtain cleaner, less polluting products, and its potential use as a medium for the efficient oxidation and destruction of environmentally hazardous materials there has been an increase in the number of reports on the basic chemistry that may be taking place in the presence of SW [1-24]. The results that are being reported are primarily concerned with the reactions of organic model compounds thought to contain functional groups representative of hazardous materials, and/or coal structures. Because of the difficulty of removing heterocyclic nitrogen, our previous experiments were initiated by extensively examining the reactivities of quinoline and isoquinoline, as well as brief examinations of the reactivities of other compounds [1]. The selection of water as the fluid was based on its physical and chemical properties [25]. Zinc chloride was chosen as a catalyst in the previous studies because of its reported catalytic activity for hydrocracking aromatic structures [26]. The current study examines the reactions of SW with 1-chloro-3-phenylpropane (CPP), 2-chlorotoluene (CT), and 4-chlorophenol (4CP). A problem that we observed in our results with SW - chlorocarbon reactions which had not been adequately addressed in previous studies [11,13] was the fate of HCl assumed to be formed. In our studies HCl was not found but significant amounts of soluble metal salts were observed. This led to the conclusions that significant corrosion of the reactor walls takes place which may also occur in the entrance lines of flow systems if reaction is initiated there, and the chemistry of the chloride - SW reaction may be affected by this wall reaction. These conclusions are consistent with the observations of previous investigators [10,24]. In addition, the HCl formed may erode oxide supported metal catalysts. Thus, experiments were conducted with Vycor ampoule inserts, the results of which are compared to those obtained from the metal reactors.

In addition, a few experiments were conducted to determine the influence of SW on the destruction of benzyl sulfide and thianaphthene.

EXPERIMENTAL

The experiments were carried out in small, cylindrical, Inconel 600, batch reactors, (10.2 cm long x 1.9 cm dia.), which were not equipped for the collection of gaseous products for analysis. The reactor was loaded with about 0.3 to 0.6g of an organic compound. The liquid reactants were introduced using about 0.5 ml. from a 1.0 ml. syringe; however since 4CP is a solid and the necks of the Vycor ampoules were too narrow for efficient solid loading, a solution of 54 wt% in toluene was used. The ampoules were constructed of standard 15mm. Vycor tubing, closed at one end and drawn to a thin capillary at the other for easy sealing once they were loaded. Their internal volumes were about 9ml. which were determined by filling with water and weighing; their external volumes were about 13ml. which were determined by water displacement. After the reactants were introduced the deionized, conductivity water was added for the SW experiments to produce the desired density or pressure at reaction temperature (the 0.255 M NiCl_2 and 0.050M FeCl_2 solutions or CaO were added as needed), then the reactor was bolted closed using a copper gasket as a seal. The reactant concentrations ranged between 1.5 and 7 mole %. For the ampoule experiments the water was added in amounts such that the internal and external densities were equal. The reactor was placed in a fluidized sand bath furnace for the required reaction time, about 5-10 minutes were required for a thermocouple embedded in the flange of the reactor to reach a temperature of 375°C. It was reasonable to assume that for those experiments with inserts the temperature rise of the reaction mixture would be more gradual due to slow heat transfer across the Vycor barrier. However, it was not possible to measure the temperatures of these mixtures. Thus, several insert experiments were run for longer reaction times than those without inserts at the same temperature setting to insure that the observed lower extents of reaction when inserts were used were not due to shorter times at the reaction temperature.

Following the reaction, the vessel was air cooled, opened, the reaction mixture or

ampoule removed, the ampoule broken open when applicable, and the water and organic layers separated. Portions of solvent, methylene chloride, were used to rinse the reactor or ampoule and extract the water layer; however some solids could not be removed from the walls of the ampoules. These portions were combined with the organic layer and additional solvent plus a known amount of an internal standard were added to a fixed volume for quantitative determinations made gas chromatographically using peak area calibrations from known solutions. The GC system consisted of a Varian model 3700 which used a 50cm x 1/8" column packed with 5% OV-101 (liquid methyl silicone) on chromosorb G-HP (100/120) and an HP 3396 A integrator. The peak areas were normalized using a ratio of compound area to area of standard/mole. The product yields and extents of reaction were determined from calibration factors (normalized area/mole compound) obtained from known solutions. Because of the pressure buildup in the ampoules when there was significant reaction some solids and gases were lost when they were opened, liquid losses appeared negligible. The components of these solutions were identified using a Hewlett Packard Model 5890 GC with a 1.2m x 0.2mm x 0.33 μ m capillary column packed with HP-1 (crosslinked methyl silicone gum), and an HP Model 5970 Mass Selective Detector. There were certain limitations on the GC-MS determinations: some products are reported as an isomer of a probable structure as deduced from the molecular weight and MS fragmentation pattern. In addition, many of the higher molecular weight minor products could be measured only with a low degree of precision by GC and calibration factors were estimated.

RESULTS AND DISCUSSION

The volatile product yields are presented as moles formed/mole of reactant consumed. The terms char and tar refer to insoluble solids and non volatile liquids respectively and are reported as mass formed/mass reactant consumed. Many experiments did not produce significant amounts of char or tar.

1-Chloro-3-phenylpropane. CPP was used to represent alkyl chlorides; Table I presents the data for its reactions. The CPP was completely consumed at all conditions and the products and their yields were very similar from the SW reactions in metal and Vycor. However, some small differences were observed, the most significant of which was that the yields of the 118 molecular wt species (isomers of dihydroindene, methylstyrene, etc.) were below detection limits from the reaction in Vycor but were easily measured from the reaction in metal. The odor of HCl was not detected in the evolved gases from any of the SW- chloride experiments without inserts, but was readily noted on breaking open the ampoules. In addition, the water layer color from experiments without inserts indicated significant concentrations of metal ions. The metal ion concentrations in the water layer were determined by Inductively-Coupled Plasma (ICP) analysis, and show an amount about equivalent to the CPP loading. Thus, the reactant, or any HCl formed, reacted with the metal walls to form metal chlorides which dissolved in the water layer on cooling. An ICP analysis of the water layer from a 1-chlorohexane - SW reaction discussed previously, [16], also showed metal ion amounts equivalent to the reactant loading. The addition of CaO did reduce the HCl attack on the metal walls but did not eliminate it. ICP analysis showed only trace amounts of metal ions in the water layers from reactions when chlorine was absent.

2-Chlorotoluene. The most interesting results were obtained with CT. Table II shows that SW had a very significant effect on the rate of consumption of CT, increasing extents of reaction at 450°C from only about 10% up to 80 to 100% at the same reaction times; similar increases were observed at 500°C. Thus, the presence of SW does facilitate the removal of aromatic chlorine at a lower temperature (450°C) where less char and tar are formed and produces good yields of toluene. At 500°C more C-C bond rupture took place increasing char/tar and benzene yields at the expense of toluene. However, the results of the experiments with Vycor inserts show that these increases in extents of reaction in the SW experiments are promoted, both directly and indirectly, by the metal walls, Table III. The extents of reaction with added NiCl₂ and FeCl₂ clearly show that these have a catalytic effect on CT consumption; however, these extents are still less than those obtained directly in the metal reactor, at 450°C and shorter times, indicating that both metal salts and metal walls are catalysts. The 0.255 and 0.050 molar concentrations for the NiCl₂ and FeCl₂ respectively were chosen since they were about the values calculated from the ICP analysis of the water layer from the CPP experiment. This catalytic effect appears to be considerably reduced in the absence of SW, however it is still present in the dry reactor, as indicated by extents of reaction at 500°C without water and at 495°C with SW in Vycor. For example, if first order kinetics are assumed and that the extents of reaction with inserts represent the uncatalyzed reaction, a very rough calculation of the activation energy leads to a predicted value for the uncatalyzed extent of reaction at 500°C and 60 min of about 17%, well below that observed in the dry metal reactor.

4-Chlorophenol. A brief examination of 4 CP indicated a similar behavior to that of CT although somewhat more reactive. Again the catalytic effect of metal walls and/or salts was evident, Table IV. The extents of reaction may have been influenced by toluene used as a solvent to aid in loading the ampoules. However, if it had reacted with radicals formed from 4 CP some bibenzyl should have been formed, but none was observed. The ampoules will be modified in future experiments to allow loading of solid reactants.

Sulfur Compounds. Table V shows benzyl sulfide reacts completely at our mildest conditions with and without SW. However, the SW reaction yielded cleaner products, in the organic layer only hydrocarbon compounds were detected. Since pyrolysis formed significant amounts of thiophenes, yields of which were estimated, the complete removal of sulfur without SW would be much more difficult, as shown by the lack of reactivity of thianaphthene discussed next. The formation of these thiophenes appears to come at the expense of the benzene yield. There were several very minor products that were detected by GC-MS but could not be measured by our GC, as well as small amounts of tar were formed. Finally, there was a strong odor of H_2S from the SW reaction which was absent from the pyrolysis.

Table VI shows that SW may promote the reaction of thianaphthene somewhat and the addition of NH_3 further increases the extents of reaction. However, these reactions were still not very rapid and a more effective catalyst, $ZnCl_2$, was used again producing some improvement. The NH_3 was tried as a catalyst because it was previously found to promote the reaction between SW and benzaldehyde [14]. It should be noted that in some experiments small amounts of styrene and a C_3 benzene were detected, however, no odor of H_2S was evident. From these data it is clear that extreme conditions are needed for heterocyclic sulfur to be removed.

ACKNOWLEDGEMENTS

Supported by, or in-part by, the U.S. Army Research Office.

REFERENCES

1. Houser, T.J.; Tiffany, D.M.; Li, Z.; McCarville, M.E.; Houghton, M.E., *Fuel*, vol. 65, 1986, p 827.
2. Houser, T.J.; Tsao, C.C.; Dyla, J.E.; VanAtten, M.K.; McCarville, M.E., *Fuel*, vol. 68, 1989, p 323.
3. Abraham, M.A.; Klein, M.T., *Ind. Eng. Chem. Prod.-Res. Dev.*, vol. 24, 1985, p 300.
4. Townsend, S.H.; Klein, M.T., *Fuel*, vol. 64, 1985, p 635.
5. Lawson, J.R.; Klein, M.T., *Ind. Eng. Chem. Fund.*, vol. 24, 1985, p 203.
6. Helling, R.K.; Tester, J.W., *J. Energy & Fuels*, vol. 1, 1987, p 417.
7. Helling, R.K.; Tester, J.W., *Environ. Sci. Technol.*, vol. 22, 1988, p 1319.
8. Webley, P.A.; Tester, J.W., *Fundamental Kinetics and Mechanistic Pathways for Oxidation Reactions in Supercritical Water*, SAE Technical Paper Series #881039; 18th Intersociety Conference on Environmental Systems: San Francisco, CA, 1988.
9. Webley, P.A.; Holgate, H.R.; Stevenson, D.M.; Tester, J.W., *Oxidation Kinetics of Model Compounds of Metabolic Waste in Supercritical Water*, SAE Technical Paper Series #901333; 20th Intersociety Conference on Environmental Systems: Williamsburg, VA, 1990.
10. Yang, H.H.; Eckert, C.A., *Ind. Eng. Chem. Res.*, vol. 27, 1988, p 2009.
11. Jin, L.; Shah, Y.T.; Abraham, M.A., *J. Supercritical Fluids*, vol. 3, 1990, p 233.
12. Thornton, T.D.; Savage, P.E., *J. Supercritical Fluids*, vol. 3, 1990, p 240.
13. Lee, D.S.; Gloyna, E.F.; Li, L., *J. Supercritical Fluids*, vol. 3, 1990, p 249.
14. Tsao, C.-C.; Zhou, Y.; Liu, X.; Houser, T.J., *J. Supercritical Fluids*, vol. 5, 1992, p107.
15. Li, Z.; Houser, T.J., *Ind. Eng. Chem. Res.*, vol. 31, 1992, p 2456.
16. Houser, T.J.; Ying, Z.; Tsao, C.-C.; Liu, X.; ACS Symposium Series No. 514, *Supercritical Fluid Engineering Science Fundamentals and Applications*, Eds. E. Kiran and J.F. Brennecke, 1993, pp 327-337.
17. Aki, S.N.V.K.; Abraham, M.A., *J. Supercritical Fluids*, vol. 7, 1994, p 259.
18. Savage, P.E.; Li, R.; Santini Jr., J.T., *J. Supercritical Fluids*, vol. 7, 1994, p 135.
19. Katritzky, A.R.; Barcock, R.A.; Balasubramanian, M.; Greenhill, J.V.; Siskin, M.; Olmstead, W.N., *J. Energy & Fuels*, vol. 8, 1994, p 487.
20. Katritzky, A.R.; Barcock, R.A.; Balasubramanian, M.; Greenhill, J.V.; Siskin, M.; Olmstead, W.N., *J. Energy & Fuels*, vol. 8, 1994, p 498.
21. Katritzky, A.R.; Shipkova, P.A.; Allin, S.M.; Barcock, R.A., *J. Energy & Fuels*, vol. 9, 1995, p 580.
22. Katritzky, A.R.; Barcock, R.A.; Siskin, M.; Olmstead, W.N., *J. Energy & Fuels*, vol. 8, 1994, p 990.

23. Li, R.; Savage, P.E.; Szmukler, D., *AIChE J.*, vol. 39, 1993, p 178.
24. Marrone, P.A.; Lachance, R.P.; DiNaro, J.L.; Phenix, B.D.; Meyer, J.C.; Tester, J.W.; Peters, W.A.; Swallow, K.C., *ACS Symposium Series No. 608, Innovations in Supercritical Fluids: Science and Technology*, Eds. K.W. Hutchenson and N.R. Foster, 1995, pp 197-216.
25. Frank, E.U., *Endeavor*, vol.27, 1968, p 55.
26. Salim, S.S.; Bell, A.T., *Fuel*, vol. 63, 1984, p 469.

Table I: 1-Chloro-3-phenylpropane Pyrolysis and SW Reaction Data at 400 °C *

Vycor Insert	No	Yes	Yes	Yes
Time (min)	60	60	120	50
Water Pressure (bar)	270	270	270	270
CaO added (g)	0	0	0	0
Volatile Product Yields (mols/mol reactant-all 100% consumed)				
Benzene	<0.01	0.026	0.017	0.021
Toluene	<0.01	0.014	0.021	<0.01
Ethyl Benzene	0.010	<0.01	<0.01	<0.01
Ethyl Toluene	0.036	0.06	0.06	0.06
Propyl Benzene	0.28	0.17	0.18	0.17
C ₉ H ₁₀ ^b	0.05	-	-	-
M.W. 196-236 ^c	0.13	0.11	0.04	0.03
Tar (g/g reacted)	0.23	0.33	0.29	0.22

^a Dashes indicate these products were not detected.

^b Estimated yield. Several isomers of 118 M.W. were present, they could be cyclopropyl benzene, dihydroindene, methyl styrene and propenyl benzene.

^c Estimated yields. These are principally isomers of diphenyl cyclohexane, with very small amounts of several compounds with molecular weights between diphenyl propane (196) and diphenyl cyclohexane (236).

Table II: 2-Chlorotoluene Pyrolysis and SW Reaction Data, without Vycor Inserts.

Temperature (°C)	400	400	450	450	450	450	500	500	500	500
Time (min)	60	60	30	60	30	60	30	60	30	60
Water Pres. (bar)	0	270	0	0	364	364	0	0	454	454
% Reaction	0	0	11	10	82	99	36	87	100	100
Volatile Product Yields (mols/mol reacted) ^a										
Benzene	-	-	0	<.01	<.01	<.01	0.02	0.04	0.18	0.15
Toluene	-	-	0.29	0.45	0.67	0.68	0.41	0.46	0.27	0.43
Char/Tar Yields (g/g reacted)	-	-	0.08	0.11	0.11	0.12	0.37	0.29	0.34	0.32

^a Very small amounts of phenol, cresol and an isomer of C₁₄H₁₃Cl were detected in some experiments.

Table IV: 4 -Chlorophenol - SW Reaction at 450 °C and 310 bar Water Pressure

Vycor Insert	No	Yes	Yes
Time (min)	60	75	120
% Reaction	100	30	41
Detectable Products			
Phenol (mol/mol reacted)	0.65	0.15	0.31
Tar (grams/gram reacted)	-	-	0.15

Table III: 2-Chlorotoluene - SW Reaction Data with Vycor Inserts

Temperature (°C)	425	450	450	495	450	450	450
Time (min)	60	120	365	260	95	95	155
Water Pressure: (bar)	280	320	320	280	320	320	320
% Reaction	0	0	8	46	54	28	83
Catalyst ^a	0	0	0	0	NiCl ₂	FeCl ₂	NiCl ₂
<i>Volatile Product Yields (mols/mol reacted)</i>							
Benzene	-	-	-	0.014	0.015	0.032	0.030
Toluene	-	-	-	0.049	0.45	0.35	0.47
C ₁₄ H ₁₃ Cl ^b	-	-	-	0.07	0.04	-	-
Tar ^c (g/g reacted)	-	-	-	0.14	0.27	-	0.19

^a The concentrations of NiCl₂ and FeCl₂ were 0.255 and 0.050 molar respectively.

^b Estimated yields; this product appears to be 2-Chlorodiphenyl methane.

^c Chars could not be removed quantitatively from inserts, thus were not measurable.

Table V: Benzyl Sulfide Pyrolysis and SW Reactions

Temperature (°C)	400	400	400	450
Time (min)	30	30	30	60
Water Pressure (bar)	0	260	260	340
<i>Volatile Product Yields (mols/mol reactant - all 100% reacted)</i>				
Benzene	0.011	0.359	0.413	0.408
Toluene	0.816	0.849	0.811	0.832
C ₁₃ H ₁₂ Isomer	-	0.011	-	0.006
C ₁₄ H ₁₄ Isomer	-	-	-	0.011
Bibenzyl	0.154	0.031	0.041	0.052
Stilbene	0.033	0.063	0.099	0.023
Phenyl Benzothiophene	0.055	-	-	-
Tetraphenyl Thiophene	0.125	-	-	-

Table VI: Thianaphthene Pyrolysis and SW Reaction Data

Temperature (°C)	450	450	475	475	475	505	500	500	500
Time (min)	120	300	300	300	300	300	360	300	360
% Reaction	1	44	28	51	62	17	39	45	55
H ₂ O Pres. (bar)	370	283	365	365	269	0	335	335	335
NH ₃ added	0	0	2M	6M	0	0	0	6M	6M
ZnCl ₂ (g)	0	0.677	0	0	0.513	0	0	0	0
<i>Volatile Product Yields (mols/mol reacted)</i>									
Benzene	-	0.06	0.08	0.05	0.05	0.08	0.09	0.05	0.05
Toluene	-	0.18	0.20	0.21	0.12	0.02	0.20	0.19	0.22
Ethyl Benzene	-	0.18	0.19	0.38	0.23	<.01	0.09	0.20	0.26
C ₆ H ₄ C ₂ HSCH ₃	-	0.03	-	-	0.01	0.03	0.02	0	0.01
C ₆ H ₄ C ₂ H ₄ S	-	0.05	-	-	0.03	-	-	-	-

CO-PROCESSING OF COAL AND RESID UNDER DELAYED COKING CONDITIONS

Shona C. Martin, Jasna Tomić and Harold H. Schobert

Fuel Science Program, Department of Materials Science and Engineering
The Pennsylvania State University, University Park, PA 16802 USA

Keywords: Coal/resid co-coking, retrogressive reactions, coal characteristics

Introduction

Delayed coking is a universal conversion process which utilizes long reaction times to produce gases, distillates and coke from relatively low value feedstocks such as vacuum resid [1,2]. It does not suffer from many of the inherent disadvantages associated with direct liquefaction, i.e. high pressure operation in hydrogen atmospheres, and hence is an attractive alternative to conventional coprocessing methods. In practice [1-3], the feed is rapidly heated to ca 500 °C in the coke drum. The vapor products (gases, naphtha and gas oil) are stripped off and sent to a fractionator tower whilst the coke remains in the drum, reacting to produce a high quality coke. The distillates can be subsequently catalytically upgraded to produce synthetic fuels. One further advantage is that the associated condensation reactions produce a highly aromatic coke enriched in S, N and metals relative to the feed. Typical product distributions from industrial coking operations are: 10-15% gas; 50-60% liquids; 30-35% coke [1-3].

Optimum coal/resid coprocessing conditions are governed by many factors including feed characteristics and reaction conditions [4-6]. Wallace and co-workers reported an improved interaction between coal and petroleum residua with resid Car values >40% [7]. Curtis and Hwang observed a decreased oil yield and increased asphaltene, preasphaltene and residue concentrations commensurate with addition of 30 wt% coal to residuum [8].

The work presented here represents a continuation of previous studies, primarily concerned with evaluation of retrogressive studies during coal/oil coprocessing [9,10]. Rather than focussing on the relative yields of soluble and insoluble product, this present work will incorporate qualitative analysis of the liquid products.

Experimental

Samples Three petroleum vacuum residua were used in the duration of this work. Elemental and NMR analyses are presented in Table 1. The residua were used as received. Six coal samples were utilized in this study from the Penn State Coal Sample Bank and Data Base. Analyses of the relevant samples are summarized in Table 2. Samples were ground to -60 mesh and dried under vacuum at 110 °C for 2 hours prior to use.

Coprocessing The reactions were carried out in vertical 25 ml microautoclave reactors with ca 8g feed (resid:coal ratio of 2:1 w/w) at 450 °C for 60 and 120 min. Tests were conducted under 3.5 MPa and atmospheric N₂ environments, respectively. The gaseous products vented and the liquid and solid products recovered and separated by sequential Soxhlet extraction into *n*-hexane solubles (oils), toluene solubles (asphaltenes) and THF solubles (preasphaltenes). The THF-insoluble residue was washed with acetone followed by *n*-pentane to remove any residual THF.

All recovered products were finally dried under vacuum at 110 °C for ca 10 hours. The conversion of coal into soluble products and gases was calculated on the basis of recovered THF-insoluble residue and reported on a dry, ash free (daf) basis. The concentration and composition of the liquid component was determined by GC/GC-MS to evaluate the contribution of the coal and resid to the overall reaction mechanism.

GC/GC-MS *n*-Hexane soluble products were analyzed by GC and GC-MS using a Hewlett Packard 5890 II GC coupled with an HP 5971 A mass spectrometer operating at electron impact mode (EI, 70 eV). The column was a DB-17 column; 30m x 0.25mm, coated with 50% phenyl 50% methylpolysiloxane with a film thickness of 0.25µm. A temperature program of 40 to 280 °C at heating rate of 4 °C/min and a final holding time of 15 min were used.

Results and Discussion

Figures 1 and 2 summarize the reaction conversions for the experiments conducted at 60 and 120 min, respectively, comparing the amount of THF-insolubles from coprocessing resid independently and in the presence of coal. Although the two sets of data were compiled under slightly different reaction conditions, they serve to illustrate that concentrations of THF-insoluble material are comparable for the two sets of feed.

At 450 °C, coking the coals and resid together for 60 min under 3.5 MPa N₂ was found to produce more solids than the sum expected from the independent reactions. Obviously, coal retrogressive reactions dominate at this higher temperature. However, it may also be that these resids coke more readily in the presence of coal, as suggested by the lower THFI concentrations from similar reactions with a more aromatic resid [10].

There are many possible reaction mechanisms in coprocessing, as each of the feedstocks can lead to a variety of products. Therefore, it must be stressed that the separation of coprocessing products into insoluble and soluble material does not discriminate between the amount of insoluble matter originating from the independent reactions of the coal or residuum or, indeed, any resultant interactions. The overall negative conversions measured at 450 °C (Table 3) may be a result of the coking reactions of each feedstock independently or the product of interactions between the two components.

From Table 3, it can be seen that the presence of coal in the coking medium presents no significant deterioration in product distribution, with the bituminous coals displaying similar conversion data, especially asphaltene and preasphaltene concentrations. However, as anticipated there appears to be a rank effect on the enhancement of coke formation. This is in agreement with the preliminary results presented here. An important criterion in behavior in coprocessing systems is that the interactions leading to retrogressive reactions are influenced by the thermoplastic properties of the feedstock. Indeed, retrogressive reactions only arise when both the coal and the residuum are undergoing active thermal decomposition. The bituminous coal were therefore chosen, in part, due to their fluidity profiles. The existence of a fluid-like state enhances mixing with the resid and enables hydrogen transfer reactions. This is illustrated by the improved liquid product distribution in reactions of Pittsburgh #8, Upper Banner and Illinois #6 with VR1; all have maximum fluidity in the temperature range of 410-447 °C. Conversely, Wyodak coal, a low-rank subbituminous sample, demonstrates no plastic behavior, as reflected by the smaller THF-insoluble residue concentration; subbituminous coals offer restricted mobility and contact in comparison to their higher rank counterparts, resulting in limited surface interactions with the residuum components.

As cited earlier, product quality is a factor in determining the "success" of any experiment. Preliminary analysis of the n-hexane soluble fraction (oils) has shown significant differences in composition between samples from the latter reactions. A selected chromatogram is shown in Figure 3. VR1 oils are characterized by mainly small chain paraffins and 1-2 ring hydroaromatic structures. However, upon reaction in the presence of coal (irrespective of rank) heavier hydroaromatics were identified; in each case, selected 4 ring structures such as benzo(a)pyrene were observed.

Conclusions

Microautoclave reactions conducted with a range of coals and commercial residua demonstrated that at 450 °C and reaction times of 60 and 120 min, vacuum residua coke more readily in the presence of coals. Continued characterization of both the soluble and insoluble products by standard analyses such as HPLC, NMR, FTIR, optical microscopy, will determine the contribution of the coal and resid to the overall reaction mechanism. Finally, the solvating capacity of petroleum feedstocks has been reported to be enhanced by addition of an aromatic species, such as anthracene oil [11]. Further work will therefore include reactions with ternary systems, e.g. addition of decant oil to resid/coal mixtures.

References

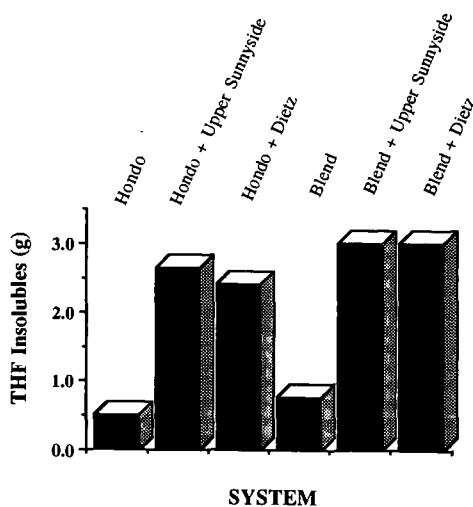
1. Speight, J.G. 'The Chemistry and Technology of Petroleum: Second Edition', Marcel Dekker, Inc. New York 1991
2. Gray, M.R. 'Upgrading of Petroleum residues and Heavy Oils' Marcel Dekker, Inc. New York (1994)
3. Rodriguez, J., Tierney, J.W., Wender, I. Fuel **73**, 1863 (1994)
4. Fouda, S.A., Kelly, J.F., Rahimi, P.M. Energy and Fuels **3**, 154 (1989)
5. Ceylan, K., Stock, L.M. Energy and Fuels **5**, 482 (1991)
6. Moschopedis, S.E., Hawkins, R.W., Speight, J.G. Fuel Proc. Tech. **30**, 205 (1982)
7. Wallace, S., Bartle, K.D., Burke, M.P., Egia, B., Lu, S., Taylor, N., Flynn, T., Kemp, W., Steedman, W. Fuel **68**, 961 (1989)
8. Curtis, C.W., Hwang, J. Fuel Proc. Tech. **32**, 47 (1992)
9. Tomic, J. PhD Thesis Dissertation, The Pennsylvania State University, 1993
10. Tomic, J., Schobert, H.H. Energy and Fuels 1997, in press
11. Rincorn, J.M., Ramirez, J., Cruz, S. Fuel **69**, 1052 (1990)

Table 1. Properties of Petroleum Residua.

Resid	Hydrogen Distribution				Elemental Composition (%w/w)				
	Har	H α	H β	H γ	C	H	N	S	H/C
VR1	6.44	12.58	62.88	18.11	85.9	10.82	0.43	1.53	1.51
Hondo	10.7	7.9	52.7	26.5	79.1	10.50	0.80	5.45	1.58
Blend	10.5	12.7	60.7	16.2	84.8	9.9	0.61	4.74	1.39

Table 2. Analysis of Project Coals.

		Coal					
		Upper Sunnyside	Dietz	Pittsburgh #8	Upper Banner	Illinois #6	Wyodak
	Rank	hvAb	subB	hvAb	hvAb	hvCb	subC
Proximate Analysis (wt%, as received)	Moisture	3.38	23.66	2.40	2.44	13.20	28.42
	Ash	7.54	5.35	10.0	6.2	11.62	9.90
	Volatile Matter	n/a	n/a	35.16	33.46	35.44	32.38
	Fixed Carbon	n/a	n/a	52.44	57.89	39.74	29.30
Ultimate Analysis (wt%, daf)	C	82.0	76.0	83.3	86.6	76.3	74.4
	H	5.8	5.2	5.7	5.5	5.3	5.2
	N	1.8	0.9	1.4	1.6	1.3	1.0
	S	0.8	0.5	1.3	0.6	6.4	0.9
	O	9.7	17.3	8.4	5.7	10.7	18.5

Figure 1. Comparison of THF-insoluble residue concentration from reaction conducted at 450 °C, under 3.5 Mpa N₂, 60 min.

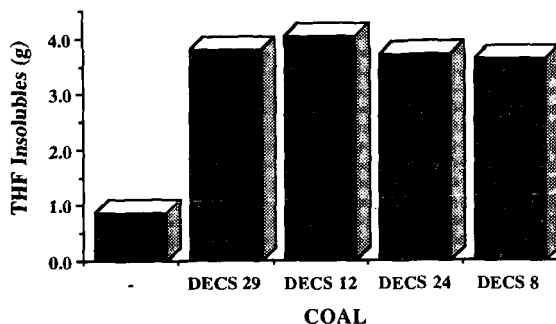


Figure 2. Comparison of THF-insoluble residue concentration from reaction conducted at 450 °C, under atmospheric N₂ environment, 120 min.

Table 3. Results of Simulated Delayed Coking of Vacuum Resid and Selected Coals at 450 °C for 2 hours, under atmospheric N₂.

Feed		Conversion (wt%, daf)	Liquid Product Distribution (wt%, daf)		
Resid	Coal		Oils	Asph	Preasph
VR1	-	80.6	4.8	2.1	0.7
VR1	Upper Banner	-37.5	10.4	5.4	2.9
VR1	Pittsburgh #8	-39.0	6.6	5.3	2.8
VR1	Illinois #6	-36.6	11.6	4.9	2.5
VR1	Wyodak	-27.4	8.0	7.2	2.8

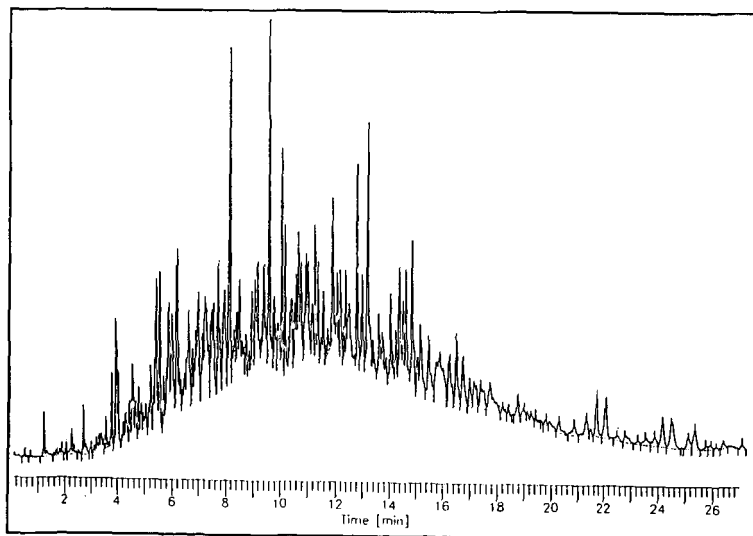


Figure 3. Chromatogram of n-Hexane Solubles from Co-coking Upper Banner with VR1, 120 min, atmospheric N₂ environment.

KINETICS OF HYDROPROCESSING OF COAL-DERIVED VACUUM RESIDS

Shaojie Wang, He Huang, Keyu Wang, M.T. Klein and W.H. Calkins*
Department of Chemical Engineering
University of Delaware
Newark, DE 19716

Key words: coal-derived resid, hydroprocessing, kinetics

Introduction

The direct liquefaction of coal produces a substantial amount of high boiling, non-distillable residuum, whose amount depends upon a number of factors such as the coal type, the hydrogen donor strength of the solvent, activity of the catalyst, and the conditions under which the direct liquefaction was run. Because of its high boiling point and potential thermal instability, this material is not suitable for processing in a conventional petroleum refinery. In a commercial liquefaction process as visualized today, therefore, this material would be recycled to the process to recover its energy value and to provide some of the solvent needed for the coal liquefaction process itself. Furthermore, this recycle oil has been shown to have a beneficial effect (i.e. increased oil yield) in the liquefaction process (1,2). Thus, it became important to determine the rates of conversion of these residual materials to products boiling in the fuel range (e.g. $< 850^{\circ}\text{F}$) and to know whether these high boilers will build up or be rapidly broken down in the recycling process. It was to follow the rates of resid breakdown (resid reactivity) under conditions approximating the conditions in the liquefaction process that this program was undertaken. Knowing the rates of resid condensation as well as breakdown are also important as retrograde processes reduce product yields and foul catalysts and equipment. This required the use of a reactor system capable of measuring hydroprocessing rates at very short contact times and the development of analytical methods for measuring the conversion and boiling ranges of the products. Resid conversion rates (both condensation and breakdown) would be correlated with composition data obtained by other analytical methods (e.g. TGA, NMR, elemental analysis etc.)

Experimental Section

Apparatus. The design and operation of the Short Contact Time Batch Reactor (SCTBR) system have been described in detail elsewhere (3). In operation, both the empty 30 cm³ reactor and the preheater and precoolers are immersed in a fluidized sand bath and brought up to reaction temperature. High pressure hydrogen gas provided the driving force to deliver the reaction mixture of solvent, coal and catalyst from a blow case into the reactor at reaction temperature in of the order of 0.3 seconds, eliminating the heat up limitations in kinetic measurements. Discharging and quenching of the reaction mixture was carried out in the similar time frame. Hydrogen bubbled through the reactor from the bottom provided the necessary agitation. Temperature control was within $\pm 2^{\circ}\text{C}$. Reaction times as short as 5 seconds could be measured with considerable precision.

Materials Studied. Thirteen resid samples (boiling above 850°F) from coal liquefaction runs made at the Wilsonville pilot plant and two resid samples from Hydrocarbon Research Institute bench scale unit were prepared and supplied by CONSOL Inc. The feed coals for the resids produced at the Wilsonville pilot plant were Wyodak-Anderson, Illinois #6 and Pittsburgh coals. Selected properties, such as elemental analysis and the ¹³C NMR patterns obtained by CONSOL Inc., of each resid are shown in Table 1.

Resid Conversion Reactions. All reactions were run as mixtures of tetralin T (the donor solvent) and resid R over a range of T/R ratios, temperatures and catalyst. For each reactor run, 5 - 10 grams of resid were used together with added tetralin to make up the desired T/R ratio. Holdup of material prevented complete recovery of the reaction products. Recoveries varied from 75 to 85 wt%, depending upon the T/R ratio used. The determination of conversion and subsequent analytical results were therefore based on representative aliquots. Molybdenum naphthenate was used as the catalyst and was sulfided *in-situ* using methyldisulfide.

Reaction Product Workup Procedure. The reaction products were worked up by separating the solids from the liquids by filtration (Figure 1). The solid filter cake was washed with methylene chloride which went into the filtrate with the product liquids. The filtrate was then distilled at low temperatures (45°C) to remove the methylene chloride. The resulting solid cake and the filtrate were analyzed separately.

Analytical Methods - Conversion. The conversion to liquid was determined using thermogravimetric analysis (TGA) on the solid cake by an ash balance calculation.

The tetralin content of the methylene chloride-free filtrate was determined by gas chromatography using an added 1-methylnaphthalene internal standard.

To determine the amount of liquid product boiling above and below 850°F (454°C), a

boiling range method, SimDis TG, was developed based on TGA (4).

The conversion of resid to the material boiling below 850 °F was estimated by Equation 1:

$$\text{Conversion} (< 850^\circ\text{F}) = \text{TSF} \times \left(1 - \frac{850^\circ\text{F}^*}{\text{RSF}}\right) \quad (1)$$

where TSF is the Tetralin Soluble Fraction of the resid (daf basis) determined by ash content in the solid resid after resid hydroprocessing; RSF is the Resid Soluble Fraction in tetralin and 850 °F* is the fraction boiling above 850 °F.

Analytical Methods - Resid Characterization. The resids studied were characterized by thermogravimetric analysis at 10°C/min in nitrogen from room temperature to 600 °C. This was followed by combustion of the remaining organic material at 100 °C/min to 850 °C in air. The derivative DTG curves, Volatile Matter (VM), Fixed Carbon (FC), and ash were determined. These TGA parameters as well as the peak temperatures and peak heights from the DTG curves are also included in Table 1.

Results and Discussion

As discussed in a previous section of this paper, conversion has been determined in part by an ash balance. Efforts to carry out hydroprocessing of resids using the Ni/Mo on alumina catalyst used in Wilsonville, however, resulted in unreliable conversions data because of the large amount of ash in the catalyst. In addition, it was found that the supported catalyst changed as the hydroprocessing progressed, making the calculations of conversion unreliable. Sulfided molybdenum catalyst, on the other hand, contributed little ash (which can be corrected for) to the system and gave very reproducible results. Preliminary experiments using a range of sulfided molybdenum naphthenate catalyst concentrations from 0.9 wt% to 5.0 wt% showed that 0.9 wt% catalyst resulted in only a barely detectable increase in conversion over uncatalyzed runs. However, 3 to 5 wt% (based on the resid) gave significant conversion to lower boiling products.

After considerable experimentation to determine appropriate reaction conditions, all 15 resids were hydroprocessed for 30 minutes at 420°C in 3 to 1 tetralin to resid weight ratio and 1500 psig hydrogen with and without sulfided molybdenum naphthenate catalyst (as 3 wt% molybdenum based on the resid charged). Each resid was also run at ambient temperature for comparative purposes.

Tables 2 and 3 show the conversions to material boiling below 850°F for the thermal and catalyzed hydroprocessed resids, respectively. It is to be noted that significant conversion to lower boiling material occurs even in the absence of catalyst. However, in the presence of the molybdenum catalyst, conversion to the lower boiling material was at least doubled. To attain as much as 30 to 40% conversion requires a significant amount of catalyst.

As Tables 2 and 3 show, there is considerable variation among the resids in terms of their reactivity and convertability to lower boiling products. Plots of the thermal and catalyzed conversions of the resids vs the feed coal types are shown in Figure 2. In the thermal hydroprocessing, there appears to be a correlation with the coal type used in the liquefaction, i.e., the lower rank coal produced resid which gave higher conversion on hydroprocessing in the absence of catalyst. On the other hand, if a catalyst is used, the resids from the three coals studied showed little or no difference in conversion under the conditions used. It will be noted in Figure 3 and Tables 1, 2 and 3 that those resids having high DTG peaks and high aromatic carbon content (by ¹³C NMR) generally show low conversions under the thermal hydroprocessing conditions while lower aromatic carbon containing resids show higher conversions in thermal hydroprocessing. Use of a strong catalyst apparently compensates in part for the high aromaticity.

SimDis TGA on the solid filter cake showed that, whereas there is considerable solubility of the resid in tetralin, up to 80 wt%, the solids themselves are not degraded to lower boiling material. Therefore, the resid must be solubilized in the recycle solvent for the resid breakdown to occur.

Summary and Conclusions

With the appropriate catalyst and conditions approximating coal liquefaction, high boiling coal-derived resids do break down to lower boiling products as they are recycled to the coal liquefaction process.

Coal-derived resids vary widely in their reactivity toward breakdown to lower boiling products under both thermal and catalytic conditions.

High catalyst activity appears to be necessary to convert these refractory materials to lower boiling materials.

Solubilization of the resid in the processing solvent is necessary for the molecular breakdown.

Acknowledgements

The support of various portions of this work by the Department of Energy and CONSOL Inc. under subcontract DE-AC22-94PC93054 is acknowledged. The guidance and assistance of Drs F.P. Burke, R.A. Winschel and S.D. Brandes in providing samples, analytical data and other assistance were also major factors in the progress of this project.

References

1. Whitehurst, D.D.; Mitchell, T.O.; Farcasiu, M. *Coal Liquefaction the Chemistry and Technology of Thermal Processes* Academic Press: New York, 1980.
2. Grint, A.; Jackson, W.R.; Larkins, F.P.; Louey, M.B.; Marshall, M.; Trehalla, M.J.; Watkins, I.D. *Fuel* 1994, 73, 381.
3. Huang, H.; Calkins, W.H.; and Klein, M.T. *Energy & Fuels* 1994, 8, 1304.
4. Huang, H.; Wang, K.; Wang, S.; Klein, M.T.; and Calkins, W.H. *ACS Fuel Chem. Div. Prep.* 40, (3) 485, 1995.

Table 1 Selected properties of the resids

Resid	Feed Coal	Number	Stream*	f _a	VM wt %	FC wt %	Ash wt %	T _{peak} C	Peak Height wt%/min (daf)
Resid L	Wyodak-Anderson Black Thunder	4	V 1067	34.0	51.3	48.7	19.1	470.7	4.59
Resid K		5	R 1235	24.6	53.6	46.4	17.2	464.8	4.60
Resid H		6	V 131B	33.3	57.1	42.9	15.2	475.3	4.67
Resid F		10	V 1067	24.3	55.2	44.8	17.5	461.5	4.36
Resid E		11	R 1235	26.0	53.4	46.6	15.6	454.4	4.24
Resid G	Illinois No. 6	12	V 131B	25.9	55.7	44.3	15.9	462.2	5.02
Resid I		7	V 1067	30.4	61.5	38.5	15.9	480.1	6.44
Resid M		8	R 1235	29.4	59.7	40.3	13.7	481.8	6.16
Resid D		9	V 131B	29.2	70.9	29.1	9.9	490.5	6.83
Resid J		1	V 1067	31.6	57.6	42.4	10.2	490.1	7.20
Resid B	Pittsburgh Ireland	2	R 1235	33.3	61.1	38.9	8.7	493.6	7.43
Resid C		3	V 131B	31.5	61.0	39.0	8.5	490.2	6.23
Resid A				38.9	51.8	48.2	17.0	472.1	4.75
Resid N				20.6			0.4		
Resid O				18.8			4.1		

*

V 1067 = interstage stream

R 1235 = 2nd stage product stream

V 131B = recycle stream

Table 2 Conversion of thermal hydroprocessing of resid

Sample	Resid Name	Solid Residue		Liquid Residue			Conversion to 850 F+	Conversion to 850 F-
		Ash	Ash	TSF	Tetralin	SRF		
Resid A	W258V-131B	17.0	50.1	79.7	88.2	11.8	9.6	15.0
Resid B	W259R-1235	8.7	33.5	81.0	88.0	12.0	9.6	15.9
Resid C	W259V-131B	8.5	35.0	82.7	86.2	13.8	10.8	17.7
Resid D	W261V-131B	9.9	45.8	87.1	87.9	12.1	9.7	17.1
Resid E	W262R-1235	15.6	43.5	76.0	88.4	11.6	8.6	19.6
Resid F	W262V-1067	17.5	47.8	76.9	87.4	12.6	9.7	17.7
Resid G	W262V-131B	15.9	46.5	78.3	88.7	11.3	8.7	18.2
Resid H	W260V-131B	15.2	46.6	79.5	87.7	12.3	9.0	21.3
Resid I	W261V-1067	15.9	50.8	81.8	88.9	11.1	8.5	19.4
Resid J	W259V-1067	10.2	38.7	82.0	86.4	13.6	11.5	12.9
Resid K	W260R-1235	17.2	49.0	78.4	86.9	13.1	9.8	19.7
Resid L	W260V-1067	19.1	51.3	77.6	89.2	10.8	8.3	17.8
Resid M	W261R-1235	13.7	45.6	81.1	90.1	9.9	7.9	16.0
Resid N	HTI POC-01, O-43	0.4	33.0	99.2	80.6	19.4	14.1	27.0
Resid O	HTI POC-02, O-43	4.1	38.0	93.1	70.6	29.4	22.4	22.1
Thermal: 420 C; 30 min; 1500 psig H ₂								
Catalytic: 420 C; 30 min; 1500 psig H ₂ ; 3 wt% Mo								
Control: 25 C; 10 min; 1500 psig H ₂								
TSF: Tetralin Soluble Fraction of resid, wt% (daf basis)								
RSF: Resid Soluble Fraction in tetralin, wt%								
850 F+: fraction of boiling above 850 F								

Table 3 Conversion of catalytic hydroprocessing of resid

Sample	Resid		Solid Residue			Liquid Residue		Conversion
	Name	Ash	Ash	SF	Tetralin	SR in Tetralin	850 F+	
Resid A	W258V-131B	17.0	51.5	80.7	82.5	17.5	9.9	35.0
Resid B	W259R-1235	8.7	40.0	85.6	79.8	20.2	11.2	38.1
Resid C	W259V-131B	8.5	41.4	86.8	81.4	18.6	11.5	33.1
Resid D	W261V-131B	9.9	54.9	91.0	77.9	22.1	14.1	32.9
Resid E	W262R-1235	15.6	44.2	76.6	80.6	19.4	11.3	32.1
Resid F	W262V-1067	17.5	49.4	78.3	79.6	20.4	10.7	37.4
Resid G	W262V-131B	15.9	48.3	79.8	79.2	20.8	11.5	35.8
Resid H	W260V-131B	15.2	50.9	82.7	75.6	24.4	11.3	44.6
Resid I	W261V-1067	15.9	56.6	85.5	76.2	23.8	11.9	42.7
Resid J	W259V-1067	10.2	43.8	85.4	76.5	23.5	11.9	42.1
Resid K	W260R-1235	17.2	52.1	80.8	78.1	21.9	12.4	35.2
Resid L	W260V-1067	19.1	53.5	79.5	79.1	20.9	11.7	35.0
Resid M	W261R-1235	13.7	53.7	86.3	80.2	19.8	11.7	35.3
Resid N	HTI POC-01, O-43	0.4	36.4	99.3	67.9	32.1	16.7	47.6
Resid O	HTI POC-02, O-43	4.1	48.3	95.4	70.2	29.8	19.1	34.3
Thermal: 420 C; 30 min; 1500 psig H ₂								
Catalytic: 420 C; 30 min; 1500 psig H ₂ ; 3 wt% Mo								
Control: 25 C; 10 min; 1500 psig H ₂								
TSF: Tetralin Soluble Fraction, wt% (daf basis)								
RSF: Resid Soluble Fraction in tetralin, wt%								
850 F+: fraction of boiling above 850 F								

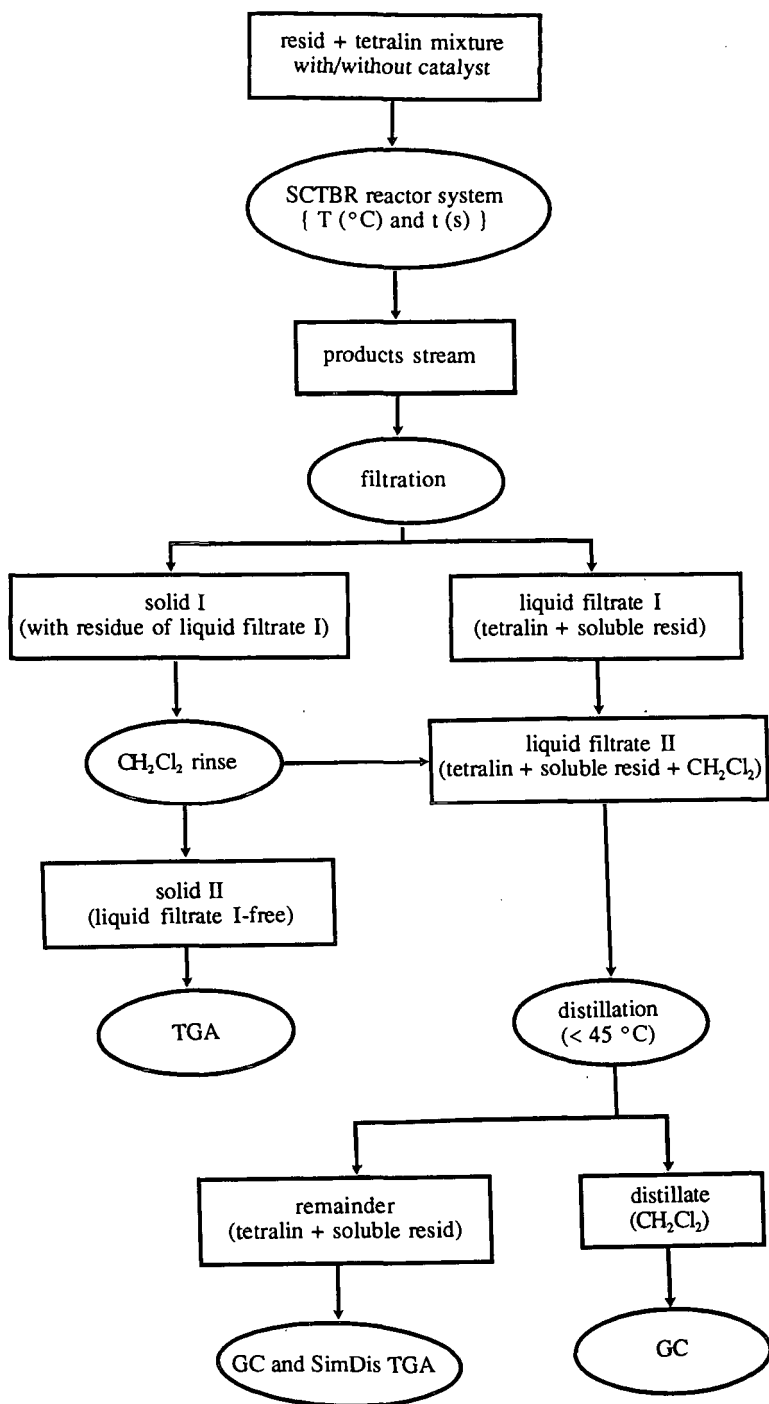


Figure 1 Scheme of the reaction product workup procedure

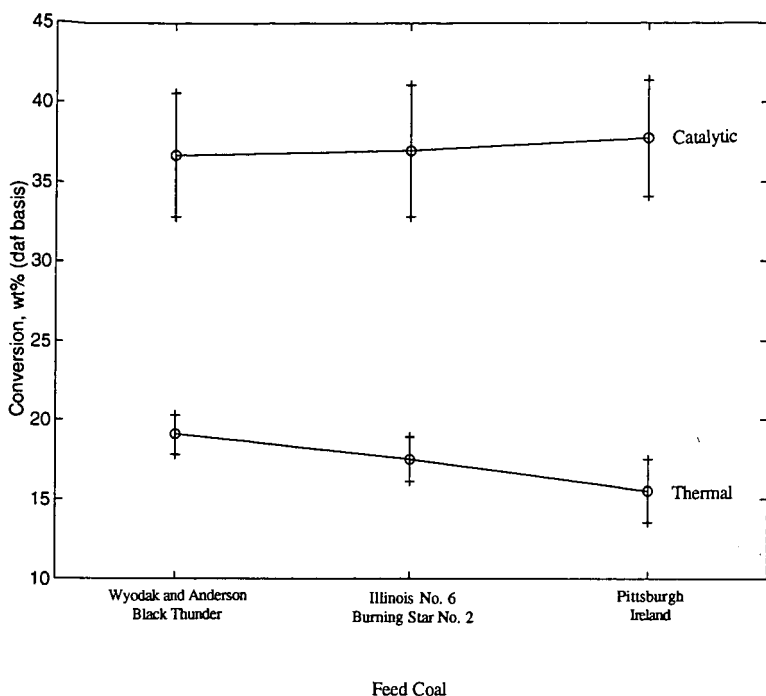


Figure 2 Thermal and catalyzed hydroprocessing conversions of the resid vs feed coal type

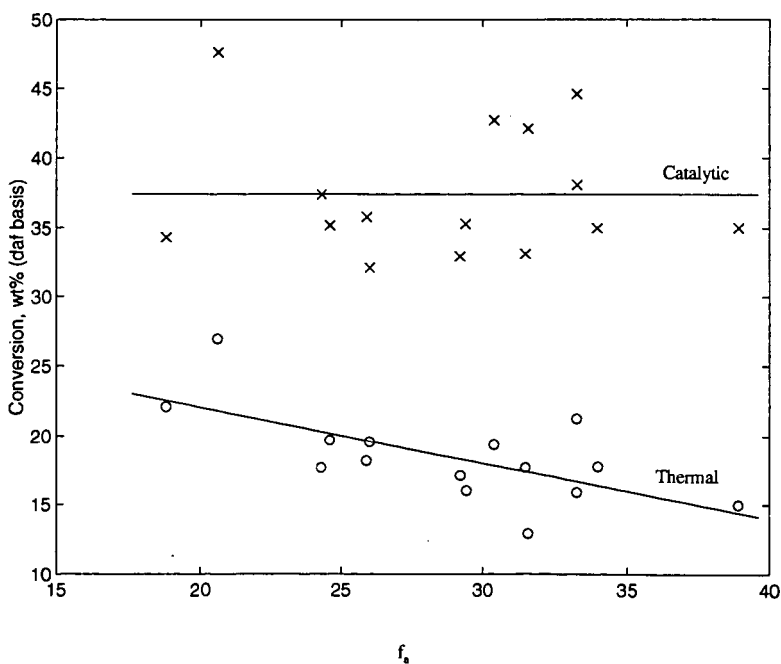


Figure 3 Thermal and catalyzed hydroprocessing conversions vs f_a of the resid

EVALUATION OF Mo CATALYST PRECURSORS FOR HYDROTREATING COAL DERIVED LIQUIDS

Richard K. Anderson, Deana R. Gibb, Geoff M. Kimber and Frank J. Derbyshire
Center for Applied Energy Research, University of Kentucky, 3572 Iron Works Pike
Lexington, KY 40511-8433

Keywords: Coal liquefaction, molybdenum catalyst, activation

INTRODUCTION

Numerous studies have examined the use of dispersed catalysts for promoting the dissolution of coal and upgrading high-boiling and residual liquids.¹ Catalysts have been added in various forms, including oil soluble organometallics and carbonyls,^{2,3,4} with industrial interest for application to a spectrum of residual feedstocks,⁵ and demonstration in coal liquefaction at the pilot plant scale.⁶ Dispersed catalysts offer certain advantages over supported catalysts for hydroprocessing such feedstocks. Because of their large molecular size, many of the feed constituents cannot access the internal pore structure of supported catalysts, and hence upgrading must proceed by an indirect process, probably involving H-transfer via lower molecular weight species. Another major deficiency of supported catalysts is their susceptibility to deactivation by reactions which cause the deposition of carbon and metals.

Dispersed catalysts can overcome the first of these obstacles and may be less susceptible to deactivation. At the same time, there are also difficulties in the utilization of dispersed catalysts. These include: attaining and maintaining adequate dispersion; and converting the precursor to the active phase. Moreover, the effective catalyst metals, such as Mo, are expensive and their application is only economically viable if they can be used at very low concentrations or efficiently recycled. In direct coal liquefaction, the presence of mineral matter and undissolved coal in the products of coal solubilization mean that a solids separation step is necessary and, inevitably, catalyst will be removed with the reject stream. However, in upgrading solids-free coal liquids and petroleum residua, there exists the potential to recycle nearly all of the catalyst with the unconverted residue. Hence, the catalyst inventory in the reactor can be maintained at a high concentration with only a low level of fresh catalyst addition. The success of such a process depends upon the ability to maintain catalyst activity during repeated recycles, and to avoid the substantial generation of solids or refractory liquid products that have to be removed in a drag stream, together with the catalyst.

With this concept in view, we have initiated a study of the effectiveness of dispersed Mo catalysts for hydroprocessing solids-free residual coal liquids that were obtained from the former Wilsonville Advanced Coal Liquefaction Research and Development Facility, while operating with Black Thunder subbituminous coal. In this work, comparisons are made between three different Mo-containing catalysts: a ground commercial NiMo supported catalyst, and two organometallics which, being oil-soluble, are expected to facilitate dispersion in the reactor feed. A series of experiments was made to examine the influence of presulfiding conditions on catalyst activity which was assessed by the extent of resid conversion and hydrogen consumption under a standard set of reaction conditions.

EXPERIMENTAL

Materials- The following reagents were used: high purity tetrahydrofuran (THF), Burdick & Jackson Brand from Baxter S/P; ultra high purity grade H₂ and a 7.93% H₂S/H₂ gas mixture, Air Products and Chemicals, Inc. A deashed resid (DAR) derived from Black Thunder mine coal processed at Wilsonville in Run 258A⁷ was provided by CONSOL, Inc. This material was used as the hydrotreating feedstock. It contained 0.13% ash, and 76% 566°C+ (1050°F+) resid (af). Three hydrotreating catalyst precursors were evaluated: Molyvan L containing 8.1% Mo, RT Vanderbilt Co.; Mo naphthenate containing 6.1% Mo, ICN Biomedicals, Inc.; and AKZO AO-60, an alumina supported Ni/Mo catalyst, Hydrocarbon Technologies, Inc. In-house determinations of the Mo and Ni content of the AO-60 were 11.3 and 2.7 wt% respectively (dried sample), compared to 12.3 and 2.6% reported by the manufacturer. Because of the small quantities of catalyst used, an equal weight of 99% anhydrous hexadecane (Aldrich) was used to dilute the organometallic precursors to improve the precision of addition to the reactor.

Liquefaction Experiments- Catalytic hydrotreating experiments were conducted in microautoclaves; the methods and microautoclaves used have been described in detail elsewhere.⁸ In a typical experiment, 3 grams of DAR and the appropriate amount of catalyst precursor (to give either 1000 ppmw Mo or Mo+Ni, total DAR feed basis) are added to the reactor. The reactor is sealed, purged with hydrogen, pressurized to 10.1 MPa total pressure (2% hydrogen sulfide, balance hydrogen) and leak tested. The reactor is heated by immersing it into a hot, fluidized sandbath. Real-time measurements of both the reaction temperature and pressure are recorded with a computer. For some experiments, a pretreating period was used where the reactor was heated at a lower

temperature before going to the final reaction temperature. At the end of the reaction period, the cooled reactor is vented into a 10-liter gas collection cylinder at atmospheric pressure. The gas mixture is analyzed with a Carle Series AGC 400 Refinery Gas Chromatograph (Application 397-B). Vacuum distillations are performed on the remaining products using a modified ASTM D-1160 procedure to give a cutpoint of 566°C. Material balances are based upon a forced catalyst balance with any loss and error being assigned to the yield of distillate product.

In order to more fully characterize the reaction products, a high-temperature simulated distillation method has been developed. The SIMDIS apparatus (a Hewlett-Packard model 6890 gas chromatograph) and application software were developed by AC Analytical Controls, Inc. The method is designed to analyze hydrocarbons up to a boiling point of 750°C.

To select one of the catalysts for detailed parametric studies, a series of hydrotreating experiments was conducted at 440°C for 60 minutes. Each precursor was evaluated in a single run, in which it was used directly or was presulfided *in situ* at 375°C for 30 minutes. A sample of the AO-60 was also sulfided *ex situ*. The presulfided AO-60, which had been delivered in its oxidic form, was prepared⁸ *ex situ* by grinding the 1/16" extruded pellets, sizing to -100 mesh, air drying, and sulfiding in the microautoclave in the H₂S/H₂ gas mixture at 400°C. The dry, black powder was stored under dry N₂. Analysis of the sulfided material showed 1.9 mol S_{added}/mol Mo, compared with the stoichiometric (including Ni) requirement of 2.3 mol S_{added}/mol Mo. Sulfur addition rates reported in the literature typically range from 1.6 to 2.0 S/Mo, depending on pre- and post-treatment conditions.

From the test results, Molyvan L was selected for further activation studies. A parametric study was conducted in which a mixture of DAR and 1000 ppmw Mo as Molyvan L was presulfided for selected times and temperatures, followed by a hydrotreating reaction. Using 2% H₂S in hydrogen to sulfide the Mo, the influences of time (0, 5 and 30 minutes), temperature (300, 340, 375 and 440°C) and hydrotreat time (30 and 60 minutes) were examined. Estimates were also made of the activity of the dispersed catalyst after reaction, to assess its utility for recycle. Two different approaches were used to simulate recycled catalyst and resid combinations. In the first, an experiment was conducted using the DAR in reactions at 440°C for 60 minutes as the single-pass condition. Molyvan L, sufficient to give 1000 ppmw Mo, was added to only 10% of the DAR, and this mixture was reacted to simulate the first pass at an equivalent Mo concentration of 10,000 ppmw. The gases were collected, the reactor opened and the remaining 90% of the DAR was added and the second pass effected (labeled Method RM1). In a parallel study, the DAR was again reacted with Molyvan L at the 1000 ppmw Mo level in a first pass, only this time feeding 100% of the feedstock. The products were distilled to 566°C, and the residual fraction recovered. Fresh DAR and heavy distillate were then added to restore the reactor feed to 3 g for a second pass with the same 566°C+ composition as in the first pass (Method RM2). Because of losses in recovering the resid, the concentration of Mo in the second pass was 200 ppmw lower than the first pass, but the effect of conversion changes due to this lower concentration is less than can be estimated from the available data.

RESULTS AND DISCUSSION

As shown in Table 1, each of the Mo precursors improved resid conversion over that found (19%) without added catalyst, increasing conversion to 34-38%, either with or without the presulfiding procedure used. The one exception was the *in situ* presulfided AO-60 catalyst, which increased resid conversion to an average of 45%. Both organometallic precursors exhibited reasonably good activity, with resid conversion somewhat less than that found for the presulfided AO-60 catalyst, and with little apparent effect from the presulfiding step.

Based on a comparison of resid conversion and hydrogen consumption data, Molyvan L was selected for the parametric study, to evaluate the benefits of presulfiding in some detail. These results are presented in Figure 1 (30 and 60 minute conversion reactions). At lower presulfiding temperatures, it appears there is little effect of this pretreatment on catalyst activity, and it may even be adverse. The data, therefore, suggest that Molyvan L attains an active form within the first few minutes of the reaction under hydrotreating conditions. This finding is consistent with other research⁹ using a dispersed Mo precursor at short reaction times. Based on these results, it was determined that presulfiding over the times and temperatures tested was not necessary to produce an active catalyst, and this step was omitted in subsequent work.

A plot of reaction time vs log (wt percent resid remaining) for three pairs of duplicate experiments is shown in Figure 2, where it is seen that the early portion of the reaction may be fairly well represented by first order kinetics with respect to the disappearance of resid. The reaction clearly slows in the 60 to 90 min period when presumably only the more refractory resid remains. The progressive reduction in rate is of interest from a presulfiding viewpoint since there is no suggestion that a more active Mo catalyst form was generated, either in combination with carbon, sulfur or other species, as the reaction steadily progressed, but lends further support to the suggestion that the active species was present fairly soon into the experiment.

Table 2 reports the results of the simulated recycle experiments with Molyvan L. Using data

from an earlier experiment with 10,000 ppmw Mo loading to calculate the total resid feed to the second pass, a second pass resid conversion of 33.7% was calculated for Method RM1. This is the same as the single pass resid conversion (33.6%) determined earlier using all fresh feedstock (ie, no recycle). However, lower conversion (24.7% vs 33.7% in RM1) was found in Method RM2, that could have reflected reduced reactivity of the recycled residual fraction, which in this experiment comprises most of the second pass reactor feed and contains the recycled catalyst. Figure 3 is a plot of the total reactor pressure for the two passes of RM2, and their nearly equal pressure histories suggest that the Mo is similarly active in both passes. A pressure profile for the same reaction without added Mo is shown for reference, where the immediate pressure reduction evident in the previous experiment is absent.

To determine the effect of fresh catalyst addition to the recycled catalyst in between the first and second pass (similar to catalyst make-up in an operating plant) 100 ppmw fresh Mo was introduced between the two reaction steps (Method RM2'). This increased the total Mo concentration from 800 to 893 ppmw. Other procedures remained the same as with the previously described experiment. Resid conversion in the second pass for this experiment was almost restored to that obtained in a single pass. Previous work has shown that resid conversion is relatively insensitive to fresh Mo concentrations above about 500 ppmw. Consequently, it may also be supposed that the freshly added catalyst is more active than the recycled Mo. The apparent reduction in recycle activity may be due to the conditions used for catalyst and resid recovery. Thus there appears to be two reasons for the reduced second pass conversion in the RM2 experiment, namely reduced resid reactivity and reduced catalyst activity. Note that for each of the recycle experiments, hydrogen consumption is reduced below that of the single pass experiment, as is hydrocarbon gas make. Relatedly, SEM/EDS studies of the hydrotreating residues at high catalyst loading showed the Mo species were well distributed across the recovered residual fractions.

CONCLUSIONS

Similar hydrotreating activity was found for the two dispersed organometallic catalyst precursors studied, and presulfiding over the times and temperatures tested was not required for high catalytic activity. Simulated recycle experiments have shown that conversion is reduced, the causes of which are attributed to reduced activity of the recycled resid and lower catalytic activity of the recycled Mo. Both of these factors could be affected by the process steps required to recover the catalyst and resid, and are the subject of continuing investigation.

ACKNOWLEDGMENTS

The authors gratefully acknowledge the support of the Department of Energy (no. DE-AC22-95PC95050), funded through a CONSOL, Inc subcontract, and the Commonwealth of Kentucky. We also thank Hydrocarbon Technologies, Inc. for providing the AKZO AO-60; the RT Vanderbilt Co. for supplying a sample of Molyvan L; Dr. Scott Carter of the CAER for his development work with the AC SIMDIS equipment; and Rebecca Cash of the CAER for her work in the laboratory.

REFERENCES

1. Derbyshire, F. J. *Catalysis in Coal Liquefaction*, IEACR/08, IEA Coal Research: London, UK, 1988, 69 pp.
2. Hawk, C. O.; Hiteshue, R. W. "Hydrogenation of Coal in the Batch Autoclave" *Bulletin* 6322 US Department of the Interior, Bureau of Mines: Washington, DC, USA, 1965, 42 pp.
3. Watanabe, Y.; Yamada, O.; Fujita, K.; Takegami, Y.; Suzuki T. *Fuel* 1984, 63, 752-755.
4. Suzuki, T.; Yamada, O.; Then, J. H.; Ando, T.; Watanabe, Y. *Proceedings 1985 International Conference on Coal Science*; Pergamon Press: New York, 1985, pp 205-8.
5. Aldridge, C.L.; Bearden, R.Jr. *Energy Progress* 1981, 1 (no.1-4), 44-48.
6. Southern Electric International, Inc., Technical Progress Report, "Run 262 with Black Thunder Mine Subbituminous Coal" *Document No. DOE/PC/90033-22*, September, 1992.
7. Southern Electric International, Inc., Technical Progress Report for Run 258 with Subbituminous coal, *Document No. DOE/PC/50041-130*, May, 1991, Advanced Coal Liquefaction Research and Development Facility, Wilsonville, AL.
8. CONSOL, Inc, Exploratory Research on Novel Coal Liquefaction Concept, Topical Report, *Document No. DOE/PC 95050-22*, December, 1996.
9. Huang, H.; Wang, K.; Shaojie, W.; Klein, M.T.; and Calkins, W.H. "Kinetics of Coal Liquefaction at Very Short Reaction Times" *Prepr. Pap.- Am. Chem. Soc., Div. Fuel Chem.* 1995, 40(3), pp 550-554.

Table 1. Results of hydrotreating tests of catalyst precursors in deashed resid.									
Catalyst precursor	Feed	none	Molyvan L	Molyvan L	Mo naph-thenate	Mo naph-thenate	AO-60	AO-60	AO-60 sulfided ex situ
Pretreat time @ °C	-	none	30 @ 375	30 @ 375	none	30 @ 375	30 @ 375	30 @ 375	none
Reaction time @ °C	-	60 @ 440	60 @ 440	60 @ 440	60 @ 440	60 @ 440	60 @ 440	60 @ 440	60 @ 440
Ni, ppmw feed	-	-	-	-	-	-	173	171	175
Mo, ppmw feed	-	-	1013	988	997	1010	817	803	825
Products, wt% maf feed									
Hydrocarbon gas, C ₁ -C ₄ +	-	6.2	6.0	6.2	9.4	6.0	9.4	7.2	5.7
CO + CO ₂	-	0.3	0.1	0.4	0.9	0.2	1.1	0.3	0.1
566°C-	24.3	32.3	43.6	45.2	42.2	45.7	41.0	51.0	47.5
566°C+	75.7	61.2	50.3	48.2	47.5	48.1	48.5	41.5	46.7
Total	100	100	100	100	100	100	100	100	100
Resid conversion, wt %	-	19.2	33.6	36.3	37.3	36.5	36.0	45.2	38.4
566°C+	-	19.2	33.6	36.3	37.3	36.5	36.0	45.2	38.4
H ₂ consumed, mg/g maf feed	-	7	22	18	17	16	19	18	16

Note: 10.1 MPa total pressure (cold, 2% H₂S in H₂ mixture) used for all hydrotreating tests.

Table 2. Evaluation of Molyvan L activity in simulated recycle.				
Method	RM1	RM2	RM2'	
Rxn temp., First pass	440	440	440	
Second pass	440	440	440	
Run time, First pass	60	60	60	
Second pass	60	60	60	
Fresh Mo, ppm feed	-	-	-	100
Recycle Mo, ppm feed	1006	800		793
Products, wt% maf feed				
Hydrocarbon gas, C ₁ -C ₆ +	4.4	4.6		5.0
CO + CO ₂	0.1	0.1		0.1
566 °C-	47.0	38.3		43.9
566 °C+	48.5	57.0		51.0
Total	100	100		100
Second-pass resid conversion, wt % 566 °C+	33.7	24.7		32.7
H ₂ consumed, mg/ g maf feed	15	12		14

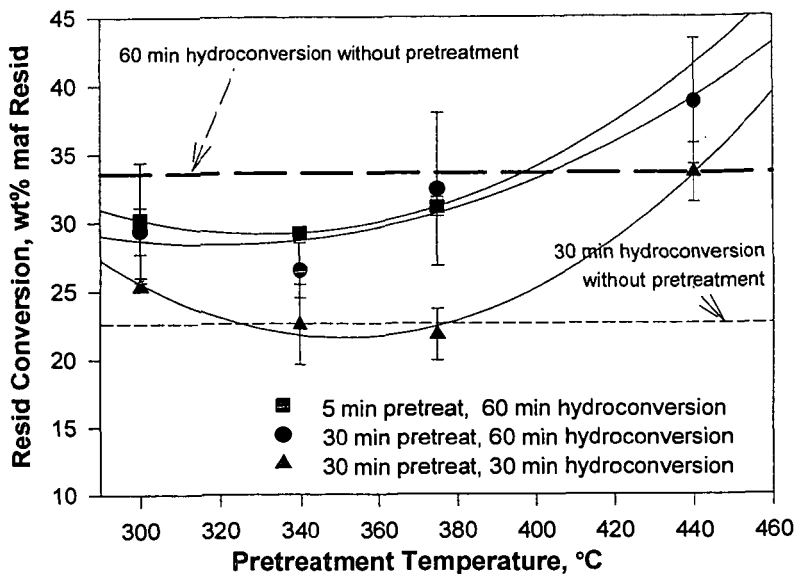


Figure 1. Effect of pretreatment time and temperature on 566°C+ resid conversion in 30 and 60 minute reactions of a deashed resid with 1000 ppmw Mo in Molyvan L, at 440°C.

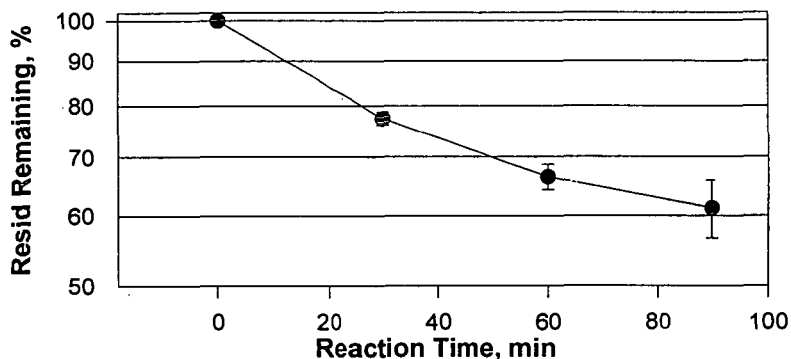


Figure 2. Disappearance of 566°C+ resid vs reaction time, hydrotreating deashed resid with 1000 ppmw Mo in Molyvan L at 440°C, without pretreatment.

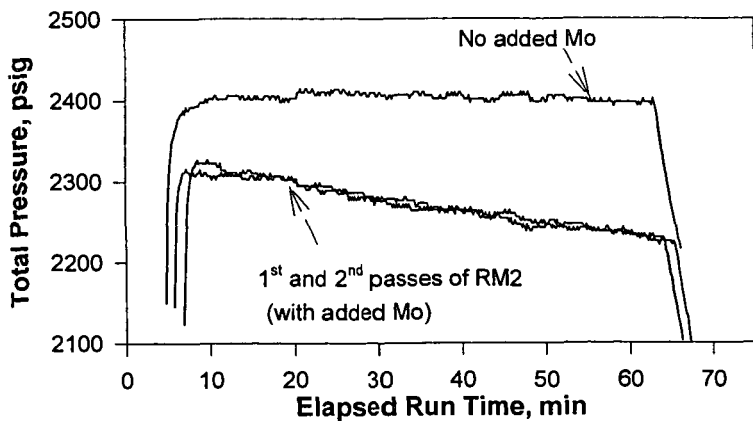


Figure 3. Impact of fresh and recycled Mo on total pressure in 60 min reactions at 440°C.

FREE RADICAL CHAIN REACTIONS OF BITUMEN RESIDUE

Carolyn M Blanchard and Murray R Gray

Department of Chemical and Materials Engineering

University of Alberta

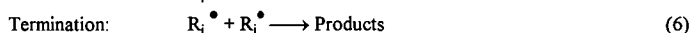
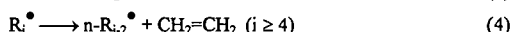
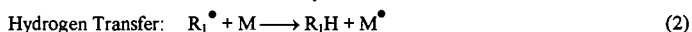
Edmonton, AB T6G 2G6

ABSTRACT

The mechanism of residue cracking was probed by diluting Athabasca bitumen with a solvent capable of accepting free radicals: 1-methyl naphthalene. The dilute solution was cracked at 400°C and 13.8 MPa hydrogen pressure. In the presence of a free radical chain reaction, this solvent would reduce the rate of cracking and give characteristic bi-naphthyl products due to recombination of radicals. Both of these trends were verified by comparing conversion of residue and liquid phase composition to data from control experiments. We conclude that the residue fraction of bitumen cracks by the same type of mechanism as lighter hydrocarbons, i.e. chain reactions involving free radical intermediates. Similar experiments under coking conditions suggest that free radical chain reactions are also important for coke formation.

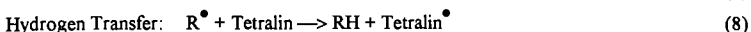
INTRODUCTION

Free radicals are formed during pyrolysis reactions due to the breakage of covalent bonds, and essentially all mechanisms for thermal cracking involve the formation and reaction of radical species. The unpaired electron in these radicals makes these highly reactive, unless the unpaired electron is stabilized, as in high viscosity pitches or in coke residues. Rice and Hertzfeld (1934) recognized that free radicals were the active intermediates in thermal cracking of n-alkanes. The main steps of the chain reaction are as follows:



where M and M[•] are the parent alkane and the parent radical, R_i[•] and R_jH are the methyl or ethyl radical and the corresponding alkane, R₂[•] is the methyl, ethyl or higher primary alkyl radical, R_i[•] is the butyl or higher radical and R_p[•] and R_s[•] are the primary and secondary pentyl or higher radicals. The simple model of Hertzfeld and Rice (1934) has been continuously expanded to allow detailed molecular modeling of ethylene cracking furnaces (Hillewaert et al., 1988). Free radical chain reactions are also observed in a variety of alkyl-aromatic and alkyl-cycloaromatic compounds. Of the thermal reaction mechanisms reviewed by Poutsma (1990), for example, all compounds with aliphatic side chains or rings with a least two carbons followed a free radical chain reaction. The predominant mechanism for thermal cracking reactions of alkanes, alkylaromatics, cycloalkanes, ethers and thioethers is free radical chain reactions.

Application of a free radical chain mechanism to a complex hydrocarbon mixture, such as coal or bitumen, is much more difficult. The reactants and products are poorly defined, and direct observation of radical species *in situ* can be obscured by highly stabilized radicals. Mechanisms proposed for thermal cracking of these complex mixtures have normally invoked free radicals as intermediates, but the crucial role of chain reactions has often been ignored. The most common type of reaction that is amenable to manipulation is hydrogen transfer, either from a hydrogen donor species such as tetralin or from molecular hydrogen. One the earliest mechanisms suggested for the role of donor solvents in coal liquefaction was proposed by Curran et al. (1967):



where M is the coal extract and R[•] is a general radical species. This mechanism spawned the idea of *capping of free radicals*. The role of hydrogen sources (donor solvents and molecular hydrogen) is to stabilize the reactive radical species, thereby giving stabilized molecular products.

The only cracking reaction in the sequence of reactions (7) through (11) is the initiation step. In fact, this reaction scheme lacks a propagation step that involves cracking. Each breakage of a carbon-carbon bond requires an initiation reaction.

Thermodynamics are clearly against this view of thermal reaction chemistry. Homolytic cleavage of a stable carbon-carbon bond requires an activation energy larger than the bond dissociation energy, or approximately 345.6 kJ/mole at 25°C. Actual activation energies for initiation reactions of alkanes consistent with this value, with reported values in the range 213 - 398 kJ/mol. In contrast, the propagation steps of a chain reaction face a much lower energy barrier. The β -scission reaction (equation 3) has an activation energy of 125 - 146 kJ/mol, while hydrogen abstraction has an energy of 46 - 71 kJ/mol. The chain reaction proceeds because the initial radical species turn over hundred or thousands of times to give many moles of cracked products per mole of initiation reactions. In contrast, the radical capping model has a chain length of unity. Observed rates of conversion by thermal cracking in the liquid phase are much higher than would be expected on the basis of scission of carbon-carbon bonds, i.e. initiation reactions only.

The concept of capping of radicals appears widely in the fuel science literature, to explain the reactions of coal liquids and other materials such as bitumens (for example, Sanford, 1994). The literature presents a paradox: model compounds follow free radical chain reactions as long as 2-carbon or longer aliphatic groups are present, while complex mixtures are presumed to generate radicals which are capped by donated hydrogen. Radical species are used to explain both processes, but one has a chain reaction and the other doesn't. A limited number of crossover studies have used insights into chain reaction mechanisms to explain observations of cracking kinetics (Thomas et al., 1989), or proposed new propagation steps for heavy hydrocarbons such as radical hydrogen transfer (McMillen et al., 1987).

Two barriers have likely prevented wider acceptance of the importance of chain reaction in thermal cracking of mixtures of heavy hydrocarbons. First, the chain reaction mechanisms are more complex, and lack the attractive simplicity of the radical capping mechanism. Second, the existence of chain reactions is difficult to prove in complex reaction mixtures. Compounds which are capable of trapping free radicals are routinely used in organic chemistry, however, such compounds are unstable at the temperatures of over 400°C typical of thermal cracking. The toluene carrier technique, developed by Swarcz (1949) to measure bond dissociation energies, offers one method of determining the significance of chain reactions. Homolytic scission of an alkyl-benzene is a slow step due to the high energy requirement: decomposes



In the presence of a large excess of toluene, the radicals will react with the toluene rather than abstracting hydrogen from the parent alkyl benzene. Abstraction of hydrogen from toluene generates a stabilized benzyl radical, therefore, the reaction is fast in comparison to initiation:



The formation of benzyl radicals diverts the chain reaction away from the parent compound, so that β -scission is suppressed. In the very dilute case, cracking of the parent compound proceeds at the rate of the initiation reaction, thereby giving an estimate of the bond dissociation energy.

Khorasheh and Gray (1993) reacted n-hexadecane in a variety of aromatic solvents in dilute solution in the liquid phase. Formation of solvent radicals was indicated by two observations; first the rate of cracking of n-hexadecane was reduced by the addition of solvent, and second the solvent radicals reacted with each other to give dimerized products. Cracking in benzene formed biphenyl, while cracking in toluene and ethylbenzene gave alkyl-diphenyl methanes and diphenyl ethanes. In general, therefore, we would expect dilution in a solvent capable of forming radicals to slow the rate of cracking by diverting the chain reaction, and to form solvent dimers.

Another important free radical reaction in vacuum residues is coking. Usually attributed to some combination of condensation reactions and phase behavior, coke formation may begin with dimerization or polymerization of residue molecules. Although cracking is favored at temperatures over 400°C, addition reactions have been observed in the liquid phase at these temperatures. For example, Khorasheh and Gray (1993) observed significant formation of addition products in the cracking of n-hexadecane in the liquid phase. The toluene carrier technique would prevent the interaction of residue radicals with other species, and thereby block any dimerization reactions.

The purpose of this study was to apply the toluene carrier technique to liquid-phase thermal cracking of vacuum residues, to verify the role of free radical chain reactions in both cracking and coking reactions.

EXPERIMENTAL

The solvent 1-methylnaphthalene (1-MN) was selected as a less volatile analog to toluene to serve as a radical acceptor in the liquid phase. Like toluene, 1-MN would form relatively stable benzyl radicals upon loss of a hydrogen to a radical. Athabasca vacuum residue (424°C+) was blended with 1-MN to give a 17 weight% solution, for an approximate molar concentration of 1.2%. The solution of residue was reacted in a 500 mL batch reactor (Parr) under hydrogen at 400°C and 13.8 MPa. The solution was degassed by pressurizing with nitrogen, purging the gas, then pressurizing twice with hydrogen and purging each time. The reactor was then pressurized for a final time at a hydrogen pressure just below the amount required to achieve 13.7 MPa at reaction temperature. As the reaction temperature was approached additional hydrogen was added to the reactor to bring it to the final pressure. The reaction time was 1 hr, measured from the time that the final temperature was achieved. Two control experiments were also conducted: reaction of solvent only to determine the background yield of dimer products in the absence of residue, and reaction of residue only to determine conversion in the absence of solvent. Reaction conditions were similar for coking, except that the reaction time was only 30 min, and the atmosphere was nitrogen at an initial cold pressure of 101 kPa.

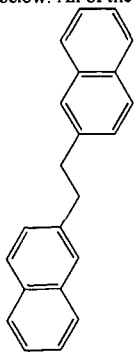
The reactor products were separated first by spinning band distillation, to remove components boiling below 343°C, particularly the solvent. Several batches of material from the spinning band distillation were then combined to give enough sample for determination of the vacuum residue by ASTM D-1160 distillation. The liquid products were also analyzed by gas chromatography using a 30 m HP-1 capillary column in a Hewlett Packard 5890 GC equipped with a flame ionization detector. Individual peaks were identified by GC-MS.

RESULTS AND DISCUSSION

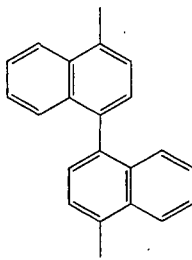
The conversion of the residue fraction with and without dilution in 1-MN is shown in Table 1. The mean conversion without solvent was 48.6%, but the conversion in dilute solution was much more variable, ranging from 1.5% to 41.6%. The distillation data from one batch of residue reacted in 1-MN (data not shown) were anomalous in giving half the amount of gas oil compared to the other experiments, therefore, the results were excluded. The remaining experiments with 1-MN diluent were more variable than without 1-MN, giving a mean conversion of 35.7%. In replicate experiments, therefore, the addition of 1-MN as a radical acceptor reduced the conversion of the residue fraction, consistent with a chain reaction mechanism.

Each set of five experiments with 1-MN diluent was pooled, then distilled. Spinning band distillation to remove of the large volume of solvent was followed by a single vacuum distillation to determine the amount of unconverted residue. This sample handling was the most likely source of variability. Other possible causes, such as variations in solvent purity, batch to batch variation in time-temperature history, sensitization by trace oxygen in the reactor or the catalytic effects of the reactor walls would all tend to average out from run to run due to the pooling of products from five reactor experiments.

Reaction of 1-MN without residue gave a series of dimers, illustrated in Figure 1. Structures of two of the compounds were identified by GC-MS, as compounds I and II shown below. All of the GC peaks in Figure 1 had the same molecular weight of 282.



I 2,2'-(1,2-ethanediyl)bis-naphthalene



II 4,4'-dimethyl-1,1'-binaphthyl

The formation of a series of termination products, including I and II, was consistent with reaction of the various resonance forms of the methyl naphthyl radicals that would form from 1-MN.

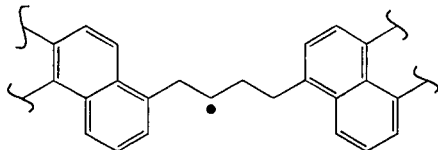
When the solvent was reacted in the presence of residue, the total concentration of termination products increased by a factor of 5.88, taking into account the interfering signals from the cracked products of the residue (Table 2). The concentration of compound I was the largest in most samples, and its concentration was increased by a factor of 3.64 when the solvent was reacted in the presence of residue (Table 3). This increase in the concentration of products from

the solvent clearly shows that radicals were transferred from the bitumen to the solvent by hydrogen abstraction, and that the cracking of the residue sensitized the solvent for free radical reactions.

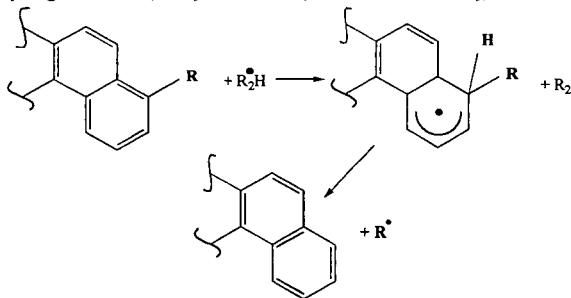
The experimental data were, therefore, consistent with both predictions of the effect of adding a free radical acceptor to the residue; reduced cracking of the residue due to the transfer of radical species to the solvent, and a concomitant increase in dimers formed from the solvent. These data can only be interpreted in light of a chain reaction mechanism for the cracking of the residue. As a non-donor compound, 1-MN should have had no effect on the rate of cracking had the radical capping mechanism been in effect.

When 1-MN was added to residue under coking conditions (i.e. a nitrogen atmosphere) the yield of coke decreased from 0.011 g coke/g feed residue to 0.022 g/g. The coke product was separated by diluting the product in methylene chloride and filtering through a 0.22 μm filter, therefore, the solids recovered would include clays and mineral solids from the feed oil. The determination was in triplicate. The concentration of termination products from the solvent in the presence of residue increased by a factor of 2.05 relative to solvent alone reacted under nitrogen. These results suggest that coking is also suppressed by addition of a radical acceptor, but further work is required at higher coke yields to verify the trend.

The main gap in the radical capping model is the lack of propagation steps that result in breakage of carbon-carbon bonds. The β -scission reaction is the most reasonable candidate in petroleum and bitumen residue materials, which contain an abundance of aliphatic carbon-carbon bonds in side chains and in bridges between aromatic clusters. A radical such as the following hypothetical structure:



can undergo β -scission to form an olefin and benzyl-type radical. The benzyl radical would then either abstract a hydrogen from another residue molecule (eqn 2) or isomerize (eqn 5) or terminate (eqn 6). Strong aryl-alkyl C-C bonds may crack by mechanisms such as the radical hydrogen transfer (RHT) mechanism (McMillen et al., 1987), an alternate propagation step:



(14)

Although the RHT mechanism remains controversial, it is consistent with some important experimental observations (Savage, 1995) and it provides for continuation of a chain reaction once a radical is formed by homolytic bond cleavage.

CONCLUSIONS

1. Residue conversion was more variable when diluted with 1-MN, but always lower than without dilution.
2. Residue cracking increased the concentration of termination products from 1-MN, consistent with and increase in radical concentration.
3. Experimental data were consistent with a free radical chain mechanism

ACKNOWLEDGMENTS

The authors gratefully acknowledge financial support and technical assistance from Syncrude Canada Ltd, particularly the encouragement from Maya Veljkovic to study mechanisms.

REFERENCES

- Curran, George P.; Struck, R.T.; Gorin, E. *Ind. Eng. Chem. Process Des. Dev.* **1967**, *6*, 166-173.
 Khorasheh, F.; Gray, M.R. *Ind. Eng. Chem. Res.* **1993**, *32*, 1864-1876.
 McMillen, D.F.; Malhotra, R.; Chang, S.-J.; Ogier, W.C.; Nigenda, S.E.; Fleming, R.H. *Fuel* **1987**, *66*, 1610-1619.

Poutsma, M.L. *Energy Fuels* 1990, 4, 113-131.

Rice, F.O.; Herzfeld, K.F. *J. Am. Chem. Soc.* 1934, 56(1), 284 - 289.

Sanford, E.C. *Ind. Eng. Chem. Res.* 1994, 33, 109-117.

Savage, P.E. *Energy Fuels* 1995, 9, 590-598.

Szwarc, M. *J. Chem. Phys.* 1949, 17, 421-435.

Thomas, M.; Fixari, B.; Le Perche, P.; Princic, Y.; Lena, L. *Fuel* 1989, 68, 318-322.

Table 1. Conversion of the Residue Fraction with Hydrogen Atmosphere

Experiment Type and #	# of Reactor Expts Mixed	Conversion of Residue, %	Average
Undiluted Residue Series A	2	50.3 %	
Undiluted Residue Series B	2	48.6 %	
Undiluted Residue Series C	2	46.9 %	48.6%
Residue in 1-MN Series D	5	26.8 %	
Residue in 1-MN Series E	5	38.9 %	
Residue in 1-MN Series F	5	41.6 %	35.7%

Table 2. Ratio of Termination Products From Residue in 1-Methyl Naphthalene Experiments to Pure 1-Methyl Naphthalene Experiments

Pure 1-MN: Replicate Experiments					
Rxn Description and Series	# of Reactor Expts Mixed	Termination Products, g/g (n=2)	Mean Concentration	Correction for Residue Contribution	Ratio of Residue in 1-MN to Pure 1-MN
Pure 1-MN (Series G)	1	0.320 E-3	0.224 E-3	1.32 E-3 g/g 1-MN	5.88
Pure 1-MN (Series H)	1	0.128 E-3	g/g 1-MN		
Residue in 1-MN (D)	5	1.23 E-3	1.63 E-3		
Residue in 1-MN (F)	5	2.03 E-3	g/g Mixture		
Correction for Background signal for Residue					
Undiluted Residue (A)	2	0.461 E-3		1.32 E-3 g/g 1-MN	
Undiluted Residue (C)	2	0.597 E-3	0.535 E-3		
Undiluted Residue (5)	2	0.548 E-3	g/g Mixture		

Table 3. Ratio of Diphenyl Ethane Found in Residue in 1-Methyl Naphthalene Experiments to Pure 1-Methyl Naphthalene Experiments

Reaction Description	Series Number	# of Reactor Expts Mixed	Termination Products in Sample g/g (n=2)	Termination Products in Sample Mean	Ratio of Residue in 1-MN to Pure 1-MN
Pure 1-MN	1	1	1.33 E-4	0.902 E-4	3.64
Pure 1-MN	4	1	0.473 E-4	g/g 1-MN	
Residue in 1-MN	1	5	1.93 E-4	3.29 E-4	
Residue in 1-MN	4	5	3.52 E-4	g/g 1-MN	

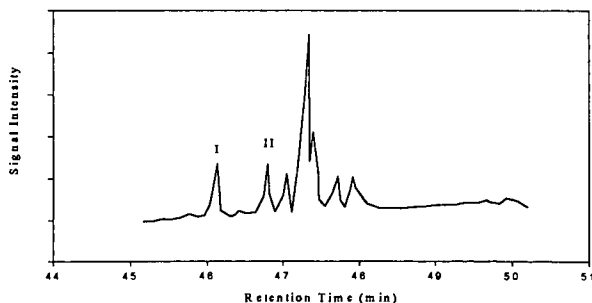


Figure 1. Chromatogram of Termination Products

HYDROGEN TRANSFER REACTIONS IN COAL/TYRE LIQUEFACTION : QUANTIFICATION OF H-DONOR CONTENTS.

Graham Harrison and Andrew B. Ross,
School of Sciences (Chemistry Division),
Staffordshire University,
College Road,
Stoke-on-Trent, ST4 2DE
England.

Keywords: coal liquefaction, H-donor, tyre pyrolysis oils

Introduction

The traditional view of the mechanism of coal liquefaction of thermal cleavage followed by radical stabilisation by hydrogen transfer explained why solvents with a good hydrogen donor potential were the best solvents for coal liquefaction. The excellent work by McMillen et al ⁽¹⁾ effectively challenged this traditional view and showed that the solvent could be even more reactive and could initiate bond cleavage. The actual situation is probably a combination of the two, with the weaker linkages between polyaromatic centres undergoing thermal cleavage followed by radical stabilisation and the stronger linkages undergoing solvent initiated cleavage followed by radical stabilisation. For the weaker bonds, the rate determining step would be radical stabilisation whereas solvent initiated cleavage would be rate determining for stronger bonds.

As shown by the research of McMillen et al, certain hydroaromatic molecules are more effective than others at initiating cleavage. Bate and Harrison ⁽²⁾ emphasised this point by showing that symmetrical octahydrophenanthrene was much more effective than its antisymmetric isomer at inducing bond cleavage. Thus ideally it would be useful to have not only a measure of the total H-donor content, but also an indication of the relative amounts of individual donors. Unfortunately, the complex composition of a liquefaction process solvent (LPS) makes identification and hence quantification of individual donors difficult if not impossible even by gc-ms so that only measurements of total H-donor contents are usually carried out.

Various methods have been developed to quantify H-donor contents. Our research has made extensive use of sulphur as a H-acceptor, following an approach developed originally by Aiura et al ⁽³⁾ and modified later by Bate and Harrison ⁽⁴⁾. This method has produced results which agree well with other methods, both for model compounds and LPS's. When other materials are introduced into the liquefaction mixture, measurement of H-donor contents becomes more difficult, especially when an highly aromatic material such as tyre pyrolysis oil (TPO) is introduced. This paper examines the sulphur test approach using various substituted aromatic compounds and relates the results to measurements of H-donor contents of TPO and TPO/LPS mixtures.

Experimental

Materials

A bulk sample of TPO was provided by Bevan Recycling and a sample of hydrogenated anthracene oil (HAO) was provided by British Coal Corporation, who also supplied a sample of Point of Ayr (POA) coal and the sulphided NiMo catalyst used for hydrogenation experiments. POA coal had the following analysis : moisture 3.8, ash 14.6, volatile matter 30.9 wt% as received basis; C 68.4, H 4.7, O 8.4, N 1.34 wt% dmmf; S 2.59 wt% dry basis

Coal dissolution

Coal, TPO (or hydrogenated TPO, HTPO) and HAO were reacted in spinning/falling basket autoclaves at 400°C for 1 h. After the autoclave had cooled, the contents were removed and filtered under vacuum through glass fibre filter paper. The dichloromethane -insoluble residue was Soxhlet extracted with THF. The solid residue was dried to constant weight and its ash content was determined to calculate percentage dissolution by ash balance.

Solvent hydrogenation

Samples (150g) of TPO were hydrogenated at 420°C for various lengths of time at an initial H₂ overpressure at temperature of 170 bar, using sulphided NiMo catalyst (5g) in the spinning/falling basket autoclave. The catalyst basket was retained above the liquid charge until the temperature reached 370°C when it was released to stir in the charge at 500 rpm. After the autoclave had cooled, the liquid contents were removed by suction and stored in sealed glass jars.

H-donor tests

Weighed amounts of sulphur and test material (approximately 0.5g each giving an excess of sulphur) were introduced into a bomb type autoclave. The bomb was connected to a pressure transducer and placed in its electrical heater. The bomb was heated to its set temperature and its pressure reading noted. For the model compound test materials, the contents of the bomb were dissolved in dichloromethane and most of the excess sulphur was removed by evaporating the

dichloromethane and extracting with diethylether. The diethylether extract was analysed by gc-ms using a VG-TRIO-1 bench top quadrupole mass spectrometer with a direct capillary interface (DB17 column) from a Carlo Erba HRGC 5160 chromatograph.

Results and Discussion

Figure 1 shows a plot of relative dissolution of POA coal in various HTPO samples against the relative H-donor content of the HTPO sample. The base line represents the situation if dissolution was not being enhanced by using HTPO rather than HAO. As expected the percentage dissolution increased with increasing H-donor content, but unexpectedly dissolution was enhanced. Figure 2 shows the influence of adding various amounts of TPO or HTPO to HAO in solvent augmented coal dissolution. The H-donor content of the HTPO sample was 85% of that of HAO and the TPO sample, 23% of HAO. On addition of TPO, dissolution was reduced but not as much as might be expected by the reduction in the H-donor content alone. This point was emphasised by the increase in dissolution when HTPO was added. This apparent improvement in coal dissolution ability can be either related to compounds in the HTPO/TPO samples having a better potential to initiate bond cleavage in POA coal than the compounds in HAO, or to the sulphur procedure underestimating the H-donor content.

Analysis of TPO samples has shown that they contain a considerable content of alkyl-substituted aromatic compounds (much more than is present in HAO), and only a very low content of hydroaromatic compounds.⁽⁵⁾ Consequently the sulphur test procedure was carried out with a series of alkyl-substituted aromatic compounds to assess their influence. Table 1 shows the results relative to a base sample of hydrogenated phenanthrene (HP) at three temperatures. The TPO sample tested had been pre-distilled to remove material boiling below 275°C. Obviously a pressure increase would result from the vapour pressure of the model compound, all of which would boil below 275°C at atmospheric pressure. As an approximation, the values for toluene could be subtracted from the other values (not TPO or HP) to indicate potential of reaction with sulphur. Certain trends can be derived from the results :- (i) the number of aromatic rings - the free radicals generated by hydrogen abstraction by sulphenyl radicals will be stabilised more effectively as the number of aromatic rings increases (a fact that is important in the relative effectiveness of H-donors to initiate bond cleavage); (ii) the degree of substitution - this dependency is not as great as the previous one and probably relates to the likelihood of occurrence of cyclisation reactions; and (iii) the position of substitution - certainly 2-methylnaphthalene reacted more than 1-methylnaphthalene and para xylene did not show the same reactivity as ortho and meta xylene, probably again as a result of the likelihood of cyclisation reactions. In addition, the high reactivity of TPO should be noted.

The reactions of a wide range of hydroaromatic compounds have been reviewed.⁽⁶⁾ The reactions were initiated by abstraction of hydrogen from a benzylic position to produce a hydroarene radical. Combination of a sulphenyl radical with the hydroarene radical produced sulphur adducts which may react to release H₂S and form the dehydrogenated hydroaromatic. The review also suggested that toluene could dimerise to stilbene and 1,1'-dimethy biphenyl could cyclise to phenanthrene, each resulting in the production of H₂S. Analysis of the reaction products confirmed these earlier observation, e.g. small amounts of stilbene together with bibenzyl were identified in the toluene reaction. The gc-ms also confirmed that cyclisation reactions had occurred, producing benzothiophenes, benzodithiophenes, dithiols and phenyl thiophenes. The production of such sulphur heterocycles may have a bearing on the direct inclusion of tyre pieces into coal liquefaction. Sulphur is included in tyre formulations and breakdown of the tyre radicals could produce sulphenyl radicals which could abstract hydrogen causing retrograde reactions and depletion of valuable H-donors.

The outcome of these results is that the sulphur test would over rather than underestimate the H-donor contents. Therefore, the presence of alkyl substitution in LPS's could be advantageous. Hydropyrenes are more effective than hydrophenanthrenes at initiating bond cleavage for model compounds, reducing the activation energy for the cleavage of the ether bond in diarylethers by about 50 kJ mol⁻¹ and the alkyl link in diarylmethanes by at least 50 kJ mol⁻¹.⁽⁷⁾ However large amounts of hydropyrenes were not found in HTPO's which tended to contain more hydroderivatives of alkyl-substituted phenanthrene. Thus addition of HTPO to liquefaction, either by addition after the coal dissolution stage as TPO or by separate hydrogenation and addition at the dissolution stage could be beneficial; but the addition of tyre pieces could have both negative (production of sulphur heterocycles) and positive (improved solvent properties) effects.

Acknowledgements

The authors acknowledge the European Coal and Steel Community for the financial support under contract 7220-EC866. Gratitude is also expressed to British Coal Corporation and Bevan Reeying for the supply of materials

References

1. McMillen, D.F., Malhotra, R., Chang, S.J., Ogier, W.C., Nigenda, S.E. and Flemming, R.H. *Fuel*, **66**, 1613 (1987)
2. Bate, K. and Harrison, G. *Fuel*, **71**, 289 (1992)
3. Aiura, M., Masunaga, T., Moriya, K. and Kageyama, Y. *Fuel* **63**, 1138 (1984)
4. Bate, K. and Harrison, G. *Am. Chem.Soc. Div, Fuel Prepr.* **34**, 839 (1989)
5. Harrison, G. and Ross, A.B. *Fuel* **75**, 1009 (1996)
6. Fu, P.P. and Harvey, R.G. *Chemical Reviews*, **78**, 317 (1978)
7. Sage, A.B. PhD Thesis, Staffordshire University, July 1996.

Table 1. Pressure readings per unit mass relative to hydrogenated phenanthrene (HP) for H-donor test using sulphur. n/v - no value.

Sample	Relative reading at temperature		
	230°C	275°C	300°C
toluene	0.24	0.24	0.28
ethyl benzene	0.28	0.78	0.79
o-xylene	0.26	0.32	0.46
m-xylene	0.26	0.32	0.44
p-xylene	0.26	0.29	0.29
1-methylnaphthalene	0.16	0.46	0.79
2-methylnaphthalene	0.18	0.74	0.90
dimethylnaphthalene	n/v	0.87	0.95
TPO	0.69	0.74	0.71
HP	1.0	1.0	1.0

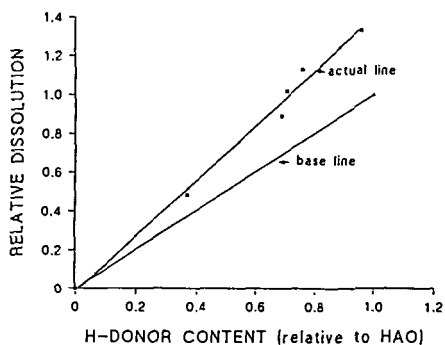


Figure 1 Graph of dissolution vs. H-donor content relative to HAO
- base line shows situation for no enhancement

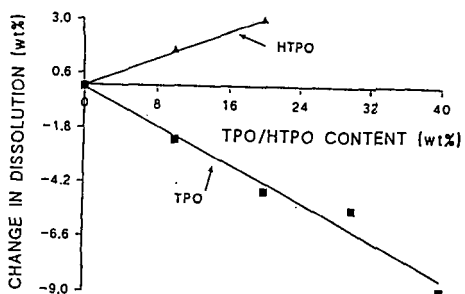


Figure 2 Graph of change in dissolution relative to HAO vs.
amount of augmenting solvent

CORRELATION OF CHEMICAL COMPOSITION OF EXTRA HEAVY OILS WITH INCIPIENT COKE FORMATION USING HOT-STAGE MICROSCOPY

P.M. Rahimi¹, T. Gentzis², K. Chung³, V. Nowlan³ and A. DelBianco⁴

¹ National Centre for Upgrading Technology, One Oil Patch Drive, Devon, Alberta, Canada T0C 1E0

² Alberta Research Council, P.O. Box 8330, Edmonton, Alberta, Canada T6H 5X2

³ Syncrude Research, 9421 17th Ave, Edmonton, Alberta, Canada T6N 1H4

⁴ Eniricerche SpA, San Donato Milanese, Italy

Keywords: Chemical composition, hot-stage, mesophase

INTRODUCTION

Upgrading bitumen to more valuable products involves a host of chemical reactions. The conversion of relatively low-value bitumen to high-value transportation fuels is usually limited due to coke formation. Bannayan et al. (1) discussed possible mechanisms for deposit formation in the reactor recycle cup and vacuum tower of a commercial unit. These authors proposed asphaltenes to be the cause of vacuum tower fouling in the H-oil unit.

In this study we investigated the coking propensities of extra heavy oil fractions from Athabasca bitumen vacuum bottoms. Athabasca bitumen vacuum bottoms (+524°C) was fractionated into 10 sub-fractions using pentane as super-critical solvent. The super-critical fluid extraction technique allowed the pitch (+524°C) to be extracted into narrow boiling point cuts with different chemical compositions. The development of mesophase was followed using hot-stage microscopy. The coking tendencies (the onset of mesophase formation) of these extra heavy oil fractions are correlated with their chemical compositions. The data from the hot-stage microscopy are also compared with the results obtained from autoclave studies of these fractions. The advantages and limitations of hot-stage microscopy for studying the hydrocracking behavior of heavy oils are discussed.

EXPERIMENTAL

Super-critical fluid extraction (SCFE) of Athabasca bitumen vacuum bottoms (+524°C) into 10 fractions was performed at the State Key Laboratory of Heavy Oil Processing (SKLHOP) of the Petroleum University at Beijing, China. The details regarding the preparation of narrow fractions of petroleum residue using SCFE have been described elsewhere (2). Hot-stage microscopy was carried out on all 10 fractions. In this paper, we report hot-stage and autoclave experiments on selected fractions whose properties are shown in Table 1. The details regarding development of the technique have been described elsewhere (3). The system was pressurized with H₂ (750 psi) and the flow of the gas was maintained at 35 mL/min during the experiments. The most critical factors in mesophase formation are temperature, residence time, heating rate, gas flow rate, and stirring rate (4). In this study, the feedstocks were heated from room temperature to 440°C at 11°C/min. The amount of material used varied between 5 and 12 mg depending on the nature of the fractions (liquid or powder form). Once at 440°C, the experiment was continued for about 3 h. Due to limitations of the experimental setup the samples were not subjected to stirring. The cooling effect of the flowing gas made it necessary to adjust the furnace temperature upward by approximately 50°C to maintain the appropriate sample temperature. This was confirmed by determining the melting points of K₂CrO₇ and Zn. The process was recorded by a video cassette recorder (VCR) for further observations. Mesophase diameter and growth with time were measured periodically using a micro scaler device. Photomicrographs were taken in polarized light under cross polars to show the optical texture of mesospheres and isochromatic regions. Combined magnification was 200X.

In order to compare the coking propensity of the heavy oil fractions obtained from hot-stage microscopy to those obtained from the autoclave, a series of experiments were carried out using fractions 1, 2B, 4, 7, and 9. Hydrocracking experiments were performed at 440°C, 2000 psi H₂ (13.9 MPa) for 30 min using a microautoclave. Hydrogen flow rate was constant at 3 L/min for all the experiments. Autoclave results are shown in Table 2.

Hydrocarbon-type analyses of maltene fractions from the selected samples were carried out before and after autoclave experiments to determine the reaction chemistry at the hydrocracking conditions. These results are shown in Table 3. The detailed experimental setup and hydrocarbon-type analyses were reported earlier (5).

RESULTS AND DISCUSSION

Autoclave results

The results are shown in Table 2. Fractions 1, 2B, 4, and 7 contain no asphaltenes. However, the amount of polar materials in these fractions increased from 9.25 wt % in fraction 1 to 22.61 wt % in fraction 7 (Table 3). Although only a negligible amount of coke (methylene chloride insolubles) was formed from fraction 1 (0.03 wt %), coke formation from fraction 7 was significantly higher (1.4 wt %). Asphaltenes were also produced in all fractions ranging from 2.67 wt % in fraction 1 to 28.38 wt % in fraction 7. Thermal reaction of fraction 9 produced a relatively large amount of coke as well as 45.94 wt % pentane-soluble maltenes. The data indicate that fractions having higher molecular weight, MCR, and aromaticity are more prone to coke formation. These results also confirm the proposed reaction mechanism for coke formation as:



In order to investigate the reaction chemistry in more detail, the maltene fractions in the feedstocks and the products were separated into saturates (M1), mono/diaromatics (M2), polyaromatics (M3), and polars (M4). Significant amounts of saturates were produced, in part, at the expense of polyaromatics and polars (Table 3). The results may indicate that dealkylation reactions are major reaction paths leading to products under the thermal conditions employed. Possible mechanisms for dealkylation are ipso attack by hydrogen radicals (6) and electron transfer from aromatic rings to metal porphyrins present in the tar sand fractions (7). Analysis of the reaction products under way indicates that dehydrogenation of cycloparaffins is also a major reaction leading to products having significantly higher aromaticity than the feedstocks.

Hot-stage microscopy results

When an organic material such as pitch is heated to temperatures between 350°C and 500°C, decomposition and polymerization reactions result in the formation of polycondensed aromatic hydrocarbons which eventually leads to mesophase. Upon further heating, mesophase spheres coalesce to form bulk mesophase and coke having different textures (4). Although hot-stage microscopy was carried out on all 10 SCFE fractions, in this paper we will discuss only the results obtained from fractions 1, 2B, 4, 7, and 9. Observations of hot-stage microscopy experiments are described below. The stated times are referenced to the beginning of the experiments which is taken as time zero (room temperature).

Fraction 1: Due to the high volatility of this fraction no mesophase was observed.

Fraction 2B: Tiny mesophase appeared approximately after 65 min. Mesophase diameter grew from 4 to 30 microns after 84 min (Figure 1a). The growth continued forming particles of more than 50 microns diameter after 94 min. Coalescence of mesophase accelerated and large isochromatic areas (>100 microns) showing domain anisotropy formed after 105 min (Figure 1b). Even at this time smaller mesospheres (< 10 microns) were forming in the isotropic matrix (Figure 1b). By 116 min, the entire field of view was covered by coke with domain anisotropy. Upon termination of experiment, the temperature of the cell decreased rapidly (from 440°C to 410°C in one minute). At the lower temperature it was observed that the previously isotropic areas had become anisotropic due to the reappearance of mesophase. When the residue in the cell was reheated to 440°C the anisotropic texture was converted to isotropic. This confirms the presence of a soluble and fusible mesophase in this fraction and shows that the phase change is reversible with temperature. This phenomenon was reported on hydrogenated coal tar pitch by Honda (4). Due to the high volatility of fraction 2B, the reproducibility of mesophase formation time was poor. Less volatile fractions (fractions 7 and 9) showed better reproducibility.

Fraction 4: Mesophase first appeared after 105 min. The growth of the spheres was as follows: 4 microns after 106 min, 9 microns after 116 min, and 33 microns after 127 min. Growth and coalescence of mesophase resulted in the formation of larger mesophase (>50 microns) after 136 min (Figure 1c). After 166 min the mesophase particles had formed a "donut-shaped" structure surrounded by mesospheres of various sizes and shapes (Figure 1d). When the residue was cooled and reheated to 440°C the same behavior as fraction 2B was observed.

Fraction 7: The time of mesophase formation was 70 min. Mesophase spheres grew from 3 microns in diameter after 74 min to 21 microns after 98 min (Figure 1e) and finally formed large coke areas with flow domain anisotropy after 153 min (Figure 1f). The flow domain was observed only in this fraction. The flow domain texture enclosed smaller patches of isotropic matrix, which, in itself, contained numerous tiny mesospheres (1-2 microns in size). The disc-like inclusions of isotropic pitch

surrounded by anisotropic pitch are similar to the results reported by Hüttinger et al. (8). Complete conversion of this isotropic phase to coke could take place only after a long time at 440°C. The behavior of this fraction in forming flow domain warrants further investigation.

Fraction 9: The first mesophase spheres were noticed after 57 min which is faster than any of the other fractions examined. After 95 min the sample had developed large isochromatic areas with domain anisotropy and rounded margins (Figure 1g). After 104 min some small mesophase spheres could still be seen floating in an isotropic matrix. The resulting coke was angular with serrated edges (Figure 1h). Upon cooling, these isotropic areas became anisotropic with a mosaic texture, which is consistent with observations in previous samples. When the residue was cooled and reheated to 440°C the same behavior as fractions 2B and 4 was observed.

The above data indicate that the incipient mesophase formation is dependent on the chemical composition of the fractions. For instance, the chemical analysis of fraction 9 (Table 1) indicates that this fraction contains 88.0 wt % asphaltenes and has the highest molecular weight, aromatic carbon, and MCR. Compared to the more aliphatic fractions 2B and 4, the molecules in fraction 9 require shorter heating time to become the lamellar molecules which eventually are involved in mesophase formation. Thermal hydrocracking of this fraction in the autoclave also produced the highest coke yield (Table 2). Overall, the results of hot-stage microscopy are consistent with the autoclave experiments for fractions 4, 7, and 9. Fraction 2B produced the least amount of coke in the autoclave runs. However, the time of mesophase formation for this fraction in the hot-stage run was earlier than expected. This was attributed to the fact that this fraction is relatively volatile and, under hot-stage conditions, evaporated significantly leaving the most refractory components behind.

The second important observation that can be related to the chemical composition of the fractions is the relative rate of mesophase formation at 440°C. Mesophase growth rate as a function of time was recorded for fractions 4 and 7. It was observed that in fraction 4 the growth rate was slower in the first 60-75 min at isothermal temperature (440°C) followed by much faster growth. In contrast, fraction 7 showed a continuous linear growth rate. These observations indicate possible differences in the reaction kinetics of the two fractions which, in turn, relates to the differences in their chemical compositions (Table 1). Fraction 9, being the most refractory according to the chemical characteristics, showed the highest rate of growth compared to the other three fractions examined. Accordingly, it was observed that mesophase growth was faster in the first 40-45 min of formation at isothermal temperature. These results are in agreement with data reported by Hüttinger et al. (8).

References

- 1- Bannayan, M.A., Lemke, H.K. and Stephenson, W.K., "Fouling mechanisms and effect of process conditions on deposit formation in H-Oil equipment", Catalysis in petroleum refining and petrochemical industries 1995. M. Absi-Halabi et al. Editor, 1996 Elsevier Science B.V.
- 2- Jiang, T., Wang, R.A. and Yang, G., "Simulated Distillation of Residue by Fractional Distraction (I)", Proceedings of the International Symposium on Heavy Oil and residue Upgrading and utilization, Fushun, China, 53 (May 1992).
- 3- Sears, P.L., "Hot-Stage Microscopy", Division Report ERL 93-03 (CF), CANMET, Energy, Mines and Resources Canada, 1993.
- 4- Honda, H. "Carbonaceous mesophase: History and prospects", Carbon, 26, (2), 139, (1988).
- 5- Rahimi, P.M., de Bruijn, T.J.W., Dawson, W.H., Charland, J.P., Heitz, M., and Chornet, S. "Thermal hydrocracking of heavy oils and their components", Division Report ERL 93-67 (CF), CANMET, Energy, Mines and Resources Canada, 1993.
- 6- McMillen, D.F., Manion, J.A., Tse, D. S., and Malhotra, R. ACS Div Petroleum Chem Preprints 39:2:422, 1994.
- 7- Franz, J.A., Camaioni, D.M., Alnajjar, M.S., Autrey, T. And Linehan, J.C., "Fundamental hydrogen transfer studies in coal liquefaction: understanding the answers and questions." ACS Div Petroleum Chem Preprints 40:2:203, 1995.
- 8- Hüttinger, K.J., Bernhauer, M., Christ, K., and Gschwindt, A., "Kinetics of mesophase formation in a stirred tank reactor and properties of the products, IV: Carbon dioxide atmosphere", Carbon, 30, (6), 931 (1992).

Figure 1

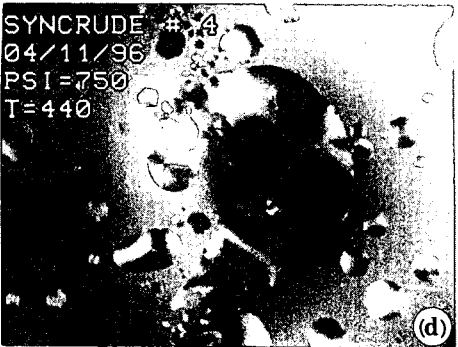
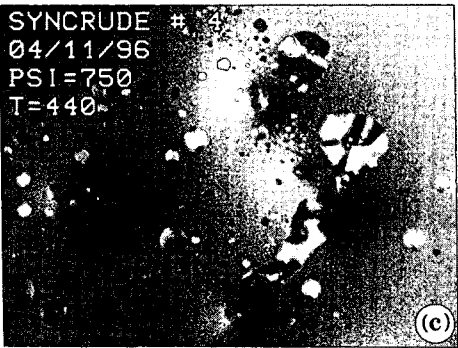
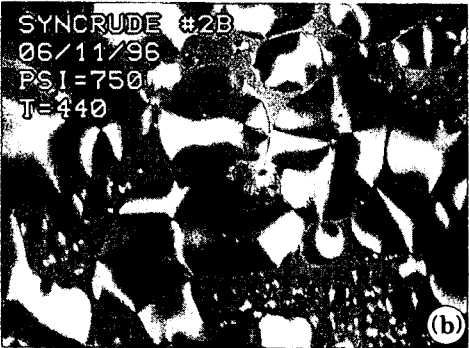
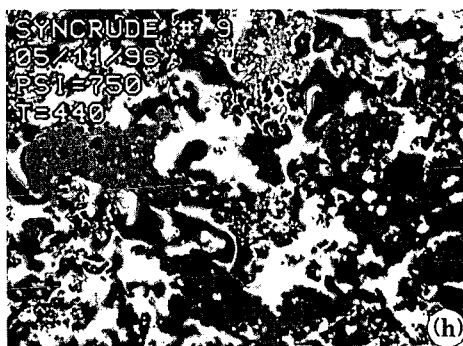
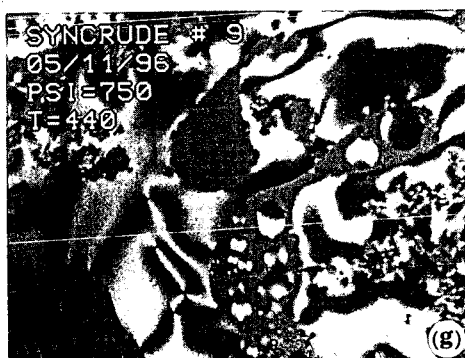
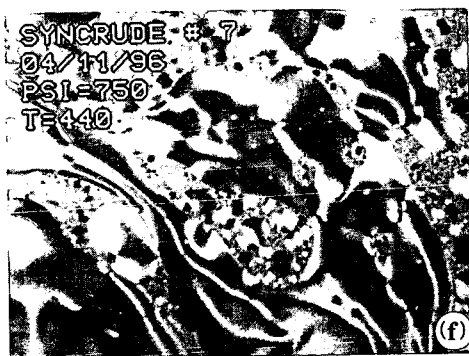
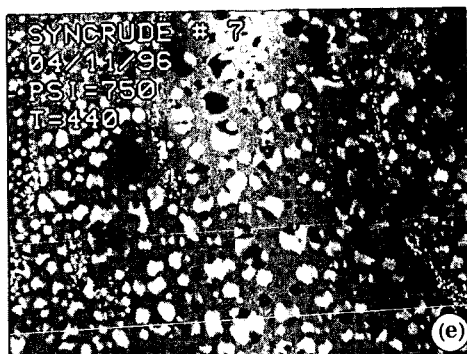


Figure 1



Description of photomicrographs

- (a) Fraction 2B- Growth of mesophase spheres from isotropic matrix after 84 min.
- (b) Fraction 2B - Coalescence of mesophase spheres after 105 min.
- (c) Fraction 4- Growth of mesophase spheres from isotropic matrix after 136 min.
- (d) Fraction 4- Coalescence of mesophase to 'donut' shape structure after 166 min.
- (e) Fraction 7 - Formation of mesophase from isotropic matrix after 98 min.
- (f) Fraction 7 - Development of flow domain and domain anisotropy after 153 min.
- (g) Fraction 9 - Formation of mesophase and coke with domain anisotropy after 95min.
- (h) Fraction 9 - Coke with angular and serrated texture after 104 min.

Table 1 - Characteristics of Athabasca bitumen vacuum bottoms fractions obtained by SPCE technique

Fraction #	1	2B	4	7	9
Pressure, MPa	4-5	5.5-6	7-8	10-11	>12
Wt% of pitch	12.7	7.6	6.5	2.6	40.4
Density, g/ml @20°C	0.9745	1.0061	1.0427	1.0678	N/a
Molecular weight, g/mol	506	711	825	1209	4185
Sulphur, wt %	4	5	6	6.8	7.6
Nitrogen, ppm	3080	4330	6160	7530	10500
Carbon, wt %	84.5	83.5	83	83	78.5
Hydrogen, wt %	11.5	10.95	10.25	9.7	8
C/H (atomic)	0.612	0.635	0.675	0.713	0.818
Aromatic carbon*, %	26	25	36	43	49
Nickel, ppm	12.8	30.1	71.1	138	339
Vanadium, ppm	30.7	69.8	166	355	877
MCR, wt %	5.64	10.83	18.16	26.46	48.94
Saturates, wt %	26.86	9.68	1.36	0.28	0
Aromatics, wt %	57.23	65.7	63.86	45.91	2.19
Resins, wt %	15.91	24.62	34.78	53.81	9.38
Asphaltenes, wt %	0	0	0	0	88.03

*¹³C NMR

Pitch = +524°C fraction

Table 2- Thermal hydrocracking products (wt %) of selected fractions

Fractions	Gases	Coke	Asphaltenes	Maltenes
1	14.61	0.03	2.67	82.69
2B	14.15	0.09	10.54	75.22
4	12.34	0.12	22.08	65.08
7	13.47	1.40	28.38	56.75
9	12.98	8.68	32.40	45.94

Maltenes = pentane solubles

Asphaltenes = pentane insolubles

Coke = methylene chloride insolubles

Table 3. Hydrocarbon-type distribution (wt % of feed) of selected fractions before and after thermal hydrocracking

fraction	feed				product			
	M1	M2	M3	M4	M1	M2	M3	M4
1	15.08	9.63	66.04	9.25	30.39	10.65	36.05	5.60
2B	5.29	5.29	75.02	14.40	23.64	9.80	36.81	4.97
4	2.34	1.08	73.97	22.61	18.24	8.62	33.83	4.39
7	0.06	0.08	72.66	27.20	18.90	6.61	27.67	3.58
9	Approximately 88 wt% asphaltenes				17.16	4.80	20.61	3.37

M1 = saturates
M2 = mono/diaromatics
M3 = polyaromatics
M4 = polars

ASSESSMENT OF COAL REACTIVITY DURING PREHEATING BY THE RELATIONSHIPS BETWEEN STRUCTURAL AND PLASTIC PROPERTIES. CHEMOMETRIC ANALYSES.

N. Pieri, L. Quoniam, J. Kister, Laboratoire GOAE, Aix-Marseille III University, Case 561,
13397 Marseille Cedex 20, France,

M. A. Diez, R. Alvarez, J.J. Pis, Instituto Nacional del Carbón (INCAR), CSIC, Apartado 73,
33080 Oviedo, España.

Key-Words: Coking coals, chemical characterization, chemometrics

ABSTRACT

Relatively little attention has been given to determine the coal structural changes induced by industrial preheating process. In this work, a series of ten coking coals was characterized, before and after industrial preheating, by FTIR and Synchronous UV Fluorescence (SF) spectroscopies and by petrography and plastic properties (e.g. mean Reflectance and Gieseler maximum fluidity, Fm). Specific structural indices derived from FTIR and SF data were defined and used in Principal Component Analysis to determine the effects of coal preheating on structural changes and to classify coals on the basis of plastic and petrography characteristics. Predicted models of plastic and petrography properties were established from FTIR and SF indices using Multivariate Linear Regression. For example, Gieseler Fm and volatile matter content, two main parameters for coal blending, can be estimated from the FTIR and SF indices for wet and preheated coals. Thus a better insight into reactivity of coking coals and a valuable estimation of their properties can be accounted.

INTRODUCTION

Recently, reserves of good coking coals have become less available and comparatively more expensive. Resources are extended by using coal blends with different coking properties and/or selective additives. Coal preheating technology has emerged as a technique to overcome some of these problems. This technology, preheating of coal at about 200°C in an inert atmosphere, in combination with the dry cooling of the resulting coke, is now incorporated into the operation of the Jumbo Coking Reactor (JRC, European Eureka Research Project)¹.

Most studies of preheating have focused on advantages in terms of technological improvements to coke quality and productivity, together with widening the range of coals suitable for coking compared to conventional wet gravity charging². Industrial preheating produces a decrease in the volatile content of the preheated coal compared to the original coal due to a devolatilization of the coal particles, accompanied by coal particle pore formation³. However, relatively little attention has been given to determining the structural changes induced in coals by industrial preheating process. These chemical transformations can be accurately evidenced by routine or more sophisticated analytical techniques.

The small molecules, trapped in the pores of coal macromolecular structure, have been defined as the mobile components in coals, and they are extractable using organic solvents⁴⁻⁵. Brown and Waters⁶ have shown that the mobile component extracted with CHCl₃ plays an important role in the development of coking ability. Previous studies have shown that UV Synchronous Fluorescence (SF) spectroscopy is interesting for qualitative and quantitative analysis of aromatic compounds present in the extractable organic matter⁷⁻⁸. Furthermore, a new ranking parameter for coals which present a large range of petrographic and chemical characteristics has been established from SF data⁹. Despite of the non applicability of this ranking parameter for coals comprised in a similar range, this technique can be used to determine the structural changes related to aromatics in the extractable phase¹⁰⁻¹². Moreover, structural information of coal residue can be assessed by Fourier transformed infrared (FTIR) spectroscopy¹³⁻¹⁵.

It may be assumed that the nature and the extent of the chemical transformations associated with the preheating process depend on the initial composition of coal i.e. its origin and its rank. In order to evidence the effects of initial composition on the rank and the coking properties of coals, a coal series was preheated and analyzed by FTIR and SF spectroscopies before and after preheating. This paper presents the results of the analysis of the different coals and emphasizes the effect of origin-preheating pair on the plastic behavior of coals, using chemometric analyses.

EXPERIMENTAL

A series of international coking coals (H) was selected for the industrial coal preheating process (Table 1). Coal preheating was carried out in the 2t/h INCAR pilot plant -Precarbon process- at 210 ± 10 °C under an inert atmosphere¹⁶. A coal sampling was performed : the wet coal before

being charged into the preheating pilot plant (H) and the preheated coal in the closed conveyor before entering to the coke-oven (P).

The particle fractions of wet and preheated coals ($< 150\mu\text{m}$) were ultrasonically extracted with CHCl_3 (100 mg coal / 30 ml solvent) for 45 min. Extract yields were about 2 wt%. After removing solvent, extracts were dissolved in THF (10 mg/l) for SF measurements. SF spectra were obtained at a fixed excitation and emission wavelength interval of 23 nm, excitation and emission beams being kept at a width of 5 nm and a scanning rate of 200 nm/s, in the 200-600 nm range. Selected indices derived from SF data using the integrated area (A) of different spectral bands are described in Table 2.

The extraction residues were analyzed by FTIR spectroscopy using KBr standard pellets (1:150 coal residue to KBr ratio). Each spectrum resulted from the accumulation of 128 scans, recorded with a spectral resolution of 4 cm^{-1} in the $4000\text{-}400\text{ cm}^{-1}$ spectral domain, was normalized to 1 mg of sample. Mineral matter interferences were eliminated by subtracting the corresponding spectrum of the low-temperature ash (LTA). The detailed band assignments of coal spectra and the integration method of these FTIR bands were widely described elsewhere^{14,17}. Selected indices derived from FTIR data using the integrated area (A) or the maximum intensity (H) of different spectral bands are described in Table 2.

Statistical analyses.

The factor analysis used is based on the Principal Component Analysis or PCA (STATISTICA software, Statsoft Inc.). The principle of this multivariate statistical method¹⁸ is to create new independent variables (*i. e.*, factors) that are the linear combination of original variables (*i. e.*, FTIR and SF indices) which are correlated to each other. The primary objective of the statistical analysis is to reduce the dimensionality of the data to a few important components or factors that best explain the variation in the data. From the data matrix, its standardized version Z and correlation matrix R were calculated. The correlation matrix R was used as a starting matrix in PCA. Principal components (PC) were determined by considering eigenvalues and associated eigenvectors. For plotting purpose only two or three PC scores were used. These must explain over 80% of the total variance. In R-mode factor analysis, the initial variables are scaled, thus the links between variables can be easily visualized. In Q-mode, the observations are scaled on the same set of factor axes. Coking coals with similar FTIR and SF index values are gathered in factor space and specific variables, which are important in distinguishing the different groups of coals, are determined.

RESULTS AND DISCUSSIONS

The chemical characteristics of coals, before and after preheating, have been studied using FTIR and SF spectroscopies in order to determine (i) the structural modification occurring during preheating, (ii) the relationships between Reflectance and Volatile Matter (VM) amount, standing for thermal maturity reference parameters, and structural parameters, (iii) the chemical structures acting on plastic properties (Gieseler maximum fluidity, GI ; Arnu dilatation)^{10, 19}.

As a matter of fact, the fluid properties (*i.e.* plastic properties) is an important step of coking because of the quality dependence of the semi-coke. However, fluidity leads to gas production increasing pressure inside the coke oven¹. The optimization of the fluidity and the gas pressure becomes necessary. Moreover, preheating produces a decrease in the volatile matter content of the preheated coal compared to the original coal¹¹. All those parameters could be maturity-/origin-dependent. To get coking performance related to structural parameters, Gieseler Index (maximum fluidity), Arnu (dilatation), Reflectance and Volatile Matter (maturity) were included in the statistical analysis.

The first step of this work was to characterize wet coking coals. Along this line, a first Principal Component Analysis was performed to relate chemical features to plastic properties as well as to visualize the main characteristics of the total sampling. The first PCA explains 87% of the total variance with 3 factors (Table 3). The factor 1 is related to the coking coal maturity with, in its positive way, a high reflectance value (*i.e.* REFLECT) and a low volatile matter amount (*i.e.* VM) (Figure 1a). This corresponds to a high aromatic structure amount in the residue (*i.e.* Aromatic H Index: H ARO and Aromatic/Aliphatic ratio : AH) and a high amount of highly polycondensed aromatics in the extract (predominance of 4-5 polycondensed aromatic rings compared to 2-3 rings, *i.e.* A3/A1). The factor 2 is characteristic, in its positive way, of an important dilatation of coal during coke making corresponding to a low branched aliphatic content in the residue (BA index). This PCA allows to classify three groups of coking coals. We can notice that the intermediate group shows the lowest expansion (Figure 1b). The third factor, representative of aliphatic structures within coking coal residues, underlines that the volatile matter amount (VM on factor 1) is independent of these structures (Figure 2).

A second PCA has been performed from spectroscopic data and plastic properties measured before and after preheating in order to know the chemical structures involved in coking property changes during preheating. This second PCA which explains 83% of the total variance with 3 factors (Table 4), underlines the main chemical changes during this step. The aromaticity of all the coals increases with a loss of aliphatic structures, in the residues (increase in Aromatic Index: AI and decrease in Factor of Aliphaticity: FA and in vCH_2 asym/ vCH_2 sym: W) in spite of their maturity rank except for one coal which underwent a low evolution (i.e. T3595H). The fluidity and the volatile matter of coals, related to factor 1, slightly decrease during preheating except for T3614H (Figure 3). In its negative sense, the third factor concurrently underlines the loss of alkane side-chains on aromatic structures (i.e. SS1) in the residues and an increase in aromatic hydrogen content (i.e. H ARO) (Figure 4). Some coals act during preheating as described above (e.g. T3637H, T3614H, T3595H, T3591H). No changes are noted for aromatic structure substitutions of the other coals. This PCA underlines that the preheating mainly consists in an aromatization and thermodesorption, the chemical structures within the more mature coals changing less than the less mature ones. Consequently, coals have a slight difference in their properties after preheating.

Then, from those spectral data, multivariate linear regressions were performed to determine the relationships between structural characteristics, petrography parameters and plastic properties.

The first model was established to estimate the Reflectance from only three independent and standardized spectroscopic variables calculated from wet coals. The following equation was obtained :

$$Y_{\text{REFLECT}} = -0.59 X_{\text{H/C}} + 0.37 X_{\text{ACI}} + 0.68 X_{\text{A3/A1}} \quad (1)$$

The first model explains 96% of the total adjusted variance (adjusted $r^2 = 0.96$), the standard error of the predicted value being 0.3. This model underlines an increase in maturity with the decrease in H/C ratio. The higher the maturity of coking coals, the higher their aromaticity in their residue and the higher their highly condensed aromatic content in their extract (Figure 5a).

Gas emission during coke making can also be evaluated by the volatile matter content in wet and preheated coals. Consequently, a second predictive model of the volatile matter amount was performed from structural indices measured before and after preheating (equation 2):

$$Y_{\text{V.M.}} = -0.63 X_{\text{BA}} - 0.34 X_{\text{H ARO}} - 0.22 X_{\text{ACI}} - 0.48 X_{\text{A3/A1}} \quad (2)$$

This model explains 85% of the total variance and the standard error of the predicted value is 2 (Figure 5b). Few changes in volatile matter amount is noted during preheating. This parameter inversely depends on the maturity (aromaticity of coking coals). The less aromatic the structures and/or the more substituted the aromatic structures within coal residues, the less polycondensed the aromatic structures within extracts, the more the volatile matter amount within coals. The V.M. also depends on the aliphatic nature in the residue because the volatile matter content inversely relates to the branched aliphatic index (i.e. BA).

Those two predictive models underline the relationships within coals between chemical structures, their reflectance and their volatile matter amount.

At last, one of the most important factors occurring on coke making has been predicted : the Gieseler Index, representing the maximum fluidity for coking coals. The optimal values of this index are between 500 and 1500 ddp^m. To simplify, GI values have been expressed in log ddp^m. Two models were established, one for wet coals and one for preheated coals (equations 3 and 4) because the predictive model of GI, after preheating, requires one more parameter which is the H/C ratio.

$$\text{For wet coals : } Y_{\text{GI}} = -0.84 X_{\text{BA}} + 0.61 X_{\text{SS1}} - 0.61 X_{\text{AH}} - 0.27 X_{\text{A3/A1}} \quad (3)$$

$$\text{For preheated coals : } Y_{\text{GI}} = 0.25 X_{\text{BA}} - 0.40 X_{\text{SS1}} - 0.74 X_{\text{AH}} - 0.34 X_{\text{A2/A1}} + 0.63 X_{\text{H/C}} \quad (4)$$

Those models respectively explain 95% and 97% of the total variance. In both cases, standard error of estimate is 0.2. Those models depend, in the coal residue, on the branched aliphatic ratio, the percentage of the highly substituted aromatic structures and the aromaticity (Figure 6). GI is inversely linked to the polycondensation of aromatic structures, in the coal extracts. However, even if trends are the same in coal extracts towards GI, before or after preheating, that is not the case in coal residues. Before preheating, the higher the maximum fluidity for coals, the more substituted the aromatic structures and the less branched the aliphatic structures. After preheating, one can observe the opposite relationships between the maximum fluidity, the aromatic substitution level and the branched aliphatic ratio. Furthermore, GI parameter decreases during preheating. Those results would underline the irreversible changes which occur in the organic matrix and pore structure of coal during preheating process and would explain the

different behaviors of the preheated coals during carbonization^{11, 20}. As a matter of fact, preheated coals cannot be compared with wet coals because of the differences noted in the relationships between chemical structures and plastic properties.

CONCLUSION

FTIR data on coal residues and SF data on coal extracts give complementary information. Coking coal chemical composition can be quantified from few spectroscopic indices. A ranking of coking coals from those data would be possible.

The main changes occurring during preheating are an aromatization with loss of alkane side-chains, in the solid residue for some coals, and a thermodesorption of the volatile compounds.

Principal Component Analysis showed the correlation between some structural indices and coal rank parameters, and the combined effects of some composition parameters on the plastic properties.

Some physical and plastic properties were predicted from few FTIR and SF indices of coking coals: Reflectance, the Volatile Matter amount and the Gieseler maximum fluidity.

Such investigations provide global as well as structural parameters that facilitate the understanding of the mechanisms involved during the different natural and industrial transformations of coals.

REFERENCES

- (1) Diez, M. A.; Alvarez, R.; Sirgado, M.; Marsh, H.; *ISIJ International* **1991**, 31(5), 449-457.
- (2) Alvarez, R.; Alvarez, E.; Canga, C.S.; Diez, M. A.; Gonzales, A. I.; Marsh, H. *Fuel Proc. Technol.* **1993**, 33, 117-135.
- (3) Menendez, J. A.; Alvarez, R.; Canga, C.S.; Diez, M. A.; Gonzales, A. I. *Fuel* **1992**, 71, 1265-1270.
- (4) Marzec, A.; Jurkiewicz, A.; Pislewski, N. *Fuel* **1983**, 62, 996-998.
- (5) Given, P. H.; Marzec, A.; Barton, W. A.; Lynch L. T.; Gerstein, B. C. *Fuel* **1986**, 65, 155-163.
- (6) Brown, H. R.; Waters, P.L. *Fuel* **1966**, 45, 17-39, 41-59.
- (7) Kister, J.; Guiliano, M.; Mille, G.; Dou, H. *Fuel* **1988**, 67, 1076-1081.
- (8) Mille, G.; Guiliano, M.; Kister, J. *Org. Geochem.* **1988**, 13(4-6), 947-952.
- (9) Kister, J.; Doumenq, P.; Mille, G.; Landais, P.; Pis, J. J. In *Synthesis, properties, analytical measurements, occurrence and biological effects*, Polycyclic Aromatic Compounds; Garrigues, P and Lamotte, M., Eds.; Gordon and Breach Science Publishers: Switzerland, 1993, pp 639-646.
- (10) Kister, J.; Pieri, N.; Diez, M. A.; Alvarez, R.; Pis, J. J. In *Coal Science; Coal Science and Technology* 24; Pajares, J. A. and Tascon, J. M. D., Ed.; Elsevier: Amsterdam, **1995**, p 381-384.
- (11) Kister, J.; Pieri, N.; Alvarez, R.; Diez, M. A.; Pis, J. J. *Energ. Fuel* **1996**, 10(4), 948-957.
- (12) Benkhedda, Z.; Landais, P.; Kister, J.; Dereppe, J. M.; Monthieux, M. *Energ. Fuel* **1992**, 6(2), 166-172.
- (13) O. Ruau, Thèse en Sciences de l'Institut National Polytechnique de Lorraine, **1996**, pp 300.
- (14) Kister, J.; Ruau, O.; Landais, P.; Alvarez, R.; Diez, M. A.; Pis, J. J. *Fuel Proc. Tech.* **1993**, 36, 313-318.
- (15) Pieri, N.; Planche J. P.; Martin, D.; Germanaud, L.; Kister, J. *Proc., Euraspalt & Eurobitume Congress* **1996**, 5.120, 1-13.
- (16) Alvarez, R.; Diez, M. A.; Menendez, J. A.; Pis, J. J.; Suarez, C.; Sirgado, M. *Cokemaking Int.* **1993**, 5(2), 36-40.
- (17) Guiliano, M.; Mille, G.; Doumenq, P.; Kister, J.; Muller, J. F. In *Advanced Methodologies in Coal Characterization*, Coal Science and Technology 19; Charcosset, H., Ed.; Elsevier: Amsterdam, **1990**, pp 399-417.
- (18) Escofier, B.; Pages, J. *Analyses factorielles simples et multiples- Objectifs, méthodes et interprétation*. Dunod, Ed.; Bordas: Paris, **1988**.
- (19) Lloyd, W. G.; Reasoner, J. W.; Hower, J. C.; Yates, L. P. *Fuel* **1990**, 69, 1257-1270.
- (20) Landais, P.; Langlois, E.; Pis, J. J.; Diez, M. A.; Alvarez, R.; Kister, J. In *Coal Science; Coal Science and Technology* 24; Pajares, J. A. and Tascon, J. M. D., Eds.; Elsevier: Amsterdam, **1995**, pp 453-456.

Table 1 : Petrography and plastic properties of a series of ten coking coals, before and after preheating. These data have been given by INCAR-CSIC, Oviedo, Spain.

Origin	Coking coals: Wet (H) Preheated (P)	H atom/ C atom : H/C	Reflectance: REFLECT	Volatile Matter VM	Dilatation: ARNU	Maximum fluidity, Gieseler Index : GI
Australia	T3631H	0.720	1.41	19.5	70	1.68
Germany	T3637H	0.695	1.18	22.4	52	1.64
Australia	T3622H	0.751	1.09	23.2	75	3.17
USA	T3639H	0.683	1.15	24.2	123	2.50
Spain	T3595H	0.726	1.25	25.6	171	3.99
Poland	T3625H	0.728	1.00	28.5	147	2.59
USA	T3658H	0.760	1.00	30.8	279	4.25
Spain	T3590H	0.720	0.96	31.4	218	4.00
USA	T3614H	0.750	0.90	33.8	143	4.01
Spain	T3591H	0.760	0.84	35.9	135	4.03
Australia	T3631P	0.669		20.4	33	0.78
Germany	T3637P	0.694		22.3	42	0.90
Australia	T3622P	0.732		23.4	66	2.57
USA	T3639P	0.713		24.1	109	2.02
Spain	T3595P	0.756		24.0	134	3.16
Poland	T3625P	0.753		28.1	88	2.60
USA	T3658P	0.763		30.6	273	3.90
Spain	T3590P	0.692		32.1	177	3.37
USA	T3614P	0.746		33.6	137	3.67
Spain	T3591P	0.724		35.8	101	3.43

Table 2 : FTIR and SF indices calculated from spectral data measured for each coking coal. A:

Area, H : Height. For FTIR data, the subscript number of Area (e.g. A₃₀₅₀) represents the wavenumber (cm⁻¹) at the top of the spectral band, integrated from valley to valley. The subscript number of Height (e.g. H₁₆₀₀) represents the wavenumber (cm⁻¹) at the top of the band at which the height is measured. For SF data, the two subscript numbers represent the area band limits (nm), used to measure the absolute value of the fluorescence emission. These indices and their significance have been well described by Kister *et al.*¹⁴

Indices calculated from :	From FTIR spectra							From SF spectra	
	H ARO A ₃₀₅₀ / A ₂₉₂₀	W H ₂₉₂₀ / H ₂₈₅₅	BA H ₁₃₈₀ / H ₁₄₄₀	ACI H ₁₆₀₀ / (H ₁₄₄₀ + H ₁₄₄₀)	FA (H ₂₉₂₀ +H ₂₈₅₀)/ (H ₁₆₀₀ +H ₂₉₂₀ + H ₂₈₅₀)	SSI A ₈₆₄ / A ₈₆₄₊₇₄₃	AH A ₈₆₄₋₇₄₃ / A ₂₉₂₀	A2/A1 A ₄₆₀₋₃₇₀ / A ₃₇₀₋₃₀₀	A3/A1 A ₅₈₀₋₄₆₀ / A ₃₇₀₋₃₀₀
T3631H	0.142	1.675	0.807	0.586	0.472	0.186	0.941	3.46	0.936
T3637H	0.108	1.695	0.850	0.511	0.504	0.201	0.811	2.85	0.667
T3622H	0.113	1.646	0.826	0.577	0.481	0.204	0.809	2.44	0.600
T3639H	0.176	1.733	0.799	0.533	0.504	0.185	0.919	2.62	0.568
T3595H	0.163	1.684	0.771	0.573	0.475	0.214	0.917	2.98	0.832
T3625H	0.113	1.692	0.807	0.519	0.491	0.182	0.863	2.55	0.604
T3658H	0.102	1.800	0.791	0.596	0.491	0.170	0.697	2.49	0.528
T3590H	0.115	1.708	0.767	0.523	0.517	0.170	0.734	2.73	0.767
T3614H	0.107	1.681	0.796	0.568	0.474	0.194	0.772	2.19	0.444
T3591H	0.091	1.667	0.779	0.566	0.457	0.154	0.713	1.82	0.308
T3631P	0.149	1.565	0.796	0.623	0.444	0.226	1.033	3.61	0.819
T3637P	0.177	1.671	0.852	0.572	0.430	0.178	1.174	2.41	0.394
T3622P	0.114	1.613	0.839	0.582	0.429	0.180	1.051	2.29	0.408
T3639P	0.190	1.657	0.806	0.550	0.474	0.173	1.044	2.92	0.571
T3595P	0.164	1.597	0.788	0.586	0.480	0.207	0.930	3.13	0.727
T3625P	0.122	1.619	0.816	0.501	0.447	0.208	0.958	2.48	0.482
T3658P	0.118	1.706	0.801	0.585	0.462	0.201	0.778	2.32	0.374
T3590P	0.126	1.626	0.804	0.543	0.465	0.166	0.809	3.20	0.706
T3614P	0.097	1.627	0.771	0.577	0.457	0.171	0.848	2.70	0.472
T3591P	0.101	1.623	0.773	0.576	0.425	0.136	0.788	1.87	0.318

Table 3 : Results of the first PCA performed from wet coal data. 9 variables (V.M., ARNU, REFLECT, H ARO, AH, BA, W, FA and A3/A1) were selected for 10 coking coals. 3 factors were extracted and explain 87 % of the total variance.

Factor	Eigenvalues	% total variance	Cumul. Eigenval.	Cumul. % total variance
1	4.4	49	4.4	49
2	2.1	23	6.5	72
3	1.3	15	7.8	87

Table 4 : Results of the second PCA performed from wet and preheated coal data. 9 variables (V.M., GI, H ARO, ACI, AH, BA, W, FA and SSI) were selected for 20 coking coals. 3 factors were extracted and explain 83 % of the total variance.

Factor	Eigenvalues	% total variance	Cumul. Eigenval.	Cumul. % total variance
1	4.0	44	4.0	44
2	2.3	26	6.3	70
3	1.2	14	7.5	83

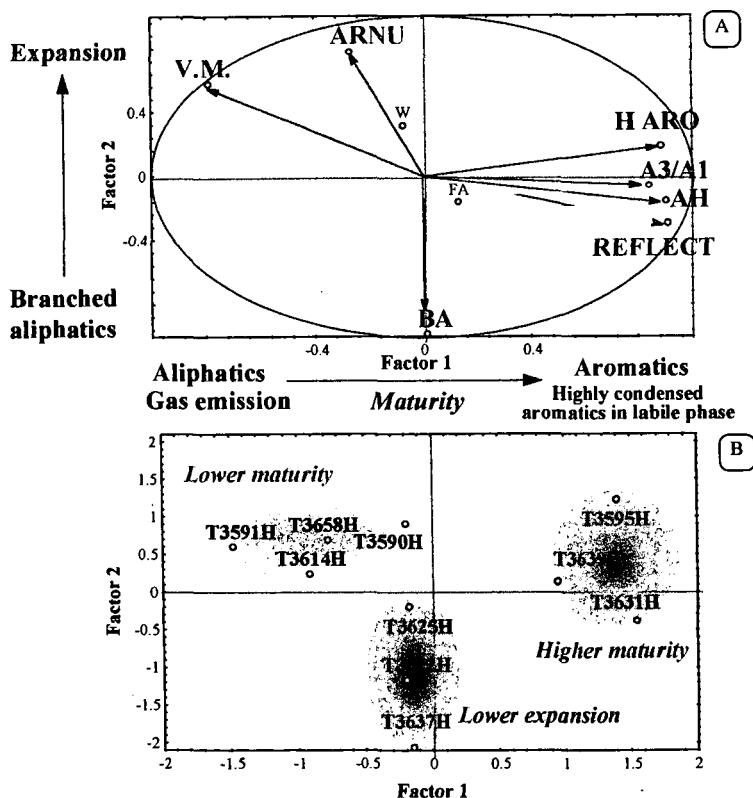


Figure 1 : First PCA performed from 9 variables (spectroscopic indices, petrography and plastic properties) and 10 wet coking coals. This PCA explains 87% of the total variance with 3 factors. This figure shows the 2 first Principal Components (PC) and visualizes the main chemical and physical characteristics of wet coals. A/ R-mode factor analysis : initial variables. B/ Q-mode factor analysis : coking coals.

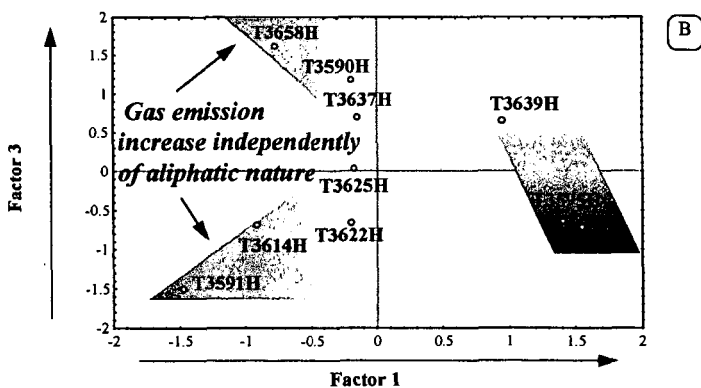
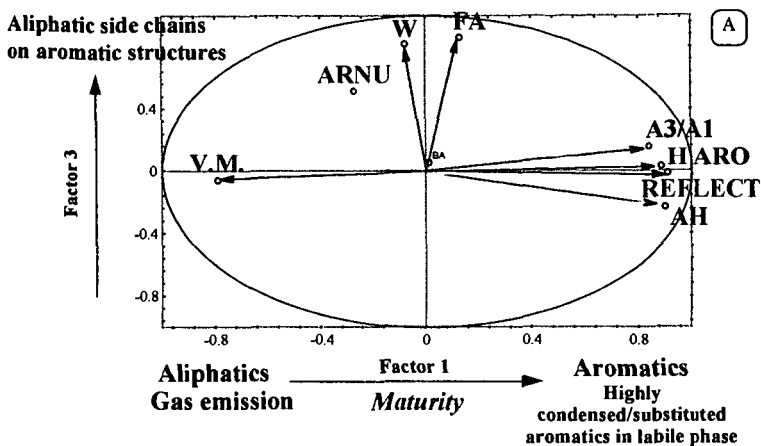


Figure 2 : First PCA performed from 9 variables (spectroscopic indices, petrography and plastic properties) and 10 wet coking coals. This PCA explains 87% of the total variance with 3 factors. This figure shows the 2nd and the 3rd Principal Components (PC). A/ R-mode factor analysis : initial variables. B/ Q-mode factor analysis : coking coals.

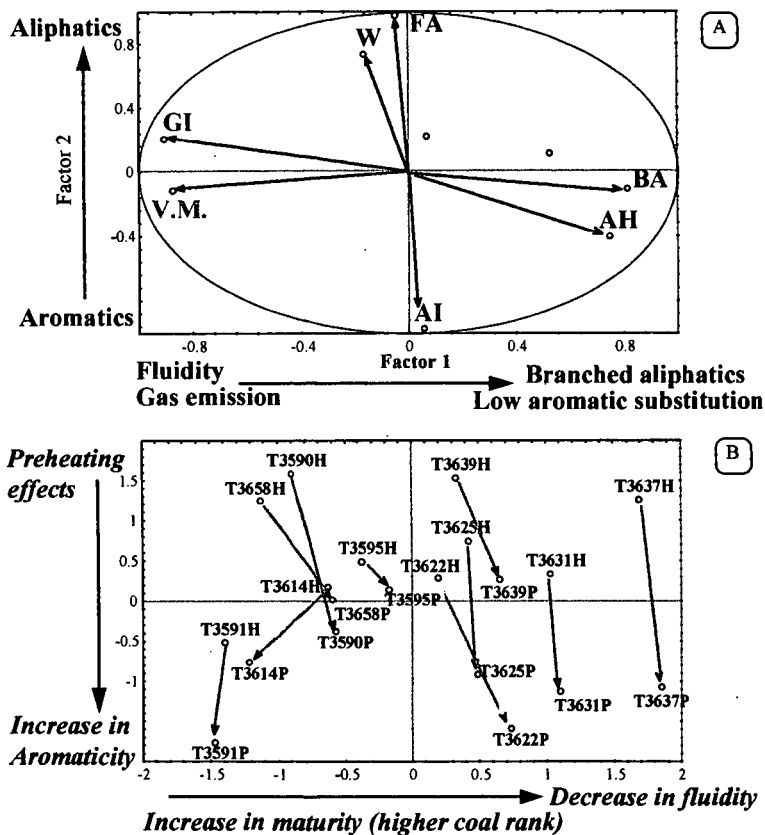


Figure 3 : Comparison between plastic property and structural characteristics changes during preheating. Second PCA performed from 9 variables (spectroscopic indices, petrography and plastic properties) and 20 (wet and preheated) coking coals. This PCA explains 83% of the total variance with 3 factors. This figure shows the 1st and the 2nd Principal Components (PC). A/ R-mode factor analysis : initial variables. B/ Q-mode factor analysis : coking coals.

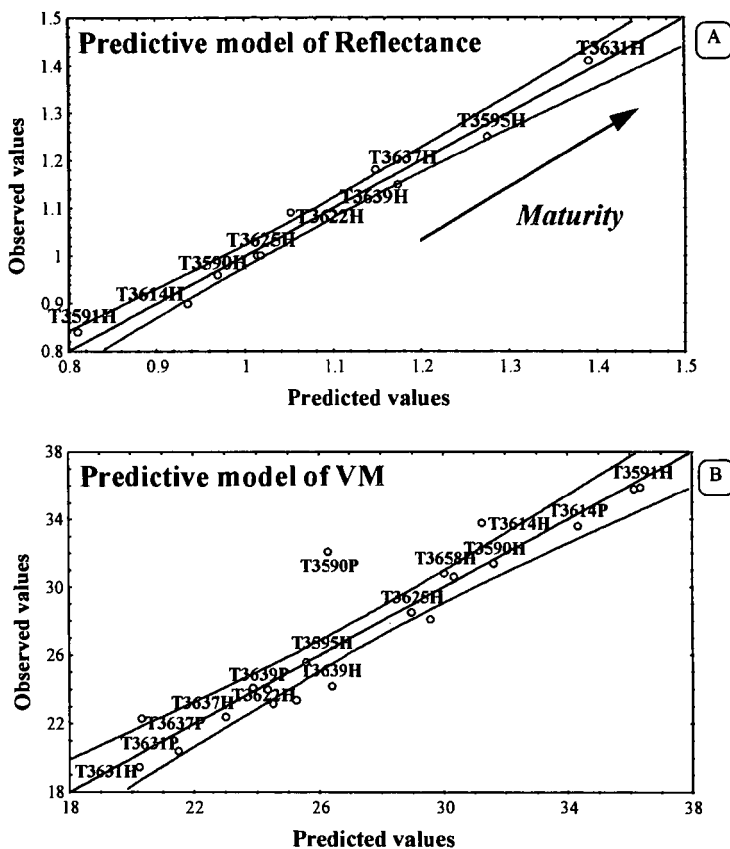


Figure 5: Prediction of the petrography properties of the coking coals by Multivariate Linear Regression (MLR) A/ Predictive model of Reflectance from wet coal data (3 indices, 10 coals, Adjusted $R^2 = 0.96$, $F(3,6)=79$, $p<0.00003$, Std. Error of estimate: 0.03). B/ Predictive model of Volatile Matter Amount (VM) from wet and preheated coal data (4 indices, 20 coals, Adjusted $R^2 = 0.85$, $F(4,15)=28$, $p<0.00000$, Std. Error of estimate: 2).

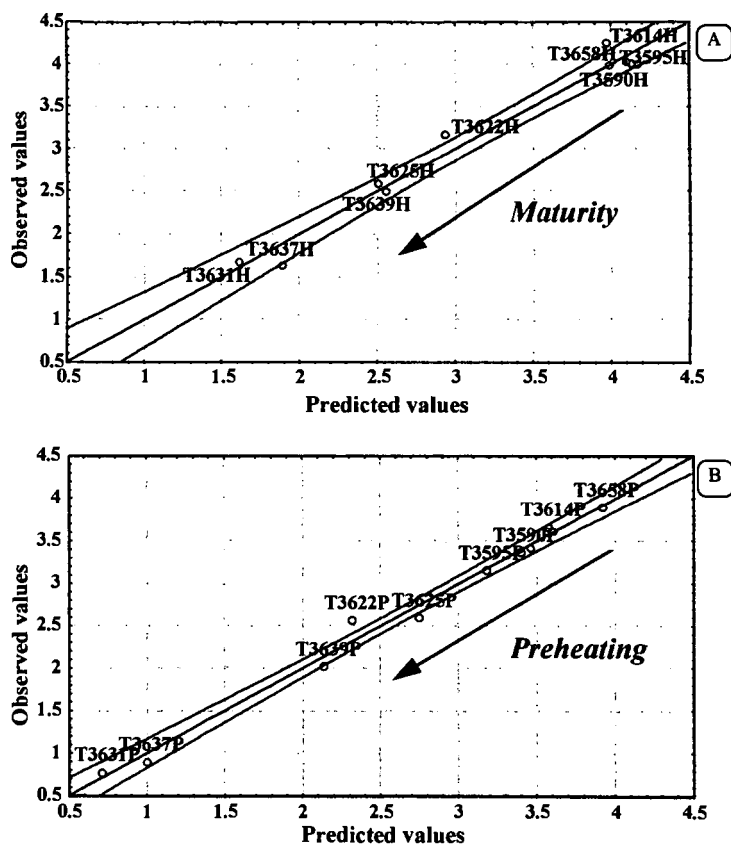


Figure 6: Prediction of the plastic properties of the coking coals by Multivariate Linear Regression (MLR) A/ Predictive model of Gieseler Index (GI from wet coal data (4 indices, 10 coals, Adjusted $R^2 = 0.95$, $F(5,4)=44$, $p<0.0004$, Std. Error of estimate: 0.2). B/ Predictive model of GI from preheated coal data (5 indices, 10 coals, Adjusted $R^2 = 0.97$, $F(5,4)=70$, $p<0.0006$, Std. Error of estimate: 0.2).

EVALUATION OF ORGANIC MATTER REACTIVITY DURING PYROLYSIS BY MICRO-FTIR TECHNIQUES.

O. Ruau, P. Landais, R. Michels and E. Langlois

CNRS-CREGU, BP 23, 54501 Vandoeuvre lès Nancy Cedex, France.

Keywords: FTIR microspectroscopy, Organic matter, Polar compounds.

INTRODUCTION

The understanding of the processes occurring, as well as reacting mechanisms taking place during organic matter maturation and oil generation is of major importance in order to develop models to be used in petroleum exploration. The artificial maturation of organic matter performed in laboratory allows to reduce the duration of experiments and to control the reacting medium components (water, polar compounds, gas, generated hydrocarbons).

Infrared spectroscopy is a well adapted technique for the characterization of organic matter as far as it provides information on the chemical composition (aliphatic, aromatic and oxygenated bearing functions) and functional distribution (hydroxyls, carbonyls, carboxyls, ethers, etc.). Coupling an infrared spectrometer with an adapted microscope and using a diamond anvil compression cell allows to facilitate the sample preparation, to improve the quality of the recorded spectra and to use quantitatively the data obtained from the solid residues. In this study, the reactivity of solid residues and polar compounds related to several artificial maturation series has been investigated thanks to these new transmission micro-FTIR techniques.

ANALYTICAL

Samples: The samples used in this study are polars and solid residues from (i) confined pyrolysis series of an immature vitrinite rich coal from the Mahakam delta¹, (ii) confined and hydrous pyrolysis of Woodford shale², (iii) confined pyrolysis of Kimmeridge Clay³.

Transmission Infrared microspectroscopy: The sample preparation protocols of the solid residues and the polar compounds have been previously described in Ruau et al.⁴ (1996). The micro FTIR analysis were performed on a Nicolet System 800 coupled with a Nic-Plan microscope which was fitted with a 250 μm narrow band MCT detector cooled to 77K. The standard analytical conditions were X 15 infrared objective, 40-60 μm diameter infrared spot, 32 to 128 scans, spectral resolution of 4 cm^{-1} , gain = 4.

Flash pyrolysis - Gas chromatography - Mass spectrometry (Py-GC-MS): Solid residues and polar compounds have been investigated by Py-GC-MS using a CDS 2000 pyrolyser coupled with a HP 5890AII chromatogram and a HP 5972A mass spectrometer. Flash pyrolysis was performed at 620°C for 20 s.

RESULTS AND DISCUSSION

Reactivity of the chloroform extracted solid residue. A detailed inspection of the transmission micro-infrared spectra of the solid residues recorded thanks to the diamond anvil compression cell reveals the presence of interference fringes between 1900 and 2800 cm^{-1} that were used for the sample thickness determination⁴. Thus the band integrations were normalized to a common sample thickness (e.g. 30 μm). This operation allowed the intensity variations of a given band to be directly investigated. The variations of the ν aromatic C-H (3000-3100 cm^{-1}), ν aliphatic C-H (2800-3000 cm^{-1}) and ν C=O (1650-1800 cm^{-1}) normalized to a sample thickness of 30 μm are reported in figure 1.

This figure shows that the removal of the C=O functions and aliphatic moieties follows a rather linear trend while the increase of aromatic CH is rather exponential. Special care was also addressed to the distribution of C=O bearing functions. The results show that the 1650 cm^{-1}

¹ band assigned to conjugated C=O first increases during maturation until 320°C and then decreases. This observation strongly suggests a functional rearrangement within the C=O groups during the maturation. This type of approach facilitates the survey of the chemical modifications the solid residues may undergo during maturation.

Transmission micro-FTIR was applied for the characterization of the fractions issued from other maturation series and particularly to successive pyrolysis-extraction experiments⁵. The results showed that the behavior of the kerogen and the polar fractions (asphaltenes and resins) strongly depends on the presence (or absence) in the reacting medium of polars, hydrocarbons, and generated water. Furthermore, a specific reactivity of polars was clearly evidenced.

Reactivity of the polar compounds. Spectra of the polar compounds can be recorded on the same micro-FTIR system than that used for the solid residues. Then, a comparison of the chemical composition of these fractions as well as their specific evolution along the maturation profile can be made. Spectra reported on figure 2 evidence major differences between the solid and the polar compounds. Generally, the solid residue spectra show more intense bands related to aromatic groups (C=C and aromatic CH), while the spectra of the polar compounds exhibit marked aliphatic CH as well as OH and C=O bands.

Data extracted from the integration of polar compounds and solid residue micro-infrared spectra provide the chemical evolution of each fraction during the artificial maturation. If the solid residue react as previously described with a removal of aliphatic moieties and oxygenated bearing functions, the polar compounds behaviour is somewhat different. The evolution of the aliphaticity of the resins suggests that resins may be considered as the kerogen relay for the hydrocarbon generation. On the other hand, it is shown that asphaltenes undergo an oxidation contemporaneous to the removal of the generated water and to the production of hydrocarbons. These results suggest that asphaltenes are implied in complex and specific reactions during maturation that should be taken into account for the modelisation of the hydrocarbon generation process.

Combined use of micro FTIR and Py-GC-MS techniques. Micro-FTIR results were also compared to PyGCMS data obtained on the solid residues and the polar fractions. This approach provides a molecular insight that is particularly suitable for the elucidation of problems related to organic matter reactivity. Parameters obtained by these two different approaches allow the same process to be evidenced by two ways. The aromatization of the solid residue during the artificial maturation can be depicted by the increase of the ratio aromatic compounds/sum of the compounds (Py-GC-MS) as well as the ratio aromatic CH/Sum of the integrated bands (μ -IRTF) (Figure 3). On the other hand, these two techniques can be used in a complementary way to explain for example the evolution the methyl/methylenes distribution of the aliphatic fraction of the asphaltenes.

CONCLUSIONS

Transmission infrared microspectroscopy appears as an improved routine technique to rapidly record high quality spectra of organic matter. The sample preparation as well as the amounts of studied material can be significantly reduced. The quality of the micro-infrared spectra facilitates the qualitative overview of the gross chemical variations occurring during laboratory simulated maturation of organic matter. Thanks to the diamond anvil compression cell, the micro-infrared spectra of solid residues can be used in a quantitative way in order to follow the chemical evolution of organic matter during maturation. The versatility of the micro-FTIR technique allows the characterization of the polar compounds of the same maturation serie. Then the specific reactivity of each fraction can be underlined. Coupling this technique with the PyGCMS provides converging and/or complementary informations on the chemical composition of the studied samples as well as their reactivity.

REFERENCES

- 1 Landais P. and Gérard L. *Int. J. Coal Geol.* **1996**, 30, 4, 285.

- 2 Michels R., Landais P., Torkelson B.E. and Philp R.P. *Geochim. Cosmochim. Acta.* **1995**, *59*, 1589-1604.
- 3 Michels R., Langlois E., Ruau O., Mansuy L., Elie M. and Landais P. *Energy and Fuels.* **1996**, *10*, 39.
- 4 Ruau O., Landais P. and Gardette J.L. *Fuel*, **1996** Accepted.
- 5 Mansuy L., Landais P. and Ruau O. *Energy and Fuels.* **1995**, *9*, 691.

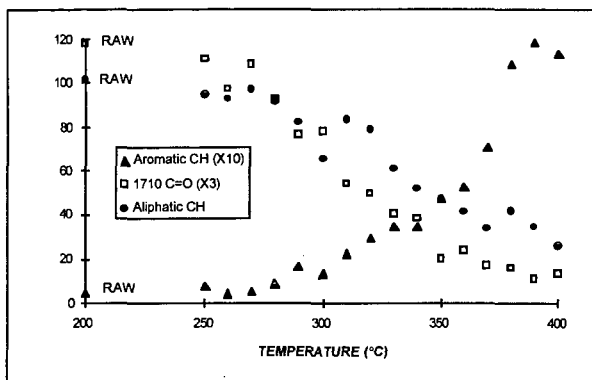


Figure 1 : Evolution of aliphatic C-H ($2800-3000\text{ cm}^{-1}$) integrated area, aromatic C-H ($3000-3100\text{ cm}^{-1}$) integrated area (X 10) and C=O (1710 cm^{-1}) integrated area (X 3), both normalized to a sample thickness of $30\text{ }\mu\text{m}$, with increasing pyrolysis temperature (Confined pyrolysis of a Mahakam coal).

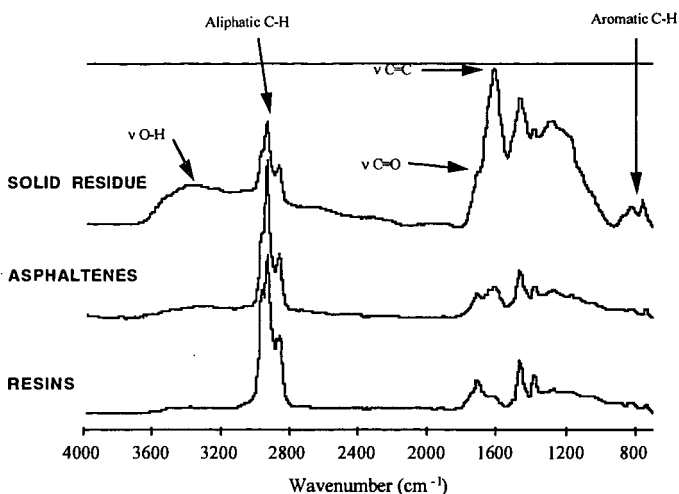


Figure 2 : Comparison between asphaltenes, resins and solid residue obtained by the confined pyrolysis of a Mahakam coal (250°C, 24 h).

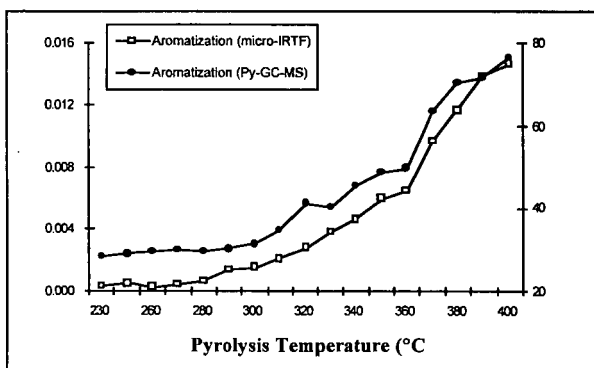


Figure 3 : Aromatization of the solid residue along the artificial maturation evidenced by micro-IRTF and Py-GC-MS data (Mahakam coal).

THE CHEMICAL STRUCTURE AND THERMAL MODIFICATION OF LOW RANK COALS

Masakatsu Nomura, Takeshi Muratani, Satoru Murata, Shigeru Maeda,* and Akira O-ki*

Department of Applied Chemistry, Faculty of Engineering, Osaka University,
2-1 Yamada-oka, Suita, Osaka 565, Japan

*Department of Applied Chemistry, Faculty of Engineering, Kagoshima University
1-21-40 Ko-rimoto, Kagoshima 890, Japan

Keywords: Chemical structure, Low rank coal, Thermal modification

ABSTRACT

For two brown coals, Australian Yallourn and Indonesian South Banko coals, measurements of SPE/MAS ^{13}C NMR spectra, OH group analysis according to acetylation and silylation, Curie-point pyrolysis, and analysis of CO_2H groups were conducted. Based on these results, plausible chemical structural units of above brown coals were proposed and submitted to CAMD calculation to understand the interactive forces of units. On the other hand, these brown coals were found to show the higher reactivities when modified in the presence of water at around 350°C . The enhancement of these reactivities was examined by supposing what kinds of reaction take place based on the unit chemical structures proposed here and the interactive forces of these units.

INTRODUCTION

In 1987, Hüttinger *et al.* had proposed molecular structure of a typical Rheinische brown coal based on elemental analysis, pyrolysis experiments, and extrapolation of literature data and successfully explained the pyrolysis and hydrolysis data of brown coals [1]. In 1992, Hatcher *et al.* [2] and Nomura *et al.* [3] proposed chemical structural units of subbituminous coal and bituminous coal by applying solid state NMR data in the combination with conventional data such as from pyrolysis and quantification of functional groups, respectively. Nomura *et al.* pointed out the importance of the following subjects concerning the elucidation of chemical structure of coals: (1) more precise and quantitative evaluation of chemical bonds connecting aromatic rings; (2) search for analysis of constituents without accompanying coke formation; (3) reliable evaluation of real molecular weight of extracts; (4) research on qualitative and quantitative evaluation of non-bonding interactions in coal organic matrix; (5) study on the quantitativity of CP/MAS ^{13}C NMR spectroscopy. These mean that, around 1992, these subjects remain uncertain. As for subject (1), Stock *et al.* proposed RuO_4 oxidation method as the means to evaluate aliphatic substituents on aromatic rings [4]. In this RuO_4 oxidation, aliphatic portion connecting aromatic rings could be converted to aliphatic dicarboxylic acid derivatives; This experiments showed that there were many different kinds of aliphatic dicarboxylic acids even though their amounts are so small. [5] However, the presence and amount of methylene bridge could not be detected and quantified by this method because resulting malonic acid is unstable under the reaction conditions. Solid state ^{13}C NMR is still powerful means, suggesting the distribution of different kinds of carbon contained in coal organic matrix. At present time, SPE/MAS ^{13}C NMR spectra are believed to be more quantitative than CP/MAS ^{13}C NMR spectra [6]. The advantage of using ^{13}C NMR spectral data for the evaluation of unit chemical structure is that the spectra can reflect the whole coal. As for subject (2) and (3) there has been no rapid progress since 1992. As for subject (4), much attention are paid to non-bonding interactions in coal organic matrix, however, there is few method to evaluate them in the quantitative way. Authors are now thinking that non-bonding interaction might be very important to consider the reaction taking place at the early stage of heating process. In that sense, the unit chemical structures proposed here and their non-bonding interactions based on CAMD study give us the meaningful clues to understand the reactivities of brown coal at the early stage of liquefaction and thermally modified brown coal.

EXPERIMENTAL SECTION

Coal samples. Two brown coals, Australian Yallourn and Indonesian South Banko coals (YL and SB), were employed in this study, which were provided by the courtesy of Nippon Brown Coal Liquefaction Co. Ltd. These were ground under 200 mesh and dried at 40°C in vacuo before use. Elemental analysis of these two coals are listed in Table 1.

Consecutive extraction and acetylation of THF-insoluble materials. A dried and pulverized coal samples (5 g) was put in a Soxhlet thimble, then being set in the apparatus. Extraction with tetrahydrofuran (THF) was conducted for one day. The resulting residue (THF-insoluble materials) was submitted to acetylation by refluxing in a solvent mixture of acetic anhydride-pyridine, then the acetylated samples being extracted again with THF. These procedures were repeated for three times (scheme of this extraction is shown in Figure 1). The resulting products were submitted to structural analysis according to GPC.

Solid state ^{13}C NMR measurement. CP/MAS and SPE/MAS ^{13}C NMR spectra were recorded on a Chemmagentic CMX-300 with MAS method (10 kHz). For the measurement, about 150 mg of coal were packed in a vessel (5 mm diameter x 8 mm long). The experimental conditions employed were as follows; 200 s pulse delay, 45° pulse width, and ca. 400 scan number. Deconvolution of the spectra was conducted on an Apple Macintosh computer with a commercial NMR data processing software, MacAlice (ver 2.0, JEOL Datum). The resulting spectra were divided into twelve Gaussian curves. For two brown coals, Yallourn and South Banko coals, SPE/MAS (Figure 2) and CP/MAS gave following f_a values, 0.77 and 0.66, and 0.60 and 0.54, respectively.

Diffuse reflectance FT/IR (DR/FT/IR) measurement. Dried sample (50 mg) and KBr (450 mg) were mixed and ground by using an agate mortar. The resulting mixture was further

dried at 90 °C for 10 h in vacuo. FT/IR spectrum of the sample was recorded on a JEOL JIR-AQS20M with diffuse reflectance method (128 scans). Data acquisition and analysis were also carried out on the computer equipped with the spectrometer.

Gel permeation chromatography.

Analysis by gel permeation chromatography (GPC) was conducted by using a Shimadzu LC-10AS liquid chromatographic system with a Shodex KF-80M GPC column (30 cm, stationary phase: polystyrene gel) and a Shimadzu SPD-10A ultraviolet detector ($\lambda=270$ nm). An extract (6.3 mg) was dissolved in 10 mL of DMF, 20 μ L of which was injected to the LC system, when either DMF or lithium bromide-containing DMF was used as eluant. Calibration of retention time-molecular weight relationships was conducted by using 14 kinds of standard polystyrene samples and benzene.

Quantitative analysis of OH groups.

(1) Acetylation Method: According to the method reported by Blom *et al.* [7], analysis of OH groups was conducted. (2) Silylation method: According to the Friedman's method [8], we conducted silylation of coal. The details are referred in his paper.

Quantitative analysis of CO₂H groups.

These analysis were conducted by ion exchange with sodium acetate [9] and ion exchange with sodium bicarbonate.

Computer simulation.

Computer simulation was conducted on an Apple Power Macintosh personal computer by using a commercial CAMD (computer-aided molecular design) software, CAChe (CAChe Scientific, Inc., Version 3.7). At first, the structure proposed in this study was input to a computer, then, molecular mechanics (MM) calculation being conducted till root-mean-square error becomes less than 0.1 kcal/mol. Then, molecular dynamics (MD) calculation was carried out for 10 ps to avoid local minimum structure. From this calculation, intermediary conformers were output every 0.1 ps. Consequently, 100 conformers could be obtained, among which five lowest energy conformers were selected and submitted to MM calculation. At last, we selected the conformer having the lowest energy and defined it as the most reliable conformer.

RESULTS AND DISCUSSION

Construction of unit chemical structures of coals.

As we cited already in the experimental section, SPE/MAS ¹³C NMR spectra were found to give higher *fa* value than CP/MAS ¹³C NMR spectra. From the carbon distribution based on ¹³C NMR, we found that α -methylene is more abundant in SB coal compared with YL coal, this indicating that SB coal is rich in methylene, polymethylene and more alkyl groups substituted on aromatic rings.

In brown coal, due to the presence of a lot of hydroxyl groups, hydrogen bonding interaction should be more significant, especially in constructing three dimensionally complicated structure. First of all, we extracted two brown coals by THF under refluxing conditions. In order to obtain much more amount of coal extract, we conducted consecutive extraction of residue after acetylation. As we pointed out the importance of molecular weight information of coal, we submitted these extracts to GPC where we found the following interesting phenomena: the use of LiBr-containing DMF as eluant, seems to be able to dissociate extracts due to breakage of hydrogen bonding. This experiments informed us of the molecular weight of the extract being around from 4000 to 6000 with the maximum peaks. Based on these findings, we firstly assumed average molecular weight of brown coals around 5000. Basing on elemental analysis and above molecular weight, following molecules are proposed for each coal; YL C₂₇₉H₂₃₅N₂O₈₇ and SB C₂₉₇H₂₇₀N₄O₆₇. From *fa* values based on SPE/MAS ¹³C NMR spectra, numbers of aromatic carbons in each unit are decided to be 215 for YL and 196 for SB. As for the constituents of aromatics in coal, Curie-point pyrolysis data (at 670 °C for 3 s) were referred to. As for the aliphatic portion, we have to conduct RuO₄ oxidation even if at present time it is not quantitative, however, in this study we consulted the NMR data, which can give the distribution of different carbons in coal. By referring to the data on oxygen-containing groups, we tentatively proposed following numbers of each group in unit structure: YL -OH 31, -CO₂H 12, -CO₂Ar 6, -O- 38; SB -OH 28, -CO₂H 7, -CO₂Ar 4, -O- 29. Table 1 is the comparison of calculated values of models and observed values of original coals. These two models are submitted to computer simulation (Figure 3).

Computer simulation.

Computer simulation of model structures was carried out using molecular mechanics and molecular dynamics in order to obtain the most stable conformation. Each energy term for the coal structural model for brown coals is listed in Table 2. As for potential energy, YL model was found to show a higher negative value than that of SB model, indicating that YL coal is more stable than SB coal. It is interesting to note that non-covalent bonding energy is higher negative value than covalent bonding energy in both models. Higher negative non-covalent bonding energy with YL model is indicating that hydrogen bonding is prevailing in this coal. We conducted liquefaction of two brown coals here and found that SB coal showed higher reactivity than YL coal (higher hexane soluble portion). At the early stage of liquefaction, OH groups are believed to play important roles in the reactivity. If we consider that YL coal, due to its high contribution of intermolecular hydrogen bonding, tends to conduct condensation reaction to a great extent, the resulting lower yield of lighter fraction could be explained in a reasonable way. In Japan, low rank coal is now processed around 350 °C in the presence of water using an 8.4/day pilot plant, the resultant coals showing good reactivities. The reactivity of modified coal could be rationalized in this context. We are now conducting the measurements of FT/IR, swelling index and SEM observation of these modified brown coals to examine their properties.

REFERENCES

- 1) Hüttinger, K. J.; Michenfelder, A. W. *Fuel* **1987**, *66*, 1164.
- 2) Hatcher, P. G.; Faulon, J.-L.; Wenzel, K. A.; Cody, G. D. *Energy Fuels* **1992**, *6*, 813.
- 3) Nomura, M.; Matsubayashi, K.; Ida, T.; Murata, S. *Fuel Process. Technol.* **1992**, *31*, 169.
- 4) Stock, L. M.; Tse, K. T. *Fuel* **1983**, *62*, 974.
- 5) Murata, S.; Uesaka, K.; Inoue, H.; Nomura, M. *Energy Fuels* **1994**, *8*, 1379.
- 6) Franz, J. A.; Garcia, R.; Linehan, J. C.; Love, G. D.; Snape, C. E. *Energy Fuels* **1992**, *6*, 598.
- 7) Blom, L.; Edelhausen, L.; van Krevelen, D. W. *Fuel* **1957**, *36*, 135.
- 8) Friedman, S.; Kaufman, M. L.; Steiner, W. A.; Wender, I. *Fuel* **1961**, *40*, 33.
- 9) Funasaka, W. ed. *Nenryo Bunseki Siken-hou*, Nankodo, 1968, p.75.

Table 1. Comparison of calculated values of model and observed values of original coal with two brown coals

Yallourn coal						South Banko coal					
Ultimate analysis (wt%, daf)						Ultimate analysis (wt%, daf)					
C	H	N	S	O		C	H	N	S	O	
67.1	4.7	0.6	0	27.6		70.7	5.8	1.1	0.7	21.7	
(66.9)	(4.7)	(0.5)	(0.3)	(27.6)		(71.3)	(5.4)	(1.2)	(0.5)	(21.6)	
Oxygen-containing functional groups (wt%, daf)						Oxygen-containing functional groups (wt%, daf)					
-OH 10.37 (10.46)						-OH 9.32 (9.44)					
-COOH 10.60 (11.02)						-COOH 6.39 (5.94)					
Carbon aromaticity, fa						Carbon aromaticity, fa					
0.78 (0.77)						0.69 (0.66)					

Table 2. Each energy term for the coal structural model for brown coals

Energy term	YL	SB
total	-732.977	-604.096
Covalent bonding	-227.871	-158.460
stretch	11.432	11.972
angle	129.207	154.672
stretch bend	0.188	0.355
dihedral	-370.588	-326.310
improp torsion	1.888	0.850
Non-covalent bonding	-505.106	-445.636
electrostatics	-69.811	-42.020
van der waals	33.205	-14.801
hydrogen bond	-468.500	-388.815

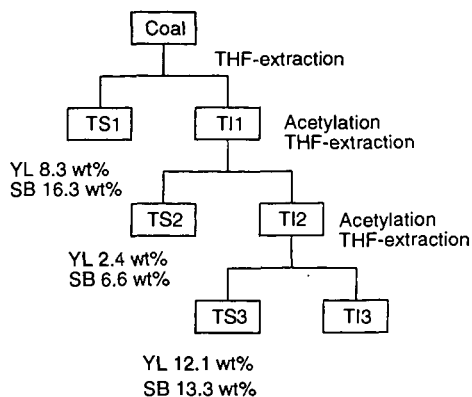


Figure 1. Procedure for consecutive extraction of two brown coals.

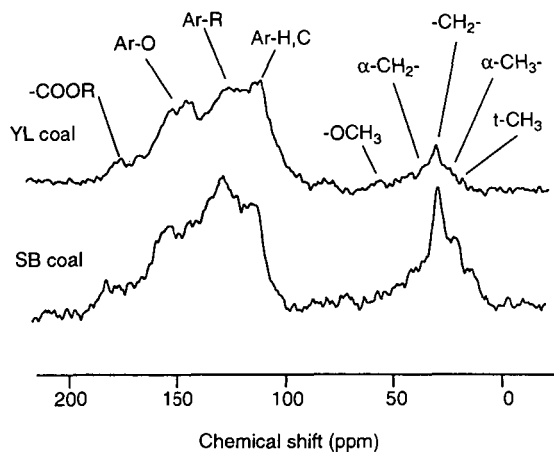


Figure 2. SPE/MAS ¹³C NMR of two brown coals

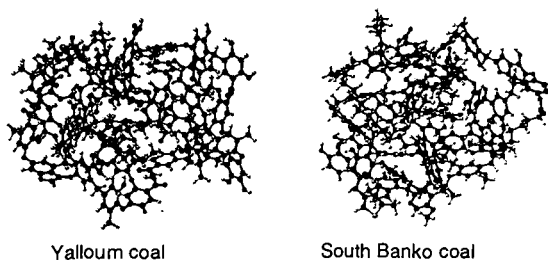


Figure 3. 3D skeeth for the model structures proposed

THE ROLE OF ETHER OXYGEN AND CARBON DOUBLE BONDS AS LINKAGES DURING THE DISSOLUTION OF KEROGENS WITH PERCHLORIC ACID

Chris W. McGowan, Kenneth J. Oestreich, Gloria Elayne Hood
Department of Chemistry, Tennessee Technological University, Cookeville, TN 38501

Deborah J. Davidson,
Chemical Technology Division, Oak Ridge National Laboratory, Oak Ridge, TN 37831

and Richard Markuszewski
Institute of Gas Technology, 1700 S. Mount Prospect Road, Des Plaines, IL 60018

Keywords: Kerogen Structure, Perchloric Acid, Coal, Oil Shale

INTRODUCTION

In 1966, Fester and Robinson (1) reported that 53.5 percent of the oxygen in the kerogen of Green River oil shale was present in ether functional groups. Fester and Robinson had measured the amount of carboxyl, ester, amide, carbonyl and hydroxyl oxygen with a series of chemical analyses. Ether oxygen was determined by measuring the difference between the sum of the amounts of each of the above functional groups and the total oxygen present. The idea that ether oxygen was a "linkage" between kerogen units was further supported by McGowan et. al. (2) in 1985. In that work, a kerogen concentrate of Green River oil shale was oxidized with solutions of perchloric acid having various concentrations and subsequent boiling points. The kerogen concentrate dissolved at boiling points between 160°C and 170°C. The dissolution range of the kerogen concentrate was compared to the dissolution ranges for a series of model compounds. The compounds (and linkages tested) were polyethylene (carbon-carbon single bonds), graphite (aromatic carbon bonds), nylon (amide bonds) and polyethylene oxide (ether bonds). Polyesters, which readily hydrolyze and dissolve in cold perchloric, were not tested. Polyethylene required a boiling point of 202°C before dissolution occurred (the polymer caught on fire inside the reaction vessel). Boiling, concentrated perchloric at 202°C did not dissolve graphite to any appreciable extent. Nylon also resisted dissolution but a portion was dissolved at 202°C. Both the dissolution ranges and infrared spectra supported the conclusion that ether oxygen was being attacked during the dissolution of the kerogen concentrate from Green River oil shale.

Several additional kerogens have also been reacted with perchloric acid. These include a kerogen concentrate from Chattanooga Shale (3); and two bituminous coals, an Illinois #6 coal and a Charming Creek coal from New Zealand (4). The kerogen concentrate from Chattanooga Shale and the Illinois #6 coal dissolved in boiling point ranges similar to the kerogen of Green River oil shale. However the Charming Creek coal dissolved between 180°C and 190°C. Since the dissolution range for the Charming Creek coal fell outside the range of that for ether oxygen, several additional model compounds were tested. In this paper, the results for the dissolution of three new model compounds and two new kerogens is reported. The new model compounds are poly-m-phenoxyene (aromatic ether bonds), polybutadiene and a polybutadiene with 20 percent styrene copolymer (carbon double bonds). The new kerogens were a Mequinenza lignite from Spain and an Elizabethtown anthracite from Pennsylvania.

When cold or dilute, perchloric acid is a non-oxidizing acid. When hot and concentrated, perchloric acid is powerful oxidizing agent. The apparent reduction potential rises slowly as the concentration and subsequent boiling point increases. The apparent potential rises from 0.8 V at a boiling point of 130°C to 2.0 V at 203°C, the boiling point of the concentrated acid (5).

EXPERIMENTAL

The poly-m-phenoxyene and the polybutadiene-styrene copolymer were obtained from Dr. Vernon Allen of the Department of Chemistry at Tennessee Technological University. The polybutadiene was a Taktene 220 sample obtained from Ms. Pat Kolda at the Bayer Plant in Orange, TX. The Mequinenza coal was obtained by the Ames Laboratory at Iowa State University and was originally supplied by Dr. Sabino Moinelo at the Instituto Nacional del Carbon in Spain. The Elizabethtown coal was supplied by Dr. John Riley of the Department of Chemistry at Western Kentucky University. The ultimate analysis of the Mequinenza coal was determined by Analytical Services at Ames Lab and that of the Elizabethtown coal by the Materials Characterization Center at Western Kentucky. The results appear in Table 1. For comparison purposes, the ultimate analyses for the Illinois #6 and Charming Creek coals as determined at Ames Lab also appear in Table 1.

Table 1. Ultimate Analysis of Coal Samples (on a dry basis)

coal (rank)	carbon	hydrogen	nitrogen	oxygen	sulfur
Elizabethville (anthracite)	83.7	2.30	1.10	0.57	0.74
Charming Creek (bitum.)	79.0	5.32	0.95	9.26	5.44
Illinois#6 (bituminous)	62.2	4.13	1.60	15.5	3.45
Mequinenza (lignite)	53.7	3.94	0.85	9.55	9.93

Safety Note

All reactions were performed under total reflux, in a perchloric acid hood and behind an explosion shield. Generally 1-g samples were reacted at low boiling points and 0.1-g samples at 203°C. An explosion occurred when a 0.2 g sample of the polybutadiene was reacted with concentrated perchloric acid having a boiling point of 203°C. A stopper in the side-arm of the reaction flask was shattered and glass was embedded in the plastic explosion shield. When the sample size was reduced to 0.1 g, no explosion occurred.

Procedure

All reactions were performed in a modified Bethge Apparatus designed to maintain a constant boiling solution. The apparatus has been described by McGowan and Diehl (6). A perchloric acid solution was added to the Bethge Apparatus and the boiling point was adjusted to the desired value. Approximately 50 mL of solution remained. After cooling, a weighed 1.0-g or 0.1-g sample of the model compound or coal was added. The reaction vessel was heated for 1.5 hrs. After cooling, the reaction mixture was filtered. The residue was dried and weighed, and the amount of undissolved material was determined.

RESULTS AND DISCUSSION

The results for the dissolution of the Mequinenza lignite and the Elizabethville anthracite appear in Fig. 1. The lignite sample dissolved between 160°C and 170°C. This dissolution was almost identical to that of the kerogen of Green River oil shale and Illinois #6 coal. The hypothesis that ether linkages were being attacked in this coal was consistent with the high oxygen content and low rank of this coal. The anthracite sample appeared to have two dissolution ranges. One from 170°C to 180°C and a second from 190°C to 203°C. The first range was similar to the dissolution of the kerogen of Chattanooga Shale and was within the range of the dissolution of ethers. The second range was consistent with the dissolution polyethylene and, as presented below, with polybutadiene. The results for the dissolution of poly-m-phenoxyene, polybutadiene and the polybutadiene-styrene copolymer appear in Fig. 2. Poly-m-phenoxyene gained weight at all boiling points up to 190°C. The infrared spectra of the undissolved material indicated that the polymer had been extensively chlorinated. This chlorination process had been previously observed for other aromatic compounds (7). The polymer was almost completely dissolved at 203°C. The polybutadiene-styrene copolymer displayed a spike in the percent undissolved material at a boiling point of 185°C before dissolving at 190°C. The infrared spectra of the residue from the 185°C reaction also indicated extensive chlorination of the polymer. Although the polybutadiene-styrene copolymer may be a better model compound to represent the kerogen of a coal, it was decided that a polymer containing a double bond without aromatic rings should also be investigated. Polybutadiene displayed a smaller spike in the amount of undissolved material at a boiling point of 190°C. The sample was partially dissolved at 195°C and completely dissolved at 203°C. There was a kinetic problem with the dissolution of the polybutadiene. Even though the polymer was cut up into small particles, they would coalesce into large particles when heated with the perchloric acid solutions; thereby decreasing the surface area of the polymer. When a 1.0-g sample of the polymer was reacted at 195°C, the percent undissolved material was 125 percent. When a 0.1-g sample was reacted at 196°C, the percent undissolved material was 68 percent. Even with this problem, the dissolution of polybutadiene was similar to the dissolution of polyethylene and the second dissolution range of the Elizabethville coal. These results showed that the presence of aromatic rings in a polybutadiene polymer resulted in the double bonds being more susceptible to oxidation by perchloric acid. This could result from just the presence of the rings or could be enhanced by the chlorination of the rings. Since the presence of aromatic rings in the kerogens of coals is highly probable and if double bonds in the kerogen were being attacked, then the dissolution of the kerogen should be similar to the dissolution of the polybutadiene-styrene copolymer.

As the molar ratio of oxygen to carbon decreased, the range of boiling points of perchloric acid solutions, over which dissolution occurred, increased. This is shown in Table 2. The obvious implication would be that as the oxygen content dropped, the available ether linkages that could be attacked would also drop. Each increase in the dissolution range was accompanied by an order of magnitude decrease in the oxygen to carbon ratio.

Table 2. Molar O/C Ratios and Dissolution Ranges for Coal Samples

coal	molar O/C	Dissolution Range (b.p HClO ₄)
Elizabethville	0.0051	190°C to 203°C (2nd)
Charming Creek	0.088	180°C to 190°C
Illinois #6	0.19	160°C to 170°C
Mequinzenza	0.14	160°C to 170°C

CONCLUSIONS

The results of this study indicated that kerogens which contain a large amount of oxygen were dissolved by boiling perchloric acid solutions when ether oxygen was attacked. However, as the oxygen content of the kerogens decreased other bonds had to be attacked in order to dissolve the kerogen. For the kerogens in this study, the Illinois #6 coal, the Mequinzenza coal and the Green River oil shale were dissolved when aliphatic ether oxygen was attacked. The Charming Creek coal dissolved when carbon double bonds were attacked. The Chattanooga Shale and the first dissolution range for the Elizabethville coal were probably the result of the attack on aliphatic ethers, although the possibility of an aromatic-aliphatic ether has not been eliminated. The second dissolution range for the Elizabethville coal was probably due to the oxidation of carbon single bonds although the oxidation of carbon double bonds was a possibility.

LITERATURE CITED

1. Fester, J.I. and W.E. Robinson, Adv. Chem. Ser. (55), 22, 1966.
2. McGowan, C.W., R.C. Pearce and H. Diehl, Fuel Process. Technol., 10, 195, 1985.
3. Stanton, B.J., R.M. Morris and C.W. McGowan, Fuel Process. Technol., 29, 85, 1991.
4. McGowan, C.W. and R. Markuszewski, Fuel Process. Technol., 17, 29, 1987.
5. Smith, G.F., Analyst, 80, 16, 1955.
6. McGowan, C.W. and H. Diehl, Fuel Process. Technol., 10, 169, 1985.
7. McGowan, C.W., K. Q. Cates and R. Markuszewski, Prepr. Pap. -Am. Chem. Soc., Div. Fuel Chem., 33, 225, 1988.

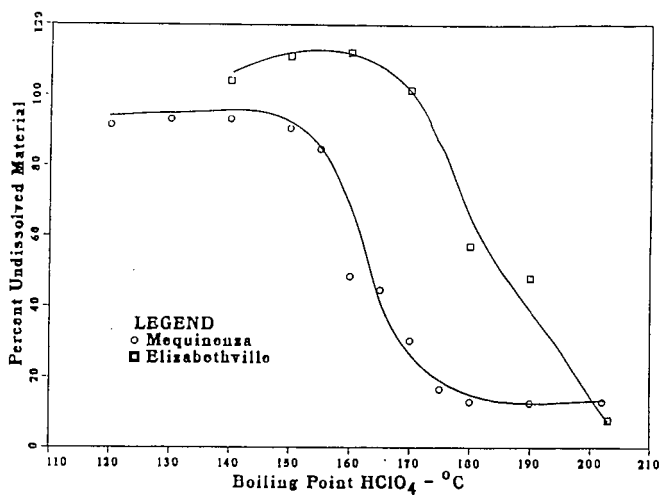


Figure 1. Dissolution Curves for the Mequinensa and Elizabethtown Coals

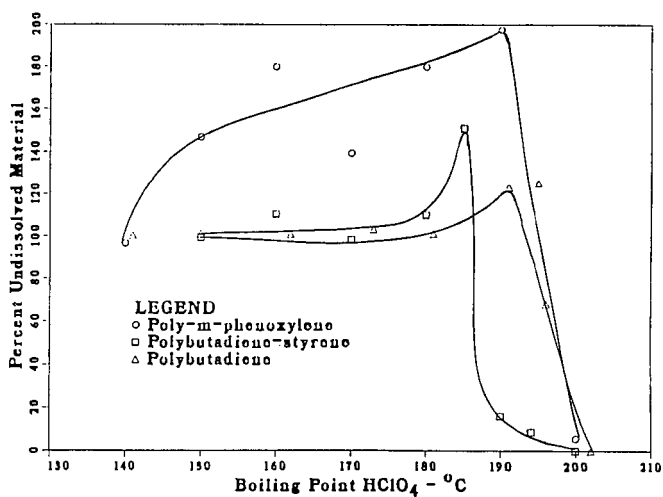


Figure 2. Dissolution Curves for the Model Polymers

SOLUBILIZATION OF AN AUSTRALIAN BROWN COAL OXIDIZED WITH HYDROGEN PEROXIDE IN CONVENTIONALLY USED SOLVENTS AT ROOM TEMPERATURE

Kazuhiro MAE, Taisuke MAKI, Jun ARAKI, and Kouichi MIURA

Department of Chemical Engineering, Kyoto University, Sakyo-ku, Kyoto 606-01, Japan

Key words: Extraction of brown coal, Liquid Oxidation of coal, Methanol based binary solvents

INTRODUCTION

It is very important to develop effective methods for utilizing low rank coals such as brown coal and lignite, which are most abundant fossil resources. One of the inherent drawbacks for utilizing the coal lies in the difficulty of handling such as transportation and storage. To overcome the drawback, several methods for fluidifying the coal have been proposed. Preparation of coal-water mixture (CWM) is one of such methods, but low rank coals are not suitable for CWM preparation, because they have lots of hydrophilic functional groups such as -COOH and -OH. Liquefaction is another means to fluidify the low rank coals, but it is a technology of the next generation. Therefore, it would be very profitable if some practical methods which are suitable to fluidify low rank coals are developed. The authors have focused on the extraction of low rank coals in conventionally used solvents as one of such methods.

Extraction and swelling of coals by various solvents have been performed for decades as a means to examine the coal structure, but only the coals of a certain rank could be extracted by 70 wt% or so with a special solvent.¹ The extraction yield of low rank coals has been less than 10 wt% even in a highly polar solvents.¹⁻⁴ To increase the extraction yield of lower rank coals, several pretreatments of coals were performed.^{5,6} However, the treatments under severe conditions and/or in highly polar solvents are required to extract the low rank coal to a large extent. On the other hand, several researchers^{7,8} found that the coal was largely swollen with alcohol based binary solvents. We have recently found that an Australian brown coal oxidized by H_2O_2 for 2 h at 60°C was extracted at room temperature by 84 wt% in a mixed solvent of methanol and 1-methylnaphthalene.⁹

In this paper we performed the extraction of low rank coals modified by several oxidation methods in several combinations of low molecule alcohol and non-polar solvent systems to examine the validity of the proposed method. Then, the extraction mechanism of coal in the mixed solvents of methanol and non-polar solvents was discussed from the viewpoint of the change in coal structure and solvent properties.

EXPERIMENTAL

Oxidation of coal

Three kinds of coals, an Australian brown coal (Morwell, MW), a Canadian brown coal (Highvale, HV), and a Japanese sub-bituminous coal (Taiheiyō, TC) were used as raw coals. The coals were ground into fine particles of less than 74 μm , and dried in vacuo at 110°C for 24 h before use. The oxidation of the coals was performed as follows: 2 g of coal particles were mixed with 20 ml of 30% aqueous hydrogen peroxide (HPO) in a flask. After treating the mixture for 2 h in a water bath kept at a constant temperature of 25 °C or 60 °C, an excess of cold water was added to the flask to terminate the oxidation. The oxidized coals were filtrated and evacuated at 60 °C for 24 h. To examine the effect of the oxidation method, MW coal was also oxidized in an air stream at 250 °C (AO) using a thermogravimetric analyzer until no weight change was detected. The oxidized coals were abbreviated to (oxidation method)(treatment temperature).(treatment time(h)) such as HPO60.2 and AO250.2, etc.

Extraction of oxidized coals

The raw coals and the oxidized coals were extracted at 25°C by alcohol based binary solvents of m-xylene (m-X), 1-methylnaphthalene (1MN), 2-methylnaphthalene (2MN), benzene (B), and tetralin (Tet), phenol (Ph) and tetrahydrofuran (THF). Methanol (MeOH), ethanol (EtOH), 1-propanol (PrOH) and 2-methyl-1-propanol (2M1P) were used as the alcohols. The extraction was performed as follows: 200mg of the oxidized coal were mixed with 6 ml of solvent and were kept for 4h at 25 °C under the irradiation of an ultrasonic wave. After centrifuging the mixture and removing the extract, 6 ml of fresh solvent were added to the residue and the mixture was treated for 3 h at 25 °C under the irradiation of the ultrasonic wave. This centrifugation-extraction cycle was repeated three times. The residue was then washed with an excess of methanol and evacuated for 24 h at 60 °C. The extraction yield was calculated from the weight difference between the oxidized coal and the residue, and was represented on the basis of dry oxidized coal.

Characterization of the oxidized coal and their extracts

The change in coal properties through the oxidation was examined from the ultimate analysis, ^{13}C -n.m.r., TG-MS, and F.T.i.r. measurements. The extracts were dissolved by

DMF, then they were served to molecular weight distribution measurement using the GPC technique.

RESULTS AND DISCUSSION

Changes in coal properties through oxidation

The oxidation pretreatment was performed to change the coal into more extractable structure. However, the oxidation inevitably causes the loss of coal itself. Therefore, the degree of the oxidation must be optimized by taking into account both the extraction yield and the loss of coal. Then, the changes in the solid yield and the loss of coal through the oxidation were examined first. Table 1 lists the carbon conversions of the coals to solid, CO_2 , and water soluble organics through the oxidation. The ultimate analyses, and the atomic H/C and O/C values for the oxidized coals are also listed. When MW coal was oxidized by air for 4 h at 250°C (AO250.4), the carbon conversion to CO_2 was 0.20, indicating that 20% of carbon is lost through the oxidation. On the other hand, when MW coal was oxidized by H_2O_2 for 2 h at 60°C (HPO60.2), the carbon conversion to CO_2 was 0.04 and the carbon conversion to the water-soluble organics was 0.17. Since the water soluble organics can be recovered and utilized,¹⁰ the loss of coal was judged to be only 4% for HPO60.2 prepared from MW. This was also the case for HPO60.2 prepared from HV. These results indicate that the H_2O_2 pretreatment is superior to the air oxidation pretreatment from the viewpoint of minimizing the carbon loss through the pretreatment.

Then, the changes in coal properties through the H_2O_2 oxidation were examined in more detail from several analyses for MW coal. Both the H/C and O/C values of the solid increased through the oxidation for HPO25.4 and HPO60.2 as listed in Table 1. We have shown that both hydrogen and oxygen are introduced into the coal, mainly as the form of OH groups, through the H_2O_2 oxidation in a previous paper.¹⁰ This is peculiar to the H_2O_2 oxidation. Comparing the F.T.i.r. spectra between the oxidized coals and the raw coal, the amount of carboxyl groups was found to increase by the oxidation. Table 2 gives the carbon distributions estimated by the ^{13}C -n.m.r. for the raw coal and the HPO60.2. The amounts of COOH , O-aliphatic (including R-OH), and aliphatic carbon increased, on the contrary, the f_a value and the amounts of Ar-OH (including Ar-O-Ar), substituted and protonated carbons decreased through the H_2O_2 oxidation. From the above results, it was judged that the H_2O_2 oxidation decomposed a part of the covalent bondings such as Ar-OH, Ar-O-Ar, and substituted carbon, then produced -COOH , C-O-C and R-OH in the coal.

Extraction of oxidized coal by methanol and 1-methylnaphthalene mixtures

The solvent extraction of lower rank coals is believed to be affected by non-covalent interactions such as hydrogen bonding as well as the solubilization ability of the solvent.¹¹ The HPO60.2 prepared from MW coal was supposed to be enriched with the hydrogen bonding sites because of the increase in the oxygen functional groups. Therefore, the solvent suitable to extract the HPO60.2 must have the potential for breaking the hydrogen bonding in addition to the potential for dissolving the coal.

Methanol is known not to dissolve but swell coal to a large extent. On the other hand, two aromatic ring compounds such as naphthalene, naphthalene derivatives, etc., which are recovered from the coal conversion process, are judged to be solvents suitable to dissolve the coal, judging from the solubility parameter. This suggests that the extraction of the HPO60.2 is expected to be enhanced by using mixed solvents of methanol and aromatic compounds.

Figure 1 shows the extraction yields of the raw coal and the oxidized coals in a mixed solvent of methanol and 1-methylnaphthalene (1MN/MeOH). The abscissa in Fig.1 represents the volume fraction of methanol (f_v) in the mixed solvent. The extraction yield of the raw coal was 10 wt% at most at around $f_v=0.6$, and the extraction yield of HPO25.4 was slightly larger than that of the raw coal. The HPO60.2 was extracted little in pure methanol or pure 1MN, but was extracted to a large extent in the mixed solvent of $f_v=0.2$ to 0.9. At $f_v=0.56$ the extraction yield reached up to 84 wt% on the oxidized coal basis, which is comparable to the extraction yield in DMF. The value of 84 wt% on the oxidized coal basis corresponds to 66 wt% on the raw coal basis for HPO60.2. Even this value of the extraction yield is much larger than the values reported by now. If we add the water soluble organic acids recovered during the pretreatment to the extraction yield, the extraction yield reaches more than 80 wt% on the raw coal basis. The molecular weight distribution (number basis) of the 1MN/MeOH ($f_v=0.56$) extract of HPO60.2 ranged from 240 to 10000, and the average molecular weight was found to be 837.

Extraction of the oxidized coal by several mixtures of small molecule alcohols and solvents

Next, we examined the effect of the solvent type on the extraction of HPO60.2 prepared from MW. Figure 2 shows the extraction yields at 25°C in the mixed solvents of 1MN and several small molecule alcohols. The extraction yields in 1MN/EtOH, 1MN/PrOH were also as high as the extraction yields in 1MN/MeOH, but the maximum yield in 1MN/2M1P was

only 42 wt%. Since 2M1P has the largest molecule size of the alcohols tested, its penetration into the coal matrix would be retarded. Figure 3 shows the extraction yields of the HPO60.2 at 25 °C in the mixed solvents of MeOH and aromatic compounds. In 2MN/MeOH the HPO60.2 was also extracted to a large extent at $f_v=0.3$ to 0.9, and reached up to 80 wt% at $f_v=0.56$. However, in Xy/MeOH the HPO60.2 was extracted by only 33 wt% at maximum at $f_v=0.76$. This small extraction yield is probably due to less solubilization potential of m-xylene. On the other hand, the extraction yields of the HPO60.2 in the mixed solvents of methanol and THF or PhOH reached up to almost 80 wt% at $f_v=0.36$ in both binary solvents. The f_v value corresponding to the maximum extraction yield for these binary solvents was smaller than that in the mixed solvents of methanol and non-polar solvents.

Effect of coal type on the extractability of the oxidized coal

The H_2O_2 oxidation pretreatment was very effective to increase the solvent extraction yield for Morwell coal. To examine the effect of the H_2O_2 oxidation pretreatment for other coals, we extracted several coals oxidized by H_2O_2 for 2 h at 60 °C. Figure 4 compares the extraction yields of the oxidized coals in DMSO and 1MN/MeOH. The HPO60.2 prepared from MW coal was extracted more than 80 wt% in both DMSO and 1MN/MeOH as described above. For the HPO60.2 prepared from HV brown coal, the yield of DMSO-extract reached 82wt%, but the yield of 1MN/MeOH-extract was 48 wt%. For the HPO60.2 prepared from TC subbituminous coal, the extraction yields in 1MN/MeOH and DMSO were 30 wt% and 37wt%, respectively. The small extraction yield of TC coal was presumed to be due to a small extent of the oxidation. The solid yield through the H_2O_2 oxidation was 0.94 for TC as shown in Table 1. So, we oxidized the TC coal by H_2O_2 for 24h at 40 °C (HPO40.24) to increase the extent of oxidation. The solid yield through the oxidation was 80 wt%, whose value was almost same as that of HPO60.2 prepared from MW. The extraction yield of the HPO40.24 in DMSO increased up to 55 wt%, but not so large as that for the brown coals. These results suggest that the extraction yield of the coal oxidized by H_2O_2 in 1MN/MeOH is strongly dependent on coal type, and that the proposed method is more effective for lower rank coals.

Role of the binary solvent mixture on the extraction of the oxidized coal

The secondary interaction of brown coal is mainly due to hydrogen bonding and ionic force as reported by Nishioka.¹² Green et al.⁸ showed that the swelling ratio of coal increased in N-N-dimethylaniline and methanol mixture, and concluded that methanol could interact with the specific sites of the coal surface and break the hydrogen bonding. Lucht et al.¹³ and Suuberg et al.¹⁴ also claimed that methanol having a small molecule easily penetrated and swelled the coal to interact with the specific site of coal. Table 3 lists several properties of methanol, ethanol, DMF, DMSO, and pyridine. The values of relative dielectric constant for methanol and ethanol are as large as those for DMF and DMSO. The values of the hydrogen bond index summarized by van Krevelen¹⁵ and Guttman's ΔH for methanol and ethanol are larger than those for DMF, respectively. In addition methanol molecule is small and easy to penetrate into coal matrix as stated above. These discussion suggests that methanol well has a potential to break hydrogen bonding in coal.

Then the extraction mechanism of HPO60.2 prepared from MW in methanol based binary solvents was presumed as follows: Methanol disrupts the hydrogen bonding in the HPO60.2 and interacts with functional groups at first, then the penetration of aromatic compounds such as 1MN is enhanced. Since the aromatic compounds have the potential to solubilize the coal molecule interacting with methanol, the HPO60.2 could be extracted to a large extent. Then the solubilization of the methanol adducted coal may be regarded as the solubilization of the bituminous coal.

The regular solution theory may not be applied to the extraction of low rank coal,¹¹ but it seemed to be applicable to the extraction of the HPO60.2 in methanol based binary solvents, judging from the above discussion. Following the regular solution theory, the extraction yield is maximized when the solubility parameters of both coal and solvent are close together.¹⁵ Since the oxidized coal is adducted with methanol through its functional groups, the coal molecule would be enveloped by methanol molecules. Then, the solubility parameter of the HPO60.2 was calculated by taking into account the contribution of methanol adducted in terms of the following equation:¹⁶

$$\delta(\text{coal}) = \frac{7.0+63.5f_a+63.5(H/C)+106(O/C)+51.8(N+S/C)}{-10.9+12f_a+13.9(H/C)+5.5(O/C)-2.8((N+S)/C)} \quad (1)$$

Figure 5 shows the change in the solubility parameter of HPO60.2, $\delta(\text{HPO60.2})$, against the amount of methanol adducted. The $\delta(\text{HPO60.2})$ value decreased with the increase of the amount of methanol adducted. If it is assumed that methanol adducts with carboxyl groups first and then ArOH of HPO60.2, the $\delta(\text{HPO60.2})$ decreased from 13.1 to 11.5 first, and finally to 10.8 (cal/cm³)^{0.5} with the increase of the amount of methanol adducted.

The solubility parameter of the mixed solvent, δ , was calculated by ¹⁵

$$\delta^2 = \delta_d^2 + \delta_h^2 + \delta_p^2 \quad (2)$$

where δ_d , δ_h , and δ_p represent the solubility parameters deriving from dispersion forces, hydrogen bondings, and polar forces, respectively. The values of δ_d , δ_h , and δ_p are calculated from the values of pure solvents by

$$\delta_i^2 = x_1 \cdot \delta_{i1}^2 + (1 - x_1) \cdot \delta_{i2}^2 \quad (\delta_i: i = d, h, p) \quad (3)$$

where x_1 is the mole fraction of alcohol, and δ_{i1} and δ_{i2} are the solubility parameters of alcohol and nonpolar solvent, respectively.

Figure 6 shows the extraction yield of HPO60.2 at 25°C against the solubility parameter of the solvent calculated by eqs.(2) and (3). The δ (HPO60.2) value was assumed to change from 13.1 to 10.8 (cal/cm³)^{0.5} with the increase of the amount of methanol adducted as stated above. The extraction yield and the solubility parameter of the solvent correlated very well and the extraction yield reached a maximum at $\delta \approx 11.5$ (cal/cm³)^{0.5}. The value of 11.5 (cal/cm³)^{0.5} corresponded to the δ (HPO60.2) value calculated by assuming that methanol adducted with all carboxyl groups of HPO60.2. Thus the regular solution theory seemed to be applicable to the extraction of HPO60.2 with the alcohol based mixed solvent.

This supports the extraction mechanism mentioned above: Methanol and/or ethanol penetrate into the coal matrix easily, break the hydrogen bonding or ionic interaction in coal, and interact with the oxygen functional groups tightly. This facilitates the penetration of the binary solvent of non-polar solvent and alcohol. The macromolecules enveloped with alcohol will be easily extracted by the mixed solvent having strong solubilization potential. This may be speculative because the extraction behavior is also affected by the phase separation equilibrium among coal, binary solvent and extracts. We will examine the extraction behavior in more detail in future work. However, it is noteworthy that the regular solution theory hold unexpectedly for the extraction of the oxidized coal with alcohol based mixed solvents.

CONCLUSION

A new method was developed for extracting a great deal of brown coal at room temperature in conventionally used solvents. When an Australian brown coal, Morwell, was preoxidized with H₂O₂ for 2 h at 60 °C, the covalent bondings were partly decomposed and many carboxyl groups and C-O-C groups were formed. The oxidized coal was extracted in several alcohol based binary solvents. The maximum extraction yields of the oxidized coal surprisingly reached more than 80 wt% in the binary solvents of methanol/1-methylnaphthalene, ethanol/1-methylnaphthalene, methanol/2-methylnaphthalene, and methanol/phenol at an suitable alcohol fraction. The average molecular weight (number basis) of the extract was 837. The proposed extraction method will be useful to develop a new coal conversion method as well as to facilitate the transportation of coal.

ACKNOWLEDGMENT

The authors give sincere thanks to Drs. Tadashi Yoshida and Hideaki Sasaki of Hokkaido National Industrial Research Institute for the ¹³C-n.m.r. measurement of our samples. This work was financially supported by NEDO International Joint Research (Coal and Wastes as Oil Alternative Energy and Chemicals).

REFERENCES

1. Iino, M.; Takanohashi, T.; Ohsuga, H.; Toda, K.; *Fuel*, **1988**, 67, 1639-1645.
2. Pugmire, R.J.; Solum, M.S.; Bai, S.; Fletcher, T.H.; Woods, S.; Grant, D.M., *Prepr. ACS Fuel Div.* vol 38, No.2, **1993** 647-654.
3. Marzec, A.; Juzwa, M.; Betej, K.; Subkowiak M.; *Fuel Process. Techn.*, **1979**, 2, 35-44.
4. Morgan, D.L.; *Prepr. ACS Fuel Div.* vol 37, No.4, **1992** 1996-2001.
5. Nishioka, M.; *Fuel*, **70**, **1991** 1413-1419.
6. Winans, R.E.; McBeth, R.L.; Hunt, J.E.; *Prepr. ACS Fuel Div.* vol 38, No.2, **1993** 561-564.
7. Hombach, H.-P.; *Fuel*, **1980**, 59, 465-470.
8. Green, T.K.; Larsen J.W.; *Fuel*, **1984**, 63, 1538-1543.
9. Miura, K.; Mae, K.; Maki, T.; Araki, J.; *Chemistry Letters*, **1995** 909-910.
10. Miura, K.; Mae, K.; Okutsu, H.; Mizutani, N.; *Energy & Fuel* in press.
11. Larsen, J.W.; Schawver, S.; *Energy & Fuels*, **1990**, 4, 74-77.
12. Nishioka, M.; *Fuel*, **1993**, 72, 1719-1724.
13. Lucht, L.M.; Peppas, N.A.; *Erdol und Kohle erdgas*, **1987**, 40, 483-485.
14. Suubarg, E.M.; Otake, Y.; Lannngner, M.J.; Leung, K.T.; Milosavljevic, I.; *Energy & Fuels*, **1994**, 8, 1247-1262.
15. van Krevelen, D.W., *"Coal" 2nd edn*, Elsevier Scientific: New York, **1981**
16. Painter, P.C.; Graf, J.; Coleman, M.M.; *Energy & Fuels*, **1990**, 4, 379-384.

Table 1 Carbon conversions through the oxidation and ultimate analysis of oxidized coals.

Sample	Carbon conversion through oxidation			Ultimate analysis of the oxidized coal [wt%, daf]				mol ratio	
	acid	CO ₂	water soluble % organics	C	H	N	O (diff)	O/C [-]	H/C [-]
MW Raw	1.00	-	-	64.0	4.7	0.7	30.6	0.359	0.881
HPO25.4	0.96	0.02	0.02	61.6	4.6	0.6	33.2	0.404	0.896
HPO60.2	0.79	0.04	0.17	60.1	4.9	0.7	34.3	0.428	0.978
A0250.4	0.80	0.20	0	68.4	3.8	1.0	26.8	0.294	0.666
HV Raw	1.00	-	-	67.0	4.3	1.0	27.7	0.310	0.770
HPO60.2	0.70	0.08	0.22	63.0	4.3	1.0	31.7	0.377	0.819
TC Raw	1.00	-	-	72.4	5.6	1.4	20.6	0.213	0.928
HPO60.2	0.94	0.02	0.04	71.3	5.9	1.5	21.3	0.224	0.993
HPO40.24	0.80	0.07	0.13	71.2	7.3	1.1	20.4	0.208	1.199

Table 2 Carbon distributions of Morwell coal and the H₂O₂ oxidized coal determined by ¹³C-n.m.r

sample	Raw	HPO60.2
Aromatic carbon		
H-C=O, =C=O	1.81	3.83
COOH	5.90	8.54
Ar-OH	9.01	6.93
Substitute	12.66	9.32
Protonated	34.09	24.55
Aliphatic carbon		
C-O-C	0.94	6.01
O-Methyl	1.63	3.69
Aliphatic	27.22	28.40
Methyl	6.73	8.73
total	36.53	46.83
Structural parameter		
f _h [-]	0.63	0.53
M ₀ [kg/kmol]	156.4	196.8

Table 3 Comparison of the solvent properties between alcohol and polar solvents

Solvent	Methanol	Ethanol	DMF	DMSO	Py	1MN	Xy
Relative dielectric constant	32.6	24.3	36.7	46.7	12.3	-	-
Guttman ΔH (=DN*AN/100)	7.8	7.4	5.7	5.8	4.5	-	-
Hydrogen bond index	8.9	8.9	6.4	-	8.7	-	-
Solubility Parameter							
δ (cal/cm ³) ^{0.5}	14.6	13.0	12.2	13.1	10.7	10.4	8.4
δ _D (cal/cm ³) ^{0.5}	7.6	7.7	8.5	9.2	9.3	10.4	8.3
δ _P (cal/cm ³) ^{0.5}	10.9	9.6	5.5	5.0	2.9	0.0	0.5
δ _H (cal/cm ³) ^{0.5}	6.1	4.3	6.7	8.0	4.3	0.2	0.5

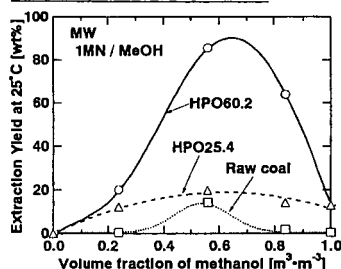


Figure 1 Extraction yield of the raw coal and H₂O₂ oxidized coal prepared from Morwell coal measured at 25°C in methanol and 1-methylnaphthalene mixture.

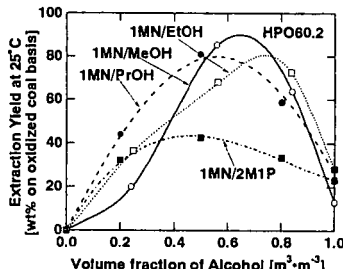


Figure 2 Extraction yield of the HPO60.2 prepared from Morwell coal measured at 25°C in the mixed solvents of several alcohols and 1-methylnaphthalene.

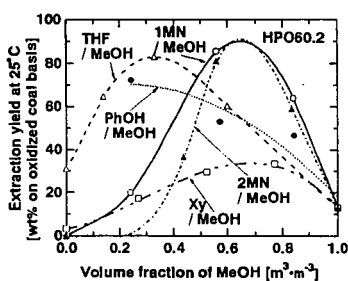


Figure 3 Extraction yield of the HPO60.2 prepared from Morwell coal measured at 25°C in various methanol based binary solvents.

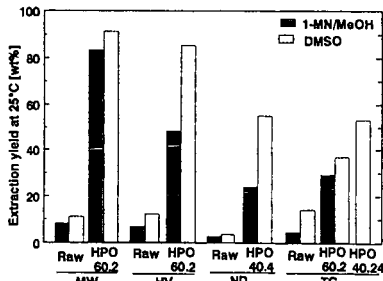


Figure 4 Effect of coal type on the extraction yield of the H₂O₂ oxidized coal.

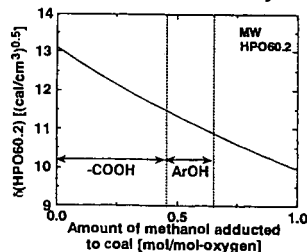


Figure 5 Change in the solubility parameter of HPO60.2 adducted with methanol.

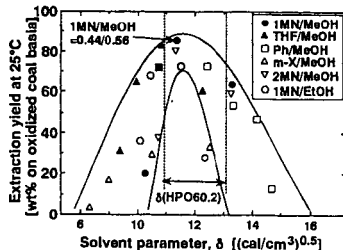


Figure 6 Relationship between the extraction yield of HPO60.2 prepared from Morwell coal and the solubility parameter of the solvent.

LINKAGES BETWEEN AROMATIC STRUCTURES IN THE ARGONNE PREMIUM COAL SAMPLES

Randall E. Winans and Nancy A. Tomczyk
Chemistry Division
Argonne National Laboratory
Argonne, IL 60439

Keywords: Argonne coals, structure lengths, mass spectrometry

ABSTRACT

The objective of this study is to elucidate the nature of the important linkages between aromatic clusters and variations of these links with coal rank. From studies using methods such as NMR and mass spectrometry, we have considerable information on the size and types of aromatic clusters in the Argonne coals. In this study, extracts, model polymers, extracted coals, and modified coals are examined by temperature resolved high resolution mass spectrometry. There is evidence that strong bond cleavage may be very important for volatile release in pyrolysis of higher rank coals.

INTRODUCTION

There is significant general information on the size and nature of the aromatic structures in coals, especially the Argonne Premium Coal Samples. A battery of methods have been used yielding global information by NMR,¹ XANES,^{2,3,4} XPS,⁵ and TGFTIR,^{6,7} and more specific class and size distribution by FIMS,⁸ HRMS,^{9,10} and LDMS.¹¹ The nature and distribution of the linkages between these clusters is less well defined but are obviously important in any thermal process. A large number of studies have been done on the pyrolysis of the Argonne coals, for example: modified Rock-Eval pyrolysis,¹² pyrolysis MS,^{8,12} and TGFTIR.^{6,7} It has been assumed that ethylene linkages are important in coals and that they are reactive. However, there is no direct evidence that this is the case.

EXPERIMENTAL

A complete description of the Argonne Premium Coal Samples is available via internet at: <http://www.anl.gov/PCS/pcshome.html> and has been published.¹³ Important analytical data on the coals and pyridine extracts¹¹ are shown in Table 1. Nitrogen values are fairly constant between 1.3-1.7 N/100 carbons.

Desorption high resolution mass spectra are taken on a 3-sector MS-50 either in electron impact or chemical ionization mode. Samples are heated from 200 to 700 °C at 200 °C/min on a probe directly in the source. The chemical ionization gas used was iso-butane. A Diels-Alder adduct of maleic anhydride and perdeuteroanthracene is used as an internal standard. Precise mass measurements are averaged from scans over the entire temperature range. Formulae are assigned and the data sorted via a procedure developed in this program. Only formulae that fit within ± 3.5 millimass units are considered.

Table A- 1. Selected Analysis and Yields for the Argonne Premium Coal Samples.

Sample #		Name	%C	Per 100 Carbons					Pyridine Solubles Yield (w%)
				H	S	O			
a	b	c							
8	Beulah-Zap	74.1	80	0.4	21	31	7.7	18	
2	Wyodak-Anderson	76.0	86	0.2	18	22	7.3	29	
3	Illinois #6	80.7	77	1.2	13	10	5.0	29	
6	Blind Canyon	81.3	86	0.2	11	12	7.4	25	
4	Pittsburgh	85.0	77	0.4	8	9	6.0	24	
7	Lewiston-Stockton	85.5	76	0.3	9	10	6.7	17	
1	Upper Freeport	88.1	66	0.3	7	8	6.4	28	
5	Pocahontas #3	91.8	59	0.2	2	4	3.7	3	

a - Coal

b - Extract

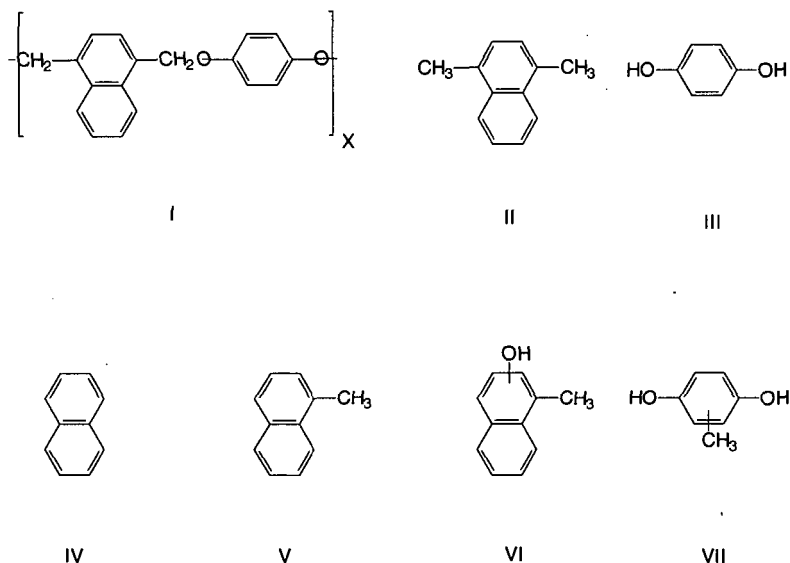
c - Furans and Ethers

High resolution mass spectrometry data can be sorted by both heteroatom content and by hydrogen deficiency which is also termed double bond equivalents and is related to z-number. From hydrogen deficiency, the size of aromatic clusters can be estimated.

RESULTS AND DISCUSSION

In absolute numbers of oxygens per 100 carbon atoms determined by HRMS, the furans plus ethers are relatively constant compared to the total oxygen in the extracts as is shown in Table 1. This would suggest that the influence of these types of structures are relatively important and constant across all ranks for vitrinite rich coals.

Because of these results, we decided to reinvestigate the reactivity of a model polymer with ether links. DCIMS results were examined since ions observed are the result of thermal fragmentation and not fragmentation in the source of the spectrometer. From the mass spectra recorded as a function of temperature a series of products were observed and are shown in Scheme 1 along with the polymer (I).¹⁴



Scheme 1

Strong bond cleavages occur at higher temperatures which would yield naphthalene (IV) and methyl naphthalene, and especially with the rearranged polymer resulting in VI and VII. For example, the naphthalene yield, which only can be formed from cleavage of strong bonds, is maximum at 500 °C. In contrast, dihydroxybenzene ($m/z = 110$) and dimethylnaphthalene peak at 300 °C. In Figure 1a, the temperature profile for dihydroxybenzene is compared between the polymer and the Illinois coal (APCS 3) extract. The coal yields below 400 °C are very small and maximize between 400-500 °C which would suggest that the bonding is not via oxygen-methylene linkages as is the case for the polymer. Ring methylated dihydrobenzene (VII) results from rearrangement of the polymer followed by cleavage. It is probably represented in the second peak for $m/z = 124$ at ~475 °C (see Figure 1b). The Illinois bituminous coal has a maximum at this temperature and several at even higher temperatures. While the low rank subbituminous coal is very broad and has a maximum at even a higher temperature; this broad type of distribution was also observed for phenol in lignite pyrolysis.¹² The oxygen functionality is likely to be undergoing some secondary reactions prior to release from the macromolecular matrix.

Burnham, et al.¹² using PyMS noticed greater high temperature tails for small unsubstituted aromatics compared to corresponding methyl derivatives for the higher rank coals. They suggested that this may be due to increased breaking of Ar-Ar bonds. We observed in the high rank coals that

larger aromatics are released in greater quantities at high temperature compared to lower temperature while substituted aromatics tend to be more abundant at lower temperature. In Figure 1c, we observed this effect for pyrene/fluoranthene ($m/z=202$) compared to C_2 -pyrene ($m/z=230$) for the Pocahontas extract. In the lower rank Pittsburgh seam coal (Figure 1d), the unsubstituted pyrene which can only be released by strong bond breaking, is still more abundant at high temperatures, but in addition, the alkylated aromatic is also released at higher temperatures.

CONCLUSIONS

The evidence suggests the strong bond breaking in pyrolysis is significant in higher rank coals and could play a role in the lower rank coal pyrolysis. We are examining methods to better quantitate the extent of these types of cleavages in coal pyrolysis.

ACKNOWLEDGMENTS

This work was performed under the auspices of the Office of Basic Energy Sciences, Division of Chemical Sciences, U.S. Department of Energy, under contract number W-31-109-ENG-38.

REFERENCES

1. T. H. Fletcher, S. Bai, R. J. Pugmire, M. S. Solum, S. Wood, and D. M. Grant, *Energy Fuels* **7**, 734 (1993).
2. G. N. George, M. L. Gorbaty, S. R. Kelemen, and M. Sansone, *Energy Fuels* **5**, 93 (1991).
3. G. P. Huffman, S. Mitra, F. E. Huggins, N. Shah, S. Vaidya, and F. Lu, *Energy Fuels* **5**, 574 (1991).
4. S. Mitra-Kirtley, O. C. Mullins, J. Branthaver, J. Van Elp, and S. P. Cramer, *Prepr., Div. Fuel Chem., ACS* **38**, 756 (1993).
5. S. R. Kelemen, M. L. Gorbaty, and P. J. Kwiatek, *Energy Fuels* **8**, 896 (1994).
6. R. Bassilakis, Y. Zhao, P. R. Solomon, and M. A. Serio, *Energy Fuels* **7**, 710 (1993).
7. P. R. Solomon, M. A. Serio, R. M. Carangelo, and R. Bassilakis, *Energy Fuels* **4**, 319 (1990).
8. N. Simmleit, H.-R. Schulten, Y. Yan, and H. L. C. Meuzelaar, "Thermochemical Analysis of U.S. Argonne Premium Coal Samples by Time-Resolved Pyrolysis FIMS," in *Advances in Coal Spectroscopy*, H. L. C. Meuzelaar (ed.), Plenum Press, New York, 1992, 295.
9. R. E. Winans, Y. Kim, J. E. Hunt, and R. L. McBeth, *Proceedings, 1995 International Conference on Coal Science, Oviedo, Spain* (1995), 87.
10. R. E. Winans, "Mass Spectrometric Studies of Coals and Coal Macerals," in *Advances in Coal Spectroscopy*, H. L. C. Meuzelaar (ed.), Plenum Press, New York, 1992, 255.
11. J. E. Hunt and R. E. Winans, *Proceedings, 1995 International Conference on Coal Science, Oviedo, Spain* (1995), 319.
12. A. K. Burnham, M. S. Oh, and R. W. Crawford, *Energy Fuels* **3**, 42 (1989).
13. K. S. Vorres, *Energy Fuels* **4**, 420 (1990).
14. T. G. Squires, B. F. Smith, R. E. Winans, R. G. Scott, and R. Hayatsu, *Proceedings, 1983 International Conference on Coal Science, Pittsburgh, PA* (1983), 292.

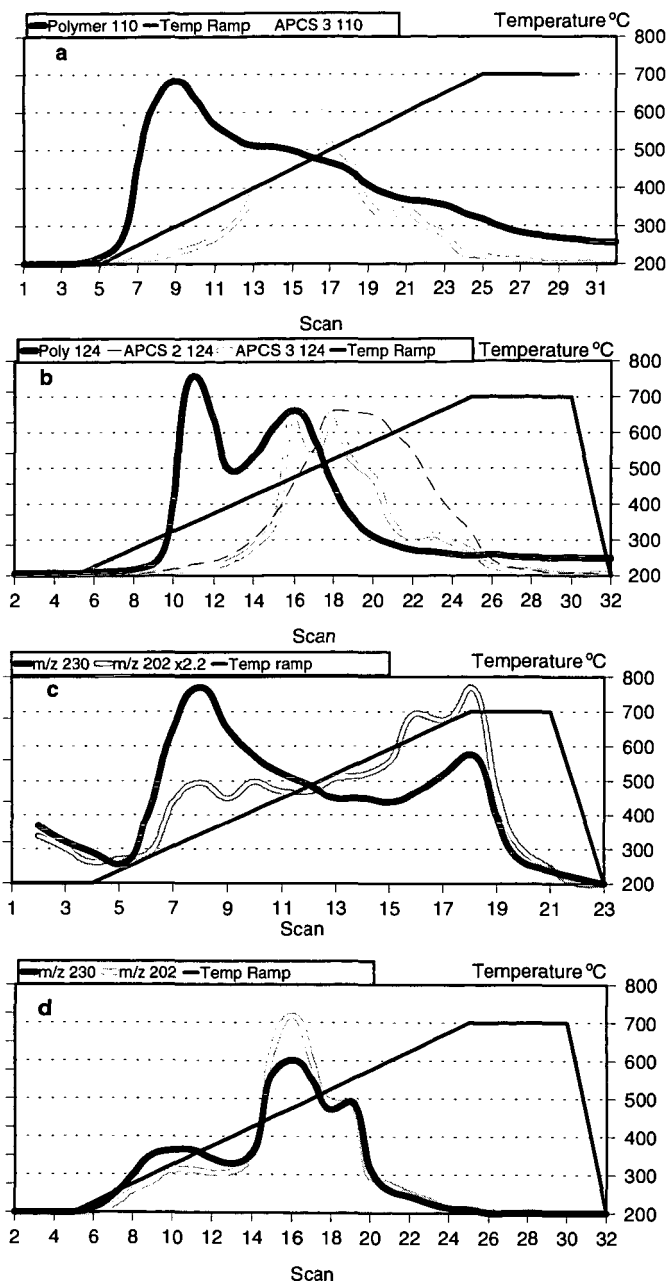


Figure 1. Individual ion pyrograms from DCIMS for (a) Pocahontas (APCS 5) pyridine extract; (b) Pocahontas whole coal; (c) Pittsburgh (APCS 4) pyridine extract; and (d) $m/z = 124$, for the polymer (I), Wyodak-Anderson subbituminous coal (APCS 2) pyridine extract, and Illinois No. 6 (APCS 3) pyridine extract.

A Question Concerning Coal Structure and/or Reactivity. The Reaction of Maleic Anhydride with Pittsburgh No. 8 Coal

John W. Larsen, James E. Roberts, Deanna Metka Quay
Chemistry Department
Lehigh University
Bethlehem, Pennsylvania 18015

ABSTRACT. Maleic anhydride reacts readily with coals under Diels-Alder conditions and the coals gain 10% or more in mass. This reaction has been carried out using ^{13}C labeled maleic anhydride and Pittsburgh No. 8 coal. The results are consistent with the occurrence of the Diels-Alder reaction. There is evidence against the occurrence of all other conceivable (to us) reactions. The amount of maleic anhydride incorporated is inconsistent with all published coal structures. Either coal structures are seriously in error by omitting a significant population of reactive diene structures or coal reactivity is strongly enhanced by mechanisms not understood.

INTRODUCTION. Several groups have studied the reaction of maleic anhydride and coals and, with one exception, concluded a Diels-Alder reaction was responsible for the mass increase.¹⁻⁵ This conclusion immediately leads to a significant dilemma. The maleic anhydride uptake observed by all workers is too large to be consistent with a Diels-Alder reaction between maleic anhydride and current published coal structures. The amount of incorporation is much higher than would be predicted by the number of reactive diene structures thought to be present. Such reactive structures in coals are primarily anthracene and higher acenes. β -naphthol undergoes a Diels-Alder reaction, but only under forcing conditions much more vigorous than those used with coal.⁶ There are two possible explanations for the large maleic anhydride incorporation. One is that the coal structures are in error and contain more reactive dienes than suspected. This is a reasonable conclusion because such reactive dienes are unlikely to survive any of the degradation conditions so far used to probe coal structure and would be spectroscopically indistinguishable from the aromatics. Another possible explanation is that functional groups, for example naphthalenes, might be reactive in coals under conditions much milder than in other situations. Stated another way, coals are showing strongly enhanced reactivity. Either of these explanations raises fundamental questions about the chemistry and structure of coals and it is this which makes the study of the maleic anhydride-coal reaction important. Reported here is a thorough re-examination of this reaction.

EXPERIMENTAL METHODS. Argonne samples of Pittsburgh No. 8 coal were reacted with maleic anhydride in chlorobenzene. The coal was dried by distilling off some of the chlorobenzene-water azeotrope. Work-up followed the procedure used by Nishioka.⁵ Samples of maleic anhydride independently labeled at both carbonyl and vinyl carbons were used. Solid state NMR spectra of the coals were obtained using a General Electric GN300 solid state NMR spectrometer operating at 75.4MHz for carbon using a Doty Scientific, Inc. 7 mm or 5 mm probe and a radio frequency feedback control circuit. The spectrometer was operated with radio frequency field strengths of 50 to 63 kHz for carbon and protons while acquiring 1 K of complex data points with a dwell time of 15 μs , a receiver gate time of 15 μs , and a filter delay of 15.75 μs . The times for the recycle delays were selected after the proton and carbon spin lattice relaxation times T_1 of 0.23-0.27 s for protons and 0.2-9.8 s for carbons were determined. Relaxation delays of 2 s for cross polarization experiments, and 60 s for Bloch decay experiments were employed. The data were processed using a baseline correction, exponential multiplication equivalent to 100Hz line broadening and one zero-fill followed by Fourier transformation. The spectra were phased using an auto phase function followed by linear baseline adjustment and another auto phase so that only minor adjustments were required. Samples were examined under magic angle spinning and high power proton decoupling. Sapphire rotors with Kel-F[®] end caps were used to minimize ^{13}C background. Bloch decay single pulse experiments were used for most of the coal spectra. A cross polarization ^{13}C - ^{13}C double quantum filter pulse sequence was also utilized.¹¹

RESULTS. Figure 1 shows solid state ^{13}C Bloch decay NMR spectra for a physical mixture of Pittsburgh No. 8 coal and maleic anhydride and Pittsburgh No. 8 coal after reactions with a mixture of 50% ^{13}C maleic anhydride labeled in the 2 and 3 (vinyl) positions or in the 1 and 4 (carbonyl) positions.

RESULTS AND DISCUSSION. The NMR spectra show that the vinyl carbons have become sp^3 hybridized carbons in the adduct and that the carbonyl carbons remain unaltered. That the carbonyl carbons have not shifted confirms earlier reports that ester formation has not occurred and rules out Nishioka's assertion that a charge transfer interaction was responsible for maleic anhydride incorporation.^{1,2,5} If charge transfer was responsible for the upfield shift of the vinyl carbons, then a large upfield shift of the carbonyl carbons must also occur due to the presence of the transferred electron in the maleic anhydride LUMO. The conversion of the vinyl carbons from sp^2 to sp^3 is consistent with the occurrence of a Diels-Alder reaction. A ^{13}C - ^{13}C double quantum experiment confirms the double bond is converted to a single bond.

There are several other reactions which might also convert the vinyl carbons to sp^3 . An ene reaction would do this, but there is no precedent in the literature for an ene reaction between maleic anhydride and either phenols or alkyl aromatics. Maleic anhydride can be homo polymerized only with difficulty and it has been demonstrated that the unshared electrons in coals are remarkably inefficient at inducing polymerizations; vitrinite radicals are not capable of initiating the polymerization of vinyl pyridine.^{7,8} The radical addition of maleic anhydride to benzylic positions is a known reaction, but adding radical initiators or using peroxide containing air-oxidized coals did not give any increase in maleic anhydride incorporation ruling out this pathway.^{7,9} Michael addition to phenols or thiols is possible.¹⁰ This reaction does not occur with phenols in coals, but does occur with coal thiol groups. The amount of thiol sulphur in this coal is much too small to explain the observed maleic anhydride incorporation.

It is clear that maleic anhydride is adding to the coals via a reaction involving the carbon-carbon double bond. The most reasonable candidate for this reaction remains the Diels-Alder. We are left with the puzzle with which we began, although this puzzle is now based on firmer ground. Either there are under characterized reactive diene structures in coals or the maleic anhydride reaction with coals is somehow enhanced. In one investigation of this latter possibility, we attempted to catalyze the Diels-Alder reaction between maleic anhydride and naphthalene by carrying it out in the presence of added coal. The added coal had no effect. It is clear from these results that major features of coal structure and/or reactivity are still not understood.

ACKNOWLEDGMENT: We are grateful to the U. S. Department of Energy for partial support of this research.

REFERENCES

1. Duty, R. C.; Liu, H. F. *Fuel* **1980**, *54*, 546-550.
2. Larsen, J. W.; Lee, D. *Fuel* **1983**, *62*, 1351-1354.
3. Quinga, E. M. Y.; Larsen, J. W. *Energy Fuels* **1987**, *1*, 300-304.
4. Zher 'akova, G.; Kochkan'an, R. *Fuel* **1990**, *69*, 898-901.
5. Nishioka, M. *Energy Fuels* **1991**, *5*, 523-525.
6. Wariyar, N. S. *Proc. Indian Acad. Sci.* **1956**, *43A*, 231-236.
7. Trivedi, B. C.; Colbertson, B. M. *Maleic Anhydride* Plenum Press: New York 1982.
8. Flowers, R. A. II; Gebhard, L. A.; Larsen, J. W.; Silbernagel, B. G. *ENERGY FUELS* **1989**, *3*, 762-764.
9. Bickford, W. G.; Fisher, G. S.; Dollean, F. G.; Swift, C. G. *J. Amer. Oil. Chem. Soc.* **1948**, 251-254.
10. Zcenty, F. G.; Vinegard, B. D.; Schlepnpnik, A. A. *J. Org. Chem.* **1962**, *27*, 3140-3146.
11. Bax, A.; Freeman, R.; Kempell, S. *J. Am. Chem. Soc.* **1980**, *102*, 4849-4851. Menger, E. M.; Vega, S.; Griffin R. G. *J. Am. Chem. Soc.* **1989**, *108*, 2215-2218.

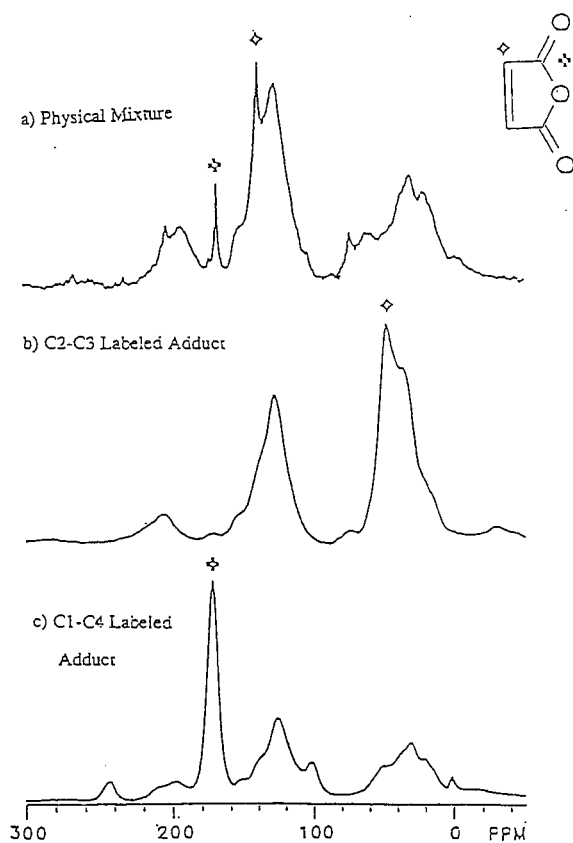


Figure 1. Solid State ^{13}C NMR spectra for a) a physical mixture of Pittsburgh 8 coal and maleic anhydride and Pittsburgh No. 8 coal reacted with b) $^{13}\text{C}_2$ $^{13}\text{C}_3$ and c) $^{13}\text{C}_1$ $^{13}\text{C}_4$ labeled maleic anhydride for 10 days in chlorobenzene at 110°C , then Soxhlet extracted with methanol for 3 days and dried.

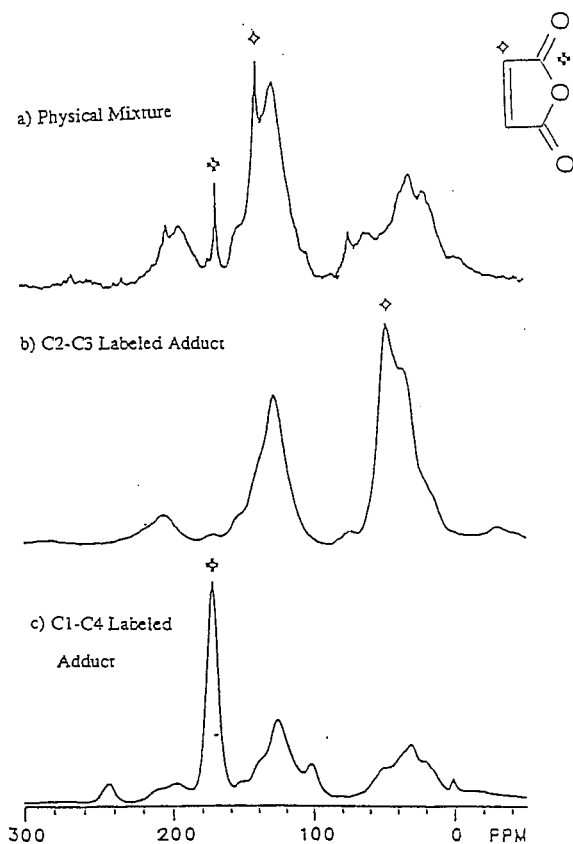


Figure 1. Solid State ^{13}C NMR spectra for a) a physical mixture of Pittsburgh 8 coal and maleic anhydride and Pittsburgh No. 8 coal reacted with b) $^{13}\text{C}_2$ $^{13}\text{C}_3$ and c) $^{13}\text{C}_1$ $^{13}\text{C}_4$ labeled maleic anhydride for 10 days in chlorobenzene at 110°C , then Soxhlet extracted with methanol for 3 days and dried.

HEAT TREATMENT OF COALS IN VARIOUS SOLVENTS AT TEMPERATURES AS LOW AS 175 - 300°C

Masashi Iino, Jianli Shen, Satoshi Ashida, Chunqi Li, and Toshimasa Takanohashi

Institute for Chemical Reaction Science, Tohoku University
Katahira, Aoba-ku, Sendai 980-77, JAPAN

KEYWORDS: Heat treatment, dissolution reaction, solvent effect

INTRODUCTION

Neavel (1) reported that more than 90% of a high-volatile bituminous coal became soluble in pyridine by coal liquefaction less than 5 min. at 400°C in tetralin. We are interested in the dissolution mechanism at this initial stage of coal liquefaction, since this stage seems to be a key step to control liquefaction yield and product selectivity. So, heat treatments of coals were carried out at temperatures as low as 175-300°C in various solvents which have different hydrogen donatability (2,3).

We are also interested in the mechanism of retrogressive reactions which concurrently occur with dissolution reactions in coal liquefaction. Although the details of retrogressive reactions are still obscure, hydrogen donation to coal fragments is essential for their suppression. Especially radicals formed during the initial stage of coal liquefaction must be stabilized to suppress efficiently the retrogressive reactions which could result in the formation of refractory, high-molecular weight substances. We have used carbon disulfide- N-methyl-2-pyrrolidinone (CS₂-NMP) mixed solvent (1:1 by volume) as an extraction solvent for the heat treated coals. The CS₂-NMP mixed solvent has been found to give high extraction yields (40-65wt%, daf) at room temperature for many bituminous coals (4). We also found that the extracts obtained with the mixed solvent include a considerable amount of the very heavy component which is not soluble in THF or pyridine, but soluble in the mixed solvent, i.e., heavier extract fraction than preasphaltene (5).

In the previous study (2,3) the heat treatments of several bituminous coals such as Upper Freeport and Illinois No. 6 coals were carried out in solvents of different hydrogen-donatability under N₂ atmosphere. In tetralin retrogressive reaction was observed at 175-250°C and dissolution proceeded at 300-350°C. While in dihydroanthracene (DHA) or hexahydroanthracene (HHA), which have higher hydrogen-donatability than tetralin, the coals used underwent dissolution reactions even at low temperatures such as 175-250°C. The quantity of hydrogen transferred from the solvents to coals, which was estimated from dehydrogenation of the solvents such as anthracene from DHA, was found to be well correlated with the extent of the dissolution reactions occurred. However, recent study on the heat treatment of coals in NMP, which seems to have little hydrogen-donatability from its chemical structure, showed that for some coals NMP gave higher dissolution yields than HHA, the strongest hydrogen donor among the solvents we used.

In this study the heat treatments of coals in NMP at 175-300°C were carried out and the dissolution mechanism in NMP will be discussed, compared with that in HHA.

EXPERIMENTAL

The coals used in this study are shown in Table 1. NMP and HHA were used as a solvent for heat treatment of coals.

Heat treatment of the coal was performed in 50ml magnetically stirred autoclave at 175, 250, and 300°C, respectively. 1g of the coal and 5g of the solvent were charged into the autoclave, which was pressurized with nitrogen to 5.0 MPa at room temperature. After the heat treatment, the coal was fractionated into the CS₂-NMP mixed solvent-insoluble fraction (MI) and -soluble fraction (MS), and then MS further into tetrahydrofuran (THF) -insoluble, the mixed solvent soluble fraction (TIMS) and THF-soluble fraction (TS), with the mixed solvent and THF at room temperature under ultrasonic irradiation, as shown in Figure 1. The quantity of MI and TIMS was determined after drying overnight in vacuum at 80°C and that of TS was calculated by difference, i. e., 100-MI-TIMS. The dissolution yield was defined here as the sum of TIMS and TS.

RESULTS AND DISCUSSION

Heat treatment of coals in NMP and HHA

Figure 2 shows the fraction distribution after the heat treatment of Upper Freeport coal in NMP and HHA at 175°C, 250°C, and 300°C, together with the fraction distribution before the heat treatment, i. e., for the raw coal, which was obtained from the extraction of the raw coal with the CS₂-NMP mixed solvent and the fractionation of the extract obtained. At 175°C NMP gave higher dissolution yield (TIMS + TS) than HHA and little effect of temperature on the dissolution yield and fraction distribution was observed in NMP, unlike the case with HHA, suggesting different dissolution mechanisms for NMP and HHA. Figure 3 shows the result for Zao Zhuang coal and the similar tendency was obtained as Upper Freeport coal. Figure 4, 5 and 6 show the results for Pittsburgh No. 8, Illinois No. 6 and Beulah-Zap coals, respectively. The heat treatments of Pittsburgh No. 8 and Illinois No. 6 coals gave nearly 80% of the dissolution yields at 300°C, higher than those in HHA. Figure 7 shows the plot of net dissolution yields for the heat treatment of the coals in NMP and HHA at 300°C versus C% of the coals. The net dissolution yields here are the dissolution yield corrected for the yield for the raw coal, i. e., (TIMS + TS)_{300°C} - (TIMS + TS)_{raw coal}. Figure 7 shows that for the low rank coals NMP gave higher net dissolution yields than HHA. Figure 8 shows radical concentrations of the raw Zao Zhuang coal and after the heat treatment for 1h at 300°C in HHA (a) and NMP (b). This clearly shows that in HHA the radical concentrations decrease as the increase of the heat treatment temperature, but in NMP the reverse tendency was obtained. As described in INTRODUCTION, hydrogen transfer from HHA to the coals was observed and it was well correlated with the dissolution yields. However, in the heat treatment in NMP no dehydrogenated derivatives of NMP was detected, indicating no hydrogen transfer from NMP to the coals.

Dissolution Mechanism in NMP and HHA

It is clear from the results described above that the dissolution reactions in NMP and HHA proceed through different mechanisms. In HHA coal radicals, which formed by the scission of very weak covalent bonds at 175-300°C and/or indigenous radicals activated by heat at these temperatures, may be responsible for the dissolution. These radicals are stabilized by the hydrogen donation from HHA and the dissolution reactions proceed. When the heat treatment was carried out in tetralin at 175 and 250°C, which is a much poorer hydrogen donor than HHA and hardly donate hydrogen to the radicals at these low temperatures, retrogressive reactions such as the addition to aromatic rings and coupling reactions occur.

The dissolution mechanism in NMP is not clear, though it is sure that hydrogen transfer from NMP to the coals does not occur. NMP is a polar solvent and a better solvent for coal extraction than pyridine, especially for low-rank coals which have many polar groups. One tentative explanation is that NMP dissolves much of coal molecules and radicals at 175-300°C and prevent retrogressive reactions which would occur in a non-polar solvent. Ionic reactions is also conceivable in NMP, though we have no evidence for it now.

Finally, it should be noted that the results above described were obtained by the use of the CS₂-NMP mixed solvent as an extraction solvent for the reaction mixture. If THF is used as a starting extraction solvent instead of the mixed solvent, we can only see small change of TS in the heat treatments carried out here.

CONCLUSIONS

Heat treatments of 7 coals were carried out in HHA which is a strong hydrogen donor, and in NMP which is a strong extraction solvent for coals, at temperatures as low as 175-300°C. HHA and NMP gave high dissolution yields for high- and low-rank coals, respectively. Hydrogen donation from HHA to coal radicals and high solubility for coal molecules and radicals are suggested to be responsible for these dissolutions.

REFERENCES

1. Nieve, R. C. *Fuel*, **1976**, *55*, 237-242.
2. Shen, J., Takanohashi, T., and Iino, M. *Energy Fuels*, **1992**, *6*, 854-858.
3. Shen, J., and Iino, M. *Energy Fuels*, **1994**, *8*, 978-983.
4. Iino, M., Takanohashi, T., Osuga, H., and Toda, K. *Fuel*, **1988**, *67*, 1639-1647.
5. Iino, M., Takanohashi, T., Obara, S., Tsueta, H., and Sanokawa, Y. *Fuel*, **1989**, *68*, 1588-1593.

Table 1 Ultimate and ash analyses of coals

Coal	Ultimate analysis (wt%,daf ^b)					Ash (wt%,db ^c)
	C	H	N	S	O ^a	
Pocahontas No.3 (PC)	89.7	4.5	1.1	0.7	4.0	4.8
Zao Zhuang (ZZ)	86.9	5.1	1.5	1.6	4.9	7.4
Upper Freeport (UF)	86.2	5.1	1.9	2.2	4.6	13.1
Pittsburgh No.8 (PB)	82.6	5.5	2.1	2.4	7.4	8.7
Illinois No.6 (IL)	76.9	5.5	1.9	5.6	10.1	10.4
Wyoming (Wy)	75.1	5.5	1.1	0.4	17.9	5.2
Beulah-Zap (BZ)	71.6	4.8	1.0	0.9	21.7	9.6

^a By difference

^b Dry ash free basis

^c Dry basis

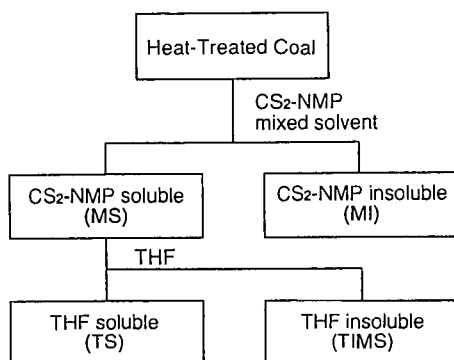


Figure 1 Extraction and fractionation procedures for the heat treated coals

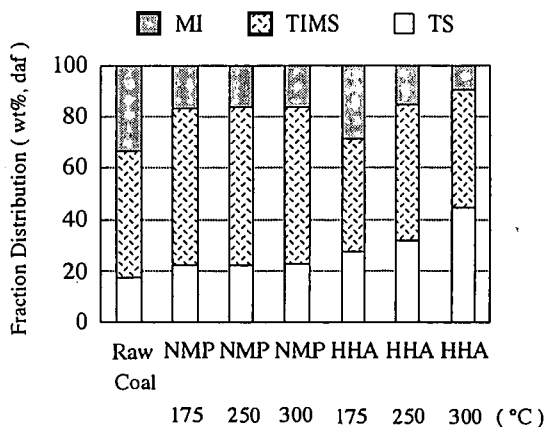


Figure 2 Fraction distribution after the heat treatment of Upper Freeport coal at 175-300°C in NMP and HHA for 1h, together with that for the raw coal.

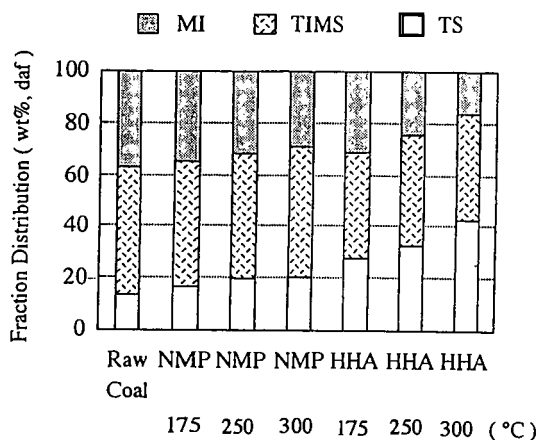


Figure 3 Fraction distribution after the heat treatment of Zao Zhuang coal at 175-300°C in NMP and HHA for 1h, together with that for the raw coal.

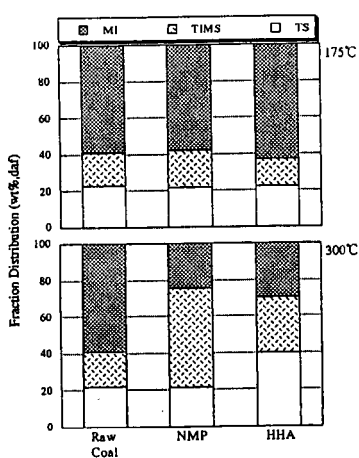


Figure 4 Fraction distribution after the heat treatment of Pittsburgh No. 8 coal at 175 and 300°C in NMP and HHA for 1h, together with that for the raw coal.

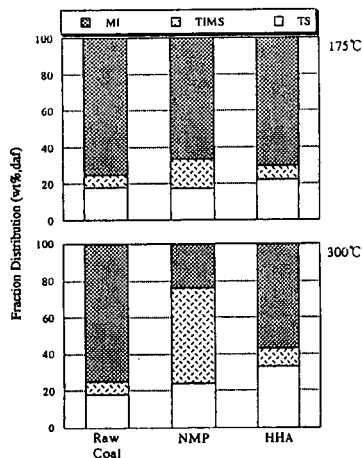


Figure 5 Fraction distribution after the heat treatment of Illinois No. 6 coal at 175 and 300°C in NMP and HHA for 1h, together with that for the raw coal.

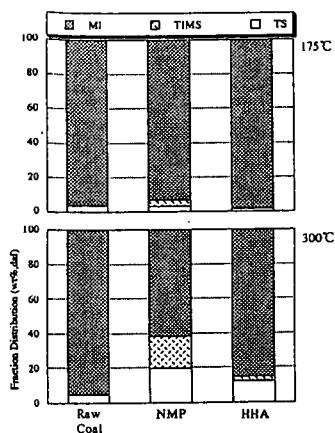


Figure 6 Fraction distribution after the heat treatment of Beulah-Zap coal at 175 and 300°C in NMP and HHA for 1h, together with that for the raw coal.

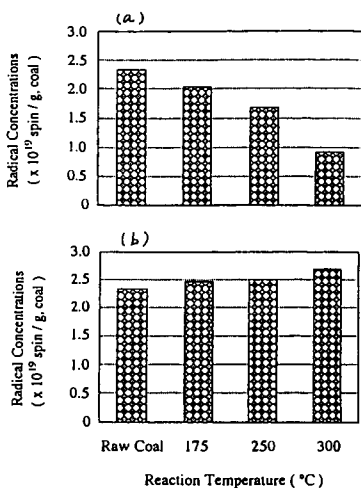


Figure 8 Radical concentrations of the raw Zao Zhuang coal and after the heat treatment for 1h at 300°C in HHA (a) and NMP (b).

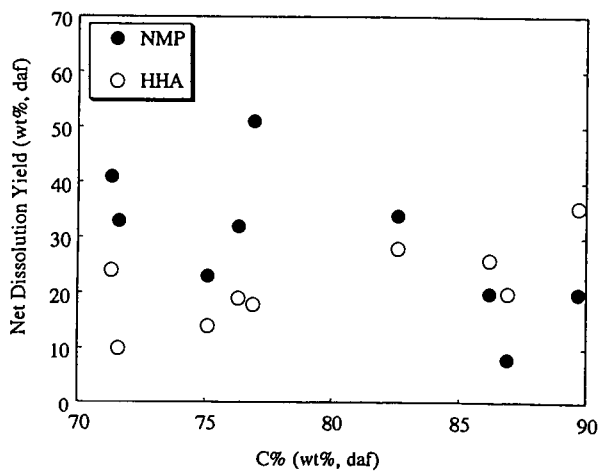


Figure 7 Plot of net dissolution yields for the heat treatment of the coals in NMP (●) and HHA (○) for 1h at 300°C versus C% of the coals.

PREDICTING ^{13}C NMR MEASUREMENTS OF CHEMICAL STRUCTURE OF COAL BASED ON ELEMENTAL COMPOSITION AND VOLATILE MATTER CONTENT

D. Genetti and T. H. Fletcher

Department of Chemical Engineering, Brigham Young University, Provo, Utah 84602

Keywords: coal structure, ^{13}C NMR

INTRODUCTION

Devolatilization models based on quantitative measurements of chemical structure, such as available through ^{13}C NMR analysis, have been successful in predicting tar volatiles yields as a function of heating rate, temperature, pressure, and coal type.¹ However, due to limited resources, ^{13}C NMR structural parameters have only been obtained for about 35 coals at the present time. Industrial interest in coal devolatilization has led to several attempts to correlate structural parameters affecting devolatilization as a function of the ultimate analysis of coals. Serio, et al.² used a triangular (i.e., linear) interpolation technique to estimate the input parameters for the FG-DVC devolatilization model.³ Niksa and Kerstein⁴ also developed a procedure that estimates the coal structural parameters based on simple linear correlations of ultimate analysis.^{5,6}

An extensive statistical analysis to determine the validity of linear correlations of ^{13}C NMR structural parameters based on ultimate analysis; preliminary results of this analysis were presented by Genetti and coworkers.⁷ A database including elemental composition, the ASTM volatile matter content, and ^{13}C NMR structural parameters for 30 coals of widely varying rank and composition was used in the analysis. The database was closely examined using the SPSS[®] statistical computer package. Using SPSS[®], a correlation matrix was calculated between all of the chemical structural parameters obtained from the NMR analysis. From the correlation matrix, the strength of relationships between the individual elements and the derived parameters were easily determined. The parameters were also examined for relationships among themselves. Multi-variate linear regression was then performed to derive equations that predict each of the parameters as a function of the elemental composition and volatile matter content. The r^2 value was then determined for each correlation.

The r^2 value is the coefficient of determination which determines the relative strength of correlation ($r^2=1$ is a perfect correlation). In this analysis the r^2 values ranged from 0.17 for $\sigma+1$ to 0.59 for M_8 ($r^2=0.49$ for P_0 and $r^2=0.38$ for MW_{cl}). The low r^2 values indicate a only weak linear correlation between the ^{13}C NMR structural parameters and the ultimate analysis. However, even when r^2 is zero, a strong non-linear correlation is possible. As a result of this study, it was determined that correlations based on linear regressions of ultimate analysis are unsuitable for predicting ^{13}C NMR structural parameters with reasonable accuracy. The purpose of this investigation is to develop non-linear correlations that predict the chemical structure parameters generally measured by ^{13}C NMR and required for the CPD devolatilization model:¹ (i) the average molecular weight per side chain (M_8); (ii) the average molecular weight per aromatic cluster (MW_{cl}); (iii) the ratio of bridges to total attachments (P_0); and (iv) the total attachments per cluster ($\sigma+1$).

CORRELATION OF M_8 , MW_{cl} , P_0 , AND $\sigma+1$

The database collected for 30 coals of varying rank used by Genetti, et al.⁷ is shown in Table 1. The database includes the elemental composition, the volatile matter content, and the measured values of the four chemical structural parameters derived from ^{13}C NMR analysis that are required in the CPD model.

Coals 1-7 are Argonne premium coals, 8-16 are coals used at Sandia National Laboratories, data for 17-18 came directly from Advanced Fuel Research, and coals 19-30 are coals from the Penn State coal sample bank. The volatile matter content data for the Penn State coals were taken directly from the Penn State coal sample database. Ultimate analysis on the Penn State coals was performed independently by Western Analytical and Huffman Laboratories and the average values are listed in Table 1. It is apparent that a diverse range of coals were used in this investigation.

Each ^{13}C NMR parameter was plotted against the different elemental constituents and the volatile matter content in order to determine relative dependence on each variables. This made it possible to see visually and quantitatively any possible correlation patterns. A non-linear (e.g., polynomial) correlation was then made for each of these plots, and the r^2 value was calculated to determine the strength of correlation. For example, it was determined that the value of M_8 depends significantly on the relative contents of carbon, hydrogen, oxygen, and volatile matter. Once it was determined that M_8 was dependent on carbon, hydrogen, oxygen, and volatile matter content, the best fit equations from the four plots were added together. Once the form of the equation was determined, coefficients were determined by minimization of the sum square error between the measured value and the predicted value of M_8 . Any obvious outlying points were removed. Only the DECS-13 coal was a consistent outlier for the M_8 correlation. The following is the equation resulting from the final optimization ($r^2=0.87$).

$$M_8 = c_1 + c_2 x_C + c_3 10^{x_H} + c_4 x_O + c_5 x_O^2 + c_7 VM + c_8 VM^2 \quad (1)$$

where C, H, O, and VM represent the mass percent carbon, hydrogen, oxygen, and ASTM volatile content on a daf basis, and the c_i are empirical coefficients. This procedure was repeated for $\sigma+1$, P_0 , and MW_{cl} . A modified cubic correlation was also determined ($r^2 = 0.88$), but this correlation gave unrealistic values of MW_{cl} and $\sigma+1$ for low rank coals ($\%O > 25\%$) and high rank coals (VM

<10%). For example, values of MW_{cl} for low rank coals were less than 100 daltons; the lowest NMR measurement for any coal was ~200 daltons. These unrealistic values seemed to be the result of extrapolations of the cubic curve fit beyond the original data set. Quadratic-type correlations did not give such poor extrapolations, and hence are shown here. Correlations for MW_{cl} , P_0 , and $\sigma+1$ were made with the following form:

$$y = c_1 + c_2C + c_3C^2 + c_4H + c_5H^2 + c_6O + c_7O^2 + c_8N + c_9N^2 + c_{10}S + c_{11}S^2 + c_{12}VM + c_{13}VM^2 \quad (2)$$

Coefficients for the quadratic fits are shown in Table 2. Coals with dry ash free carbon contents exceeding 95% (i.e., anthracites) were removed from the correlation. Thus, this model is only useful for coals with up to 95% C (daf). Additional ^{13}C NMR data are needed for coals with high carbon contents before a reliable correlation can be made for these coals.

It is anticipated that elemental composition may correlate with the coal structure parameters for many coals. However, it is recognized that often it is the exception to the rule that causes problems, and hence the need for additional ^{13}C NMR data, especially for "problem" coals. Therefore, these types of correlations should be used as a representation of the average of a database of coals and will fail occasionally for unique coals. Also, note that no cross correlations were used in Eqs. 1 or 2; this may be a subject of future work.

To determine the accuracy of the models, the measured values were plotted against the predicted values for each of the four structural parameters and the r^2 values were determined. The following r^2 values were determined: for M_5 , $r^2=0.87$; for MW_{cl} , $r^2=0.53$; for P_0 , $r^2=0.71$; for $\sigma+1$, $r^2=0.73$ (see Table 2). The outlier coals for each correlation are listed and were omitted from the r^2 calculation.

CORRELATION FOR C_0

The CPD model requires an estimation for the number of stable bridges existing in the parent coal or that are formed early in the pyrolysis process for low rank coals. This parameter has generally been used for low volatile bituminous coals to represent bi-aryl linkages and for lignites to represent early crosslinking. In the past, this has been a tuning parameter for these types of coals, and had to be changed as a function of heating rate, since crosslinking occurs at different rates as a function of heating rate. Based on the research performed before, a rough correlation for C_0 was developed for high heating rate applications. For low rank coals, oxygen content in the parent coal was used, since this correlates well with early crosslinking. For high rank coals, carbon content was used, since this may correlate well with the bi-aryl linkages. The correlation for C_0 becomes:

$$C_0 = \max\{(0.0177 \%C - 1.4542), 0.0\} + \max\{(0.0143 \%O - 0.1136), 0.0\} \quad (3)$$

Equation 5 was used below for all CPD model predictions that used the correlated chemical structure parameters. It is hoped that additional research on bi-aryl linkages and the chemistry behind early crosslinking in low rank coals will eliminate the need for such empiricism.

CPD MODEL PREDICTIONS

Five coals for which ^{13}C NMR and devolatilization data are available were tested in the CPD model. Volatiles yields were taken from the FFB experiments reported by Fletcher and Hardesty.⁸ Ultimate analysis and volatile matter data were used in the correlations to estimate the ^{13}C NMR parameters required as input for the CPD model. The CPD model was then used to predict tar and total mass release. The CPD model predictions made using the correlation were then compared against the measured experimental yields as well as versus yields predicted using the actual ^{13}C NMR measurements (from Table 1). Figure 1 compares the measured values and the predicted values of mass release for the five coals tested. It can be seen that the use of the structural parameters from the correlation gives predictions of total mass release that are as good or better than the use of the actual NMR data. This may be due to the fact that the correlation tends to smooth the NMR data.

Seventeen coals reported by Xu and Tomita⁹ were also used to test the reliability of this correlation. Table 3 lists these coals with their ultimate analysis and the four ^{13}C NMR parameters estimated by the correlation. It appears by looking at the estimated ^{13}C NMR values that the correlation works quite well overall; all estimated values are within expected ranges. Table 4 lists the predicted and measured values of mass and tar release for the 17 coals. Figure 2 shows the predicted and measured mass release vs. %C in the parent coal for the data from Xu and Tomita.⁹ The predicted mass release compares relatively well to the measured mass release for most of the coals tested. The correlation coefficient between the predicted and measured total volatiles yield was 0.89. The predictions of tar yield are lower than measured experimentally, especially for the low rank coals. The exact cause for this discrepancy is not known. In the Xu and Tomita experiment, the mass of char and the concentrations of major light gases are measured, and the tar yield is obtained by difference. This may lead to errors if light gases are present that are not measured, or if some fragmentation occurs. The tar yields reported by Xu and Tomita for low rank coals seem to be much higher than reported elsewhere in the literature.

The CPD model currently subtracts 7 daltons from the value of M_5 in order to account for some methyl ($-CH_3$) groups attached permanently to the aromatic cluster. However, since M_5 for the Hongay coal was 6 daltons, a minimum corrected value of 1 dalton was used in all CPD calculations. It may be necessary to develop a separate correlation for coals with carbon contents greater than 90% daf.

CONCLUSIONS

The non-linear correlation of ^{13}C NMR measurements with ultimate analysis and volatile matter content is a promising approach to obtain data to model devolatilization behavior where ^{13}C NMR data are not available. The correlation, combined with the CPD model, works very well in predicting total volatiles yield for low to high rank coals. Coals of very high rank ($>95\% \text{C}$) were not included in this correlation due to drastically different structure and lack of sufficient data. Flat flame burner devolatilization tests are planned on a number of these coals to obtain provide additional volatile yield data.

REFERENCES

1. Fletcher, T. H., A. R. Kerstein, R. J. Pugmire, and M. D. Grant, *Energy and Fuels*, **6**, 414-431 (1992).
2. Serio, M. A., P. R. Solomon, and Y. Zhao, 25th Symposium (International) on Combustion, 553-560 (1994).
3. Solomon, P. R., D. G. Hamblen, R. M. Carangelo, M. A. Serio, and G. V. Deshpande, *Energy and Fuels*, **2**, 405-422 (1988).
4. Niksa, S. and A. R. Kerstein, *Energy and Fuels*, **5**, 647-665 (1991).
5. Niksa, S. and A. R. Kerstein, *Energy and Fuels*, **5**, 673-683 (1991).
6. Niksa, S. and A. R. Kerstein, *Energy and Fuels*, **8**, 659-670 (1994).
7. Genetti, D. B., T. H. Fletcher, and R. J. Pugmire, "Predicting ^{13}C NMR Measurements Based on Coal Elemental Composition," in *Coal Science*, edited by J. A. Pajares and J. M. D. Tascon, **1**, 331-334, Elsevier, New York (1995).
8. Fletcher, T. H. and D. R. Hardesty, "Compilation of Sandia Coal Devolatilization Data: Milestone Report," for DOE/PETC under contract FWP 0709, Sandia Report No. SAND92-8209, available NTIS (May, 1992).
9. Xu, W.-C. and A. Tomita, *Fuel*, **66**, 627-631 (1987).

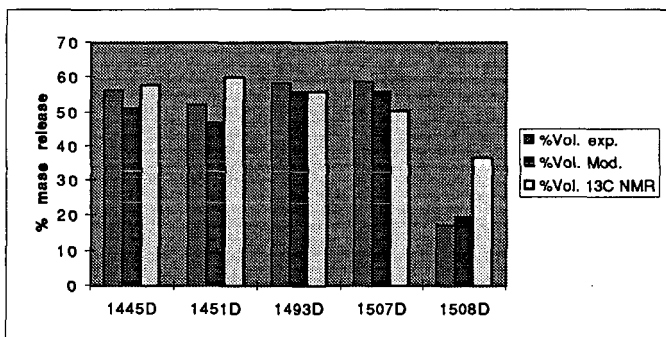


Figure 1. Comparison of total mass release with measured total volatile yields in a flat flame burner (Fletcher and Hardesty⁸).

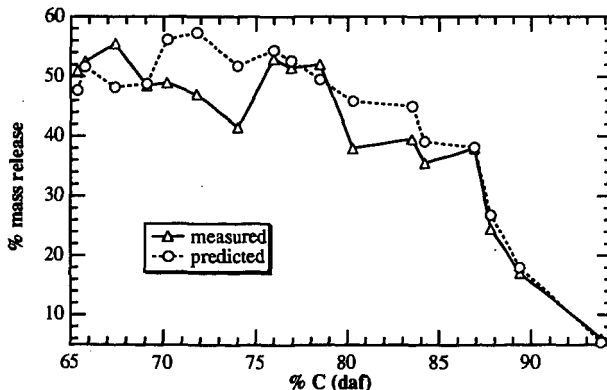


Figure 2. Predicted and measured mass release vs. $\% \text{C}$ in the parent coal for the data from Xu and Tomita.⁹

Table 1
Coal Data Set Used for Development of Empirical Correlations

#	COAL SAMPLE	C	H	O	N	S	VM	$\sigma+1$	P _o	MW _{cl}	M _s
1	NORTH DAKOTA	72.94	4.83	20.34	1.15	0.70	49.78	4.10	0.64	269	40
2	WYODAK	75.01	5.35	18.02	1.12	0.47	49.03	5.60	0.55	408	42
3	BLIND CANYON	80.69	5.76	11.58	1.57	0.37	48.11	5.10	0.49	366	36
4	ILLINOIS #6	77.67	5.00	13.51	1.37	2.38	47.39	5.00	0.63	322	27
5	PITTSBURGH #8	83.20	5.32	8.83	1.64	0.89	41.67	4.70	0.64	330	28
6	STOCKTON	82.58	5.25	9.83	1.56	0.65	37.64	4.80	0.69	272	20
7	UPPER FREEPORT	85.50	4.70	7.51	1.55	0.74	31.62	5.30	0.67	312	17
8	POCAHONTAS	91.05	4.44	2.47	1.33	0.50	19.53	4.40	0.74	307	13
9	PSOC 1443	72.34	5.21	20.11	1.35	0.94	78.67	4.80	0.59	297	36
10	PSOC 1488	76.00	5.23	17.27	0.94	0.53	44.22	4.70	0.54	310	37
11	PSOC 1468	95.36	1.38	1.86	0.84	0.53	3.92	4.70	0.89	656	12
12	PSOC 1445D	75.60	5.26	17.33	1.32	0.49	48.17	5.00	0.48	384	45
13	PSOC 1451D	84.23	5.54	7.56	1.65	1.01	38.69	4.80	0.48	329	33
14	PSOC 1493D	74.12	4.96	13.18	1.45	6.29	43.37	5.50	0.52	402	39
15	PSOC 1507D	66.56	4.26	25.16	1.12	2.89	49.59	4.40	0.59	392	58
16	PSOC 1508D	88.83	4.37	5.14	1.06	0.60	17.18	4.20	0.70	285	18
17	GOUDEY A	87.90	3.77	4.65	1.31	2.37	36.94	4.80	0.64	264	21
18	GOUDEY B	88.49	4.94	1.40	3.42	1.75	19.27	5.00	0.65	295	19
19	DECS-1	71.62	7.11	18.84	1.33	1.10	56.52	5.80	0.42	505	55
20	DECS-7	73.67	6.04	18.22	1.08	1.00	48.11	5.10	0.55	381	43
21	DECS-11	67.81	6.85	23.66	0.91	0.76	62.01	4.60	0.88	329	42
22	DECS-13	87.03	5.19	5.48	1.65	0.65	26.08	4.50	0.72	483	72
23	DECS-18	80.15	6.04	7.44	1.62	4.75	46.93	5.30	0.48	370	35
24	DECS-20	85.16	5.81	6.49	1.52	1.01	39.70	4.70	0.64	247	21
25	DECS-21	93.61	2.77	2.90	0.17	0.56	5.08	3.80	1.00	216	13
26	DECS-27	76.73	6.14	15.03	1.32	0.79	41.50	5.20	0.55	361	34
27	PSOC-1515	89.23	4.13	4.95	0.90	0.78	11.92	6.00	1.00	231	4
28	PSOC-1516	87.34	4.92	4.12	1.37	2.24	20.83	4.50	0.35	354	21
29	PSOC-1520	69.55	6.45	21.70	0.91	1.39	62.47	3.70	0.64	282	46
30	PSOC-1521	89.96	4.67	2.79	1.70	0.88	22.11	4.40	0.69	225	14

$\sigma+1$: Attachments per cluster

MW: Average molecular weight per cluster

P_o: Intact bridges

M_s: Average molecular weight per side chain

VM: ASTM volatile matter (daf)

Table 2
Coefficients for Quadratic Correlation of ¹³C NMR data

	M _s	MW	P _o	$\sigma+1$
C ₁	161	-587.73	-0.39	-2.2
C ₂	-1.76	22.32	-4.0E-03	0.32
C ₃	5.28E7	-0.17	2.0E-04	-2.6E-03
C ₄	-2.37	90.31	-5.4E-02	-2.1
C ₅	-1.27	-8.40	5.3E-03	0.19
C ₆	3.42E-2	-0.52	5.9E-03	0.10
C ₇	8.76E-1	0.04	6.3E-04	-4.5E-03
C ₈	-9.04E-3	1.28	5.5E-03	1.321
C ₉		-0.01	2.5E-04	-0.20
C ₁₀		-5.67	0	0
C ₁₁		2.49	0	0
C ₁₂		0.37	-1.8E-05	-1.2E-02
C ₁₃		-0.02	1.1E-06	3.9E-05
r ²	0.87	0.535	0.71	0.73
Outliers	DECS-13	PSOC-1468	PSOC 1516	PSOC-1515
	PSOC-1468		DECS 1	PSOC-1468
			PSOC-1515	

Table 3
17 Coals Tested by Xu and Tomita⁹.

	Cdaf	Hdaf	Odaf	Ndaf	Sdaf	VMdaf	c+1	P _o	MW	M ₆
Yallourn	65.40	4.90	28.80	0.6	0.3	53.93	3.33	0.75	362	59.3
Rhein Braun	65.80	5.50	27.60	0.8	0.3	58.46	3.67	0.71	358	57.5
Morwell	67.40	5.00	26.80	0.5	0.3	52.54	3.52	0.71	362	54.7
Velva	69.10	4.80	23.90	1.4	0.6	52.34	4.77	0.64	356	50.3
Soyakoishi	70.20	5.20	22.40	1.8	0.2	46.42	5.18	0.62	366	48.0
South Baulah	71.80	4.70	19.20	1.4	2.9	44.70	5.25	0.55	364	44.6
Colowyo	74.00	5.00	18.60	1.9	0.4	38.75	5.56	0.59	363	40.0
Taiheiyō	76.00	6.50	16.00	1.2	0.3	56.02	5.19	0.57	318	37.1
Millmerran	76.90	6.60	15.40	0.5	0.6	54.80	4.54	0.58	313	35.8
Wandoan	78.50	5.80	14.40	0.9	0.4	49.76	4.69	0.59	327	33.5
Hunter Valley	80.30	5.00	12.20	2	0.4	37.18	5.55	0.59	337	30.0
Liddell	83.50	5.40	8.40	2.1	0.6	37.58	5.30	0.60	318	26.6
Newvale	84.20	5.00	8.90	1.4	0.5	34.18	4.87	0.63	316	24.3
Yubari Shinko	86.90	5.60	5.20	1.9	0.3	40.51	4.73	0.66	293	23.7
Vicary Creek	87.80	4.70	4.90	2.1	0.4	24.74	4.97	0.68	298	17.8
Keystone	89.40	4.40	3.10	2.2	0.8	16.83	4.91	0.71	284	12.8
Hongay	93.70	3.30	1.30	1.2	0.8	7.66	4.66	0.85	207	5.3

Table 4
Predicted and Measured Mass Release and Predicted Tar Yield
(data from Xu and Tomita⁹)

COAL	% mass release (daf)		% tar release (daf)	
	pred.	meas.	pred.	meas.
Yallourn	48	51	14	20
Rhein Braun	52	53	14	22
Morwell	48	56	15	26
Velva	49	49	17	18
Soyakoishi	56	49	9	21
South Baulah	57	47	14	17
Colowyo	52	42	10	19
Taiheiyō	54	53	16	30
Millmerran	53	52	22	30
Wandoan	50	52	21	28
Hunter Valley	46	38	15	22
Liddell	45	40	19	22
Newvale	39	36	19	19
Yubari Shinko	38	38	17	22
Vicary Creek	27	25	12	12
Keystone	18	17	10	8
Hongay	5	6	4	3

A SIMPLIFIED METHOD TO DETERMINE $f(E)$ AND k_0 IN THE DISTRIBUTED ACTIVATION ENERGY MODEL FOR COAL PYROLYSIS

Kouichi Miura and Taisuke Maki
Department of Chemical Engineering, Kyoto University
Kyoto 606-01, Japan

Keywords: Coal pyrolysis, Distributed activation energy model, Argonne premium coal

INTRODUCTION

To analyze complex reactions such as pyrolysis of fossil fuels, thermal regeneration reaction of activated carbon *etc.*, the so called distributed activation energy model (DAEM) has been widely utilized. The model has been applied to represent the change in overall conversion¹⁻³ and/or the change in the yield of a given component⁴⁻⁶ during the coal pyrolysis. The model is represented as follows when it is applied to represent the change in total volatiles.

$$1 - V/V^* = \int_0^\infty \exp(-k_0 t) e^{-E/RT} f(E) dE \quad (1)$$

where V is the total volatiles evolved by time t , V^* is the effective volatile content of the coal, $f(E)$ is a distribution curve of the activation energy to represent the differences in the activation energies of many first-order irreversible reactions, and k_0 is the frequency factor corresponding to the E value. The distribution curve $f(E)$ is defined to satisfy

$$\int_0^\infty f(E) dE = 1 \quad (2)$$

The focus of the analysis is the estimation of k_0 and $f(E)$. The distribution curve $f(E)$ is generally assumed by a Gaussian distribution with mean activation energy E_0 and standard deviation σ . On the other hand, the frequency factor k_0 is assumed to be a constant in general for all reactions to avoid the complexity of the analysis.

Since k_0 and $f(E)$ are interrelated as clarified by several investigators^{7,8}, k_0 is assigned on some basis first, and $f(E)$, namely E_0 and σ , is determined to fit experimental data. Therefore, eq 1 becomes just a correlation equation when we can not determine k_0 on some sound basis. Even the assumption of a constant k_0 value may not be valid when $f(E)$ spreads over wide range of E values. Furthermore, the assignment of the Gaussian distribution to $f(E)$ does not always reflect real situations.

Recently one of the authors has presented a simple method to estimate both $f(E)$ and k_0 from three sets of experiments performed at different heating profiles without assuming any functional forms for $f(E)$ and k_0 ⁹. The procedure to estimate $f(E)$ and k_0 is summarized below:

1. Measure V/V^* vs. T relationships at three different heating rates at least.
2. Calculate nominal rates $\bar{k} = dV/dt/(V^*-V)$ at several but same V/V^* values at the different heating rates, then make Arrhenius plots of \bar{k} at the same V/V^* values.
3. Determine activation energies from the Arrhenius plots at different levels of V/V^* , then plot V/V^* against the activation energy E .
4. Differentiating V/V^* by E gives $f(E)$, because the following relation holds approximately:

$$V/V^* = 1 - \int_{E_a}^\infty f(E) dE = \int_0^{E_a} f(E) dE \quad (3)$$

5. Calculate k_0 corresponding to each E_s value at all the heating rates using

$$0.545aE_s/k_0RT^2 = e^{-E_s/RT} \quad (4)$$

then employ the averaged k_0 value as a true k_0 value.

No *a priori* assumption is required for the functional forms of $f(E)$ and $k_0(E)$. In other

words we can determine k_0 and E at any levels of V/V^* .

In this paper the method was applied to estimate $f(E)$ and k_0 for the pyrolysis of 19 coals including the Argonne premium coals. It was found that $f(E)$ was significantly dependent on coal rank. However, the k_0 vs. E relationships were found to be classified into three groups depending on coal rank. Using the three k_0 vs. E relationships, we presented to estimate $f(E)$ from a single experimental run performed under a constant heating rate.

EXPERIMENTAL

Table 1 lists the ultimate analyses for the 19 coals used in this work. The weight change accompanying the pyrolysis of coal was measured by use of a sensitive thermobalance (Shimadzu TG-50) under three different heating rates (α) of 5, 10, and 20 K/min in a nitrogen atmosphere. The measured weight-time relationships were converted to the relationships of V/V^* vs. T . Pyrolysis using a Curie point pyrolyzer (Japan Anal. Ind. JHP-2S) was also performed for several coals. The coal particles were heated at 3000 K/s to 280, 386, 485, or 578°C and kept for 10 s at the temperature. The change in V/V^* was calculated from the total weight change of the coal particles.

RESULTS AND DISCUSSION

$f(E)$ curves and k_0 vs. E relationships estimated by the proposed method for 19 coals

Figure 1 shows the relationships of V/V^* vs. T measured at $\alpha = 20$ K/min. The temperature at which the reaction starts and the shape of the curves are significantly different among the coals.

The relationships between V/V^* vs. E can be obtained through the procedures 1 to 3 mentioned above and are shown for the Argonne premium coals in the figure above and for the other coals in the figure below in Figure 2. Differentiating the curves graphically by E , $f(E)$ curves for the coals could be obtained as shown in Figure 3. The shape of the curves are significantly different among the coals: the peaks appear at $E=220$ – 280 kJ/mol, and the activation energy E spreads from 150 to 400 kJ/mol. These results clearly show that $f(E)$ can not be represented by a single Gaussian distribution. For the Argonne premium coals, the peak position shifted to higher E values with the increase of coal rank. This is well expected because the higher rank coals are decomposed at higher temperatures as shown in Fig. 1. For the other coals, the order of peak position does not always follow the order of coal rank as shown in Fig. 3b. This is probably because the coals were collected from various countries.

Figure 4 shows the k_0 vs. E relationships estimated for all the coals. Interestingly, the relationships were little dependent on coal types except three low rank coals, SY, MW, and BD. The difference in k_0 was only the order of 10^2 at maximum at a same E without the lower rank coals. This means that the coal pyrolysis consists of similar reactions having almost same rates for these coals. Only the proportions of the reactions are judged to be different among the coals, which is represented by the difference of $f(E)$ curves. The k_0 value increased from the order of 10^{10} to the order of 10^{25} s⁻¹ while E increases from 150 to 400 kJ/mol. The following compensation effect approximately held between the k_0 values and E for all the coals.

$$k_0 = \alpha e^{\beta E} \quad (\alpha, \beta; \text{constants}) \quad (5)$$

It is obvious that k_0 can not be assumed as constants for the pyrolysis of these coals.

Figure 5 compares the experimental TG curves and the curves calculated using $f(E)$ and k_0 estimated for MW coal. Not only the curves ($\alpha = 5, 10$, and 20 K/min) utilized for obtaining $f(E)$ and k_0 but the data obtained at $\alpha=3000$ K/s showed good agreement with the calculated curves. This clearly indicates the validity of the presented method.

Figure 6 shows the $f(E)$ curves obtained by Burnham et al.¹⁰ for the Argonne premium coals by the conventional method. The peak position of $f(E)$ is not in the order of the coal rank: the peak position of the lowest rank coal, ND coal, is at $E=260$ kJ/mol, whereas the peak position of the highest rank coal, POC coal, is at $E=220$ kJ/mol. This would be because the k_0 value assigned to ND coal is larger than that assigned to POC coal. In the conventional method the $f(E)$ curve is dependent on the value of k_0 assigned as stated above. Therefore, we must be careful in interpreting the meaning of the activation energy when we resort to the conventional method.

A method to determine $f(E)$ from a single experiment

Figure 4 shows that the k_0 vs. E relationships are little affected by the coal type. This means

that the k_0 vs. E relationships may be represented by several relationships. Then the k_0 vs. E relationships in Fig. 4 were examined in more detail, and they were found to be grouped into three relationships depending on the coal rank as shown in Figs. 7a to 7c, where the relationships were approximated by eq 5.

Once we can know the k_0 vs. E relationship, we can obtain the relationship between E vs. T by using eq 4 for a selected heating rate α . Then $f(E)$ can be estimated from a single TG curve obtained at the heating rate. The procedure is given as follows:

- (1) Measure V/V^* vs. T relationship at a heating rate α .
- (2) Calculate the E vs. T relationship using eq 4 by choosing the k_0 vs. E relationship corresponding to the coal rank from three correlating equations.
- (3) Convert the V/V^* vs. T relationship into V/V^* vs. E relationship using the k_0 vs. E relationship obtained in (2).
- (4) Differentiate the V/V^* vs. E relationship by E gives $f(E)$.

Although the procedure is rather simple, the procedure (2) requires trial and error calculation. Then, the E vs. T relationships for $\alpha = 20\text{K/min}$ were calculated, and shown in Figure 8. Measuring the V/V^* vs. T relationship at $\alpha = 20\text{K/min}$ and using Fig. 8, one can obtain $f(E)$ curve straightforwardly.

Figure 9 compares the $f(E)$ curves estimated by the simple method using the V/V^* vs. T relationship measured at $\alpha = 20\text{K/min}$ and those estimated by the original method for several coals. The $f(E)$ curves estimated using the simple method are rather smooth and the peak intensities are smaller than those estimated using the original method. However, the E values at the peak positions obtained by the two methods are almost same. The V/V^* vs. T relationships were well reproduced using the $f(E)$ curves estimated by the simple method. One of the difficulties in applying the original method was to obtain E at smaller V/V^* region ($V/V^* < 0.1$) and at higher V/V^* region ($V/V^* > 0.1$). This was because the V/V^* vs. T curves obtained under three different heating rates become so close. Using the simple method, we can the procedure to obtain E . This largely facilitates the estimation of $f(E)$. Since the $f(E)$ curves estimated by the simple method are rather close to those obtained by the original method, the simple method is well utilized to estimate $f(E)$ curve.

CONCLUSION

The new method presented by the authors for estimating both the distribution curve $f(E)$ and the frequency factor $k_0(E)$ in the distributed activation energy model (DAEM) was applied to the analysis of pyrolysis reaction of 19 coals. It was found that the $f(E)$ curve spreads over 150 to 400 kJ/mol and that the frequency factor k_0 increases from 10^{12} to 10^{26} s^{-1} with the increase of E . The assumption of a constant k_0 value could not be employed for these coal. The validity of the proposed method was clarified through these works. Furthermore, a simple method was presented for estimating $f(E)$ from a single experiment. The $f(E)$ curves estimated by the simple method are rather close to those obtained by the original method, indicating the validity of the simple method. Using the simple method, we can estimate $f(E)$ easily and straightforwardly.

REFERENCES

1. Pitt, G.J., *Fuel*, **1962**, *41*, 267-274.
2. Suuberg, E.M.; Peters, W.A.; Howard, J.B., *Ind. Eng. Chem. Process Des. Dev.*, **1978**, *17*, 37-46.
3. Reynolds, J.G.; Burnham, A.K., *Energy & Fuels*, **1993**, *7*, 610-619.
4. Solomon, P.R.; Hamblen, D.G.; Carangelo, R.M.; Serio, M.A.; Deshpande, G.V., *Energy Fuels*, **1988**, *2*, 405-422.
5. Grant, D.M.; Pugmire, R.J.; Fletcher, T.H.; Kerstein, A.R., *Energy Fuels*, **1989**, *3*, 175-186.
6. Niksa, S.; Kerstein, A.R., *Energy Fuels*, **1991**, *5*, 647-665.
7. Anthony, D.B.; Howard, J.B., *AIChE J.*, **1976**, *22*, 625-656.
8. Du, Z.; Sarofim, A.F.; Longwell, J.P., *Energy & Fuels*, **1990**, *4*, 296-302.
9. Miura, K., *Energy Fuels*, **1995**, *9*, 302-307.
10. Burnham, A.K.; Oh, M. S.; Crawford, R. W., *Energy & Fuels*, **1989**, *3*, 42-55.

Table 1. Ultimate analyses of the coals used

Coal	Ultimate analysis [wt% d.a.f.]			
	C	H	N	O(diff.)
Beulah-Zap (ND)	72.9	4.8	1.2	20.1
Wyodak (WY)	75.0	5.4	1.1	18.5
Illinois#6 (IL)	77.6	5.0	1.4	16.0
Blind Canyon (UT)	80.6	5.8	1.6	12.0
Lewiston-Stockton (ST)	82.5	5.3	1.6	10.6
Pittsburg#8 (PITT)	83.2	5.3	1.6	9.9
UpperFreeport (UF)	85.5	4.7	1.6	8.2
Pocahontas (POC)	91.0	4.4	1.3	3.3
Soya (SY)	66.1	5.2	1.5	27.2
Morwell (MW)	67.1	4.9	0.6	27.4
Baiduri (BD)	72.3	4.7	1.4	21.6
Onbilitin(OB)	78.3	5.6	1.7	14.4
Taiheiyu(TC)	78.7	6.2	1.2	13.9
Ebeneza(EN)	81.2	6.1	1.6	11.1
Tiger Head(TH)	82.3	5.6	1.8	10.3
Taung(TT)	82.7	4.7	1.1	11.5
Ensuyutokson(ET)	82.8	5.6	1.5	10.1
Blair Athol (BA)	82.9	4.7	1.8	10.6
Newlands(NL)	85.9	4.9	1.7	7.5

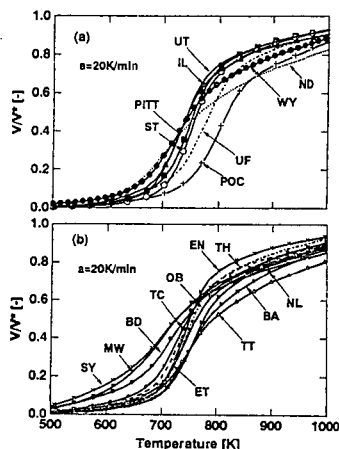


Figure 1. V/V^* vs. T relationships measured at $a=20K/min$ for 19 coals.

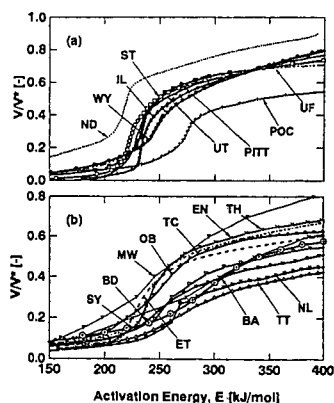


Figure 2. V/V^* vs. E relationships estimated by the proposed method.

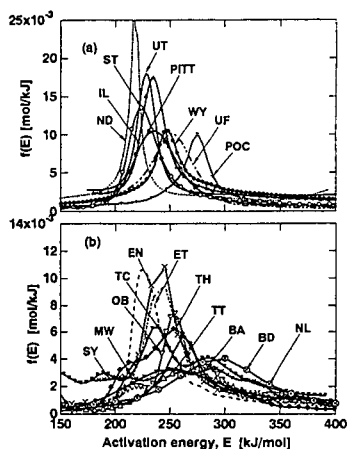


Figure 3. $f(E)$ curves estimated by the proposed method.

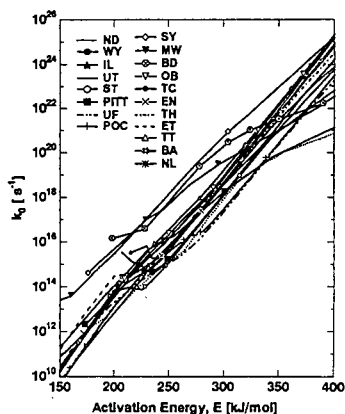


Figure 4. k_0 vs. E relationships estimated by the proposed method.

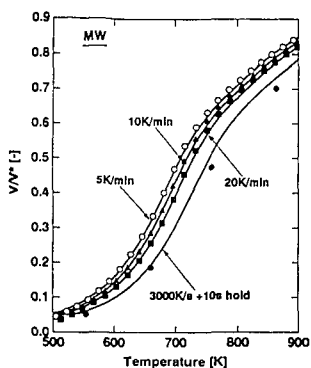


Figure 5. Comparison between the experimental V/V^* vs. T curves and calculated ones using $f(E)$ and k_0 estimated.

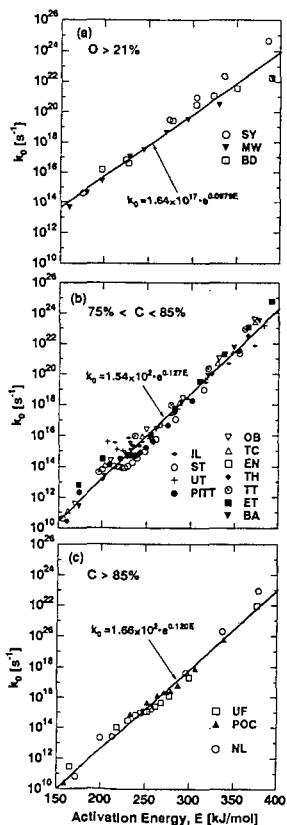


Figure 7. k_0 vs. E relationships approximated for three groups of coal rank.

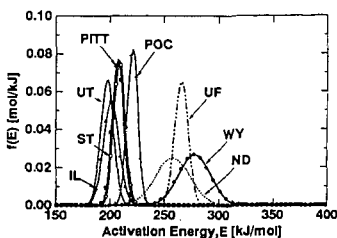


Figure 6. $f(E)$ curves for the Argonne coals estimated by Burnham et al. using the conventional method.

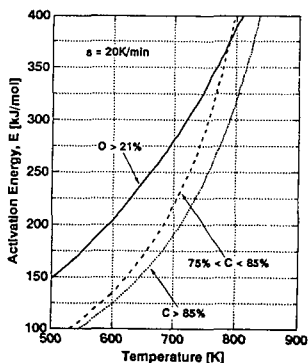


Figure 8. E vs. T relationships for $a = 20$ K/min for three groups of coal rank.

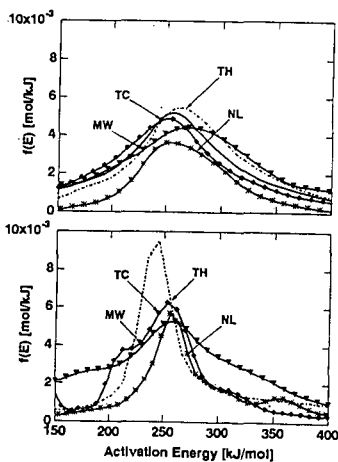


Figure 9. Comparison of the $f(E)$ curves estimated by the simple method (above) and those estimated by the original method (below).

PORPHYRIN- AND METALLOPORPHYRIN-DERIVED CARBONS AS MODELS FOR COAL CHARs

Jenny M. Jones, Jonathon Agnew, James Kennedy and Ben Watts
Department of Fuel and Energy, University of Leeds, Leeds, U.K., LS2 9JT

Keywords: Coal, porphyrins, NO_x, catalysis.

INTRODUCTION

Factors which govern the release of fuel-nitrogen as NO_x (rather than N₂) during coal combustion are of interest because of the environmental implications. Coal is a complex material which can be considered to be composed of large polymeric, molecules comprising aliphatic cross-linked polyaromatic structural units which contain many heteroatom types and functionalities. Within this polymeric matrix smaller molecules are dispersed, together with mineral particles, metal salts etc. Model coals derived from carbonisation of organic precursors offer an approach for examining the role of some of these variables (nitrogen-functionality, oxygen content, metal type, environment and content etc.) on NO_x formation during combustion. In principle, such models are easier to characterise, compared to coal, with regards to their chemical and physical properties.

The nitrogen in coal is virtually exclusively organic and typical nitrogen contents are in the range 0.7-2.1 wt%. The chemical form of the nitrogen is mainly pyrrolic and pyridinic, with smaller amounts of quaternary nitrogen within the aromatic units. Lower rank coals may possess other functional groups such as amines. As a consequence model coals derived from carbazole, acridine, or ammonia-treated carbons etc. have been studied for their combustion behaviour.¹⁻⁵

One source of this nitrogen in coal is derived from porphyrin and other plant protein structures which are degraded via different routes during coal diagenesis. These types of systems have been identified in coals as well as coal extracts.^{6,7} Such systems are of interest because of their ability to chelate metals, in particular vanadium and iron. Nitrogen chelates and chelated metal species are expected to have very different nitrogen release behaviour during combustion, compared to free pyrrolic or pyridinic systems because: (i) the nitrogen:carbon ratio is unusually high in the porphyrin chelate; (ii) the nitrogen atoms are in close spatial proximity within the chelate; (iii) there exists intimate contact between the chelated metal and the nitrogen atoms.

In the present study, model coals derived from porphyrin and metalloporphyrin chelates have been characterised for their chemical and physical properties with particular emphasis on their behaviour during pyrolysis and combustion. To the authors' knowledge such types of systems have not been studied previously.

EXPERIMENTAL

The model carbons were prepared by atmospheric pressure co-carbonisation of a 10:1 by weight acenaphthylene and the porphyrin (or metalloporphyrin) mixture under an argon atmosphere. The heating rate was 1 K/min and initially the carbons were heat-treated at 873 K for 1 h. Carbons treated at higher temperatures were heated again in argon at 4 K/min to the desired temperature and held for 1 h. Surface areas were measured by the BET method using a Quantachrom Quantasorb QS-13 surface area analyser. Pyrolysis studies at 1273 K were performed using a Chemical Data Systems, Inc., 190 Pyroprobe pyrolysis system interfaced to a Perkin-Elmer 8700 capillary GC, with FID and NPD detectors. Combustion studies were performed in a Shimadzu TGA-50H thermogravimetric analyser (15 K/min heating rates) in air, or in 20% O₂/Ar using a Stanton Redcroft STA 1500 thermogravimetric analyser coupled to a VG Quadrupole mass spectrometer by means of a heated capillary sampling probe. Further details are described elsewhere.¹

RESULTS AND DISCUSSION

The elemental analyses of the model coals are given in Table 1, together with surface areas, where available. The surface areas of the carbons were, in general, quite low which may be expected for the anisotropic acenaphthylene derived carbons, due to small pore sizes. The N:V ratio in the carbon prepared from pure tetraphenyl porphine (CTTPV) is much larger than that in the precursor suggesting that much of this metal is no longer chelated, and may be present as the oxide. In contrast, the N:M ratio for the 873K heat-treated Fe- and Co-containing co-carbonised carbons are essentially unchanged compared with the corresponding metalloporphyrin precursors, which may indicate that the chelate is intact, to some extent.

The evolved gas profiles during the temperature programmed combustion (TPC) of the tetraphenyl porphine starting material are given in Figure 1. The main fuel-N product is N_2 , and relatively large amounts of NO, HCN and other cyano species were detected. The cyano species are seen to be evolved during the onset of combustion, while the majority of fuel-N is evolved as N_2 towards the latter stages of combustion. This type of behaviour is often seen for coals and coal chars, where nitrogen is retained in the char until its eventual release at high levels of burnout.

The evolved gas profiles during TPC of the carbonised tetraphenylporphyrin and carbonised vanadyl porphyrin are given in Figures 2 and 3 respectively and Table 2 quantifies the differences in the fuel nitrogen conversions. Comparison of Figures 1 and 2 show that the differences in the fuel nitrogen conversions which occur during carbonisation have profound effects on the fuel-N released. In particular, the HCN gas evolution profile is quite different, and far more N_2 is evolved after carbonisation. This N_2 is evolved at almost the same temperature as observed during the TPC of the pure tetraphenylporphine precursor, suggesting structural similarities. The evolution of N_2 during combustion may be indicative of N atoms in the carbon structure which are close spatially. Alternatively mobile C(N) surface species may participate. The presence of the metal (Figure 3, and Table 2) also has a marked effect on the fuel-N conversions. This may be the result of a catalytic effect of vanadium on the reduction of NO to N_2 . The catalytic effects of the metal on combustion is illustrated dramatically when comparisons of Figures 2 and 3 are made. Catalysis was seen to occur for the combustion of all the co-carbonised carbons, and a compensation effect on the rates was apparent, as shown in Figure 4.

During pyrolysis of the co-carbonised samples, the major products observed were hydrogen cyanide and acetonitrile. The presence of the metal decreased the amount of both these species which may be indicative of the persistence of M-N interactions in the carbons.

CONCLUSIONS

Carbons derived from porphyrin and metalloporphyrin precursors can be used to investigate the influence of such moieties on the conversion of fuel-nitrogen in coals. The presence of metals catalyses the combustion and appears to lower the amount of fuel-N converted to HCN in the volatiles, and increase the fuel-N to N_2 conversions. It is unclear, at the present time, as to whether chelated or unchelated metals are responsible for this.

REFERENCES

1. Jones, J. M., Harding, A. W., Brown, S. D., and Thomas, K.M. *Carbon* 1995, **33**, 833.
2. Grant, K. A., Zhu, Q., and Thomas, K. M. *Carbon* 1994, **32**, 883
3. Wang, W. and Thomas, K. M., *Fuel* 1993, **72**, 293.
4. Jones, J. M., and Thomas, K. M. *Carbon* 1995, **33**, 1129.
5. Thomas, K. M., Grant, K., and Tate, K. *Fuel* 1993, **72**, 941.
6. Bonnett, R., Burke, P.J., Dewey, C.R., Fairbrother, A.E., and Major, H.J.; *Fuel*, 1991, **70**, 1227;
7. Haenel, M.W.; *Fuel*, 1992, **71**, 1211.

ACKNOWLEDGEMENT

The TG-MS data was obtained in the Northern Carbon Research Laboratories, Department of Chemistry, University of Newcastle upon Tyne, U.K.

TABLE 1: Properties of the model carbons

sample i.d.†	HTT (K) ‡	wt% C	wt% H	wt% N	wt% O*	wt% metal	surface area (m ² /g)
CTPP-873	873	83.1	2.4	8.8	5.7	-	nm
CTPPV-873	873	52.1	1.4	5.5	13.5	27.5	nm
ACE-TPP-873	873	94.1	2.1	0.5	3.3	-	5
ACE-TPP-V-873	873	93.1	1.7	1.6	0.9	2.7	5
ACE-TPP-Fe-873	873	92.1	1.8	1.6	3.0	1.5	5
ACE-TPP-Co-873	873	89.6	1.7	1.8	5.0	1.9	3
ACE-TPP-Cu-873	873	89.5	1.8	1.6	5.0	2.1	3
ACE-PC-873	873	92.2	2.1	0.8	4.9	-	2
ACE-PC-V-873	873	88.6	1.8	2.8	3.2	3.6	11
ACE-TPP-1073	1073	97.4	0.9	0.6	1.1	-	2
ACE-TPP-V-1073	1073	93.2	1.0	1.5	1.4	2.9	6
ACE-TPP-Fe-1073	1073	96.2	0.3	0.7	1.2	1.6	149
ACE-TPP-Co-1073	1073	94.6	0.3	0.7	2.2	2.2	57
ACE-TPP-Cu-1073	1073	94.5	0.7	1.5	1.2	2.1	3
ACE-TPP-1273	1273	95.9	0.3	0.5	3.3	-	3
ACE-TPP-V-1273	1273	95.2	0.3	1.1	0.5	2.9	2

†ace - acenaphthylene; tpp - tetraphenylporphyrin (free base or chelated to denoted metal); nm: not measured. *By difference. ‡HTT: Heat treatment temperature.

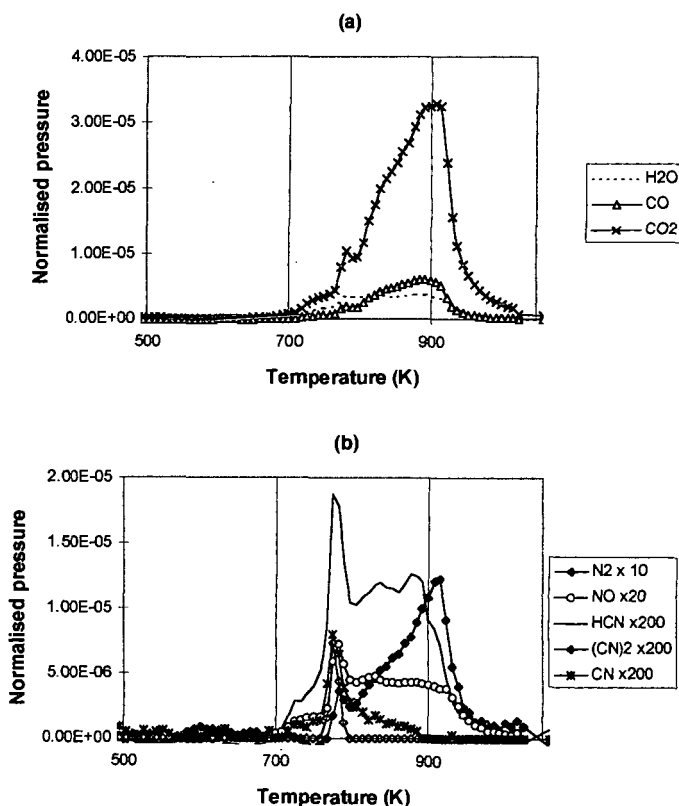


FIGURE 1: Gas evolution profiles during the temperature programmed combustion of tetraphenylporphyrine in 20% O₂/Ar (a) major products, (b) fuel nitrogen products.

TABLE 2: Product distribution ratios during temperature programmed combustion.

Product Ratio	TPP	CTPP-873	CTPPV-873
CO/CO ₂	0.173	0.713	0.235
NO/N	0.090	0.213	0.033
HCN/N	0.021	0.0005	0.041
N ₂ /N	0.452	0.807	0.822
C ₂ N ₂ /N	0.002	-	-
CN/N	0.004	-	-
Total N/fuel N	0.569	1.0205	0.896

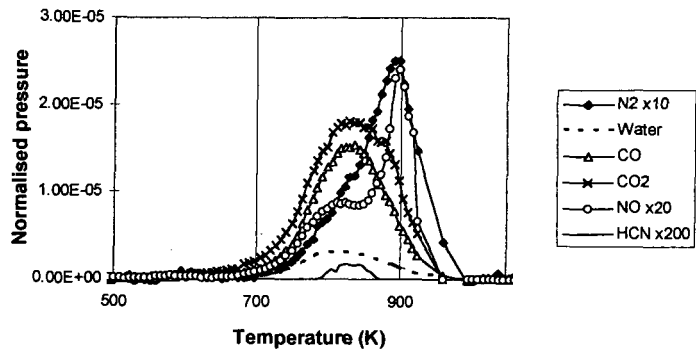


FIGURE 2: Gas Evolution profiles during the temperature programmed combustion of CTPP-873 in 20% O₂/Ar

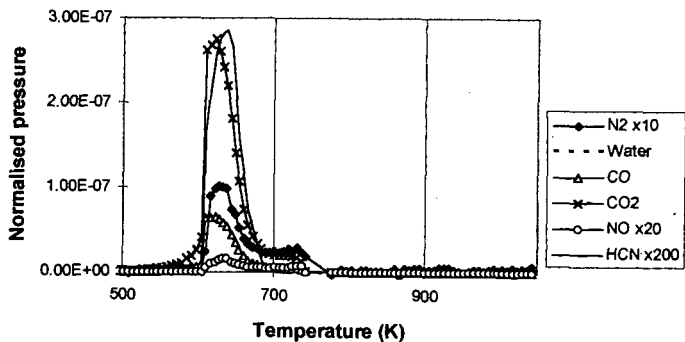


FIGURE 3: Gas Evolution profiles during the temperature programmed combustion of CTPPV-873 in 20% O₂/Ar

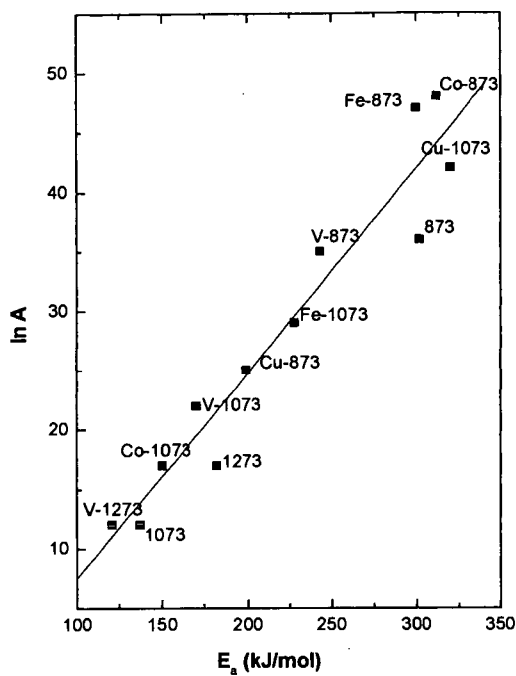


FIGURE 4: Compensation effect for metal-free and metal containing carbons. The ACE-TPP prefix has been dropped from the sample designation.

A NEW METHOD TO ESTIMATE HYDROGEN BONDINGS IN COAL BY UTILIZING FTIR AND DSC

Kouichi MIURA, Kazuhiro MAE, and Fumi-aki MOROZUMI

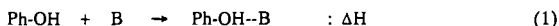
Department of Chemical Engineering, Kyoto University, Kyoto 606-01 JAPAN

Key words: Strength distribution of hydrogen bonding in coal, Wavenumber shift of O-H stretching vibration, Enthalpies of hydrogen bonding

INTRODUCTION

Several attempts have been made to estimate the change in the macromolecular network of coal using DSC and F.T.i.r. techniques. Lucht et al.,¹ Mackinnon et al.,² and Yûn et al.³ examined the glass transition of coal by the DSC measurement. Mackinnon et al.² observed the 2nd order phase glass transition at around 110 °C during the heating of various coals. They speculated that the 2nd order phase glass transition at low temperature was caused by the change in hydrogen bondings, although the direct evidence was not shown. We also demonstrated that a part of hydrogen bondings in coal are released between 100 and 200 °C from in-situ F.T.i.r. analysis.⁴ Painter et al.⁵ examined in detail the hydrogen bondings in coal using F.T.i.r., and classified the hydrogen bondings into 5 types.

In liquid phase, on the other hand, hydrogen-bonded adduct formation reactions between the OH functional groups of phenols and various bases have been examined in detail. The reaction is represented by



where Ph-OH \cdots B represents the hydrogen-bonded adduct, and ΔH is the enthalpy change of the reaction. When the hydrogen bonding is formed, the wavenumber of the O-H stretching vibration shifts to a low wavenumber and generates heat ($\Delta H < 0$). The enthalpy change, ΔH , and the OH wavenumber shift, $\Delta\nu_{\text{OH}}$, were measured for various phenol-base combinations, and a linear relation was found to hold between ΔH and $\Delta\nu_{\text{OH}}$ by many investigators.⁶⁻⁹ The relation obtained by Drago et al.⁶, for example, is given by

$$-\Delta H = 0.067 \Delta\nu_{\text{OH}} + 2.64 \quad [\text{kJ/mol}] \quad (2)$$

The values of $-\Delta H$ was interpreted as the energy related to hydrogen bonding Ph-OH \cdots B by many investigators.¹⁰⁻¹³ However, Drago et al. thought that ΔH consists of two contributions: the change in the phenol O-H bond energy, δD_{OH} , and the bond dissociation energy of hydrogen bond formed, D_{HB} , as

$$\Delta H = \delta D_{\text{OH}} - D_{\text{HB}} \quad (3)$$

They thought that D_{HB} is an index better than ΔH for the strength of the hydrogen bond. Then a relationship between δD_{OH} and $\Delta\nu_{\text{OH}}$ as well as a relationship between D_{HB} and $\Delta\nu_{\text{OH}}$ are required. They approximated the stretching of the hydrogen-bonded OH by the anharmonicity stretching of free OH, and related δD_{OH} with $\Delta\nu_{\text{OH}}$ as follows:

$$\delta D_{\text{OH}} = (hcN/4x_e) \delta\nu_{\text{OH}} = D_{\text{OHf}} (\delta\nu_{\text{OH}}/\nu_e) = 0.131\Delta\nu_{\text{OH}} \quad (4)$$

where h is Planck's constant, c is the speed of light, D_{OHf} is the bond dissociation energy of free O-H in kJ/mol and ν_e is the wavenumber of harmonic vibration of the free OH in cm^{-1} , and x_e is the anharmonicity constant for the oscillator.

From eqs.(2) and (4) D_{HB} was assumed to be represented by

$$D_{\text{HB}} = k \delta D_{\text{OH}} + \text{const.} \quad (5)$$

Substituting eq.(4) into Eq.(5), the following equation is obtained.

$$D_{\text{HB}} = k_1 \Delta\nu_{\text{OH}} + k_2 \quad (k_1, k_2: \text{const.}) \quad (6)$$

If the constants k_1 and k_2 can be determined, the relationship between D_{HB} and $\Delta\nu_{\text{OH}}$ is obtained. In liquid phase the following equation has been established for the $D_{\text{HB}}\text{-}\Delta\nu_{\text{OH}}$ relationship⁶:

$$-D_{\text{HB}} = 0.198 \Delta\nu_{\text{OH}} + 2.64 \quad [\text{kJ/mol}] \quad (7)$$

In this paper an equation relating the bond dissociation energy of the hydrogen bonding, D_{HB} , and $\Delta\nu_{\text{OH}}$ for coal was derived by extending the method of Drago et al. Then the strength distribution of hydrogen bondings in coal was estimated using the equation. Finally, the change in the hydrogen bondings through the heating of coal was examined.

EXPERIMENTAL

Sample preparation

A Japanese sub-bituminous coal, Taiheiyô (TC, C; 74.5%, H; 6.0%, N; 1.3%, S; 0.2%, O; 18.0% daf), was used as a raw coal. The coal was ground into fine particles of less than 74 μm , and dried in vacuo at 70 °C for 24 h before use. Irreversibly swollen coals (VDC) were prepared as follows: the coal particles were mixed with tetralin in a mass ratio of 1 to 0.6 in a stainless steel tube, and they were pressurized up to 1 MPa by nitrogen. The tube was immersed in a sand bath which was kept at a constant temperature at 150 or 220 °C and kept there for 1 h to prepare the swollen coal. Then, the swollen coal was evacuated at 70 °C for 24 h to remove completely the solvent retained. Even after removing the solvent the coal was still swollen to some extent. Then the coal was abbreviated to

VDC (vacuum dried coal). The VDCs prepared from the coals swollen at 150 and 220 °C were abbreviated to VDC(150°C) and VDC(220°C), respectively. The VDC(220°C) was further cooled to -100 °C using liquid nitrogen to prepare the sample in which some hydrogen bondings were restored. This sample was abbreviated to VDC(-100°C). The chars were prepared by pyrolyzing the coal at 5 K / min up to several temperatures to examine the change in hydrogen bondings during the pyrolysis.

F.T.i.r. and Calorimetric Measurement

The F.T.i.r. spectra of the raw coal, the VDCs and the pyrolysis chars were measured by the KBr method using a F.T.i.r. spectrometer (Shimadzu, FTIR 4300). The DSC profiles and the TG curves of the raw coal and the VDCs were measured under a constant heating rate of 5 K / min by use of a differential scanning calorimeter (Shimadzu, DSC 50) and a thermobalance (Shimadzu, TGA 50), respectively.

RESULTS AND DISCUSSION

Comparison of F.T.i.r. spectra between the raw coal and VDCs

The F.T.i.r. spectra were measured for all the samples. The spectrum of the O-H stretching vibration related to hydrogen bonding appears between 2600 and 3600 cm^{-1} ,⁵ so the base line was drawn between these wavenumbers by a usual method.^{14,15} Two sharp peaks at around 2800 cm^{-1} are due to aliphatic C-H vibrations, these peaks were eliminated following Solomon's method,¹⁶ then the absorption peak related to hydrogen bondings was 3000 to 3600 cm^{-1} for TC coal. The spectra obtained after the treatment are shown by the dotted lines in Figure 1. Comparing the spectra, the intensity of peak at 3630 cm^{-1} , which is assigned as the free OH, is almost same for all the samples, indicating that free OH groups are not produced through the solvent swelling and the heat treatment. Many peaks are involved between 3000 and 3600 cm^{-1} in the spectrum. Painter et al. showed that absorption bands of five hydrogen-bonded OH groups are involved in the spectrum: OH- π bonds (3516 cm^{-1}), self-associated OH groups (3400 cm^{-1}), OH-ether hydrogen bonds (3300 cm^{-1}), tightly bound cyclic hydrogen bonds (3200 cm^{-1}) and OH-N hydrogen bonds (2800-3100 cm^{-1}).⁵ Following these assignments, each spectrum was fitted by five Lorentz-Gaussian distributions as shown by the solid lines in Fig.1. The OH wave number shift, $\Delta\nu_{\text{OH}}$, for each hydrogen bonding is exactly estimated from the five peaks for the raw coal. The intensity of peak at around 3300 cm^{-1} was the strongest for the raw coal. As compared with the spectrum of the raw coal, the intensity of peak at around 3300 cm^{-1} decreased, and the intensities of peaks at around 3400 cm^{-1} and 3520 cm^{-1} increased for VDC(220°C). The intensities of peaks at around 3400 cm^{-1} and 3520 cm^{-1} decreased, and the intensity of peak at around 3300 cm^{-1} increased for VDC(-100°C). The intensities of peaks at around 3130 and 3040 cm^{-1} were almost same for all the samples. These results clearly show that the strong hydrogen bond and free OH were not affected by the solvent swelling and the heat treatment. Only the ether-OH, the self-associated OH groups, and the OH- π bonds were released or restored through the treatments.

Then we can visualize the change in the hydrogen bonding in coal as shown in Figure 2. When the coal is heated to as high as 200 °C or so, relatively weak hydrogen bonds such as OH-ether bond are released, but strong hydrogen bonds assigned at low wavenumber do not change. As a result the movement of the macromolecule of coal is restricted, then the OH in the hydrogen bonds released can not become free OH. It will form another weak hydrogen bonds.

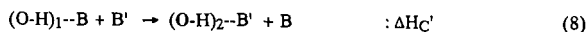
Figure 3 shows the DSC profiles measured for the raw TC and the VDCs. Thermogravimetric (TG) curves were measured under the same conditions. Distinct differences were found among the DSC profiles at the temperature region of 100 to 300 °C, whereas no difference was found among the TG curves of the four samples. The DSC profile of the raw coal showed the largest endothermicity of the three samples: the endothermic rate started to increase at around 100 °C, reached a maximum at ca. 250 °C, decreased to reach a minimum at 300 °C or so, and finally increased rapidly with the further increase of temperature. On the other hand, the endothermic rate of VDC(220°C) whose swelling ratio was largest was almost constant up to 200 °C, then started to increase, and finally almost coincided with that of the raw coal. The endothermic rate of VDC(150°C) which was slightly swollen lay between the endothermic rates of the raw coal and VDC(220°C). The DSC profile of VDC(-100°C) was close to that of VDC(150°C) up to 200 °C, but over 200 °C it was closer to that of the raw coal. The difference between the DSC profiles of the raw coal and the VDCs is judged to arise from the differences in the hydrogen bondings among the samples. The difference of the enthalpy levels between the raw coal and the VDC at 25 °C, ΔH_C , is obtained by heating both samples up to 220 °C where both enthalpy levels are considered to be same as shown in Fig.4. The enthalpy ΔH_C could be related to the difference of the strength of hydrogen bondings between the samples.

Estimation of the hydrogen bondings in coal using F.T.i.r. and DSC

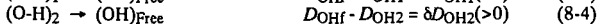
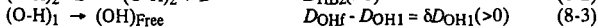
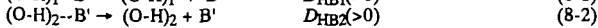
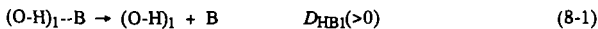
a) Formulation of equation relating D_{HB} and $\Delta\nu_{\text{OH}}$ in coal

The equation developed by Drago et al.⁶ for relating D_{HB} and $\Delta\nu_{\text{OH}}$ may not be applied to analyze the hydrogen bonding in coal, because it was obtained in liquid phase and coal contains several types of hydrogen bondings. However, the equation relating δD_{OH} and $\Delta\nu_{\text{OH}}$, eq.(4), was assumed to hold for the hydrogen-bonded OH in coal, because it is for intramolecular movement. Then the concept developed by Drago et al.⁶ was extended to formulate the equation relating D_{HB} and $\Delta\nu_{\text{OH}}$ using the experimental data, ΔH_C and $\Delta\nu_i$, obtained above.

First, we consider the change of a hydrogen bond, (O-H)₁-B, into another hydrogen bond, (O-H)₂-B', as a chemical reaction.



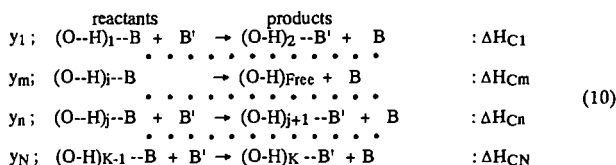
where B and B' represent electron donor atoms or molecules. The enthalpy change through the reaction, $\Delta H_C'$, is positive when the hydrogen bond becomes weaker through the reaction and vice versa. If we assume that $\Delta H_C' > 0$, the OH wavenumber shift decreases from $\Delta \nu_{OH1}$ to $\Delta \nu_{OH2}$, and the O-H bond dissociation energy increases from D_{OH1} to D_{OH2} as shown in Fig.5. The above reaction was apparently divided into the following reactions:



where $(O-H)_i$ represents the hydrogen-bonded OH groups, $(OH)_{Free}$ represents the free OH, D_{HBi} is the bond dissociation energy of hydrogen bond defined by Drago et al.,⁶ and δD_{OHi} ($i = 1, 2$) is the difference between the dissociation energy of the free O-H bond, D_{OH1} , and that of hydrogen bonded O-H, D_{OHi} . Since eq.(8-1) - eq.(8-2) + eq.(8-3) - eq.(8-4) makes eq.(8), $\Delta H_C'$ is represented by

$$\Delta H_C' = (D_{HB1} - D_{HB2}) - (\delta D_{OH1} - \delta D_{OH2}) \quad (9)$$

Next, eq.(8) was extended to all the reactions of the hydrogen bondings in coal as follows:



where all the possible reactions are taken into account in the N reactions, y_n is the contribution of each reaction defined so as to satisfy $\sum y_n = 1$, and the electron donors, B and B', for different reactions are not always same. The sum of $(O-H)_k$ and free OH, N_{OH} [mol/kg], is the total amount of OH groups in coal. The enthalpy change for each reaction, ΔH_{Cn} , is represented in the same manner as eq.(9). Then, summing up the reactions in eq.(10), the difference in the enthalpy between the products (p), and the reactants (r), ΔH_C [kJ/kg-coal], is represented by

$$\begin{aligned} \Delta H_C &= N_{OH} \sum y_n \Delta H_{Cn} \\ &= N_{OH} [\{ \sum (\sum y_n)_i D_{HBi} \}_r - \{ \sum (\sum y_n)_i D_{HBi} \}_p] \\ &\quad - N_{OH} [\{ \sum (\sum y_n)_i \delta D_{OHi} \}_r - \{ \sum (\sum y_n)_i \delta D_{OHi} \}_p] \end{aligned} \quad (11)$$

where y_n is set equal to 0 when i-th species is not involved in the n-th reaction. Then the term $(\sum y_n)_i$ is equal to the fraction of hydrogen-bonded $(O-H)_i$ of the all OH, and it was represented by f_i . The terms $\sum (\sum y_n)_i D_{HBi}$ and $\sum (\sum y_n)_i \delta D_{OHi}$, therefore, correspond to the average values of D_{HB} and δD_{OH} , respectively. They were represented by \bar{D}_{HB} and $\bar{\delta D}_{OH}$, respectively. By using the representation eq.(9) is rewritten as

$$(\bar{D}_{HB})_r - (\bar{D}_{HB})_p = \Delta H_C / N_{OH} + [(\bar{\delta D}_{OH})_r - (\bar{\delta D}_{OH})_p] \quad (12)$$

By inserting eqs.(4) and (6) into δD_{OHi} and D_{HBi} in eq.(11), eq.(13) is rewritten as

$$k_1 \{ (\Delta \bar{\nu}_{OH})_r - (\Delta \bar{\nu}_{OH})_p \} = \Delta H_C / N_{OH} + 0.131 \{ (\Delta \bar{\nu}_{OH})_r - (\Delta \bar{\nu}_{OH})_p \} \quad (13)$$

where

$$\Delta \bar{\nu}_{OH} = \sum (\sum y_n)_i \Delta \nu_{OHi} = \sum f_i \Delta \nu_{OHi} \quad (14)$$

Thus a general equation relating ΔH_C and $\Delta \nu_{OHi}$ was formulated. When the raw coal and one of the VDCs are chosen as the reactants and the products in eq.(13), respectively, ΔH_C was measured by DSC, and $\Delta \nu_{OHi}$ ($i = 1 \sim 5$) were measured by F.T.i.r. for both the raw coal and the VDC as stated above. The value of N_{OH} could be determined from ¹³C-n.m.r. Then, knowing f_i , the k_1 value in eq.(13) can be determined. The value of f_i can be determined from the F.T.i.r. spectra if the relative sensitivities of the five peaks are known. Since the sensitivities are not known now, they were assumed to be same as a first approximation. Then the relations between D_{HB} , ΔH and $\Delta \nu_{OH}$ could be obtained as

$$D_{HB} = 0.20 \Delta \nu_{OH} \quad (15)$$

$$\Delta H = 0.069 \Delta \nu_{OH} \quad (16)$$

Figure 6 compares the D_{HB} - $\Delta \nu_{OH}$ and ΔH - $\Delta \nu_{OH}$ relationships obtained here (eqs.(15) and (16)) with those obtained by Drago et al. in liquid phase (eqs.(7) and (2)). The experimental data in liquid phase obtained by several researchers⁶⁻⁹ are also shown. Eqs.(16) and (2) were very close, and they correlate the experimental data very well. Eqs.(15) and (7) also almost coincided. This shows that same D_{HB} - $\Delta \nu_{OH}$ and ΔH - $\Delta \nu_{OH}$ relationships hold in liquid phase and solid phase, and that eq.(15) is valid to estimate the hydrogen bondings in coal.

(b) Estimation of the strength distribution of hydrogen bonding in coal

Once eq.(15) is found to be valid, the strength distribution of hydrogen bond in coal is straightforwardly estimated. The hydrogen bondings in coal were represented by 5 types, and they were approximated by Gauss-Lorentz functions as stated earlier. The amount of OH corresponding

to each hydrogen bonding, n [mol/mol], is calculated from the intensity of each peak, and D_{HB} corresponding to the peak is calculated from $\Delta\nu_{OH}$ using eq.(15). Then, plotting the n values against D_{HB} , we can obtain the strength distribution of hydrogen bonding. The values of D_{OH} and $\Delta\nu_{OH}$ are also obtained using eqs.(3), (15) and (16).

Figure 7 shows the strength distributions of hydrogen bondings in the raw TC coal and the VDCs. The values of D_{HB} , D_{OH} , and ΔH at maximum n value were 68.0, 42.0 and 23.8 kJ/mol-OH, respectively, for the raw coal. The value of 23.8 kJ/mol-OH for ΔH is reasonable, judging from the values reported.¹⁰⁻¹³ The strength distribution for VDC(220°C) shows that the hydrogen bondings of D_{HB} = 68.0 and 90.0 kJ/mol-OH decreased, but the hydrogen bondings of D_{HB} = 22.8 and 42.0 kJ/mol-OH increased through swelling.

(c) Change in the strength distribution of hydrogen bonding during the pyrolysis

The change in the strength distribution of hydrogen bonding during the pyrolysis was examined by applying eq.(16) to the pyrolysis chars prepared at several pyrolysis temperatures as shown in Fig.8. When TC coal was heated to 280 °C, the 2nd phase glass transition temperature, the hydrogen bonding of D_{HB} = 68 to 90 kJ/mol-OH decreased, and the hydrogen bonding of D_{HB} = 42 kJ/mol-OH increased, indicating that the macromolecular network of the coal was altered to a loose network. The strong hydrogen bondings of D_{HB} = 90 kJ/mol-OH was disappeared first when the coal was heated from 386 to 485 °C, then the weak hydrogen bondings disappeared at around 500 °C. These results indicate that the stronger hydrogen bonding sites become the crosslinking site at low temperature. This well coincides with the fact that the value of D_{OH} decreases as the hydrogen bonding becomes stronger.

Thus, the presented equation was found to be very useful for estimating directly the hydrogen bonding in coal. We have made several assumptions and approximations to derive the equation. We will examine the validity of the assumptions and the approximations in future works.

CONCLUSION

A new method was presented for estimating the strength distribution of hydrogen bonding in coal by use of F.T.i.r. and DSC. An equation relating the dissociation energy of hydrogen bonding, D_{HB} , with the OH wavenumber shift, $\Delta\nu_{OH}$, was established by utilizing the change of hydrogen bonding between a Taiheiyu coal and irreversibly swollen coal prepared from the coal. Using the equation, we could estimate the strength distribution of hydrogen bonding in the coal. The peak D_{HB} value of the raw coal was found to be about 68 kJ/mol-OH. The change in the hydrogen bondings through the pyrolysis of coal was well represented by the method.

ACKNOWLEDGMENT

This study was supported by "Research for the Future" project of the Japan Society for the Promotion of Science (JSPS) through the 148 committee on coal utilization technology of JSPS.

REFERENCES

1. Lucht, L.M.; Larson, J.M.; Peppas, N.A., *Energy & Fuels*, **1987**, 1, 56-58.
2. Mackinnon, A.J.; Hall, P.J., *Energy & Fuels* **1995**, 9, 25-32.
3. Yun, Y.; Suuberg, E.M., *Fuel* **1993**, 72, 1245-1254.
4. Miura, K.; Mae, K.; Sakurada, K.; Hashimoto, K., *Energy & Fuels* **1992**, 6, 16-21.
5. Painter, P.C.; Sobkobiak, M.; Youtcheff, J., *Fuel*, **1987**, 66, 973-978.
6. Purcell, K.F.; Drago, R.S., *JACS*, **1967**, 89, 2874-2879.
7. Drago, R.S.; Epley, T.D., *JACS*, **1969**, 91, 2883-2890.
8. Arnett, E.M.; Mitchel, E.J.; Murty, T.S.S.R., *JACS*, **1974**, 96, 3875-3891.
9. Arnett, E.M.; Mitchel, E.J.; Murty, T.S.S.R.; Gorrie, T.M.; Schleyer, P.v.R., *JACS*, **1970**, 92, 2365-2377.
10. Larsen, J.W.; Green, T.K.; Kovac, J., *J. Org. Chem.* **1985**, 50, 4729-4735.
11. Lucht, L.M.; Peppas, N.A., *Erdol und Kohle-Erdgas* **1987**, 40, 483-485.
12. Green, K.; Kovac, J.; Brenner, D.; Larsen, J.W. in *Coal Structure*; Academic Press: New York, **1982**, pp.199.
13. Painter, P.C.; Park, Y.; Coleman, M.M., *Energy & Fuels*, **1988**, 2, 693-702.
14. Maddams, W.F., *Appl. Spectroscopy*, **1980**, 34, 245-267.
15. Painter, P.C., in *Coal and Coal Products: Analytical Characterization Techniques, ACS Symp. Ser. 205*, **1982**, pp.47-75.
16. Solomon, P.R.; Carangelo, R.M., *Fuel*, **1988**, 67, 949-959.

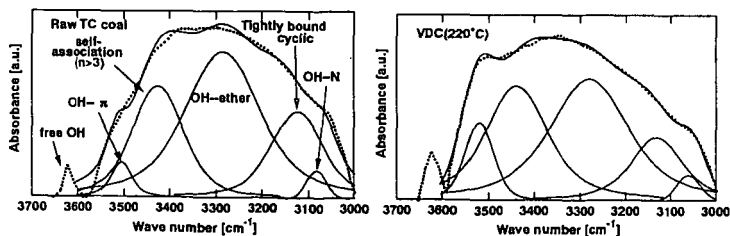


Figure 1 Comparison of the OH stretching vibration between the raw TC and a swollen coal.

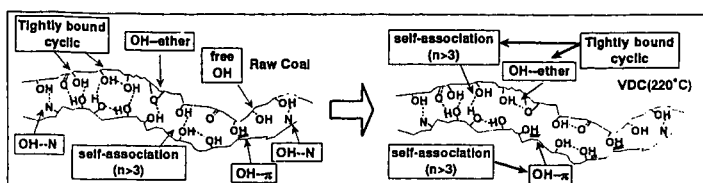


Figure 2 Image of the change in hydrogen bondings in coal through the treatment.

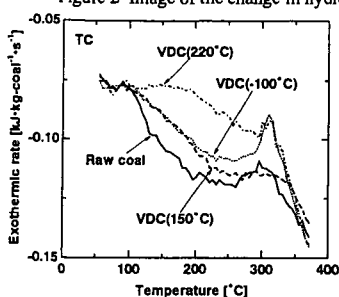


Figure 3 DSC profiles of the raw TC and the VDCs.

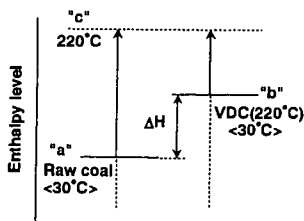


Figure 4 Enthalpy levels of the raw TC and VDC(220°C).

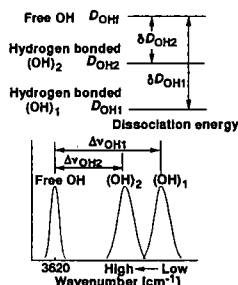


Figure 5 Changes in OH bond energy, D_{OH} , and wavenumber shift, $\Delta\nu_{OH}$, accompanied the change of a hydrogen bonding in coal.

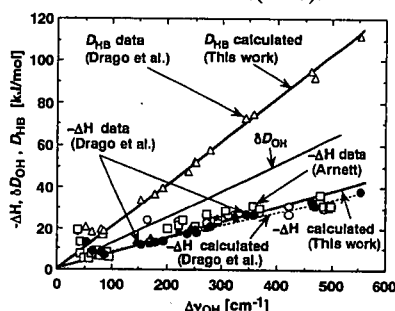


Figure 6 Comparison of the values of D_{HB} and ΔH calculated by eqs. (15), (16) with the experimental data.

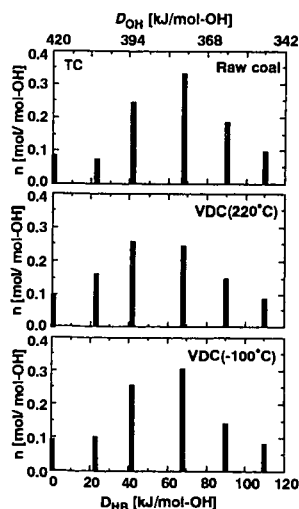


Figure 7 Strength distributions of hydrogen bondings in TC coal and the VDCs.

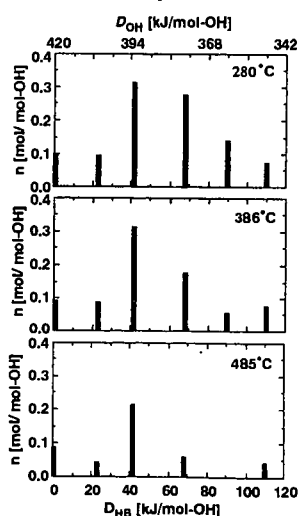


Figure 8 Change in strength distributions of hydrogen bondings in TC coal through the heat treatment.

INFLUENCE OF CHEMICAL STRUCTURE ON THE FLUIDITY OF RAPIDLY HEATED BITUMINOUS VITRINITES

Jonathan P. Mathews, Patrick G. Hatcher, Alan W. Scaroni
Energy & Fuels Research Center and Fuel Science Program, 211 CUL, The Pennsylvania State University, University Park PA 16802

Keywords: Vitrinite, char morphology and thermoplastic transformations.

ABSTRACT

When heated rapidly, many coal particles undergo thermoplastic transformations which change the particle size, shape and morphology. In the current work, vitrinites with subtle differences in rank and bulk chemical composition but significant differences in chemical constitution produced chars with different particle size and helium density. The particle size of an Upper Freeport (UF) sample increased by a factor of 2.5, and the helium density increased to 2.1 g/cm^3 (daf). In contrast, a Lewiston-Stockton (LS) vitrinite swelled by a factor of 1.8 and the helium density increased slightly then decreased to 1.3 g/cm^3 . The LS vitrinite had more aliphatic hydrogen than the UF vitrinite, which should promote thermoplasticity. However, less aromatic hydrogen and more oxygen in the LS sample contributed to increased "cross-linking", presumably increasing the lamella size in the thermoplast, thus reducing the extent of thermoplasticity.

INTRODUCTION

Much of the published work on the properties of chars produced from coals that have undergone thermoplastic transformations has been with whole coals. However, macerals have different extents of thermoplasticity, hence by using whole coals individual maceral behaviour has been masked (1-3). While new separation techniques produce maceral concentrates (4), the associated particle size is typically less than pulverised coal. Although similar in rank and bulk chemical composition, two Illinois No. 6 coal samples were found to develop different extents of thermoplasticity during rapid heating (5). Since maceral analyses were not reported, fluidity differences manifested as different char properties might be explained by differences in the maceral composition. A relationship between chemical structure (total aliphatic hydrogen) and a modified Giesler fluidity has been reported for vitrinites, with an abrupt increase in fluidity over a relatively narrow range of aliphatic hydrogen (6). Furthermore, it has been proposed that three criteria must be met for plasticity to occur in bituminous vitrinites: 1) the presence of lamellae-bridging structures that can be thermally ruptured, 2) a supply of hydroaromatic hydrogen and 3) an initial, intrinsic potential for micellar and lamella mobility (not related to the rupture of chemical bonds), which provides opportunity for the free-radicals formed by bond rupture to contact potentially transferable hydrogen (7). Thus, the relationship between thermoplastic behaviour and chemical constitution can be explored utilizing vitrinites of subtly different bulk composition but different chemical constitution. In this study, particle swelling and helium density of the resulting chars were measured and related to differences in the vitrinite chemical structure.

EXPERIMENTAL

The vitrain samples were collected from *Sigillaria* (a type of Lycopod) tree remains in the roofs of coal mines in the Upper Freeport (UF) and Lewiston-Stockton (LS) coal seams. The samples were comminuted in a Holmes 501XLS pulveriser. A narrow particle size separation was achieved by wet sieving with a series of (U.S. Standard) sieves. Char particles were collected after rapid heating to 1500°C in a drop-tube reactor similar to that discussed previously (8). Coal was fed by an Acrison GMC-60 feeder through a water-cooled injector at a rate of 0.33 g/min and entrained by 1.0 L/min of primary nitrogen. The tip of the injector was level with the bottom of a mullite flow-straightener. Secondary nitrogen (3.0 L/min) was preheated to 830°C and exited the flow straightener with the primary nitrogen. Char particles were collected using a water-cooled probe with a cold suction flow of 4.0 L/min . Char particles were obtained from various locations by raising and lowering the collection probe.

The particle size distributions of vitrinite and collected vitrinite-chars were determined with a laser light scattering instrument (9). Helium densities were obtained using a commercially-available pycnometer. Changes in the morphology of the char were followed using gold-coated samples in a SEM. Ultimate analyses were performed using commercially-available instrumentation. Proximate analyses were determined using a thermogravimetric analyser (5 mg sample size) utilizing a modified ASTM methodology (10). The mean maximum vitrinite reflectance was calculated in accordance with ASTM procedures (11). CPMAS ^{13}C NMR and dipolar dephasing experiments were performed in ways similar to those reported previously (12).

RESULTS AND DISCUSSION

The mean maximum vitrinite reflectance values were 0.97 (sd 0.04) and 0.93 (sd 0.08) for the UF and LS vitrinites, respectively. Both samples were determined to be monomaceral in composition using polished briquettes with reflected white and blue light. The elemental compositions of the vitrinites normalized to 100 carbon atoms were $C_{100}H_{75.5}N_{1.2}O_{4.4}S_{0.0}$ and $C_{100}H_{77.9}N_{1.4}O_{6.3}S_{0.6}$ (oxygen determined by difference) for the UF and LS vitrinites, respectively. The elemental compositions differed subtly, however in that, the LS vitrinite was slightly richer in hydrogen, nitrogen, sulphur and oxygen. Aromaticities determined by ^{13}C NMR were 0.77 and 0.81 for the UF and LS vitrinites, respectively (Table 1). Thus, the vitrinites were of the same maceral composition, with close particle size distributions (Table 2), yet subtle differences in the rank (mean maximum vitrinite reflectance) and aromaticities (Table 1). The volatile matter (daf basis) for the 200x400 mesh cuts were 37 and 30% for the UF and demineralized LS vitrinites, respectively. This indicates that, although there were only subtle differences in the bulk chemical composition, the constitution of the two vitrinites was substantially different. Structural parameters derived from the elemental composition and ^{13}C NMR experiments are reported in Table 1. The LS sample was richer in total aliphatic hydrogen (H/C_{ali}) in comparison to the UF vitrinite and had less aromatic bound hydrogen. The lower aromatic hydrogen and higher oxygen content are consistent with a more "cross-linked" structure for the LS vitrinite.

SEM micrographs of the wet sieved 200x400 mesh UF and LS vitrinites and drop-tube generated vitrinite-char particles are presented in Figure 1. The UF vitrinite and chars are shown at different magnifications to aid in following morphological changes. The LS vitrinite and vitrinite-chars are shown at the same magnification to allow visual representation of the swelling. The wet sieved vitrinite fraction for both samples was characterized by angular particles with generally sharp edges. The char particles collected at 13 cm showed that some of the UF particles had undergone thermoplastic transformations, resulting in the rounding of edges and occasional cenosphere formation. However, many of the particles retained their angular shape and sharp edges. In contrast, most of the LS vitrinite chars at the 13 cm sampling location remained angular. The light-scattering-obtained volumetric weighted average size ($D_{[v,0.5]}$) indicated little swelling for both samples at the 13 cm location (Table 2).

The vitrinite-char particles for both samples collected at the 23 cm location displayed the characteristics of greater fluidity, in that very few particles retained their original morphologies and there was a slight increase in the $D_{[v,0.5]}$ (Table 2). The char particles collected at the 33 cm location had increased in size, swelling by a factor of 2.5 for UF vitrinite chars with the distribution of particle sizes increasing by a factor of 3.9 as shown by the Δ value (the difference between the $D_{[v,0.9]}$ and $D_{[v,0.1]}$ diameters). In contrast, the LS vitrinite-chars were less swollen, only expanding by a factor of 1.8 with the Δ value increasing by a factor of 1.6. As both vitrinite particle size cuts had similar Δ 's, indicating similar particle size distributions, the swelling of the UF sample was more sensitive to particle size. For both samples the char particles were almost all cenospheres. The outer skins of the cenospheres appeared wrinkled in many cases, which may be indicative of contraction. Decreasing $D_{[v,0.5]}$ values for both samples after the 33 cm location supports the occurrence of contraction. It might be expected that contraction would occur immediately after the jet release phenomenon (13), where the internal pressure is released suddenly and violently. However, cenospheres collected at the 23 cm location contained rents and blowholes, indicative of a sudden jet-release of volatiles, yet the skins remained smooth. Thus, contraction appears to post-date the jet-release event. It is speculated that the contraction of the particles may therefore be linked to chemical changes affecting fluidity rather than physical changes affecting the internal pressure (3). The cenospheres collected at the 33 cm location contained soot agglomerates on their skins. Chars collected at the 43 and 53 cm locations (not shown) were thin walled, having undergone some structural collapse.

Helium densities for the demineralized vitrinites and vitrinite-chars for both samples are shown in Figure 2, and compared to the reported density of graphite (14). The UF vitrinite chars showed a slight increase in helium density with increasing reactor length until after the 23 cm location where a substantial increase in the helium density occurred. In contrast, the LS vitrinite-chars experienced a slight increase in helium density (at the 13 cm location) and then a decrease to 1.3 g/cm³. A lower helium density is consistent with the observed reduced thermoplasticity of the LS vitrinite.

CONCLUSIONS

Two vitrinites with only subtle differences in bulk chemical composition exhibited different extents of thermoplastic transformations upon rapid heating as manifested by particle swelling and the helium densities of the resulting chars. The Lewiston-Stockton sample, although richer in total aliphatic hydrogen, did not experience enhanced thermoplastic transformations in comparison to the Upper Freeport vitrinite. The higher concentration of oxygen and less aromatic hydrogen in the Lewiston-Stockton vitrinite are consistent with a more cross-linked structure. This appears to reduce the fluidity, presumably by increasing the size of the lamellae, and produced chars with lower helium density and smaller particle size in comparison to the UF vitrinite.

REFERENCES

1. Tsai, C.-Y. and Scaroni, A. W., *Fuel*, 1987, **66**, (2), 200.
2. Street, P. J., Weight, R. P. and Lightman, P., *Fuel*, 1969, **48**, 343.
3. Anson, D., Moles, F. D. and Street, P. J., *Combustion & Flame*, 1971, **16**, 265.
4. Taulbee, D., Poe, S. H., Robl, T. and Keogh, B., *Energy & Fuels*, 1989, **3**, 662.
5. Cai, M. F., Guell, A. J., Dugwell, D. R. and Kandiyoti, R., *Fuel*, 1993, **72**, (3), 321.
6. Senftle, J. T., Kuehn, D. W., Davis, A., Brozoski, B., Rhoads, C. and Painter, P. C., *Fuel*, 1984, **63**, (2), 245.
7. Neavel, R. C., Coal Agglomeration and Conversion, West Virginia Geological and Economic Survey, 1975, Morgantown, WV, 120.
8. Artos, V. and Scaroni, A. W., *Fuel*, 1993, **72**, (7), 927.
9. Allen, T., Particle size measurement, Vol 4, 1990, London, Chapman and Hall.
10. ASTM, Designation: D 5142 - 90, Standard test methods for proximate analysis of the analysis sample of coal and coke by instrumental procedures, in Annual book of ASTM standards, Section 5, Petroleum products, lubricants and fossil fuels, 1994, 442.
11. ASTM, Standard test method for microscopical determination of the reflectance of vitrinite in a polished specimen of coal, in Annual book of ASTM standards, Section 5, Petroleum products, lubricants and fossil fuels, 1995, 274.
12. Hatcher, P. G., *Energy & Fuels*, 1988, **2**, 40.
13. Grey, V. R., *Fuel*, 1988, **67**, (9), 1298.
14. Franklin, R. E., *Fuel*, 1948, **27**, (1), 46.

Table 1. Chemical parameters

Parameter	UF	LS
f_a (CPMAS)	0.77	0.82
aryl-O content	0.20	0.17
f_a^H	0.49	0.37
H/C	0.76	0.78
H/C _{ali}	1.7	2.7

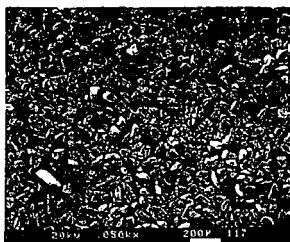
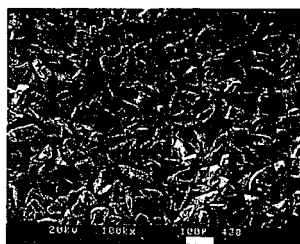
f_a is the aromaticity, aryl-O content is the ratio of aryl-O bonded carbons to total aromatic carbons, f_a^H is the fraction of aromatic carbons that are protonated, H/C is the atomic hydrogen to carbon ratio, H/C_{ali} is the aliphatic atomic hydrogen to carbon ratio.

Table 2. Particle size distribution for the vitrinite and vitrinite-chars

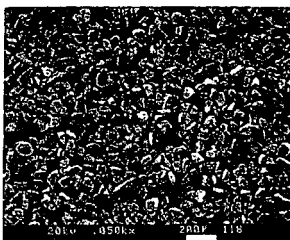
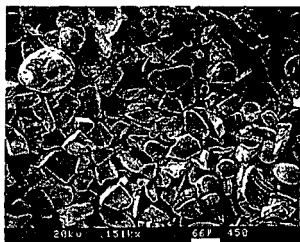
Sampling Location (cm)	D _[v,0.5] μm	D _[v,0.9] μm	D _[v,0.1] μm	Δ μm	Swelling
Vitrinite (UF)	65	110	44	66	1.0
13	69	120	48	72	1.1
23	76	132	48	86	1.2
33	160	298	42	255	2.5
43	148	223	54	169	2.3
53	132	210	59	151	2.0
Vitrinite (LS)	61	92	39	53	1.0
13	75	106	49	57	1.2
23	76	139	46	93	1.2
33	109	191	55	136	1.8
43	103	185	49	136	1.7

Analysis is based on volume, D_[v,0.5] is the volumetric weighted average size. D_[v,0.90] is the particle diameter such that 90% of the total volume is in particles of smaller diameter. D_[v,0.1] is the particle diameter such that 10% of the total volume is in particles of smaller diameter, Δ is the difference between the D_[v,0.90] and D_[v,0.1] diameters, swelling was calculated from the D_[v,0.5] diameter, particles were assumed to be spherical and no shape correction was performed. Data were collected in the model independent mode.

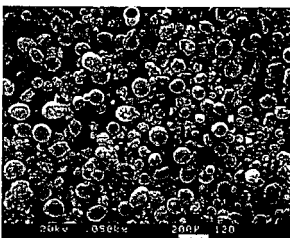
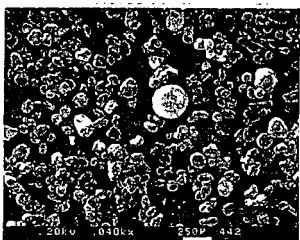
vitritine



13 cm



23 cm



33 cm

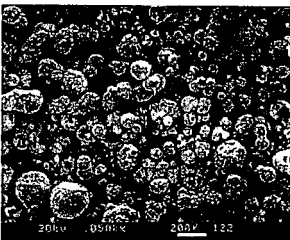
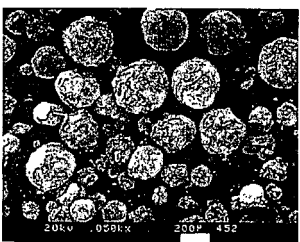


Figure 1. SEM micrographs of Upper Freeport (left) and Lewiston-Stockton (right) vitritine and vitritine-chars.

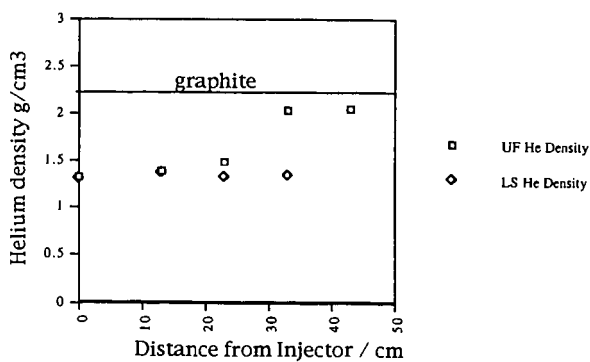


Figure 2. Helium densities for demineralized UF and LS vitritines and vitritine-chars

THERMAL BEHAVIOUR OF CARBOXYLIC ACID FUNCTIONALITY IN COAL

Tetsuo Aida, Noriyosi Hiram and Yukinari Tsutsumi
Department of Industrial Chemistry
Faculty of Engineering, Kinki University at Kyusyu
11-6 Kayanomori, Iizuka, Fukuoka 820, JAPAN

Keywords: Coal, carboxylic acid functionality, thermal decomposition

INTRODUCTION

Coal contains various chemical functionalities. Among them, the oxygen-containing functionalities are considered to play very important role to control its physical and chemical properties. Particularly, a carboxylic acid functionality has a relatively strong acidic characteristic comparing with other functionalities such as alcoholic and phenolic hydroxyl functionalities, so that it can make strong cohesive forces with a hydrogen bonding to other functionalities bearing electron negative atoms such as oxygen, nitrogen and sulfur. This means that the solubility of coal extracts for various solvents must be greatly affected by its concentration, as well as the apparent cross-linked structure formation in coal by molecular interactions such as hydrogen bonding, charge-transfer bonding or π - π -bonding.

Nevertheless, it has long been a kind of common-sense in the coal science community that the bonding contribution from a carboxylic acid functionality to the chemical and physical property of coal could be negligible toward higher ranked coals like a subbituminous and a bituminous coals. Simply because the previously reported analytical data concerning a carboxylic acid functionality content was too small, which used to be determined by the chemical method developed by Blom et al.(1) about 40 years ago. Although the recent development of sophisticated instrumentalations such as FT-ir, ^{13}C -CP-MAS-NMR, XPS, etc., has made it possible to provide quite reliable informations about such hetero-atom-functionalities as sulfur-, nitrogen- and oxygen-containing functionalities, they seem to have a common problem in the accuracy to determining a small amount of functionality.

At the recent ACS Meeting, we had asked a following question in public with our experimental data obtained by newly developed chemical method(2). However, the low public attention had made us very disappointed.

"Is it true that a bituminous coal contain such a small amount of carboxylic acid functionality in the macromolecular network structure as shown in the Shinn's model(3)(one unit over 660 carbon skeleton) ??".

In Figure 1, our experimental data determined by the new method are summarized. It is just amazing and unbelievable that a wide range of high ranked coals still have a significant amount of carboxylic acid functionality in their macromolecular network structures. Based on these experimental results, Illinois No.6 coal contains at least 6units of carboxylic acid functionality over 660 carbon skeleton which means 6 times more than the Shinn's Model. Furthermore in the case of its pyridine extract, it reached upto 8units/660-carbon. Thus, the conclusion in our previous paper was that there was a possibility of very serious misleading preconception concerning the carboxylic acid functionality in coal, particularly to the higher ranked coals.

Actually, as Niksa pointed out in his recent personal communication and paper(4), it was well-known contradiction that the most of the CO_2 -release during the pyrolyses of subbituminous and bituminous coals could not rationalize by the unimolecular decomposition chemistry of carboxylic acid functionality in coals, because the previously reported quantity of the functionality was too small to use.

This is the strategical background for us to initiate the study on the thermal behaviour of carboxylic acid functionality in coal by means of the direct chemical determination.

EXPERIMENTAL

The chemical reagents were commercial products(Aldrich's gold label grade) which were used without further purifications. Pyridine for the chemical determination of carboxylic acid functionality was dried over calcium hydride and distilled before use. Coals from the Argonne National Laboratory(premium), the Ames Coal Library and BRAIN-C(5) were ground, seized, dried in a silica-gel desiccator at room temperature under vacuum for three days, and stored under a dry nitrogen atmosphere. The thermal treatment of coals(their analytical data shown in Table 1) and model compounds were carried out by using a thick-wall Pyrex glass sealed tubing of which inside atmosphere was replaced by an argon gas, and heated in a molten salt bath for 30 minutes at an appropriate temperature. After the reaction, the sealed tube was cooled down at a liquid nitrogen temperature, and then broken the seal for analyses.

The principle of our chemical determination method of carboxylic acid functionality is described as follows: The chemical reaction with tetra-n-butylammonium borohydrides was adopted for the determination of the carboxylic acid functionality as shown below. Since this reaction proceeds toward different hydroxyl functionalities with very different reaction rates, we can easily discriminate the carboxylic acid functionality from others. The detailed experimental procedure is available in our previous paper(2).



in pyridine solvent
(R = Aryl, Alkyl)

RESULTS AND DISCUSSION

1. Thermal stability of carboxylic acid functionality in coals

In order to examine the thermal stability of carboxylic acid functionality in coals, we have chosen two young coals (Yallourn, Dietz No.1&2) and two relatively old coals (Illinois No.6, Pittsburgh No.8). These coals were carefully handled under a nitrogen atmosphere to prevent an auto-oxidation by air, and also the heat-denaturation for which the drying operation was performed by using a silica-gel vacuum desiccator at room temperature for three days.

In Figure 2, the degree of the decomposition of the carboxylic acid functionality in each coals for 30 minutes were demonstrated versus temperatures.

Very interestingly, the pattern of the decomposition seems to be quite different between these two groups, that is, the carboxylic acid functionalities in the old coals were relatively stable below 350°C, and started to decompose over 400°C, meanwhile the young coals seemed to contain significant amount of reactive(unsafe?) carboxylic acid functionality. Almost 40% of carboxylic acid functionality in coal destroyed under 300°C within 30 minutes heating condition. These results are consistent with a general understanding of a coalification process which is considered to predominantly destroy the reactive functionality in coal. Based on this assumption, the thermal decomposition pattern of the old coal, i.e., Pittsburgh No.8 coal, represents that of the stable form of carboxylic acid functionality in coal. Namely, the decomposition rate is accelerated over 400°C, and about 80% of the total content can be destroyed within 30 minutes at 450°C.

Meanwhile, in the case of the young coals (Lignite) the total content of carboxylic acid functionality are 2-3 times more than those of the old coals, and the most of the functionalities are reactive form which can be decomposed below 400°C. Obviously, the thermal decomposition pattern around 450°C suggest that some amount of stable form of functionality exists in the coal. It is also interesting that the fine structure of the decomposition pattern appeared between 200°C to 350°C suggests that the reactive functional group consisted from further different groups of the functionalities. Although at this moment it will be too early to draw a conclusion, there seems to be interesting coincidence between our data and the CO₂-release rate of the coal pyrolysis reported by Solomon, et al. (6) shown in Figure 3. We have not yet enough stoichiometric data concerning the decomposition of carboxylic acid functionality and the amount of the released CO₂ during the pyrolyses. But, it is quite plausible that the yield of CO₂ in the coal pyrolysis can be rationalized in terms of unimolecular decomposition chemistry of carboxylic acid functionality.

2. Thermal stabilities of model compounds

It has been found that coal contained several groups of carboxylic acid functionalities which had a different thermal stability. So, we have decided to assume the chemical structure of the functionality by comparing with those of the structure-known model compounds.

The first group of the model compounds chosen are the simple aromatic and aliphatic carboxylic acid compounds such as toluic acid, 1- and 2-naphthoic acid, and n-hexanoic acid which are assumed to be thermally quite stable.

Figure 4, summarized the experimental data obtained under the same reaction conditions as used for the coals, previously. The thermal decomposition patterns of the aromatic carboxylic acid, i.e., toluic acid, 1-and 2-naphthol seemed to be quite similar to those of higher ranked coals (Figure 2). The thermal stability of the alkyl derivative seems to be quite stable compared to others, which was decomposed over 450°C.

All of these results strongly suggest that the major component of carboxylic acid functionality in the old coal such as Illinois No.6 and Pittsburgh No.8 coals, must be simple aromatic and/or aliphatic derivatives. This assumption seems to be consistent with our previous understanding, for example, Shinn's model adopted a single aromatic carboxylic acid functionality.

The second group of the model compounds chosen are mainly the nature-oriented form of carboxylic acid compounds such as malic acid and fumaric acid, of which existence in coal are not sure, but it is considered to be one of the candidates for the possible functionality in younger coals like a lignite.

The results obtained are summarized in Figure 5.

As expected, these model compounds started to decompose under relatively mild conditions, around 250-300°C.

Of course it is quite difficult to assume with these data that the actual chemical structure of the reactive carboxylic acid functionality in coals are just like these chemical structure. But at least, we may be able to say that the younger coals like a lignite have much of a nature-oriented (raw) form of carboxylic acid functionality in the macromolecular network structure. Also, the carboxylic acid functionality of which chemical reactivity can be significantly enhanced by the specific substituents or hetero-atoms like a 9-anthracenecarboxylic acid seems to be responsible for such a mild decompositions.

CONCLUSION

It was found that the coal contains both stable form and relatively unstable form of carboxylic acid groups in the macromolecular network structure. The former seem to be a simple aromatic carboxylic acid, and the later is assumed to be more natural product like carboxylic acid functionality. It is also likely that the previous observation of the CO₂-release during the pyrolyses of coals can be rationalized by the unimolecular decomposition chemistry of carboxylic acid functionality in coal.

ACKNOWLEDGEMENTS

A part of this research was supported by the grant from The Japanese Ministry of Education through The Nippon Gakujutu Shin-koukai.

REFERENCES

- (1) Blom, L., Edelhause, L., and van Krevelen, D.W., *Fuel*, **36**, 135(1957)
- (2) Aida, T, et al., *Prepr. Am. Chem. Soc. Div. Fuel Chem.*, **41**(2), 744(1996)
- (3) Shinn, J.H., *Fuel*, **63**, 1187(1984)
- (4) Niksa, Stephen, *Energy & Fuels*, **10**, 173(1996)
- (5) Coal Bank sponsored by NEDO through CCUJ(Japan)
- (6) Solomon, P. R., et al., *Energy & Fuels*, **4**, 319(1990)

Table 1. Analytical Data of Coals

Coal	(dmmf wt %)					(mmol / g)		
	Ash	C	H	N	O	S	COOH	Ph-OH
Yallourn*	1.6	66.9	4.70	0.48	27.7	0.26	1.28	4.61
Dietz No.1 & 2	5.5	74.4	5.26	1.09	18.9	0.44	1.27	-
Illinois No.6**	14.3	80.7	5.20	1.43	10.1	4.82	0.67	2.52
Pittsburgh No.8**	9.1	85.0	5.43	1.68	6.90	2.19	0.37	2.04

* Australian brown coal

** Argonne premium coal

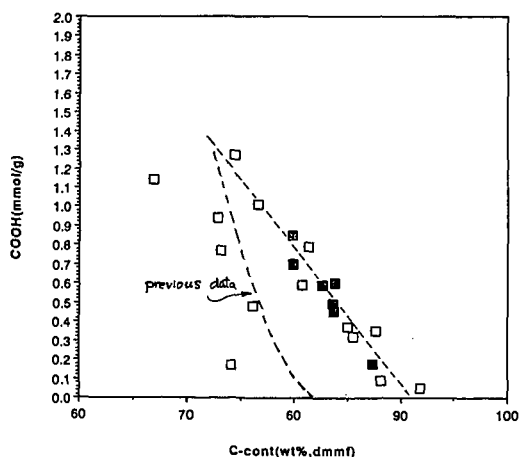


Figure 1. Coal rank dependency of Carboxylic acid functionality content

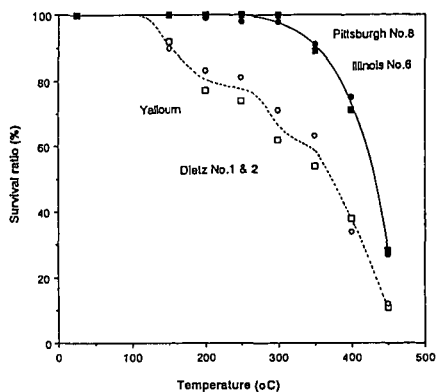


Figure 2. Thermal stabilities of carboxylic acid functionality in coals

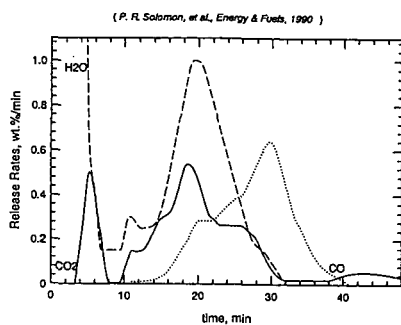


Figure 3. Release rates of gaseous products from thermal decomposition of subbituminous coal (6)

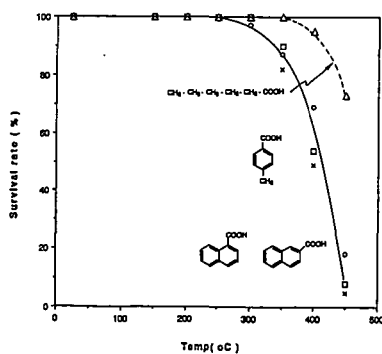


Figure 4. Thermal stabilities of model compounds

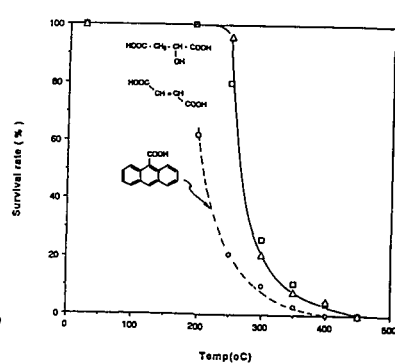


Figure 5. Thermal stabilities of model compounds

THE OXIDATIVE REACTIVITY OF COAL CHARs IN RELATION TO THEIR STRUCTURE

by

M-L Chan*, J. M. Jones, M. Pourkashanian, and A. Williams

Department of Fuel and Energy, The University of Leeds,
Leeds, West Yorkshire, UK, LS2 9JT

*British Gas Research Centre, Ashby Road, Loughborough.

Keywords: coal, porosity, reactivity

Abstract: In the oxidation of highly porous carbons, the internal surface area can increase as a function of conversion due to pore growth and the opening up of sealed internal pores or cavities. Consequently, rate expressions for carbon oxidation are more accurately described in terms of the intrinsic reactivity, where differences in surface area and porosity are accounted for.

The oxidative reactivity of coal chars is complicated by a number of different factors which are explored in this paper. These include (i) the development of the pore structure during devolatilisation of the coal, (ii) the ash content and its distribution in the carbon matrix, (iii) the H and N functional groups present on the solid matrix, and the interrelation with volatile species present, (iv) the graphitic nature of the carbon surface and, the active surface area available for reaction.

Introduction

Coal char structure is influenced, not only by coal properties, but also by the temperature-time history which the coal particles experience within the combustor, i.e. heating rate, maximum temperature experienced, residence time at this temperature, and the gaseous atmosphere. This is because these variables, together with coal properties all influence the amount and nature of the volatile, as well as their rate of release. These factors determine both the macroscopic morphology and the microscopic porosity of the resultant char. The porosity is particularly important because it can control the rates of diffusion of chemical species into and out of the char particle. The rate of combustion of coal chars is an important parameter on combustion efficiency because of its impact on the unburnt carbon in the ash. Rationalization of the relationship between char reactivities in combustion and coal/char chemical and physical properties has therefore been attempted. In the chemical kinetic regime these include structural and chemical properties which increase the active surface area of the chars.

This paper considers the effect of some of these properties on porosity of coal chars and hence active surface area and reactivity. Particular emphasis will be placed on the following: (i) effect of devolatilisation conditions on porosity, (ii) effect of porosity on reactivity of coal chars and (iii) effect of mineral and heteroatoms content, and their distribution, on reactivity

Experimental methods

Coal chars were prepared from three British bituminous coals (70-90 μm), Markham Main (MM), Kiverton Park (KP), and Goldthorpe (G), by heating in an inert atmosphere to different heat-treatment temperatures (400-900 $^{\circ}\text{C}$) and at different heating rates (10 K/min (slow) or $1-10^4$ K/s (rapid)). The coal chars were characterized for their surface areas (N_2 and CO_2 adsorption at 77 or 195 K respectively), density, and porosity (mercury porosimetry). Chars were also examined by SEM. Isothermal char reactivities in air were measured in the temperature range 395-764 $^{\circ}\text{C}$ using a Beckman LM 600 microbalance.

Results and Discussion

The physical properties of the coal chars produced at slow pyrolysis are given in Table 1. For all three coals the surface area of the char is seen to pass through a minimum with increasing heat-treatment temperature. The surface areas measured by CO_2 adsorption are much higher than those measured by N_2 adsorption which is indicative of the presence of micropores which are

inaccessible at 77K due to activated diffusion. The density of the chars increase with increasing heat-treatment temperature, while the effect on porosity is more subtle.

The general trends in the changes in surface areas with heat-treatment can be explained in terms of the expected behavior for bituminous coals. At temperatures of between 200-500 °C the coals begin to soften and some volatile gases are evolved resulting in a loss of disordered material within the coal and an improvement in the stacking of the lamellae. A consequence of this is decreasing surface area. Upon further heating (500-600 °C), loss of tars begins resulting in swelling and an increase in the porosity (micro, meso and macro) hence both N₂ and CO₂ surface areas begin to increase again, as do the pore volume and porosity. At still higher temperatures (600-900 °C) resolidification of the coke structure occurs and the lamellae begin to grow with loss of H₂, resulting in increasing meso- and microporosity. These structural changes are validated by the spectroscopic properties and by elemental analysis of the chars. The role of N is also identified in this way.

The reactivity of coals in an oxygen atmosphere were obtained from experimental measurements. These apparent reactivities of the coals were converted into the values per unit surface area of the sample at one atmosphere oxygen partial pressure (i.e. the intrinsic reactivity R_i). The intrinsic reactivity, p_i, is used to normalize carbon reaction rates for differences in porosity:

$$p_i = R_i p_{O_2}^n \quad (1)$$

$$R_i = \frac{R_c}{A_g \gamma \sigma_a \eta} \quad (2)$$

Where R_i is the intrinsic reaction rate coefficient, P_{O₂} is the oxygen partial pressure, n the reaction order, A_g is the specific (pore) surface area, γ is the characteristic dimension of the particle, σ_a is the apparent density of the char and η is the effectiveness factor, calculated using Thiele's modulus in a unimodal pore system. The chemical rate coefficient, R_c, can be obtained from:

$$R_c = R_D p_{O_2}^{-(n-1)} \frac{X}{(1-X)^n} \quad (3)$$

where, R_D is the rate coefficient for oxygen diffusion to the particle, and X is the ratio of the actual burning rate to the maximum burning rate.

Figure 1 shows the Arrhenius plots of the R_i values not only for the coals examined in present study but includes values collected by the authors (1) for 6 different types of coal including petroleum coke. Figure 1 also includes values of intrinsic reactivity for 32 samples collected by Smith (2). Figure 1 shows R_i at a specific temperature ranging over up to two orders for the coal-types investigated. Values for the char activation-energies obtained from the intrinsic reaction rates were between 172 ± 12 kJ/mole and the pre-exponential factor was approximately 50 g/cm²s for the temperature ranges under investigation. As R_i is the reactivity per unit surface area of the coal, the differences in intrinsic reactivities must be attributed to other factors than porosity of the char sample. To clarify the relative importance of the other factors likely to affect the char oxidation process, relationships between R_i and some physical properties of the coals were examined.

Relationship between char reactivity and ash, H and carbon content: It is well established that overall coal reactivities are affected by the presence of minerals (3,4). The relationship between mineral matters and char reactivity R_i, is explored in (Figure 2). Although the number of coals studied during this investigation is very limited, it appears that reactivities R_i of the chars of higher rank coals are influenced by ash concentration. At low oxidation temperatures (<600 °C) the non-linear behavior of the R_i with ash concentration indicates that char reactivity may be controlled by the catalytic activity of coal minerals. However, at higher oxidation temperature (>600 °C) the intrinsic reactivity depends linearly on the char's ash content which may represent a non-catalytic reaction of carbon. Therefore, reduction in R_i with increasing ash content would be due to an inhibition of the carbon reactivity by the ash.

The relationship between R_i and hydrogen content of the coals is shown in Figure 3. The results imply a relationship very similar to the ash-char reactivity relationship. It is known that coal hydrogen content is directly related to the volatile content of the coal, and the number of carbon active sites on char can be related to the devolatilisation process and volatile concentration.

Therefore, the decrease in reactivity of char with hydrogen content can be related to the reduction in active sites.

Figure 4 shows the relationship between intrinsic reactivity and carbon content of the sample coals. At higher oxidation temperatures the intrinsic reactivity decreases monotonically with carbon content. Lower oxidation temperatures result in a optimum carbon concentration for maximum reactivity.

Reactivity and char structure: In a previous investigation by the authors (5), a correlated chemical reactivity is evaluated for 24 chars and cokes. The correlated chemical reactivity was based on all the chemical and physical variables of the coal. The resulting relationship is:

$$R_c = [1.4 (Vit_m + 0.83 Vit_{ps})] - 0.6(\ln_R + 1.6 \ln_{LR}) \exp^{(-89)} \sigma_a^{(-7.5)} Ag^{(-0.5)} C^{(3.5)} T_p^{(9.5)} \quad (4)$$

where \ln_R and \ln_{LR} are the fractions of low reflectance (reactive) and high reflectance (less reactive) inertinite respectively, and Vit_m and Vit_{ps} is the fraction of matrix and pseudo vitrinite respectively, C the carbon content and T_p the particle temperature.

The class of empirical formulations, of which equation 4 is an example, is of paramount importance to computational modelling. Other investigations have also produced a number of similar classes of formulations (6). Careful consideration of the results indicates that statistical analysis of char burn-out is necessary to describe the reactivity characteristic because of the complicated interplay of factors.

Conclusions

Values for the char activation-energies obtained from the intrinsic reaction rates were between 172 ± 12 kJ/mole for the temperature ranges under investigation. The current studies indicate strong interactions between carbon content, ash, and hydrogen content during the char-oxidation process. These interactions have been quantified for the coals studied.

References

1. Hargrave, G., Pourkashanian, M., and Williams, A., Twenty first Symposium (international) on Combustion, The Combustion Institute, 1987.
2. Smith, I. W., 19th Symposium on Combustion, The Combustion Institute, p1045, 1982.
3. Fung, D.P.C. and Kim, S.D., Fuel, 63, p1197, 1984.
4. Hippo, E.J., Jenkins, P.L. Fuel, 58, p338, 1979.
5. Hampartsoumian, E., Pourkashanian, M. and Williams, A. J. Inst. E. p.48, 1989.
6. Charpenay, S., Serio, M.A. and Solomon, P.R., International Conference on Coal Science, Banff, Canada, Vol. II, 189, 1993.

Table 1: Physical properties of Markham Main coal chars produced by slow pyrolysis

Char	HTT (°C)	Surface Area (m ² /g)		Density (g/cm ³)		Pore vol. (cm ³ /g)	Porosity (%)
		N ₂ @ 77K	CO ₂ @ 195 K	He	Hg		
MM-400	400	5.8	257.3	0.99	0.95	0.040	4.04
MM-500	500	0.7	113.7	1.01	0.98	0.030	2.97
MM-600	600	1.1	181.5	1.07	1.02	0.046	4.67
MM-700	700	3.6	179.7	1.15	1.07	0.065	6.96
MM-800	800	10.8	272.1	1.23	1.18	0.034	4.07
MM-900	900	11.3	210.0	1.46	1.33	0.067	8.90
KP-400	400	4.1	91.3	0.98	0.94	0.043	4.08
KP-500	500	0.4	73.1	0.99	0.96	0.032	3.03
KP-600	600	0.8	67.9	1.01	0.98	0.030	2.97
KP-700	700	5.6	221.7	1.03	1.01	0.020	1.94
KP-800	800	8.1	211.6	1.06	1.03	0.030	2.83
KP-900	900	9.6	184.4	1.19	1.12	0.050	5.88
G-400	400	3.6	48.3	1.05	0.95	0.100	9.52
G-500	500	0.3	49.9	1.01	0.97	0.040	3.96
G-600	600	0.2	29.1	1.08	1.01	0.064	6.48
G-700	700	0.9	262.6	1.11	1.09	0.016	1.80
G-800	800	5.9	215.1	1.13	1.10	0.024	2.65
G-900	900	5.1	-	1.27	1.19	0.053	6.30

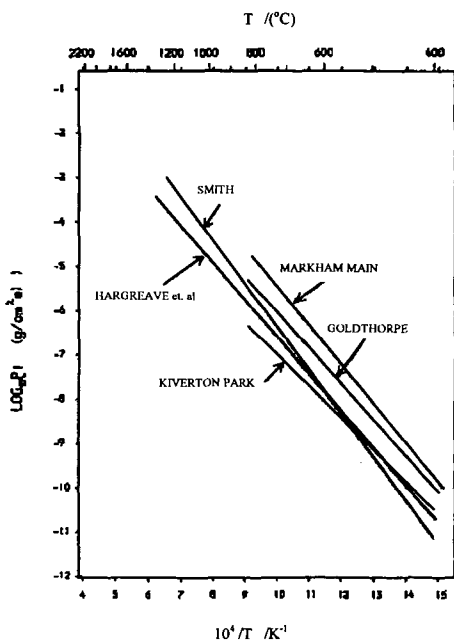


Figure 1: Comparison of Intrinsic chars reactivity in air

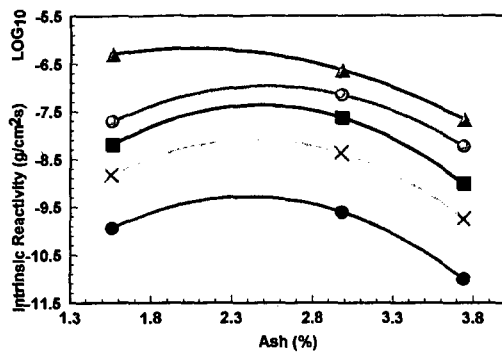


Figure 2: Relationship between Intrinsic reactivity and % ash in char. Oxidation temperature Δ 900C, \circ 800C, \blacksquare 700C, \times 600C and \bullet 500C.

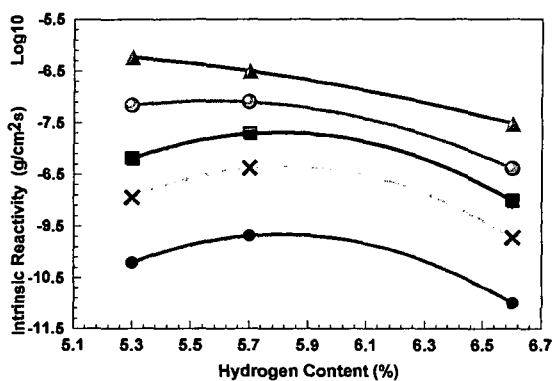


Figure 3. Relationship between Intrinsic reactivity and H in coal samples. Symbols as in Fig. 2.

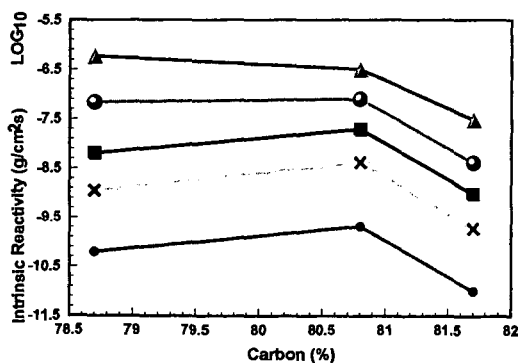


Figure 4: Relationship between intrinsic reactivity and %carbon of the char. Symbols as in Fig. 2.

IN-SITU ^1H NMR STUDY OF FLUIDITY ENHANCEMENT BY HYDROGEN-DONOR AND NON-DONOR PITCHES FOR A BITUMINOUS COAL

M. Mercedes Maroto-Valer, John M. Andrésen and Colin E. Snape

University of Strathclyde, Department of Pure and Applied Chemistry,
295 Cathedral Street, Glasgow G1 1XL, Scotland, UK

Keywords: Hydrogen-donor, pitch, fluid phase, high temperature ^1H NMR.

Hydrogen-donor ability has been ascribed as one of the factors responsible for the stabilisation of the plastic phase during coal carbonisation. In-situ high temperature ^1H NMR has been used here to quantify the interactions between a low-volatile bituminous coal and both a normal coal tar pitch (CTP) and a hydrogen-donor pitch (HDP) obtained from a coal liquefaction process. When the CTP was added to the coal (25% w/w, 150-250 μ), the amount of fluid material increased by nearly 20% more than that predicted at maximum fluidity close to 450°C. Indeed, a larger synergistic effect was observed with the HDP. By 400°C, 90% of the fluid phase concentration observed at 450°C had already been generated, corresponding to an enhancement of 50% over that predicted. However, particle size appears to be a dominant factor under the slow heating regime used in that no enhancement in fluidity was detected when the coal size was <45 μ .

INTRODUCTION

Coal and pitch carbonisation has previously been investigated using high temperature in-situ ^1H NMR by Sanada and coworkers ⁽¹⁾ and, more recently, by Lynch et al, who refer to the technique as "Proton Magnetic Resonance Thermal Analysis" (PMRTA) ^(2,3). The thermoplastic stage of coal is characterised by a ^1H NMR signal that consists of a mobile (Lorentzian) and a rigid (Gaussian) component ⁽²⁻⁵⁾. The authors recently have used a high temperature Doty NMR probe to rationalise a number of coal carbonisation phenomena, including the effects of particle size and mild oxidation, in terms of both the concentration of rigid and fluid material present, as well as the mobility or T_2 of the later ^(4,5).

The stabilisation of the plastic phase present during coal carbonisation has been reported to be connected with its hydrogen transfer and donor abilities ^(6,7). Indeed, aromatic additives that soften upon heating and include coal extracts, pitch and individual polycyclic aromatic compounds can improve fluid properties considerably. For example, using Gieseler fluidity measurements for a series of New Zealand coals, Clemens and Matheson ⁽⁸⁾ reported that both decacyclene and solvent extracts can improve plasticity development. Fortin and Rouzaud used TEM to view the beneficial effects of N-methyl-2-pyrrolidone and boiling anthracene oil extracts on the formation of coke microtexture ⁽⁹⁾. Indeed, the addition of coal tar pitch (CTP) to coal blends is widely used as a means of enhancing fluidity in coke production. To rationalise the role of solvent extractable material present on the development of a potentially much larger pool of fluid material, Neavel and Marsh ⁽¹⁰⁾ proposed a parallel between coal liquefaction and carbonisation. The development of plasticity can be considered as a pseudo liquefaction process, in the sense that the extractable material acts as a hydrogen-donor and transfer agent, stabilising the unstable radical species produced by pyrolytic-reaction pathways. In this study, in-situ high temperature ^1H NMR has been used here to quantify the interactions between a low-volatile

bituminous coal and both a normal (CTP) and a hydrogen-donor pitch (HDP) obtained from a coal liquefaction process.

EXPERIMENTAL

Table 1 lists the atomic H/C ratios, aromaticity and softening points for the low volatile Australian coal (20% daf volatile matter, $R_{o,max}$ of 1.46), the CTP and the HDP investigated. The CTP was obtained by distillation of a coal tar at 380°C and under 125 mm Hg vacuum for 2 hours. The HDP was produced in the liquid British Coal Liquid Solvent Extraction (LSE) process at the Point of Ayr facility, and comprises material boiling above 450°C in the product from the hydrocracker. The coal was ground manually using a mortar and pestle to give <45 and 150-212 μ fractions. Mixtures of coal and pitch (4:1 w/w) were prepared and stirred for one hour to ensure homogeneous blends were obtained.

The high temperature measurements were carried out using a Doty probe on a Bruker MSL-100 spectrometer as described previously ^(4,5). Approximately 50 mg of sample was packed in a zirconia container, except for the pitch samples, where only around 30 mg was used due to their high fluidity and the fact that a significant amount of sample distills off below 450°C. The average heating rate was around 4°C min⁻¹. Spectra were obtained at a number of different temperatures and fitted to Lorentzian and Gaussian components, as appropriate.

RESULTS AND DISCUSSION

General aspects Figure 1 compares the peak widths at half height, $\Delta H_{1/2}$, at temperatures up to 550°C for the coal, CTP and their mixture (4:1 w/w) with a particle size of 150-212 μ . The softening process for the coal is similar to other coking coals ^(4,5); the maximum fluidity at 470°C is reflected by the minimum in $\Delta H_{1/2}$, corresponding to a maximum in T_2 . During the fluidity range, the peak width of the plastic phase (this dominates $\Delta H_{1/2}$) is only 20-35% of that for the initial coal. At maximum fluidity, the fluid phase accounts for 26% of the hydrogen observed (Table 2). After the onset of resolidification at 490°C, the peak width increases to reach a value similar to that of the initial coal. As anticipated for the CTP, the overall $\Delta H_{1/2}$ decreases markedly after softening at ca. 190°C and then stays constant close to 1000 Hz (Figure 1). Indeed, as discussed later, the overall peak width of only 10 ppm for both pitch samples means that aromatic and aliphatic hydrogen peaks are resolved. No rigid material was observed in the spectra of the pitch samples above their softening points.

Particle size effect Figure 1 shows that for the peak width for the coal (150-212 μ)/CTP mixture below 350°C is dominated by the softening of the pitch. For the mixture, the $\Delta H_{1/2}$ of ca. 1100 Hz is the same as for the pitch alone indicating that the coal particles do not impair the motion of the pitch constituents. In contrast, for the mixture with <45 μ particles, the $\Delta H_{1/2}$ (ca. 10 kHz) is nearly ten times larger between 200 and 400°C. This difference in halfwidth is also apparent in the ¹H NMR spectra obtained at maximum fluidity (460°C) for the two mixtures (Figure 2). The increase in peak halfwidth with decreasing particle size has previously been reported as playing an important role in fluidity development ^(4,5). The mobility or T_2 of the fluid material falls with decreasing particle size, but the amount of fluid material remains constant. These findings suggest that the fluid material - both pitch and coal extract - is weakly adsorbed on the coal and the extent of this interaction increases with decreasing particle size as more of the surface becomes available.

Synergism with coal tar pitch In order to ascertain whether there was any synergism between coal and CTP in terms of plasticity development, the spectra obtained at maximum fluidity were deconvoluted to derive the proportions of fluid and rigid material. The observed and predicted values for the proportion of

hydrogen in the fluid phase are listed in Table 2. The latter were derived from the amounts of fluid material generated when the coal and CTP were heated separately, the hydrogen contents of the coal and CTP and the hydrogen lost during the heating. For the smaller particle size ($<45\ \mu$), the predicted value of 37% is extremely close that of 38% for the proportion of fluid hydrogen at maximum fluidity, indicating no synergism has occurred. In contrast, the predicted proportion of 37% for the fluid hydrogen was significantly lower than that of 45% observed with the larger particle size (150-212 μ , Table 2). This difference corresponds to an enhancement of 20% in the amount of fluid material generated (Table 2). The same treatment at 400°C indicates that the enhancement in fluidity is 15%, although the total concentration is only about two-thirds that observed at 450°C (Table 2). Thus, a synergistic effect is evident only when the coal particles are sufficiently large (ie. 150-212 μ) so as not to impair the motion of the pitch.

Hydrogen-donor pitch The structural differences of the two pitches are listed in Table 1, the HDP having a higher atomic H/C ratio and lower carbon aromaticity (0.75 compared to 0.99 for the CTP). Figure 3 presents the ^1H NMR spectra for the two pitches obtained in the fluid stage at 300°C before any significant proton weight loss. Both pitches display two peaks from aromatic (5-10 ppm) and aliphatic (0-5 ppm) hydrogen, respectively. As expected from the relatively low aromaticity, the HDP spectrum is dominated by the aliphatic peak.

The amount of fluid material generated at 460°C from the coal (150-212 μ)/HDP mixture is 44% (Table 2), indicating a positive interaction as for the coal/CTP mixture. However, since the HDP loses more weight during the heating process (ca. 60% of its hydrogen) than the more aromatic CTP (only 25%), the degree of synergism is larger with 30% more fluid material being generated than predicted (Table 2). By 400°C, 90% of the fluid phase concentration observed at maximum fluidity (460°C) has already been generated, corresponding to an enhancement of 50% over that predicted. Thus, the HDP extends the range of high fluidity to a significant degree. Moreover, the halfwidths of the fluid components at maximum fluidity for the coal (150-212 μ)/pitch mixtures (Table 3) indicate that the HDP also mobilises the fluid phase to a much greater extent than the CTP, further demonstrating the ability of this pitch to solubilise the coal.

CONCLUSIONS

This study has confirmed the ability of high temperature ^1H NMR to quantify the enhancement of coal fluidity by pitch additives. Particle size appears to be a dominant factor with slow heating, in that positive interactions were not detected with the $<45\ \mu$ coal fraction. The synergistic effect observed with the HDP was considerably larger than that with the normal CTP, particularly at temperatures below maximum fluidity with the proportion of fluid material being 50% more than that predicted at 400°C.

ACKNOWLEDGEMENTS

The authors thank the European Coal & Steel Community (Contract No. 7220-EC/870) and the Basque Government (studentship for M.M. Maroto-Valer) for financial support. We are also grateful to British Steel and CRE for supplying the coal and HDP, respectively.

LITERATURE CITED

- 1 K. Miyazawa, T. Yokono and Y. Sanada, Carbon, 1979, 17, 223.
- 2 L.J. Lynch and D.S. Webster, American Chemical Society Symposium Series, 1983, 230, 353.

- 3 L.J. Lynch, D.S. Webster, R. Sakurovs, W.A. Barton and T.P. Maher, Fuel, 1988, **67**, 579.
- 4 M.M. Maroto-Valer, J.M. Andrésen and C.E. Snape, Prep. Am. Chem. Soc., Division of Fuel Chemistry, 1996, **41**, 1147.
- 5 M.M. Maroto-Valer, J.M. Andrésen and C.E. Snape, Energy & Fuels, in press.
- 6 R.C. Neavel, in Coal Science, vol 1, M.L. Gorbaty, J.W. Larsen, and I. Wender, 1982, Academic Press.
- 7 T. Yokono, T. Obara, Y. Sanada, 1984, Carbon, **22**, 2, 169.
- 8 A.H. Clemens, and T.W. Matheson, 1992, Fuel, **71**, 193, and 1995, Fuel, **74**, 57.
- 9 F. Fortin and J.N. Rouzaud, 1993, Fuel, **72**, 245, and 1994, Fuel, **73**, 795.
- 10 H. Marsh and R.C. Neavel, 1980, Fuel, **59**, 511.

Table 1 Atomic H/C ratios, aromaticities and softening points for the coal and pitches investigated.

	Atomic H/C	Aromaticity ^a	Softening point / °C
Coal	0.61	0.89	470 ^b
Coal tar pitch (CTP)	0.49	0.99	190
Hydrogen donor pitch (HDP)	0.78	0.75	175

^a The aromaticity fraction was determined by using the quantitative ¹³C NMR SPE methodology.

^b The softening temperature for the coal refers to the maximum fluidity temperature as determined by the standard Gieseler plastometer.

Table 2 Proportion of the fluid component at maximum fluidity temperature for the coal, pitches and coal/pitch mixtures (4:1 w/w).

	Observed mobile H / %		Weight average mobile H / %		Enhancement	
	400°C	460°C	400°C	460°C	400°C	460°C
Coal	12	26	10 / 10 ^a	22 / 23 ^a		
CTP	100	100	16	15		
HDP	100	100	17	11		
Coal (<45 μ) / CTP	27	38	26	37	NONE	NONE
Coal (150-212 μ) / CTP	31	45	26	37	15 %	20 %
Coal (150-212 μ) / HDP	41	44	27	34	50 %	30 %

^a The first and second values are for the coal in the coal/CTP and coal/HDP mixtures, respectively.

Table 3 Peak widths at half height, $\Delta H_{1/2}$, of the fluid component at maximum fluidity for the coal, pitches and coal/pitch mixtures (4:1 w/w).

	Observed $\Delta H_{1/2}$ / Hz	Calculated $\Delta H_{1/2}$ for mixtures / Hz	Enhancement
Coal	5260		
CTP	1000 ^a		
HDP	1000 ^a		
Coal (150-212 μ) / CTP	3000	4700	36%
Coal (150-212 μ) / HDP	1920	4800	60%

^a Peak width is for aromatic and aliphatic hydrogen bands combined, each band having a $\Delta H_{1/2}$ of only 300-400 Hz.

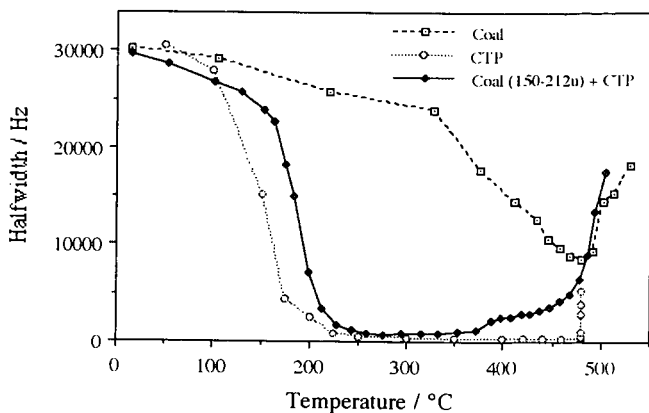


Figure 1 Evolution of the peak halfwidth for the coal (150-212 μ), CTP and the coal / CTP mixture.

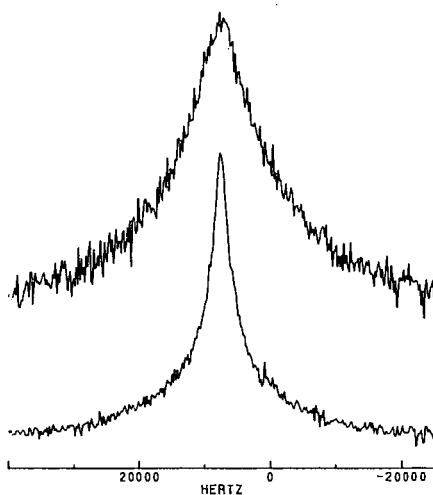


Figure 2 ^1H NMR spectra at maximum fluidity (460°C) for the coal / coal tar pitch mixtures (4:1), coal particle size <45 μ (top) and 150-212 μ (bottom).

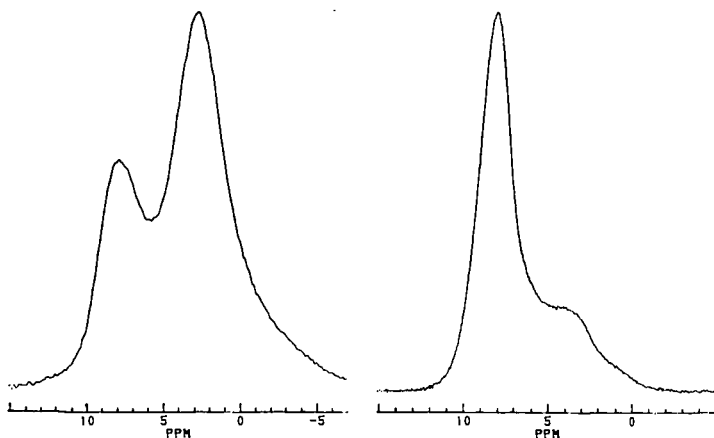


Figure 3 ^1H NMR spectra at 300°C prior to significant weight loss for the CTP (right), and HDP (left).

AN ^{19}F AND ^{13}C NMR STUDY OF CF_x PREPARED BY VARIABLE TEMPERATURE FLUORINATION OF CHARCOAL WITH ELEMENTAL FLUORINE.

D. K. Murray, E. W. Hagaman and G. D. Del Cul,
Chemical & Analytical Sciences Division, Oak Ridge National Laboratory,
P. O. Box 2008, Oak Ridge, TN 37831-6201.

Key Words: charcoal, fluorine, carbon monofluoride, nmr

Abstract

The preparation of CF_x by elemental fluorination of charcoal is studied using solid state ^{13}C and ^{19}F NMR spectroscopy. ^{19}F - ^{13}C CP/MAS NMR experiments are used to determine the extent of fluorination vs. reaction temperature. Four types of carbon species are observed over the temperature range -80°C to 350°C , assigned to graphitic carbon (C), CF, CF_2 and CF_3 . These species are assigned and quantified using dipolar dephasing and variable contact time experiments. NMR results are presented along with gravimetric and ESCA results to provide new insights into charcoal structure and fluorination.

Introduction

Probing heterogeneous carbonaceous solids with selective reagents is a useful approach to study their chemical and physical properties.¹ Elemental fluorine is a particularly effective probe, adding to unsaturated carbon, and displacing O and H from organic materials.^{2,3} Fluorine is easily detected by ^{19}F NMR spectroscopy.⁴ It also provides a useful polarization source for investigating carbon structure by ^{19}F - ^{13}C CP NMR spectroscopy.⁵

Here we describe changes in the structure of charcoal as it is converted to CF_x by reaction with elemental fluorine. These studies demonstrate the utility of fluorine as a probe and provide insight into the fluorination process in more complex solids. Both radical and ionic mechanisms are reported upon elemental fluorination of model organic compounds.^{2,3} CF_x made from graphite is reported as a solid lubricant and as an excellent cathode material for Li batteries.⁶ Gravimetric, NMR and ESCA analyses are used to investigate charcoal structure and the fluorination process.

Experimental

Preparation of CF_x . Coconut-based activated charcoal (6x16 mesh size) was provided by Calgon Carbon Corporation. The microstructure is that of graphite, consisting of stacked planar platelets of fused aromatic carbon.⁷ The C-C bond distance is 0.141 nm and the interplatelet distance is 0.335 nm. According to the manufacturer's data a large portion of the micropore volume consists of pores in the range 1.5 to 2.0 nm and a system of macropores larger than 100 nm. A suite of ten CF_x samples were prepared over the temperature range -80 to 350°C using the following method. Ten to fifteen gram batches were loaded into a passivated-nickel U-tube reactor (1/2" OD) having monel bellows vacuum valves at each end. The activated charcoal was pre-conditioned by heating to 200 - 250°C under helium flow. The reactor was then fully immersed in a thermostatic bath to maintain the desired fluorination temperature. To minimize formation of gaseous products and to better control the highly exothermic reaction, dilute fluorine gas was used. A 5 % by volume F_2/He

gas mixture was prepared in three liter batches in a passivated-nickel tank. The preparative manifold has a titanium getter to remove water, oxygen or nitrogen impurities. Dilute fluorine was introduced into the reactor at a very low flow rate. A temperature difference of $<3^{\circ}\text{C}$ was maintained between the charcoal and reactor wall by controlling gas flow. Flow was maintained for several days until these temperatures equalized. Finally, pure fluorine was slowly flowed for several hours to ensure complete reaction. The reaction vessel was then purged with helium and transferred to a dry-helium glove box for disassembly and storage of the fluorinated product.

NMR Spectroscopy. NMR spectroscopy was performed on 50-100 mg samples in a Bruker MSL-100 (2.35 T) spectrometer. The samples were spun at 5 kHz in a doubly tuned single coil magic angle spinning probe. Single pulse ^{19}F spectra were obtained at 94.200 MHz and MAS = 12 kHz. ^{13}C spectra were obtained at 25.184 MHz by ^{19}F - ^{13}C cross polarization (CP) with ^{19}F decoupling during acquisition. Dipolar dephasing (DD) delays in the range of 0-100 μs were used to aid in assignment of fluorinated species, while 0-2 ms delays were used for graphitic carbons. To obtain quantitative CP data, variable contact time (VCT) experiments were performed.⁸ Signal intensity (I) is acquired vs. contact time (τ) over a wide range of contact times (25 μs to 100 ms), and fit to equation (1) to

$$I = \frac{I_0}{T_{\text{CF}}} * \frac{e^{-(\tau/T_{1\rho})} - e^{-(\tau/T_{\text{CF}})}}{(1/T_{\text{CF}}) - (1/T_{1\rho})} \quad (1)$$

obtain I_0 , T_{CF} and $T_{1\rho}$. I_0 represents the $T_{1\rho}$ relaxation-independent intensity of the resonance, while T_{CF} and $T_{1\rho}$ are the time constants associated with the buildup and decay of intensity. Fitting is accomplished by least squares minimization. Composition of each carbon type is reported as a percentage of total observed carbon. The precision of the percentage composition reported are on the order of $\pm 5\%$.

ESCA Analysis. ESCA data were obtained using a PHI (Perkin Elmer) 5000 series XPS spectrometer equipped with a dual anode (Al: $h\nu = 1486.6\text{ eV}$ and Mg: $h\nu = 1253\text{ eV}$). The Al anode was utilized at a power of 400 W (15 kV). The instrument was operated in the fixed analyzer transmission (FAT) mode with a pass energy of 17.9 eV for high resolution scans. Pressure was $< 1.0 \times 10^{-7}$ torr.

Results and Discussion

NMR Analysis. ^{13}C NMR spectra of charcoal fluorinated at different temperatures are presented in Figure 1. Four distinct resonances are observed, assigned to graphitic C, CF, CF_2 and CF_3 species. In the -80°C spectrum, the downfield feature found at 129 ppm is initially assigned to graphitic carbon (C). This chemical shift is consistent with model fused aromatic carbons (121-133 ppm). Its relatively slow signal accrual ($T_{\text{CF}} > 100\text{ }\mu\text{s}$) and decay ($T_{\text{DD}} \sim 500\text{ }\mu\text{s}$) indicate that these carbons are at least 0.3 nm (2-3 bonds) from fluorine nuclei. The resonance observed at 86 ppm is assigned to CF. Fast signal accrual and dephasing (T_{CF} and $T_{\text{DD}} \sim 50\text{ }\mu\text{s}$) confirm that these carbons are strongly coupled (directly bonded) to fluorine. A third resonance (CF_2) becomes apparent at 112 ppm in charcoal fluorinated at higher temperatures. A fourth resonance (136 ppm) is observed only in the charcoal fluorinated at 250°C and is assigned

to CF_3 . A ^{19}F spectrum of the charcoal fluorinated at 250°C (Figure 2) supports these ^{13}C CF_x assignments. The broad feature in the region -60 to -220 ppm contains unresolved isotropic peaks which are flanked by spinning sidebands outside this range. The isotropic peaks indicate the presence of CF (-170 ppm), CF_2 (-128 ppm) and CF_3 (-85 ppm).

The relative percentages of each carbon type in the ^{13}C spectra are listed in Table 1. The F/C atomic ratio indicates the extent of fluorine incorporation. Fluorination is evident even at -80°C , but is not complete until 350°C . CF, CF_2 , and CF_3 percentages determined by ^{13}C NMR and ^{19}F NMR are comparable (within 5 %), supporting structural assignments and justifying the fitting procedure used to quantify species in CP spectra. CF_3 is lost upon fluorination at 350°C , indicating platelet degradation above 250°C . Carbons at the platelet edge produce CF_2 rather than CF upon fluorination. The CF_2/CF ratio is a measure of edge to bulk carbon and is thus useful in determining platelet size. A simple hexagon-shaped model platelet with 5 aromatic rings per side (assuming a C-C distance of 0.14 nm) has an edge to bulk carbon ratio of 0.20 and a 2.2 nm diameter. The CF_2/CF ratio obtained by NMR studies of the 250°C material is 0.19 ± 0.09 . A platelet diameter of 2 ± 1 nm is obtained if a hexagonal shape is assumed. Small angle neutron scattering experiments gave a platelet size of roughly 2 nm.

Two graphitic carbon species are assigned to the 129 ppm resonance based on VCT results. This bimodal character is revealed in a plot of intensity vs. contact time for the charcoals fluorinated at -80°C , 23°C and 65°C (Figure 3). Bulk graphitic carbon (C_b), with $T_{\text{CF}} = 5$ ms and $T_{1\rho} = 30$ ms, dominates the -80°C plot. It consists of carbon further than 0.32 nm from fluorine nuclei. At higher preparation temperatures, an increasing amount of graphitic carbon displays $T_{\text{CF}} = 0.2$ -1 ms and $T_{1\rho} = 1$ -5 ms. This species becomes dominant at 65°C as indicated by the change in lineshape and is defined as interfacial graphitic carbon (C_i). C_i is adjacent to CF with a $\text{C}_i\text{-C-F}$ distance estimated at 0.24 nm. Fluorine must be widely dispersed in small CF clusters at -80°C to account for the percentage C_i observed. The C_i/CF ratio is an indicator of CF cluster size. It shows the growth of CF regions in the graphitic plates with increasing temperatures. Initially, 2-3 F/cluster are indicated, increasing to about 8 F/cluster at 23°C , and >40 F/cluster at 180°C .

ESCA Analysis. Results of ESCA analyses are given in Table 2. The generation of fluorinated carbon species follow trends observed in the NMR data, although relative percentages are lower by 10-20 %. CF_2 is detected even at -80°C , but is never more than 4 %. Two species of graphitic carbon are also observed. Bulk graphitic carbon (CC), analogous to C_b , is initially the dominant species but is entirely consumed at 250°C . $\text{C}(\text{CF})$ is analogous to C_i . Its concentration (35-40 %) is remarkably constant over the sample temperature range. The ratio $\text{C}(\text{CF})/\text{CF}$ follows trends observed for C_i/CF . CF_2/CF is nearly constant at 0.11 throughout the temperature range. Assuming a hexagon-shaped platelet, the platelet diameter that produces this ratio is about 4 nm.

Comparison of Analyses. Gravimetric analysis is the most direct measure of fluorine incorporation into charcoal. The F/C ratios determined by attributing net weight gain to fluorine (See Tables 1 & 2) are very similar to results from NMR and ESCA. Gravimetry does not take into account weight loss from the displacement of edge oxygen and hydrogen by fluorine. This atomic replacement can lower the F/C ratio measured

gravimetrically by as much as 20 %. Differences in F/C ratios are generally within experimental error except at 250°C where the F/C ratio from the ESCA analysis is significantly lower than the NMR result. The F/C ratio is very sensitive to CF₂ and CF₃ concentrations which are consistently lower in the ESCA results. This lower ratio is most pronounced in studies of the sample fluorinated at 250°C where the CF₂ and CF₃ concentrations is greatest. An F/C ratio of 1.1-1.25 is calculated for fluorinated charcoal with platelets roughly 2-3 nm, a value more consistent with NMR results.

Structural Features and Fluorination Mechanism. Charcoal consists of planar fused aromatic carbon platelets having an average diameter on the order of 2-4 nm. The platelet interlayer distance (0.33 nm) is large enough for F₂ to diffuse between platelets. F₂ is not limited to surface reaction in micropore void spaces. The platelets separate to 0.57 nm upon complete fluorination.⁶ Paramagnetic sites were detected based on NMR observations. Carbonaceous materials generally contain free electron spin density as a result of their aromatic character and/or the presence of trace amounts of metals. A ¹H-¹³C CP experiment was attempted on the original charcoal used in this study to search for edge functionality. Edge sites in this material are assumed to consist of hydrogen and oxygen containing functional groups. Edge resonances were not detected, but the experiments did confirm the presence of free spin density. The probe tuning characteristics changed significantly with this material, an effect sometimes observed for conductive or paramagnetic materials. A ¹H-¹³C CP spectrum could not be obtained. The spinning sample also slowed significantly (4953 Hz to 4860 Hz) when the probe was raised into the magnetic field. This effect was reversible. ¹⁹F T_{1ρ} time constants were on the order of 50 ms for the charcoal fluorinated at -80°C, a value common for diamagnetic materials. The free spin density present in the charcoal had evidently been quenched by fluorine reaction at -80°C. At higher CF_x preparation temperatures, ¹⁹F T_{1ρ} grows significantly shorter (to 1 ms for the 250°C material) and returns to 50 ms for the 350°C material. Iron is also present in this charcoal (1 %) as a possible paramagnetic source. Demineralization did not remove the paramagnetic sites, so we conclude that iron is not the source of free spin density in the charcoal or its fluorination products. The tuning, spinning, and T_{1ρ} behavior strongly suggest the presence of paramagnetic organic radicals.

Summary

Carbon monofluoride is prepared by elemental fluorination of charcoal. Two graphitic and three fluorinated carbon species are quantified in NMR studies and confirmed by ESCA analysis. Fluorination occurs to a limited extent at -80°C by a radical mechanism. Small widely dispersed CF regions grow larger and more numerous when charcoal is fluorinated at higher temperatures. CF_{1.1-1.2} is produced above 250°C. The charcoal platelet has an average diameter on the order of 2-4 nm and is stable to at least 250°C.

Acknowledgments

This research was sponsored by the Division of Chemical Sciences, Office of Basic Energy Sciences, U. S. Department of Energy, under Contract No. DE-AC05-84OR21400 with Lockheed Martin Energy Research. The ESCA analysis was done by Joseph Fiedor.

References

- (1) Hagaman, E. W.; Lee, S. K. *Energy & Fuels*, **1995**, *9*(5), 727-734.
- (2) Purrington, S. T.; Kagen, B. S.; Patrick, T. B. *Chem. Rev.* **1986**, *86*, 997-1018.
- (3) Wilkinson, J. A. *Chem. Rev.* **1992**, *92*, 505-519.
- (4) Harris, R. K.; Jackson, P. *Chem. Rev.* **1991**, *91*, 1427-1440.
- (5) Hagaman, E. W.; Burns, J. H. *Fuel*, **1993**, *72*(8), 1239-1243.
- (6) Kamarchik, P.; Margrave, J. L. *Acc. Chem. Res.* **1978**, *11*, 296-300.
- (7) Greenwood, N. N. And Earnshaw, *Chemistry of the Elements*, Pergamon Press, New York, 1984; p304.
- (8) Hagaman, E. W.; Chambers, R. R.; Woody, M. C. *Anal. Chem.*, **1986**, *58*(2), 387-394.

Table 1. Composition and ratios of carbon components in fluorinated charcoal as determined by ^{19}F - ^{13}C CP/MAS NMR

Carbon Component	Fluorination Temperature							
	-80	0	23	65	120	180	250	350
C _i	27%	38%	33%	36%	29%	21%	0%	0%
C _b	<u>57%</u>	<u>37%</u>	<u>33%</u>	<u>21%</u>	<u>17%</u>	<u>5%</u>	<u>0%</u>	<u>0%</u>
C (=C _i + C _b)	84%	75%	66%	57%	46%	26%	0%	0%
CF	16%	25%	34%	39%	48%	67%	81%	78%
CF ₂				4%	6%	8%	15%	22%
CF ₃							4%	0%
C _i /CF	1.64	1.50	0.96	0.91	0.61	0.31	0	0
CF ₂ /CF				0.10	0.12	0.11	0.19	0.28
F/C by NMR	0.16	0.25	0.34	0.47	0.59	0.82	1.19	1.22
F/C by Wt.	0.27	0.32	0.38	0.45	0.50	0.77	0.91	

Table 2. Composition and ratios of carbon components in fluorinated charcoal as determined by ESCA Analysis

Carbon Component	Fluorination Temperature						
	-80	0	23	65	120	180	250
C(CF)	38%	39%	34%	39%	43%	38%	35%
CC	<u>43%</u>	<u>39%</u>	<u>36%</u>	<u>13%</u>	<u>9%</u>	<u>10%</u>	<u>0%</u>
Total C	81%	78%	70%	52%	52%	48%	35%
CF	19%	18%	22%	32%	44%	47%	60%
CF ₂	2%	2%	2%	4%	4%	4%	4%
CF ₃	0%	0%	0%	0%	1%	1%	1%
C(CF)/CF	2.00	2.17	1.55	1.22	0.98	0.81	0.58
CF ₂ /CF	0.11	0.11	0.09	0.13	0.09	0.09	0.07
F/C by ESCA	0.24	0.26	0.30	0.42	0.53	0.56	0.77
F/C by Wt.	0.27	0.32	0.38	0.45	0.50	0.77	0.91

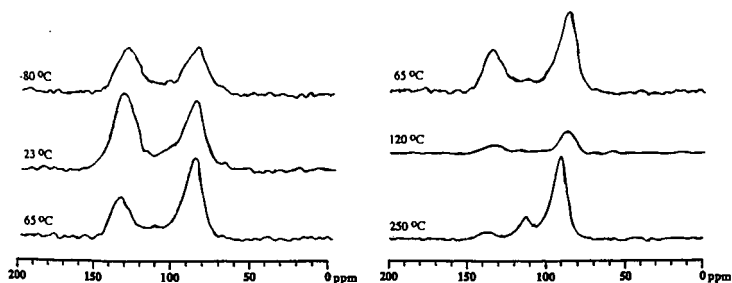


Figure 1. ^{19}F - ^{13}C CP/MAS NMR spectra of charcoal fluorinated at various temperatures. Typically 20k scans were signal averaged using a 2.5 ms contact time and a 2 s recycle delay.

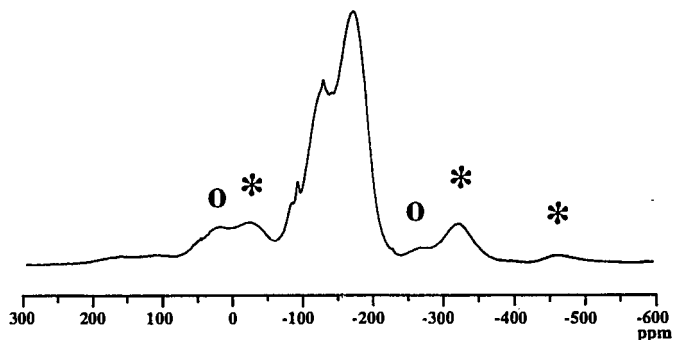


Figure 2. ^{19}F MAS NMR spectrum of charcoal fluorinated at 250°C. Spin rate is 12 kHz (127 ppm). * indicates spinning sidebands of the CF peak (-170 ppm). O indicates sidebands of the CF_2 peak (-128 ppm).

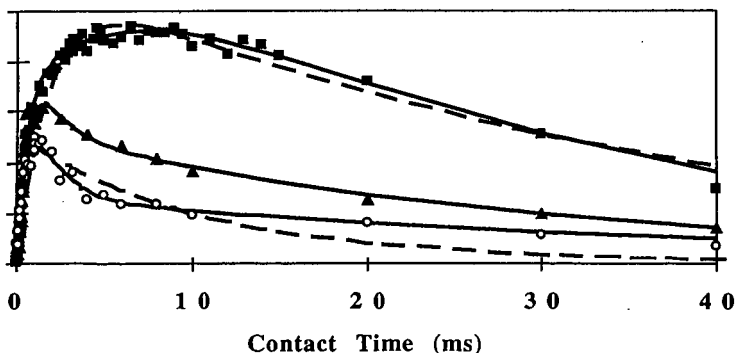


Figure 3. Graphitic carbon intensities from ^{19}F - ^{13}C CP/MAS NMR studies plotted vs. contact time for several fluorinated charcoal samples: (■) -80°C, (▲) 23°C, (○) 65°C. Two component fits are displayed as solid lines. Selected one component fits are displayed as dashed lines.

TYPE OF WATER ASSOCIATED WITH COAL

K. Norinaga, H. Kumagai, J.-i. Hayashi and T. Chiba
Center for Advanced Research of Energy Technology (CARET), Hokkaido University
N13, W8, Kita-ku, Sapporo 060, Japan

M. Sasaki
Hokkaido National Industrial Research Institute (H-NIRI)
2-17, Tsukisamu-Higashi, Toyohira-ku, Sapporo 062, Japan

Key words: crystallization, proton mobility, non-freezing water

INTRODUCTION

The authors¹ have evaluated changes in physical structure of a lignite induced by drying by means of swelling in water and proton NMR relaxation measurements. They have found that the water removal reduces considerably and irreversibly the swelling ratio and the relaxation time of protons in the macromolecular phase meaning that it makes the macromolecular network more rigid, as has been observed for solvent loading and removal processes.² It has been also found that the dryings carried out at different temperatures of 303 K and 380 K give rise to difference in the above properties even at the same extents of water removal. This result reveals that physical structure of macromolecules in the lignite is not determined only by the water content but also other factors such as properties of water in its matrix. The systematic analysis of water sorbed on coal should be therefore established for understanding its roles in physical structure of coal.

Differential scanning calorimetry (DSC) has been applied to evaluate the crystallization property of water sorbed on polymers carrying polar functional groups. Nakamura et al.³ investigated the property of water in polyhydroxystyrene employing this technique. When the water content reached a certain level, they observed two exothermic peaks due to the crystallization of water centering at 273 K and 235 K respectively arisen from bulk (or free) water and freezable bound water. They also found another type of water, called as non-freezing water, no crystallization of which was observed. An advantage of this technique is that water can be quantitatively classified by assuming its crystallization heat and it can be also applied for characterization of water sorbed on coal.⁴ The freezing-point temperature depends on the size of space where water is condensed and it is not observed when the size is smaller than a critical value. The distribution of water elucidated by DSC may give informations on the size distribution of assemblies of water molecules. The non-freezing water has been recognized to be directly hydrogen-bonded to polymer functionalities and would be the most important type of water relevant to properties of the macromolecular network of coal. However, the non-freezing water is not directly observed by DSC.

The crystallization of free and bound waters is also expected to be observed in proton NMR relaxation measurements as the conversion of 'mobile proton' giving Lorentzian magnetization decays into 'immobile proton' doing Gaussian ones. Furthermore, the non-freezing water would be observed and its abundance and mobility would be also evaluated. Recently the NMR measurements have been adopted for determination of water content in coal^{5,7}. Lynch et al.⁷ observed a Lorentzian-Gaussian transition in a brown coal around 273 K and thereby estimated the content of free water contained in the coal.

The present study aims first to quantify the amounts of free, bound and non-freezing waters sorbed in coals ranging from lignite to bituminous ranks on the basis the crystallization characteristics measured by DSC. The second objective is to observe the non-freezing water and to evaluate changes in its mobility in the course of cooling as well as the other types of water and coal hydogen.

EXPERIMENTAL

Coal samples

Table 1 presents the moisture and ash contents as well as the elemental compositions of coal samples so far used. Experiments were conducted with four Argonne PCSP coals and four brown coals supplied from the Nippon Brown Coal Liquefaction Co. Ltd.. The particle sizes were smaller than 150 μm for all samples. The samples other than the PCSP ones were stored in a gas tight vessel which was filled with atmospheric nitrogen saturated by water vapor at 293 K for a week prior to analyses. The moisture contents in the brown coals were determined from fractional mass release from them by a drying under nitrogen flow at 380 K for 2 h, while for the PCSP coals the literature values were used⁸. The PCSP samples were subjected to analyses immediately after opening the ampules.

Drying

Among the coal samples BZ coal was partially or completely dried at 303 K under dried or humidified nitrogen atmosphere. The extent of water removal was controlled by varying the relative humidity in a drying vessel from zero to 84% using conc. H_2SO_4 and aqueous solutions

saturated by selected salts.¹

DSC

DSC measurements were made employing a calorimeter (DSC 200, Seiko Co. Ltd.) equipped with a liquid nitrogen cooling accessory. The coal sample was cooled from 293 K to 123 K at a rate of 2 K/min and then heated up to 293 K at 2 K/min under atmospheric nitrogen gas flow of 80 ml/min.

Solid-state proton NMR

A proton magnetic resonance was adopted to elucidate spin-spin relaxation characteristics for the coal samples. The relaxation measurements were carried out on a JEOL Mu-25 spectrometer operated at 25 MHz. A 90° - τ - 90° solid echo sequence was used to obtain the entire free induction decays (FID). The FID was measured at temperature intervals of 2-5 K in the course of cooling from 293 K to 203 K. At each temperature the signal was recorded after a time period of 15 min since the temperature was reached for confirming homogeneous temperature distribution in the specimen. The FID curves were analyzed by a sequential linear-least-squares fitting method which has been commonly employed to deconvolute the total FID into two Gaussian and a Lorentzian functions with different specific relaxation times, i.e., T_2 . The following equations were used to fit the FID signal.

$$I(t) = I_L(t) + I_G(t) \quad (1)$$

$$I_L(t) = I_L(0) \exp[-t/T_{2L}] \quad (2)$$

$$I_G(t) = I_{G1}(0) \exp[-t^2/2T_{G1}] + I_{G2}(0) \exp[-t^2/2T_{G2}] \quad (3)$$

where $I(t)$ and $I_L(t)$ are the intensity observed and that attributed to the component i at time t . In Figure 1 natural logarithm of the FID intensity of YL, BZ and WY coals at 293 K are shown versus the relaxation time. The long-decaying component observed after 30 μ s for each coal is evidently a Lorentzian function. After fitting the Lorentzian component by Eq. (2) to determine $I_L(0)$ and T_{2L} and subtracting it from the signal, the rest was further fitted by Eq. (3) to obtain $I_{G1}(0)$, $I_{G2}(0)$, T_{G1} and T_{G2} . This procedure was successful for all curves observed. FID curves of dried BZ coal shown in Figure 2 were also analyzed by the same procedure.

RESULTS AND DISCUSSION

DSC results

Figure 3 exhibits the DSC curves for four different coals together with that for pure water. The positive peaks appearing on the curves mean exothermic processes. Though not shown here such peaks were never observed for the coals dried at 380 K. Negligible weight change was confirmed for all samples during the measurements. These peaks are thus arisen from a transition of water sorbed on the coal into ice, i.e., crystallization. For YL coal two peaks centering at 226 K and 258 K are evident. The larger one appears in the same temperature range as that for pure water and is ascribed to the crystallization of water having no specific interactions with the coal. The water can be defined as 'free water' or 'bulk one'. On the other hand, the smaller peak is attributed to 'bound water' being frozen at temperatures lower than that for the free water. Water condensed in capillaries with diameters of less than several microns has been known to be frozen around 220-230 K. Hence the bound water defined here can be also regarded as water condensed in macropores. The curves for the other coals indicate the existence of the bound water, while no free water. The peaks around 226 K are common among the curves for all coals, and in addition, for BZ and SB coals they overlap with the peaks observed at higher temperatures which are also assigned to the bound water.

The amounts of the free and bound waters can be estimated by assuming their crystallization heat. The heat for the free water was calculated as 333 J/g by analyzing the DSC curve for pure water. The value is nearly equivalent to that for the transition of bulk water into ice having Type-I polymorphic form, an only one that can be formed under the present conditions, i.e., 334 J/g.² This literature value was thus employed for estimating the free water content. This was also used to estimate that of the bound water content assuming its crystallization into Type-I ice.

Calculated fractions of the free and bound waters are summarized in Table 2. It should be noted that these types of waters account only for a portion of total for the all coals tested. This means the existence of another type of water that is not frozen at any temperatures examined. This type of water is here defined as 'non-freezing one' according to Nakamura et al.³ as well as the other types of waters.

In Figure 4(a) the amount of the non-freezing water per unit mass of coal on a dry basis is plotted against the sum of oxygen and nitrogen molar contents in them, which is a measure for the amount of polar and hydrophilic functional groups. The non-freezing water seem to be more abundant in the coal carrying more oxygen and nitrogen. This tendency can be reasonably explained by that water molecules as the non-freezing water are dispersed in the coal matrix at molecular levels being hydrogen-bonded to polar functional groups, a necessary condition of which is that the water is not frozen at any temperatures scanned in the DSC measurements. It is also noted in Figure 4(b) that the coal having more oxygen and nitrogen functionalities binds the larger number of water molecules as the non-freezing water per that of oxygen and nitrogen atoms. There is a wide variation in the number ranging from 0.3 for IL coal to 1.5-1.8 for the brown coals. Although the values indicated

in the figure are averaged ones, they are small enough to support that water molecules directly interact with oxygen and nitrogen-containing groups.

The above DSC results reveal that the coals contain freezable water which is classified into the free water and bound one based on their crystallization temperature. They also indicate the existence of the non-freezing water, the crystallization of which is not observed. As suggested from the result shown in Figure 4(b), when water molecules are dispersed on a molecular scale, the crystallization as a phase transition should be not observed even if their mobility as liquid is lost by the cooling. The NMR relaxation measurements were therefore made to examine the mobility of molecules as the non-freezing water and its temperature dependence as well as to observe the crystallization of the free and bound waters as the conversion of the Lorentzian component into Gaussian one.

NMR results

In Figure 5 are shown relationships between the amount of proton assigned to the Lorentzian component at 293 K and that as water sorbed on the coals. The former, given as $I_L(0)/I(0)$ multiplied by the total amount of hydrogen in water-containing coal, is larger than the latter without an exception, suggesting that a portion of coal hydrogen has mobilities characteristic to those in a liquid environment. Under an assumption that all protons as water are attributed to the Lorentzian component at 293 K, fractions of coal hydrogen having such mobility to the total are 9-38 % as indicated in the figure. The effect of water content on the amount of mobile coal hydrogen is shown for BZ coal in Figure 6. It is seen that the amount increases with an increase in the water content. This suggests that both non-freezing and bound waters mobilize coal hydrogen. The authors previously reported that water contained in the coal plays a role of solvent as a swelling agent based on volumetric shrinkage due to its removal.¹ Yang et al.,¹⁰ who studied the proton relaxation characteristics of dried and pyridine-swollen high-volatile bituminous coals by means of a spin-echo NMR technique, found that the fraction of the Lorentzian component in the coals increases from zero to 70-80% due to the swelling. The results shown in Figs. 5 and 6 are therefore quite reasonably accepted.

Figure 7 presents the amount of hydrogen giving the Lorentzian decay, H_L , normalized by that as water contained in the coal as a function of temperature ranging from 213 K to 293 K. For MW coal, the reduction of H_L is first observed at 273 K. There seems to be two different temperature dependences of the H_L reduction in the ranges of 263-273 K and 213-263 K. Similar profiles were obtained for LY and YL coals. Considering that such sharp decrease in H_L at 263-273 K is not observed for the other coals, it can be mainly attributed to the crystallization of free water which is also observed in the DSC measurements. The liquid-solid transition should be observed as the conversion of the Lorentzian component to the Gaussian one. Moreover, the decrease in H_L in the range of 213-263 K should involve that due to the phase transition of the bound water, while it may also involve other Lorentzian-to-Gaussian transitions for hydrogen as the non-freezing water and/or coal hydrogen. The total decrement of H_L is thus expected to be at least equivalent to the amount of hydrogen as the free and bound waters, or larger if other transitions are also observed. The extents of H_L reduction for MW and YL coals are respectively 52 and 57 % and are in good agreement with the total fractions of the free and bound waters in these coals, i.e., 52 and 58 %. Hence the decrease in H_L can be referred to the crystallization of these types of waters, and hydrogen of the non-freezing water and coal hydrogen being mobile at 293 K both give the Lorentzian decay even at 213 K.

Table 3 summarizes the decrement of H_L in the range of 213-293 K for six different coals. For the coals other than the brown ones, the decrement is evidently larger than the amount of hydrogen as the bound water, while H_L at 213 K also appears to be larger than that as the non-freezing water. The result means that the reduction of H_L involves the transition of a portion of coal hydrogen being mobile at 293 K, that of hydrogen as the non-freezing water or both of them. Although their contributions to the reduction are not clear at present, it can be said that at least most of the non-freezing water is in a liquid environment even at 213 K by postulating higher mobility of water molecules than that of coal macromolecules based on much smaller mass of the former than the latter.

Figure 8 shows T_{2L} of the four different coals as a function of temperature. Although there is a wide variation in the temperature dependence of T_{2L} with the coals, the relaxation time seems to reach a value of 60 μ s at 213 K for the all coals. Such a coal-independent relaxation time implies that the Lorentzian components observed for the different coals at the temperature, which consist mainly of the non-freezing water, have similar mobilities.

CONCLUSIONS

The eight coals were subjected to the DSC and proton solid-state NMR relaxation analyses. Water sorbed on/in their matrices can be classified into three types on the basis of the crystallization characteristics, namely free water, bound water and non-freezing water. The abundances of the free and bound waters can be quantified using the crystallization heat of water, while the non-freezing water by difference. The crystallization of the freezable waters is also observed in the NMR as the conversion of the Lorentzian component into Gaussian one at 213-273 K where the conversion for coal hydrogen is also observed for the coals other than the brown ones. All or at least most of the non-freezing water is in a liquid environment to give Lorentzian decays even at 213 K.

REFERENCES

1. K. Norinaga, H. Kumagai, Y. Sanada, M. Sasaki and T. Kotanigawa, *Coal Science and Technology* 1995, 24, 35.
2. R. P. Warzinski and G. D. Holder, *Fuel* 1992, 71, 993.
3. K. Nakamura, T. Hatakeyama and H. Hatakeyama, *Polymer* 1983, 24, 871
4. S. C. Mraw, D. F. Orourke, *Science* 1979, 205, 901.
5. B. C. Gerstein, C. Chow, R. G. Pembleton, R. C. Wilson, *J. Phys. Chem.* 1977, 81, 565
6. X. Yang, A. R. Garcia, J. W. Larsen, B.G. Silbernagel, *Energy Fuels* 1992, 6, 651.
7. L.J. Lynch, D. S. Webster, *Fuel* 1979, 58, 429.
8. K. S. Vores, 1993. *USERS HANDBOOK FOR THE ARGONNE PREMIUM COAL SAMPLE PROGRAM*. Argonne National Laboratory, Argonne, Illinois, p. 20.
9. D. Eisenberg and W. Kauzmann, 'The Structure and Properties of Water', Oxford University Press, London, 1969
10. X. Yang, J. W. Larsen, B.G. Silbernagel, *Energy Fuels* 1993, 7, 439.

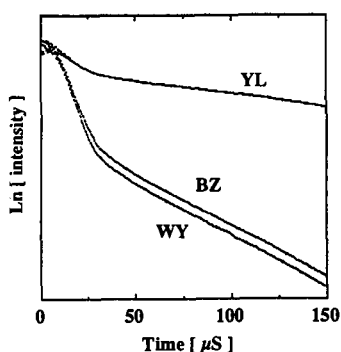


Figure 1. Natural logarithm of FID intensity versus relaxation time at 293 K for LY, BZ and WY coals.

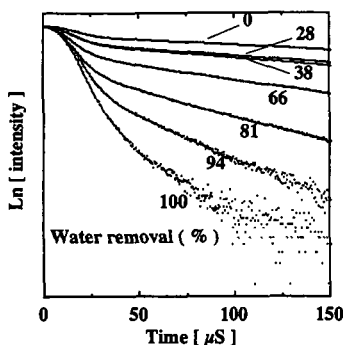


Figure 2. Natural logarithm of FID intensity versus relaxation time at 293 K for BZ coal with different water removal.

Table 1. Properties of coals so far used.

Coal	(Symbol)	Moisture [wt. % -sample]	Ash [wt. % db-coal]	C	H	N	S	O(diff.)
				[wt. % daf-coal]				
Blind Canyon	(BL)	4.6	4.7	80.7	5.8	1.6	0.4	11.6
Illinois #6	(IL)	8.0	15.5	77.7	5.0	1.4	2.4	13.5
Wyodak	(WY)	28.1	8.8	75.0	5.4	1.1	0.5	18.0
Beulah Zap	(BZ)	32.2	9.7	72.9	4.8	1.2	0.7	20.3
South Banko	(SB)	31.5	3.2	70.4	5.8	1.2	0.4	22.2
Yallourn	(YL)	57.5	1.4	62.6	4.6	0.7	0.3	31.9
Loy Yang	(LY)	56.7	1.1	62.7	4.7	0.7	0.3	31.6
Morwell	(MW)	55.5	2.6	64.2	4.7	0.7	0.3	30.1

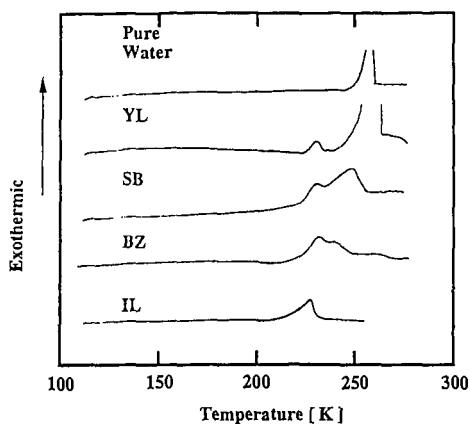


Figure 3. DSC profiles of LY, SB, BZ and IL coals and pure water.

Table 2 Summary of DSC results

Coal	Peak at higher temp.		Peak at lower temp.		Water type		
	ΔH	Temp.	ΔH	Temp.	Free	Bound	Non freezing
	J/g	K	J/g	K	[% to total]		
BL	0	-	1.1	226.2	0	7	93
IL	0	-	5.0	227.0	0	19	81
WY	0	-	25.1	227.6	0	27	73
BZ	0	-	23.0	226.4	0	21	79
SB	0	-	31.0 (248.1, 227.6)		0	29	71
YL	86.7	258.5	25.4	226.3	45	13	42
LY	93.6	258.4	18.4	227.1	49	10	41
MW	83.6	257.9	13.9	227.0	45	7	48

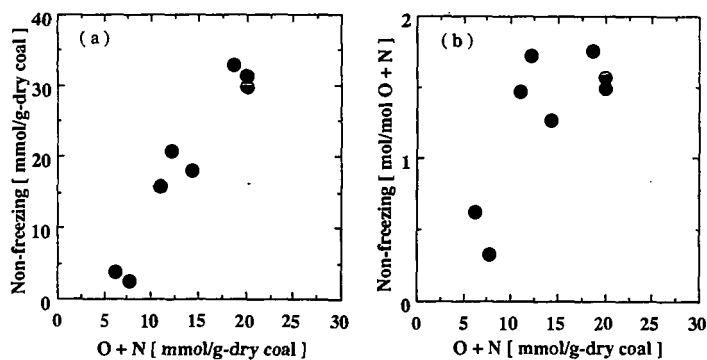


Figure 4. Plots of abundance of non-freezing water against sum of molar oxygen and nitrogen contents (a) and those of number of water molecules as non-freezing water per that of oxygen and nitrogen atoms (b).

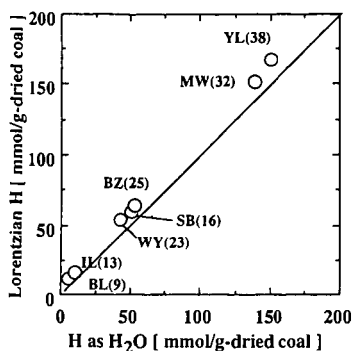


Figure 5. Comparison of amount of proton giving Lorentzian decay with that as water sorbed on coals. Values in (): % fraction of Lorentzian coal hydrogen to total.

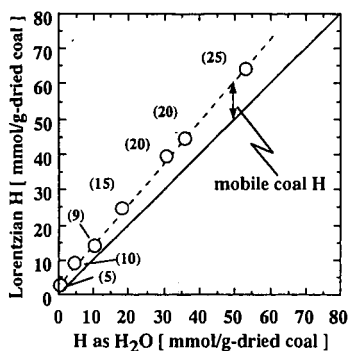


Figure 6. Comparison of amount of proton giving Lorentzian decay with that as water for BZ coal with different water contents. Values in (): % fraction of Lorentzian coal hydrogen to total.

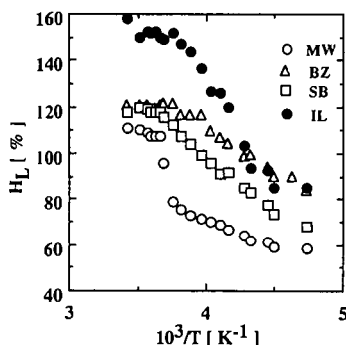


Figure 7. Temperature-dependent changes in H_L being amount of Lorentzian proton normalized by molar amount of proton

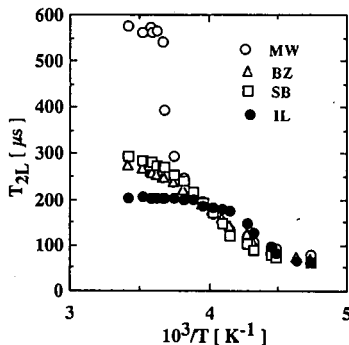


Figure 8. Temperature-dependent changes in relaxation time of Lorentzian component.

Table 3. H_L 's at 293 and 213 K and difference between them.

Coal	H as H ₂ O [mmol/g-dried coal]	H_L [%]		
		293 K (1)	213 K (2)	(1)-(2)
IL	9.6	158	85	73
WY	43.4	126	79	47
BZ	52.9	120	84	36
SB	51.1	118	68	50
YL	150.6	112	55	57
MW	138.7	111	59	52

THE PREPARATION AND CHARACTERIZATION OF LINEAR AND CROSS-LINKED POLY(FLUORENYL).

Edward W. Hagaman and Suk-Kyu Lee.

Chemical and Analytical Sciences Division
Oak Ridge National Laboratory
Oak Ridge, Tennessee 37831-6201

Keywords: Cross linking, Poly(fluorenyl), CP/MAS ^{13}C NMR

INTRODUCTION

Retrogressive reactions in coal processing are that class of reactions that lead to the formation of high molecular weight materials that are more intractable than those present in the coal prior to processing. This outcome almost always is regarded as deleterious. The present work focuses on the characterization of the acid-catalyzed polymerization of benzylic fluorides, and in particular the synthesis of poly(fluorenyl), as an example of the type of chemistry that may occur in the cross-linked organic matrix of coals when in contact with strong acids. Solution and solid state ^{13}C NMR spectroscopy was used to characterize the soluble and insoluble polymers. The change in the value of $f_a^{A^H}$, the fraction of aromatic carbon that is protonated¹, is the criterion used to monitor the extent of cross-linking in these polymer preparations.

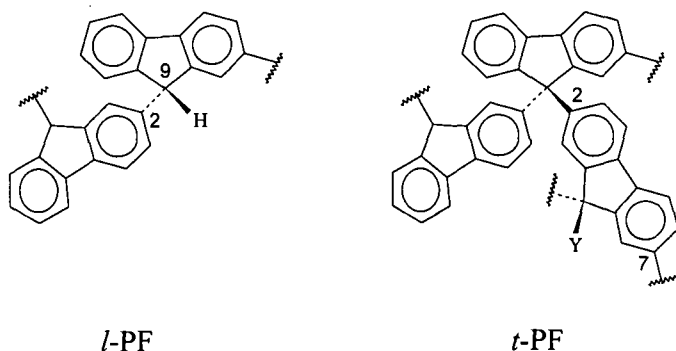
Benzylic fluorides are sensitive substances, prone to further reaction via acid catalyzed heterolytic scission of the C-F bond. The electron deficient reactive intermediate formed in this reaction undergoes electrophilic aromatic substitution. This reaction can be started with catalytic traces of acid and is self-sustaining as HF is generated in equivalent concentrations as the reaction proceeds. The relevance of this naturally non-occurring functional group in coal processing stems from the similar reaction pathway followed by both benzylic fluorides and benzylic alcohols. In the coal matrix, the operation of two exogenous processes- air oxidation and strong acid treatment of the coal (deminerallization) creates a situation in which the polymerization discussed herein may occur in the coal. In addition to the polymerization reactions that produce poly(fluorenyl), the subsequent cross-linking of the linear polymer is also reported. In subsequent work, similar chemistry will be applied to soluble lignin as a model more similar to low rank coals.

RESULTS AND DISCUSSION

The generation of poly(fluorenyl), PF, is most easily effected by impurity- or self-catalyzed decomposition of solid 9-fluorofluorene. The solid state reaction proceeds unattended by storing the monomer in a closed, dry glass container at room temperature. In a matter of days the white, crystalline 9-fluorofluorene is completely converted into a white, fluorine-free, *soluble* polymer. This material is identical (except in molecular weight distribution) to the polymer generated from 9-fluorofluorene in hexane or THF solution that has been treated with catalytic trifluoroacetic acid. A polymer that is virtually indistinguishable from that derived from 9-fluorofluorene is obtained from the reaction of 9-hydroxyfluorene in HF/pyridine.

The gross structure of the polymer follows from the change in $f_a^{A^H}$ between the monomer, 9-fluorofluorene (0.67 ± 0.02) and the polymer (0.59 ± 0.02), i.e., a change from 8 to 7 aromatic methines out of 12 aromatic carbons. The identification of protonated and non-protonated aromatic carbon resonances is made through dipolar dephasing experiments.² In Figure 1 the two resonances with chemical shifts greater than 140 ppm represent the non-protonated aromatic carbons in this polymer. In addition, the C(9) fluoromethine resonance (92.6 ppm, $^1J_{CF} = 180$ Hz) of 9-fluorofluorene is absent in the polymer. Indeed, no fluorocarbon resonance appears in the polymer.

The tetrahedral carbon resonance in the polymer occurs at 54.5 ppm (Figure 1a). These data indicate the loss of the carbon-fluorine bond and the formation of a carbon-carbon bond between C(9) and an aromatic carbon of another fluorene moiety. The C(9) resonance of the model 9-phenylfluorene is 54.4 ppm, an excellent match for the corresponding resonance in the polymer. The site of attachment of C(9) of one residue to the aromatic ring of the next monomer unit is C(2) [see the structure for numbering]. This attachment is supported by (1): chemical shift additivity arguments, (2): the well established electrophilic substitution pattern observed in fluorene, e.g., nitration of fluorene produces solely 2-nitrofluorene, and (3): a proof of structure based on long range ^1H - ^{13}C coupling in 2-(pentamethylbenzyl)fluorene, prepared by the acid-catalyzed reaction of pentamethyl benzyl fluoride with fluorene. The polymer has the structure shown below labeled linear PF, *l*-PF. The line widths of the resonances in the solid state spectrum are on the order of 125 Hz. The high resolution ^{13}C NMR spectrum of this highly soluble *l*-PF, obtained at low concentration in CDCl_3 to keep solution viscosity low, shows an order of magnitude better resolution than the solid state spectrum. The spectrum contains evidence of conformational heterogeneity of the polymer, with most carbons represented by a narrow manifold of chemical shifts that produces an asymmetric or split resonance band shape. This distribution in chemical shifts is too small to be an indication of the presence of structural isomers.



The *l*-PF formed from the solid state reaction of 9-fluorofluorene has a number average molecular weight, $M_n = 568$ and polydispersity, $M_w/M_n = 2.5$ determined by GPC. The weight average molecular weight, 1420, is in good agreement with that determined from end group analysis in the solid ^{13}C NMR spectrum, 1245. The end group resonance in this spectrum occurs at 36.0 ppm, the chemical shift of C(9) in the fluorene itself. It is possible that the polymer could bite back on itself, generating a ring or branch point in the polymer. The linkage so generated would be indistinguishable from the linear C(9) polymer resonances on the basis of chemical shift. Such structures, if present in high concentration would be reflected in low f_a^{CH} values.

Treatment of *l*-PF with F-TEDA or with $\text{HF/pyridine/NO}^+\text{BF}_4^-$, reagents used to introduce a fluorine substituent at unactivated aliphatic sites, fails to generate the intended product, poly(9-fluorofluorenyl). The products are *fluorine-free*, have a ^{13}C NMR spectrum similar in appearance to the starting material (cf. Figure 1a,b), and are *highly insoluble*. Integration of the aromatic resonances reveals $f_a^{\text{CH}} = 0.56 \pm 0.020$.³ These facts indicate that the polymer has been cross-linked by this chemical treatment. The implication is that the reagents do in fact generate the 9-fluoro *l*-PF, but that this product, like the 9-fluoro monomer, undergoes cationic polymerization. The f_a^{CH} of the product indicates that one of every three fluorenyl residues in the product, *l*-PF, has a new intra- or inter-chain C(9)-C(2) connection. The statistical repeating structural unit

of *t*-PF is shown above. In the limit of complete cross-linking the aromatic CH/C ratio would become 6/6, i.e., $f_a^{ar} = 0.50$. The inter-chain cross-links imbue the polymer with its high insolubility. All samples of *t*-PF that we have synthesized are cross-linked to about the same extent ($f_a^{ar} = 0.55 \pm 0.02$). This may represent a limiting degree of polymerization dictated by the physical constraints of the polymer chain. In addition to the 54 ppm resonance representing mono- and di-aryl substituted C(9) carbons of the fluorenyl residues, a new resonance at 83 ppm appears in the spectrum of *t*-PF produced using F-TEDA (Figure 1b). This is the region of the spectrum for oxygenated aliphatic carbon resonances. The resonance represents the incorporation of 9-aryl-9-fluorenol residues in the *t*-PF polymer ($Y = OH$ in the above structure). The C(9) resonance of the model, 9-phenyl-9-hydroxyfluorene, is 83.4 ppm. This functionality likely arises from quenching of fluorenyl cation sites with water during reaction work-up, sites that can not react by the usual pathway due to physical constraints built into the cross-linked polymer.

REFERENCES

1. M. A. Wilson, R. J. Pugmire, J. Karas, L. B. Alemany, W. R. Woolfenden, and D. M. Grant, *Anal. Chem.*, **56**, 933, (1984).
2. P. D. Murphy, B. C. Gerstein, V. L. Weinberg, and T. F. Yen, *Anal. Chem.*, **54**, 522, (1982).
3. The error limits on the aromaticity determinations reflect the absolute error in this quantity. The theoretical value of f_a^{ar} for the linear polymer is 0.583. The value from the direct NMR integral, splitting the area at the saddle point, is 0.60. Peak fitting with an assumed Gaussian line shape yields 0.59, while allowing the line shape to be treated as a mixed Gauss-Lorentz line produces the best line fit (smallest residuals) and a value of 0.61. The ± 0.02 error limits reflect these uncertainties as well as the deviations from linear response that may accrue in the actual experiment. However, in comparisons between two similar materials, taking care to use the same evaluation criterion for both, the relative error is small. The 0.03 difference in f_a^{ar} between *l*-PF and *t*-PF is reproducible, indicating a small relative error.

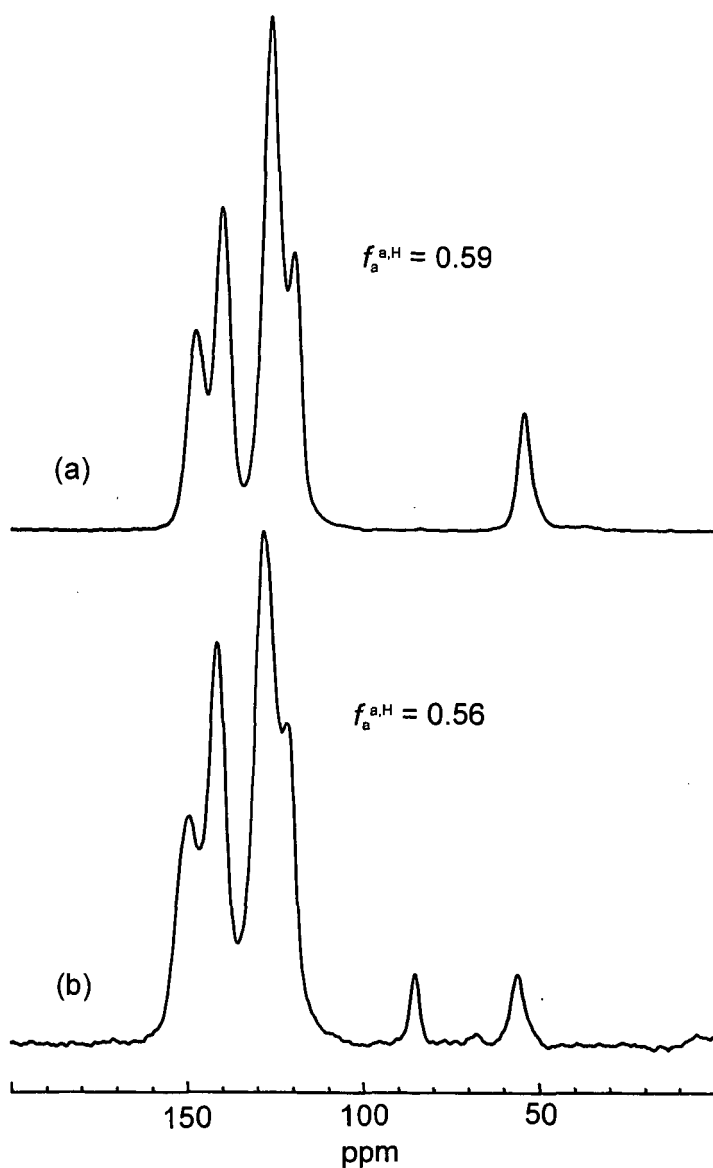


Figure 1. ^{13}C NMR spectra of (a) *t*-PF from the solid state polymerization of 9-fluorofluorene and (b) *t*-PF from the reaction of *t*-PF with F-TEDA. Broadening of the aromatic peaks in 1b relative to 1a and the change in $f_a^{a,H}$ evidence the increase in conformational heterogeneity and cross linking in *t*-PF. The $f_a^{a,H}$ values are calculated from areas derived from peak deconvolution of the aromatic resonances.

THE INCREASE OF THE EXTRACTION YIELD OF COALS BY THE ADDITION OF AN ELECTRON ACCEPTOR

Masashi Iino, Hongtao Liu, Nobuyuki Hosaka, Hideyuki Kurose, and Toshimasa Takanohashi
Institute for Chemical Reaction Science, Tohoku University
Katahira, Aoba-ku, Sendai 980-77, JAPAN

KEYWORDS: Coal extraction, additives, electron acceptor

INTRODUCTION

We have reported(1) that the extraction yield with carbon disulfide - *N*-methyl-2-pyrrolidinone (CS_2 -NMP) mixed solvent (1:1 by volume), which gave very high extraction yields for bituminous coals at room temperature(2), increases by the addition of a small amount of tetracyanoethylene(TCNE) to the solvent. The yield of the room temperature extraction of Upper Freeport coal with the 1:1 CS_2 -NMP mixed solvent increases from 59 wt%(daf) to 85 wt%(daf) by adding only 5%(based on coal) of TCNE to the mixed solvent. *p*-Phenylenediamine is also an effective additive for the mixed solvent extraction (3).

We have also found (4) that when the extracts obtained with the CS_2 -NMP mixed solvent were fractionated with pyridine to yield pyridine-insoluble (PI) and -soluble (PS) fractions, part of PI became insoluble in the mixed solvent. The addition of a small amount of TCNE, tetracyanoquinodimethane (TCNQ) or *p*-phenylenediamine to the mixed solvent, PI became soluble in the mixed solvent.

While, the aggregation state of coal molecules and its change with heating or contact with solvent and reagent play an important role in structure and reactivity of coal, but the details on them are still unknown. Coal extracts and coal-derived liquids are known to readily associate between themselves to form complex aggregates(5-7). The effect of TCNE on the extraction yields above mentioned can be explained by its breaking ability of noncovalent bonds through which the aggregates form(1). However, another explanation is possible, i. e., covalent bonds in coal such as ether bonds break after electron transfer from coal to TCNE, which is a strong electron acceptor. Solubility limit of coals, i. e., maximum extraction yield without the breaking of covalent bonds is one of the key points to clarify a kind of cross-linking bonds, i. e., covalent or non-covalent (physical)cross-links. If coal has developed covalent cross-links, its extractability is low, as observed in the extraction with conventional solvents such as pyridine which gave the yields less than 30-40wt% (daf) of coal. So, 85wt% of the extraction yield for CS_2 -NMP-TCNE solvent system suggests that Upper Freeport coal has little covalent cross-links, if no covalent bond breakings occur during this extraction.

In this study the effect of various electron acceptors on solubility of PI in the mixed solvent and also the effect of TCNE retained in PI on the solubility of PI were investigated. The mechanisms for the enhancement of the extraction yield of coal and solubility of PI by electron acceptors are discussed.

EXPERIMENTAL

Upper Freeport(Argonne Premium coal, 86.2 wt% C(daf)) and Zao Zhuang(Chinese coal, 87.8 wt% C(daf)) coals were extracted with the 1:1 CS_2 -NMP mixed solvent repeatedly at room temperature (2). The extract obtained was fractionated with acetone and pyridine, respectively, to give acetone-soluble(AS), pyridine-soluble and acetone-insoluble(PS), and pyridine-insoluble (PI) fractions, as shown Figure 1. Solubility of PI in the CS_2 -NMP mixed solvent was examined using 0.4g of PI and 50ml of the mixed solvent at room temperature under ultrasonic irradiation with or without an electron acceptor such as TCNE. The quantity of an electron acceptor added is 8×10^{-3} mol to 0.4g of PI. This quantity corresponds to 2.5wt% (10wg) of TCNE to 0.4g of PI.

RESULTS AND DISCUSSION

The Effect of Electron Acceptors on the Solubility of PI

Table I shows the solubility of PI in the mixed solvent when an electron acceptor was added, together with its electron affinity, which is a measure of the electron acceptability of electron acceptor. Table I shows that only TCNE and TCNQ gave high solubility as expected from their high electron affinities. However, other electron acceptors used here do not show the solubility enhancements. So, it is not clear whether charge-transfer (donor-acceptor) interactions is responsible for the solubility enhancement by the addition of TCNE and TCNQ, or not.

The Effect of TCNE Retained in PI on the Solubility of PI

Figure 2 shows the result of the repeated dissolution experiments of PI(PI-1 in Figure 2) from Zao Zhuang coal in the 1:1 CS₂-NMP mixed solvent with or without TCNE. A part(40.4%) of PI becomes insoluble in the mixed solvent, though PI is a part of the mixed solvent extract, but almost completely(97.6%) soluble in the mixed solvent containing TCNE, as already reported (4). Figure 1 shows that PS(PS-2) and AS(AS-2), in addition to PI(PI-2), were also obtained from PI-1 in the yield of 9.2% and 5.0%, respectively, probably due to the change of the aggregation state, as described later. PI-2 was well washed with pyridine to remove PS. It was reported that most of TCNE retained in PI could be removed by its washing with pyridine (1). In fact, from Figure 3, which shows that the FT-IR spectra of soluble and insoluble fractions of PI in the CS₂-NMP-TCNE solvent, PI-2, and PS-2, the peak at 2200cm⁻¹ due to TCNE (nitrile group) was almost disappeared in PI-2 (Figure 3-c), compared to soluble fraction (Figure 3-a) and PS-2 (Figure 3-d), indicating the removal of TCNE retained in PI-2 by washing with pyridine. PI-2 was then tried to redissolve in the CS₂-NMP mixed solvent and again a considerable part(31.6%) of PI-2 became insoluble, and 99.0% of PI-2 was dissolved in the mixed solvent containing TCNE, as shown in Figure 2. Fractionation of PI soluble in CS₂-NMP-TCNE solvent gave again 9.1% of PS+AS. A similar result was obtained for the PI from Upper Freeport coal, as shown in Figure 4.

If the solubility increase by TCNE addition is caused by the covalent bond breaking through the electron transfer from coal to TCNE, the insolubilization of PI in the mixed solvent after the removal of TCNE from the PI, just described above, should not be observed. So, the solubility increase of PI by TCNE is considered to be caused by the breaking of noncovalent bonds in the aggregates among coal molecules and the new associates with TCNE is more soluble than the original aggregates, as shown in Figure 5. In Figure 5, two kinds of noncovalent bonds, weak and strong, are assumed. The CS₂-NMP mixed solvent can break the weak bonds, but not the strong bonds, and the mixed solvent containing TCNE, which has strong interaction with coal molecules, can break even the strong bonds. The interaction between TCNE and coal molecules may be charge-transfer (donor-acceptor) and/or other interactions. The solvents such as pyridine and THF seem not to break easily even the weak noncovalent bonds, resulting in low extraction yields. The mechanism shown in Figure 5 can also explain the reason why the extraction yield increased by TCNE addition.

Figures 2 and 4 show that lighter fractions such as AS and PS formed from PI by the treatment with CS₂-NMP mixed solvent containing TCNE. This suggests that they are included in PI due to the formation of the aggregates which are not soluble in pyridine nor acetone and became soluble in those solvents by the change of the aggregation state. So, the fraction distribution obtained here is considered to be a reflection of not only solubility of coal molecules themselves, but aggregation state among coal molecules.

TCNE is very efficient for the extraction yield enhancement of Upper Freeport coal. The addition of TCNE more than 0.05g to 1g of the coal reached an almost constant extraction yield of about 85 wt% (daf). Using the structural parameters of *f*_a and degree of aromatic ring condensation for Upper Freeport coal reported by Solum et al.(8), 0.05g of TCNE per 1g of coal is calculated to correspond to 1 molecule of TCNE per about 8 aromatic clusters of the coal.

These results obtained strongly suggest that at least some bituminous coals, which gave high extraction yields with the CS₂-NMP-TCNE solvent, have chemical structure consisting of complex mixture of the aggregates among coal molecules, and having no giant covalently bound cross-linked network.

CONCLUSIONS

The effect of various electron acceptors on the solubility of pyridine-insoluble extract fraction (PI) in the CS₂-NMP mixed solvent was investigated. The other electron acceptors than TCNE and TCNQ do not show the solubility enhancement. So, it is not clear whether the solubility enhancement by TCNE and TCNQ is ascribed to their charge-transfer interactions with coal molecules or not. The results obtained for the effect of TCNE retained in PI on solubility of PI suggest that the solubility increase by the electron acceptors is caused by the breaking of noncovalent interaction in aggregates of coal molecules.

ACKNOWLEDGEMENT

This work was supported by "Research for the Future" project of Japan Society for the Promotion of Science (JSPS) through the 148 committee on coal utilization technology of JSPS.

REFERENCES

1. Liu, H., Ishizuka, T., Takanohashi, T., and Iino, M. *Energy Fuels*, 1993, 7, 1108-1111.
2. Iino, M., Takanohashi, T., Osuga, H., and Toda, K. *Fuel*, 1988, 67, 1639-1647.
3. Ishizuka, T., Takanohashi, T., Ito, O., and Iino, M. *Fuel*, 1993, 72, 579-580.
4. Sanokawa, Y., Takanohashi, T., and Iino, M. *Fuel*, 1988, 69, 1577-1578.
5. Sternberg, H. W., Raymond, R., Schweighardt, F. K., *Science*, 1975, 188, 49-51.
6. Sternberg, V. I., Baltisberger, R. J., Patel, K. M. et al. in *Coal Science*; Gorbarty, M. L., Larsen, J. W., Wender, I., Ed.; Academic Press: New York, 1983; pp125-171.
7. Nakamura, K., Takanohashi, T., Iino, M. et al. *Energy Fuels*, 1995, 9, 1003-1010.
8. Solum, M. S., Pugmire, R. J., Grant, D. M. *Energy Fuels*, 1989, 3, 187-192.

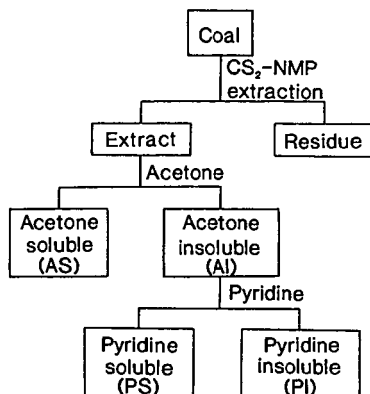


Figure 1 Extraction and fractionation procedures

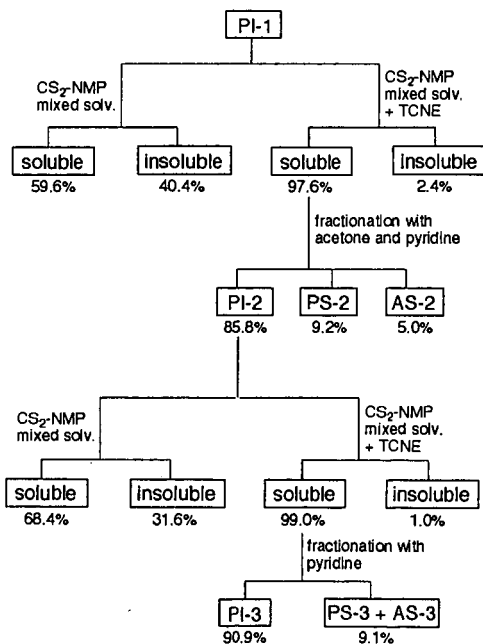


Figure 2 Repeated solubility experiments for PI from Zao Zhuang coal in the CS_2 -NMP mixed solvent with or without TCNE (2.5 wt% based on PI).

Table1 The effect of the addition of electron acceptors on the solubility^{a)} of PI from Zao Zhuang coal in the CS₂-NMP mixed solvent at room temperature

Electron acceptor	Solubility of PI (wt%)	Electron affinity ^{b)} (eV)
None	51.0	—
Tetracyanoethylene(TCNE)	99.5	2.2
7,7,8,8-Tetracyanoquinodimethane(TCNQ)	81.0	1.7
2,3-Dichloro-5,6-dicyano- <i>p</i> -benzoquinone(DDQ)	53.8	1.95
1,2,4,5-Tetracyanobenzene	47.7	0.4
<i>p</i> -Benzoquinone	44.1	0.77
2,6-Dichloro- <i>p</i> -benzoquinone	37.0	1.2
<i>p</i> -Chloranil	34.8	1.37

a) Wt% of PI soluble in the mixed solvent when 8×10^{-5} mol of an electron acceptor was added to 0.4g of PI in 50ml of the mixed solvent.

b) Electron affinity of the electron acceptor.

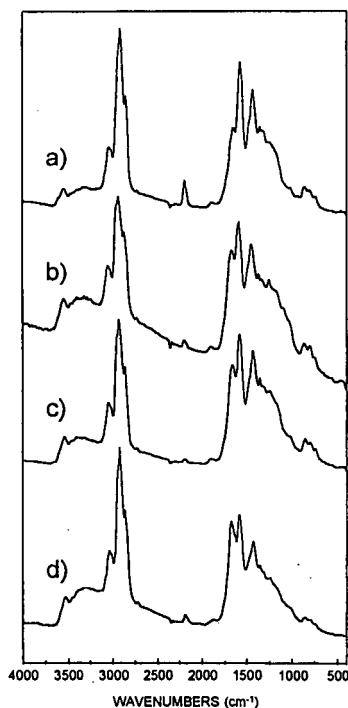
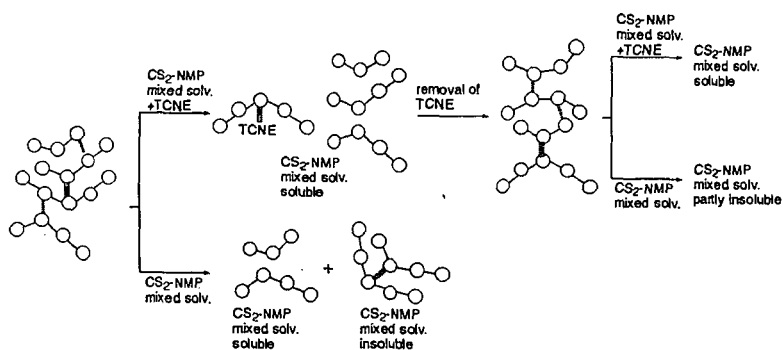
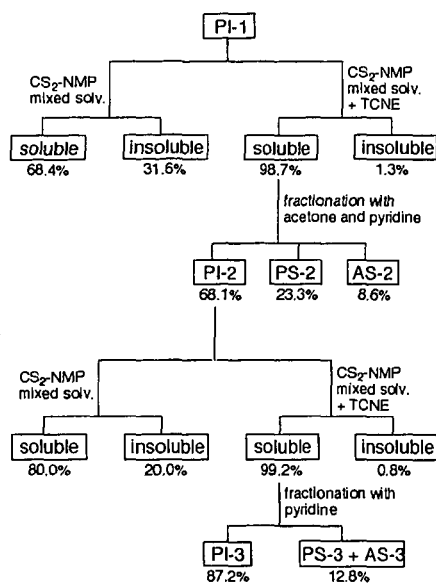


Figure 3 FT-IR spectra of soluble(a) and insoluble(b) fractions of PI-1 in the CS₂-NMP-TCNE solvent, PI-2(c) and PS-2(d).



SMALL ANGLE NEUTRON SCATTERING STUDIES OF COAL-EXTRACT SOLUTIONS

P. Thyagarajan Intense Pulsed Neutron Source, Argonne National Laboratory Argonne, IL 60439 George D. Cody, Geophysical Laboratory Carnegie Institution of Washington 5251 Broad Branch Rd. Washington, DC 20015

key words SANS, Coal Extracts, Fractals

INTRODUCTION

Interest in the physics and chemistry of coal extracts has extended for over 100 years. Early on it was recognized that pyridine was a particularly good solvent capable of extracting a significant weight percent of intermediate rank coals. Many of the current theories regarding the macromolecular structure of coals (type III kerogens) are based on the fact that there exists a physically definable limit in the extractability of soluble organics from coal in pyridine¹. The non-extractable residue is generally considered to be a cross-linked macromolecular network². The extract-solvent "solutions", although acknowledged to be far from ideal (thermodynamically), are presumed to be "molecular solutions" in the sense that random mixing of the constituents occurs within a single solution phase³.

Recently, a number of investigations have challenged this established model of coal structure. In particular, studies by Iino and colleagues⁴, using mixed solvent systems (most notably, a *n*-methyl-2-pyrrolidinone (NMP) mixture with CS₂), have demonstrated increases in extractabilities of more than twice that by pyridine in the case of some coals⁴. These results suggest that either there exists a set of non-covalent interactions unperturbed by pyridine but disrupted by the mixed solvents or that the mixed solvents are degrading the network and enhancing the extraction yields through some, as yet unknown, chemical reaction.

In the present work we set out to characterize the solution structures of coal extracts to gain insight on the nature of coal-solvent interactions. The characterization of solution structures of dilute mixtures of macromolecules in various solvents is readily attainable using small angle neutron scattering⁵⁻¹⁷. The theory of small angle scattering is well established and the method has been used by many researchers for the purpose of elucidating the configurational state of polymers in solution⁶, the structure of asphaltenes in apolar solvents⁷⁻¹², the study of proteins¹³, as well as dilute coal extract "solutions"^{5,14,15}.

Neutron scattering is particularly useful in revealing the spatial characteristics of structures composed of low atomic number (Z) elements. This is due to the fact that neutrons, uncharged and with spin (I) = 1/2, interact with a given element through their respective angular momenta. The magnitude of this interaction has no correlation with Z. X-rays, on the other hand, interact with the electronic shell surrounding the nuclei and the magnitude of the coherent scattering amplitude varies as a strong function of Z. Although lighter elements are nearly "invisible" to X-rays, the unique nature of the interaction of the neutron with spin (I) > 0 nuclei results in the coherent scattering cross-section of low Z elements being similar in magnitude to that of many of the higher Z elements¹⁶; e.g. deuterons scatter neutrons as efficiently as gold.

In the following the results of small angle neutron scattering (SANS) experiments are described in reference to assessing the solution structure of solvent extract "solutions" from a number of coals. The goal of this study is to identify features or characteristics of the mixtures which may highlight the mechanism behind the exceptional solvating capabilities of the mixed solvents as compared with other polar solvents such as pyridine. For the present study we chose a lignite (APCS No. 8), a sub bituminous C rank coal (APCS No. 2), a High volatile bituminous coal (APCS No. 3), and a medium volatile bituminous coal (APCS No. 1) (see Table I).

In addition to characterizing the solution structure of the neat extracts, O-methylated extracts were also studied. The purpose of O-methylation was to neutralize the predominant interaction between coal and pyridine. The medium volatile coal was not O-methylated.

Experimental Section

Solvent Extraction: In the case of pyridine extraction, approximately 5 grams of 100 mesh coal was extracted with pyridine in a Soxhlet extraction apparatus for periods exceeding 24 hours. The extract was separated from the solvent using roto-evaporation. The extractability of the Upper Freeport (UF) coal in the mixed solvent (NMP/CS₂) is over twice that in pyridine as is presented in Table I. Extraction of the Upper Freeport coal (APCS No. 1) with NMP/CS₂ follows the procedure of Iino et al.⁴ with minor

modifications. Approximately 5 grams of 100 mesh APCS No. 1. was stirred in 150 ml of a 1:1 mixture (by volume) of *n*-methyl-2-pyrrolidinone (NMP) and carbon disulfide (CS₂) (mixed solvent, MS) for approximately 6 hours. The solvent extract was decanted and then centrifuged up to 14 K rpm to sediment out any entrained solids.

Throughout the paper below, the various soluble fractions from different coals are designated as presented in Table II.

Small Angle Neutron Scattering: Solutions of the extracts (5 wt. %) were prepared by mixing dry extract with either of the per-deuterated solvents. This concentration was selected to yield sufficient scattering intensity without introducing scattering intensity due to interparticle interactions. Previous work on the SANS behavior of coal extract solutions in pyridine exhibited no dependence on scattering behavior with solvent concentration (at 1, 5, and 10 wt. %) other than a linear increase in incoherent and coherent scattering intensity with increasing wt. % of extract.⁵

Solutions were contained in Suprasil cylindrical cells with a 2 mm path length (volume = 0.7 ml) for the SANS analysis. SANS data were measured at the Intense Pulsed Neutron Source of Argonne National Laboratory, using the Small Angle Diffractometer (SAD). This instrument uses pulsed neutrons derived from spallation with wavelengths in the range of 1-14 Å and a fixed sample-to-detector distance of 1.54 meters. The scattered neutrons are measured using a 64 x 64 array of position sensitive, gas filled, 20 x 20 cm², proportional counters with the wavelengths measured by time-of-flight by binning the pulse to 67 constant $\Delta t/t = 0.05$ time channels. The size range in a SANS experiment is constrained by both the geometry of the instrument and the wavelength of the neutrons which determine the working range of momentum transfer Q .

$$Q = 4\pi\lambda^{-1} \sin \theta \quad (1)$$

where θ is half the Bragg scattering angle and λ is the wavelength of the neutrons. Given the characteristics of the SAD¹⁷ at the Intense Pulsed Neutron Source (IPNS), useful SANS data in the Q range of 0.006-0.25 Å⁻¹ can be obtained in a single measurement. The reduced data for each sample is corrected for the backgrounds from the instrument, the Suprasil cell, and the solvent as well as for detector nonlinearity. Data are presented on an absolute scale by using the known scattering cross-section of a silica gel sample. The absolute cross-section for this sample has been measured at the SANS instrument at ORNL. Standard Guinier analysis in the region of $QR_g < 1.0$ can be used to extract the radius of gyration, R_g and $I(0)$ values by using the equation below.

$$I(Q) = I(0)\exp(-Q^2 R_g^2 / 3) \quad (2)$$

R_g is the root-mean-squared distance of all of the atoms from the centroid of neutron scattering length density of the particle and $I(0)$ is the absolute scattering cross-section at $Q=0$ which is defined as follows.

$$I(0) = N_p (\rho - \rho_s)^2 V^2 \quad (3)$$

Here N_p corresponds to the number density of particles, V is the volume of the particle, and ρ and ρ_s are the scattering length densities of the particle and the solvent, respectively. The absolute scattering data of the silica gel standard give $R_g = 44.7 \pm 0.2$ Å and $I(0) = 70$ cm⁻¹. The magnitudes of R_g and $I(0)$ for this sample are routinely measured in the same Q region and are used to determine scale factors to place the scattering data on an absolute scale in units of cm⁻¹.

RESULTS

SANS of Soluble Fractions in Organic Solvents:

The SANS data, on an absolute scale, for each coal extract in pyridine-d₅ is presented in Figures 1-4, where the intensity of the scattered neutrons $I(Q)$ is plotted against the magnitude of the momentum transfer (Q); note that all of the plots are log-log. The SANS data for UF-PyS/dPy, UF-MS/dPy and UF-MS/dM solutions on an absolute scale are presented in figure 5.

The scattering behavior of the lowest rank coal (APCS No. 8) (Figure 1) exhibits power law scattering behavior in the low Q region; the power law exponent is 2.13 for the

untreated extract and 2.29 for the O-methylated. Similar behavior is observed for the sub bituminous extract (APCS No. 2) (Figure 2), with exponents of 1.79 and 2.46, for the untreated and O-methylated extracts, respectively. The high volatile C rank coal exhibits scattering behavior that is "bounded" at low Q for the untreated extract, but exhibits power law scattering at low Q in the O-methylated case ($d = 1.7$) (figure 3). The medium volatile bituminous coal (APCS No. 1) exhibits scattering behavior that is remarkably similar to that of the (APCS No. 3) (Figure 4). The scattering behavior of the medium volatile coal (APCS No. 1) in the mixed solvent (Figure 5) exhibits only incoherent scattering, i.e. there are no large structures in this particular system.

Discussion

In a number of liquid-phase systems there exist random solution structures that exhibit scattering behavior resulting from self similar or fractal topology. An elegant theory, formulated by Freltoft et al.¹⁴, accounts for power law scattering behavior, with $d < 3.0$, to systems with mass fractal characteristics. Such solution structures are aggregates with structure factors governed by interparticle correlations which decay exponentially from the center of the aggregate. Thus, changes in d , as seen in figures 1-3 reveal changes in the density of the mass fractal aggregates.

In the case of APCS No.s 3 and 1, in pyridine, aggregates also exist, however, they do not exhibit mass fractal characteristics, rather they are readily described using the Guinier approximation. Incidentally, The remarkable similarity between the SANS behavior of the two extracts exhibited in Figure 4 strongly suggests that, in both the IL-PyS/dPy and UF-PyS/dPy samples, the molecular aggregates are nearly identical in their chemical composition, size, shape, and number density.

In complete contrast to the aforementioned results, the solution of mixed solvent solubles in NMP/CS₂ (UF-MS/dM) exhibits virtually no coherent scattering intensity across the accessible Q range of the SAD. SANS analysis of the UF-MS/dM solution, therefore, reveals a well dispersed "molecular" solution of small particles. The fact that aggregation does not occur in UF-MS in NMP/CS₂ indicates that the mixed solvent solvates the extractable molecules much more effectively than pyridine, a result which is clearly consistent with the observation of overall enhanced extractability.

The presence of aggregated structures in solutions of coal extracts with pyridine is contradictory to the hypothesis that pyridine is an exceptionally good solvent for coal in a thermodynamic sense. Although, pyridine clearly exhibits a strong interaction with acidic functional groups in coal, in the case of coal extracts, pyridine does not appear to have exceptional solvating capabilities. The clustering or aggregation, clearly evident in all of the pyridine solutions suggests that coal-pyridine interactions may not be sufficient to solvate all non-covalently bound material in coal. This implies that the limits in extractability may be the result of limits in pyridines solvating capability, rather than limits dictated by a covalently cross-linked, "infinite", macromolecular network.

Acknowledgments

The neutron scattering experiments were performed at the Intense Pulsed Neutron Source at Argonne National Laboratory. The authors gratefully acknowledge the help of Denis Wozniak of IPNS, Argonne National Laboratory. Insightful discussions related to the mixed solvent/Upper Freeport system with Profs. Masashi Iino and Toshimasa Takanohashi of the Institute of Chemical Reaction Science, Tohoku University, Sendai Japan, are greatly appreciated. This work was performed under the auspices of the Office of Basic Energy Sciences, Division of Chemical Sciences, U. S. Department of Energy, under contract No. W-31-1090ENG-38. The Intense Pulse Neutron Source is a Department of Energy supported facility.

References

- (1) van Krevelan, *Coal*, Third Edition, Elsevier, Amsterdam, 1993, 979.
- (2) Larsen, J. W.; Green, T. K.; Kovac, J., *J. Org. Chem.*, 1985, **50**, 4729
- (3) Painter, P. C.; Park, Y.; Coleman, M. M., *Energy & Fuels*, 1988, **2**, 693-702
- (4) Iino, M.; Takanohashi, T.; Ohsuga, H.; Toda, K., *Fuel*, 1988, **67**, 1639-1647
- (5) Cody, G. D.; Thiagarajan, P.; Botto, R. E.; Hunt, J. E.; Winans, R. E., *Energy & Fuels*, 1994, **8**, 1370-1378
- (6) Bates, F. S., *J. Appl. Cryst.*, 1988, **21**, 681.
- (7) Herzog, P.; Tchoubar, D.; Espinat, D., *Fuel*, 1988, **67**, 245
- (8) Ravey, J. C.; Ducret, C.; Espinat, D., *Fuel*, 1988, **67**, 1560.
- (9) Overfield, R. E.; Sheu, E. Y.; Sinha, S. K.; Liang, K. S. *Fuel Sci. Technol. Int.*, 1989, **7**, 611.
- (10) Senglet, N.; Williams, C.; Faure, D.; Des Courieres, T.; Guillard, R. *Fuel*, 1990, **69**, 72
- (11) Storm, D. A.; Sheu, E. Y.; DeTar, M. M. *Fuel*, 1993, **72**, 977.
- (12) Thiagarajan, P. Hunt, J. E., Winans, R. E., Anderson, K. B.; Miller, J. T. *Energy & Fuels*, 1995, **9**, 829.

- 13) Stuhmann, H. B.; Miller, A. *J. Appl. Cryst.*, 1978, **11**, 325.
 (14) Ho, B.; Briggs, D. E. *Colloids Surf.*, 1982, **4**, 285.
 (15) Triolo, R.; Child, H. R. *Fuel*, 1984, **63**, 274.
 (16) Bacon, G. E. in *Neutron Diffraction*, Clarendon Press, Oxford, 1975, pp.38-40
 (17) Thiyagarajan, P.; Epperson, J. E.; Crawford, R. K.; Carpenter, J. M.; Hjelm, R. P. In *Proceedings of International Seminar on Structural Investigations on Pulsed Neutron Sources*; Dubna, 1993; pp 194.
 (18) Freltoft, T.; Kjems, J. K.; Sinha, S. K., *Phys. Rev. B*, 1986, **33**, 269

Table I

Sample	Rank	Samples and Their Physical Characteristics				
		%C*	%H	%O	%S	%E(NMP/CS ₂)** %E(Pyr)***
APCS No. 8	Lignite	73	4.8	20	0.8	NA 15.0
APCS No. 2	Sub.bit	75	5.4	18	0.6	NA 29.0
APCS No. 3	HvC	78	5.0	14	4.8	NA 29.0
APCS No. 1	mv	86	4.7	8	2.3	56.0 25.5

*Dry ash free basis

**percent extractable (wt.) in NMP/CS₂

***percent extractable (wt.) in pyridine

Table II

Sample Designations

Sample: Lignite (Lig) Sub.bit (Sub) HvC Bit (HV) Med. Vol.(MV)

Solvent

Pyridine Lig-PyS/dPy* Sub-Pys/dPY HV-PyS/dPy MV-PyS/dPy

NMP/CS₂

MV-PyS/dM**

* where PyS - pyridine solubles, dPY-deuteropyridine

** where dM - perdeutero-n-methyl-pyrrolidinone and carbon disulfide

Figure Captions.

Figure 1: Absolute differential SANS cross-section of APCS No. 8 pyridine extract 5 % (wt.) in pyridine D₅, Untreated (filled) and O-methylated (unfilled).

Figure 2: Absolute differential SANS cross-section of APCS No. 2 pyridine extract 5 % (wt.) in pyridine D₅, Untreated (filled) and O-methylated (unfilled).

Figure 3: Absolute differential SANS cross-section of APCS No. 3 pyridine extract 5 % (wt.) in pyridine D₅, Untreated (filled) and O-methylated (unfilled).

Figure 4: Absolute differential SANS cross-section of APCS No.1 pyridine extract 5 % (wt.) dispersed in pyridine-D₅ (filled o) and APCS #.3 pyridine extract 5 % (wt.) dispersed in pyridine-D₅ (o).

Figure 5: Absolute differential SANS cross-section of APCS No.1 pyridine extract 5 % (wt.) dispersed in pyridine-D₅ (Square), APCS No. 1 pyridine extract 5 % (wt.) in NMP/CS₂ (filled o) APCS No. 1 NMP/CS₂ extract 5 % (wt.) in NMP-D₉/CS₂ ((o).

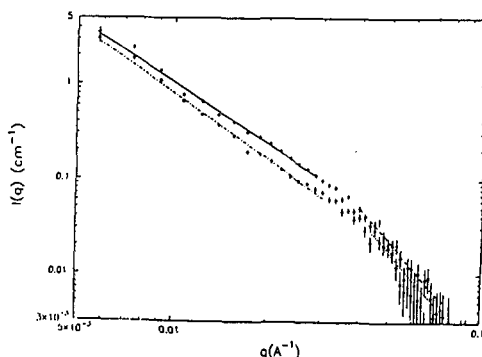


Figure 1

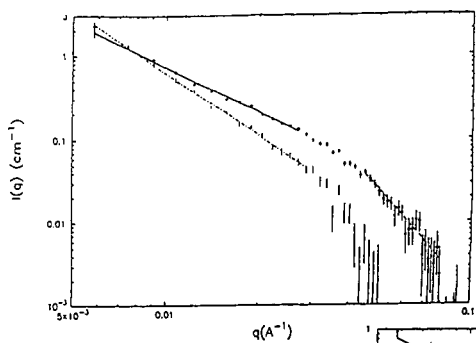


Figure 2

Figure 3

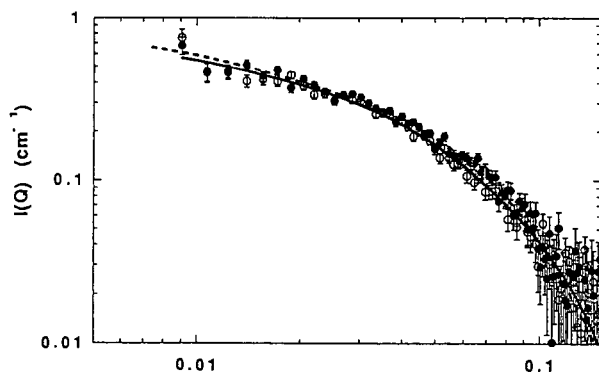
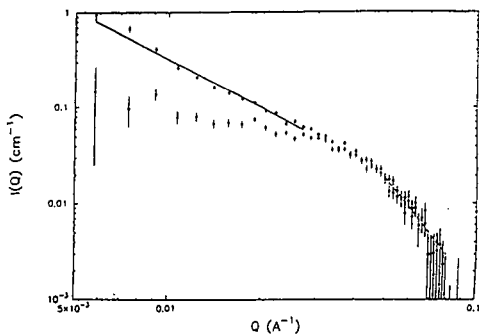
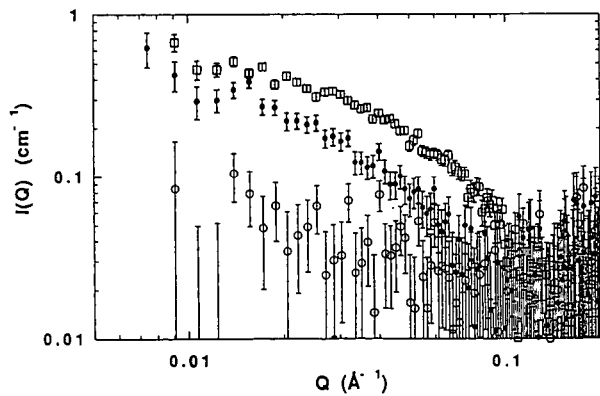


Figure 4

Figure 5



**EFFECTS OF LITHIUM IODIDE DOPING ON
THE ASSOCIATED MOLECULAR STRUCTURE OF BROWN COAL.**

H.Kumagai, J.-i.Muraoka, J.-i.Hayashi, T.Chiba,
Center for Advanced Research of Energy Technology, Hokkaido
University,
Kita-ku, Sapporo 060, Japan,

D.S.Webster, R.Sakurovs, D.Phan,
CSIRO, Division of Coal and Energy Technology,
North Ryde, NSW 2113, Australia

Keywords: Associated molecular structure, Hydrogen bonding, Low rank coal

ABSTRACT

Effects of lithium iodide (LiI) doping on the associated molecular structure of brown coal have been investigated. Devolatilization of the coal is enhanced with LiI doping at lower temperature range ($<300^{\circ}\text{C}$). The devolatilization enhanced with LiI doping proceeds without thermal decomposition and cleavage of cross-linkage structure. High temperature ^1H -NMR results indicate that the LiI doping increases the fractions of mobile structure, and also enhances the mobility of molecules. During heat treatment, LiI maintains the enhanced molecular mobility resulting in an increase in the evolution of volatile matter.

INTRODUCTION

Coal is complex macromolecular compounds containing several types of noncovalent interactions, such as hydrogen bonding, van der Waals, aromatic π - π and charge transfer interaction. Chemical and physical properties of coal are strongly affected with associated structure as well as chemical structure of coal molecules. The associated structure of coal molecules is governed the type and strength of noncovalent interactions exist in coal. Low rank coals, such as lignite and brown coal, have a high oxygen content, and a considerable proportion of the oxygen is present in the form of carboxyl and phenolic functional groups. These oxygen containing groups are forming hydrogen bonds with each other resulting in the associated structure of molecules. Thus, it can be considered that inter- and intra-molecular hydrogen bonding interactions are responsible for the properties of low rank coal.

The role of hydrogen bonding in the properties of coal has already been recognized. Painter and co-workers [1] have discussed the band assignment of hydroxyl groups forming hydrogen bonding interaction in coal. They also discussed the significance of hydrogen bonding on the structure of coal. The classical solvent induced swelling techniques of polymer chemistry have been applied to investigate the associated structure of coal molecules [2-6]. Larsen et al. [4] estimated that bituminous coal contain about 5 times as many hydrogen bond cross-link as covalent cross-link. Brenner [3] pointed out the effects of hydrogen bonding interaction on the glass transition temperature and glassy properties of coal. The importance of the hydrogen bonding interaction in the formation and stabilization of coal macromolecular structure has also demonstrated by computer aided molecular design technique [7,8].

Cross-linking reactions at hydroxyl sites during heat treatment have been postulated to suppress the fluidity and volatile matter formation of coals [9-14]. Van Krevelen and co-worker [9] provided direct evidence on the role of hydroxyl groups in suppressing fluidity by model compound study. The mechanism of the suppression by the presence of hydroxyl groups has been modeled as involving cross-linking reactions at hydroxyl sites. The solvent induced swelling techniques have been employed also to determine cross-link density changes during heat treatment. The results obtained from the swelling techniques have demonstrated that cross-linking in low rank coals occurs prior to tar evolution, and the temperature is lower than that for bituminous coals [10-12]. Comparison of char solvent swelling behaviour and gas evolution has indicated that the low temperature cross-linking occurs simultaneously with CO_2 and H_2O evolution [13]. The cross-linking at lower temperature was also inferred with the Proton Magnetic Resonance Thermal Analysis (PMRTA) [15,16]. The mobile phase of low rank coal determined from NMR

relaxation time decreased at a substantially lower temperature, below that for tar evolution.

In this paper, to clarify the effects of hydrogen bonding interaction on the associated molecular structure of Loy Yang brown coal, the devolatilization of the coal subjected to modification of hydrogen bonding interaction with lithium iodide doping have been investigated by means of a thermogravimetric analysis (TGA), a high temperature electron paramagnetic resonance spectroscopy (HT-EPR) and PMRTA.

EXPERIMENTAL SECTION

Coal Sample and Reagents.

The coal sample used for the present study is Loy Yang brown coal (LY, C;70.6wt%, H;5.0wt%, N;0.8wt%, O+S;23.6wt% diff.). The sample coal was ground to pass through 100 Tyler mesh and dried under a vacuum at 40°C for 24 hours. Methanol (G.R. grade) as a solvent and lithium iodide (G.R. grade) were used without further purification.

Preparation of LiI Doped Coal.

A known amount of lithium iodide (LiI), i.e., 4.17×10^{-3} mol/g-coal, dissolved in methanol was added to dried coal particles. The coal suspension was placed in an ultrasonic bath for 10 minutes and stirred for 2 hours at room temperature. After standing the suspension over night, the solvent was evaporated off. The LiI doped sample thus obtained, was dried under a vacuum at 40°C for 24 hours and then cooled down in a flow of nitrogen.

TGA.

Typically, 10mg of sample in platinum TG cell was placed in a thermogravimetric equipment (ULVAC TGD 5000). The sample was heated at 105°C under a flow of nitrogen for 2 hours to remove moisture. TG curves of the sample were measured at a heating rate of 5°C/min up to 500°C in a flow of nitrogen. For kinetic studies, the sample removed moisture at 105°C was heated at a rate of 200-400°C/min to a prescribed temperature of 200-400°C and kept at final temperature for 30 minutes.

HT-EPR.

The sample in a HT-EPR quartz tube of 6mm o.d. was inserted directly into a cavity where the sample was heated at 105°C in a flow of nitrogen to remove moisture. The variation in EPR spectra was monitored with a Varian E-109 EPR spectrometer equipped with a cylindrical high temperature cavity (Micro-device Co.Ltd.) in a flow of nitrogen at a heating rate of 5°C/min. The details of the HT-EPR operation have been reported previously [17].

PMRTA.

For a PMRTA experiment, 500mg of sample was contained in a 10mm o.d. glass tube and dried at 105°C in a flow of nitrogen prior to analysis with PMRTA. The solid-echo pulse sequence (90°x-t-90°y) was used to generate ¹H-NMR transverse magnetization signal. The solid-echo signal, I(t), was recorded at regular intervals (1-2 minute) while the sample was heated from room temperature to 500°C at a rate of 4°C/min in a flow of nitrogen. The details of PMRTA operation have also been reported previously [17].

RESULTS AND DISCUSSION

TGA Studies

The effects of LiI doping on the devolatilization properties of Loy Yang brown coal (LY) were investigated with TGA. TGA curves for LY and LiI doped LY (LILY) are shown in Figure 1 where the weight loss of coal sample is expressed on an ash and LiI free basis. The weight loss of LY starts at about 200°C, and increases gradually with increasing temperature. LILY always shows higher weight loss than that for LY over the range of measurement temperatures. The weight loss of LY increases from 25wt% to 44wt% at 400°C with LiI doping.

In Figure 2, the variation in the differential weight loss curves, i.e., the rates of volatile matter evolution, for LY and LILY are plotted as a function of temperature. The rate of evolution for LY monotonously increases, and reaches a maximum value at 400°C. In contrast, the rate for LILY increases immediately at the initial stage of heating. These results indicate that LiI doped in LY enhances the evolution of volatile matter at lower temperatures. It should be noted that the temperature at which the maximum rate of

volatile matter evolution is obtained shifts down from 400°C to 250°C with LiI doping and the temperature for LILY seems to be much lower than that of thermal decomposition and cleavage of cross-linkage structure in the coal.

For kinetic analysis of the devolatilization, a systematic series of experiments were carried out on change of the yields of devolatilization products (weight loss), Y , with time, t , at different temperature. Considering the appreciable and rapid decrease in the weight of coal, the reactions in early stage appear to proceed mainly with evolution of volatile matter. Figure 3 shows a typical result of analysis where $\ln(1-Y)$ are plotted against t assuming a first-order irreversible reaction. In the figure, straight line can be seen within the first 1 minutes, implying that evolution of volatile matter in the early stage can be described by a first-order irreversible reaction.

The first-order reaction rate constant, k , for evolution of volatile matter was obtained analyzing data of Y at different time and temperature for LY and LILY. The Arrhenius plots of these reaction rate constants are shown in Figure 4. It is seen that k 's for LILY is higher than k for LY within the present range of reaction temperature, reflecting the promotion of volatile matter evolution by LiI doping. The activation energy, E , for LILY (34.3kJ/mole) is found to be appreciably smaller than that for LY (50.3kJ/mole). This less temperature-sensitive devolatilization may be attributed to the modification of associated molecular structure of the coal with LiI doping

HT-EPR Studies

The spin concentrations for LY and LILY were monitored by using HT-EPR. With HT-EPR technique, relatively stable radicals are detected, such as stable π and/or s radicals with relatively long life. As shown in Figure 5, the spin concentration for LY starts to increase at about 170°C and increases drastically beyond 380°C. The drastic increase in the spin concentration observed beyond 380°C in LY may be attributed to the increase in stable π and/or s radicals produced with thermal decomposition and cleavage of cross-linkage structure during heat treatment [18]. For LILY, however, the spin concentration remains almost constant at temperature below 350°C, where marked increase in weight loss is seen. A drastic increase in the spin concentration similar to that for LY is seen beyond 380°C. This result suggests that the reaction mechanism for weight loss for LILY at lower temperature is somewhat different from that for LY and evolution of volatile matter at lower temperature proceeds without thermal decomposition and cleavage of cross-linkage structure. Since the temperature at which LILY gives the maximum evolution rate is much lower than usual pyrolysis temperature, the enhancement of devolatilization at lower temperature, therefore, might be resulted from the evolution of volatile matter which linked physically and/or noncovalently to the coal.

PMRTA Studies

Residual Hydrogen

The PMRTA technique was employed to elucidate the effects of LiI doping on the thermal transformation behaviour of LY. The initial amplitude of solid-echo signal, $I(0)$, is closely proportional to the hydrogen content in the specimen. Therefore, the variation in $I(0)$ plotted in Figure 6 is akin to that of weight loss (TG curves) in Fig. 1. For LY, $I(0)$ decreases rapidly as heating above 350°C relative to the decrease in weight loss. This fact means that disproportionation of hydrogen in the specimen occurs at this temperature range. From the HT-EPR study, the disproportionation is considered due to the evolution of hydrogen rich compounds, such as methane and water, produced by the thermal decomposition and cleavage of cross-linkage structures. The variation in $I(0)$ for LILY is nearly in accordance with that in the weight loss at temperatures below 350°C (Fig.1), where a significant increase in volatile matter was observed. Thus, it appears that the composite of volatile matter evolved at lower temperature (<350°C) is analogous to that of parent coal (LY). The disproportionation is seen to occur slightly above 350°C.

Mobile Remaining Hydrogen

The separation of the solid-echo signals permits hydrogen-weighted mobile and rigid fractions of the molecular structure in coal [17]. The fractions of remaining hydrogen in mobile structures, H_m , on the

basis of the initial amplitude of signal are plotted in Figure 7 against temperature. H_a for LILY is high even at the initial stage of heating, increases with temperature, and then reaches a maximum value at about 150°C. On further heating, H_a maintains the high value up to 400°C where evolution of volatile matter occurs. The result indicates that the LiI doping increases the fraction of mobile structures in LY and keeps it at the higher level up to 400°C. H_a for LY shows a maximum value at about 320°C, and then decreases rapidly on further heating. For LY, the drastic increase in the spin concentration (>380°C) and the rapid decrease in $I(0)$ (>350°C) were observed at a higher temperature range. The rapid decrease in H_a , therefore, could be attributed not only to the evolution of volatile matter, but also to the condensation and recombination reactions, which follow the thermal decomposition and cleavage of cross-linkage structures in coal.

CONCLUSIONS

1. Devolatilization of LY is enhanced with LiI doping at lower temperature range (<300°C).
2. The activation energies for the devolatilization decrease with LiI doping. This less-temperature sensitive devolatilization may be attributed to the modification of associated molecular structure of the coal with LiI doping.
3. The devolatilization enhanced with LiI doping proceeds without thermal decomposition and cleavage of cross-linkage structure.
4. The doping LiI increases the fractions of mobile structure, and also enhances the mobility of LY molecule.
5. During heat treatment, LiI maintains the enhanced molecular mobility resulting in an increase in the evolution of volatile matter.

ACKNOWLEDGMENT

H.K. gratefully acknowledge the financial support of Ministry of Education, Science and Culture, Japan (Japan-Australia Joint Research Program, No. 06044017, Coordinator: Prof. Y. Nishiyama of Tohoku University).

REFERENCE

- (1) Painter, P.C.; Sobkowiak, M.; Youtcheff, J. *Fuel* 1987, 66, 973
- (2) Brenner, D. *Fuel* 1984, 63, 1324
- (3) Brenner, D. *Fuel* 1985, 64, 167
- (4) Larsen, J.W.; Green, T.K.; Kovac, J. *J. Org. Chem.* 1985, 50, 4729-4735
- (5) Cody, G.D.; Larsen, J.W.; Siskin, M. *Energy Fuels* 1988, 2, 340
- (6) Aida, T.; Fuku, K.; Fujii, M.; Yoshihara, M.; Maeshima, T.; Squires, T. *Energy Fuels* 1991, 5, 79-83
- (7) Carlson, G.A. *Energy Fuels* 1992, 6, 771
- (8) Kumagai, H.; Nakamura, K.; Sasaki, M.; Yoneda, J.; Sanada, Y. *Proc. Int. Conf. Coal Sci.* 1993, Vol. 1, 136
- (9) Wolfs, P.M.J.; van Krevelen, D.W.; Waterman, H.I. *Fuel* 1960, 39, 25
- (10) Suuberg, E.M.; Lee, D.; Larsen, J.W. *Fuel* 1985, 64, 1668
- (11) Suuberg, E.M.; Unger, P.E. Larsen, J.W. *Energy Fuels* 1987, 1, 305
- (12) Solomon, P.R.; Hamblen, D.G.; Carangelo, R.M.; Serio, M.A.; Deshpande, G.V. *Energy Fuels* 1988, 2, 405
- (13) Solomon, P.R.; Serio, M.A.; Deshpande, G.V. Kropo, E. *Energy Fuels* 1990, 4, 42
- (14) Ibarra, J.V.; Moliner, R.; Gavilab, M.P. *Fuel* 1991, 70, 408
- (15) Sakurovs, R.; Lynch, L.J.; Maher, P.; Banerjee, R.N. *Energy Fuels* 1987, 1, 167
- (16) Lynch, L.J.; Webster, D.S.; Sakurovs, R.; Barton, W.A.; Maher, P. *Fuel* 1988, 67, 579
- (17) Sanada, Y.; Lynch, L.J. In *Magnetic Resonance of Carbonaceous Solids*; Botto, R.E.; Sanada, Y., Eds.; ACS Symposium Series 229; American Chemical Society: Washington, DC, 1993; 139
- (18) Petrakis, L.; Grandy, D. In *Free radicals in Coals and Synthetic Fuels*; Coal Science and Technology Series No. 5; Elsevier: Amsterdam, Netherlands, 1983; 71

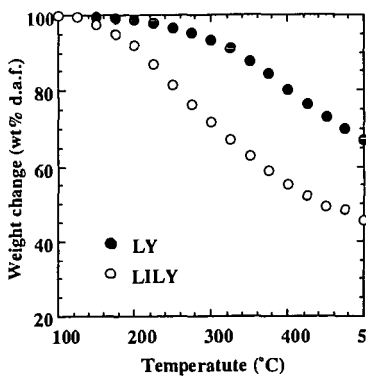


Figure 1. Effects of LiI doping on the devolatilization properties of LY

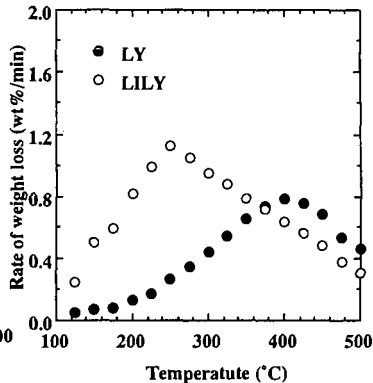


Figure 2. Differential weight loss curves for LY and LILY

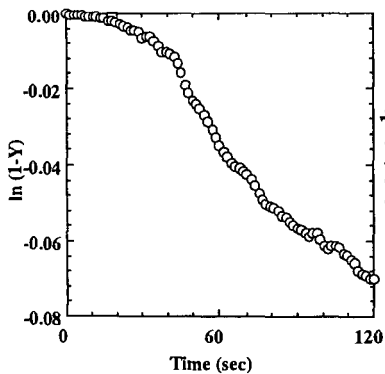


Figure 3. Variation of $\ln(1-Y)$ against reaction time for LILY at 250°C

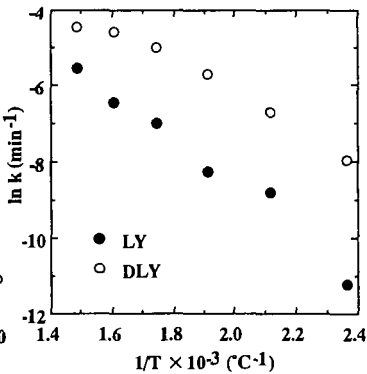


Figure 4. Arrhenius plots of weight loss rate constants for LY and LILY

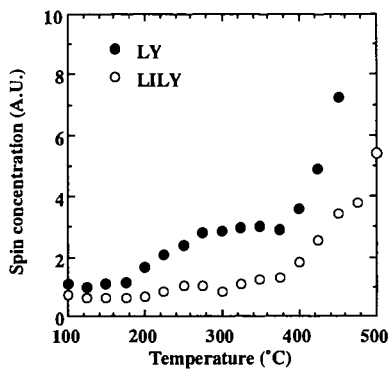


Figure 5. Variation in spin concentration for LY and LILY

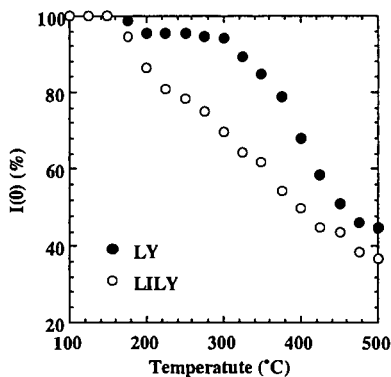


Figure 6. Residual hydrogen, $I(0)$, pyrograms derived from PMRTA data for LY and LILY

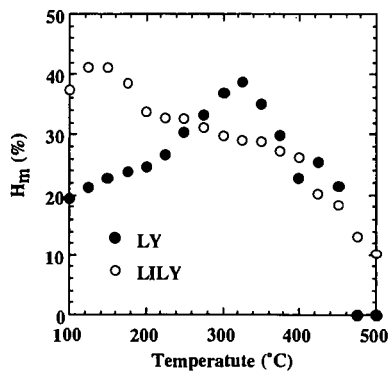


Figure 7. Mobile remaining hydrogen, H_m , pyrograms derived from PMRTA data for LY and LILY

COAL: CROSS-LINKED NETWORKS OR ASSOCIATED STRUCTURES?

Paul Painter, Maria Sobkowiak and Mike Coleman

Polymer Science and Engineering Program
Penn State University
University Park, PA 16802

Introduction

For many years the "standard model" for coal structure has essentially considered most coals to consist of covalently cross-linked networks with a cross-link density and "sol" fraction that varies systematically with rank (this model excludes anthracites and high rank coals that are more graphitic in their structure). Recently, this view has been challenged on a number of grounds. One view, based on some seminal and very important experiments on the mechanical response of swollen coal particles, is that coal is indeed a macromolecule but the network essentially consists of entangled rather than covalently linked chains (1). We have remained somewhat skeptical of this model because it would suggest that there should be a solvent that could completely dissolve coal. More on this later. Another fairly recently proposed model considers coal to be an associated structure, held together by secondary forces acting in some undefined cooperative manner (2-6). Although space in this preprint does not allow us to fully review the evidence for this view, it is largely based on three lines of evidence

1) There is a solvent induced association that occurs upon soaking in organic solvents 2) There is an increase in extraction yields using certain mixed solvents 3) Experiments involving the swelling of extracts compared to the swelling of residues

The latter experiments have been largely interpreted in terms of secondary forces such as hydrogen bonds acting as cross-links, thus by extension indicating that the parent coal itself may be held together by such forces.

We have addressed this latter point in a note (7). If, for example, one were to take a pyridine soluble extract and then try to swell it in pyridine, one would not get any useful result, because the extract would simply redissolve. In this type of work the extracts are placed in contact with a *poor solvent*, like benzene or methanol. The phase behavior of such mixtures is such that there will be a solvent rich phase (e.g., benzene with some dissolved extract) and a solvent poor phase (a "swollen" extract rich phase). It is not our intention in this paper to rehash this issue but to consider some of the other evidence that has been cited as favoring an associated structure. Some recent work in the polymer literature will also be discussed because of the light it throws on what role secondary interactions can play in terms of forming crosslinks.

Solvent Soaking and Extraction of Coal

Nishioka (2-5) has argued that the evidence for associative equilibria in coal has not been fully recognized. The basis for this view is the change in extraction yields upon pre-soaking in pyridine (or other solvents) and the enhanced yields obtained in multi-step extraction. These experiments, however, are seriously flawed. Take, as an example, the soaking experiments. A coal is soaked in pyridine for various periods of time. The pyridine is evaporated and the treated coal is washed with methanol. This coal is then Soxhlet extracted with pyridine. The yield of soluble material obtained in this latter step is found to be less than the yield obtained by Soxhlet extraction of the original untreated coal. It is then argued that there is some solvent induced conformational change that results in the coal being more "associated" than the original structure.

We have repeated these experiments with an Illinois #6 coal and obtained very similar results. We found 20.1% of the weight of the original coal could be extracted with pyridine (the residue accounted for 80.7 wt%, giving a total of 100.8% because of tightly bound residual pyridine). The pyridine soaked coal only gave an extraction yield of 16.9%, however, an apparently significant reduction. The problem is that Nishioka ignored the material that dissolves in the methanol washing step, which accounts for 2.8% of the original coal, giving a total extraction yield of 19.7%, within error of the extraction yield of the original coal. Of course methanol by itself does not extract appreciable amounts of soluble material from the original coal, but this is because it does not swell the coal to any detectable amount, so that low molecular weight material that may be soluble remains trapped in the network. Upon treating with pyridine, soluble material is extracted from the coal particles into the solvent phase and upon evaporation of solvent this material remains sitting on the surface of the coal particles. A portion of this, probably the low molecular weight end, can then be dissolved in the methanol wash step. In other words, the arguments concerning the effect of soaking immediately collapse once a complete mass-balance is performed.

The evidence concerning multi-step extraction is similarly flawed. For example, Nishioka asserts, with no evidence, that covalent bonds are not broken in these experiments. However, reactive solvents, such as phenol at 180°C, are used! At these temperatures phenol can break ether linkages.

Experiments involving mixed solvents, particularly the CS₂/NMP mixture used by Iino and co-workers (8), provide far more compelling evidence that many coals have a much larger soluble fraction than originally suspected. This does not mean that they are associated structures simply held together by secondary forces, however. Figure 1 shows the extraction yields obtained from just U.S. Eastern and Interior coals (we have found in previous work that comparing coals from similar sources gives superior correlations). In this figure the yields obtained using a CS₂/NMP mixture are compared to pyridine extraction yields as a function of coal rank. The first thing to note is that many samples of equivalent rank give comparable yields. However, a large proportion gave significantly high yields, the largest being an Upper Freeport Coal giving a 54% extraction yield in CS₂/NMP. (Iino et al (8) also reported a Zao Zhuang coal that gave a 65% extraction yield). As we mentioned above, this does not mean that these coals are purely associated structures. At the gel point in the formation of polymer networks only about 16% of the material (by volume) needs to be in the "gel" or network phase to give a continuous structure, the rest can be the "sol" or soluble phase (9,10). Furthermore, it would not be surprising, giving the heterogeneous character of coal, that a few coals are indeed significantly different in their structure to most of their counterparts, being largely soluble in the appropriate solvents. Finally, there are other compelling reasons to believe that coal is not a collection of relatively small molecules held together by secondary forces such as hydrogen bonds and these relate to the nature and character of these interactions.

The nature of cross-linking and cooperative processes in physical gels

There are various types of cross-links that can exist in networks. It is useful to subdivide these into two categories, "point" cross-links and junction zones. In the first category are covalent cross-links, entanglements and specific interactions such as hydrogen bonds. The first of these, covalent linkages, can be considered "permanent", in the sense that if we confine our experiments to conditions of temperature, stress, etc., where bond rupture does not occur, then they confer certain elastic properties on the network (e.g., reversible deformation). Entanglements and non-covalent linkages are dynamic, so that in the "melt" or liquid state (i.e., above the T_g of the system), they have a "lifetime" or, more precisely, there is a relaxation time associated with their behavior. Thus under fast loads a non-covalently cross-linked polymer like "silly putty" behaves elastically, because the rate of loading is much faster than the "disentanglement" time. Under slowly applied loads the material deforms permanently, because the chains have time to disentangle.

This brings us to secondary interactions such as hydrogen bonds; can they act as crosslinks? We have to be careful about semantics here. Of course, there is a "network" of hydrogen bonds in materials such as coal, but in order for them to act as cross-links they must maintain their integrity during the course of a deformation experiment (e.g., swelling), thus causing the interlinked segments to be displaced in such a way as to maintain a certain spatial relationship with respect to one another (i.e., there are configurational constraints relative to a non cross-linked system). As with entanglements, this comes down to the dynamic properties of the cross-link relative to the time frame of the mechanical experiment. For small molecules in the liquid state the lifetime of hydrogen bonds appears to be in the range 10⁻⁵ to 10⁻¹¹ secs, much too short to act as a cross-link. In macromolecular systems the dynamics of the hydrogen bond can be coupled to those of the chain, so that the situation may be very different. The work of Stadler and co-workers (11-13), however, demonstrates unequivocally that at temperatures well above the T_g the lifetimes are still very short (~ 10⁻³ to 10⁻⁶ secs, depending on the experiment).

Stadler and his group have published an extensive body of work concerning the effect of hydrogen bonds on mechanical and rheological properties. They introduced urazole groups, which form hydrogen bonded pairs with an enthalpy of about -7 kcal/mole (i.e., somewhat stronger than most of the hydrogen bonds found in coal), into various elastomers and compared properties to those of the unmodified rubbers. The transient network formed by the hydrogen bonds was found to affect viscoelastic properties through an apparent increase in the viscoelastic effective molecular weight, but the equilibrium network modulus remained unaffected (i.e., the hydrogen bonds were not behaving like covalent cross-links). In a theoretical analysis Leibler et al. (14) demonstrated how the properties of these transient networks depend upon the dynamics of the hydrogen bonded complex. At frequencies that are higher than the characteristic frequency of the complex, the hydrogen bond acts like a covalent cross-link, but at lower frequencies they hydrogen bonds simply retard the terminal relaxation. However, as a system is cooled through the T_g there is a point where the dynamics are such that a hydrogen bond could act as a cross-link (11-13).

Now we must consider the implications of this work for coal extraction and swelling. The quantity we work with is the change in free energy of the swollen coal/solvent gel relative to that of the initial pure coal and pure solvent. The initial coal is a glassy solid. Are the hydrogen bonds and perhaps other interactions acting as cross-links in this state? If we neglect various relaxation processes we can argue that all contacts are essentially frozen in place, so they are all cross-links! What is important is this; we must consider the change in free energy on going to the swollen state. Larsen and co-workers (15,16) have demonstrated that swollen in a good solvent a coal such as Illinois #6 has a T_g of about 210°K, well below room temperature (naturally, we are only discussing coals that are capable of appreciably swelling in a good solvent). In this state point interactions such as hydrogen bonds (and anything weaker such as π - π^* interactions) cannot act

as cross-links in the time-frame of a swelling measurement. Covalent cross-links, however, contribute to the free energy through terms that account for the distribution of chain configurations between cross-link points and the distribution of cross-link junctions over the volume of the swollen gel relative to volume of the initial coal (at least in the Flory model). In other words, it is only those contacts that are crosslink points or junctions in both the original pure coal and the swollen coal gel that determine the free energy change. Other types of contacts contribute to the free energy through mixing terms, where a proportion of coal/coal contacts are replaced by coal/solvent contacts to an extent that depends upon composition. We have made this point before, although not in this way, and demonstrated how coal will not swell in a non-hydrogen bonded solvent because the mixing part of the free energy changes are unfavorable, not because the hydrogen bonds act as cross-links (i.e., if the coal and solvent don't mix, the hydrogen bonds don't break!)

This finally brings us to the question of whether secondary forces can act in a cooperative manner to give so-called "junction zones". In various coal papers such cooperative processes are often invoked, but never specified. This should be against the law, because the types of cooperative processes that occur in physical gels are well-known and occur through specific identifiable mechanisms, such as the formation of triple helical regions, as in gelatin; microcrystalline regions, as in poly(vinyl chloride) gels; or by the intersection of a liquid-liquid phase separation and a glass transition, as in polystyrene gels formed upon cooling certain solutions (see reference 17). These processes are all subject to physical characterization and detection. If cooperative processes are to be invoked in coal, their nature must be specified, together with the evidence leading to this conclusion, otherwise we are left with the "standard model"; coal is a covalently cross-linked network.

Acknowledgments

The authors gratefully acknowledge the support of the Office of Chemical Sciences, U. S. Department of Energy, under grant No. DE-FG02-86ER13537.

References

- 1 Cody, G. D., Davis, A. and Hatcher, P. G. *Energy and Fuels*, 1993, 7 455.
- 2 Nishioka, M., Gebhard, L. A. and Silberragel, B. G. *Fuel*, 1991, 70, 341.
- 3 Nishioka, M. *Fuel*, 1991, 70, 1413.
- 4 Nishioka, M. *Fuel*, 1992, 71, 941
- 5 Nishioka, M. *Energy and Fuels*, 1991, 5, 487.
- 6 Takanohashi, T., Iino, M., and Nishioka, M. *Energy and Fuels*, 1995, 9, 788
- 7 Painter, P. C. *Energy and Fuels*, 1992, 6, 863.
- 8 Iino, M., Takanohashi, T., Ohsuga, H. and Toda, K. *Fuel*, 1988, 67, 1639.
- 9 Flory, P. J. *Principles of Polymer Chemistry*. Cornell University Press, 1951.
- 10 Zallen, R. *The Physics of Amorphous Solids*. John Wiley and Sons, 1983.
- 11 Muller, M., Kremer, F., Stadler, R., Fischer, E. W. and Seidel, U. *Colloid Polym. Sci.*, 1995, 273, 38
12. Muller, M., Stadler, R., Kremer, F. and Williams, G. *Macromolecules*, 1995, 28, 6942.
- 13 Muller, M., Seidel, U. and Stadler, R. *Polymer*. 1995, 36 3143
14. Liebler, L., Rubinstein, M., and Colby, R. H., *Macromolecules*, 1991, 24, 4701
15. Hall, P. J., and Larsen, J. W., *Energy and Fuels*, 1993, 7, 47
16. Yang, X., Silberragel, B. G., and Larsen, J. W., *Energy and Fuels*, 1994, 8, 266
17. Burchard, W. and Ross-Murphy, S. B. *Physical Networks*, Elsevier Applied Science, London and New York, 1990.

Plot of the extraction yield versus carbon content of coals

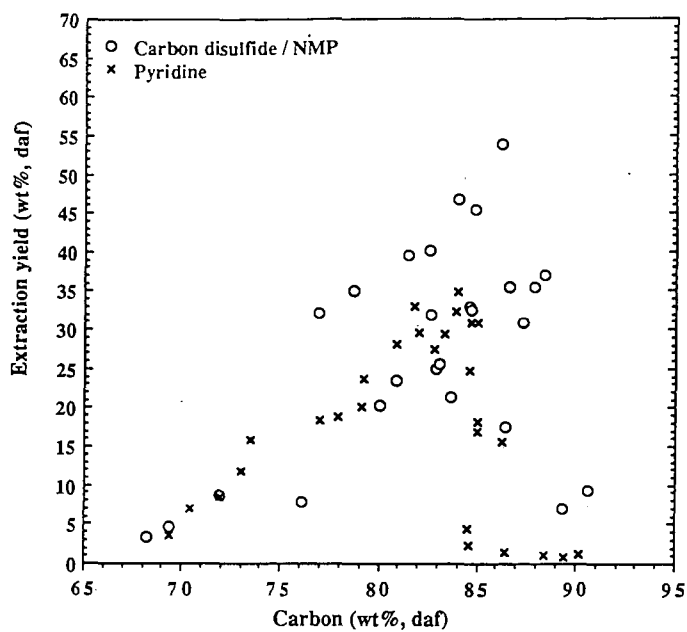


Figure 1.

THE TEMPERATURE DEPENDENCE ON THE STRAIN DYNAMICS OF SOLVENT-DILATED COAL

George D. Cody
Geophysical Laboratory
Carnegie Institution of Washington,
5251 Broad Branch Rd., NW
Washington, DC 20015

Key Words: Coal, Viscoelastic, Solvent Swelling

Introduction

The "rubbery" properties of pyridine dilated coals has been recognized for several decades (1). The physical properties of rubbery materials are related to macromolecular structure. For example, measurement of the time-dependent response of a rubber material to applied stresses is one means of obtaining fundamental information on macromolecular structure, such as short range chain flexibility, and long range network topology (2). Previous work exploring the time-dependent compliance of solvent-dilated coals revealed upon the application of a uniaxial compressive stress, numerous coals exhibited both a reversible, viscoelastic strain and an irreversible, viscous strain (3); the irreversible strain was confirmed with creep recovery experiments. This later observation was unexpected as it requires that the coal macromolecule not be covalently cross-linked. It was further noted, however, that the enormity of the viscous coefficients ($\eta \sim 10^{12}$ Poise), coupled with the relatively short time required to reach steady state compliance indicated a structure composed of highly entangled chains with long chain branches. Thus, although the coals are technically not cross-linked, the very small self diffusion coefficients of the entangled macromolecules preclude extraction over reasonable time scales.

In order to characterize the viscoelastic and viscous behavior further, creep compliance experiments have been applied as a function of temperature. By monitoring the temperature dependence on the various dynamic parameters insight can be gained on the molecular scale features that constitute the building blocks of coals macromolecular structure.

Experimental

A sample of the Illinois No. 6 coal, PSOC 1539 was selected for study. This coal is characterized with 81.9 % C, 5.5 % H, 9.4 % O, 1.4 % N, and 2.2 % S. Sections of vitrain (over 95 % vitrinite) were identified and separated from larger blocks with a wafer saw. Small rectangular blocks were sectioned with dimension on the order of 1 x 2 x 2 mm. The blocks were exhaustively extracted in pyridine prior to analysis. Uniaxial stress ($\sim 0.5 \text{ Kg/cm}^2$) was applied to the sample, strain was measured using a microdilatometer employing a linearly variable differential transformer (LVDT). Details on measuring apparatus have been published previously (4). To control temperature, the entire sample holder was placed within a reservoir of pyridine, which was surrounded by an oil bath. Heating tape and a temperature controller were used to establish the temperatures of interest; 25, 50, and 76° C, in this case. During the experiment the inner bath temperature was monitored with a thermocouple; details on the measuring protocol for the variable temperature experiments have been published elsewhere (5).

Results

Figure 1 presents data from a typical creep compliance run. Following the application of uniaxial compressive stress, the swollen coal exhibits a rapid, essentially instantaneous, initial compliance. This evolves into a more gradual viscoelastic compliance spanning several tens of minutes. After approximately 40 minutes the system has reached steady state viscous flow characterized by a constant strain rate. The strain in this during time is totally irreversible. Previous creep experiments were monitored for up to 72 hours. The present experiments were run only long enough to establish steady state deformation.

In general, creep compliance data can be decomposed as the sum of three independent strain components, e.g.

$$J(t) = \frac{t}{\eta} + J_i + \sum_{i=1} J_a(1 - e^{-t/\tau}) \quad (1)$$

Where the first term corresponds to viscous strain, governed by the coefficient of viscosity, η ; the second term corresponds to instantaneous compliance, i.e. very high frequency or glassy strain; the third term corresponds to viscoelastic strain in the so-called "transition

zone", i.e., in the frequency range spanning the "glass transition" (2). This final term is expressed as a sum of exponentially relaxing strain elements. In reality, it would be more appropriate to consider a continuous spectrum of relaxation times as opposed to this discrete representation, e.g.

$$\int_0^{\infty} J(\tau_n)(1 - e^{-t/\tau_n})d\tau \quad (2)$$

The creep compliance, $J(t)$, can be separated into purely viscoelastic and viscous contributions using equation 1, given data that is acquired over a sufficiently long interval of time. Figure 2 presents the purely viscoelastic strain at $T = 25, 50$, and 76°C . The data are normalized to magnitude of the final steady state reversible compliance.

$$\alpha(t)/\alpha_f; \alpha(t) = \Delta L(t)/L; \alpha_f = \Delta L_f/L \quad (3)$$

Each curve is best described by a multiexponential "spectrum" of viscoelastic elements (equation 1 or 2). Significant shifts in the relaxation "spectra" with temperature are clearly evident. One question that arises is whether the different viscoelastic strain elements have the same temperature dependence. For example, a simple chain may exhibit Rouse-like (2) dynamics, where backbone vibrations all contribute to the viscoelastic response. In this case the viscoelastic spectrum is given as proportional to the normal mode frequencies of the coupled oscillators that constitute the simple polymer chain. Of course the temperature dependence of the viscoelastic elements across the frequency spectrum will be the same in such a system. As a consequence of such behavior, each creep compliance curve will be self-similar, when scaled by a time-temperature shift factor a_T^{-1} (6). Indeed, many simple polymers exhibit such behavior.

To test if such behavior is exhibited by the Illinois No. 6 Coal we attempt to scale each curve to match the $T = 76^\circ\text{C}$ viscoelastic curve. We plot the natural log of the shift factors, a_T^{-1} , obtained for the time it takes to reach 50 % and 80 % of the steady state compliance. These are plotted against, $1/T$ (K), in figure 3. If all of the strain viscoelastic strain elements shared the same temperature dependence, then $\ln(a_T^{-1})$ vs $1/T$ for 50% should equal that for 80%. The fact that they do not equate, reveals that viscoelastic elements in different frequency regimes exhibit different temperature dependences. Clearly, the lower frequency modes exhibit a stronger temperature dependence than the higher frequency modes.

This type of behavior has been observed in the case of polymers with side chains, e.g. poly[ethylmethacrylate]. The favored interpretation is that the side chain motion dominates the high frequency, "glassy", deformation, while chain backbone motions dominate the lower frequency, "transition zone", deformation. One can only speculate as to the molecular origin of such variations in the temperature dependence of the viscoelastic properties of solvent dilated coals. It is likely that in place of side chains, oscillations of phenyl groups along the molecular chains within coal may contribute to the high frequency deformation. The lower frequency backbone motion, including the coupled motion of the "virtual" bonds that span the phenyl groups, contributes to the stronger temperature dependence of strain at longer times. This simple picture is complicated, however, by additional factors as described in the discussion section below.

In consideration of the temperature dependence on the viscous deformation it is generally noted that viscous strain (terminal relaxation) follows Arrhenius type behavior, with the temperature dependence being governed by an apparent activation energy given by

$$\eta \propto e^{E_a/RT}$$

Figure 4 presents the viscous coefficients, η , plotted as the natural log of η against $1/T$ (K). Apparent Arrhenius behavior is observed yielding an apparent activation energy of 6.9 Kcal/mol. This value is similar to that of high molecular weight polymer melts and solutions. In general the magnitude of the viscous coefficient in polymeric systems is considered to be related to a molecular friction coefficient (2). Reduction in the molecular friction coefficient with increases in temperature is classically interpreted to be the result of an increase in "free volume" within the system. The viscous data is therefore interpreted to indicate that there is a small positive coefficient of expansion for this solvent dilated coal.

Discussion

At the molecular level, the exact nature of creep in solvent dilated polymers is complex. In general there are two different moduli (both time dependent) that warrant consideration. It is important to recognize the the swelling equilibrium is a balance between

the osmotic stress given by mixing component of the chemical potential and the elastic "pressure" given by the elastic component of the chemical potential (6). Stress applied to one surface of the sample will act with the elastic "pressure" to oppose the osmotic stress leading to compression of the swollen gel through the expulsion of solvent. Calculation of the pure osmotic compressibility for a sample with the dimensions described above, an equilibrium swelling value of $v_2 = 0.42$, and subjected to a uniaxial stress of 0.5 Kg/cm^2 indicates that up to 22 % of the elastic/viscoelastic compliance may be the result of osmotic deswelling.

The osmotic deswelling is clearly time-dependent, subject to requirement that the solvent diffuse out of the network to restore "swelling" equilibrium. The small osmotic strain component corresponds to a 1.4 mol% reduction (calculated) in pyridine. Given that rate of diffusion will be proportional to the chemical potential gradient of solvent inside and out of the network, it is clear that the osmotic deswelling contributes only to the low frequency strain behavior. It is quite possible that the rate of osmotic deswelling is so slow as to be buried within the viscous strain. For example, De-swelling kinetics experiments on similarly sized samples required many hours for full solvent expulsion (7). Additional experiments will need to be run to fully account for the time dependences of the various strain mechanisms. It is clear, however, that the temperature dependence of viscoelastic strain in solvent diluted coals is complex, hence may be some value in characterizing the macromolecular structure of coals.

References

- 1) van Krevelan, Coal, Elsevier Scientific, New York, 1981.
- 2) Ferry, J. D., The Viscoelastic Properties of Polymers; John Wiley & Sons, New York, 1980.
- 3) Cody, G. D., Davis, A., Hatcher, P. G., Energy & Fuels, 7, 455-462
- 4) Cody, G. D., Davis, A., Hatcher, P. G., Energy & Fuels, 1993, 7, 463-468.
- 5) Cody, G. D., Eser, S., Hatcher, P.G., Davis, A., Sobkowiak, M., Shenoy, S., Painter, P. C. Energy & Fuels, 1992, 6, 716
- 6) Flory, P.J., Rehner, J. Chem. Phys., 1944, 12, 412.
- 7) Lei, H., Cody, G. D., French, D. C., Botto, R. E., Hatcher, P. G, Energy & Fuels, 1995, 9, 84

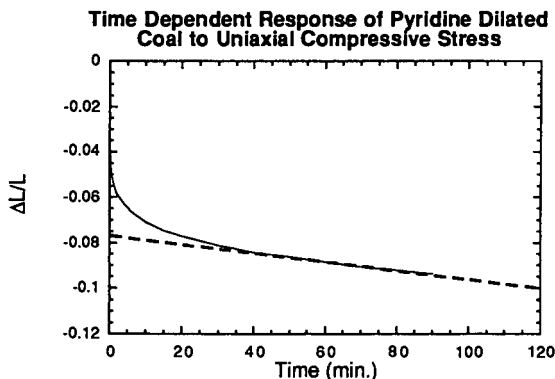


Figure 1: Time dependent Compliance of Solvent Dilated Illinois No. 6 Coal following application of uniaxial compressive stress ($\sim 0.5 \text{ Kg/cm}^2$). Rapid (high frequency) elastic strain grades into viscoelastic (Transition zone) strain, followed by purely viscous (terminal zone) strain. The viscous strain is irreversible.

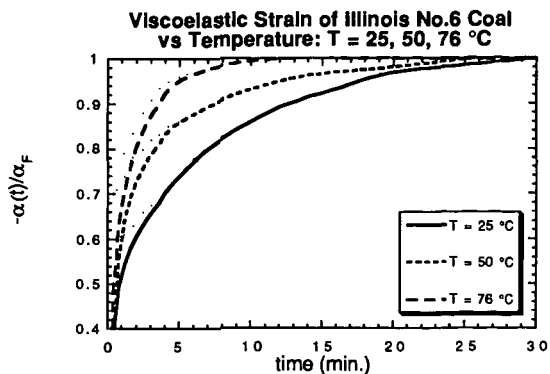


Figure 2: Purely viscoelastic strain (scaled). Temperatures are 25, 50, 76°C. Large shifts towards the higher frequency strain components is clearly evident.

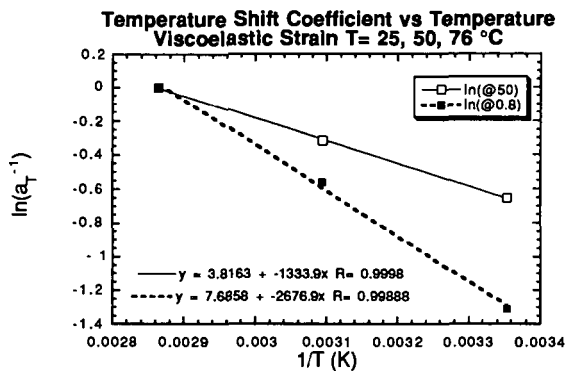


Figure 3: The temperature dependence of the inverse time-temperature shift factor, a_T^{-1} . The different slopes at different extents of total viscoelastic strain reveal that the viscoelastic deformation is not self-similar at different temperatures. The lower frequency modes clearly, exhibit a stronger temperature dependence than the higher frequency modes. This may indicate that different structural elements are dominating different regions of frequency response.

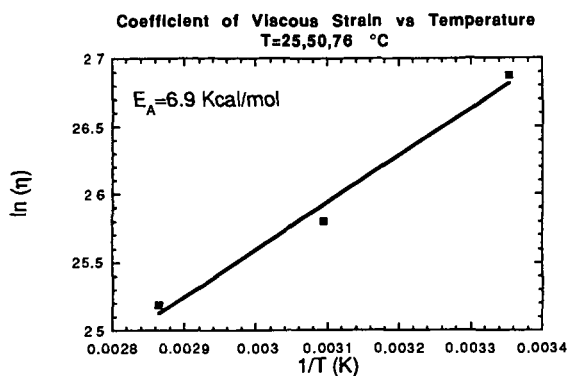


Figure 4: The inverse temperature dependence of the viscous coefficient. The viscosity of polymer/macromolecular melts and solutions typically exhibit Arrhenius type temperature dependences described by an apparent activation energy, E_A . The magnitude of E_A is similar to that of high molecular weight polymer melts, e.g. polyethylene. The positive slope is generally considered to indicate a reduction in the molecular friction factor through a temperature dependent increase in the free volume of the system.

VISCOELASTICITY OF COAL GEL FILMS PREPARED FROM SOLVENT-SOLUBLE CONSTITUENTS OF COALS

Toshimasa Takanohashi, Shigeki Isoda, Satoshi Doi, and Masashi Iino
Institute for Chemical Reaction Science, Tohoku University
Katahira, Aoba-ku, Sendai 980-77, JAPAN

KEYWORDS: Coal, Gel Film, Viscoelasticity

ABSTRACT

A large amount of solvent-soluble constituents of coals were mildly extracted with a carbon-disulfide - *N*-methyl-2-pyrrolidinone mixed solvent at room temperature. Various gel films containing a solvent was successfully prepared by using the solvent-soluble constituents and polar solvents such as *N*-Methyl-2-pyrrolidinone and *N,N*-dimethyl-formamide. A thermomechanical analysis (TMA) of the gel films was carried out and the creep compliance behaviors of the gel films showed the viscoelastic properties, suggesting that the gel films have mainly physical cross-linked networks through coal - coal interaction and coal - solvent interaction, since the solvent-soluble constituents have little original covalent cross-links. When the weight fraction of solvent in the gels was decreased, the viscous strain and the viscoelastic strain decreased, while the elastic strain was almost unchanged, suggesting no participation of a solvent. The network structure of homogeneous coal - solvent gel films and the coal - solvent interactions are discussed.

INTRODUCTION

Coal is considered to have cross-linked network structure consisting of various macromolecules, but the nature of network structure has not been well understood. Recently, it has been reported¹⁻³ that the network consists of physical cross-links through noncovalent interactions between coal molecules, not a covalently bound cross-linked network. The study on viscoelasticity of coal and coal-derived materials is one of the key to clarify cross-link structure of coal. To investigate the elasticity of coal network, coal thin sections were prepared and viscoelasticity of the pyridine swollen coal has been measured by Brenner⁴ and Cody et al.^{1,5} The pyridine swollen coals have been reported^{4,6} to show a rubbery elasticity. However, raw coal contains mineral matter and has a significant amount of pores and cracks on the surface, being liable to influence the measurement of elasticity of coals.

In our research groups, it has been found⁶⁻⁸ that by using a carbon disulfide - *N*-methyl-2-pyrrolidinone (CS₂-NMP) mixed solvent 40 wt % - 79 wt % of organic components in coals can be extracted at room temperature. The extract obtained is relatively homogeneous and has no ash.⁹ Since the extraction procedure includes no chemical reaction such as cleavage of covalent bonds in coals and addition reaction of the solvents with coals, the organic constituents originally existing in the raw coals are extracted.^{6,9} Recently, it has been succeeded¹⁰ to prepare gel films by mixing the homogeneous solvent-soluble constituents and polar solvent such as NMP or *N,N*-dimethyl-formamide at room temperature. In the present study, viscoelasticity of the gel films is measured and the network structure is discussed.

EXPERIMENTAL

Sample Preparation.

Upper Freeport coal (Argonne Premium Coal, 86.2 Cwt%) and Zao Zhuang coal (Shan Tong Province in China, 86.9 Cwt%) were used in this study. The coals (<150 μ m) were extracted with the mixed solvent under ultrasonication at room temperature. The two bituminous coals have been reported^{6,7} to give the high extraction yields with the CS₂-NMP mixed solvent, 59 wt% (daf), and 63 wt% (daf), respectively. The extract obtained was further fractionated with acetone and pyridine into acetone soluble (AS) fraction, acetone insoluble-pyridine soluble (PS) fraction and pyridine insoluble (PI) fraction under ultrasonication at room temperature. The PS and PI fractions were washed with acetone, while AS fraction was washed with acetone-water mixed solvent to remove the retained solvents. The extract fractions (AS, PS, PI) were dried under vacuum at 80 °C for 12 h. The fractionation procedure and the yields of each fraction of two coals are shown in Figure 1.

Gel Film Preparation.

Approximately 2 mL of solvent was added to 0.1 g of the coal extract fraction and was mixed under ultrasonication. After filtration with a membrane filter (0.8 μ m), the solution was placed in a glassware. The solvent in the solution was gradually removed under vacuum at room temperature. At some range of solvent wt % in the mixture, the

mixture became a lustrous gel film. By changing the evacuation time of solvent, the gel films containing different solvent composition (W_s) were prepared. The thickness of the films are the range of 50 μm – 200 μm .

Thermomechanical Analysis.

Viscoelasticity of the gel film was measured by a thermomechanical analysis apparatus (Shimadzu-TMA50). The small section of gel film was placed on the bottom plate. A load (stress) of 1 g was applied to the film section by using a detector bar, and a strain was measured from the decreased thickness of the film. Creep compliance measurements in which constant stress (5 g or 10 g load) was applied to the film, and stress-strain analyses in which the weight of load was changed were carried out.

RESULTS AND DISCUSSION

The Nature of Gel Film.

Figure 2 shows the weight fraction of NMP (W_s) in the Upper Freeport-PS fraction + NMP mixture (UFPS-NMP) when NMP was vaporized under vacuum. The W_s was decreasing with time by vaporization of NMP from the mixture and the slope became small around at $0.35 > W_s > 0.25$. In this range of W_s , it was observed that the mixture became lustrous gel film. For other fractions, PI, AI (PS+PI), the formation of similar gel films was observed, while for AS fraction which is a lighter fraction than the others, the mixture kept pasty even when W_s became little unchanged, i.e., no gel film formation. It has been reported that the AS fraction has lower average molecular weight and lower polar functional groups than other heavy fractions, suggesting that a physical cross-linked network by coal-solvent interaction and coal-coal interaction is important for the formation of gel films.

Creep measurements.

Figure 3 shows the creep compliance behaviors of three gel films with different W_s (0.70, 0.47, 0.30) which were obtained from UFPS-NMP mixture. The load of 5 g applied on the film was kept for 15 min, and then the load was released and the relaxation behavior was also measured. The procedure was repeated three times. In the case of $W_s = 0.70$, the strain was greatly changed with an increase and a decrease in the load, showing the breaking of gel structure due to the stress. The strain is considered to be mainly due to viscous strain by the flow of solvent. On the other hand, for $W_s = 0.47$ and 0.30, in the second and third scans, the reproducible data was obtained. Cody et al. analyzed² the creep compliance behavior of pyridine-swollen coal using a four-element Kelvin-Voigt model, which separates the strain into three strain elements, i.e., instantaneous elastic strain, ϵ_E , time-dependent viscoelastic strain, ϵ_{VE} , which decayed exponentially to a constant strain rate, and irreversible viscous strain ϵ_v , which was linear with time.

We also treated similarly. For the second and third scans for two gel films ($W_s = 0.47$ and 0.30), total strain is represented as the following equation.

$$\epsilon(t) = \epsilon_E + \epsilon_{VE}(1 - \exp(-t/\tau)) + 100\sigma t/\eta \quad (1)$$

where t is time (s), τ is retardation time constant (s), σ is stress (Pa), and η is coefficient of viscosity (Pa s). In the eq. (1), the third term on the right describes viscous strain, $\epsilon_v(t)$. The calculated lines assuming ϵ_E , ϵ_{VE} , ϵ_v , τ and η in the eq. (1), for the second and third scans on the UFPS-NMP gel film ($W_s = 0.30$) are shown in Figure 4. It was found that the calculated lines are well consistent with the experimental points for the both scans. A half of total strain is produced near $t = 0$, i.e., instantaneous elastic strain. The strain at the second scan is more greatly increasing with time than that for the third one. The values of elastic strain, ϵ_E , viscoelastic strain, ϵ_{VE} , and coefficient of viscosity, η , are shown in Table I. For both samples, the changes of elastic strain, ϵ_E and viscoelastic strain, ϵ_{VE} were small between the second and the third scan, while coefficient of viscosity, η greatly increased, showing that the viscous strain is gradually decreasing. In $W_s = 0.30$, the viscoelastic strain and the viscous strain were small, while the elastic strain was a little large, compared to the case in $W_s = 0.47$, suggesting that the elastic strain may originate from physical cross-links through noncovalent interactions between macromolecules in the heavy extract fraction, as well as relatively strong interactions between coal macromolecules and the solvent.

Stress-Strain Curve.

A load was increased from initial 1 g to 10 g at a constant rate, 1 g/min, and then the load was decreased at the same rate. The procedure was repeated several times. The stress-strain curves of UFPS-NMP gel films with $W_s = 0.53$ and 0.30, are shown in Figure 5 and 6,

respectively. Figure 5 shows that the first and the second scan gave a large strain. The first large strain is considered to be attributed to the structural changes by the viscous strain. While after the forth scan a similar stress-strain curve was obtained, suggesting that the structural changes of gel becomes reversible with repeating the increase and decrease in the stress. Figure 6 shows that the strain change is small compared to that for $W_s = 0.53$ shown in Figure 5. This result suggests that the gel film is more elastic, since the amount of the solvent is small and relatively strong interactions must have still remained in the gel film, resulting in the large contribution of the elastic component.

CONCLUSIONS

Homogeneous gel films containing no mineral matter could be prepared from the mixture of the solvent-soluble constituents with polar solvents such as *N*-methyl-2-pyrrolidinone and *N,N*-dimethyl-formamide. It is suggested that the gel films have physical cross-linked networks through coal-coal interaction and coal-solvent interaction, since the solvent-soluble constituents themselves have little extended covalent cross-links. When the weight fraction of solvent in the gels was decreased, the viscous strain and the viscoelastic strain decreased, while the elastic strain was almost unchanged. It was found that a similar stress-strain curve is obtained after several cycles of the increase and decrease in the stress, indicating that a constant structural change with changing the stress occurs.

ACKNOWLEDGMENT

This work has been carried out as one of "Research for the Future" project of the Japan Society for the Promotion of Science (JSPS) through the 148 committee on coal utilization technology of JSPS.

REFERENCES

1. Cody, G. D. J.; Davis, A.; Hatcher, P. G. *Energy Fuels* **1993**, *7*, 463.
2. Fujiwara, M.; Ohsuga, H.; Takanohashi, T.; Iino, M. *Energy Fuels* **1992**, *6*, 859.
3. Takanohashi, T.; Iino, M.; Nishioka, M. *Energy Fuels* **1995**, *9*, 788.
4. Brenner, D. *Fuel* **1985**, *64*, 167.
5. Cody, G. D. J.; Davis, A.; Hatcher, P. G. *Energy Fuels* **1993**, *7*, 455.
6. Iino, M.; Takanohashi, T.; Ohsuga, H.; Toda, K. *Fuel* **1988**, *67*, 1639.
7. Takanohashi, T.; Iino, M.; *Energy Fuels* **1990**, *4*, 452.
8. Iino, M.; Takanohashi, T.; Ohkawa, T.; Yanagida, T. *Fuel* **1991**, *70*, 1236.
9. Iino, M.; Takanohashi, T.; Obara, S.; Tsueta, H.; Sanokawa Y. *Fuel* **1989**, *68*, 1588.
10. Iino, M.; Watanabe, H.; Takanohashi, T. *Inter. Conf. Coal Sci.*, Oviedo, **1995**, vol. 1, p.59.

Table 1 The Values of Elastic Strain(ϵ_E), Viscoelastic Strain(ϵ_{EV}), and Viscosity (η)

	$W_s = 0.30$		$W_s = 0.47$	
	second	third	second	third
ϵ_E (%)	0.55	0.53	0.47	0.43
ϵ_{EV} (%)	0.08	0.06	0.13	0.13
$\eta \times 10^{10}$ (Pa s)	11.3	19.0	5.0	8.5

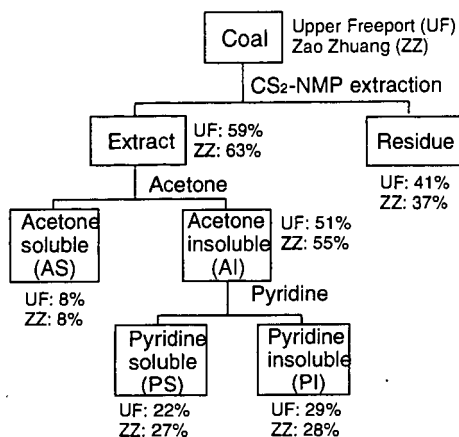


Fig.1 Extraction and Fractionation Procedures

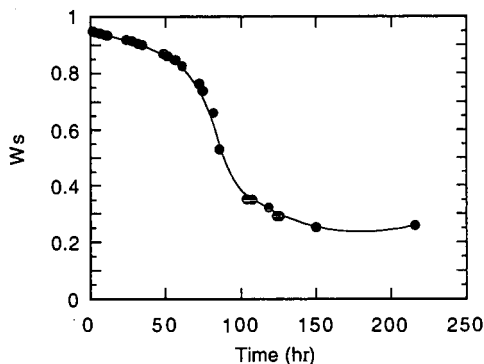


Fig.2 Weight Fraction Change of UFPS+NMP under vacuum at room temperature

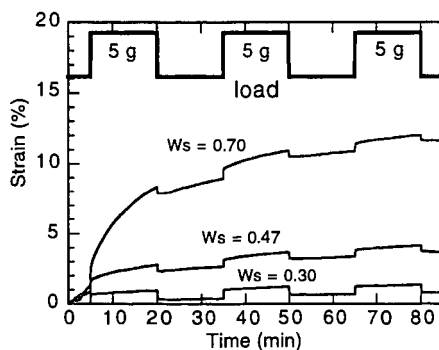


Fig.3 Creep Compliance of UF-PS - NMP gel: ($W_s = 0.30, 0.47, 0.70$)

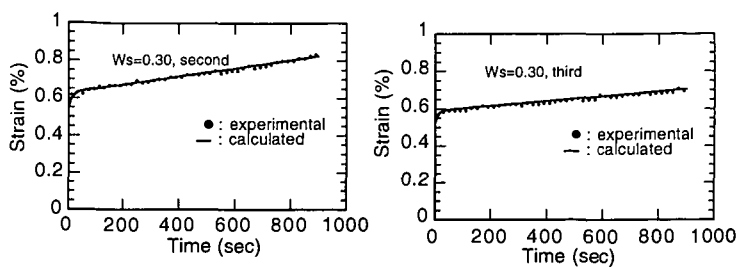


Fig.4 The Fitting Curves for the Second Scan (a) and the Third Scan (b) of Creep Compliance of UFPS - NMP Gel ($W_s = 0.30$)

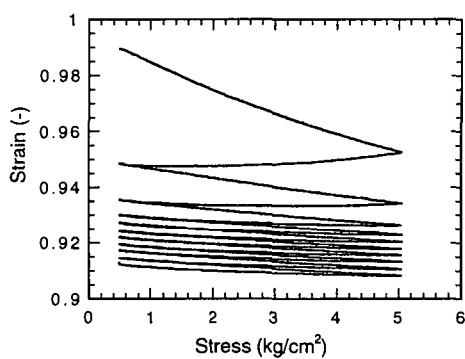


Fig. 5 The Stress-Strain Curve of UFPS - NMP Gel Film ($W_s = 0.53$)

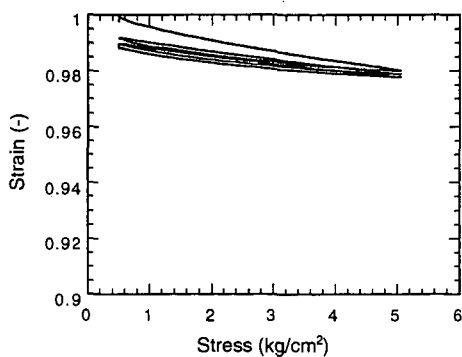


Fig.6 The Stress-Strain Curve of UFPS - NMP Gel Film ($W_s = 0.30$)

DIFFUSION RATES OF ORGANIC SOLVENTS IN COALS: ACTIVATION ENERGIES

Yoshinobu Otake and Eric M. Suuberg
Division of Engineering
Brown University, Providence, RI, 02912

Keywords: Coal, Diffusion, Swelling

INTRODUCTION

Diffusional limitations are of concern in virtually all aspects of coal utilization. As a result, over the last few years there have been a number of studies of the factors that influence diffusion [1-24]. These studies, which have been mostly concerned with transport of solvents through coals, have generally indicated that diffusion in coals is similar in many respects to the diffusion of solvents through glassy polymers. The process of relaxation of coal structure by the solvents plays an important role in determining how fast the coal can take up additional solvent. The rates of solvent uptake are strongly influenced by factors such as the nature of the coal, the size of the coal particles [1], the strength of the solvent [15,17,18], the size and shape of the solvent molecules [7,8, 24], the temperature [5,6,17-19,23], the moisture content of the coal [19], and other features of its pretreatment [9,10,14,19,20,21]. The present paper presents results that shed further light on the role of temperature on the rates of diffusion. This is a key aspect of the process that requires further consideration, since most coal conversion processes are performed at elevated temperatures.

It is important to note at the outset that the diffusional processes that are of concern in this study involve movement of individual molecules of solvent through molecular scale openings in the coal. Thus we are not concerned with diffusion or flow in the macropores of coal, which would generally be much faster processes than those of interest here.

The main experimental method that is applied in this study is solvent swelling of coal. This method has been applied in earlier studies of diffusion in coals [7,8,15,17-21,23,24]. To be useful, this technique requires working with coal-solvent pairs that strongly interact, and that the coal measurably swell. This limited the study to solvents that are strong electron donors [25]. In our particular application of the technique, measurements of the extent of swelling were made manually, *vide infra*, which required at least a few minutes per measurement. This limited the study to systems that did not swell on a timescale faster than a few minutes. The timescale of experiments could be adjusted by variation of either temperature (lower temperatures slowed the process) or particle size (larger particles swelled more slowly). This limited the experimental matrix that could be conveniently studied, but a broad range of conditions was still available, as will be apparent below. It should be noted that the automated techniques for measuring swelling rates [7,8,15,23,24] were considered, but felt to pose certain problems with respect to heat transfer and maintenance of constant packing. The vapor sorption techniques require pre-extraction and corrections for pore filling [3,4,26,27], which made these unattractive for present purposes.

In this paper, discussion is limited to the effects of temperature on the swelling process. The temperature influences not only the kinetics of swelling, but also the nature of the swelling (whether Fickian or non-Fickian).

EXPERIMENTAL

The data were obtained on the coals from the Argonne Premium Coal Sample Program [28]. Since the composition and properties of these coals have been carefully tabulated elsewhere, the information will not be repeated here. To assure uniformity among samples, all were dried for 3 hours at 373 K in vacua. As we have noted before, the effects of drying can be quite significant [19]. Studies of dried coals are nevertheless relevant, both because in practical applications coals are first dried, and because the fundamental phenomena of interest here are not changed in basic nature by the drying procedure (even if the kinetics are affected).

It was learned early in this study that particle size has a significant effect upon the results obtained. One major reason is that if a broad range of particle sizes is employed, packing of fine particles into the interstices between larger particles can cause significantly higher packing of the particles, and

lead to artifacts in the volumetric swelling measurements. Thus efforts were made to always work with relatively well-defined particle size fractions, even though the means of the size fractions varied widely from experiment to experiment, for the reasons noted above. When the results are given below, the size fractions will be indicated.

The swelling experiments were performed as described in an earlier paper [17]. The technique involved immersion of the prepared coal samples in pure, reagent grade solvents. The measurements were performed in constant diameter glass tubes of 3 mm inner diameter and about 5 cm in length. After a 30 to 100 mg sample was placed in the tube, it was centrifuged at 7500 rpm for 3 minutes in a 30 cm diameter horizontal rotor centrifuge, to permit accurate measurement of an initial dry packed height of coal. Solvent, prewarmed or precooled as necessary to the experimental temperature, was then added to the tube, and the contents were vigorously stirred with a thin rod. Such stirring is important to prevent the coal from rapidly swelling and forming a solid plug in the tube. The tube was then placed in a thermostatted water bath, for the desired time, and was agitated as noted during this immersion. The temperature of the water bath was controlled to about 0.1°K.

The coal was then allowed to swell for the desired time, and then was removed from the bath and placed in an ice bath to slow the swelling to a negligible rate. Then the sample was again centrifuged as above, and the height of the column of coal remeasured. The ratio of the swollen height to the initial height is what is reported here as the volumetric swelling ratio. Several different samples were employed to determine the extent of swelling as a function of time, in cases in which the swelling was rapid. It was often necessary during the course of the swelling measurements to change the solvents, as they became visibly extract-laden. This was done by carefully decanting the extract-containing solvents, and replacing with fresh solvents. No attempt was made to pre-extract the coals prior to these measurements, since it was desired that the diffusion rates be studied in what was as close to the virgin coal state as possible, except that the coals were dried.

RESULTS AND DISCUSSION

Effect of Temperature on the Extent of Swelling of Coals

There are two potential effects of temperature on the swelling behavior of coals. Temperature may influence both the ultimate extent of swelling as well as the rate of swelling. Many workers have noted the insensitivity of ultimate swelling ratio on temperature [17, 23, 29]. In the present experiments, we have again confirmed that there is no significant effect of temperature on the extent of swelling, at least in the range from 10 to 60°C. This is understood in terms a near zero enthalpy of swelling near the equilibrium extent of swelling [25]. The near thermoneutrality of the swelling process is what dictates a temperature-independent final equilibrium, which may be easily seen as a consequence of the Gibbs-Helmholtz equation of classical thermodynamics.

It has also been argued that the weak dependence of the extent of equilibrium coal swelling on temperature could be a consequence of a rather special form of the equation describing the partial molar Gibbs free energy of elastic deformation [29]; in this case, the partial molar energy of coal elastic deformation must be temperature independent. The recognized need for inclusion of the combinatorial entropy of mixing raises questions about the validity of this theory, however, since this reintroduces the temperature dependence to the expression governing equilibrium.

It should be noted that there is one report of great sensitivity of the swelling ratio to temperature [1]. The experiments in question were conducted by allowing solvent uptake from a *vapor* phase, as opposed to the *liquid* phase, as in the other studies. In this case, there is always a significant (exothermic) enthalpy of solvent condensation, which dictates that condensation, and swelling, would be less extensive, the higher the temperature.

Solvent Swelling Kinetics

The diffusion of solvents into coals, as governs their swelling, has been noted by virtually all workers to be highly non-Fickian in nature, in many cases. The behavior is often that observed in glassy polymers, and involves "Case II" diffusion, as defined by Alfrey et al. [30]. The Case II situation involves a solvent uptake process which is controlled by the relaxation of the macromolecular network structure, as opposed to diffusion itself. It is characterized by a sharp front separating the swollen and unswollen regions of the coal.

To the extent that solvent swelling is linearly related to mass uptake, it is possible to relate the two

quantities via:

$$M/M_{\infty} = (Q-1)/(Q_{\infty}-1) \quad (1)$$

where M refers to mass uptake of solvent by the coal, Q is the coal's volumetric swelling ratio, and the subscript ∞ refers to the final equilibrium values. The error associated with the neglect of small amounts of empty voidage is generally negligible. Analysis of the nature of the diffusional process has been greatly aided by a simple empirical approach, which relates M/M_{∞} to time [2]:

$$M/M_{\infty} = k t^n \quad (2)$$

where k is a constant related to the rate of swelling, and n is a number that crudely indicates the nature of the diffusion. For nearly spherical particles and for mass uptakes up to about 60% of the equilibrium value, $n = 0.43$ for Fickian diffusion, and $n = 0.85$ for Case II diffusion. Values above $n = 0.85$ are possible, and are termed "super-Case II" [2].

Table 1 gives the results for the Argonne Premium Coal Samples, swollen by pyridine. All results were obtained on particles of 150-212 μm size range, unless noted otherwise. The results show the measured values of the parameter n , as a function of temperature. Generally speaking, the values of n are reasonably constant with temperature, though in two cases, they showed a significant decrease with temperature above 40°C. The values indicate a range of behaviors ranging from clearly Fickian (Illinois No.6) to clearly Case II (or even super-Case II, in Pittsburgh No.8). This range of behaviors is precisely the same as has been recently reported for a suite of British coals [23]. It should be noted that we provide no values for two Premium Sample Coals (Pocahontas and Upper Freeport), because as has been noted earlier, these coals swell to a negligible degree until thermally relaxed at much higher temperatures [21].

Given the values of n from Table 1, it is possible to evaluate activation energies for the swelling process, from:

$$E = -nR \left[d(\ln 1/t_r)/d(1/T) \right] \quad (3)$$

where E is the activation energy, R is the gas constant and t_r refers to the time at a fixed extent of swelling. This definition of activation energy is based upon the rate law (2), and is slightly different from that which we used earlier [17,18]. The values from (3) are more directly comparable with other values recently published [23]. The results for the Argonne Coals are again shown in Table 1. The values range from about 20 to 50 kJ/mol. It may be noted that the coals with the higher rates of swelling (indicated by the time to achieve 50% swelling, t_{50}), generally exhibit lower activation energies for swelling. It is logical to associate a lower energy barrier to swelling with a higher rate. In fact, swelling in the coal with the lowest activation energy, Illinois No. 6, apparently was limited by ordinary Fickian diffusion, though with a reasonably high activation energy of 20 kJ/mol.

Earlier, we reported that low rank coals generally exhibit higher activation energies for swelling than do higher rank coals [18]. The opposite conclusion was more recently presented by another group [23], but they examined a somewhat narrower range of rank. Here, we again see a low rank coal show a high activation energy, but now there is no clear trend with rank. The conclusion is that there is no definite trend of activation energy with rank. The actual rates of swelling were also earlier reported to show no correlation with rank [18, 23]. Again, this is seen to be the case here as well.

There is a strong dependence of activation energy on the nature of the solvent. The results obtained using various solvents to swell the Pittsburgh No. 8 sample are shown in Table 2. It has been earlier concluded that the degree of coal swelling is strongly correlated with the electron donor strength of the swelling solvent [25], or equivalently, the basicity of the solvent [23]. It was also earlier reported that the basicity is an important factor only during initial swelling, prior to initial relaxation of the coal structure [23]. In the case of raw coals it was suggested that the stronger the base, the faster the initial swelling. The results of Table 2 show that there is little correlation of activation energy for swelling of raw coals with basicity alone. Butyl- and hexyl-amines are stronger bases than is pyridine, which is stronger than THF. Recently, this issue was addressed in another similar study with alkyl amines, in which it was shown that activation energy increases with the size of the amine [24], as is seen also in Table 2. The conclusion that both size and electron donor strength need to be considered in predicting activation energies is supported by the present results. The present results, however, suggest that the shape of the molecule has an enormous influence, as the much weaker electron donor THF exhibits an activation energy intermediate between the much larger and stronger bases butylamine and hexylamine. It should be recalled that despite this, THF swells the coal less and much more slowly than either of the two

bases.

We have earlier shown that this Pittsburgh No. 8 coal can be thermally relaxed by heating to 350°C at 8°C/min [20,21]. We explored the swelling kinetics of samples treated in this manner. The results are also shown in Table 2. These results show that the activation energies for swelling are only slightly decreased by the thermal relaxation and that in pyridine, the ultimate degree of swelling is unaffected, but that the rate is slightly increased. In THF, both the ultimate extent and rate of swelling are significantly increased. These pre-pyrolytic effects are a result of relaxation of the structure. The relaxation does not, however, change the activation energy. This appears to suggest that the activation energies for swelling are determined by a relaxation which is distinct from that which is thermally induced, and from its magnitude, might be speculated to be associated with breaking single hydrogen bonding interactions. Hydrogen bonding interactions have long been known to be a key in determining swelling behavior [e.g.,31]. The range of activation energies observed is in the ranges typically reported for hydrogen bonding in coals [e.g., 32,33].

CONCLUSIONS

The swelling kinetics of several raw coals have been examined in various solvents at various temperatures. These data have been examined in terms of apparent activation energies. Both size and shape of the solvent molecules appear to play a role in determining the values, as does the electron donor strength of the solvent. The overall rates of diffusion were naturally lower, the bigger the solvent. There was generally an enormous variability in diffusional/swelling rates, which did not correlate well with coal rank. In cases in which the swelling was relaxation-controlled, the activation energies for diffusion were of the same order of magnitude as hydrogen bonding interactions.

ACKNOWLEDGEMENTS

We gratefully acknowledge the financial support of this work by the U.S. Department of Energy through Contract DE-AC22-91PC91027 and Grant DE-FG22-90PC90308.

REFERENCES

- 1 Ritger, P.L.; Peppas, N.A. *Fuel*, **1987**, *66*, 1379.
- 2 Ritger, P.L.; Peppas, N.A. *Fuel*, **1987**, *66*, 815.
- 3 Peppas, N.A.; Lucht, L.M., *Chem. Eng. Commun.*, **1985**, *37*, 333.
- 4 Barr-Howell, B.D.; Peppas, N. A.; Winslow, D. *Chem. Eng. Comm.*, **1986**, *43*, 301.
- 5 Olivares, J.M.; Peppas, N.A. *Prepr. Pap.- Am. Chem. Soc. Div. Fuel Chem.*, **1990**, *35*(2), 292.
- 6 Barr-Howell, B.D.; Howell, J.M.; Peppas, N.A. *Thermochim. Acta*, **1987**, *116*, 153.
- 7 Aida, T.; Squires, T.G. *Prepr. Pap.- Am. Chem. Soc. Div. Fuel Chem.*, **1985**, *30*(1), 95.
- 8 Aida, T.; Fuku, K.; Fujii, M.; Yoshihara, M.; Maeshima, T.; Squites, T.G. *Energy Fuels*, **1991**, *5*, 79.
- 9 Larsen, J.W.; Lee, D. *Fuel*, **1983**, *62*, 1351.
- 10 Hsieh, S.T.; Duda, J.L. *Fuel*, **1987**, *66*, 170.
- 11 Brenner, D.; Hagan, P.S. *Prepr. Pap.- Am. Chem. Soc. Div. Fuel Chem.*, **1985**, *30*(1), 71, also Brenner, in same volume, p83.
- 12 Maturro, M.G.; Liotta, R.; Isaacs, J.J. *J. Org. Chem.*, **1985**, *50*, 5560.
- 13 Green, T.K.; Kovac, J.; Brenner, D.; Larsen, J.W., *Coal Structure*, R. Meyers, Ed., **1982**, Academic Press, Chapter 6.
- 14 Green, T.K.; Ball, J.E.; Konkright, K. *Energy Fuels*, **1991**, 609.
- 15 Hall, P.J.; Thomas, K.M.; Marsh, H., *Fuel*, **1992**, *72*, 1271.
- 16 Cody, G.D.; Botto, R.E. *Energy Fuels*, **1993**, *7*, 561.
- 17 Otake, Y.; Suuberg, E.M. *Fuel*, **1989**, *68*, 1609.
- 18 Otake, Y.; Suuberg, E.M. *Proc. 1989 Int. Conf. Coal Sci.*, Vol. I, **1989**, I.E.A., p 17.
- 19 Suuberg, E.M.; Otake, Y.; Yun, Y.; Deevi, S.C. *Energy Fuels*, **1993**, *7*, 384.
- 20 Yun, Y.; Suuberg, E.M. *Energy and Fuels*, **1992**, *6*, 328.
- 21 Yun, Y.; Suuberg, E.M. *Fuel*, **1993**, *72*, 1245.
- 22 Cody, G.D.; French, D.C.; Botto, R.E. *Prepr. Pap.- Am. Chem. Soc. Div. Fuel Chem.*, **1994**, *39*(1), 59.
- 23 Ndaji, F.E.; Thomas, K.M. *Fuel*, **1993**, *72*, 1525 and 1531.
- 24 Ndaji, F.E.; Thomas, K.M. *Fuel*, **1995**, *74*, 842.
- 25 Suuberg, E.M.; Otake, Y.; Langner, M.; Leung, K.T.; Milosavljevic, I. *Energy Fuels*,

- 1994, 8, 1247.
 26 Nelson, J.R.; Mahajan, O.P.; Walker, P.L., Jr. *Fuel*, **1980**, 59, 831.
 27 Nelson, J.R. *Fuel*, **1983**, 62, 112.
 28 Vorres, K. *Energy Fuels*, **1990**, 4, 420.
 29 Cody, G.D.; Eser, S.; Hatcher, P.G.; Davis, A.; Sobkowiak, M.; Shenoy, S.; Painter, P.C. *Energy Fuels*, **1992**, 6, 716.
 30 Alfrey, T.; Gurnee, E.F.; Lloyd, W.G. *J. Poly. Sci.*, **1966**, C2, 249.
 31 Larsen, J.W.; Green, T.K.; Kovac, J. *J. Org. Chem.*, **1985**, 50, 4729.
 32 Glass, A.S.; Larsen, J.W. *Energy Fuels*, **1994**, 8, 284.
 33 Miura, K.; Mae, K.; Takebe, S.; Wakiyasu, H.; Hashimoto, K. *Ener. Fuels*, **1994**, 8, 874.

Table 1- Summary of Swelling Results on Argonne Premium Coal Samples in Pyridine

Coal	Q_{∞}	$T(^{\circ}\text{C})$	$t_{50}(\text{min.})$	n	$k \cdot 10^3$	$E(\text{kJ/mol})$
Beulah-Zap Lignite	2.33	25.8	230.0	0.67	12.7	51.1
		45.8	35.5	0.70	40.2	
		59.5	11.3	0.72	87.8	
Wyodak Subbit.*	2.42	11.9	47.0	0.65	41.5	36.8
		24.2	12.8	0.77	72.8	
		42.1	5.1	0.47	231.4	
Illinois No. 6 hvb*	2.23	11.9	4.5	0.53	206.9	20.1
		24.0	1.7	0.43	378.6	
		44.7	0.7	0.50	588.0	
Blind Canyon hvb*	2.22	11.9	92.0	0.76	16.2	44.9
		24.3	30.0	0.70	47.1	
		42.1	7.3	0.67	129.4	
Lewiston - Stockton hvb	1.94	20.0	41.0	0.67	40.2	37.3
		40.7	9.4	0.77	92.6	
		50.9	5.3	0.70	151.1	
Pitts. No. 8 hvb	2.14	11.7	90.0	1.04	5.0	51.9
		24.1	30.5	0.81	30.1	
		41.0	8.5	0.68	113.4	

* Particle size: 212-300 μm .

Table 2. Swelling of Pittsburgh No. 8 Coal in Various Solvents

Solvent	Q_{∞}	$T(^{\circ}\text{C})$	$t_{50}(\text{min.})$	n	$k \cdot 10^3$	$E(\text{kJ/mol})$
Pyridine (80.9)*	2.14	11.7	90.0	1.04	5.0	51.9
		24.1	30.5	0.81	30.1	
		41.0	8.5	0.68	113.4	
Butylamine (98.8)*	1.93	25.3	16.2	0.82	36.6	22.2
		35.5	10.5	0.90	43.1	
		46.7	8.1	0.85	58.8	
Hexylamine (132.1)*	2.28	25.3	117.0	1.09	2.6	55.0
		35.5	62.0	1.31	2.3	
		46.7	35.2	1.23	6.4	
THF (81.0)*	1.41	24.2	143.0	0.92	5.6	39.3
		34.9	80.0	0.94	8.7	
Pyridine (Heat Treated) ^o	2.18	15.5	35.0	0.79	32.2	48.3
		24.1	15.4	0.94	39.0	
THF (Heat Treated) ^o	1.76	19.1	16.2	0.67	96.1	38.5
		24.2	8.9	0.86	81.1	
		34.9	4.6	ND	ND	
		40.0	3.0	ND	ND	

* Molar volume of solvent, in cc/mol

^o Samples heat treated at 8 $^{\circ}\text{C}/\text{min}$ to 350 $^{\circ}\text{C}$, then quenched

RECENT ADVANCES IN MAGNETIC RESONANCE MICROSCOPY TO THE PHYSICAL STRUCTURE CHARACTERIZATION OF CARBONACEOUS AND INORGANIC MATERIALS**

D. M. Gregory, R. E. Gerald, G. D. Cody and R. E. Botto
Chemistry Division
Argonne National Laboratory
9700 South Cass Avenue, Argonne, IL 60439

Abstract

Magnetic resonance microscopy (MRM) techniques have been employed to study the molecular architectures and properties of structural polymers, fossil fuels, microporous carbons and inorganic catalysts.

Keywords: solid state NMR, imaging, microscopy, materials

INTRODUCTION

In recent years, the field of magnetic resonance microscopy (MRM) has been advanced by the introduction of several new experimental techniques for the study of materials [1]. Our research has focused on specific methods that facilitate proton MRM of rigid solids, by utilizing proton multipulse line-narrowing in the presence of high gradient fields [2]. We have also developed new chemical-shift imaging strategies, which have been devised to highlight specific chemistries. We have used these techniques to investigate molecular transport of solvents and gases within polymers, catalysts and coals. Time-sequenced imaging of solvent uptake within macromolecular solids have been used to differentiate between Fickian and anomalous, or Case II, transport processes, analytical solutions to which form the basis of a model yielding information on the nature of transport in these systems, and ultimately, on their molecular architecture [3]. Current research in our laboratory is focussed on MRM to monitor porosities, pore-size distributions and diffusivities of methane and other gases in inorganic catalysts and high surface-area carbons.

In this paper, we highlight three recent developments in our laboratory: Applications to the areas of porosity measurements and the characterization of polymeric materials will be presented.

EXPERIMENTAL

Samples

A porous ceramic catalyst sphere (brand X) approximately 1.6 mm in diameter was prepared by immersing in water for several hours prior to the imaging experiment. The treated sample was then placed in a sealed teflon tube for imaging; the specimen contained 3.2 mg of water or the equivalent of about 10^{20} proton spins. The polymethylsilicone rubber sample was rectangular with initial dimensions of 2 x 2 x 1 mm, and the upper and lower sample surfaces protected from solvent infiltration by glass cover slips.

For chemical-shift imaging experiments, a test phantom was assembled from two concentric tubes: a 5-mm NMR tube was placed inside a 10-mm NMR tube. The inner tube contained acetone ($^1\text{H} \delta_B = 2.1$ ppm) and the annular region contained chloroform ($^1\text{H} \delta_A = 7.3$ ppm). A small amount of relaxation agent added to each solvent reduced the spin-lattice relaxation times by approximately one order of magnitude. The values of τ_{null}^A and τ_{null}^B were determined in a separate experiment by the inversion recovery method and found to be 35 and 50 ms, respectively.

MRM System and Experimentation

The MRM experiments were implemented on a portable, home-built Tecmag system operating at a proton Larmor frequency of 100.2 MHz. The system is capable of operating at frequencies between 50 and 400 MHz. Spectrometer control and data processing were executed by the software program MacNMR operating on a Macintosh Quadra 950 host computer.

The imaging probe having an outside diameter of 70 mm was constructed to fit within the room temperature shim stack of a wide-bore (89-mm) 2.35 T superconducting magnet, and could accommodate samples up to 28-mm in diameter. The design included rf coils for excitation and detection of the nuclear signals, and a set of gradient coils to create orthogonal gradient fields with respect to the three spatial coordinates. To maximize the filling factor of the rf coil and allow for different samples shapes, various coil and resonating structures ranging in diameter from 3-mm to 25-mm were interfaced to the probe. The probe was force-air cooled and was capable of operating with duty cycles in excess of 20% while producing a highly linear magnetic field gradient of up to 58 G/cm over a volume 30 mm in diameter.

MRM experiments were performed on the spherical catalyst specimen using 256 complex data points and a total of 3600 projections (30 θ angles over $\pi/2$ radians \times 120 ϕ angles over 2π radians). A gradient field of 25 G/cm and a sweep width of 60 kHz were employed. A total of 16 scans were collected for each projection using a 90°-pulse width (4- μ s duration) and a recycle delay time of 1 s, resulting in a total acquisition time of 16 hr.

In order to obtain sufficiently high quality images on the polymethylsilicone rubber specimen, it was necessary to acquire 32 (128 point) transients with a recycle delay of 500 ms for each of 128 phase-encoded gradient positions using a standard imaging spin-echo pulse sequence. This yielded a resolution on the order of 70 μ m, which was obtained over intervals of approximately 30 min. Typically a 64-kHz spectral width was chosen, establishing an echo time of 0.5 ms. Signal-to-noise improvement for the series of phase encoded echos was accomplished by apodization using a biexponential weighting function developed within the Macro subroutine of MacNMR.

RESULTS AND DISCUSSION

Determination of Porosity of Catalysts

In the first application, we have explored the potential of MRM to further the development of advanced formed absorbents and heterogeneous catalyst materials. Formed absorbents and catalyst systems on porous oxide supports are currently in use and are continually being improved in applications involving the production of upgraded hydrocarbon fuels or specialty chemicals. A detailed knowledge of the spatial distribution of the pore network is essential to the evaluation and improvement of catalyst and absorbent performance. MRM, utilizing filler fluids, offers the potential of spatially mapping the porosity of a variety of porous media. With application to spent catalysts, imaging techniques can be utilized to study the chemistry of catalyst coking, and has the ability to detect the spatial distributions of coke and other agglomerates in the pore matrix.

Figure 1 shows sequential 3D surface-rendered images with 20- μ m thick 2D slices displayed of internal portions throughout the catalyst sphere. The MRM experiment required a total of 3600 projections, or about 16 hr. for data acquisition. In this manner, an image resolution of 20 μ m was attained in each of the three spatial dimensions. Some thirty-two 2D image projections of proton spin density (where spin density scales linearly with image brightness) were used to provide estimates of total porosity and spatial distributions of pores throughout the specimen.

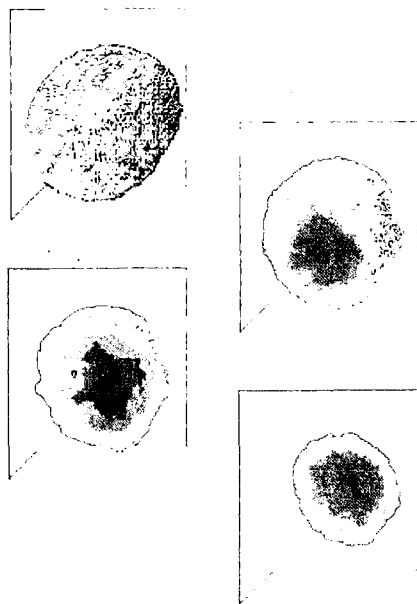


Figure 1. Three-dimensional MRM images of catalyst sphere.

Performing MRM experiments on the catalyst sphere presents the opportunity to discuss the limits of resolution in image reconstruction, on a sample for which the spectral resolution of individual projections is very high ($< 1 \mu\text{m}$) because of its inherently narrow proton linewidth. For example, given our catalyst sample of maximum radius equal to 0.8 mm (a diameter of 1.6 mm), the total number of projections required to obtain an image having a resolution of $20 \mu\text{m}$ is calculated to be 10,953. If lower resolution can be tolerated in the resultant images, the number of projections becomes even more reasonable. In order to achieve a resolution of $40 \mu\text{m}$, for example, the number of projections required is only 3,943. In practice, these numbers can be reduced by a factor of two or three if one employs significant filtering in the reconstruction algorithm. Thus, acquiring 3600 projections for our catalyst specimen is sufficient to achieve the desired resolution provided that appropriate filtering is applied. Finding that an adequate SNR ratio for each projection can be attained in 16 acquisitions employing a 1 s pulse repetition time translates into a total experimental averaging time of about 16 hr.

^{19}F MRM of Solvent Transport In Rubbers

Significant insight into the character of solvent transport has been obtained through time-resolved, ^{19}F NMR imaging of solvent concentration and network dilation changes that occur during solvent uptake within rubbery polymer networks. Complications found in proton NMR imaging experiments, because contributions to the signal intensity can arise from both the protons of the solvent and protons of the mobile polymer backbone, can be averted using fluorinated solvents. In the present study, ^{19}F imaging has been employed to investigate Fickian transport of hexafluorobenzene within a specimen of polymethylsilicone (PMS) rubber.

Sequential 2D ^{19}F images of a specimen of PMS swelling in hexafluorobenzene, observed at early (top), intermediate (middle) and advanced (bottom) solvent diffusion times are shown in Figure 2. Clearly evident is the smooth, exponential, solvent gradients directed into the core of the sample, indicating a Fickian transport mechanism.

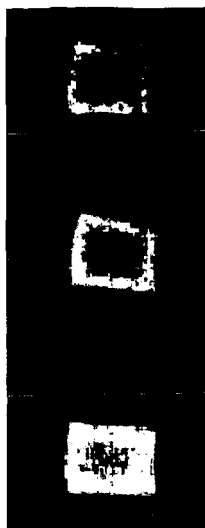


Figure 2. Sequential ^{19}F images of hexafluorobenzene transport in polymethylsilicone.

The measured front velocities from MRM provide a valuable and quantitative constraint for the parameterization of the uptake data. Direct measurement of linear dilation accompanying swelling is a simple means to quantify the overall swelling behavior of rubbery networks. Linear dilation behavior for PMS was consistent with Fickian transport in rubbery networks. Given the uptake data, it was trivial to derive a mass-fixed diffusion coefficient through linear fitting of the experimental data. The generation of a curve for Fickian transport, in the present case, requires solving the two-dimensional diffusion equation and integrating this solution with respect to time. Fitting of the dilation data results in values of $D_R = 1.1 \times 10^{-6} \text{ cm}^2/\text{s}$ for PMS-hexafluorobenzene. These relatively large values of D_R reflect the high degree of inter- and intra-molecular mobility of the network, which explains the rapidity with which the rubbery systems respond to applied stresses that are osmotic in nature.

Chemical-Shift MRM of Binary Systems

In this last section, we present a new method for chemical-shift selective MRM, selective-echo chemical-shift imaging (SECSI), which is easily implemented and can be executed in a short time period ($<1 \text{ ms}$). The SECSI pulse sequence is designed to select the magnetization from one of two chemical species. Subsequently, this magnetization is used to form a spin-echo in the conventional manner. The magnetization of the second chemical species is initially placed antiparallel to the Zeeman field and is then allowed to decay to zero via T_1 relaxation; therefore, it does not contribute

to the spin-echo. In the simplest case, each chemical species is represented by a single NMR resonance; however, a cluster of closely spaced resonances for each species is also suitable for NMR imaging by the SECSI method. The full Boltzmann magnetization is used for imaging either chemical species; this approach presents an advantage over many other pulse methods. Both chemical species can have any value for T_1 and concentration. Additionally, the method employs only hard pulses of quadrature phase and is easily implemented using standard spectrometer hardware.

The SECSI pulse sequence is a *chemical-shift filter* consisting of two 90° pulses and two delays $(90^\circ_x - \tau_{\text{antiphase}} - 90^\circ_x - \tau_{\text{null}})$ and is executed prior to a standard spin-echo imaging sequence [4]. The RF transmitter is centered on one of the NMR resonances of a two-component system A and B where $\delta_A > \delta_B$. In a reference frame rotating (clockwise) at ω_A (component A on resonance), the magnetization vector for the A spins is stationary, while the magnetization vector for the B spins precesses (counterclockwise) at $\omega_A - \omega_B$. The initial 90°_x pulse tips the magnetization of both components on to the $+y$ axis in the xy -plane. An antiphase period, $\tau_{\text{antiphase}}$, equal to $\pi/(\omega_A - \omega_B)$ is allowed to elapse such that the magnetization vectors from both components become mutually out of phase by 180° . The second pulse, 90°_{-x} , restores the Boltzmann magnetization of component A along the $+z$ axis while inverting the spin population of component B . After an inversion recovery delay, τ_{null}^B , equal to $\ln 2 T_1^B$, the only net z magnetization remaining is that of component A (restored along the $+z$ axis following the second RF pulse). At this point a standard 2D spin-echo imaging pulse sequence is executed, which yields the chemical-shift selective image of component A . The complementary image, the chemical-shift selective image of component B , is obtained by placing component B on resonance and repeating the pulse sequence. The antiphase period remains the same, however, the inversion recovery delay in this case is set to τ_{null}^A , given by $\ln 2 T_1^A$.

The antiphase period, $\tau_{\text{antiphase}}$, defines the duration of the transverse spin evolution within the pulse sequence and, therefore, the time during which T_2^* processes play a role in diminishing the final signal intensity. A general expression for the antiphase period is given by

$$\tau_{\text{antiphase}} = \frac{\pi \times 10^6}{\Delta \gamma_N B_0} \quad [1]$$

where Δ is the separation between the two resonances in parts per million ($\Delta = \delta_A - \delta_B$), γ_N is the gyromagnetic ratio of the nuclear spins ($2.67506 \times 10^8 \text{ rad T}^{-1} \cdot \text{s}^{-1}$ for ^1H), and B_0 is the external magnetic field strength. The antiphase period decreases monotonically for higher field strengths. For systems in which the bandwidths of the resonances are inhomogeneously broadened, the inversion recovery delay following the antiphase period serves a second purpose. Following the second RF pulse, any off-resonance contribution to the magnetization of the species returned to the $+z$ axis will not have been returned completely to the Boltzmann equilibrium position. Therefore, during the inversion recovery delay this off-resonance magnetization recovers towards Boltzmann equilibrium. This added feature of the pulse sequence compensates for effects of the antiphase period, during which the net magnetization may be reduced by the inhomogeneity of the magnetic field, a dispersion of chemical shifts, and spin-spin relaxation.

Figure 3 represents a proton 2D NMR image of the phantom that was acquired by using the conventional spin-echo imaging technique. The central region of this image appears brighter because of the greater concentration of protons in acetone; the proton concentration ratio is 6.54 : 1.00 for acetone vs. chloroform. Although the large difference in proton concentrations provides substantial contrast between the two solutions, one cannot determine from the image alone which regions represent chloroform or acetone *a priori*. The SECSI method was used to selectively image the protons of acetone at $^1\text{H}\delta_b = 2.1$ ppm (Fig. 3b) and the protons of chloroform at $^1\text{H}\delta_a = 7.3$ ppm (Fig. 3c). In images 3b and 3c there is no ambiguity as to what the bright regions represent, and no inference is necessary to describe the spatial distribution of either chemical species. Furthermore, note the large dynamic range obtained for suppressing the image intensity of the unwanted magnetization.

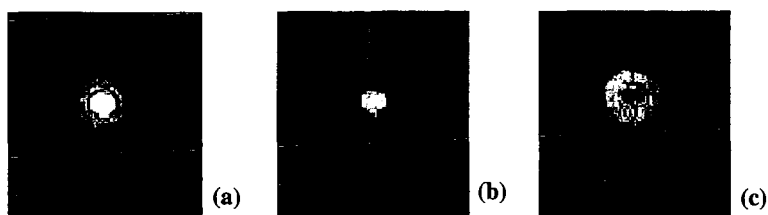


Figure 3. Proton MRM images of acetone-chloroform phantom: (a) conventional 2D spin-echo image; (b) chemical-shift selective image of acetone in the 5 mm NMR tube; (c) chemical-shift selective image of chloroform in the annular region between the 5 and 10 mm NMR tubes.

For systems containing three NMR resonances, representing different chemical species, the SECSI sequence may be applied sequentially to preferentially select one of the chemical species for imaging. The method requires phase cycling to cancel interfering transverse magnetization and can only be executed optimally for certain ratios of the T_1 's. Simultaneous selective excitation and subsequent imaging of two groups of resonances in a complex ^{19}F NMR spectrum was effectively demonstrated by Börnert and coworkers [5]. For the ubiquitous cases of water/fat or water/oil systems the SECSI technique offers simplicity, fast execution, and the highest sensitivity.

ACKNOWLEDGMENT

This work was performed under the auspices of the Office of Basic Energy Sciences, Division of Chemical Sciences, U. S. Department of Energy, under Contract No. W-31-109-ENG-38.

REFERENCES

1. "MRI of Materials", R. E. Botto, Ed., *Solid State NMR*, **6**, No. 4 (1996).
2. S. L. Dieckman, P. Rizo, N. Gopalsami, J. P. Heeschen and R. E. Botto, *J. Am. Chem. Soc.*, **114**, 2717 (1992).
3. G. C. Cody and R. E. Botto, *Energy Fuels*, **7**, 561 (1993).
4. S. L. Talagala and I. J. Lowe, *Concepts Magn. Reson.* **3**, 145-159 (1991).
5. P. Börnert, W. Dreher, A. Gössler, G. Klee, R. Peter, and W. Schneider, *J. Magn. Reson.* **81**, 167-172 (1989).

CHANGE IN THE ASSOCIATED MOLECULAR STRUCTURE OF COALS IN PYRIDINE/CS₂ MIXED SOLVENTS.

H.Kumagai, K.Matuoka, K.Norinaga T.Chiba,
Center for Advanced Research of Energy Technology, Hokkaido
University,
Kita-ku, Sapporo 060, Japan,

M.Sasaki,
Hokkaido National Industrial Research Institute,
Toyohira-ku, Sapporo 062, Japan

Keywords:Swelling, noncovalent interactions, Mixed solvent

ABSTRACT

In order to evaluate noncovalent interactions in coal, change in the associated molecular structure of coals in pyridine/CS₂ mixed solvents have been investigated. For bituminous coal, variation in L-band EPR spectra with mixing ratio of the solvents is in a close correspondence to that in equilibrium swelling ratio and in molecular mobility obtained from ¹H-NMR. The EPR spectra for lignite show similar variation to that for bituminous coal, however, does not correlate with equilibrium swelling ratio and molecular mobility. Since the L-band EPR characteristics appear to reflect the situation of aromatic π - π and charge transfer interactions in coal, these results indicate that swelling in the mixed solvents proceed with the declining of non-covalent interaction, such as aromatic π - π and charge transfer interaction, in coal.

INTRODUCTION

The chemical and physical properties of coal are affected not only with the chemical structure of coal molecules, but also with the associated molecular structure. Coal is believed to be complex macromolecular compounds containing several types of noncovalent interactions, such as hydrogen bonding, van der Waals, charge transfer and aromatic π - π interaction. The type and strength of noncovalent interactions existing in coal have been postulated to govern the associated molecular structure. Since the noncovalent interactions play an important role in the physical and chemical properties of coal, it has become of general interest in recent years.

Larsen and Kovac [1,2] have proposed two components (phase) coal structure model, in which coal consists of two components, i.e., a covalently cross-linked macromolecular network component (MM phase) and a low molecular weight component (M phase) trapped noncovalently inside the network. Based on the two components coal structure model, Marzec and co-worker [3,4] have attempted to elucidate the extraction mechanism of bituminous coal with electron-donor-acceptor interaction between M phase in the coal and solvents. The contribution of noncovalent interactions to cross-linked structure was also suggested from coal swelling and extraction studies [5,6]. While, it was argued that such noncovalent interactions are too weak to from and stabilize the cross-linking structure which affects swelling behaviour of coal [7].

Mixed solvent systems, such as NMP/CS₂ and pyridine/CS₂, have a high potential to get large amount of extracts from many bituminous coals at room temperature [8,9]. Iino and Takanohashi have indicated that no significant reaction between coal and the solvent, which results in an increase of the extraction yields, occur for this extraction [8]. In spite of the extensive studies of swelling and extractability of coal with the mixed solvent systems [10-12], the mechanism of coal extraction and swelling with the mixed solvent systems has not been clarified in detail.

In this paper, in order to evaluate the effects of noncovalent interactions on the associated molecular structure of coals, swelling behaviour of coals in the mixed solvents has been investigated by means of ¹H-NMR relaxation time and L-band EPR spectroscopy. EPR spectroscopy is one of the useful techniques to investigate noncovalent interactions such as aromatic π - π and charge transfer interaction. X-band EPR is, however, not allowed to measure the spectrum of sample in solvents with high permittivity. Thus, we have attempted to build L-band EPR from which favorable results are provided. Measurement L-band EPR for swelling and extraction of coal

may bring deep information about noncovalent interaction in coals.

EXPERIMENTAL SECTION

Coal Samples and Reagents.

Upper Freeport bituminous coal (UF) and Beulah Zap lignite (BZ) were selected from Argonne Premium coal samples and used in this study. Pyridine-d5 and CS2 (G.R. grade) for solvent were used without further purification.

Sample Preparation.

Coal sample was dried under a vacuum at 40°C for 24 hours. The dried coal sample was placed in glass sample tube (10mm o.d.). The initial height (h1) of the coal particle bed was measured by a caliper. The mixed solvent was then poured into the sample tube. The coal suspension was standing for 7 days under nitrogen atmosphere. Swollen coal bed height (h2) was measured prior to the EPR and NMR measurement. Equilibrium swelling ratio was expressed as the ratio of h2 and h1.

¹H-NMR Measurement.

Spin-spin relaxation time (T_2) of the swollen coal sample was measured with JEOL JNM-Mu25 spectrometer (25MHz) employing solid-echo ($90^\circ\text{x}-\tau-90^\circ\text{y}$) pulse sequence at 20°C under nitrogen atmosphere.

L-band EPR Measurement.

L-band EPR spectra were monitored with a Varian E-109 EPR spectrometer equipped with Micro Device Co.Ltd. MWG-2L L-band microwave bridge and MSC-2LG loop-gap resonator. In order to get the high signal sensitivity, 10mm (o.d.) sample tube was used. The effective portion of sample tube to be irradiated with microwave is 22mm. L-band EPR measurement was carried out at 20°C under nitrogen atmosphere. Spectral intensities of coals in the mixed solvents were corrected by the effects of dielectric characteristics (permittivity) of solvents and density decrease of coal particles due to swelling.

RESULTS AND DISCUSSION

Equilibrium Swelling Ratio

The equilibrium swelling ratio of UF and BZ in the mixed solvents are shown in Figure 1 and 2 as a function of mixing ratio of pyridine and CS₂ (pyridine vol%). The swelling ratio of UF increases with the fraction of pyridine and reaches a maximum value at about 50vol% pyridine. Then, the swelling ratio decreases with the increase in pyridine vol%. For BZ, the swelling ratio increases with increase in pyridine vol%, and show maximum value at about 80-100vol% pyridine. These results suggest that the swelling characteristics, i.e., change in the equilibrium swelling ratio with mixing ratio, is dependent on the chemical and associated structure of coal molecules. Since the swelling of coal in polar solvents is results from declining of noncovalent interactions in coal [13], the difference of the swelling characteristics with mixing ratio of the solvent appear to be reflecting the type and strength of noncovalent interactions existing in the coals.

¹H-NMR Relaxation Time.

The solid-echo signals obtained from coal in the mixed solvents contained two components, namely the relatively slowly relaxing tail of the signals and rapidly decaying signals. The former can be attributed to the hydrogen in mobile molecular structures, and later can be attributed to the hydrogen in rigid-like (immobile) molecular structure. The variations of T_2 values for two components of UF and BZ are plotted as a function of pyridine vol% in Figure 3 and 4, respectively. For UF, T_2 for mobile structures (T_{2m}) increases with increase in pyridine vol% in the mixed solvent and reaches a maximum value at about 50vol% pyridine. T_2 for immobile structures (T_{2im}) remains almost constant value with increase in pyridine vol%. The T_{2m} for BZ increases monotonously with increase in pyridine vol%.

The separation of the solid-echo signals permits hydrogen-weighted mobile and immobile fractions of the molecular structure in coal. The distribution of the mobile and immobile fractions for UF and BZ are shown in Figure 5 and 6. Variations in the fraction of mobile components for both UF and BZ are well correlated with the variation of T_{2m} . The ¹H-NMR relaxation characteristics described above are in a close correspondence with swelling characteristics. The spin-spin relaxation time and the fraction of mobile components

vary in proportion to equilibrium swelling ratio. The enhancement of molecular mobility due to solvent induced swelling may result the ¹H-NMR relaxation characteristics.

L-band EPR spectroscopy.

The intensity of EPR spectra for UF coal decrease with increase in the mixing ratio of pyridine. It is noted that the intensities decrease at the mixing ratio from 0 to 50% and reach a minimum in the vicinity of 50 vol% of pyridine. The EPR characteristics for UF in the mixed solvents reflect the swelling behaviour of coal. For BZ, the characteristics are almost similar to those of UF, but independent of the swelling behaviour.

The EPR spectra for UF and BZ consist two components, one broad (BC) and one narrow (NC) components. Variations in the components with pyridine vol% in the mixed solvents are shown in Figure 7 and 8. It can be clearly seen that the narrow components for both UF and BZ do not change with pyridine vol%, while the broad components show minimum values at pyridine 50vol%. With EPR spectroscopy, not only stable free radical, but also the sifted and transferred electrons can be detected. The swelling in the mixed solvents proceed without significant reaction between coal and the solvents [8]. Therefore, variation in the intensities for BC might be due to disappearance of the sifted and transferred electrons result from declining of noncovalent interactions, such as aromatic π - π and charge transfer interactions.

CONCLUSIONS

1. L-band EPR characteristics are considered to have a close relation to the aromatic π - π and charge transfer interaction in coals.
2. The molecular mobility of coals obtained from ¹H-NMR vary in proportion to swelling behaviours.
3. For UF, L-band EPR characteristics are well correlated with swelling behaviour and molecular mobility, indicating that the associated structure of UF is affected strongly with the aromatic π - π and charge transfer interactions.
4. For BZ, the characteristics are almost similar to those of UF, and independent of the swelling behaviour and molecular mobility. These facts indicate that the interaction is much less effective for the associated structure of BZ than that for UF.

REFERENCE

- (1) Larsen, J.M.; Kovac, J. In *Organic Chemistry of Coal*; Larsen, J.W., Eds.; ACS Symposium Series 71; American Chemical Society: Washington, DC, 1981; 43
- (2) Kovac, J.; Larsen, J.W. *Prepr. Am. Chem. Soc., Div. Fuel Chem.* 1975, 20(2), 122
- (3) Marzec, A.; Juzwa, M.; Betlej, K.; Sobkowiak, M. *Fuel Processing Technology* 1979, 2, 35
- (4) Marzec, A. *Proc. Symposium on Chemistry of Coal Liquefaction and Catalyst*; Hokkaido Univ.: Sapporo, Japan, 1985, 42
- (5) Nishioka, M. *Fuel* 1972, 71, 941
- (6) Fujikawa, M.; Ohsuga, H.; Takanohashi, T.; Iino, M. *Energy Fuels* 1992, 6, 859
- (7) Painter, P. *Energy & Fuels* 1992, 6, 863
- (8) Iino, M.; Takanohashi, T.; Ohsuga, H.; Toda, K. *Fuel* 1988, 67, 1639
- (9) Iino, M.; Takanohashi, T.; Ohsuga, H.; Tsueta, H.; Sanokawa, Y. *Fuel* 1989, 68, 1588
- (10) Ishizuka, T.; Takanohashi, T.; Ito, O.; Iino, M. *Fuel* 1993, 72, 579
- (11) Liu, H.-T.; Ishizuka, T.; Takanohashi, T.; Iino, M. *Energy Fuels* 1993, 7, 1108
- (12) Yun, Y.; Suuberg, E.M. *Fuel* 1993, 72, 1245
- (13) Larsen, J.W.; Green, T.K.; Kovac, J. *J. Org. Chem.* 1985, 50, 4729-4735

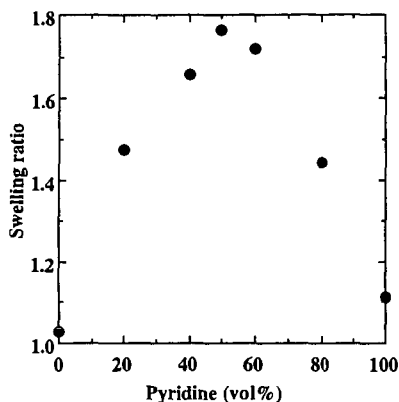


Figure 1. Change in equilibrium swelling ratio for UF with pyridine vol.% in mixed solvent

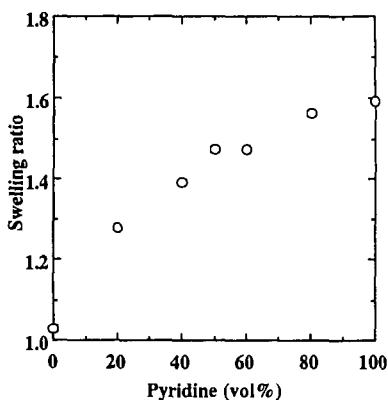


Figure 2. Change in equilibrium swelling ratio for BZ with pyridine vol.% in mixed solvent

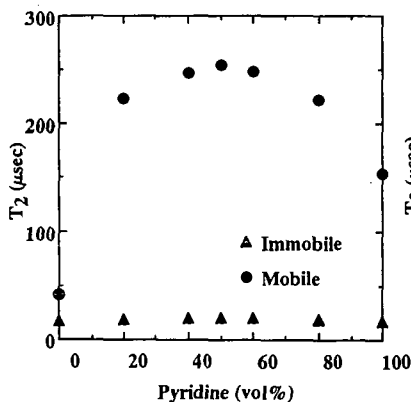


Figure 3. Effects of pyridine vol% in mixed solvent on spin-spin relaxation time, T_2 , for UF

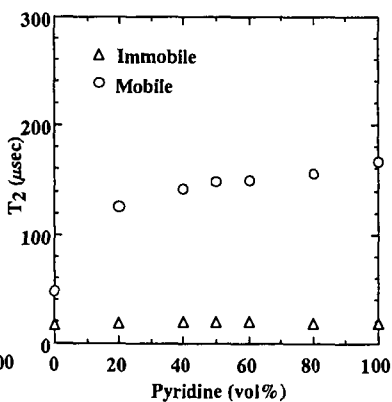


Figure 4. Effects of pyridine vol% in mixed solvent on spin-spin relaxation time, T_2 , for BZ

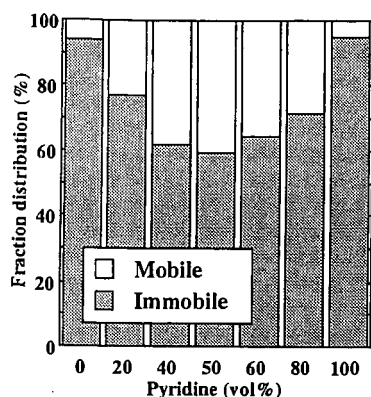


Figure 5. Distribution of mobil and immobile fractions for UF in mixed solvent

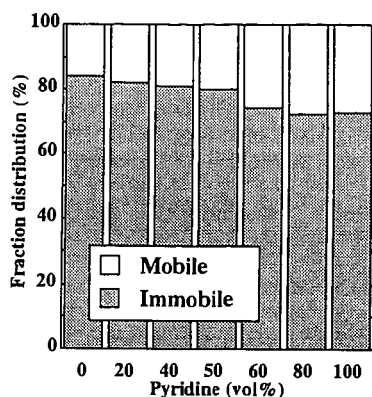


Figure 6. Distribution of mobil and immobile fractions for BZ in mixed solvent

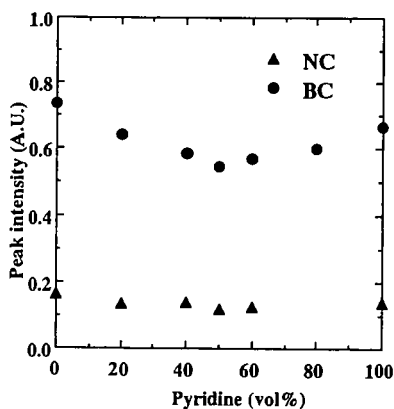


Figure 7. Change in the peak intensity of NC and BC for UF with pyridine vol% in mixed solvent

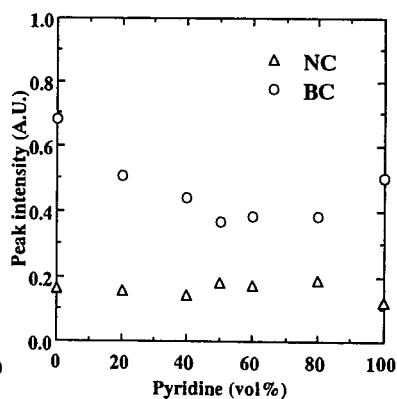


Figure 8. Change in the peak intensity of NC and BC for BZ with pyridine vol% in mixed solvent

INVESTIGATION OF THE POROUS STRUCTURE OF COAL USING ^{129}Xe NMR WITH SELECTIVE PRESATURATION AND SATURATION TRANSFER.

Stasia A. Anderson¹, Patrick G. Hatcher², Ljubisa R. Radovic² and Alan J. Benesi*¹

¹Pennsylvania State University, Department of Chemistry, University Park, PA

²Pennsylvania State University, Department of Materials Science and Engineering
Fuel Science Division, University Park, PA

Keywords: ^{129}Xe NMR, low power presaturation, saturation transfer, coal porosity, microporosity.

ABSTRACT

The technique of selective low power presaturation applied to ^{129}Xe NMR of xenon adsorbed in coal can clearly demonstrate the existence of a distribution of similar adsorption sites for xenon, where the signals from xenon in these sites are not resolved as individual signals. Differences in inter/extra particle exchange in two coals of different rank, available from a saturation transfer technique, are significant. This technique can be used to investigate pore connectivity in microporous materials of unknown pore structure.

INTRODUCTION

Coal Microporosity. Coal microporosity accounts for most of its surface area. The largely amorphous physical structure of many coals, and the small dimensions of micropores (<20 Å), have made accurate assessment of the dimensions, size distribution, and connectivity of microporous networks in coal very difficult. Techniques such as SAXS (Bale et al., 1984; Lin et al., 1978; Larsen et al., 1995), X-ray diffraction (Hirsch, 1954), TEM (Lin et al., 1978; Harris and Yust 1976; 1981), gas adsorption (reviewed by Walker, 1981; Larsen et al., 1995), and others have all contributed to our understanding of coal porosity but, when applied to the characterization of microporosity, continue to have severe limitations.

There is wide acceptance of the following general model, however: "coals contain an interconnected pore network of high surface area, the slit-shaped pores having constricted openings of molecular dimensions...[and] coals contain both open and closed porosity." (Mahajan, 1991). The question of the extent of open or closed porosity is an area of continuing controversy, the major source of which is the large difference in coal surface area determined by adsorption of gases of similar molecular dimensions, or the molecular sieving effect. There are several critical reviews on the subject (Marsh, 1987; Mahajan, 1991; Walker and Mahajan, 1993). Molecular sieving effects are open to conflicting interpretations in terms of the pore structure of coal. Larsen et al. (1995) contend that the magnitude of the molecular sieving effect, along with the high fractal dimensionality of coal as determined by SAXS, are inconsistent with an interconnected, bottlenecked micropore network model; and that microporosity in coal exists primarily as isolated 'bubbles' in the solid matrix. This is a controversial conclusion; Larsen's results do not eliminate activated diffusion, as opposed to closed porosity, as a cause of molecular sieving according to Walker and Mahajan (1993). This issue is likely to remain unresolved without additional information that does not depend on gas uptake measurements.

Our approach to characterizing coal microporosity uses ^{129}Xe NMR spectroscopy (reviewed by Dybowski et al., 1991). ^{129}Xe NMR offers a way to derive different and more extensive information about xenon gas in its adsorbed state than would be available from classical adsorption experiments. The ^{129}Xe NMR signal contains information about both adsorption-site environment and dynamics of adsorbed xenon. In order to clarify the terminology used in this paper, we will note here that differences in adsorption sites in coal that affect the ^{129}Xe NMR signal chemical shift are size differences among micropores and possibly mesopores. However, given the heterogeneity of coal, it is possible that variations in pore wall chemistry may also affect the chemical shift. We will use the term adsorption site, meaning porosity of different size and/or chemistry, where appropriate. The results presented in this study can be used to address the question of whether the broad NMR signal from xenon adsorbed in coal arises from a distribution of similar adsorption sites and will demonstrate the differences in intra/extra particle exchange in two different pore networks, which can be interpreted in terms of whether the pores are open or closed, and how porosity changes with coal rank.

Theoretical basis of the NMR experiment. ^{129}Xe NMR spectra in this study detect xenon gas adsorbed on or in contact with the solid surface of coal. ^{129}Xe NMR has been previously applied to coal as a possible tool to determine micropore sizes (Wernett et al., 1990; Tsiao and Botto, 1992). The basic NMR concepts employed in this study are selective saturation and saturation transfer, which have widely varied utility in NMR spectroscopy, as reviewed in Freeman (1988). There are several studies that, while not the same as the experiment described here, utilize similar basic concepts. Selective inversion has been used in ^{129}Xe NMR studies to monitor interstage exchange in a zeolite (Larsen et al., 1993; Jameson et al., 1994), to demonstrate that two xenon

populations are coupled (Ripmeester and Ratcliffe, 1993), and to measure diffusion coefficients in polystyrene (Simpson et al., 1995).

In the presaturation experiment we irradiated only a portion of the frequency range covered by the adsorbed xenon signal, using a low power presaturation pulse followed by a high power 90 degree pulse. We are interested in whether and to what extent the irradiation produces saturation of the signal. If saturated, the xenon atoms do not give an NMR signal when the 90 degree pulse is applied. The key ideas used in conceptualizing this experiment are as follows: NMR signals from ^{129}Xe adsorbed in and outside the coal particle are distinguishable; and the possibility that xenon atoms are to some degree mobile means that a xenon atom that is saturated while in one environment can move to another in a given time frame, carrying the saturation with it. (Spin-lattice relaxation is a competitive process.) Possible outcomes of a presaturation experiment are as follows:

(1) The xenon atoms are in distinct internal adsorption sites and are effectively immobile during the time the pulse is applied. In this case we would expect to see a well defined break or a dip in the outline of the adsorbed gas signal in the area where the low power pulse was applied.

(2) The xenon atoms do have distinct internal adsorption sites, but exchange among them during the presaturation time. Here we would expect to see saturation of the adsorbed gas signal, or overall loss of signal intensity, which may be accompanied by a change in the signal shape.

Note that outcomes (1) and (2) are related in that they are only distinguished by the time frame of site to site motion. For example, if the xenon atoms sample all the sites in 100 ms, then in a 10 ms period they are effectively immobile in their adsorption sites. A 10 ms presaturation pulse, assuming it is sufficiently narrow and delivers enough power to cause saturation, would be able to selectively saturate a portion of the overall adsorbed gas signal. A 100 ms pulse, however, should saturate the entire signal. Variation of the time frame of the experiment can identify the transition from one effect of presaturation to another.

(3) Xenon atoms are exchanging both into and out of the particle during the time the sample is presaturated. In this case, we would expect the intensity of both adsorbed and external surface signals to decrease or completely saturate.

(4) The linewidth is not due to a distribution of sites, but to a short T_2 and/or magnetic field inhomogeneity. The signal intensity could be decreased by presaturating the peak maximum, but the shape should remain the same, and presaturating the signal off center should have much less or no effect.

EXPERIMENTAL

Powdered samples of Wyodak subbituminous (subB; 76.3% C) and Sewell medium volatile bituminous (mvb; 88.9% C) coals were obtained from the Penn State/DOE coal sample bank and sieved to 60-100 Tyler mesh particle size. They were dried overnight in 10 mm NMR tubes with rototite valves (Wilmad), heated to 90° C for 2 to 4 hours, then kept under vacuum at room temperature for 24 hours or more. Once dry, the samples were charged with xenon to ~ 1 atm pressure (730-760 torr). Equilibration time was 8-12 hours.

NMR spectra were acquired on a Bruker AMX 360 NMR spectrometer operating at 99.61 MHz. A low power presaturation pulse was applied with the carrier frequency centered on the signal of interest followed by a 90 degree high power pulse and 3 s delay. The low power pulse length was varied as described in the next section. Spectra were run 300 to 1000 scans depending on the individual sample. All sets of spectra for a particular sample were run the same number of scans. Xenon gas at 700 torr was used as an external chemical shift reference.

RESULTS AND DISCUSSION

The ^{129}Xe NMR spectrum of coal and effect of presaturation. The ^{129}Xe NMR spectrum of xenon gas adsorbed on Sewell coal is shown in Figure 1a.

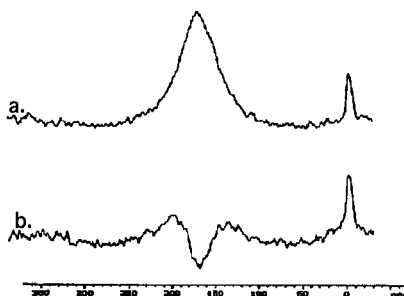


FIGURE 1. ^{129}Xe NMR spectrum of Sewell coal with (a) 80dB presaturation pulse, which has negligible effect and (b) 37 dB presaturation pulse centered at 21870 Hz (approx. 174 ppm).

A presaturation pulse of negligibly low power was applied. The appearance of this spectrum is like that of a ^{129}Xe NMR spectrum of a high rank coal without presaturation. The signal centered at 174 ppm is from xenon adsorbed on the internal surfaces of the coal, and that at 0 ppm is the interparticle or external gas signal. Figure 1b shows the loss of a portion of the signal when a 37 dB presaturation pulse was applied for 0.3 ms at the center of the signal.

Two coals were presaturated on the principal adsorbed xenon signal for increasing lengths of time. The reference spectra for both coal samples are presaturated on the center of the adsorbed gas signal at very low power (80 dB power for 0.1 ms). All subsequent spectra for a given sample were phased relative to the reference.

The Sewell coal was presaturated at 37 dB on the 174 ppm adsorbed xenon signal (21,870 Hz) for increasing times from 0.3 ms to 800 ms. The results are shown in Figure 2. There is a 'hole' in the signal at 0.3 ms accompanied by overall intensity loss. A spectral hole, or the loss of a portion of the adsorbed xenon signal, is evidence that some of the xenon atoms contributing to a broad signal have a resonant frequency close to the applied pulse; some do not, however, hence the residual portions of the signal. This is evidence that the signal is broad due to an overlap of chemical shifts, which in turn indicates that there exist slightly different adsorption sites from which the different xenon chemical shifts arise. At 1 ms the signal is almost saturated. There was no effect on the interparticle gas signal. Upon increasing the pulse length the saturation extends to the remainder of the signal it is focused on, and to the external gas signal. This clearly illustrates the motion of saturated xenon through the solid and out into the interparticle space. At 200 ms, the adsorbed signal in Sewell coal was completely saturated while the interparticle gas signal was less intense. At 400 ms the gas signal intensity decreased noticeably, and at 800 ms it was nearly saturated.

The Wyodak coal was presaturated at 40 dB power at about 150 ppm (20,000 Hz) for increasing times from 1 ms to 40 ms. The results are shown in Figure 3. The spectra show a 'hole' at 1 and 2 ms which is almost saturated at 5 ms. From 1 to 5 ms, the interparticle gas signal at 0 ppm is unchanged. At 10 ms, the adsorbed signal is completely saturated and the interparticle gas signal has some intensity loss. At 30 ms the gas signal is reduced to a little over the noise level, and at 40 ms it is saturated.

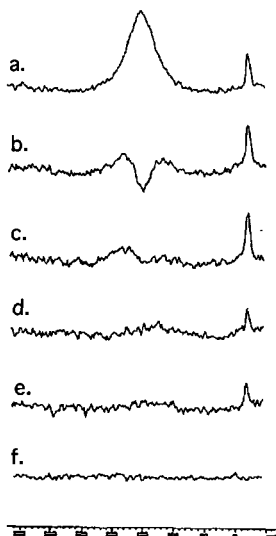


FIGURE 2. Effect of increasing presaturation pulse length on ^{129}Xe NMR spectra of Sewell coal. (a) Reference; (b) 0.3 ms; (c) 1 ms; (d) 200 ms; (e) 400 ms; (f) 800 ms.

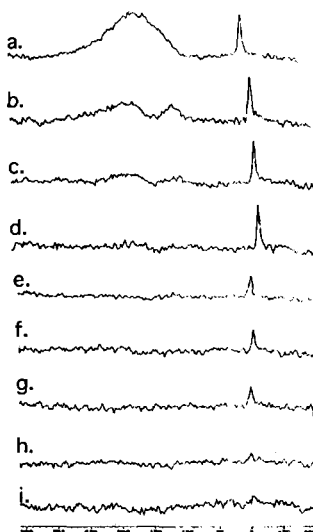


FIGURE 3. Effect of increasing presaturation pulse length on ^{129}Xe NMR spectra of Wyodak coal. (a) Reference; (b) 1 ms; (c) 2 ms; (d) 5 ms; (e) 10 ms; (f) 15 ms; (g) 20 ms; (h) 30 ms; (i) 40 ms.

Implications for the porous structure of the coals. In the Wyodak coal, the adsorbed gas signal survives presaturation longer than the Sewell coal. The longer time for the saturation transfer from the 'hole' effect to saturation of the entire signal is coupled with much shorter time to saturate the external surface signal compared to the Sewell coal. We interpret this as indicating that in the Wyodak coal, it takes a longer time for saturated xenon atoms to exchange among the internal sites and a shorter time for their exchange with gas at the external surface. This indicates that the Wyodak coal has a wider distribution of internal adsorption sites and greater connectivity of the pore network to the outside. The Wyodak coal, at 76.3%C, has meso- as well as microporosity as determined by N₂ and CO₂ adsorption, as is expected based on its rank (Gan et al. 1972). The NMR data in this study is in keeping with the presence of larger pores, in which diffusion of xenon would be faster, acting as feeder pores to the microporosity in this coal.

In the Sewell coal, an apparently shorter time to exchange among the internal sites indicates a narrower distribution of adsorption sites than in the Wyodak coal. It should be noted that the signal itself, without presaturation, is narrower than in the Wyodak coal. This too is an indication of greater site homogeneity. The longer time saturate to the external surface gas signal shows that the access of adsorbed xenon to the external surface in the Sewell coal is far more restricted than in the Wyodak coal. This indicates a significantly different type of pore network in the two coals. The evidence points to a greater number of internal pore network connections than there are openings to the external surface in the Sewell coal. This is consistent with the notion of a highly interconnected microporous system lacking a significant amount of larger porosity.

In both coals the complete saturation of the adsorbed xenon signal, with no portion resistant to saturation after allowing 1-20 ms for xenon to exchange among internal sites with the presaturation pulse applied, demonstrates *interconnection* of porosity. This information could be useful in resolving the continuing controversy on whether coal micropores are primarily open or closed (Larsen et al., 1995; Walker and Mahajan, 1993). There was no isolated adsorbed xenon signal for either coal, an indication that the xenon atoms are moving through an open porous network. If a significant portion of the porosity existed as isolated pockets, movement of xenon through the coal would require passing through regions of both solid matrix and pores. If dissolved in the solid, an NMR signal would be expected either resolved from xenon that is in porosity, or overlapped but detectable as a portion of the signal with a longer lifetime in the saturation transfer experiment. It is very unlikely that xenon can diffuse through the solid matrix at a rate comparable to its passage through pores, and this experiment reveals no indication in either coal that a detectable proportion of the adsorbed xenon is dissolved in solid coal.

REFERENCES

- Bale, H. D., Carlson, M. L., Kalliat, M., Kwak, C.Y., and Schmidt, P.W. in The Chemistry of Low Rank Coals, A.C.S. Washington, D.C. pp. 79-94 (1984).
 Dybowski, C. Bansal, N., and Duncan, T. M. *Ann. Rev. Phys. Chem.* **42**, 433 (1991).
 Freeman, R. A Handbook of Nuclear Magnetic Resonance, J. Wiley, N.Y. pp. 198-202 (1988).
 Gan, H., Nandi, S. P., and Walker, P. L. Jr., *Fuel* **51**, 272 (1972).
 Harris, L. A. and Yust, C. S. *Fuel* **55**, 233 (1976).
 Harris, L. A. and Yust, C. S. in Coal Structure, A.C.S. Washington, D. C. pp. 321-336 (1981).
 Hirsch, P. B. *Proc. Royal Soc., (London)* **A226**, 143 (1954).
 Jameson, A. K., Jameson, C. J., and Gerald, R. E. *J. Chem. Phys.* **101**, 1775 (1994).
 Lin, J. S., Hendricks, R. W., Harris, L. A., and Yust, C. S. *J. Appl. Cryst.* **11**, 621 (1978).
 Larsen, R. G., Shore, J., Schmidt-Rohr, K., Emsley, L., Long, H., Pines, A., Janicke, M. and Chmelka, B. F. *Chem. Phys. Lett.* **214**, 220 (1993).
 Larsen, J. W., Hall, P., and Wernett, P. C. *Energy Fuels* **9**, 324 (1995).
 Mahajan, O. P., *Carbon* **29**, 742 (1991).
 Marsh, H. *Carbon* **25**, 49 (1987).
 Ripmeester, J. A. and Ratcliffe, C. I. *An. Chim. Acta* **283**, 1103 (1993).
 Simpson, J. H., Wen, W.-Y., Jones, A. A., Inglefield, P. T., and Bendler, J. T. *Appl. Magn. Reson.* **8**, 349 (1995).
 Tsiao, C. and Botto, R. E. *Energy Fuels* **5**, 87 (1992).
 Walker, P. L. Jr *Phil Trans. Royal Soc. Lond. A* **300**, 65 (1981).
 Walker, P. L. Jr., and Mahajan, O. P. *Energy Fuels* **7**, 559 (1993).
 Wernett, P. C., Larsen, J. W., Yamada, O., and Yue, H. J., *Energy Fuels* **4**, 412 (1990).

MICROSCOPIC OBSERVATION AND IMAGE ANALYSIS FOR THE EVALUATION OF TOPOLOGICAL FEATURES OF SINGLE COAL PARTICLES IN PYRIDINE

Hong Gao, Satoru Murata, and Masakatsu Nomura
Department of Applied Chemistry, Faculty of Engineering, Osaka University,
2-1 Yamada-oka, Suita, Osaka 565, Japan

Keywords: Single coal particle, Pyridine, Image Analysis.

ABSTRACT

Time dependent solvent swelling behavior of six different rank coal particles in pyridine was observed by the application of a microscopy combined with a video camera: the time-resolved swelling ratios were evaluated quantitatively by an image analysis system. The topological features of the coal particles with three dimensional macromolecular structure in pyridine are classified into four types among six different rank coals. We also found that the solvent-swelling ratios of single coal particles at quasi-equilibrium state are rank dependent.

INTRODUCTION

Coal is a complex and heterogeneous material. This heterogeneity leads to difficulties in accurately characterizing its structure, so that there is no universally accepted model for the chemical structure of coal. However, it appears to have been generally conceived that coal consists of a small chain substituted aromatic and hydroaromatic units linked by covalent bonds and non-covalent bonds like hydrogen bonding and van der Waals interactions, with entanglements of skeletal chain structure to form a three-dimensional network structure [1-4]. Apart from its three-dimensional cross-linked macromolecular structure, coal is viscoelastic and largely does not dissolve in conventional solvent, but swells when exposed to a solvent. The extent of swelling is thought to be controlled by the cross-link density and the magnitude of its interaction with the solvent [5-7]. In general, the density of cross-link is evaluated in terms of volumetric swelling ratio (Q_v), defined simply as the swollen sample volume divided by the unswollen sample volume. In evaluation of coal swelling, three methods of measurement have been adopted: volumetric measurement based on packed bed [8-10]; gravimetric measurements using solvent sorption from the vapor phase [11]; microscopy coupled with image analysis [12] and Malvern laser diffraction particle sizer [12] based on the measurement of particle distribution.

The important problem existing in volumetric techniques, with which the cross-link density of macromolecular level is evaluated with packed bed, is that the topological features of particles and interactions among the particles in solvent are not yet clear. Another problem of volumetric techniques is that the soluble fractions in polar solvent are present in coal. When the solvent like pyridine is introduced into the tube, a significant amount of dissolution occurs, resulting in the reduction of solvent activity. Therefore, it is clear that there is an enthusiastic need for the more reasonable method on the measurement of coal swelling in solvent on the macromolecular level. The methods based on particle size distribution measurement [12] offers a significant advantage over volumetric method, since the ambiguity of the packing of particle beds is removed, and the method employs a coal solid concentration which is sufficiently low for solubilization of the coals not to markedly affect the solvent activity. However, two implicit assumptions were made in this approach. They are particles of all sizes swell to the same average extent and the particles must not fracture or agglomerate during swelling. In practice, because of heterogeneity of coals, the distribution of equilibrium swelling ratios and the fracture exist in some kinds of coal particles, especially for the high-solvent-swelling coal. It is clear that the systematic investigation on the dynamical behavior and characteristics of single coal particle in solvent are in need for further understanding of the change of macrostructure of coal in solvent at the macromolecule level.

EXPERIMENTAL

Coal Samples. In the present study, six kinds of coal sample with different rank used in this study ranging from low rank to anthracite, were Witbank [weak coking coal, 83.1 C% (daf), Canada], Prima [coking coal, 81.0 C% (daf), Indonesia], Goonyella [coking coal, 84.6 C% (daf), Australia], Blue Creek [coking coal, 80.0 C% (daf), USA], K-9 [coking coal, 90.1 C% (daf), Russia], and Honken [anthracite coal, 93.2 C% (daf), Vietnam].

Swelling measurements on six kinds of coals in pyridine were conducted. Pyridine used in this study was of analytical reagent grade.

Experimental Apparatus and Procedure. As shown in Figure 1, the experimental apparatus consists of a microscope coupled with a TV camera system for observing and recording the behavior of the coals in solvent container. An image analysis system was used for quantitative evaluation of time-resolved swelling ratio of the single coal particles.

The microscope (Japan Olympus Co. Ltd.) fitted with a video camera provides input to an image analysis system (Japan Nireco Co. Ltd., LUZEX-3). A 6.3 \times objective was used with the microscope which, with the other optical components used, gave a magnification, at the analyzer monitor, from 20 to 100 \times objective.

Under the conditions of atmospheric pressure and ambient temperature (20 $^{\circ}$ C), pyridine (3 ml) was injected into the cell and then single coal particle was placed into pyridine and the recording was started until to the quasi-equilibrium-state of swelling. The recorded images were directly examined

and analyzed with the image analyzer. The time-resolved swelling ratio of single coal particles were evaluated with an equivalent volume converted from particle projection area under the assumption of spherical coal particle.

RESULTS AND DISCUSSION

As shown in Figure 2, Witbank coal particle (850-1000 μm) swells up to 2.47 times within 28 h. During this period the cracks largely developed, and no change was observed during an additional time exposure both in shape and size. The massive cracks may be caused by any stresses built up from the resultant swelling gradients or uneven swelling of sample. Other cracks may have been due to non-uniform swelling which causes some stresses not being sufficiently relieved. It is also likely that the stresses were caused by heterogeneities in the structure or by differences in the equilibrium swelling of different regions of the specimens. It is clear that transport process of pyridine in the coal macromolecule is greatly enhanced locally by the formation of a large discernible crack for the large specimen. This result suggests the new interface between coal macrostructure and solvent is important for solvent-swelling for high solvent-swollen coals. This phenomenon is consistent with the results of Cody and Botto [13], and Motsegood and Clarkson [28]. It is known that the chemical heterogeneity of coal leads to anisotropic swelling [18]. And coal swelling has been found to be greater in perpendicular direction to the bedding plane than in parallel to it [27]. Cracking at mineral-organic interfaces is also expected due to differential swelling of the organic matrix relative to mineral matter because diffusion of pyridine through areas is different with susceptibility differences, particularly at organic-mineral interfaces and at surface of microfractures.

As shown in Figure 3, the swelling ratio at quasi-equilibrium state of the sample with small size (210-250 μm) is 2.10 which is somewhat smaller than the larger one (2.47). The time required for reaching quasi-equilibrium state is about 10 hours. Moreover, only a few sizable cracks developed during swelling.

The reasons why the smaller sample apparently tended to reduce fracturing of the sample could be interpreted as follows: First, it caused the penetration of the swelling agent into the coal rapid and fairly uniform over the area of the sample so that uneven swelling of the sample was minimized. Second, the smaller sample has limitation of the distance over which liquid concentration gradients could develop perpendicularly to the surface, so any stresses built up from the resultant swelling gradients would be less likely to induce fracture.

For the case of Prima coal, the quasi-equilibrium swelling ratio is 2.34 for the case of smaller coal particle (210-250 μm) and 2.78 for the case of larger particle (850-1000 μm). The times for reaching the equilibrium state were about 5 h for smaller sample (210-250 μm) and 10 h for the larger one (850-1000 μm). During the swelling there is no cracks developed, the shape of the swollen coal particle samples being close to that of the initial specimens. These phenomena were different from the case of Witbank coal.

As described previously, the cracking at mineral-organic interfaces and surface of microfractures is due to differential swelling of the organic matrix relative to mineral matter because the diffusion of pyridine is through areas with susceptibility differences, particularly at organic-mineral interfaces and at surface of microfractures. The difference in solvent-swollen deformation characteristics, therefore, is caused by difference in degree of physical and chemical heterogeneity existing among the coals. The present results suggest that physical and chemical heterogeneity of Witbank coal is much larger than that of Prima coal. On the other hand, it is obvious that energetic interactions between solvent molecules and the coals play an important role in the swelling phenomena. For the coal to expand, the macromolecule chains must be able to reorient. Since the solvent-swollen coal was observed to be substantially more flexible than the dry coal, some bonds among macromolecular chains are apparently broken by solvation. The substantial decrease in modulus which occurs on swelling demonstrates that the bonding is significantly different in the dry and the swollen coal; it indicates that the effective molecule weight between crosslinks in the highly swollen coal is substantially greater than in the original dry coal. This suggests that the elasticity of the swollen sample may have much more of an entropic or rubbery nature than that of the original sample. Therefore, the difference in deformational features between Witbank and Prima is also related to the difference in energetic interactions between solvent molecular and the coal macrostructure. The present results suggest that the interactions of Witbank coal and Prima coal with pyridine are larger than that of other coals or pyridine has sufficient force to destroy the non-covalent bonds existed in Witbank coal and Prima coal.

For the case of Goonyella coal, the quasi-equilibrium swelling ratio was 1.11 for the coal particle of 210-250 μm and 1.16 for the coal particle of 850-1000 μm . The times for reaching the equilibrium state are about 16 h for the smaller sample (210-250 μm) and 20 h for the larger sample (850-1000 μm), respectively. Moreover, during swelling there is a few sizable cracks developed with distortion, and in the initial swollen stage there is a shrinking period for both particle size although the appearance of this stage is much faster in the case of small coal particle than the case of large one. These phenomena are different from the cases of Witbank coal and Prima coal. The shrinking phenomena may be caused by transition from glass to rubbery or change in amount of the coal microporosity, although it is unclear how much the change occurs.

For the cases of Blue Creek coal, K-9 coal and Honken coal, there are almost no swelling and deformation in pyridine.

The detailed discussion on above phenomena will be conducted from the view point of non-covalent interaction existed in different rank coals in the following parts.

The physical properties of solvent-swollen coal are related to its three dimensional macromolecular architecture. The dynamic nature of the macromolecular structure of coal governs the time dependence of its response during the solvent-swollen processes. The extent of swelling is thought to be controlled by the cross-link density and magnitude of interaction between coal and solvent [19-21]. The mechanism of coal swelling in polar basic solvents such as pyridine involves the disruption of hydrogen bonding cross-links of the network [29-31]. Pyridine is often used in solvent swelling

experiments on coal and, because of its basic character [5], is capable of reacting with many of the hydrogen bonds in coal to cause swelling, if these hydrogen bonds are cross-links [22]. Brenner [23] demonstrated that swelling of coals in pyridine involves the transformation of the coal from glassy to a rubbery state. In the differential scanning calorimetric investigation on solvent-swollen coals, Hall and Larsen [30] demonstrated the existence of second-order phase transitions well below room temperature. It has been hypothesized that these phase transitions are glass to rubber transitions. Usual state of coal is glassy at room temperature. When hydrogen bonds are disrupted by pyridine, the effective cross-link density decreases. There is an associated change in the viscoelastic properties of the coal as it becomes more rubbery. The degree to which coal becomes rubbery is a function of the density of hydrogen bonds disrupted and hence the solvent swelling. It is reasonable and sufficient to assume that when swollen with pyridine, the coals behave as if some or all of the hydrogen bonds or other non-covalent bonds have been eliminated. The fact that the diffusion mechanism is a strong function of the number of hydrogen bonds disrupted suggests that this in some way limits the extent to which coals can become rubbery. Solvent sorption into glassy polymers contains contributions from both concentration gradient controlled diffusion and relaxation controlled swelling. It was reported that particle size was a factor with case-II [24] behavior being observed for large particles and Fickian diffusion for small particles. Swelling of coal in pyridine involves the disruption of hydrogen bonds in the coal and the formation of bonds between the solvent and functionalities in the coal. It has also been suggested that solvent will disrupt only those coal-coal hydrogen bonds whose bond strengths are lower than those of the coal-solvent hydrogen bonds [25]. It has also been suggested that pyridine, because of its strong basicity, is capable of breaking nearly all hydrogen bonds in coal [26]. Therefore, when coal containing an appreciable amount of hydrogen bonding is exposed to pyridine, it swells to a limitation that is primarily a function of the covalent cross-link density.

As for the present study, the swelling ratio of single coal particles (850-1000 μm) in pyridine at ambient temperature versus time are 2.47 for Witbank coal, 2.34 for Prima coal, 1.12 for Goonyella coal, 1.04 for Blue Creek coal, 0.983 for K-9 coal and 1.04 for Honken coal, respectively. These results suggested that Witbank and Prima coal contain rather more hydrogen bonds, Goonyella coal has small amount of hydrogen bonds, while few hydrogen bond exists in Blue Creek coal, K-9 coal and Honken coal (As for Blue Creek coal, detailed study on oxygen-containing functionalities seems to be needed).

As to the time required for reaching to quasi-equilibrium state, for the case of 850-1000 μm coal particle size, they are 24 h for Witbank coal, 10 h for Prima coal, 16 h for Goonyella coal, respectively. For the case of 210-250 μm coal particle size, the times required for reaching to equilibrium state is almost same each other (10 h) for three kinds of coal (Witbank, Prima, Goonyella). Therefore, it seems that the diffusion velocity of pyridine molecules in the larger coal particles and relaxation velocity of the coals in pyridine are in the order: Prima > Goonyella > Witbank.

As shown in Figure 4, for the case of large particle size (850-1000 μm), the equilibrium swelling ratios are rank-dependent with decrease of carbon content from 77 to 93 wt % (daf). The pattern is consistent generally with the previous analysis on molecular weight between crosslinks [32,33] and network mobility analysis [34-35]. For the case of particle size of 210-250 μm , the change of swelling ratio with rank is similar to the case of large one.

From the observation on the recorded images, as shown in Figures 5-10, the general features of solvent-swelling behavior of the large coal particles (850-1000 μm) in pyridine seem to be classified into four types: (1) high swelling with massive crack deformation (Witbank); (2) high swelling ratio with non cracks deformation that the shape of swollen coal sample was close to that of the initial specimen (Prima); (3) no-crack shrinkage and distortion with low swelling ratio (Goonyella); and (4) no swelling with no deformation (Blue Creek, K-9, and Honken).

For comparison of the results, it should be noted that measured particles differ in size, shape and in mineral and maceral content. We observed that the distribution of equilibrium solvent swelling ratios exists in some kinds of coals. These results suggest that available data measured by conventional volumetric method may be, at most, an average expression on the equilibrium solvent swelling ratio of the coals. The systematic analysis on the distribution of equilibrium solvent swelling ratios of coals with wide range ranks is in progress in our laboratory.

CONCLUSIONS

Solvent swelling behavior of single coal particles of six different rank coals in pyridine was observed with the application of microscopy combined with video camera and the changes of solvent swelling ratio with time were evaluated quantitatively by an image analysis system. The deformation of the large coal particles seems to be classified into four types: (1) high swelling ratio with massive cracking (Witbank); (2) high swelling ratio with non-cracking and the shape of the swollen sample was close to that of the initial specimen (Prima); (3) non cracking shrinkage and distortion with low swelling ratio (Goonyella); and (4) non-swelling and non-deformation (Blue Creek, K-9, and Honken). In the case of coal particle size being 850-1000 μm , the quasi-equilibrium swelling ratios were 2.47 for Witbank coal, 2.34 for Prima coal, 1.12 for Goonyella coal, 1.04 for Blue Creek coal, 0.983 for K-9 coal and 1.04 for Honken coal, respectively. In the case that the coal particle size is 210-250 μm , the quasi-equilibrium swelling ratios are 2.10 for Witbank coal and 2.78 for Prima coal, respectively. On the other hand, it seems that the diffusion velocity of pyridine molecules in the larger coal particles and relaxation velocity of large coal particles in pyridine are in the order: Prima > Goonyella > Witbank.

ACKNOWLEDGMENTS

This work was supported by Grant-in-Aid for Scientific Research No. 07455323 from the Ministry of Education, Science and Culture, Japan.

REFERENCES

- 1 Van Krevelen, D. W., 'Coal', Elsevier, Amsterdam, 1981.

- 2 Lucht, L. M.; Peppas, N. A. *Fuel* 1989, 66, 803.
- 3 M. Vahrman, *Fuel* 1970, 49, 5.
- 4 Spence, J. A.; Vahrman, M. *Fuel* 1970, 49, 395.
- 5 Sanada Y.; Honda, H. *Fuel* 1966, 45, 295.
- 6 Marzec, A.; Kisielow, W. *Fuel* 1983, 62, 971.
- 7 Mastral, A. N.; Izquierdo, M.; Rubio, T., B. *Fuel* 1990, 69, 892.
- 8 Liotta R.; Brons, G.; Isaacs, J. *Fuel* 1983, 62, 781.
- 9 Larsen, J. W.; Green, T. K. *Fuel* 1984, 63, 1538.
- 10 Ndaji, F. E.; Thomas, K. M. *Fuel* 1993, 72, 1525.
- 11 Hsieh, S. T.; Duda, J. L. *Fuel* 1987, 66, 170.
- 12 Turpin, M.; Rand, B.; Ellis, B. *Fuel* 1996, 57, 107.
- 13 Cody, G. D.; Botto, R. E. *Energy Fuels* 1993, 7, 561.
- 14 Lynch, L. J.; Peppas, N. A. *Fuel* 1987, 66, 803.
- 15 Ritger, P. L.; Peppas, N. A. *Fuel* 1987, 66, 1379.
- 16 Barton, W. A.; Lynch, L. J. *Energy Fuels* 1989, 3, 402.
- 17 Barton, W. A.; Lynch, L. J. In 'Proceedings of 1989 International Conference on Coal Science' Tokyo, 1989, pp. 13-16.
- 18 Brenner, D. *Fuel* 1984, 63, 1324-1328.
- 19 Suuberg, E. M.; Otake, Y.; Langner, M. J.; Leung, K. T.; Milosavljevic, I. *Energy Fuels* 1994, 8, 1247-1262.
- 20 Ndaji, F. E.; Thomas, K. M. *Fuel* 1995, 74, 842-845.
- 21 Cody, G. D.; Davis, A.; Hatcher, P. G. *Energy Fuels* 1993, 7, 455.
- 22 Marzec, A.; Kisielow, W. *Fuel* 1983, 62, 971.
- 23 Hall, P. J.; Marsh, H.; Thomas, K. M. *Fuel* 1988, 67, 863.
- 24 Nishioka, M.; Larsen, J. W. *Energy Fuels* 1988, 2, 351.
- 25 Larsen, J. W.; Green, T. K.; Kovac, J. J. *Org. Chem.* 1985, 50, 4729.
- 26 Brenner, D. *Fuel* 1985, 64, 167.
- 27 Cody, G. D.; Larsen, J. W.; Siskin, M. *Energy Fuels* 1988, 2, 340.
- 28 Motsegood, A. G. W.; Clarkson, R. B. *Fuel* 1993, 72, 1235-1237.
- 29 Green, T. K.; Kovac, J.; Brenner, D.; Larsen, J. W., in 'Coal Structure' (Ed. R. A. Meyer), Academic Press, New York, 1982.
- 30 Cody, G. D.; Larsen, J. W.; Siskin, M. *Energy Fuels* 1988, 2, 342.
- 31 Hall, P. J.; Thomas, K. M.; Marsh, H. *Fuel* 1988, 67, 863.
- 32 Lynch, L. J.; Peppas, Nikolaos A. *Fuel* 1987, 66, 803-809.
- 33 Ritger, Philip L.; Peppas, Nikolaos A. *Fuel* 1987, 66, 1379-1388.
- 34 Barton, W. A.; Lynch, L. J. *Energy Fuels* 1989, 3, 402.
- 35 Sakurovs, R.; Lynch, L. J.; Barton, W. A., In 'Coal Science II', Symposium Series 461 (Eds Schobert, H. H.; Bartle, K. D.; Lynch, L. J.), American Chemical Society, Washington, DC, 1991, pp. 111-126.

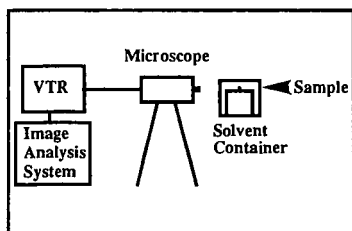


Figure 1. Schematic diagram of the apparatus for the observation and measurement of solvent swelling of single coal particles.

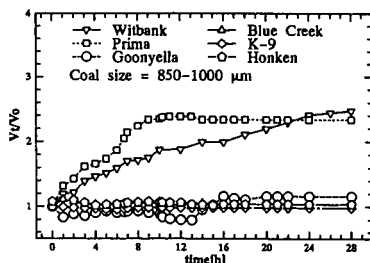


Figure 2. Changes of solvent swelling ratio with time in pyridine at ambient temperature.

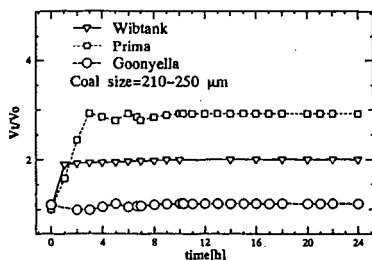


Figure 3. Changes of solvent-swelling ratio with time in pyridine at ambient temperature.

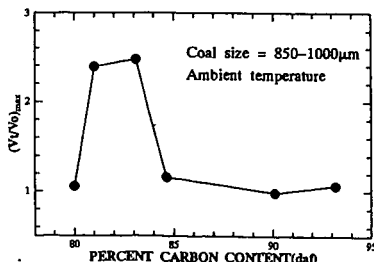


Figure 4. Relationship between maximum solvent swelling ratio in pyridine and carbon content.



Figure 5. Frame photographs of swelling of Witbank coal particle (850-1000 μm) in pyridine at ambient temperature (a: 0 h, b: 1 h, c: 2 h, d: 3 h, e: 4 h, f: 5 h, g: 6 h, h: 7 h, i: 8 h, j: 9 h, k: 10 h, l: 11 h, m: 11.25 h, n: 12 h, o: 13 h, p: 14 h, q: 14.5 h, r: 24 h).

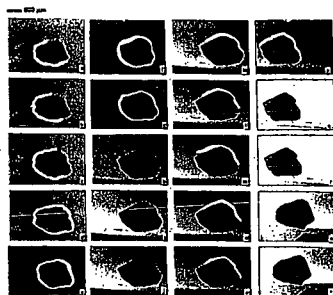


Figure 6. Frame photographs of swelling of Prima coal particle (850-1000 μm) in pyridine at ambient temperature (a: 0 h, b: 1 h, c: 2 h, d: 3 h, e: 4 h, f: 5 h, g: 6 h, h: 7 h, i: 8 h, j: 9 h, k: 10 h, l: 11 h, m: 12 h, n: 13 h, o: 14 h, p: 15 h, q: 16 h, r: 17 h, u: 18 h, v: 20 h, w: 21 h, x: 24 h).

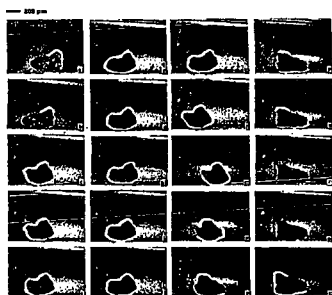


Figure 7. Frame photographs of swelling of Goonyella coal particle (850-1000 μm) in pyridine at ambient temperature (a: 0 h, b: 1 h, c: 2 h, d: 3 h, e: 4 h, f: 5 h, g: 6 h, h: 7 h, i: 8 h, j: 10 h, k: 12 h, l: 14 h, m: 14.25 h, n: 14.5 h, o: 15 h, p: 16 h, q: 18 h, r: 20 h, u: 22 h, v: 24 h).

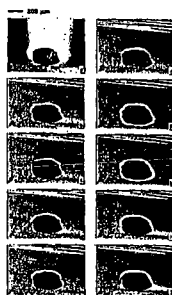


Figure 8. Frame photographs of swelling of Blue Creek coal particle (850-1000 μm) in pyridine at ambient temperature (a: 0 h, b: 1 h, c: 2 h, d: 3 h, e: 4 h, f: 6 h, g: 8 h, h: 10 h, i: 18 h, j: 24 h).



Figure 9. Frame photographs of swelling of K-9 coal particle (850-1000 μm) in pyridine at ambient temperature (a: 0 h, b: 2 h, c: 4 h, d: 6 h, e: 8 h, f: 10 h, g: 12 h, h: 24 h).

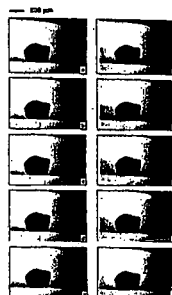


Figure 10. Frame photographs of swelling of Honken coal particle (850-1000 μm) in pyridine at ambient temperature (a: 0 h, b: 2 h, c: 4 h, d: 6 h, e: 8 h, f: 10 h, g: 12 h, h: 16 h, i: 18 h, j: 24 h).

SORPTION MECHANISM OF VARIOUS ORGANIC VAPORS TO ARGONNE PREMIUM COAL SAMPLES

Toshimasa Takanohashi, Kazuhiko Shimizu, and Masashi Iino
Institute for Chemical Reaction Science, Tohoku University
Katahira, Aoba-ku, Sendai 980-77, JAPAN

KEYWORDS: Coal, Sorption, Organic Vapor

ABSTRACT

Sorption of various organic vapors into Argonne Premium coals was systematically investigated to clarify coal-solvent interaction, sorption mechanism, and micropore and cross-linking structure of coals. Especially, the sorption at low vapor pressures was measured under temperature- and pressure-controlled gravimetric sorption system. Methanol was not only quickly sorbed into all ranks of coals used, but also easily desorbed under vacuum at 30 °C. While, pyridine was slowly sorbed into lignite and a significant pyridine was retained after desorption process. Methanol sorption isotherm for all ranks of coals could be explained by the dual-sorption model, i.e., a physical adsorption described by a Langmuir isotherm and a dissolution into bulk of coals described by Henry's law. For Illinois # 6 coal, in relative vapor pressures of 0.01-0.6, the sorption could be treated by the dual-sorption model, regardless of the kinds of organic vapors (methanol, benzene, pyridine, and cyclohexane). The adsorption mechanism by a BET equation did not fit the sorption data. At high relative vapor pressures, an equilibrium sorption could not be obtained, i.e., the sorbed amount was increasing with time, probably due to condensation of organic vapors in the pores and relaxation process of coal macromolecular structure.

INTRODUCTION

When a coal sorbs a solvent, several phenomena occur i.e., coal surface (functional groups)-solvent interaction, adsorption of solvent on the coal surface, coal cross-link-solvent interaction (specific interacting sites), diffusion of solvent into the bulk of coal (cross-link), extraction, swelling, and structural relaxation etc. Although the mechanism of solvent penetration into coal has no well been clarified, the study on the sorption of various organic substances including solvents is considered to be very useful for understanding coal chemistry such as the porosity structure and cross-linking structure of coals.

Hsieh and Duda have reported¹ that organic vapor sorption by coal particles can involve the several complex phenomena including the migration of mobile molecules in the coal and solvent-induced changes in coal structure, and that several analyses which have been used to investigate the structure of synthetic macromolecules were not directly applicable for coals. On the other hand, recently, Green and Selby² proposed that pyridine sorption isotherms can be modeled by a dual-mode sorption mechanism which have been widely used to explain the sorption isotherms of glassy polymers.³ This model is represented by two phenomena, i.e., a physical adsorption described by a Langmuir isotherm and a dissolution described by Henry's law. The linear portion of the pyridine isotherms represents dissolution of pyridine according to the Henry's law, i.e., sorption is linear with pressure. However, pyridine is sometimes troublesome for analysis of the sorption behavior, since pyridine strongly interacts with coals. Pyridine is considered to interact preferentially with the sites such as hydroxyl group in coals, attack the hydrogen-bonds, and disrupt all hydrogen-bonds. Pyridine also can cause the structural changes by diffusion into coal and it makes coals rubbery.^{4,5} Thus, the mechanism of solvent sorption can be dependent upon the chemical properties of solvents, and coal porosity and coal cross-links. The steric hindrance of the pore and the density of coal cross-links may be also an important factor on the vapor sorption.^{6,9}

In the present study, organic vapor sorption experiments were carried out by using Argonne Premium Coal Samples which are suitable for the sorption experiments since they have been stored under oxygen-free condition. The sorption mechanisms of various coal-vapor systems, coal porosity, and cross-linking structure of the coals will be discussed.

EXPERIMENTAL

Sample Preparation.

Argonne Premium Coal Samples were obtained in ampoules of 5 g of -150 μm . The coals were dried at 80 °C for 12 h under vacuum. As a organic solvent vapor, benzene, pyridine, cyclohexane, methanol were used without purification.

Sorption Experiments.

Sorption experiments was carried out in an acrylic box under temperature-control condition, using a quartz spring balance at 30 °C. The sorption was estimated by measuring the extension of a spring by a cathetometer with a telescope. Approximately 50 mg of the coal sample was placed in the quartz bucket, weighed, suspended from the quartz spring, vacuumed overnight at 30 °C. The deaeration treatment of organic solvent was carried out three times through freeze-thaw cycles three times to remove gases in the system. Two experiments were carried out. At a saturate vapor pressure, sorption change with time was measured. After 1 day, the desorption was measured under vacuum. In the other experiment, approximately 0.01 of relative vapor pressure of solvent was set and the sorption was measured until it attains an equilibrium. As the relative pressure was stepwise raised, the equilibrium sorption was measured.

RESULTS AND DISCUSSION

Sorption Behaviors.

For Pocahontas # 3, Illinois # 6, and Beulah Zap coals, the sorption was measured under at a saturate vapor pressure.

<Pocahontas # 3 Coal> Figure 1 shows the result for Pocahontas # 3 coal using methanol, pyridine, benzene, and cyclohexane as an organic vapor. For all vapors, the quantity sorbed was small, due to developed aromatic ring systems in which a vapor is difficult to penetrate the coal. The rate of methanol sorption was the fastest of all and total sorption was also large after 1 day, although pyridine and benzene sorption contain even 1 day, suggesting that the sorption rate of pyridine and benzene was relatively slow. A similar tendency was obtained for Upper Freeport coal. We have reported^{10,11} that the swelling ratios of high-rank raw coals in solvents were small, compared to those of its extraction residues and extract fractions. These results suggests that the diffusion of a solvent in the coals might be retarded by structural factors in the coals, such as stacking among aromatic rings. We have also reported^{8,9} that the size exclusion effect of coal macromolecular structures is an important factor for penetration of aromatic compounds in the coals from a inverse liquid chromatography study. Even in liquid phase, pyridine could not extract all pyridine-extractables in the coals at room temperature, indicating that the penetration of pyridine into the coals was incomplete.¹² We have also found¹² that a carbon disulfide-N-methyl-2-pyrrolidinone mixed solvent gave high extraction rates as well as high extraction yields for some bituminous coals. The kinetics of solvent diffusion into the coals may greatly influence the extraction yield and the swelling ratio of the coals.

<Illinois # 6 Coal> Figure 2 shows the result for Illinois # 6 coal. Generally, the initial rate of sorption was high and the amount sorbed was large, compared to other coals, suggesting that Illinois # 6 coal has porosity and cross-linking structure which a solvent easily diffuses. The sorption of pyridine was the largest of the solvents used, while those of benzene and cyclohexane were small. Polar solvents such as pyridine and methanol was greatly sorbed by Illinois # 6 coal. These results suggest that adsorption on the surface and the diffusion easily occurs through interaction between polar solvents and the coal. Illinois # 6 c is known to contain more functional groups than higher rank coals such as Pocahontas # 3 and Upper Freeport coals.

<Beulah-Zap Coal> Figure 3 shows the result for Beulah-Zap coal. As expected, the sorption by benzene and cyclohexane was very small as well as for Illinois # 6 coal as indicated in Figure 2. Methanol gave a high initial rate of sorption and a high equilibrium sorption. Since Beulah-Zap coal has much more oxygen functional groups than the other coals used, polar solvents would preferentially diffuse through interaction between coal and solvent. Coal is considered¹³ to have two types of interacting sites, i.e., one is free interacting sites which have not interacted with other sites, and the other is interacting sites which interacted already with other sites of coal. The methanol sorption in Figure 3 suggests that methanol may diffuse the coal through disrupting noncovalent bonds such as hydrogen bonds, since it has a high polarity. While, it is noted that the pyridine sorption rate was unexpectedly slow compared to the case of methanol. Pyridine is known to disrupt almost of hydrogen bonds in coals, since pyridine forms a strong hydrogen bond with hydroxyl groups. However, the slow diffusion of pyridine suggests that the disruption is not so much fast as methanol. The difference of pyridine sorption between Illinois # 6 coal and Beulah-Zap coal may be attributed to a difference in the distribution of strength of hydrogen bonds in the both coals.

Dual-Mode Sorption Model.

Figure 4 (a)-(d) shows sorption isotherms for Illinois # 6. In the range of 0.1 - 0.7 of relative vapor pressure, sorption was linear with the pressure for all the cases. The

isotherms was examined to be interpreted by the dual-mode sorption model. The equilibrium isotherm of the model can be expressed by the following equation:

$$C = C_H + C_D = \{C_H \times b \times p / (1 + b + p)\} + k_D \times p \quad (1)$$

where C is the quantity of the sorption, and the first term represents physical adsorption followed by a Langmuir isotherm and the second term represents dissolution into the bulk of coals followed by Henry's law. C_H is the pore saturation constant, b is the pore affinity constant, p is the relative vapor pressure, and k_D is Henry's law dissolution constant. Figure 4 shows that the observed values are consistent with the calculated lines from the model, especially at low pressures, suggesting that the isotherm behaviors can be explained by the dual-mode sorption model. The calculated C_H and C_D lines are also shown in the Figure, respectively. For benzene, cyclohexane and methanol, in the low vapor pressure ranges the physical adsorption (C_H) predominates, while for pyridine there is a large contribution of dissolution even at low pressure ranges. The value of C_H was similar, 0.37, 0.32, and 0.33 (mmol / g-coal) for benzene, cyclohexane, and pyridine, respectively, although their total sorptions are considerably different, as shown in Figure 4.

4. Their adsorption area per molecule, i.e., van der Waals radius, is also similar. These facts indicate that the number of the solvent molecules adsorbed is independent of types of solvents. The Henry's law dissolution constant, k_D , was in the order of cyclohexane < benzene < methanol < pyridine, being consistent with the order of the extraction yield and the swelling ratio for Illinois # 6.

Figure 5 and 6 show the results of Pocahontas # 3 - methanol and Beulah-Zap - methanol systems, respectively. The data could be also analyzed by the dual-mode sorption model and the calculated lines are shown in Figure 5 and 6. It should be noted that for Pocahontas # 3 coal the physical adsorption was predominant for the sorption, indicating that the most of sorption is attributed to the adsorption on the surface. The result also corresponds a very low swelling ratio and extraction yield for Pocahontas # 3 coal in methanol. On the other hand, for Beulah-Zap lignite a significant amount of methanol diffused the coal, as shown in Figure 6. The dissolution constant, k_D , of methanol in Beulah-Zap coal was much higher, while the pore saturation constant, b , was much lower than those in Illinois # 6 coal, reflecting the affinity of methanol to the pore surface and cross-links of both coals.

Thus, measurements of isotherms using various organic vapors are an useful method to elucidate interaction between coal and solvent, coal surface, chemical properties, and cross-linking structure (the distribution of the molecular weight between cross-links) of coals. Further works is continued by changing the experimental parameters such as temperature, types of organic vapors, coal samples (extract and extraction residue).

ACKNOWLEDGMENT

This work has been carried out as one of "Research for the Future" project of the Japan Society for the Promotion of Science (JSPS) through the 148 committee on coal utilization technology of JSPS.

REFERENCES

1. Hsieh, S. T.; Duda, J. L. *Fuel*, **1987**, *66*, 170.
2. Green, T. K.; Selby, T. D. *Energy Fuels* **1994**, *8*, 213.
3. Vieth, W. R. *Diffusion in and Through Polymers*, Hanser Publishers: Munich, 1991.
4. Brenner, D. *Fuel* **1985**, *64*, 167.
5. Cody, G. D. J.; Davis, A.; Hatcher, P. G. *Energy Fuels* **1993**, *7*, 455.
6. Larsen, J. W.; Hall, P. J.; Wernett, P. C. *Energy Fuels* **1995**, *9*, 324.
7. Aida, T.; Fuku, K.; Fujii, M.; Yoshihara, M.; Maeshima, T.; Squires, T. G. *Energy Fuels* **1991**, *5*, 79.
8. Morino, M.; Kaneko, H.; Takanohashi, T.; Iino, M. *Energy Fuels*, **1996**, *10*, 1012.
9. Kaneko, H.; Morino, M.; Takanohashi, T.; Iino, M. *Energy Fuels*, **1996**, *10*, 1017.
10. Fujiwara, M.; Ohsuga, H.; Takanohashi, T.; Iino, M. *Energy Fuels* **1992**, *6*, 859.
11. Takanohashi, T.; Iino, M.; Nishioka, M. *Energy Fuels* **1995**, *9*, 788.
12. Iino, M.; Takanohashi, T.; Ohsuga, H.; Toda, K. *Fuel* **1988**, *67*, 1639.
13. Suuberg, E. M.; Otake, Y.; Langner, M. J.; Leung, K. T.; Milosavljevic, I. *Energy Fuels* **1994**, *8*, 1247.

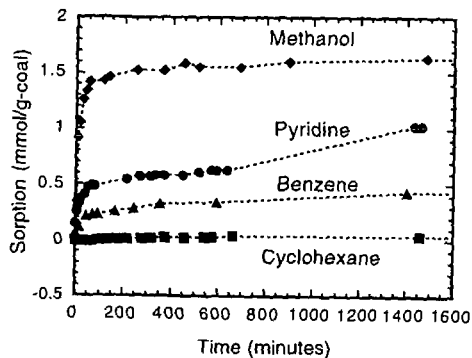


Figure 1 Sorption Behaviors Various Solvent Vapors by Pocahontas #3 Coal at 30 °C

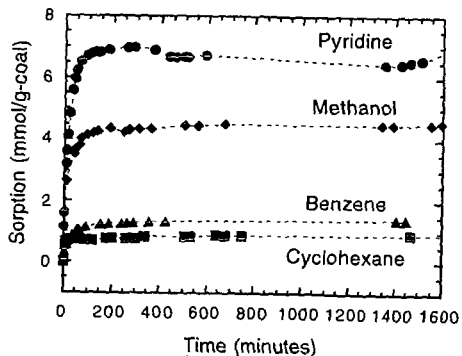


Figure 2 Sorption Behaviors Various Solvent Vapors by Illinois #6 Coal at 30 °C

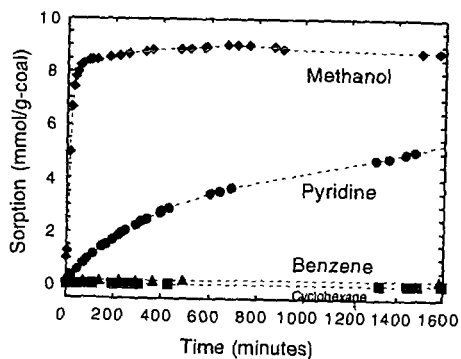


Figure 3 Sorption Behaviors Various Solvent Vapors by Beulah-Zap Coal at 30 °C

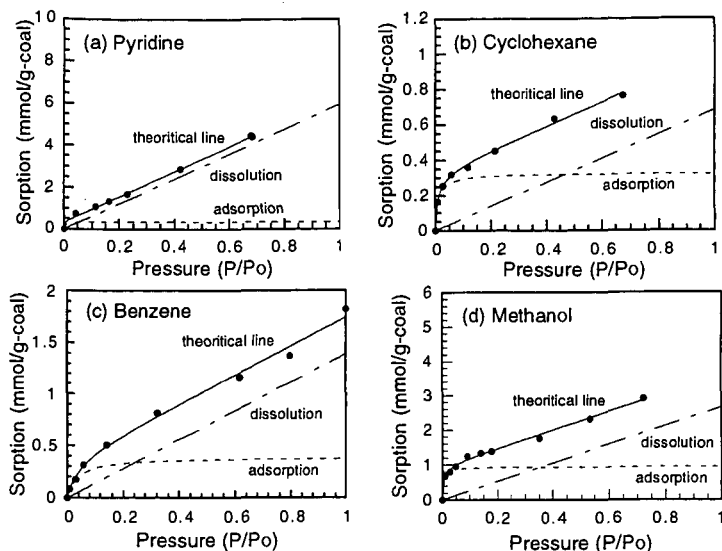


Figure 4 Pyridine Sorption Isotherm of Illinois #6 Coal at 30 °C and the theoretical lines.

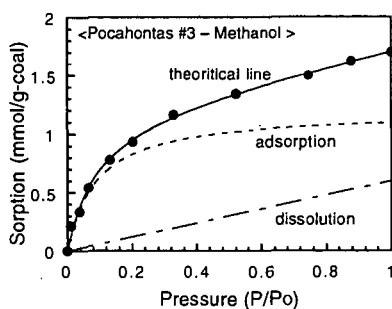


Figure 5 Methanol Sorption Isotherm of Pocahontas #3 Coal at 30 °C and the theoretical lines.

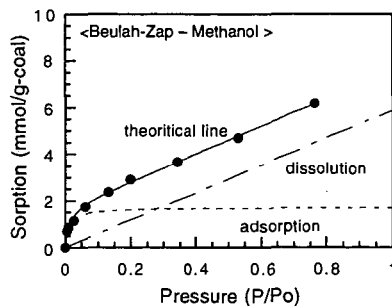


Figure 6 Methanol Sorption Isotherm of Beulah-Zap Coal at 30 °C and the theoretical lines.

A History of Coal Liquefaction in United Kingdom, 1967-1992

Geoff M. Kimber
Coal Science & Technology Consultant
(formerly Technical Manager, British Coal Corporation
Liquefaction Project)

20 King William Drive
Cheltenham
Gloucs. GL53 7RP
United Kingdom

Keywords: Coal, Liquefaction, U.K. History 1967-1992.

ABSTRACT

This paper gives an overview of the coal liquefaction studies carried out by the British Coal Utilisation Research Association, (BCURA), the National Coal Board (NCB), and the British Coal Corporation (BCC), between 1967 and 1992 at their research establishments in Leatherhead, Stoke Orchard and Point of Ayr. It is based upon a recently published ~100 page report⁽¹⁾ which condensed into a single reference document the contents of several hundred internal reports not generally available outside of BCC.

INTRODUCTION

Coal liquefaction is not new. Although Berthelot observed as early as 1869 that coal could be converted to an oil-like product by chemical reduction, practical processes using hydrogenation really date from 1913, when Bergius showed that brown coal could be converted to a heavy crude oil.

The main early developments took place during the 1920s and 1930s in Germany, while in the U.K. Imperial Chemical Industries built a plant at Billingham to produce 100,000t/year of liquid fuels from bituminous coal. This operated until 1939, after which it was used instead to convert creosote oil to aviation fuel. At this time, Germany continued to depend heavily upon coal liquefaction and built several plants, in total producing 3 million t/year, with the largest complex requiring 50,000 workers to produce 600,000t/year.

The price and availability of crude oil throughout most of the world since the 1950s has meant that coal liquefaction has not been economically attractive. However, in the mid 1960s in the USA there was interest in desulphurising coal to reduce environmental problems caused by the release of large amounts of sulphur oxides during coal combustion for power generation. It was thus to de-ash (and thereby reduce sulphur content) that the Solvent-Refined Coal (SRC) direct coal liquefaction process was developed, initially by the Spencer Chemical Company with an 80kg/h continuous unit funded by the Office of the Coal Research Council.

This revival of interest stimulated the preparation of a paper describing the BCURA work on solvent extraction of coal. The paper summarised three sets of laboratory-scale experiments that were carried out during the period 1955 to 1962 to examine whether a useful balance of products could be obtained economically via the solvent-extraction of low- or medium-rank coals. There had been three periods of activity: (1) from 1956, when the objective was to make available quantities of coal extract for assessment by industry, while removing the minimum amount of volatile material consistent with yielding a residue with smokeless fuel properties; (2) 1961, when the purpose was to make a similar extract by the simplest method available, to satisfy further enquiries from industry; and (3) 1962, when the objective was to test the extracts potential for conversion to jet fuel.

These experiments were conducted at atmospheric pressure, with high solvent to coal ratios (eg 10:1), and temperatures around 200°C. In some tests, ultrasonic energy was applied to promote extraction of the coal. The yield of the pitch-like extract was usually around 10% and never reached 20%. Though the experiments were not taken to the pilot scale, it was found that the residues obtained after this moderate degree of solvent extraction could be pressed into briquettes which withstood typical handling and weathering. These could be ignited readily, and burned without producing substantial smoke. The solid extracts, which had low ash and very low (<1ppm) boron contents, were considered to have potential application as binders or more probably as sources of carbon for graphite manufacture. It appeared that these carbon artifacts might be produced at little more than their fuel value. Using the simple hydrogenation equipment then available (limiting conditions to a maximum of 500°C and 300 bar) and stannous sulphide or stannous chloride as catalyst, 20-30% yields (based on extract) of partially-hydrogenated cyclic hydrocarbons were obtained. While these boiled in a suitable range for use as jet fuels, the calorific value (66MJ/kg) was lower than desired.

The results of an economic assessment, for an integrated plant producing annually 250,000t of smokeless fuel and a solid extract, suggested a case could be argued for investigations to be carried out at the pilot-scale level. However, in 1967 it was decided to focus on experiments to establish the feasibility of markedly increasing the yield of extract from the 20% level.

ELECTRODE COKE VIA THE SOLVENT-EXTRACTION PROCESS 1967-1979

BCURA as part of a collaborative project with NCB, initially concentrated its investigations into the solvent extraction of coal, upon the influence of operating conditions on extraction yields and product distributions. The range of variables studied included temperature, pressure, gaseous atmosphere, residence time, coal feed size, coal rank, and solvent type, and explored their impact upon engineering problems of solids separation and distillation. This information was to be obtained in the first place from batch equipment, although it was appreciated that the product yields and operating conditions would not be identical to those pertaining to a continuous-extraction process of the type which would be needed for any large-scale exploitation of the solvent-extraction process. The experiments showed that UK coals could be solvent-extracted but when a USA economic study of the SRC process was converted to the UK situation, it was evident that the process was not at that time economic in the UK; the relative cost of coal and oil in the USA was much more favourable for liquefaction than in the UK. Other factors that favoured the economic viability of the process in the US in comparison to the UK included the relatively high sulphur content of US coals, combined with the incentives to reduce atmospheric emissions - in the UK at that time it was argued that abatement of SO₂ emissions was unnecessary, in part as a consequence of climatic and geographic conditions that led to dispersion of chimney plumes. In the US a positive value was assigned to the high sulphur ash residues for landfill applications.

During the experimental work at BCURA, however, quantities of coal extracts were prepared under different conditions to those used in the SRC process. UK outlets for this re-constituted, de-ashed coal were sought, eg as potentially high value feedstocks for the manufacture of electrode binders and carbon fibres. Particularly encouraging was the discovery, during testing of the coal extracts at BCURA, that the properties of coke made from the coal extract compared favourably with premium-grade petroleum coke used in the manufacture of electrodes. At that time, such a grade of coke had about three times the value of coal, thus providing the basis for a potential economic process. The electrode-coke process which did not require the use of expensive hydrogen and the associated high-pressure equipment was thus developed.

Following a series of tests, culminating in a nine-cycle demonstration run, based around a 2 litre autoclave reactor, the decision was taken by the NCB-led research committee to build a 0.5/day plant at BCURA. Construction of this was scheduled to begin in February 1971 but in the event BCURA'S status as a Research Association ceased in the week before the contractors were due to start site operations at Leatherhead, and it was decided to transfer the whole project to the Coal Research Establishment (CRE) at Stoke Orchard, near Cheltenham. Virtually all of the equipment was moved and reinstalled within a few months. At the same time, W.C. Holmes and Co Ltd began construction at Stoke Orchard of the larger rig, now termed the 'extract plant'. Erection was completed during the latter half of 1971 and instrumentation and ancillary engineering aspects, carried out by NCB staff, were completed shortly afterwards. Commissioning was completed in February 1972 and coal first fed in March 1972.

During the following six years nearly 90 runs were carried out. By far the most significant was Run 45 which started on 13 January 1975 and continued for 168 days, during which time over 30t of coke were produced. In general, this was a period when the project size increased considerably, mainly due to the increased manpower needed to operate the extract plant; the team of six at BCURA increased in about a year to 24 at CRE.

Assessment of coke quality in terms of its suitability for electrode manufacture was carried out initially by Anglo Great Lakes (AGL) using 2kg samples and later on 250kg batches from the extract plant. AGL'S long experience was extremely useful but much of the assessment was empirical and based solely upon experience with petroleum cokes and, thus, possibly not applicable to coal-extract cokes.

During 1973, the Atomic Energy Research Establishment (AERE), Harwell was contracted to fabricate some 25mm- and 75mm-diameter graphite electrodes which were subsequently submitted directly to British Steel Corporation (BSC) for testing in arc-steel furnaces. These electrodes performed much better in BSC'S tests than would have been predicted by AGL (or any other graphite manufacturer) in that they had improved resistance to thermal shock compared to electrodes made with premium-grade petroleum coke. Although having a relatively high coefficient of thermal expansion, the cracks formed in the extract-coke electrodes propagated only slowly, reducing the rate of electrode degradation.

Much encouraged by these results and the economics based upon a capital costing carried out under contract by Kelloggs, plans were made to make enough coke to fabricate 300mm-diameter electrodes that could be tested by BSC on production arc-steel furnaces. This required the extract

plant to run continuously for six months. To improve the project's ability to assess the coal-extract coke, facilities were set up at Stoke Orchard to produce and test small-diameter graphite rods. Samples of coal-extract cokes were assessed under a collaborative agreement with SIGRI (Germany) and a new agreement was negotiated with AGL. AGL used 20t of calcined extract coke supplied by NCB to fabricate 300mm-diameter graphite electrodes. The NCB graphite electrodes were vigorously tested at the Craigneuk works of BSC and normal production levels were maintained throughout the test period. It was concluded that coal-extract coke should be suitable for manufacture of electrodes up to and including 610mm-diameter, the largest in use at the time.

New designs and costings of larger plants, based upon specifications produced by the project, were obtained in 1977 from Catalytic Inc. However, the market for electrode coke was shrinking due to the severe contraction of the steel industry, particularly in Europe. Furthermore Conoco, at Immingham, were producing 200,000t/year of coke and Phillips, at Moerdijk in the Netherlands, were about to bring on-stream another premium-grade coke plant using a new feedstock, ethylene cracker tar. This new product also had problems getting market acceptance.

Much had been learnt about the various unit operations that made up the coal-to-electrode coke process. This was invaluable in the development of a process to produce transport fuels from coal when interest in this reemerged because of world crises in crude oil supply in the mid-1970s.

TRANSPORT FUELS FROM COAL-THE LIQUID SOLVENT EXTRACTION (LSE) PROCESS 1973-1986.

The first coal hydrogenation studies in the UK since the 1960s at BCURA began in June 1973 using a 2 litre autoclave. At this time, a number of factors were threatening world crude oil supplies and the possibility of meeting at least a portion of the UK demand by synthesising oil from UK coal was considered strategically desirable. The extract plant sited at CRE was capable of supplying various streams which could have been hydrogenated (or pyrolysed) to liquids of which coal solution (the filtrate from the coal digest) and coal extract (evaporated filtrate, a solid at room temperature) were favoured technically because:

- they contain little inorganic material to contaminate catalysts and cause blockages in the plant
- the relatively unreactive inertinite portion of the coal has been removed
- they can be made fluid easily e.g., by the application of heat.

Coal extracts contain higher proportions of coal-derived material than coal solutions, so that changes in the coal material can be detected more readily. However, the higher softening points of coal extracts make them more difficult to pump.

The primary aim of the preliminary investigation was to hydro-treat coal extracts using the autoclave in order to explore possible process configurations and identify those with potential for development. However, the work had the additional aim of detecting possible problems at the more extreme conditions likely to be encountered during scale-up. An extra function was the production of liquid samples for evaluation as chemical feedstocks by the Dutch State Mines. This work was carried out in the period June to December 1973 and was the precursor to a substantial programme of research supported and partially funded by European Economic Community (EEC) between 1974 and 1986.

Autoclaves were the only equipment available in the first few years but by 1976 coal-extract solutions were provided to British Petroleum (BP) for tests in their continuous-hydrocracking unit (CHU). Although originally it was hoped to continue this arrangement, separation of the extraction and hydrocracking stages between two sites hindered detailed recycle experiments. Consequently, additional funding was obtained and BP built a new CHU, installed it at CRE and provided training for operators and maintenance engineers. This unit, together with associated facilities built at various times, eg extract production using a dedicated integrated solvent-extraction plant (ISEP), was the key experimental facility for the research programme. Many aspects of liquefaction, eg catalyst selection, were first studied or screened on smaller equipment but the aim was always to confirm potential process improvements in recycle runs on the CHU-ISEP equipment [or the Integrated Liquefaction Plan (ILP) as it was renamed in 1983].

The main criteria by which success during repeated recycling was gauged were that 100% recovery of solvent was achieved, that the power of the solvent to dissolve the coal remained adequate and that pitch-plus-filter cake represented no more than 40wt% (dmmf) of the coal. Solvent quality during repeated recycling demanded much attention; obtaining the balance between hydrocracking (of the extract) and hydrogenation (of the solvent) proved to be particularly difficult. However, solutions to all the problem areas were found and in 1984 what was deemed a totally successful run was carried out.

During the period 1977-1986, over 30,000h running of the ILP were achieved with nearly 6000h in 1984. Such long periods of operation were essential to prove catalyst life. Mass balances were carried out for virtually every day of operation and closures of over 95% became standard. The complexity of the plant, plus the amount of handling necessary to take the many samples that

were needed to assist interpretation, meant that these good balances were only achieved by continued vigilance by operators and supervisors. The success of the ILP programme owed much to the teamwork of the over 30 people involved. In addition to the studies supporting the ILP programme, much work was carried out during this period on the various unit operations, particularly on filtration using both small- and large-scale equipment (eg the extract plant in which other filters were installed). Secondary refining facilities were constructed with which finished gasolines and diesels were prepared, tested and also demonstrated in various vehicles (a lawnmower driven by Sir Derek Ezra, then Chairman of the NCB, a dumper truck by John Moore, Energy Minister, Automobile Association vans in the Lord Mayor of London's procession, as well as tests to measure fuel consumption, emissions, etc).

Proposals to build demonstration plants were made in the late 1970s and subsequently the siting of such a plant at Point of Ayr, North Wales, was agreed upon at an early stage. Consequently, Point of Ayr coal was chosen as the standard coal for use in experiments from 1981. Many other coals from around the world were tested on the small-scale and several in the ILP, including Illinois No. 6 coal which proved extremely easy to process. One of the major advantages of the LSE process that has emerged is its ability to handle virtually any coal regardless of rank or ash content.

The design specification for the Point of Ayr plant was based upon information obtained up to 1983. Many configurations were considered and four incorporated into the design, ie

- single-stage hydrocracking
- two-stage parallel hydrotreatment
- two-stage series hydrotreatment
- pitch recycle to hydrocracking

LSE PROCESS DEVELOPMENT PILOT PLANT, POINT OF AYR 1980-1992.

During the mid-1970s there were proposals to build larger electrode-coke plants, and these were considered in the Coal Industry Examination carried out in 1974. Its terms of reference were: *"To consider and advise on the contribution which coal can best make to the Country's energy requirements and the steps needed to secure that contribution"*.

With regard to the LSE project at the time, to quote the report: *"The NCB have pointed out that the prime objective of the project is the development of a liquid fuel from coal process, and that whilst the economics of electrode-coke production look attractive, the market is limited and a commercial venture could not carry the cost of developing the whole process. The extract hydrogenation stage provides the bridge to lighter hydrocarbon liquids, both fuels and chemical feedstocks, but this is still in the laboratory stage"*.

The report concluded: *"We consider that the combination of NCB expertise, relevance to the UK economy, and commercial prospects, justifies concentration on three areas, fluidised bed combustion, coal liquefaction by solvent extraction and pyrolysis"*.

Support came relatively quickly for the fluidised bed combustion project (at Grimethorpe, UK) but it was some time before an acceptable pilot plant project for the LSE process was formulated. However, in 1980 Matthew Hall Ortech (MHO) were chosen as contractors to perform design and costings of 25t/day pilot plants comprising LSE and supercritical-gas extraction (SGE) front-ends with a common hydrocracking facility. SGE was abandoned soon after in 1982, partly as a result of MHO's reservations about further scale-up of this process.

However, the LSE 25t/day plant plan did not receive UK Government support. In late 1982, ICI were called in by the Chief Scientist at the Department of Energy as consultant to advise on the scale of the development proposed by the NCB. ICI in their 'audit' proposed that engineering information could be obtained at a scale of 1t/day; NCB continued to consider that 25t/day was necessary on the basis of the process information that had been produced at CRE. However, in order to proceed, a compromise was reached in which a throughput of 2.5t/day was agreed (the base case in the specification, therefore, was 100kg/h of dry, mineral matter-free coal).

The EEC had always been highly supportive and initial approval to provide significant funding for the 25t/day plant had been granted but had to be cancelled. The UK Government stipulated that to receive their support for the 2.5t/day plant, EEC funding had also to be obtained, project management should be strengthened and at least one private company should participate. Oil company support was not forthcoming for various reasons. However, this impasse was finally resolved by an agreement between Ian McGregor (Chairman of NCB) and Peter Walker (Secretary of State for Energy) in which funding from the Department of Energy and the EEC was released on the understanding that the NCB would make every endeavour to find a commercial partner. (This was eventually achieved when Ruhrkohle Oel und Gas GmbH and Amoco Corporation joined the Project in 1987 and 1991, respectively.)

A steering committee was responsible for the project and it set the following objectives:

"The next stage in the development of the NCB's Liquid Solvent Extraction (LSE) process is to

design, build and operate a 2.5t/day Process Development Pilot Plant (PDPP).

The primary objective is to demonstrate that the LSE process can be operated continuously using solvent derived from the feed coal; this requires that solvent quality and quantity be satisfactorily maintained and controlled and satisfactory yield pattern of distillates obtained.

The project was nominally separated into four phases, ie specification, construction, commissioning and operation, and each phase was contracted separately. During the first phase, funded by the Department of Energy and BCC (the successor to NCB), the overall project costs and scheduling were ascertained. Following this, the complete project was approved in October 1985 by BCC's Board and agreements reached with the Department of Energy and the EEC.

There were contractual and other problems during the construction phase which delayed commissioning and the planned recruitment, and the full project operating time was rephased accordingly. However, the delay at Point of Ayr provided the opportunity to review again all aspects of the process and as a result additional experimental projects were proposed with separate funding arranged with the European Coal and Steel Community (ECSC) and BCC. This made particularly good use of CRE staff who were to form the core of the Point of Ayr staff and significant advances in certain areas were made.

In addition to the CRE experimental work, studies have also been made on economic aspects. This included a commercial plant design and costing performed by Costain Ltd. The design reflected the evolved LSE process and the costing procedure enabled variations in the process (eg when using different coals) to be estimated with some confidence. The objective of this particular study was two-fold. In addition to giving up-to-date economic figures, it was intended to guide the Point of Ayr plant's operating programme such that the variables studied were those that could have the biggest economic impact rather than those which were academically perhaps more interesting.

Another study commissioned in 1991 was to consider how coal liquefaction might be introduced into the European refinery scene. This required the contractor, Trichem Consultants Ltd, first to predict the future European oil refinery situation well into the next century and then to estimate the value to refiners of coal-derived liquids.

A way of expressing the process economics is to calculate what the price of crude oil has to be for a coal liquefaction plant to give a nominal internal rate of return, eg 10%. Currently, this 'break-even oil price' is around \$35/bbl (for coal priced at \$60/t) although this could be reduced in several ways. For example, if the coal price was reduced to \$20/t, the break-even oil price could be as low as \$25/bbl. Clearly, a liquefaction plant located near a cheap source of coal would seem to be a good solution. Unfortunately, most locations of cheap coal are such that the plant construction costs would be much higher (than for the base-case coastal location) and no net benefit would accrue. Consequently, the search for the ideal combination of cheap coal and cheap plant construction costs continues.

CONCLUSIONS

Direct liquefaction technology in the UK has advanced considerably from the stage in 1967, when little was known of the way in which UK coals behaved. Work on the electrode coke process not only extended knowledge of liquid solvent-extraction of coals but also showed conclusively that coal-based carbon materials were technically feasible and could be produced commercially. The LSE process, extended the first development to show that petrol and diesel fuels could be produced with high efficiency, not only from UK coals but also from essentially any coal worldwide.

Knowledge accumulated from developing and proving these processes has been achieved through the efforts of many individuals and organisations, including those who ensured the availability of funds, those who were creative in overcoming problems and those who engineered the solutions. The key benefit of all these contributions and developments is that UK liquefaction technology has been advanced to the point that when, as it eventually will, the price of oil rises, action can be taken to enable coal to provide a realistic, alternative source for transport fuels.

REFERENCE

(1) G.M. Kimber, "A History of U.K. Coal Liquefaction" COAL, R078, ETSU, Harwell, U.K., Dec. 1996.

RECENT ADVANCES AND FUTURE PROSPECTS FOR DIRECT COAL LIQUEFACTION PROCESS DEVELOPMENT

F. P. Burke and R. A. Winschel
CONSOL Inc.
Research & Development
4000 Brownsville Road
Library, PA 15129

David Gray
Mitretek Systems
7718 Old Springhouse
McLean, VA 22102-3481

Keywords: Direct Liquefaction, Process Development, Economics

ABSTRACT

Over the last fifteen years, the technology for the direct conversion of coal to liquid fuels has undergone significant development. This has been most evident in improvements in product yields (i.e., barrels per ton of coal), product quality, and, ultimately, in projected product costs. These advances have occurred through the optimization of process conditions and, particularly, a better understanding of the selection and use of catalysts. In addition, engineering and economic evaluations of the liquefaction process alternatives, and macroscopic analysis of global fuel production and consumption have been essential in guiding process development and providing a justification for investment in further R&D. This paper will highlight some of the important technical achievements in reaching the current state of direct liquefaction process development, and provide some speculation on the opportunities and obstacles for future research and commercial implementation.

THE WORLD AND UNITED STATES OIL SITUATION

Petroleum use worldwide is about 65 million barrels per day (MMBPD), and the Energy Information Administration (EIA) predicts that by 2015, worldwide demand will increase to between 89 and 99 MMBPD.¹ Over 55% of world petroleum is used in the transportation sector. Liquid hydrocarbon fuels are ideal for transportation since they are convenient, have high energy density, and a vast infrastructure for production, distribution and end use is already in place. The estimated ultimate world resource of oil and natural gas liquids (NGL) is 2.5 trillion barrels; the sum of 1.2 trillion barrels for OPEC and 1.3 trillion barrels for non-OPEC.¹ Estimates of proven reserves of oil vary over time because more of the oil resource moves into the reserve category as a result of variations in the world oil price (WOP) and available technologies. However, the estimated ultimately recoverable world conventional oil resource (EUR) has been remarkably similar for the last 25 years. James MacKenzie of the World Resources Institute² cites an analysis of 40 estimates of ultimately recoverable oil, for the years 1975 to 1993, conducted by David Woodward of the Abu Dhabi Oil company. In this analysis, Woodward concluded that "there is a fair degree of consistency among the estimates with the average being 2,000 billion barrels (BBO) and 70% falling in the range of 2,000 to 2,400 BBO."

Mitretek has performed analyses of world oil demand and potential supply from the present until 2100.³ The results of these analyses show that when the projected world oil demand is plotted on the ultimate resource curve whose integral is equal to 2.5 trillion barrels, it becomes clear that conventional world oil production will peak in a timeframe from about 2015 to 2020 and then irreversibly decline because of resource limitations.

Because oil is the primary fuel in the transportation sector, Mitretek also examined the potential impact of the above world oil supply scenario on the U.S. transportation sector.³ This analysis concludes that, even with a rapid penetration schedule for alternatively fueled vehicles, there is likely to be a significant shortfall in petroleum supply in the United States before 2015.

THE DEVELOPMENT OF DIRECT COAL LIQUEFACTION TECHNOLOGY

Direct coal liquefaction is the process by which coal is converted to liquids through the addition of hydrogen or the removal of carbon. Hydrogen can be provided directly from the gas phase, through transfer from a chemical source such as a hydrogen donor, or carbon can be removed by a disproportionation reaction in which the coal is converted to (relatively) hydrogen-rich and carbon-rich products. The reaction generally requires temperatures above the softening point of coal (typically around 600 K) to facilitate mass transport and to achieve adequate rates of reaction. Although liquids of some description can be produced by a number of approaches, the objective usually is to produce

transportation grade fuels as substitutes for petroleum-derived gasoline or diesel fuel. The reactions involved include hydrogenation and cracking, and removal of nitrogen, oxygen and sulfur from the coal (primarily as NH_3 , CO , CO_2 , H_2O , and H_2S). The mechanisms of these reactions generally involve both hydrogenation and bond cleavage, although opinions differ as to the reaction sequence.

The cost of producing coal liquids is implicit in these chemical reactions. There is a theoretical minimum amount of hydrogen that is necessary to convert the (empirical) coal structure to liquid products of some specified composition. In practice, the amount of hydrogen consumed (typically 6-7 wt % on a moisture-ash-free coal basis) will be greater than the theoretical minimum because of undesirable side reactions, such as methanation of carbon oxides and C_1 - C_4 gas formation due to cracking. Because hydrogen is expensive, there is a strong incentive to minimize its consumption, but the quality of the product liquid must be known for a comparison of hydrogen consumption values to be meaningful.

The liquefaction reactions require elevated temperatures to proceed at reasonable rates; this requires some pressure containment (~500 psig) to keep the reactants in the liquid phase. If molecular hydrogen is used as the hydrogen source, higher operating pressure (2000-3000 psig) is required for adequate mass transfer. The combination of elevated pressure and temperature is an important factor in determining the capital cost of the liquefaction train, including heat-transfer units, reactors, pumps, pressure let-down systems, etc. Effective catalysts can decrease both the reaction pressure and temperature. Given the heterogeneous nature of coal, the presence of mineral matter, and the variety of functional groups present, it is likely that some form of catalysis occurs, even if an external catalyst is not used. In fact, catalysts are universally employed in practical liquefaction processes, with solid heterogeneous catalysts being the most common. Historically, the first commercial liquefaction plants in Germany used the I. G. Farben process, in which coal was liquefied at 760 K and 10,000 psig in a liquid phase reactor using a relatively inactive iron catalyst. Because of the reaction severity, the German plants produced high hydrocarbon gas yields (30 wt % MAF coal) with a correspondingly high hydrogen consumption (~14 wt % MAF coal).

In the United States, the development of direct liquefaction technology was stimulated by the petroleum shortfalls and price increases of the 1970s. By 1980, three process concepts (SRC-II, EDS and H-Coal) had been sufficiently advanced to merit consideration for commercialization. An interest in producing a substitute fuel oil for electric utility boilers led the Southern Company and Electric Power Research Institute to explore the Solvent Refined Coal (SRC) process on the 6 tpd Wilsonville, Alabama facility. This was a one-stage thermal process in which coal was solubilized in a recycle solvent, and the product was deashed to remove mineral matter and some sulfur. A variant of this was the SRC-II process, developed by Gulf Oil Company and others. In the SRC-II process, coal was hydrogenated in a one-stage reactor with no catalyst addition, but the distillation bottoms were recycled to take advantage of the catalytic activity of the coal mineral matter. The SRC-II process was piloted on a 50 tpd unit at Ft. Lewis, WA. The Exxon Donor Solvent (EDS) process was developed through the 250 tpd pilot plant scale at Baytown, TX. In the EDS process, the coal was fed to a plug-flow reactor in a recycle solvent (the donor solvent) that was hydrogenated catalytically in an external reactor. The donor solvent provided the hydrogen for the liquefaction reaction. In later development, a bottoms recycle stream was added to the EDS feed to provide additional residence time for conversion, and perhaps to utilize the catalytic activity of the mineral matter. One common feature of these processes, and others such as the CONSOL CSF process and the British Coal LSE process, was that the primary coal liquefaction reactions took place in the absence of any added catalyst, ostensibly to avoid the rapid deactivation of the catalyst that was presumed to occur in the presence of the coal mineral matter.

In the HRI H-Coal process, the issue of catalyst deactivation was addressed by utilizing an ebullated bed reactor which allowed a supported catalyst to be added and withdrawn continuously. The ebullated bed reactor also offered superior performance in terms of heat and mass transfer. The H-Coal process was developed at HRI's bench-scale and PDU facilities in Lawrenceville, NJ, and piloted on a 250 tpd unit in Catlettsburg, KY. Representative operating conditions and yields for the H-Coal pilot plant operations with Illinois basin bituminous coal are shown in Table 1. The process made a relatively light product (proportion of naphtha) but also had a sizeable yield of hydrocarbon gases and unconverted resid, which reduced overall liquid yield.

One problem with the single catalytic stage is that hydrogenation reactions are best done at relatively low temperatures where the equilibrium is more favorable, but conversion

(i.e., cracking) reactions are faster at higher temperature. To overcome this, research was conducted on the use of multiple reaction stages, exemplified by work by Lummus and Cities Service in New Brunswick, NJ. In the Lummus/Cities bench unit, the coal was converted to a soluble form in the first stage at relatively high temperature (~720 K) but short contact time (~2 min). The first-stage product was deashed, and converted to distillate liquids at around 670 K in an ebullated bed LC-Finer unit, which simultaneously produced a hydrogenated solvent for recycle to the first stage. A similar configuration was installed at the Wilsonville SRC pilot plant, which employed a Kerr-McGee Critical Solvent Deasher between a thermal first stage and an ebullated bed second stage supplied by HRI.

Lummus first recognized, and Wilsonville later confirmed, that the location of the deashing unit between the two stages had little effect on catalyst life. The most important factor in catalyst deactivation was carbon laydown, not poisoning by metals in the mineral matter. This led to "close coupling" of the two reactor stages, with deashing applied to the second-stage product. It also allowed for "ashy recycle", in which a portion of the second-stage product is recycled directly to the first stage. By concentrating solids in the recycle stream, the amount of material processed by the deasher was significantly reduced, and the unconverted coal was given additional residence time. The Wilsonville unit subsequently was used to explore a variety of staged reactor configurations, including two ebullated bed catalyst stages ("catalytic/catalytic" mode), the use of a dispersed iron oxide as a first-stage catalyst with subbituminous coals ("thermal/catalytic" mode), and alternative temperature staging. As shown in Table 1, this resulted in substantial reductions in hydrocarbon gas and resid production for bituminous coal, with a corresponding increase in distillate liquids, although the product was higher boiling than that of the H-Coal process. Results with subbituminous coal (Table 2) were similar, although a high first-stage temperature was still required to achieve adequate coal conversion. One advantage of the "thermal" first stage is a greater removal of oxygen as carbon oxides. In the single-stage system, carbon oxides are converted catalytically to methane and water, with increased hydrogen consumption.

Although the first stage in the thermal/catalytic mode did not contain a supported catalyst, the Wilsonville unit was fed a powered iron oxide catalyst to promote coal conversion. This was consistent with research at Mobil R&D showing that solid catalysts promote the conversion of coal to soluble forms. Subsequent work at Wilsonville, HRI, and a number of academic institutions explored the use of dispersed catalysts based on iron, molybdenum, and other metals. In a current collaborative project, CONSOL, the University of Kentucky, LDP Associates, Hydrocarbon Technologies Inc. (HTI), and Sandia National Laboratories have been exploring several advanced concepts for improving direct liquefaction process economics through modifications to the feed coal and recycle solvent and the use of dispersed and impregnated slurry catalysts. This work has progressed through laboratory studies to evaluation of the process concepts in bench-scale continuous unit runs at HTI, the former experimental facilities of HRI. The first run (ALC-1) was made in the all-slurry catalyst mode with molybdenum and iron catalysts. Potential advantages of operation with all-slurry catalysts include: simplified reactor design; simplified operations, constant catalyst activity, more efficient use of reactor volume (no volume needed for catalyst support); and catalyst can be recycled with solids to reduce the fresh catalyst requirements. Raw subbituminous coal was used in condition 1 of Run ALC-1; the same coal cleaned by oil agglomeration was fed in condition 4 (Table 2). In condition 5 (not shown in Table 2), the distillate portion of the recycle solvent was dewaxed and hydrogenated to improve solvent quality. As shown in Table 2, these operations produced exceptional distillate yields of 66% to 69% MAF from subbituminous coal. This was accomplished by near-extinction conversion of residual oils, including unconverted coal. The somewhat higher hydrogen consumptions in these operations resulted, in part, from the higher gas yields due to the higher reaction temperatures, but they also resulted from the use of an in-line gas-phase hydrotreater for the distillate product. These operations produced a low-heteroatom, highly hydrogenated product with low boiling point.

OPPORTUNITIES FOR FUTURE RESEARCH AND DEVELOPMENT

As summarized above, the analysis by Mitretek indicates that the time when worldwide petroleum demand begins to deplete resources may come within the next two decades, even without significant political or economic disruptions. Therefore, it is essential simultaneously to pursue a number of options to mitigate the future shortfall in domestic petroleum. These options are: to continue domestic exploration and production using the best technologies available, to continue to develop and deploy alternatively fueled vehicles, and to continue to improve efficiencies in all sectors of transportation. Yet, even with these steps, this analysis indicates that the domestic demand for liquid fuels will exceed our potential sources of supply. Continuing our reliance on oil imports to alleviate the shortfall is not a long-term solution. Rapidly increasing world oil demand will put ever-increasing pressure on the oil supply and the WOP will rise. The inevitable conclusion is that

additional options will be necessary to ensure that the United States will have the necessary liquid fuels supply to be able to continue economic growth into the 21st century. One of these additional options is to produce liquid fuels from our huge domestic coal resources.

Current direct coal liquefaction technology is technically feasible, but not economically competitive. However, with world oil prices over \$25/bbl at this writing, it is clear that, in the long term, the upward pressure on oil prices persists. Research should be directed toward reducing the cost of liquid products so that these alternative technologies are available as early as possible to have the greatest economic benefit. Several technical issues are pertinent to achieving that objective.

Catalysts. Despite all the research that has been done on catalyst development and testing, improved catalysts still offer the single best opportunity for affecting many of the cost features in a liquefaction process, including yields, selectivity, product quality, hydrogen utilization, and capital cost (through reduced pressure and temperature and increased space velocity). A problem with much catalyst research is that it is done at unrealistic conditions, with results that are not easily translated to a process context. For example, identifying a catalyst that improves coal conversion from 40% to 60% is of little value when the process goal is produce specification products at high yield. On the other hand, identifying a truly improved catalyst could open significant opportunities for redefinition of the basic process concept.

Feedstock Selection. The principal feedstocks are coal and hydrogen. Most coals have been shown to be suitable for most processes. If there is an "opportunity" coal, it will be the result of economic opportunity; for example, the current emphasis on U.S. low-rank coal recognizes its low mine-mouth cost. Reduction in hydrogen cost is problematic. Production of hydrogen from coal involves a large unavoidable capital expenditure for the gasification plant. Production from natural gas is unlikely to be economical in the long term, particularly if petroleum prices have risen. Coprocessing feedstocks, such as waste plastics and heavy resid, may be useful in providing an economic justification for early "pioneer" plants which will demonstrate commercial viability.

New Reaction Mechanisms. Despite its variations, current liquefaction technology remains based in the early German technology, i.e., thermal free radical or radical-initiated hydrogen transfer. There are other possible hydrogen transfer chemistries, including carbonium ion, hydride ion and biochemical mechanisms. Although these have been explored, they have yet to yield a promising candidate. As with the catalyst research, much of the problem may lie in a failure to establish exploratory research goals of such a nature that they can be used to justify further development. A realistic candidate must be able to achieve high yields of liquids that meet some minimum standard of quality or upgradability.

REFERENCES

1. Annual Energy Outlook 1996 With Projections To 2015. Energy Information Administration, January 1996. DOE/EIA-03893 (96).
2. MacKenzie, James J. *Oil as a Finite Resource: When is Global Production Likely to Peak?* Paper from the World Resources Institute, March 1996.
3. Gray, David, and Glen Tomlinson, *Rationale and Proposed Strategy for Commercial Deployment of Coal-Derived Transportation Fuels*, Mitretek Report MP 96W0000209, June 1996.

TABLE 1

OPERATING CONDITIONS AND YIELDS FOR H-COAL, ITSL, AND CMSL,
ILLINOIS BASIN COAL

	H-Coal Pilot Plant Run 8	ITSL Wilsonville Run 252B1	ITSL Wilsonville Run 257J	CMSL HTI Run PB-05/2
Year	1981	1987	1989	1996
Conditions				
Stage 1				
T, K	728	705	705	720
H ₂ Partial pressure, psi, inlet	2500	2500	2600	2500*
Catalyst age, lb coal/lb	1690	~1300	645	Dispersed
S.V., lb coal/hr/ft ³ reactor, each stage	29	-	-	42
Stage 2				
T, K	None	672	678	731
Catalyst age, lb coal/lb	None	~470	1309	Dispersed
Yields, wt % MAF				
H ₂ O	7.5	9.6	10.2	4.3
H ₂ S, NH ₃ , COx	3.8	5.1	5.0	6.1
C, x C ₃ Gas	12.8	6.5	5.4	6.7
Naphtha	22.9	17.5	14.5	18.4
Middle Distillate	20.0	7.8	7.1	16.0
Gas Oil	7.6	44.1	44.2	39.0
Total Distillate	50.5	69.4	65.8	73.4
Resid	31.3	16.4	19.7	14.8
H ₂	-6.0	-7.1	-6.0	-5.2
Coal Conversion	96.1	93.0	91.7	96.2

*Unit back-pressure

TABLE 2

OPERATING CONDITIONS AND YIELDS FOR H-COAL, ITSL, AND CMSL,
POWDER RIVER BASIN COAL

	H-Coal PDU Run 10	ITSL Wilsonville Run 262D	CMSL HTI Run ALC-1/1	CMSL HTI Run ALC-1/4
Year	1980	1991	1996	1996
Conditions				
Stage 1				
T, K	719	713	715	716
H ₂ Partial pressure, psi, inlet	2500	2800	2500*	2500*
Catalyst age, lb coal/lb	742	Dispersed	Dispersed	Dispersed
S.V., lb coal/hr/ft ³ reactor, each stage	25	-	42	26
Stage 2				
T, K	None	694	726	726
Catalyst age, lb coal/lb	None	727	Dispersed	Dispersed
Yields, wt % MAF				
H ₂ O	16.3	13.9	13.8	16.2
H ₂ S, NH ₃ , COx	3.5	6.7	5.9	5.1
C, x C ₃ Gas	11.0	5.3	9.4	12.4
Naphtha	24.3	12.9	18.6	23.0
Middle Distillate	14.5	7.7	11.3	9.7
Gas Oil	11.9	40.1	39.2	33.4
Total Distillate	50.7	60.8	69.0	66.1
Resid	24.1	18.7	9.4	7.1
H ₂	-5.6	-5.5	-7.5	-6.8
Coal Conversion	91.0	90.1	95.0**	97.5**

*Unit back pressure

**SO₃-free ash basis

COAL PHOTOLUMINESCENCE: MODIFICATION OF SURFACE PROPERTIES AND GEOCHEMICAL AND TECHNOLOGICAL IMPLICATIONS

Alan Davis and Gareth D. Mitchell

Coal & Organic Petrology Laboratories, Department of Geosciences,
105 Academic Projects, Penn State University, University Park, PA 16802

Keywords: coal luminescence, coal fluorescence, coal hydrophobicity

INTRODUCTION

The luminescence behavior displayed by vitrinite across the coal rank range upon exposure to microscopic blue- and UV-light irradiation, has been explained by Lin et al. (1) using the molecular-phase concept. Two peaks occur in the trend of vitrinite luminescence intensity with rank. The first of these, at the low maturity end of the series represented by peats and lignites, displays the highest intensity levels. This "primary fluorescence," is considered to be due to the presence of lignin-derived structures (2); it is almost eliminated by about the subbituminous C/B boundary owing to the progressive luminescence quenching which accompanies condensation. It is the second peak, centered at high volatile A bituminous rank (reflectance of about 0.9%), which Lin et al. have attributed to the development of the mobile or molecular phase within the vitrinite. The same coals give the highest yields of chloroform solubles. It is these extractable components which are responsible for the luminescence response of the vitrinites; whereas the aromatic and polar fractions of hexane solubles were highly luminescent, the chloroform-extracted residue of mildly pre-heated vitrinite was not visibly luminescent. This residue is considered to represent the aromatic network which is too highly condensed to luminesce in bituminous coals; delocalization of electrons in the macromolecules within this rank range causes intense quenching.

With increasing time of exposure to UV or blue light under an air objective, the luminescence intensity displayed by vitrinite undergoes progressive or variable changes in patterns which are rank dependent. Davis et al. (3) have shown that this phenomenon, termed "alteration", results mainly from photochemical oxidation; it does not occur when an inert medium is used instead of air. A cationic dye, Safranin O, which is sensitive to oxidized coal surfaces, responds positively to the air-irradiated surfaces. FTIR spectroscopy reveals that a major change resulting from the air irradiation is an increase in carbonyl functional groups.

One purpose of this paper is to review some of the geochemical factors, in addition to rank, which influence the luminescence response of vitrinite. Another is to discuss how the molecular-phase concept has been applied to the results of quantitative luminescence photometry of the products of dry, catalytic hydrogenation. However, most of the results reported here are concerned with an investigation of the relationship between oxygen functionality and hydrophobicity. Advantage has been taken of the photo-oxidation technique to modify the surface chemistry of vitrinites so that variation in contact angle and floatability can be related to specific changes in FTIR-determined oxygen functionality.

INFLUENCE OF DEPOSITIONAL ENVIRONMENT UPON VITRINITE LUMINESCENCE

Although rank has a dominant influence in determining the luminescence behavior of coals, there is also some influence exerted by the depositional environment. Several investigators have observed higher luminescence intensities displayed by vitrinites deposited in a marine-influenced environment compared to those not so influenced. Rathbone and Davis (4) reported a positive correlation between luminescence intensity and total sulfur of an iso-rank series of bituminous coals; they discussed the possibility that the phenomenon might be related indirectly to a greater incorporation of bacteria-derived lipids into coals deposited in a marine setting. Zhang et al. (5) have suggested an alternative mechanism through which sulfur-linked aliphatic structural units acquired during early coalification has directly enhanced vitrinite luminescence intensity. Py-gc/ms and solid-state ^{13}C nmr of vitrinites and luminescence measurements on model compounds led to the conclusion that bacterially reduced sulfur species can vulcanize functionized lipids onto the macromolecular phase. In contrast, increased levels of phenolic compounds present in low-sulfur freshwater vitrinites are associated with lower luminescence intensities.

LUMINESCENCE PHOTOMETRY OF LIQUEFACTION RESIDUES

Quantitative luminescence photometry was one technique used to interpret the structural changes involved during dry, catalytic hydrogenation (6,7). Measurements were taken on the unextracted

liquefaction products and on the subsequent extracts. For example, hydrogenation experiments were performed using a high volatile bituminous coal and an impregnated molybdenum catalyst at 400°C for four different reaction times. The absence of a liquid vehicle is essential so that the liquid products are not removed from the coal. With increase in time up to 60 min, the luminescence intensity of the unextracted residues increased progressively and markedly from the zero reading obtained with the fresh coal. This increase closely paralleled the proportion of chloroform extracts obtained from the series of hydrogenated coals, a correspondence suggesting that the luminescence is a response from relatively low molecular weight materials representing both the molecular phase of the coal and products from the breakdown of the network. Indeed, the luminescence of the vitrinite residue, induced by hydrogenation, showed a red shift (increase in wavelength) as hydrogenation temperature was increased from 350 to 400°C; this shift is consistent with the increased generation of asphaltenic materials from the network. The chloroform extract of the 400°C residue was highly luminescent (the residue was not); two physically distinct components were recognizable. The component with by far the highest luminescence intensity had a spectral peak wavelength corresponding to that of the oil (hexane-soluble) fraction of the hydrogenation products, whereas that of the less luminescent component had a spectral peak corresponding to that of the asphaltene fraction.

PHOTO-OXIDATION AND HYDROPHOBICITY OF BITUMINOUS COALS

Severe oxidative weathering has a negative influence on the behavior of coals in most industrial processes including cleaning. As coals are increasingly oxidized they become less hydrophobic and more difficult to separate from mineral matter by flotation.

The surface photo-oxidation of bituminous coals which occurs as a result of blue- and UV-light irradiation shares many similarities with naturally weathered coal. Therefore, light of 390-490 nm has been used to prepare oxidized vitrain surfaces. These have been employed in experiments to establish correlations among surface oxygen functionality, surface hydrophobicity, flotation yield and, as a readily measurable index of oxidation, luminescence intensity.

An optical microscope was used to measure luminescence intensity (in N_2) and alteration (in air), and to photo-oxidize freshly polished surfaces of vitrains collected from a suite of coals of varying bituminous rank (hVcb to mvb) using a blue-light flux. Irradiations were conducted for 0, 1, 5 and 10 mins. The change in near-surface chemical functionality was measured using reflectance-mode FTIR. Contact-angle measurements were made on these same irradiated surfaces to obtain a correlation among chemical changes, luminescence intensity and wettability.

Scribe marks were cut perpendicularly across selected vitrain bands on polished blocks of coal, and successive 200 μ m diameter areas were irradiated in two adjacent lines parallel to each mark to create 0.4mm wide oxidized zones. During the course of the irradiations, photometric readings were obtained of the change in luminescence intensity with time (alteration).

A sessile drop technique was used to determine the change in surface wettability. Using a syringe and micro-pump, a drop of distilled water was advanced from the fresh vitrain surface across the photo-oxidized area and contact angles measured at regular intervals. These same areas were subsequently relocated for measurement of variation in functional group chemistry using reflectance-mode FTIR.

A comparison of the luminescence, contact angle and FTIR spectra for the fresh and varyingly photo-oxidized vitrain surfaces for three of the coals studied is given in Figures 1 and 2. Luminescence intensity changes characteristically during irradiation in air; for fresh bituminous coals there is either a negative (intensity decrease) or dual (decrease followed by increase) response, depending upon coal rank (first column, Figure 1). The reflectance FTIR spectra (Figure 2) show a progressive increase in absorbance in the carbonyl region (~ 1775 - 1650 cm^{-1}) and a decrease in the aliphatic region (~ 3030 - 2850 cm^{-1}) with irradiation time. The spectra also suggest that the O-H region near 3450 cm^{-1} may increase upon irradiation. Considering these results, the influence of photo-oxidation on surface wettability (second column, Figure 1) is predictable, i.e., the magnitude of change in contact angle increases with irradiation time. These effects decrease with rank.

The results suggest that the luminophores on the surface of fresh bituminous coals are initially quenched by oxygen, causing a decrease in emission intensity, with only marginal influence upon

near-surface chemistry and wettability. However, with increasing exposure, an increase in the spectral region occupied by ketones, aldehydes and esters suggests a variety of reactions involving carboxylic acid groups and anhydrides that would affect the intensity of luminescence alteration.

CONCLUSIONS

Rank is the dominant influence in determining the luminescence behaviors of coals; however, measureable effects representing the depositional environment can also be encountered. In marine-influenced environments, lipoidal material may have become incorporated into the coal precursor molecule through a sulfidization process, leading to an enhancement of luminescence intensity.

The results of quantitative luminescence spectrometry support the conclusion that the more intense levels of coal hydrogenation in a series of dry, catalytic experiments were achieved by disruption of the macromolecular network and the production of asphaltenes.

Blue-light irradiation using photometric microscopy provides a means of progressively oxidizing the surfaces of vitrains. The reflectance FTIR measurement on irradiated areas shows an increase in the carbonyl and decrease in aliphatic regions that are similar to results observed in laboratory and natural oxidation studies. The changes in infrared spectra and wettability are more pronounced with increasing radiation time and with lower rank. Some contribution to the oxidation of coals exposed at the face of strip mines and in stockpiles may have arisen as a result of exposure to the ultraviolet irradiation of sunlight.

ACKNOWLEDGEMENTS

The authors gratefully acknowledge the financial support of U.S. Dep. Energy Grant No. DE-FG22-93PC93223. Much of the work referenced was undertaken in collaboration with past and present colleagues within the College of Earth and Mineral Sciences at Penn State.

REFERENCES

1. Lin, R., Davis, A., Bensley, D.F. and Derbyshire, F.J., *Internat. J. Coal Geol.*, 6, 215 (1986).
2. Stout, S.A. and Bensley, D.F., *Internat. J. Coal Geol.*, 7, 119 (1987).
3. Davis, A., Rathbone, R.F., Lin, R. and Quick, J.C., *Org. Geochem.*, 16, 897 (1990).
4. Rathbone, R.F. and Davis, A., *Org. Geochem.*, 20, 177 (1993).
5. Zhang, E., Mitchell, G. D., Davis, A. and Hatcher, P.G., *ACS Div. Geochem., Geochemistry Newsletter*, Pap. 27, Spring (1994).
6. Derbyshire, F.J., Davis, A., Lin, R., Stansberry, P.G., and Terrer, M.-T., *Fuel Proc. Technol.*, 12, 127 (1986).
7. Lin, R., Davis, A., Bensley, D.F. and Derbyshire, F.J., *Org. Geochem.*, 11, 393 (1987).

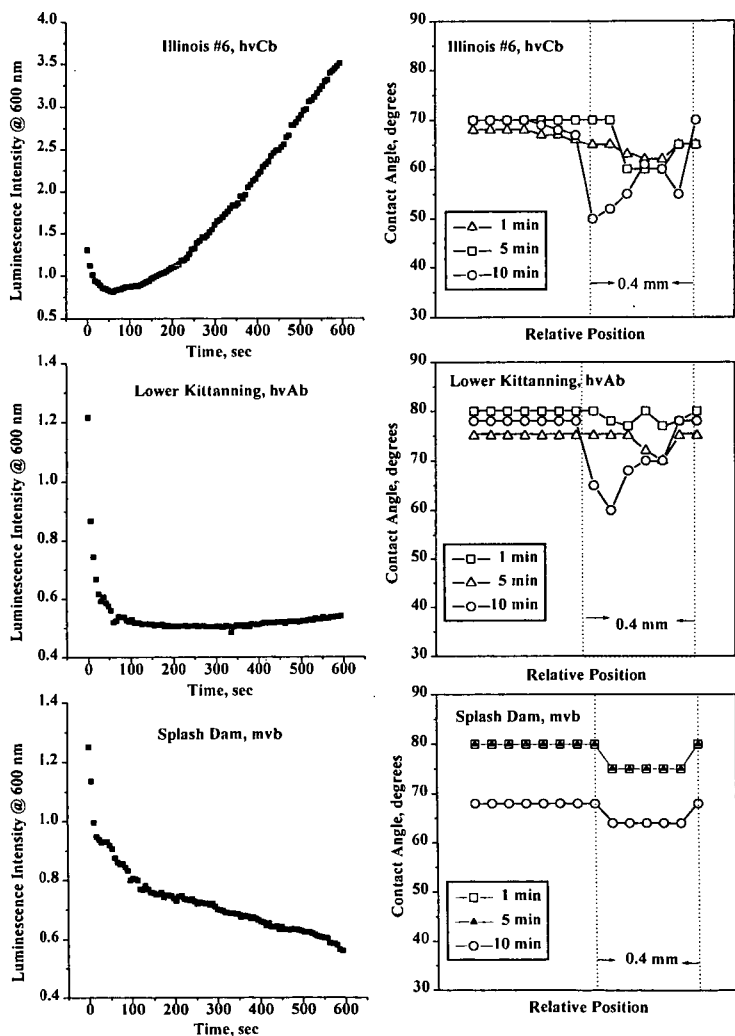


Figure 1. Comparison of luminescence alteration and contact angle measurements on fresh and photooxidized areas of three bituminous coals

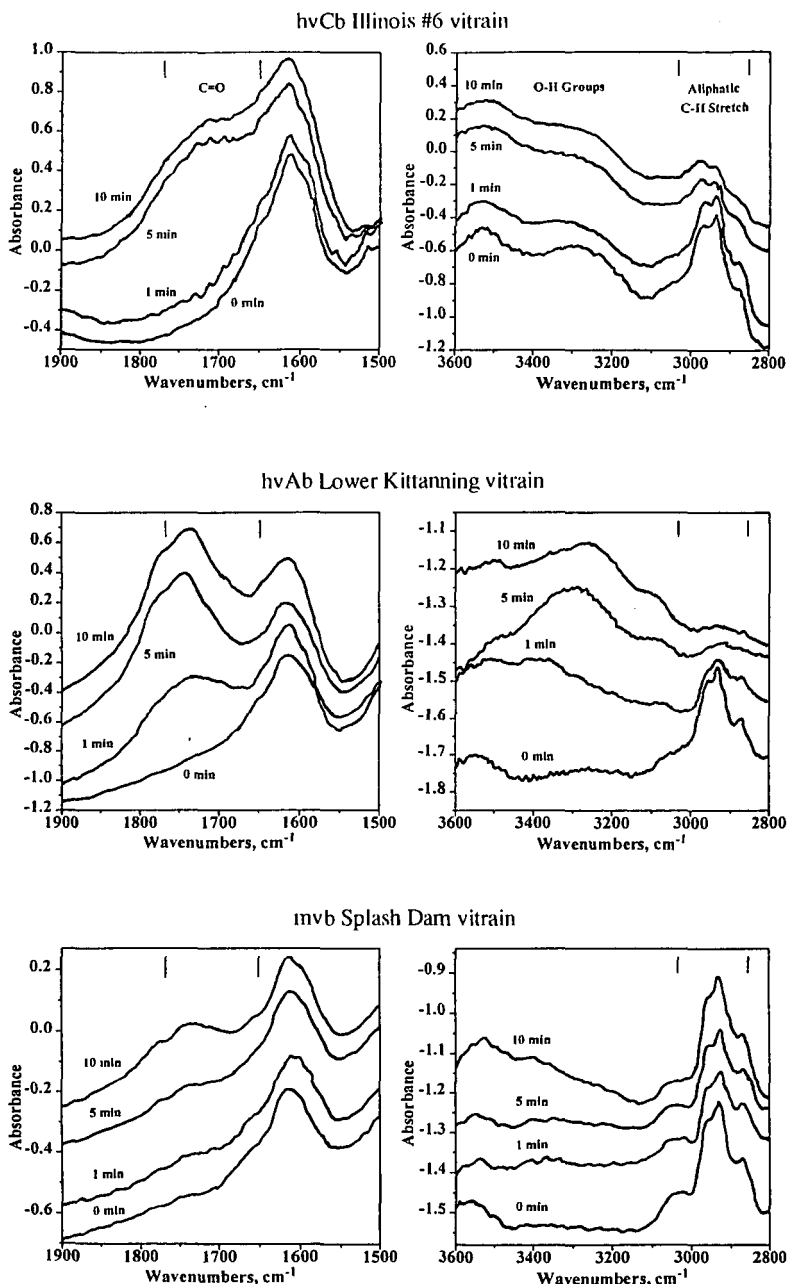


Figure 2. Comparison of FTIR spectral regions for fresh (0 min.) and irradiated surfaces (1, 5 and 10 min.) of three bituminous coals.

CARBON AS AN OXIDATION CATALYST

D.D. Whitchurst*
Mobil Research and Development Corp.
Central Research Division
Princeton, NJ 08540

* Present address - Institute of Advanced Material Study, Kyushu University, Kasuga, Fukuoka 816, Japan

KEYWORDS Oxidative dehydrogenation, Carbon catalyst, Mechanism, Surface chemistry

INTRODUCTION

There are numerous reports in the literature that carbonized metal oxides [1-7], carbons [8] and quinone containing polymers [9,10] can function as oxidative dehydrogenation catalysts. These reports, in combination with earlier work by Roth et al. [11], which showed that carbons can catalyze paraffin dehydrogenation, prompted our interest in assessing the utility of carbons or carbonized metal oxides as light paraffin upgrading catalysts.

It appeared as though there may be a common mechanism or surface chemistry operating in that reported work, so we conducted an extensive review of the literature to help our understanding of the fundamental processes before initiating our work. The purpose of that review was to gain some understanding of the stability and nature of surface functional groups formed on oxidation of carbon surfaces under conditions commonly used in the oxidative dehydrogenation of hydrocarbons in order to interpret mechanisms and potential improvements in oxidative dehydrogenations over carbonaceous catalysts. Several very good reviews on the surface chemistry of carbon do exist, but these do not attempt to interrelate surface chemistry to oxidation catalysis [12-15]. These reviews were utilized extensively in the formulation of our conclusions.

The information which we found relevant to oxidation catalysis from the diverse sources of information on carbon surface chemistry is illustrated in Figure 1. This may be summarized as follows. Carbons heated in inert atmospheres to above 1000-1200°C contain only carbon at their surfaces. All hydrogen and oxygen containing functional groups decompose (degas) below these temperatures to yield water and volatile carbon oxides respectively [12-18]. In degassed graphite, the edges of the basal planes must be composed of carbon in which all of the potential valance orbitals are not satisfied. This chemistry is believed to extend to high surface area carbons as well where the structures are much less developed and the size of the graphitic sheets is very small. One basic question is, just what is the nature of this pure carbon surface? It is known that degassed carbons contain high concentrations of unpaired electrons on their surfaces (as much as 0.2 meq/gm) [14]. In addition, Donnet has proposed that aroxylic radicals may account for many of the free radicals observed on carbons which contain some chemisorbed oxygen [14]. Certainly the surface is rich in free radicals, but what is their geometric configuration and what chemistry do they exhibit?

Two geometric orientations of the edges are possible and these have been referred to as zigzag and armchair. The preference for a given configuration has been shown to be influenced by the atmosphere used in preparation of the surface. Dry conditions favor the armchair configuration and wet conditions favor the zigzag configuration. It is also believed that only these edges interact with oxygen. Apparently, oxygen does not penetrate and react within the lamellar structure [19].

Three possible electronic structures have been proposed [20,21] for the edge carbons in which all of the valance orbitals are not satisfied. These structures contain either (1) one unpaired electron (e.g. free radical), (2) paired electrons (e.g. divalent carbon or carbene), (3) adjacent unpaired electrons or triple bond character (e.g. benzyne).

All of these structures would be expected to interact with oxygen to produce chemisorbed oxygen. The electrical properties of the carbon change drastically as oxygen is chemisorbed. The thermoelectric power of graphite has been shown to increase algebraically with oxygen concentration on the surface [16a].

Depending on the nature of the carbon structure and the conditions of reaction, one would expect to favor the production of different types of carbon-oxygen functionalities. Freshly degassed carbons begin to chemisorb oxygen at -40°C. Clean carbon surfaces, on contact with oxygen at as low as 200°C evolve volatile carbon oxides simultaneously with the formation of chemisorbed oxygen [17]. At this temperature carbon dioxide is the only gas evolved and about 1 molecule of carbon dioxide is evolved for each three oxygens chemisorbed on the surface [16b]. As the temperature of oxidation is increased, both the rate of chemisorption and volatile carbon oxide evolution increase. The maximum rate of chemisorption occurs at about 400°C [16]. Above 500°C, decomposition of chemisorbed oxygen species becomes significant [16b] and at about 650°C one molecule of CO₂ is evolved for each oxygen chemisorbed. Above 950°C chemisorbed oxygen species are not stable and very little steady state chemisorbed oxygen exists on the surface [16b]. Chemisorbed hydrogen is somewhat more stable and is not completely removed until about 1100°C [16c].

Walker has proposed that there exist two different kinds of reactive surface carbon species [16c]. Both species produce carbon monoxide on reaction with carbon dioxide at gasification temperatures (900-1100°C). One type produces more stable chemisorbed oxygen species $C<O>1$. The other is much more reactive and produces a less stable chemisorbed oxygen species $C<O>2$ which decomposes rapidly to gaseous CO and regenerates the free carbon surface. In a parallel reaction $C<O>2$ also converts to $C<O>1$ which decomposes much more slowly. The overall rate of gasification thus goes through a maximum and declines to a steady state rate as $C<O>1$ builds up on the surface. Hydrogen sources, such as H₂ or water inhibit the rate of gasification due to build-up of $>CH_2$ species which are more stable than carbon oxide surface species. Walker also showed that 2 hydrogens are adsorbed for each site that adsorbs 1 oxygen and he proposed that these sites were carbonyl like [22].

The chemical nature of chemisorbed oxygen has been studied extensively and several excellent reviews are available. Almost every conceivable oxygenated organic functional group has been proposed and detected on

carbon surfaces. Characterization has been done using infra-red spectroscopy, polarography and a variety of diagnostic wet chemical reactions [12,13,14,23].

Methods are well established for the quantitative estimation of acidic groups using selective titrations with bases of varying strength. However, there are some arguments about subtleties in distinguishing between carboxylic acid groups on adjacent vs isolated carbons [12,14]. Quantitative estimation of the content of other functionalities are less reliable and in most types of carbons only about 75% of the oxygen has been accounted for [12,24].

The nature of the functional groups on the surface is very important to the adsorption properties of the carbon and much effort has been devoted to relating functionality to selectivity for gas adsorption [12,15]. It has also been shown that catalyst preparation by impregnation with metal salts is very sensitive to the nature of the functional groups on the carbon surface [23].

The distribution of oxygen containing functional groups on carbon surfaces is dependent on the reagents used to produce the functional groups and the conditions under which the carbon is treated [12,13,14,23]. As our work deals with functionality relevant to oxidative dehydrogenation little discussion will be given on chemical oxidants at low temperatures, other than to say that treatments with strong oxidants, such as HNO_3 lead to very high concentrations of carboxylic acid groups on the surfaces [23]. As will be discussed later, such carboxylic functional groups decompose at the temperatures commonly used in oxidative dehydrogenation.

For a large number of commercial carbons, Studebaker has shown that the relative concentrations of carboxyl, phenol and carbonyl groups are about 3/1/1 respectively. Carbonyl groups represented about 18% of the total chemisorbed oxygen. However only 75% of all of the chemisorbed oxygen was accounted for [24a].

Donnet has shown that gasification of carbons with steam at 900°C yields distributions of carbonyl, lactone and hydroxyl groups that is constant and independent of the degree of gasification of the carbon. This indicates a definite mechanism and stoichiometry for steam gasification [14].

In relating oxygen functionality to oxidative dehydrogenation chemistry, one must consider the conditions under which the reaction is conducted, the rate of oxygen chemisorption, the co-production of volatile carbon oxides, the thermal and oxidative stability of different functional groups and the reactivity of the functional groups with hydrocarbons. Complicating reactions include direct reaction of hydrocarbons with free carbon surfaces, the formation of stable C-H species on the surface and the subsequent oxidation of C-H species on the carbon surface.

Much is known of the thermal stability of different surface functional groups. Table 1 summarizes the temperature ranges of thermal decomposition for the different functional groups and the corresponding gases evolved on decomposition [12-18]. We have previously shown that aromatic ketones and quinones stoichiometrically abstract hydrogen from alkylaromatics, such as tetralin, at 400°C [25]. Thus, one might expect that carbons which form such groups easily and retain them on their surfaces under oxidative dehydrogenation conditions would be good catalysts or potential oxygen carriers. It is interesting to note that the groups which would not be expected to stoichiometrically dehydrogenate hydrocarbons are either quite unstable (decomposing below 500°C) or very stable (decomposing above 700°C).

Putting together the known chemistry of carbon surfaces, reactivity of different organic oxygen functionalities and the observations on oxidative dehydrogenation catalyzed by carbonaceous surfaces, it is possible to propose a catalytic sequence of surface reactions which can explain how carbons can catalyze the oxidative dehydrogenation of hydrocarbons. This proposed mechanism is illustrated in Figure 2.

The desired sequence of surface reactions would be as follows.

- (A) Formation of a reactive free carbon surface, <C>_s
- (B1) Oxidation of the surface to produce an active carbonyl species, <C=O>_s
- (C) Stoichiometric dehydrogenation of the reactive hydrocarbon, forming surface hydrides, $\text{<CH}_2>_s$
- (D1) Regeneration of the catalyst by oxidation of surface hydrides

This step can also proceed directly to a free carbon surface or surface carbonyl species (A or B).

Side reactions which lead to low selectivity are as follows.

- (E) Excessive Coke Deposition
- (F) Over Oxidation of Surface Carbonyl Species
- (G) Thermal Decomposition of Surface Carbonyl Species
- (H) Over Combustion of Carbon-Overlayers to Pure Metal Oxides
- (B2) Direct Oxidation of Free Carbon Surface to CO and CO_2

Thus there are a number of competitive surface reactions which dictate catalyst selectivity.

- o Formation of the desired carbon-overlayer is required (A), yet over condensation of hydrocarbons with free carbon surfaces (E) leads to excessive coke formation and eventual loss of catalyst surface area.
- o Formation of the desired surface carbonyl species (B1) is competitive with over condensation (E), carbon-overlayer combustion (B2) and over-oxidation of the carbonyl species (F).
- o Oxidative dehydrogenation to produce the desired product (C) is competitive with surface carbonyl species thermal decomposition (G) and over oxidation of the surface carbonyl species (F).
- o Catalyst regeneration to remove surface hydride species (D1) may be excessive and can remove the carbon-overlayer (D2 or B2).

In the sequence $\text{A} \xrightarrow{\text{RCH=CH}_2} \text{B} \xrightarrow{\text{O}_2} \text{C}$, a parallel reaction $\text{A} \xrightarrow{\text{RCH=CH}_2} \text{E}$ can occur which leads to product loss by excessive coke formation and perhaps coke which is too labile toward combustion. Thus, catalysts which promote non-selective condensation may exhibit poor selectivity by promoting coke formation. Literature reports on metal oxide catalysts do indicate that excessive acidity of catalysts lead to poor selectivities because of excessive coke build-up and product cracking [6c].

In the sequence $B \xrightarrow{\text{CO}_2} C$, a parallel reaction $B \xrightarrow{O_2} \text{CO}_2$ (reaction G) can occur which leads to non-productive loss of surface carbonyl species and poor selectivity due to the eventual formation of CO_2 . As was discussed earlier, surface species such as carboxyl, lactone and lactol are less thermally stable than carbonyls and would be expected to thermally decompose much more readily than the desired surface carbonyl species. Unfortunately, another parallel side reaction, $B \rightarrow C \rightarrow F$ (thermal decomposition of $<\text{CO}>$ s) also can occur which would lead to non-productive loss of surface carbonyl species. Thus, high hydrocarbon partial pressures should enhance reaction C over competitive reactions G and F. Alternatively, high hydrocarbon partial pressures would appear to inhibit reactions G and F.

If the above proposed mechanism is correct, one should be able to produce, isolate and identify oxidized carbon surfaces which will stoichiometrically react with hydrocarbons to produce olefinic products in the temperature range of 400-500°C. To test this postulate, we obtained a series of different carbons, oxidized them under a variety of conditions, determined their thermal stability and reacted them with selective reagents to determine the reactive oxygen content of their surfaces. The results of those studies is the subject of this paper.

EXPERIMENTAL

The carbons used in this study were obtained from the following sources.

Amoco AX-21 - Dr. K.K. Robenson of Amoco Corporation.
 Anderson AX-21 - Anderson Development Company, Adrian, Michigan
 Barneby-Sutcliffe 207-C & 209-C - Barneby-Sutcliffe Corp., Columbus Ohio.
 Darco activated carbon - American Norit Co. Inc.
 Animal Bone Charcoal - EM Sciences - Macalaster-Bicknell Co.
 Wood Charcoal - Matheson Colman & Bell Manufacturing Chemists
 PVDC Carbon - Dr. D.F. Quinn of the Royal Military College, Kingston, Ontario.
 Si/C carbon, whisker by-product - Dr. D. J. Rhodes of Advanced Composite Materials Corp.
 C60 Soot - MER Corporation.
 Graphite flake - Aldrich Chemical Co. Inc.

Thermogravimetric analyses were obtained on a DuPont Series 99 Thermal Analyzer, using ultra pure purge gases. Each analysis consisted of a sequence of three programmed heatings and is referred to as STPD.

- 1) Argon Purge 20°C/min 25 to 750°C Cool to 25°C
- 2) Air Purge 20°C/min 25 to 450°C Cool to 25°C
- 3) Argon Purge 20°C/min 25 to 750°C Cool to 25°C

The % active oxygen ($<\text{O}>$ s) was estimated from the weight loss between 550 and 750°C in step 3.

The procedure for estimating the % active oxygen ($<\text{O}>$ s), by chemical reaction, consisted of preoxidizing the material to be studied in air in a muffle furnace at 450°C for 15-60 min to provide about 30% burnoff of the carbon. The sample (0.2 to 0.4g) was then weighed into a 10cc tubing bomb and 1.4g of a reagent consisting of 48wt% tetralin, 4wt% 1-methylnaphthalene and 48wt% diphenylether was added. The tube contents were purged with N_2 then sealed. The tube was placed in a muffle furnace, set at 450°C, for the desired reaction time then removed from the furnace and quenched in a water bath. A sample of the liquid product was taken and analyzed by gas chromatography.

Oxidative dehydrogenation reactions were conducted at atmospheric pressure in a quartz down flow reactor. Reactions were carried out by feeding EB to the preheated quartz reactor bed, which was then blended with a mixture of 5% N_2 /95% O_2 . Liquid samples were collected in a chilled trap (2°C), while gas samples were collected in collection tubes. Good liquid mass balances could be obtained at times on stream of greater than 20 min. Liquid analyses were aided by dilution of the liquid products with acetone containing 10.0 % 3-hexanone as an external standard, this solvent also provided a means to overcome nuscibility problems associated with water.

RESULTS AND DISCUSSION

Thermal stability of oxidized carbon surfaces - In the carbon community, a standard procedure has evolved for the characterization of carbons by programmed thermal decomposition is and referred to as TPD [16] and references therein. This procedure consists of linear programmed thermal decomposition (3°C/min) of the carbon being studied in nitrogen atmosphere from 300 to 1300°C coupled with simultaneous detection of CO , CO_2 and often water and hydrogen. Typically, CO_2 is predominantly evolved below 550°C. For almost all carbons the maximum rate of evolution of CO_2 occurs at 500°C and CO at 600°C [12]. Coltharp has shown that for a wide variety of carbons, the pattern of CO_2 evolution varies considerably, perhaps due to different conditions in which the carbons were oxidized. However, the patterns of evolution of CO were quite similar for diverse carbons [18].

Unfortunately, this procedure only provides the total amount and distribution of gases from the carbon surface. In its present form, it cannot be used to estimate the concentration of reactive chemisorbed oxygen that is needed for oxidative dehydrogenation catalysis. As discussed above, carbonyl groups (ketones and quinones) are the most likely oxygen containing species which can promote oxidative dehydrogenation of hydrocarbons. Therefore if one could estimate the concentration of such carbonyl species on carbon surfaces, it may be possible to predict the dehydrogenation activity of carbons. The content of carbonyl groups on carbon surfaces have been estimated to be about 18% of the total chemisorbed oxygen [12a].

From the known thermal behavior of different chemical functionalities on carbons, it may be possible to estimate the concentration of carbonyls by determining the weight loss or amount of carbon monoxide evolved from a given carbon in a specific temperature range. As shown in Table 1, carbonyl groups have reasonable thermal stabilities below 550 °C but decompose in the range of 550-750°C. Functional groups which decompose at low temperatures ($<550^\circ\text{C}$) or at very high temperatures ($>750^\circ\text{C}$) are not expected to be important in oxidative dehydrogenation catalysis. On this assumption, we conducted a series of thermal analyses on a variety of carbons to see if major differences could be observed in a systematic way.

The carbons we used are described in the experimental section. Their physical properties varied widely in terms of surface area, degree of carbonization and ash content. To evaluate their thermal behavior each carbon was pretreated at 750°C in oxygen free argon to clean its surface. Each carbon was then oxidized in diluted air (14.7% O₂) by programming to 450°C and cooling to room temperature in that atmosphere. The thermal decomposition profile of the oxidized carbon was then determined by programmed decomposition up to 750-800°C in oxygen free argon. The sequential programmed thermal decomposition analysis will be referred to as SPTD.

Table 2 summarizes the observed rates of weight loss in each cycle at 400°C and the estimated amounts of chemisorbed oxygen found as either CO₂ or CO assuming that weight loss below 550°C was primarily CO₂ and between 550 and 750°C oxidatively active carbonyls decomposed to evolve primarily CO, as discussed above.

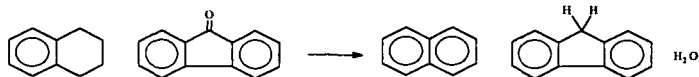
With the exceptions of animal bone charcoal and C60 soot the data appear to fall within the range of oxygen contents reported in the literature [12a]. The animal bone charcoal results may have been exaggerated due to the high correction factors necessary for this high ash content material. In the case of C60 soot it is believed that high contents of low molecular weight species vaporized from the sample simultaneously with the carbon oxide decompositions. The initial Argon cycle resulted in the loss of a great deal of weight in the temperature range in which a pure sample of C60 also rapidly volatilized. This result is interesting in that the C60 soot is believed to be contain high concentrations of tubular fullerenes. This oxidation-thermal decomposition cycle may offer a route to the production of higher yields of lower molecular weight fullerenes from C60 soots.

In comparing the rates of weight loss in each cycle of the SPTD analyses 400°C, where the maximum rate of oxygen chemisorption has been reported [12a], it is interesting to note that only C60 soot showed a positive weight change at this temperature. There appeared to be two sets of sample behavior. Those with high ash (particularly alkaline ash) and those with low ash. For low ash samples, the surface area of the parent carbon offered the best correlation with the rate of weight loss. In the case of high ash samples, the rates of weight loss correlated well with ash content. However, two high ash samples had low rates of oxidation, silicon carbide by-product and coal derived charcoal (Darco). The majority of the ash constituents of the silicon carbide by-product was in fact SiC and would be expected to be inert. Coal charcoal ash is primarily silica-alumina and would not be expected to catalyze carbon oxidation. The other carbons ashes were found to be alkaline and would therefore be expected to catalyze such oxidations. Animal bone charcoal was not found to be highly alkaline but is composed primarily of calcium phosphate (hydroxyapatite) [26]. Calcium is known to be an active catalyst for carbon oxidation [16d].

On comparing the rates of thermal decomposition of oxidized carbons with the rates of oxidation in Table 2, it appears that carbons which oxidize rapidly also decompose rapidly. At this time it is not clear if ash components affect the thermal decomposition or they change the selectivity in the formation of different functional groups on the carbon surface during the oxidation cycle.

The results of these studies indicate that oxidized carbon surfaces can accommodate 1 to 10% by weight oxygen in the form of carbonyl functional groups. Such groups should have potential as stoichiometric oxidation reagents. In all cases the formation of these active groups occurs simultaneously with the oxidation of a portion of the carbon to volatile oxides. Thus, the selectivity for oxygen utilization in the formation of these groups will always be limited. This selectivity appears to be lower for carbons containing alkali or alkaline earth impurities. Thus supported carbons may require careful preparation. However, it may be possible to use carbons as oxygen carriers in which active oxygen species are formed in air then utilized as oxidation reagents in contact with hydrocarbons.

Measurement of the active oxygen capacity of carbons by stoichiometric reactions. Unfortunately, the STPD results does not give a quantitative measure of the reactive oxygen content of carbons. In past work involving hydrogen donor chemistry, we have described how it is possible to quantitatively measure either hydrogen abstraction capacity of a solid or hydrogen donor capacity of a liquid by a test chemical reaction. We showed that aromatic ketones and quinones stoichiometrically abstract hydrogen from alkylaromatics, such as tetralin, at 400°C [25]. Thus, one might expect that carbons which form such groups easily and retain them on their surfaces under dehydrogenation conditions would be good catalysts or potential oxygen carriers. We endeavored to use this same technique at 450°C to assess the potential of various carbons as dehydrogenation reagents and the results are presented in this section. The test reaction may be illustrated simply with model compounds as follows.



The results of model compound scoping experiments are presented in Table 3. It can be seen that the results are quite quantitative. However, the chemistry of quinones was not found to agree with proposals in the literature that quinones would convert to hydroquinones. Instead, we found that only one of the carbonyls of phenanthrene type quinones were active, as after hydrogen abstraction by the first carbonyl, the intermediate monocarbonyl rearranged to a stable monophenol which did not react further. Anthracene type quinones behaved like two independent carbonyls and did not form hydroquinones. Instead, they converted to dihydroanthracene. This compound was metastable under the reaction conditions and underwent some disproportionation.

In addition to stoichiometric hydrogen abstraction it was anticipated that some catalysis of hydrogen transfer or equilibrium dehydrogenation might occur. Roth reported that carbons supported on alumina were extraordinary catalysts which in some cases rivaled the performance of commercial supported noble metal catalysts [11]. Indeed, when oxidized carbons were tested with the test reagent, catalysis was observed. Thus, when attempting to relate the amount of naphthalene formed from tetralin in these tests, it was necessary to subtract out catalytic contributions of the carbons. This correction was possible by the inclusion of 1-methylnaphthalene in the reagent mixture which measured the kinetically parallel reactions of catalytic tetralin dehydrogenation and catalytic hydrogen transfer between tetralin and 1-methylnaphthalene. In addition corrections also had to be made for thermal isomerization of tetralin to 1-methylindan, the thermal dehydrogenation of tetralin and a small amount of hydrogenolysis of the diphenylether co-solvent.

Two methods of estimation were used. For low conversions of tetralin, direct stoichiometric calculations were employed. For high conversions of tetralin, the equilibrium distribution of tetralin/naphthalene/H₂ was calculated assuming that hydrogen lost in the formation of water was an indicator of the active oxygen content of the carbons.

Surprisingly, some carbons were almost as catalytically active as 5%Pd/charcoal for hydrogen transfer and dehydrogenation. A general observation was that highly graphitic carbons exhibited high catalytic activities and non-graphitic carbons exhibited high activities for stoichiometric reactions of active oxygen. Several carbons, when oxidized, were found to contain as much as 10wt% active oxygen. Petroleum cokes could also be oxidized to produce materials with as much as 5wt% active oxygen. Carbonized CaPO₃ catalysts produced during oxidative dehydrogenation studies were found to contain active oxygen contents (carbon only basis) that were comparable to some of the most active, highest capacity pure carbons examined. The results are summarized in Table 4.

CONCLUSIONS

The results of these studies indicate that oxidized carbon surfaces can accommodate 1 to 10% by weight oxygen in the form of carbonyl functional groups which are potential stoichiometric oxidation reagents. In all cases the formation of these active groups occurs simultaneously with the oxidation of a portion of the carbon to volatile oxides. Thus, the selectivity for oxygen utilization in the formation of these groups will always be limited. This selectivity appears to be lower for carbons containing alkali or alkaline earth impurities. Thus, supported carbons may require careful preparation. However, it may be possible to use carbons as oxygen carriers in which active oxygen species are produced in air and then utilized as oxidation reagents in contact with hydrocarbons. The mechanism of oxidative dehydrogenation over carbonaceous catalysts appears to be consistent with this chemistry.

REFERENCES

1. T.G. Alkhazov, A.E. Lisovskii, M.G. Safarov and A.M. Dadasheva, *Kinet. Katal.* 13, 509 (1972).
2. P. Ciambelli, S. Crescitelli, V. DeSimone and G. Rosso, *Chim. Ind. Milan* 55, 634 (1973).
3. K. Tazaki, R. Kitahama, F. Nomura and T. Yokoji, *Japan Pat.* 74-39246; *Chem. Abst.* 83, 44002v (1975).
4. R. Fiedorow, W. Przyslawski, M. Sopa & I.G. Dalla-Lana, *J. Cat.* 68, 33 (1981).
- 5a. G. Emig & H. Hofmann, *J. Cat.* 84, 15 (1983).
- 5b. A. Schraut, G. Emig & H.-G. Sockel, *Appl. Cat.* 29, 311 (1987).
- 5c. A. Schraut, G. Emig & H. Hofman, *J. Cat.* 112, 221 (1988).
- 6a. G.E. Vrieland, *J. Cat.* 111, 1 (1988).
- 6b. G.E. Vrieland, *J. Cat.* 111, 14 (1988).
- 6c. G.E. Vrieland & P.G. Mennon, *Appl. Cat.* 77, 1 (1991).
7. L.E. Cadus, O.F. Gorziz and J.B. Rivarola, *Ind. Eng. Chem. Res.*, 29, 1143 (1990).
- 8a. G.C. Grunewald & R.S. Drago, *J. Mol. Cat.* 58, 227 (1990).
- 8b. G.C. Grunewald & R.S. Drago, *J. Am. Chem. Soc.* 113, 1636 (1991).
9. J. Manassen & S.H. Khalif, *J. Cat.* 13, 290 (1969).
- 10a. Y. Iwasawa, H. Nobe and S. Ogasawara, *J. Cat.* 31, 444 (1973).
- 10b. Y. Iwasawa & S. Ogasawara, *J. Cat.* 37, 148 (1975).
- 11a. J.F. Roth & A.R. Schaefer, *Belgain Patent* 682,863 (1966).
- 11b. J.F. Roth & A.R. Schaefer, *U.S. Patent* 3,356,757 (1966).
- 11c. J.F. Roth, J.B. Abell & A.R. Schaefer, *I&E Prod. R&D*, 7, 254 (1968).
- 11d. J.F. Roth, J.B. Abell, L.W. Fannin & A.R. Schaefer, *ACS Petr. Div. Prep. New York*, Sept. 1969, p.D146.
- 11e. J.F. Roth, J.B. Abell, L.W. Fannin & A.R. Schaefer, *Adv. Chem.* 97 193 (1970).
- 12a. B.R. Puri, *Chem. & Phys. of Carbon*, 6, 191 (1970).
- 12b. B.R. Puri, G.K. Sharma & S.K. Sharma, *Proc. 5th Conf. on Carbon*, 65 (1962).
- 12c. B.R. Puri, G.K. Sharma & S.K. Sharma, *J. Indian Chem. Soc.* 44, 64 (1967).
- 13a. H.-P. Boehm, *Angew. Chem.*, 5, 533 (1966).
- 13b. H.-P. Boehm, *Adv. Cat.* 16, 179 (1966).
14. J.B. Donnet, *Carbon*, 6, 161 (1968).
15. J.S. Mattson & H.B. Mark Jr., *Activated Carbon*, Marcel Dekker Inc., New York, Chapt. 3 (1971).
- 16a. P.L. Walker Jr., L.G. Austin & J.J. Tietjen, *Chem. & Phys. Carbon*, 1, 327 (1965).
- 16b. F.J. Vastola & P.L. Walker Jr., *J. Chim. Phys.* 58, 20 (1961).
- 16c. M. Shelef & P.L. Walker Jr., *Carbon*, 5, 93 (1967).
- 16d. P.L. Walker Jr., M. Shelef, & R.A. Anderson, *Chem. & Phys. of Carbon*, 4 287 (1968).
- 16e. G. Tremblay, F.J. Vastola & P.L. Walker Jr., *Carbon*, 16, 35 (1978).
17. W. V. Lobenstein & V.R. Deitz, *J. Phys. Chem.*, 59, 481 (1955).
18. M.T. Coltharp & N. Hacherman, *J. Phys. Chem.*, 72, 1171 (1968).
- 19a. G.R. Henning, *Proc. 5th Conf. on Carbon*, 1, 143 (1962).
- 19b. G.R. Henning, *Z. Elektrochem.*, 66, 629 (1962).
20. C.A. Coulson, *Proc. 4th Conf. on Carbon*, Pergamon Press (1962) p.215.
21. F.J. Salzano, *Carbon*, 2, 73 (1964).
22. J.F. Strange, Ph.D. Thesis, Penn. State U. (1964).
- 23a. F. Rodriguez-Reinoso and A. Linares-Solano, *Chem. & Phys. of Carbon*, 21, 1 (1988).
- 23b. C. Prado-Burguete, A. Linares-Solano, F. Rodriguez-Reinoso & C. Salinas-Martinez De Lecea, *J. Cat.* 115, 98 (1989).
- 23c. F. Rodriguez-Reinoso, M. Molina-Sabio & M.A. Munecas, *J. Phys. Chem.* 96, 2707 (1992).
- 23d. M. Molina-Sabio, M.A. Munecas-Vidal & F. Rodriguez-Reinoso, "Characterization of Porous Solids", Elsevier Science, Amsterdam (1991), p. 329.
- 24a. M.L. Studebaker, E.W.D. Huffman, A.C. Wolfe & L.G. Nabors, *I & E Chem.* 48 162 (1956)
- 24b. M.L. Studebaker, *Rubber Age (N.Y.)*, 80, 661 (1957).
- 25a. D.D. Whitehurst, M. Farcasiu, T.O. Mitchell & J.J. Dickert Jr., "The Nature and Origin of Asphaltenes in Processed Coals", *EPRI- AF-480*, July 1977, Chapt. 8.
- 25b. D.D. Whitehurst, M. Farcasiu & T.O. Mitchell, "Coal Liquefaction: The Chemistry and Technology of Thermal Processes", Academic Press, New York (1980), Chapt. 8.
26. *Encyclopedia Britannica William Benton, Publ.*, Vol.B (1964) p.906.

TABLE 1
THERMAL DECOMPOSITION OF ORGANIC OXYGEN COMPOUNDS

Functional Group	Decomposition Temp. Range (°C)	Gas Evolved
Carboxylic acid	200-600	CO ₂
Aldehyde	<400	CO
Lactone/Lactol	200-600	CO ₂ & CO
Ketone/Quinone	600-1000	CO
Phenol	600-1000	CO
Aromatic Ether	>700	CO
Anhydride	>700	CO ₂ & CO

TABLE 2
ESTIMATED REACTIVITIES AND OXYGEN CONTENTS OF CARBONS VIA STPD
(Ash free carbon basis)

Carbon	Rates of Weight Loss at 400°C (wt%/min)					Calculated % Chemisorbed O		
	% Ash	% Burnoff				From CO ₂	From CO	Total
	Initial	After air	Argon-1	Air	Argon-2			
C60 Soot	0	93	-4.78	0.72	-0.51	0.38	21.89	22.26
Animal Bone Charcoal	86	12	-5.24	-50.1	-15.7	22.47	15.38	37.85
Wood Charcoal	13	49	-4.82	-16.6	-2.37	3.31	8.40	11.71
PVDC Carbon	0	21	-0.72	-0.72	-0.37	1.61	4.61	6.22
Amoco AX-21	2	25	-1.51	-4.45	-0.24	2.57	2.55	5.12
Darco (20-40 mesh)	12	10	-0.84	-0.12	-0.56	1.15	1.70	2.84
Si/C By-product	34	8	-0.36	-1.36	-0.05	1.30	1.57	2.87
Barneby-Sutcliffe 207C	3	15	-0.97	-6.29	-0.47	0.87	1.28	2.15
Graphite	0	2	-0.19	-0.07	-0.02	0.12	0.32	0.43

TABLE 3
Stoichiometry and Rate Constants for Reactions of Model Compounds With the Test Reagent

Compound	Mol. Wt.	Wt% O	Rx Time (min)	% Conv	Hydrogen Consumption		Reaction Rate Constants (1000xmmol prod/g.rgn/g.matrl/min)		
					Theory	Observed	k _{mind}	k _{expd}	k _{met}
Benzophenone	182	8.8	30	7.2	4	4.3	21	21	0
Benzophenone	182	8.8	60	27.8	4	4.1	33	21	0
Fluorenone	180	8.9	60	16.4	4	4.9	21	54	0
9-Anthrone	194	8.2	60	97	4.4	4.7	28	100	1
Antraquinone	208	15.4	30	97	6.6	6	24	364	1
Phenanthrenequinone	208	15.4	30	100	4.2	4.2	10	255	1
Bi2O3 (42%)*	466	10.3	60	6	4.6		31	41	0
V2O5 (52%)*	182	17.6	60	4	3.9		20	94	2

* Metal oxides were supported on inert carriers, values shown are for pure metal oxides

TABLE 4

COMPARISONS OF THE ESTIMATED VALUES FOR ACTIVE OXYGEN CONTENTS OF CARBONS
(Weight % <O>s, ash corrected values)

Material	Rx Time (min)	%	Estimated wt% <O>s		
			Stoich.	Equil.	SPTD
PVDC	60	100	4.8	4.6	
AX-21 (41)	240	97	25.6	28.8	2.6
AX-21 (41)	60	97	7.1	7.0	2.6
AX-21 (41)	60	97	6.9		2.6
AX-21 (41)	30	97	2.0		2.6
Used AX-21 (41)	60	97	3.2		
AX-21 (93)	60	71	16.7		
Barneby-Sutcliff 207c	240	95	8.2	6.0	1.3
Barneby-Sutcliff 207c	60	95	3.9	1.7	1.3
Barneby-Sutcliff 207c (dry)	30	95	2.8	1.3	
Barneby-Sutcliff 207c (wet)	30	95	2.2	1.3	
Barneby-Sutcliff 209c	60	95	1.0		
Darco (20-40 mesh)	60	82	6.1	5.2	1.7
Darco (20-40 mesh)	60	82	2.6	1.7	
Norit Activated Carbon	60	84	2.2		
Wood Charcoal	60	78	6.6	8.4	
Animal Bone Char	60	2	44.8	15.4	
Petroleum Shot Coke	60	100	5.3		
Petroleum Sponge Coke #1	60	100	4.1		
Petroleum Sponge Coke (as rec)	60	100	1.1		
No Cat. Max.					
C60 Soot	60	100	0.3	9.4	21.9
Si/C By-product	60	52	-1.6	2.0	1.6
Graphite	60	100	-1.8	0.2	0.3
Graphite	60	100	-1.7	0.2	0.3
C/CaPOx (Run 228-4)	60	2.2	1.4	13.4	
C/CaPOx (Run 228-5)	60	1	-14.1	14.4	
CaPOx (Starting material)	60	0	-0.2	0.0	

FIGURE 1

CHEMISTRY OF CARBON SURFACES

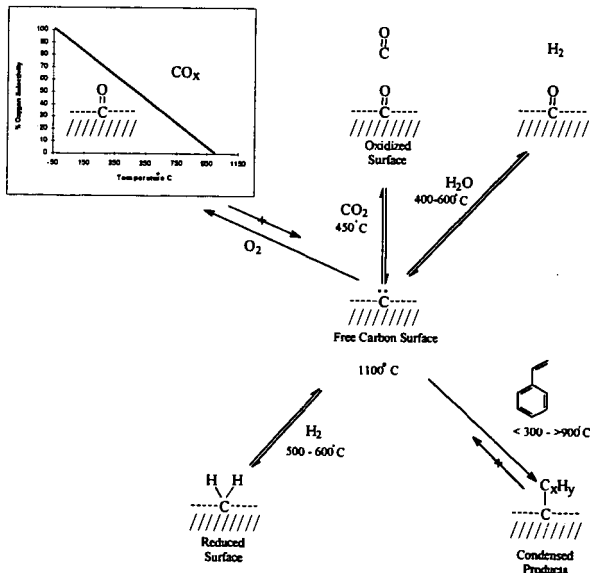


FIGURE 2
CATALYTIC SEQUENCE IN OXIDATIVE DEHYDROGENATION

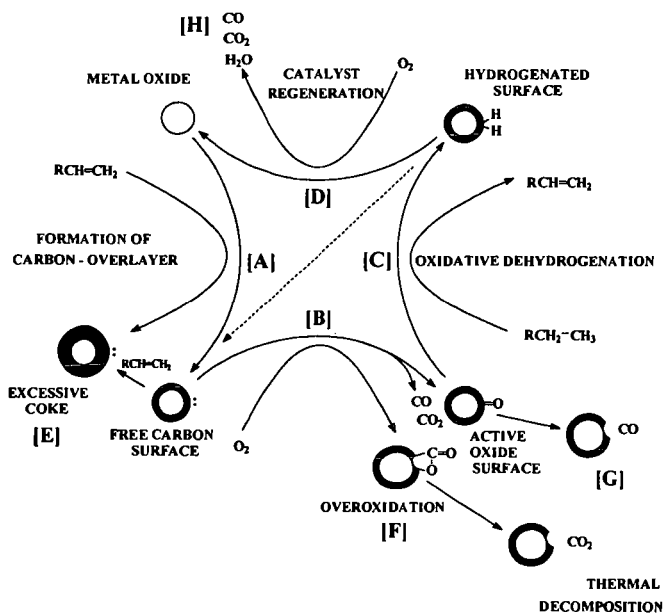
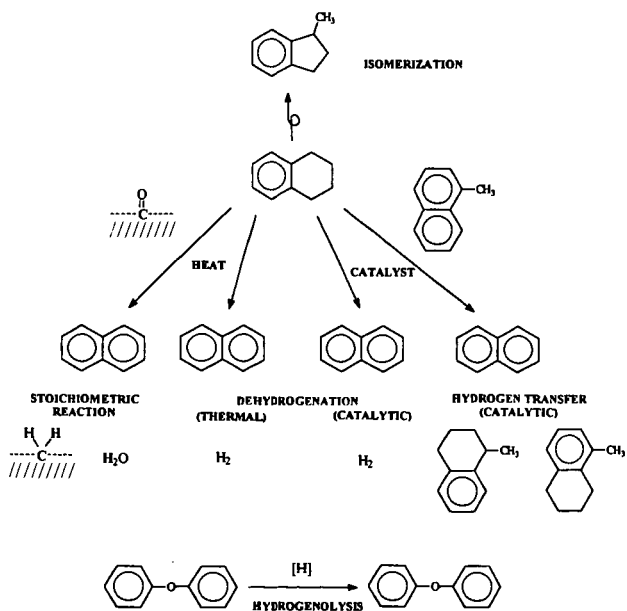


FIGURE 3
REACTIONS OF THE TEST REAGENT



OPTICAL SPECTROSCOPY OF A QUANTUM CARBON WIRE

Peter C. Eklund¹

Center for Applied Energy Research and
Department of Physics and Astronomy
University of Kentucky, Lexington, KY 40506

Keywords: carbon nanotubes, Raman scattering, quantum confinement

Abstract Raman Spectroscopy has been used to probe the vibrational modes of carbon nanotubes. The Raman spectrum of this new form of carbon is very different from that observed for graphite (the nanotube's flat parent) and these differences can be understood as a result of the cyclic boundary condition imposed on a graphene sheet rolled up to form a seamless nanotube. Optical resonances are observed which are associated with the one dimensional character of the electronic states of these novel quantum wires.

INTRODUCTION

Single wall nanotubes (SWNTs) were discovered in 1993 in the carbonaceous by-products from an arc discharge between carbon electrodes in an inert atmosphere [2,3]. They have been observed directly in electron microscopes and in scanning tunneling microscopes. In this paper, we wish to explore the special nature of these one dimensional (1D) carbon quantum wires using Raman spectroscopy. The quantum effects we observe here cannot be observed in the so-called "multiwall carbon nanotubes" (MWNTs) which were discovered a few years earlier also in the soot from a carbon arc[4]. These MWNTs are comprised of a series of concentric SWNTs with an inter-shell spacing of about 3.4 Å. The inner diameter of the MWNT is typically 5-10 times larger than a SWNT. As small as these diameters are in terms of a micron scale, they are too large to observe the quantum size effects we observe in SWNTs with diameters ~ 1nm.

In Fig. 1 the sp^2 based structure of a seamless carbon nanotube is shown schematically. The hexagonal arrangement of C-atoms, identical to that in flat carbon sheets of graphite, are apparent in the figure. Three different subclasses of seamless nanotubes can be formed: armchair (n, n), zigzag ($n, 0$) and chiral ($n, m \neq n$) where the integers n and m are used to define the symmetry of the nanotube [4]. Understanding how to compute (n, m) are not important to understanding the principle results discussed here. It is of interest to know only that "armchair" and "zigzag" tubes have rows of hexagons aligned parallel to the tube axis and chiral tubes can be formed such that the hexagon rows spiral up along the tube axis. The tube shown in Fig. 1 is a (9,9) armchair tube. The diameter of an armchair tube is given by $D(\text{\AA}) = 1.357n$, so that a (10,10) nanotube has a diameter of 13.57 Å.

Until recently, research on the physical properties of these quantum carbon wires have been slowed by the fact that previous arc discharge methods produced mostly carbon soot and only a few % carbon nanotubes[4]. Thus experimental signals in these samples were often dominated by the response of the soot. Recently, a laser ablation technique was discovered at Rice University which produced over 70% tubes [5]. Using microfiltration, we have been able to separate the carbon nanosoot from the tubes and study reasonably pure tube samples by Raman spectroscopy. Details of the laser-assisted process developed at Rice University are available elsewhere [5]. Briefly, a carbon target containing 1-2% Ni/Co catalyst is maintained in flowing Ar in an oven (1200 °C). The carbon target is vaporized by a two-pulse sequence from a YAG and frequency-doubled YAG laser at a 10 Hz repetition rate. Nanotubes (>70%) and carbon nanospheres (~30%) and fullerenes (~1-2 %) form in the hot carbon plasma and drift downstream under flowing Ar where they are collected on a water-cooled cold finger. The carbon material was first soaked in CS₂ to remove solubles (i.e., fullerenes) and the insolubles were then subjected to microfiltration to physically separate the tubes and soot. This was accomplished by dispersing the material in benzalkonium chloride using ultrasound.

The resulting carbon material appears in scanning electron microscopy (SEM) images as a mat of carbon fibers. Transmission electron microscopy (TEM) was used to measure the fiber diameter. Under high resolution it was observed that the tubes were arranged into regular bundles of single-wall carbon nanotubes. These bundles, or crystalline ropes, can be seen directly in the bright field TEM image or indirectly by the electron diffraction pattern which stems from the ordered stacking of carbon cylinders. Looking at the bundle end-on, the individual tubes can be seen to organize into a two-dimensional triangular lattice. The TEM images of, and electron diffraction patterns from these crystalline ropes are shown in Figs. 2a,b. In Fig. 2c we show the size distribution determined from bright field TEM images. The mean tube diameter was also determined by x-ray diffraction (XRD). XRD and TEM yielded slightly different values for the mean tube diameter D which must stem from a non-statistical distribution of tubes selected for study in the TEM. A mean value for D consistent with a (10,10) tube was determined by XRD, in

¹ This paper is based, in part, on results to appear in Ref. 1.

agreement with previous XRD data on similar tubes[5]. Our bright field TEM data (Fig. 2c), however, arrived at a slightly smaller mean D value, more consistent with a (9,9) tube. As can be seen from Fig. 2c, the diameter distribution for the tubes is consistent with armchair symmetry tubes (see the tick marks in the figure) associated with the range of n-values 8-11.

In Fig. 3, we display the Raman spectrum (300 K) for purified single wall nanotubes obtained in the backscattering geometry using 514 nm Ar laser radiation. For comparison, the calculated Raman spectrum is shown below for n=8-11 armchair tubes. The frequencies were calculated in a phenomenological force constant model using the same C-C force constants used to fit vibrational data for a flat graphene sheet [6]. Note that sections of the experimental spectrum have been scaled vertically (as indicated) to best expose the rich detail. Furthermore, the frequency scale has been expanded for the highest frequency region. The theoretical Raman intensities were calculated using a bond polarizability model by Subbaswamy and co-workers [7]. The mode assignments are summarized in Table 1 and compared with theory. Further polarized Raman studies will be necessary to confirm the symmetry assignments. It may be noticed that the some of the experimental bands are narrow and some are broad. This difference is attributed to an inhomogeneous line-broadening mechanism based on the theoretical observation that particular vibrational modes exhibit a strong tube diameter dependence, while others exhibit a rather weak dependence. Thus considering that our sample contains a distribution of tube diameters, the Raman lines can be sharp (similar to a linewidth in graphite $\sim 6 \text{ cm}^{-1}$) or much broad, depending on whether or not the mode frequency is strongly diameter-dependent. The intense line seen at 186 cm^{-1} in Fig. 3 is identified with the radial breathing mode in which all C-atoms are displaced radially outward in phase and the strong lines observed near 1600 cm^{-1} are related to the intralayer vibrations in graphite which are observed at 1582 cm^{-1} . In the nanotube, the cyclic boundary conditions around the tube waist activate new Raman and IR modes that are not observable in a well-ordered flat graphene sheet or in graphite--this is the first consequence of the one-dimensional (1D) nature of the nanotube. The second, to be discussed below, is the quantum confinement of the conduction electrons which gives rise to resonant Raman scattering.

The resonant nature of the Raman scattering process is clear from Fig. 4 which shows the dramatic effect on the distribution of line intensity on the frequency (or wavelength) of the excitation laser. The data were all taken at the same temperature on the same sample. Shown in the figure are spectra taken with four different lasers at the (low) power densities indicated. A closer inspection of the figure reveals that not only are the intensities changing dramatically with laser frequency, but so are the Raman line frequencies!! The former effect is typical of resonant Raman scattering in many solid, gas and liquid samples, whereas the latter is a manifestation of a series of resonances each identified with different tube diameters (e.g., (n,n)). In general, resonantly enhanced Raman scattering occurs when the energy of the incident photon matches the transition energy of a strong optical absorption band [8]. Normally, the Raman line intensity can jump by several orders of magnitude, but the Raman line frequency is fixed or varies very slightly. In the present work, large shifts in frequency are also observed which is quite unusual.

We now provide a simple explanation for this observation based on tube-diameter-dependent optical absorptions which stem from the 1D nature of the single wall carbon nanotube. A more complete theoretical explanation will be forthcoming [7]. For large enough tube diameter, the character of the electronic states in a carbon nanotube should be essentially independent of tube diameter (or n in (n,n)) and should resemble closely that of a flat graphene sheet. These larger tubes therefore should respond to the excitation laser as does graphite, or more precisely a single graphene sheet, exhibiting no strong resonance(s) in the region of interest here and only one Raman line at $\sim 1582 \text{ cm}^{-1}$. This is what is observed, for example, in much larger diameter multiwall carbon nanotubes. A change in laser excitation wavelength (or frequency) is found to produce small changes in the Raman intensity and extremely small (if detectable) changes in the frequency of the 1582 cm^{-1} mode. The large shifts in Raman line frequency we observe are therefore identified with a diameter-dependent optical absorption which promotes resonant scattering from particular diameter tubes. The shifting frequency is both the result of the sample being a collection of different diameter tubes and the fact that these different diameter tubes have different optical resonances. In 1D systems it is well known that $E^{-1/2}$ singularities exist in the electronic density of states (DOS). These singularities manifest themselves as spikes in the DOS calculated for n=8,11 armchair tubes and shown in Fig. 5; the Fermi energy (E_F) is taken as the energy zero. The allowed optical transitions for these tubes can be shown to be between filled states in spikes below E_F (v_1, v_2) to empty states above E_F (c_1, c_2). As required to explain our experimental results, the energy separation between these mirror image spikes must be diameter (n) dependent consistent with the results of Fig. 4. As one can now appreciate, Raman scattering from a (n,n) tube will dominate the spectrum when the laser photon energy matches the energy difference between spikes for that (n,n) DOS. The center of gravity of each Raman band then shifts to the frequency of the (n,n) vibrational mode being resonantly driven by the laser field.

Thus, the unusual laser frequency dependence of the Raman spectra of carbon nanotubes shown in Fig. 4 is a direct consequence of 1D quantum confinement effects in carbon nanotubes. Further work is underway to more quantitatively understand the results described above.

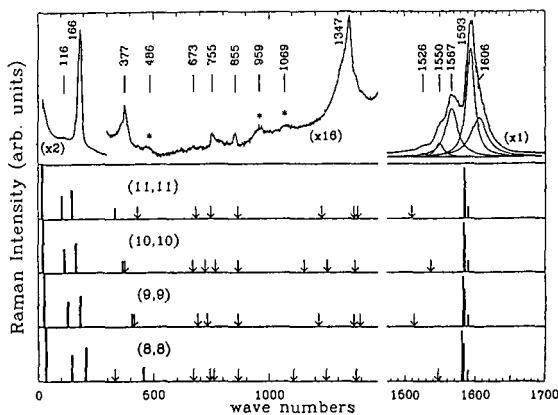


Fig. 3: Raman spectrum (top panel) of a SWNT sample taken using 514.5 nm excitation at ~ 2 W/cm². The “*” in the spectrum indicates features that are tentatively assigned to second-order Raman scattering. The four bottom panels are the calculated Raman spectra for armchair (n,n) nanotubes, $n = 8 - 11$. The downward-pointing arrows in the lower panels indicate the positions of the remaining weak, Raman-active modes [1].

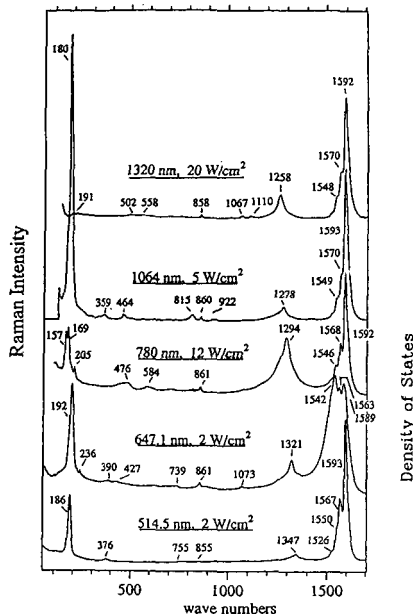


Fig. 4: Room-temperature Raman spectra for purified SWNTs, excited with five different laser frequencies. The power density for each spectrum is indicated, as are the vibrational frequencies.

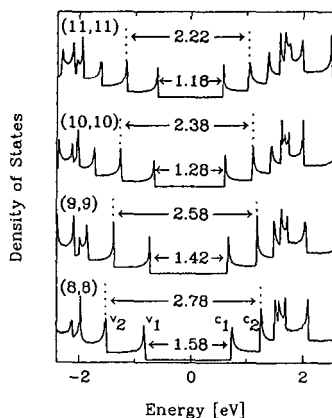


Fig. 5: Electronic density of states (DOS) calculated using a tight-binding model for $(8,8)$, $(9,9)$, $(10,10)$, and $(11,11)$ nanotubes. The Fermi energy E_F is located at 0 eV. Wavevector-conserving optical transitions can occur between mirror-image spikes, e.g., $v_1 \rightarrow c_1$ and $v_2 \rightarrow c_2$.

Acknowledgements

The author wishes to thank the NSF and DOE for his support during the course of this research. This paper is based on many of the results to appear in Ref. 1 and represents the fruits of a dynamic, multi-university collaboration between experimentalist and theoreticians.

REFERENCES:

- [1] A. M. Rao, E. Richter, S. Bandow, B. Chase, P. C. Eklund, K. A. Williams, S. Fang, K. R. Subbaswamy, M. Menon, A. Thess, R. E. Smalley, G. Dresselhaus and M. S. Dresselhaus, *Science* (in press)
- [2] D. S. Bethune et al., *Nature* 363, 605 (1993).
- [3] S. Iijima and T. Ichihashi, *Nature* 363, 603 (1993).
- [4] For more details on carbon nanotubes see "*Science of Fullerenes and Carbon Nanotubes*" by M.S. Dresselhaus, G. Dresselhaus, and P. C. Eklund, Academic Press, New York, NY 1996.
- [5] A. Thess et al., *Science*, 273, 483 (1996).
- [6] R. A. Jishi et al., *Chem. Phys. Lett.*, 209, 77 (1993).
- [7] E. Richter and K. R. Subbaswamy (unpublished).
- [8] W. Hayes and R. A. Loudon, in *Light Scattering by Crystals*, (Wiley, New York, NY 1978).

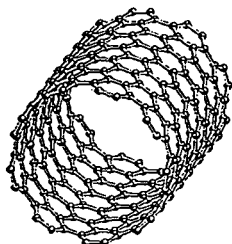


Fig. 1: Schematic model of a seamless (9,9) nanotube.

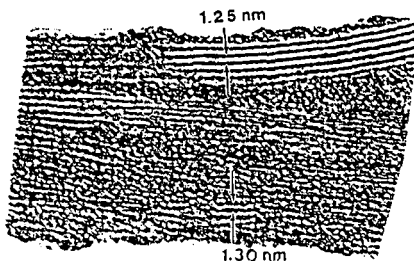


Fig. 2(a): Bright-field TEM image of a nanotube bundle. The bundles are found to be organized in triangular lattices. The arrows indicate measured approximate diameters of nanotubes within two bundles.

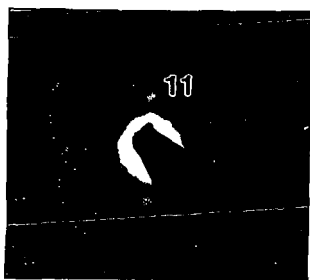


Fig. 2(b): Electron diffraction pattern with d_{11} spots corresponding to the diameter of an isolated nanotube.

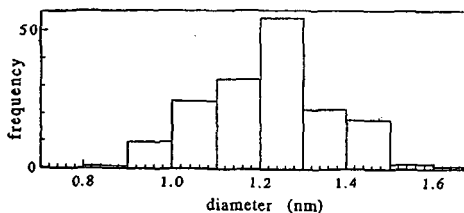


Fig. 2(c): Nanotube-diameter distribution tabulated from bright-field TEM images.

TABLES

TABLE I. First-order Raman-active vibrational mode frequencies in cm^{-1} for single-wall carbon nanotubes (SWNT): Experimental (514.5 nm excitation) and calculated. The experimental frequencies vary with laser excitation wavelength (see text and Fig. 4). The SWNT sample is thought to be an ensemble of $n = 8 - 11$ armchair nanotubes.

Expt.		Ident.	Theory ^c				
ω_0	I^d	n^b	Sym. ^a	(8,8)	(9,9)	(10,10)	(11,11)
-			E_{2g}	34	27	22	18
116	w	10	E_{1g}	146	130	117	106
186	s	8,9,10	A_{1g}	206	183	165	150
377(s)	m	10 ^e	E_{2g}	333	-	368	-
377(b)	m	9,10 ^e	E_{2g}	458	408	371	335
-		-	E_{1g}		420		431
673	w	8,10	A_{1g}	671	-	670	-
-		-	E_{1g}	-	690	-	683
-		-	E_{2g}	-	732	-	746
-		-	E_{2g}	742	-	722	-
755	w	8,10	E_{1g}	762	-	766	-
855	w	8,9,10,11	E_{2g}	866	866	866	866
-		-	E_{2g}	1106	-	1152	-
-		-	E_{1g}	-	1216	-	1229
-		-	A_{1g}	1247	-	1252	-
1347	m	$\left\{ \begin{array}{l} 9,11 \\ 8,10 \end{array} \right.$	A_{1g}	-	1369	-	1369
			E_{1g}	1377	-	1374	-
1526	w	9,11	E_{1g}	-	1513	-	1510
1550	m	10	E_{2g}			1543	
1567	s	8	E_{2g}	1547	-	1531	-
1593	s	$\left\{ \begin{array}{l} 8,9,10,11 \\ 8,9,10,11 \\ 8,9,10,11 \end{array} \right.$	A_{1g}	1583	1584	1585	1586
1609	m		E_{1g}	1581	1582	1584	1585
			E_{2g}	1589	1589	1590	1590

^aMode symmetry as determined by model calculation.

^bThe n values of the armchairs nanotubes (n, n).

^cEmpirical force constant model, see text.

^dIntensity: w = weak, m = moderate, s = strong.

^eThis line at 377 cm^{-1} is a superposition of a broad (b) and a sharp (s) peak.

Carbon Materials From Coal

Frank Derbyshire

Center for Applied Energy Research
3572 Iron Works Pike
University of Kentucky
Lexington, KY 40511-8433

Keywords: coal, conversion, carbon materials

INTRODUCTION

The production and consumption of coal is overwhelmingly directed to its use as a fuel for the generation of heat and power. At the same time, coal also represents a significant resource for the production of chemicals and carbon materials. Although, in this context, the current importance enjoyed by coal is much less than in former times, it can be anticipated that the non-fuel uses of coals will increase in years to come: coal is the most abundant fossil fuel; it is globally available; it is obtained at low cost; and the structure of coal is suited to the production of a broad range of products.

This paper will consider how the structure and composition of coals of different rank and origin can give rise to carbon materials with very different properties and fields of application. While the markets for these products can only have a small direct impact on coal consumption, they can exert a considerable indirect influence through materials applications that enhance the clean efficient use of energy. Examples include the control of emissions through adsorption and catalysis, energy storage devices and delivery systems, and the fabrication of strong lightweight structures for various forms of transport.

STRUCTURE OF COAL AND CARBONS

The ability to produce a spectrum of carbons from coal can best be understood in relation to its basic structure. As depicted in a model developed by Oberlin¹, coal consists of relatively low molecular weight structural units that are connected by different types of chemical bond. The structural units tend to be planar and consist of cyclic carbon (aromatic and hydroaromatic) and heterocyclic rings. Attached to the rings are alkyl, and oxygen and sulphur-containing groups. The structural units are connected by covalent (alkyl, or etheric - oxygen, and sulphur - bridges) and non-covalent bonds, hydrogen bonds and van der Waals forces. A proportion of weakly bonded or physically trapped material is also present, some of which can be extracted by solvents. While the overall structure is amorphous, there are limited regions of short-range order that are defined by the parallel alignment of two (or more) structural units.

As the rank of the coal increases, there are changes to the structure that include: an increase in aromaticity and a reduction in aliphatic content; the elimination of oxygen functionalities; and changes in the nature of the connecting linkages between structural units - a decrease in the extent of hydrogen bonding and covalent linkages, and an increase in aromatic-aromatic interactions^{2,3}. There are accompanying changes in the spatial arrangement of the structural units that improve the extent of short-range order: increases in the average number of atoms per structural unit, in the number of structural units or layers that are aligned in parallel, and in the mutual orientation of sets of parallel layers⁴. The model predicts, as confirmed by other studies, that coals possess inherent porosity, and that with increasing rank, the pore structure becomes narrower.

For the production of some carbon materials, coal serves simply as a source of elemental carbon and its structure and composition are not of any great relevance. These processes tend to involve high energy input, and the rearrangement of carbon atoms and carbon fragments in the vapor phase, or via vapor-solid reaction, to produce highly ordered carbons such as fullerenes and nanotubes^{5,6} and filaments⁷. However, in the majority of cases, the conversion process takes advantage of the structure of coal with the aim either of preserving its amorphous configuration or of promoting increased structural order.

With the exceptions of diamond, diamond-like materials, and closed-cage structures (fullerenes and nanotubes), the structure of most carbons is related to that of crystalline graphite. Nascent elements of the graphite structure are recognizable in coal in the form of planar cyclic carbon structures, and their propensity for parallel orientation. Upon the thermal treatment of coals (or any other solid or liquid carbonaceous precursor) the thermodynamic driving force is towards improved structural order through the aromatization, growth and alignment of structural units. The potential for ultimately producing a graphitic structure is determined by the changes that occur between about 400-600°C, as illustrated in Figure 1. The formation of crosslinks between structural units can impede improvements in structural order, preserving the random order present in the parent coal, and resulting in a hard, porous, isotropic char. Such materials are termed non-graphitizing carbons, as there is little further improvement in crystalline growth and ordering upon heat treatment to temperatures as high as 3000°C. Low-rank coals, oxidized bituminous coals, and anthracites follow this pathway.

Under conditions where there is minimal crosslinking, the formation of a fluid state allows planar aromatic structures to grow in size and diffuse into positions of parallel alignment, leading to the nucleation and growth of a separate anisotropic phase within the parent isotropic liquid. The anisotropic phase is a liquid crystal known as carbonaceous mesophase. If continued, the process is eventually arrested by solidification of the melt. The anisotropic carbon content of the resulting char is determined by the precursor composition and carbonization conditions, and the duration of the fluid phase. In the carbonization of (bituminous) coking coals and coking coal blends, mesophase development is limited because, in the coke oven, there is a mixture of fluid and solid phases, and the heating conditions are such that the existence of the plastic condition is transient. The char or coke consists of a mixture of isotropic, and small and larger anisotropic regions: in the terminology of optical microscopy, mosaic and flow domains, respectively. With pitch precursors, a fluid condition can be maintained for longer periods, allowing the possibility of extensive mesophase development through the continued formation of nuclei, their growth and coalescence. The highly anisotropic chars thus produced are composed of small, well-ordered pseudo-graphitic crystallites that are oriented with their basal planes in approximately parallel orientation. They are weaker, due to the low density of crosslinks, and are of lower porosity than isotropic chars produced from thermosetting precursors. These are graphitizing carbons, which experience a sharp improvement in structural order and crystallite size upon heat treatment to temperatures above about 2200°C.

DIRECT CONVERSION OF COALS TO CARBONS

Activated Carbon

In the production of activated carbons from coal, it is desirable to preserve, as far as possible, the amorphous nature of the parent coal structure: the porosity of activated carbons derives from the small size of the constituent disordered crystallites and their random packing. As discussed, this is achieved via crosslinking reactions during low-temperature carbonization. Low-rank coals and anthracites can be processed directly, while the thermoplastic behavior of bituminous coals is first suppressed by air oxidation, or other means such as the use of additives or coal blending.

Coals are carbonized at 500 - 700°C to produce isotropic chars with pore structures that reflect those of the starting coals. However, partly because of volume contraction that is caused by heat treatment, most of the pores are closed or too narrow to be of practical value. Porosity is then developed by activation in which carbon is removed through controlled gasification at 800-1000°C in steam or CO₂. The pore structure in the final carbon product is therefore not created but is a development of the basic structure that is inherent to the starting material and translates through the processes of carbonization and activation. For this reason, activated carbons produced from coals of different rank reflect the same changes in pore size distribution as do the original coals: those from low-rank coals have high mesopore volumes, those from bituminous coals have a broad pore size distribution, and those from high rank coals are microporous. Together, coals and lignite constitute about 50% of the raw materials used to manufacture activated carbons. They are produced with a broad range of product properties, in the form of both powders and larger sized products (granules, pellets or extrudates).

Activated carbons with novel properties can be produced from coal by chemical activation using KOH. Extremely high surface area carbons can be produced from bituminous coals and petroleum coke precursors by reaction with KOH at temperatures up to 1000°C, followed by leaching to recover the reagent⁸. Despite the unusual properties of this activated carbon (surface area > 3000 m²g⁻¹, and total pore volume 2.0 - 2.6 ml/g), only limited quantities have been produced. The cost, low bulk density, and difficulties in handling have presented obstacles to successful commercialization, although a recent development has allowed the powder to be incorporated into a more tractable monolithic form⁹. In variants of the same process, KOH has also been used to produce high surface area, hard extruded carbons from low-rank coals¹⁰ and preoxidized bituminous coals¹¹, high surface area activated mesocarbon microbeads (see below)^{12,13}, and catalysts with high activity and selectivity for the hydrodehalogenation of halogenated aromatic compounds - reactions that are of interest for environmental protection^{14,15}.

Metallurgical Coke

The manufacture of metallurgical coke represents the single largest non-fuel use of coal for the production of a carbon material, accounting for approximately 10% of world coal consumption. The phenomenon of fluidity development in coking coals and coking coal blends is critical to producing the characteristics required of metallurgical coke. An associated outcome is the development of anisotropy through mesophase formation. Its significance to many of the properties of coke that are of importance to metallurgical practice is a matter of some debate, but it does appear to influence coke strength¹⁶.

CARBONS FROM COAL-DERIVED LIQUIDS

The range of carbons that can be obtained from coal is considerably expanded through the derivation of high molecular weight liquids or pitches. Liquids can be obtained by a number of different methods, such as solvent extraction, hydrolysis, direct liquefaction, and coking, each of which effectively serves to liberate the coal structural units. The composition of the liquids can be altered to a greater extent through the selection of the coal and reaction parameters, allowing

considerable latitude in the preparation of precursors for different end-products.

Isotropic and Mesophase Pitch Carbon Fibers

Different types of carbon fibers can be classified according to the precursor or process method: polymers, rayon and polyacrylonitrile (PAN); vapor-grown; and pitch. The last of these groups is divided into fibers produced from isotropic pitch, and from pitch that has been pretreated to introduce a high concentration of carbonaceous mesophase. The former are so-called general purpose fibers that are sufficiently strong to be used in a wide range of applications, while the latter are high performance materials, possessing very high tensile strength and modulus. Extensive discussions of the synthesis and applications of isotropic pitch-based and mesophase pitch-based carbon fibers has been given by Edie¹⁷, and Singer¹⁸ has written a more general account of carbon fiber technology.

The production of isotropic pitch-based carbon fibers by melt-blowing was first commercialized in 1970, using a pitch prepared from ethylene cracker tar. Subsequently, commercial processes were developed to produce isotropic fibers from coal-tar pitch, and petroleum pitch prepared from decant oils produced by fluidized catalytic cracking¹⁹. During the 1970's, the National Coal Board (now the British Coal Corporation), United Kingdom, conducted extensive research on the formation of continuous carbon fibers from coal extracts produced by a liquid solvent extraction process, LSE²⁰. Although the starting material was isotropic, the aim was to produce fibers with high strength and modulus, and a final high temperature heat treatment step under tension was used to improve fiber strength - a technique that has also been applied to rayon-based and isotropic pitch carbon fibers¹⁸. Although these fibers were unable to compete with the later-developed PAN and mesophase fibers, the work demonstrated that other sources of coal liquids could be used as effective fiber precursors. Recent work has shown that continuous filaments of isotropic carbon fibers can be produced from coal liquefaction products^{21,22}.

The discovery of carbonaceous mesophase in the 1960s^{17,18} led to the development of mesophase fibers, in which the orientation of the molecular structure along the fiber axis allows the development of a graphitic structure. Because the intermolecular interactions in the liquid crystal phase are so weak, they can be oriented by any small shear force such as in extrusion or elongation, to produce an oriented fiber. Moreover, the orientation and resulting structure can be modified by spinning conditions, and especially the spinnerette design.

The preparation of the starting material for isotropic and mesophase pitch fibers involves quite different treatments. For isotropic pitch fibers, the principal steps involve the removal of volatile components by distillation, and solids separation. Distillation increases the softening point and aromaticity of the pitch. For mesophase fibers, the pitch must be further treated in one of several different ways to generate a high mesophase content product that is suitable for melt spinning. Spinnability is a critical requirement, since the production of continuous filaments is essential for most applications of high performance fibers. In both cases, the as-formed, "green" fibers require to be stabilized to render them thermosetting before carbonization. Stabilization is normally accomplished by air oxidation, with a weight gain of up to 10%. The introduction of oxygen functionalities leads to the formation of crosslinks during oxidation and subsequent carbonization. Oxidation must be initiated at temperatures below the glass transition temperature of the fibers to prevent melting, and for mesophase fibers, to prevent loss of molecular orientation. With continuing reaction, oxidative crosslinking progressively raises the glass transition temperature, such that the reaction temperature (and rate) can be increased. Eventually, the glass transition temperature is sufficiently elevated that pyrolysis reactions precede plasticity development, and the fibers can be carbonized.

To develop strength, the stabilized fibers are carbonized in inert atmosphere at temperatures up to about 1200°C. This is the final chemical processing step for isotropic fibers: due to the lack of molecular orientation, there is little further gain in strength upon heat treatment to higher temperatures. Conversely, there are large increases in the tensile strength and modulus of mesophase fibers upon graphitization (up to 3000°C). The final fiber properties are determined by the degree of orientation of layer planes along the fiber axis, and the size and perfection of individual crystallites. The modulus of isotropic fibers is about 1/20 of that of mesophase fibers, while their tensile strength is around 1/3.

Lower cost makes isotropic pitch fibers attractive for applications where high tensile strength or modulus are not required. Examples include: enhancing the properties of composite friction materials; the reinforcement of engineering plastics; ablation materials; acoustic and thermal insulation; electrically conductive fillers for polymers; electromagnetic shielding; filter media; paper and panels; the production of hybrid yarns with other fibers; reinforcing concrete to improve flexural strength and other properties; and as potential replacements for asbestos. Mesophase pitch fibers are used in advanced composite materials. Graphitized mesophase pitch fibers tend to have higher modulus and lower tensile strength than the PAN-based equivalents: the former have advantages in applications requiring high stiffness, high electrical and thermal conductivity, low thermal expansion, and high temperature oxidation resistance, while the latter are employed where high strength is required. Because of their high modulus, mesophase fibers are often used in

aerospace structures, and the very high thermal conductivity of recently developed fibers has opened applications for heat dissipation in areas such as high speed machinery, aircraft structures, and electronics.

Activated Carbon Fibers

There is a growing interest in the development and application of activated isotropic carbon fibers (ACF). They can be produced with high surface area, and the narrow fiber diameters (usually 10 to 20 microns) lead to much faster adsorption, desorption, or catalytic reaction than for granular carbons. The novel properties of ACFs make them more attractive than other, more conventional activated carbons for certain applications¹⁹. In this laboratory, we have examined the synthesis of isotropic pitch fibers and activated fibers from non-conventional pitches. Whereas most commercial ACFs are microporous, activated carbon fibers produced from shale oil asphaltene and from coal liquefaction products are found to possess high mesopore volumes^{21,22}. Through the selection of appropriate precursor pitches, it is possible to produce ACFs with substantially different properties in terms of pore size distribution and surface chemistry, as well as potentially allowing more rapid processing. In this context, coals present a fertile resource as heavy coal liquids can be produced relatively cheaply, and with a wide range of composition.

Individual fibers (and powders) present difficulties in handling, containment, and regeneration, and in fixed bed operations they would present an unacceptably high pressure drop. These problems can be surmounted by their incorporation into forms such as felt, paper, woven and nonwoven fabrics, and rigid monolithic structures. Potential advantages of the monolithic forms are: they allow facile handling; they can be highly permeable; they permit the possibility of regeneration; where there is good contact between the carbon constituents and if they are adequately conducting, electrical energy can be used as a method of rapid and uniform heating to drive the processes of desorption or regeneration²³⁻²⁶; and they can be fabricated to a given size and shape, a consequence of which is that completely novel adsorber/ reactor designs are possible.

In this laboratory, we have developed rigid activated carbon fiber composite materials^{27,28}. Using pre-activated carbon fibers, 80-90% of the surface area of the free fibers is retained in the composite. Alternately, the formed composite can be carbonized and activated in steam or carbon dioxide. The composites are strong, highly permeable to fluids, and can be machined. They can be used to efficiently separate CH_4 and CO_2 ²⁸. In liquid and gas phase column tests, the composites have been compared to commercial granular activated carbons, where it has been found that there is much more effective use of the adsorptive capacity of the carbon before column breakthrough. The higher efficiency of the composite is attributed to: the uniform structure which ensures that the feed is distributed evenly through the column: the presentation of the adsorbent surface in fiber form which allows high rates of adsorption; and the open architecture which renders the pore structure readily accessible.

Mesocarbon Microbeads

By arresting the process of mesophase development at the nucleation stage, mesophase microbeads can be obtained by separation using techniques such as centrifugation and solvent extraction. The diameter of the beads is typically in the range 1 - 80 μm ^{12,13}. The microbeads are used in the "green" form to produce so-called sintered or binderless carbons²⁹. These are high density, high strength, shaped carbons that are formed by molding the microbeads. Upon carbonization, strong bridging bonds are created at the points of contact between the microbeads. Under applied pressure, deformation of the microbeads helps to minimize the porosity of the resulting artefact. Heat treatment to graphitizing temperatures greatly enhances strength and produces a material that is composed of graphitic microbeads but is macroscopically isotropic due to their random orientation. Carbonized and graphitized microbeads are used in the production of new composite materials, including electrode materials for Lithium batteries. The various applications of the microbeads take advantage of the basic properties of graphite - high resistance to corrosion and oxidation, and excellent electrical and thermal conductivity.

Needle Coke

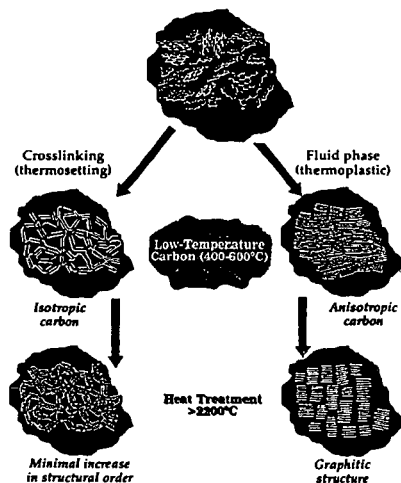
Highly anisotropic cokes are obtained by solidification after extensive mesophase development. The structure renders them relatively friable or "soft", with low porosity, and the anisotropy is reflected in the acicular shape of the coke particles, which are termed needle coke. Needle cokes are readily graphitizable and are used for the manufacture of graphite electrodes for arc-steel furnaces. Normally, needle coke is produced from selected petroleum feedstocks: one example is decant oils from fluid catalytic cracking. Feedstock properties such as high aromatic carbon content are important. The aromatic character of coals implies that they could present an attractive alternative source for the production of needle coke, and it has been shown that highly aromatic, pretreated coal tar pitches can give excellent needle cokes. It has further been demonstrated that a suitable needle coke can be obtained from coal via solvent extraction³⁰. Bituminous coal is slurried with about three times its mass of anthracene oil (itself a product of coal tar distillation), and heated to 415°C for 60 min at 0.8 MPa (autogenous pressure), when approximately 70-80% of the coal (dmmf) is solubilized. The mineral matter and undissolved coal are separated by hot pressure filtration to afford a coal extract solution (filtrate) containing around 0.1% ash. The extract is then preheated to ~ 520°C and fed to a delayed coker to produce needle coke, and the coker overhead is

recycled as solvent. The process has been successfully demonstrated on a large scale in which sufficient coke was produced to fabricate graphite electrodes (using coal tar pitch binder) that were tested in a 25 ton steel production furnace³⁰. Approximately 10% of needle coke is now produced from pretreated coal tar: annual world production is about 1.3 Mt.

REFERENCES

1. Oberlin A (1989) In: Chemistry and Physics of Carbon, 22 (Ed. P. A. Thrower), Marcel Dekker 1989, 1-143.
2. Nishioka M, Larsen J W (1990) Energy & Fuels, 4 (1), 100-106.
3. Barton W A, Lynch L J (1989) Proc. Int. Conf. Coal. Sci. Tokyo, 13-16.
4. Cartz L, Hirsch P B (1960) Phil. Trans. R. Soc., 252, 557-602.
5. Howard J B et al (1991) Nature, 352, 139-141.
6. Wilson M A, Pang L S K, Quezada R A (1995) Proc. Eighth International Conference on Coal Science (Eds. J. A. S. Pajares and J. M. D. Tascón), 2, Elsevier, 1177-1180.
7. Burton D, Lake M, Alig R (1996) Am.Chem.Soc.Div.Fuel Chem. Preprints, 41 (1), 349-353.
8. Wennerberg A N, O'Grady T M (1978) US Patent 4,082,694.
9. Robinson, K, Mievillie, R (1996) Megacarbon Inc., personal communication
10. Guy P J et al (1989) Proc. Int. Conf. Coal. Sci. Tokyo, 23-27.
11. Verheyen V et al (1995) Carbon, 33 (6), 763-772.
12. Kasuh, T, Morino, G (1992) US Patent 5,143,889
13. Matsumura, Y, Maeda, T (1992) Tanso, 155, 403-406.
14. Farcasiu M et al (1994) J. Catal., 146, 313-316.
15. Kaufman P B et al (1996) Am.Chem. Soc. Div. Fuel Chem. Preprints, 41 (1), 447-450.
16. Patrick, J W, Reynolds, M J, Shaw, F H (1982) Proc. 64th CIC Coal Symposium (A. M. Al Talweel, Ed.), C. S. Ch. E., 550-559.
17. Edie, D D (1990) In: Carbon Filaments and Composites (J. L. Figueredo et al, Eds.), Kluwer Academic Publishers, 43-72.
18. Singer, L S (1994) In: Materially Speaking, 9 (2), Materials Technology Center, Southern Illinois University at Carbondale, IL, USA.
19. Derbyshire, F J et al (1994) Am.Chem. Soc. Div. Fuel Chem. Preprints, 39 (1), 113-120.
20. Jorro, M A A, Ladner, W R (1974) Proc., 4th Int. Carbon Conference, London, Sept., 287.
21. Fei Y Q et al (1993) Proc. Eastern Oil Shale Symposium, Lexington, KY, Nov. 16-19, 38-45.
22. Kimber et al (1996) Proc. Pittsburgh Coal Conference, 553-558.
23. Economy J et al (1996) Am.Chem. Soc. Div. Fuel Chem. Preprints, 41 (1), 321-325.
24. Lordgooei M et al (1996) Am.Chem. Soc. Div. Fuel Chem. Preprints, 41 (1), 369-373.
25. Kimber G M, Johnson A (1996) Proc. European Carbon Conference - Carbon '96, Newcastle, UK, July, 52-53.
26. Le Cloirec P et al (1996) Am.Chem. Soc. Div. Fuel Chem. Preprints, 41 (1), 379-384.
27. Jagtoyen M et al (1994) Materials Research Society Symposium Proceedings, 344, 77-81.
28. Kimber G M et al (1996) Gas Sep. Purif., 10 (2), 131-136.
29. Dollin, P, Ting, D N, Rand, B (1996) Proc. European Carbon Conference - Carbon '96, Newcastle, UK, July, 421-422.
30. Kimber, G M, Brown, A, Kirk, J N (1981), High Temperatures-High Pressures, 13, 133-137.

Figure 1. Production of disordered and ordered carbons from coal



PRELIMINARY EXPERIMENTS ON THE CHARACTERISTICS AND POTENTIAL USES OF COAL FLY ASH FROM ISRAEL.

Henry A. Foner*, Thomas L. Robl, James Hower and Uschi M. Graham
University of Kentucky, Center for Applied Energy Research, 3572 Iron Works Pike, Lexington
KY 40511

Keywords: Coal fly ash, Utilization, Israel

INTRODUCTION

Traditionally electric power in Israel has been produced from heavy fuel oil. Starting in 1982, the government-owned electric utility began to build coal-fired power stations and about 55% of the current output is now derived from coal. The switch to coal was made for strategic, economic and environmental reasons and future plans call for a continuing replacement of oil by coal for power generation.

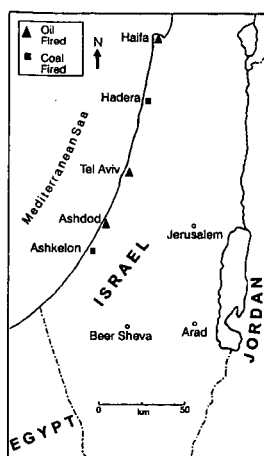


Figure 1. Location of Power Stations

All power stations in Israel are on the Mediterranean coast (as shown in Figure 1) due to the need for copious supplies of cooling water which are unavailable elsewhere in the country. The coastal plain of Israel contains a large shallow aquifer which supplies a considerable part of the country's potable water. Most of the population is concentrated in this part of the country and this aquifer is already in considerable danger from anthropogenic pollution. Hence, there is much understandable concern about the effects of dumping large quantities of extraneous material anywhere on the coastal plain. It is for this reason that coal fly ash has been declared a hazardous waste material by the Israel Ministry of the Environment who put strict controls on its disposal. The only suitable site for dumping the ash is in the Negev desert south of Beersheva, and this entails considerable transportation costs. The practice of dumping the ash at sea at carefully chosen deep sites has now been stopped.

This paper surveys the present position and describes preliminary experiments on representative samples of coal fly ash. These experiments are intended to fully characterize the properties of the ash as a preliminary step to suggesting

ways to utilize it as a useful material instead of treating it as an industrial waste.

ASH PRODUCTION AND DISPOSAL

The ash produced from the coal fired power stations has been disposed of as follows:

- Dumping in ash embankments at the Hadera power station.
- Use as an additive to cement by the Nesher Cement Co. (up to 10% allowed by the appropriate Israel Standard).
- A small amount as raw material for cement production.
- Dumping at sea (a limited amount under supervision of the Ministry of the Environment).

Table 1, reproduced from Metzger⁽¹⁾, summarizes the position - past and present.

TABLE 1

Amounts of ash produced, utilized and disposed of in Israel: Total and recent years
(thousands of tonnes)

	1993	1994	1995	1982-95
Total Production	640	650	735	6060
<u>Utilization/disposal:</u>				
Cement production	420	440	630	3910
Embankments	150	160	20	1120
Disposal at sea	70	50	85	1030

* Permanent affiliation: Geological Survey of Israel, 30 Malkhei Yisrael St., Jerusalem 95501, Israel

Israel's electricity consumption is growing rapidly due to natural development and a rising standard of living and also because of the accelerated increase in population due to immigration. The current coal-fueled generating capacity is about 3,700 MW and this is scheduled to rise to 4,900 MW by the year 2000 with the addition of extra units to existing power stations. Total imports of coal for the year 1996 were about 7.5 million tonnes and of this all but 30,000 tonnes was used for electricity generation. As long term plans for electricity production are linked to coal, it is obvious that the amount of ash produced will increase and the problem of its disposal will become more acute. Ash production is expected to be 1,000,000 tonnes in 1997 and to reach 1,300,000 tonnes by the year 2001. In the year 2001 ash production will exceed the current level of utilization by approximately 700,000 tonnes. As the amount of ash used by the cement industry is near saturation, new uses must be developed, old uses expanded or the material must be exported if the undesirable prospect of ash disposal is to be avoided.

At present there are no flue gas desulfurization (FGD) plants on any of the coal fired power stations in Israel, so the potential problems of disposing of the by-products of such plants will not be considered here. However, FGD units will be erected in the Ashkelon power station by the year 2001 and subsequently may also be retrofitted in the Hadera power station.

EXPERIMENTAL and RESULTS

The Israel Ash Authority recently collected two carefully homogenized samples of fly ash for a study of the environmental effects of ash disposal and these were also used for the present study. These samples were chosen to represent the two main types of fly ash produced in Israel according to the type of coal burnt. The samples are designated as South African (SA) and Colombian (CO) after the (approximate) source of the parent coal.

Aqueous extracts of the fly ash samples are strongly alkaline (approximately pH 12 to 12.5) and the major chemical composition of the ashes is shown in Table 2⁽³⁾.

TABLE 2
Analyses of reference samples of South African and Colombian Fly Ash

Element	South African %	Colombian %
SiO ₂	44.0	56.5
Al ₂ O ₃	33.2	23.5
TiO ₂	1.8	1.2
Fe ₂ O ₃	2.9	6.5
CaO	9.5	4.0
MgO	2.2	1.5
SO ₃	0.8	0.6
P ₂ O ₅	1.5	0.8

The samples were dry sieved into four fractions as shown in Table 3 and the carbon content of the fractions determined. The individual fractions were examined under both optical and scanning electron microscopes and the mineralogical properties of each fraction determined by X-ray diffractometry (XRD).

Table 3 shows the proportions of the various fractions present and the amount of carbon in each.

TABLE 3
Size fractions of the ash components and their carbon contents

Size		South African		Colombian	
Fraction	micron	%	carbon %	%	carbon %
>100 mesh	>150 μ	1.9	24.6	4.5	46.8
100-200	150-75	8.2	13.7	10.0	16.2
200-325	75-45	51.6	2.88	55.0	4.21
<325	<45	38.3	1.91	30.5	3.03

The original samples and the various fractions were examined under the optical microscope and the proportions of the following components determined: glass, mullite, spinel, quartz, isotropic coke, anisotropic coke and inerteite. The predominant component (>90%) in both samples is glass. The total amount of carbon determined by this method for the original samples was 5.0% for SA and 7.4% for CO. These values compare with 4.2% and 7.1%, respectively, determined by a chemical method. Microscopic examination also shows that there is considerably more anisotropic coke (as defined by optical activity) present in the CO sample than in the SA sample.

Examination under the scanning electron microscope showed that the samples are typical fly ashes composed mainly of small aluminosilicate spheres. The carbon particles are relatively large and are porous with many glass spheres embedded in the interstices (Figure 2).

XRD spectra of the two samples showed some distinct differences. These were originally thought to be related to the presence of graphitic domain structures in the CO sample, but this aspect of the work needs further investigation. The graphitic character of anisotropic coke in fly ash has been commented on previously by Graham *et al.* ⁽³⁾. The other minerals identified by XRD were: quartz, mullite and traces of lime.

DISCUSSION

The first step in any plan to encourage the use of fly ash as a raw material must be to supply a standard product with well defined properties. This product should conform to existing national or international standards. Perhaps the foremost of these is ASTM C 618 ⁽⁴⁾ which relates to the use of fly ash as a pozzolanic additive to Portland cement. This is an end use with a particularly high added value and Israeli ash is already used to some extent for this purpose. However, larger additions of fly ash to cement are quite common and, on the whole, improve the properties of the finished product. When the materials are examined on a size basis, distinct differences in the chemical and physical characteristics of the ash are found. These differences suggest that the separation of the ash into two fractions, a coarse +200 mesh (>75 μm) and a fine -200 mesh (<75 μm), would result in more usable products.

Carbon is preferentially fractionated to the larger sizes. The concentration of carbon found in the coarsest fraction of the material (+100 mesh or >150 μm) is probably sufficient to sustain combustion and may be recycled to the furnace to recapture its fuel value and increase overall fuel efficiency. The coarse fraction could also be further processed to concentrate the carbon for high value uses such as an adsorptive carbon as suggested by Graham *et al.* ⁽⁵⁾.

Carbon, however, is undesirable in fly ash used as a cement additive in concrete. It reacts with air entrainment reagents, is non-pozzolanic and may color the concrete if present in high enough concentrations. Because of these characteristics the loss on ignition (LOI), which for the most part is carbon, is limited by the ASTM C-618 standard to 6%. The fine fraction (-200 mesh or 75 μm) of both samples would easily meet this criterion. This may allow the proportion of fly ash currently used in cement in Israel to be increased beyond the current 10%. A substitution of 16% to 20% is typical for fly ash used in the U.S. The classification of the ash may also improve its pozzolanic properties. This would make it a more desirable material and encourage the development of an international export market.

The other suggested high volume use for fly ash is as a light-weight aggregate for building blocks. These could serve as a substitute for the no-fines concrete blocks which are now ubiquitously used, with the additional advantage of reducing the amount of quarrying and crushing needed for aggregate production.

Some other possible uses of fly ash are:

- as a light weight aggregate for aerated insulating building blocks.
- as a low strength flowable fill for trenches and around building foundations and basements.
- as the sand component of cement - Israel has a shortage of sand for concrete production in the densely populated parts of the country.

All these potential applications would be more profitable than using the fly ash as road-bed material and would be without the possible ecological disadvantages of this use.

REFERENCES

- (1) Metzger, A.L. The Environmental Status of Coal Ash Produced in Israel. Proceedings of the 13th Annual International Pittsburgh Coal Conference, Pittsburgh, PA, September 3-7, 1996, 749-754.
- (2) Cohen, H., Shepf, S., Dorfman, E. and Foner, H.A. Preparation of an Analytical Scheme for Coal Ash Leachates. Report to the Israel Ash Authority, May 1996.
- (3) Graham, U.M., Robl, T.L., Rathbone, R.F. and McCormick, C.J. Adsorptive Properties of Fly Ash Carbon. Preprints of Papers presented at the 211th ACS National Meeting, New Orleans, LA, March 24-28, 1996, Vol. 41, No. 1, 1996, 265-269.
- (4) Standard Specification for Fly Ash and Raw or Natural Pozzolan for use as a Mineral Admixture in Portland Cement Concrete. Annual Book of ASTM Standards, Vol. 4.02, ASTM, Philadelphia, PA, 11990.

ACKNOWLEDGMENTS

The authors wish to thank Dr. Samuel Grossman of the National Coal Supply Company, Israel, for his generous help with both the supply of samples and information. We also wish to thank our colleagues at CAER, Gerald Thomas and Margaret Grider, for carrying out analyses.

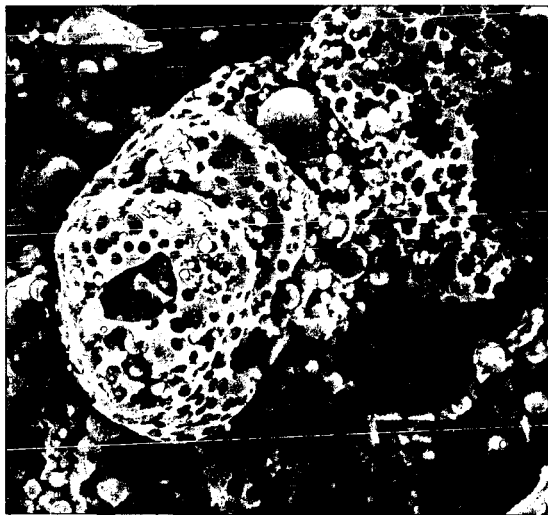


Figure 2. Porous carbon particle with embedded aluminosilicate spheres
(Photomicrograph size approx. 80 x 80 μm)

STUDIES OF FLY ASH AND ASH DEPOSITS FROM AN AFBC SYSTEM

Wei Xie, Shi Su, H. Li, Wei-Ping Pan and John T. Riley
Materials Characterization Center and Department of Chemistry
Western Kentucky University
Bowling Green, KY, 42101

Keywords: combustion, fly ash, chlorine, sulfur

INTRODUCTION

The combustion of coal in a fluidized bed combustor with a limestone bed is one method of controlling sulfur oxides emission. Atmospheric Fluidized Bed Combustion (AFBC) results in two different kinds of solid residues, bed ash and fly ash. The formation of both bed ash and fly ash during the combustion of coal is a very complex environmentally dependent reaction. Significant parameters include the combustion conditions and the characteristics of the limestone used. If a high chlorine coal is used in an AFBC system, the addition of limestone may help reduce hydrogen chloride emission. On the other hand, due to the large amount of ash produced by a power plant, the use of these materials in an environmentally acceptable manner should be considered. The analysis of how the composition of the limestone changes during combustion can provide fundamental data, not only to evaluate the way the limestone functioned during combustion, but also to possibly determine how to use the residue.

During the last decade several studies have been conducted to characterize AFBC residues. Most of these activities focus on the physical properties of fly ash, such as particle size distribution, specific density, the morphological properties, and chemical properties which include the analysis of trace elements, organic compounds and chemical compositions. Knowledge of the distribution of elements such as sulfur and chlorine in fly ash is necessary, not only to understand the principle and efficiency of sulfation of limestone, but also to evaluate the role of the limestone in the capture of sulfur oxides.

EXPERIMENTAL

Experiments were conducted with the 12-inch (0.3 m) laboratory AFBC system at Western Kentucky University using operating conditions similar to those at the 160-MW system at the TVA Shawnee Steam Plant located near Paducah, KY. Two kinds of coal were used in this study, one is a low-chlorine (0.012% Cl and 3.0% S) western Kentucky # 9 coal (95011), the other is high-chlorine (0.28% Cl and 2.4% S) Illinois # 6 coal (95031). The limestone was from Kentucky Stone in Princeton, KY. Six moveable heat exchanger tubes are located within the bed area of the AFBC system. Typical operation involves setting the correct coal/limestone feeds and air flows and then using the moveable tubes to adjust the bed temperature to the desired setting. The combustor's operating parameters (air flow, coal/limestone feed, temperature) were adjusted according to the experimental requirements during combustion.

A TGA-501 thermogravimetric analyzer from the LECO Corporation in St. Joseph, MI was used for determination of the moisture and ash contents of the fly ashes. Carbon, hydrogen and nitrogen contents in the fly ashes were determined using a LECO CHN-1000 system. The sulfur contents were determined with a LECO SC-432 sulfur analyzer. Chloride contents were measured by bomb decomposition followed by determination of chloride with an ion selective electrode.

RESULTS AND DISCUSSION

Several parameters and their effects on the absorption of sulfur dioxide and HCl by the bed ash and fly ash were investigated. The parameters to be discussed in this paper include the bed temperature, the calcium-to-sulfur ratio in the combustion mixture, and the type of coal used.

The Effect of Bed Temperature on the Absorption of SO₂ and HCl. The sulfur contents of fly ash and bed ash reflect the different trends in ash composition that occur with changes in bed temperature. Figure 1 illustrates that the sulfur content in the fly ash increases as the bed temperature is increased. In contrast, Figure 2 shows that the sulfur content of the bed ash decreases with an increase in the bed temperature. At the lower temperature of 1116 K most of the sulfur dioxide produced during combustion is absorbed by the calcined limestone in the bed ash. The optimal sulfur retention is obtained around 1120K, where the sulfur retention reaches around 96%. With an increase in temperature, several factors may contribute to the reduction in the amount of SO₂ captured by the calcined limestone. At higher temperatures (>1120K) the active internal surface of the limestone particles is decreased, which may be due to the effect of sintering of limestone particles. At higher temperatures the equilibrium involving the formation of CaSO₄ from CaO, O₂, and SO₂ is shifted away from the formation of the sulfate salt and toward the free SO₂. As a result, more SO₂ is available to react with particles of lime in the fly ash and the sulfur concentration increases in the fly ash at the higher operating temperatures.

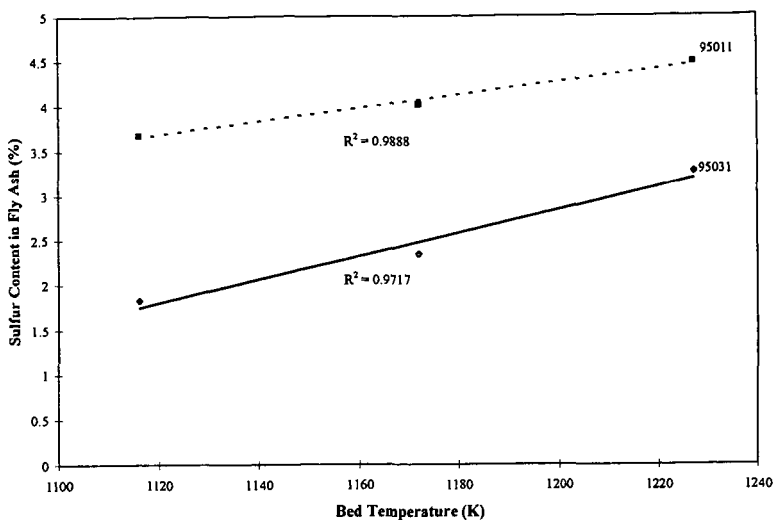


Figure 1. The effect of bed temperature on the concentration of sulfur in the fly ash of the AFBC system.

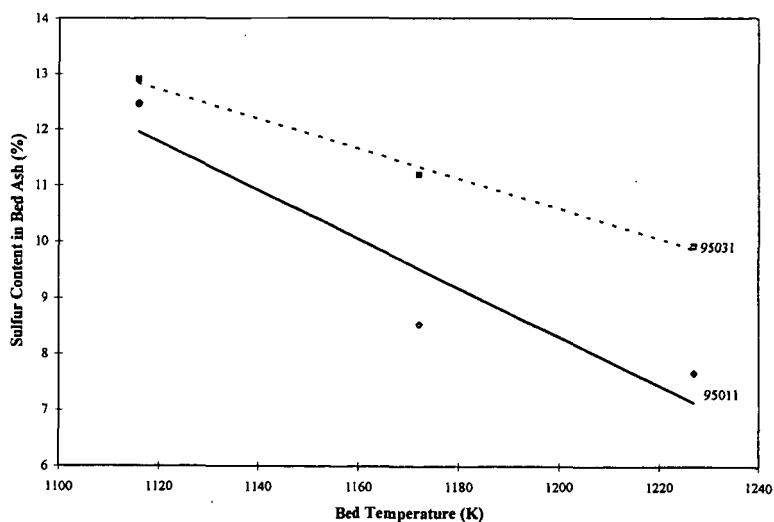


Figure 2. The effect of temperature on the concentration of sulfur in the bed ash of the AFBC system.

The effect of bed temperature on the chloride content in fly ash and bed ash are shown in Figures 3 and 4. It is obvious that the chloride content in the source coal is a decisive factor in the distribution of chloride in ash. The low chlorine coal (95011) released less hydrogen chloride during combustion and there are almost no temperature effects on the absorption of HCl in both the fly ash and bed ash from the combustion of this coal. For the high chlorine coal (95031), both Figures 3 and 4 show that chloride retention is more favorable at low temperatures.^{1,2}

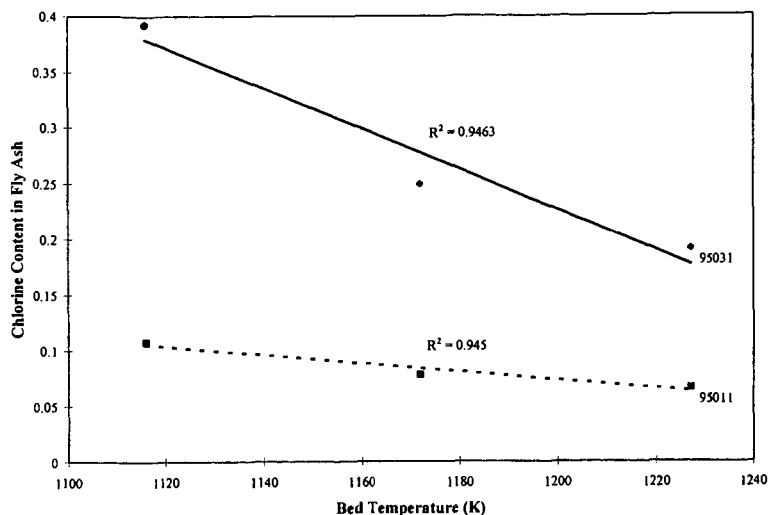


Figure 3. The effect of bed temperature on the chloride content in the fly ash from the AFBC system.

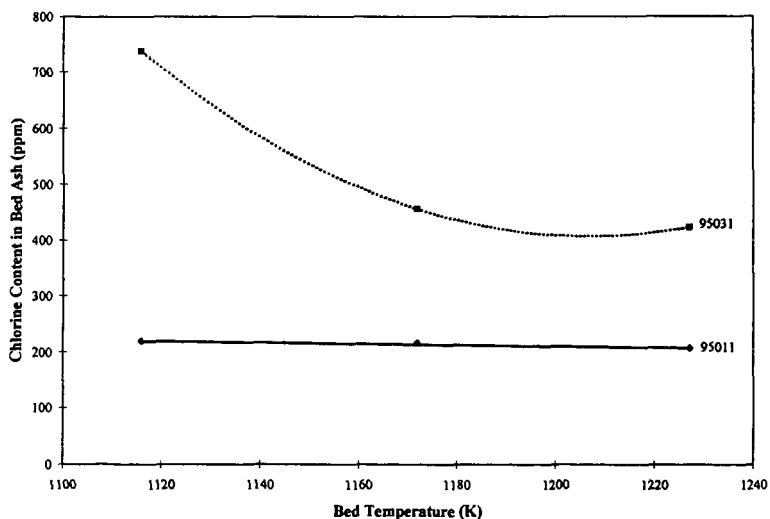


Figure 4. The effect of the bed temperature on the sulfur content in the bed ash of the AFBC system.

The Effect of Ca/S Ratio and Coal Type. Figures 5 and 6 show the effect of Ca/S ratio on the sulfur and chlorine retention in ash. One can see from these figures that the Ca/S ratio has more influence on the sulfur retention for the high sulfur content coal (95011). With the increase of the Ca/S ratio, the sulfur content in fly ash increased. Also, it can be seen that there is little effect of Ca/S on the chloride content in fly ash. On the other hand, Figure 6 shows that the Ca/S ratio is more important for the capture of chloride compared to sulfur for high chlorine content coal (95031). It is assumed that the HCl is probably captured in the low bed temperature region when the flue gas is passing through the heat exchange tube region because the reaction between HCl and CaO is more favorable at the low temperature.^{1,2}

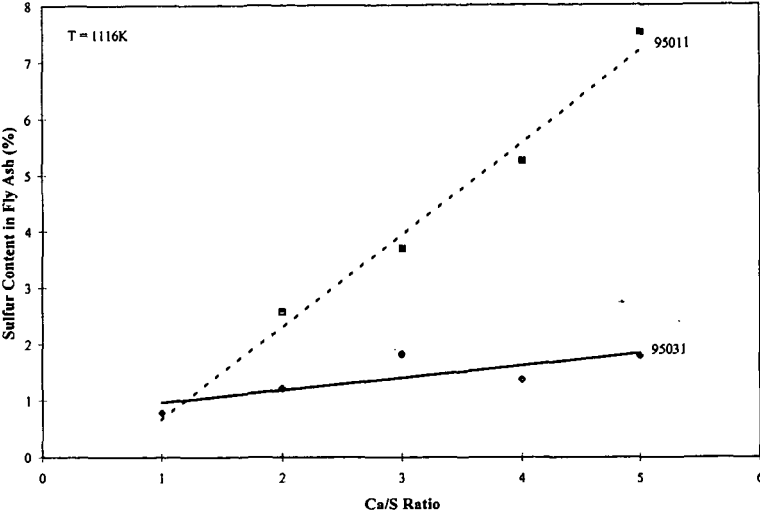


Figure 5. The effect of the Ca/S ratio on the sulfur content in the fly ash.

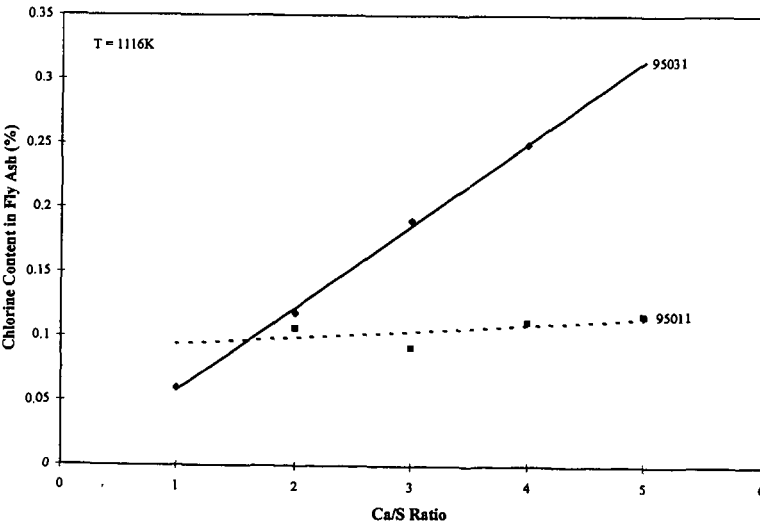


Figure 6. The effect of the Ca/S ratio on the chloride content in the fly ash.

CONCLUSIONS

Based on the data presented in this paper the following observations and statements can be made.

- The bed temperature in an AFBC system plays a key role in the retention of sulfur and chloride in ash. When the bed temperature is too high, less SO_2 is absorbed in the bed ash and more is absorbed in the fly ash.
- The chloride content of a coal is an important factor in the retention of chloride in the ash. Chloride retention in both the fly ash and bed ash is more favorable at low operating temperatures.
- When the sulfur or chlorine content in coal reaches a certain point, the Ca/S ratio in the combustion mixture will be an important factor in the absorption of SO_2 and HCl.

ACKNOWLEDGMENTS

The financial support for this work received from the Electric Power Research Institute is gratefully acknowledged.

REFERENCES

1. Bramer, E.A. "Flue gas emission from Fluidized Bed Combustion" in *Atmospheric Fluidized Bed Coal Combustion*, Elsevier, 1995.
2. Julien S.; Brereton, C.M.H.; Lim, C.J.; Grace, J. R.; Anthony, E.J. *Fuel*, 1996, 75(4), 1655.

LONG TERM LYSIMETRIC LEACHING STUDIES OF FLUE GAS DESULFURISATION MATERIALS FROM THE COOLSIDE TECHNOLOGY.

Thomas L. Robl, Uschi M. Graham and Robert Rathbone, University of Kentucky, Center for Applied Energy Research, 3572 Iron Works Pike, Lexington, KY 40511, USA

Keywords

Flue Gas Desulfurization Material (FGD), Elemental Leaching, Mineralogic Transformations

Abstract

Flue gas desulfurization materials generated by a commercial test of the Coolside duct injection flue gas desulfurization technology was emplaced under controlled compaction conditions in a field lysimeter. Leachates were collected over a period of three years and the soil gases were monitored, as were the changes in the mineralogical and geotechnical properties of the materials. The dominant early reactions include the hydration of anhydrite (CaSO_4) to gypsum and the formation of ettringite ($\text{Ca}_6\text{Al}_2(\text{SO}_4)_3(\text{OH})_{12}\cdot 26\text{H}_2\text{O}$). The dominant weathering reactions include the breakdown of gypsum and then ettringite through dissolution and carbonation reactions. The ultimate residual minerals being calcite and quartz. The original state of compaction was found to have a strong influence on the leachate chemistry with the highest compaction resulting in lower elemental concentrations and material wastage. The leachates were composed primarily of Ca, Na, K and chloride and sulfate ions. The high pH's (10-12.5) favored the mobility of oxyanions.

Background and Methodology

This study was initiated during a successful test of the Coolside flue gas desulfurization technology at Ohio Edison's Edgewater generating station in 1991^{1,2}. Coolside is a lime duct injection technology which is installed on the downstream side of the last heat exchanger. As tested by Ohio Edison, it also employs an alkali reagent, in this case NaOH, to enhance sulfur capture.

The overall goal of this study was to develop sufficient chemical and physical data to insure the environmentally safe disposal of the material. The elemental release or leaching characteristics of the material was targeted for study.

Field studies included the controlled emplacement of the material under varying degrees of compaction in a field lysimeter (Figure 1). During the fill the geotechnical properties of the materials were measured. The lysimeters were excavated at the end of the project and the physical properties of the materials were again measured to determine the changes which had taken place.

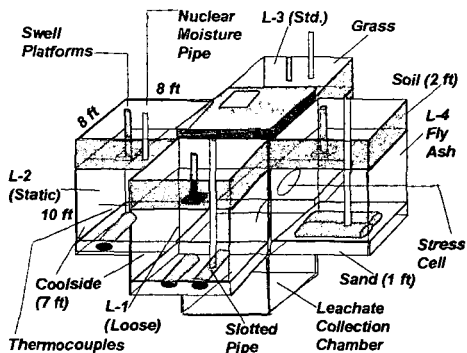


Figure 1. Diagram of Field Lysimeter.

The leaching properties of the material investigated included the determination of the chemistry of the leachate under laboratory column leaching and batch extraction (TCLP) conditions. The leachates from the field lysimeters were also collected and analyzed over a three and a half year period.

The physical and chemical properties of the materials are dependent upon complex mineral solution reactions. In an attempt to determine the overall controls on the system, detailed mineralogical determinations were made of the materials. Also, investigations were made into the state of the thermodynamic data available. A publicly available database and computer program was obtained from the United States Geological Survey and modified for this project³.

Summary of Findings

Physical Properties of the Materials. Ninety-five percent (95%) of the Coolside material passed a 200 mesh sieve (-75 micron) and had a specific gravity of ~2.5. Index properties tests indicated that the Coolside materials were non-plastic and classified as ML (silt) in the Unified Classification System and A-4 under the ASSHTO System.

Table 1. Summary of chemistry from field leachates for first project year (March 1, 1993-February 28, 1994). Data in ppm except for pH and conductivity. Means not computed where more than 50% of samples were below detection limits.

	L1-3 N=44			L2-3 N=38			L3-4 N=52		
	Year 1 Mean	Year 1 Min	Year 1 Max	Year 1 Mean	Year 1 Min	Year 1 Max	Year 1 Mean	Year 1 Min	Year 1 Max
Na	15767	5000	30000	15863	5300	33000	5480	3200	9100
Ca	800	335	1350	640	220	1340	45	18	90
K	5378	1640	8100	4764	1610	8000	1856	1000	3300
Al	ns	dl	dl	ns	dl	0.93	14.26	6.00	29.00
As	0.70	0.30	1.50	1.17	0.40	2.30	4.88	0.80	11.20
B	1.79	0.70	3.70	1.37	0.50	2.60	0.96	0.20	2.80
Ba	0.06	0.02	0.08	0.05	0.01	0.10	ns	dl	0.03
Cr	ns	dl	0.04	ns	dl	0.05	ns	dl	0.18
Fe	ns	dl	0.49	ns	dl	1.29	ns	dl	0.62
Mg	1.34	0.09	4.94	1.16	0.02	4.00	ns	dl	0.15
Mn	0.01	dl	0.04	ns	dl	0.05	0.03	dl	0.62
Mo	56.21	6.00	110.00	50.69	6.10	138.00	20.31	5.50	41.00
Se	2.44	0.30	3.70	1.85	0.25	3.55	1.09	0.24	2.00
Si	11.89	4.10	19.70	14.02	4.20	32.00	44.39	23.00	58.00
Ti	0.08	0.03	0.12	0.07	0.02	0.13	0.01	dl	0.02
V	0.54	0.28	0.98	0.85	0.07	1.80	1.56	0.92	3.47
Alk8.3	72	0	126	125	9	315	1905	275	4710
Alk4.5	186	139	314	249	143	550	3366	1573	7735
Cl	23908	1645	37590	23940	2380	46230	6897	2446	13200
Sulp.	17304	9000	20580	14311	2450	21410	2202	1214	3460
Br	nd	nd	nd	nd	nd	nd	1018	506	1960
pH	9.77	8.64	11.10	10.37	8.38	12.24	12.26	12.06	12.48
Cond.	70.18	19.40	102.00	66.21	19.80	108.30	28.56	14.90	48.50
D. Sol.	65677	16452	112500	59165	15772	107676	18462	8472	31122
S. Sol.	43	5	136	35	5	84	27	5	427

nd=not determined, ns=not significant, dl= below limits of detection

Table 2. Summary of chemistry from field leachates for third project year (March 1, 1995-March 29, 1996).

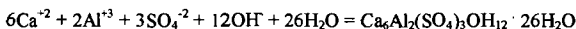
	L1-3 N=39			L2-3 N=26			L3-4 N=35		
	Year 3 Mean	Year 3 Min	Year 3 Max	Year 3 Mean	Year 3 Min	Year 3 Max	Year 3 Mean	Year 3 Min	Year 3 Max
Na	604	495	774	876	352	1635	1436	1035	2180
Ca	109	48	167	83	40	122	33	23	47
K	241	180	330	530	368	715	594	410	780
Al	0.47	0.20	0.92	1.11	0.45	1.74	12.69	10.50	16.20
As	0.30	0.21	0.44	0.47	0.15	0.77	1.16	0.85	1.60
B	0.57	0.30	0.85	0.68	0.30	0.95	0.21	0.05	0.48
Ba	0.01	0.01	0.02	0.02	0.01	0.03	0.01	0.01	0.02
Cr	0.01	0.01	0.03	ns	dl	dl	ns	dl	dl
Fe	ns	dl	0.28	ns	dl	0.20	ns	dl	0.12
Mg	ns	dl	0.10	0.06	dl	1.01	ns	dl	0.05
Mn	0.01	0.01	0.10	ns	dl	0.01	ns	dl	dl
Mo	0.93	0.52	2.00	1.36	0.61	2.90	3.40	1.75	5.00
Se	0.06	dl	0.11	0.09	dl	0.18	0.16	dl	0.45
Si	25.10	18.70	34.00	22.03	13.50	28.00	28.45	23.00	34.00
Ti	0.01	0.01	0.02	0.01	0.01	0.02	0.01	0.01	0.01
V	0.84	0.68	0.96	0.44	0.19	0.65	0.58	0.40	0.70
A8.3	129	0	262	144	66	258	563	288	920
A4.5	175	121	318	215	104	336	1033	799	1500
Cl	109	75	219	46	21	75	1408	838	2213
Sulp.	1506	1031	2052	2652	1671	5680	886	562	1510
Br	nd	nd	nd	nd	nd	nd	319	0	523
pH	11.15	10.95	11.34	11.32	10.91	11.54	12.00	11.84	12.19
Cond.	3.64	2.77	4.97	5.64	3.47	8.08	1.97	1.60	2.36
D. Sol.	2654	1850	3584	4276	2576	6870	5404	3872	7294
S. Sol.	5	5	10	5	5	5	6	5	25

Specimens compacted to 95% of maximum dry density ($\sim 1120 \text{ kg/m}^3$ or $\sim 70 \text{ lbs/ft}^3$) and with optimum moisture (36.5%) were found to develop unconfined compressive strengths of between 1,000 psi and 2,500 psi ($\sim 6,900$ to $\sim 17,200 \text{ kPa}$). The compacted Coolside materials achieved permeabilities from 4×10^{-5} to $3 \times 10^{-6} \text{ cm/sec}$ (low to very low) in the lab.

Field Results. The field lysimeters were filled at three differing levels of compaction. Lysimeter L1 was loose filled (i.e. uncompacted) and had average dry density and moisture content of 706 kg/m^3 (44.1 lbs/ft^3) and 37.5%, respectively. Lysimeter L2 was compacted to the density designed to simulate the compactive efforts of a D9 bulldozer (117.3 kPa or $\sim 17 \text{ psi}$). Dry density and moisture contents averaged 788 kg/m^3 (49.2 lbs/ft^3) and 38.9% in this lysimeter. The third lysimeter (L-3) was filled with Coolside material compacted near 95% of standard maximum dry density and optimum moisture content. Average values of dry density and moisture content were 1060 kg/m^3 (66.2 lbs/ft^3) and 37.0%, respectively.

After 3.5 years of weathering, the materials were excavated and their geotechnical properties determined. The average strengths of the materials in the three lysimeters were 44.1, 46.4 and 1,629 psi for the L1, L2 and L3 lysimeters respectively. Average permeabilities were 1.55×10^{-4} , 4.6×10^{-4} and 2.2×10^{-6} for L1, L2, and L3 respectively. Thus, compaction had an overarching effect on the physical properties of the material. Achieving optimum compaction resulted in a fill which had substantial strength (layers of L3 achieved compressive strengths as high as 2,600 psi) and greatly reduced permeability (layers with permeabilities as low as 10^{-8} to 10^{-9} cm/sec were measured).

Mineralogy of the Materials The Coolside material as received was composed of quartz (SiO_2), mullite ($\text{Al}_6\text{Si}_2\text{O}_{13}$), portlandite ($\text{Ca}(\text{OH})_2$), calcite (CaCO_3), hannebachite ($\text{CaSO}_3 \cdot 0.5\text{H}_2\text{O}$) and minor anhydrite (CaSO_4). A glassy phase is also present in the raw Coolside material and typically consists of spherical Si-Al fly ash particles. Upon hydration ettringite ($\text{Ca}_6\text{Al}_2(\text{SO}_4)_3 \cdot \text{OH}_{12} \cdot 26\text{H}_2\text{O}$), the principal cementitious mineral in the system rapidly forms,



The state of compaction of the materials was found to have a strong impact on the chemistry of the leachates. Two distinct patterns emerged over the study. Lysimeters L1 and L2 initially had much higher elemental concentrations compared to L3 which was compacted to optimum density (Table 1). Sodium, Cl, K and sulfate were all higher in concentration by factors of 3 to 4 and Ca by a factor of more than 10 in L1 and L2 leachates. The longer term elemental release pattern showed a more rapid decline in elemental concentrations in the L1 and L2 leachates (Table 2). For example, Na in L1 dropped from an average value of 15,767 ppm—which is approaching the concentration of a brine—the first year, to an average value of 1,637 ppm the second year, and 604 ppm the third. The L3 leachates declined in concentration at a lower rate, with an average of 5,480 ppm the first year followed by averages of 2,302 ppm and 1,436 ppm the second and third year.

The leaching pattern for minor and trace elements did not necessarily show a similar pattern to that of the major elements. For example, Al and Si increased in concentration during the second year of the study in the L1 and L2 leachates as a function of pH of the leachates which increased over time.

The average pH of the L1, L2 and L3 leachates was 9.7, 10.4, and 12.3 during the first year of collection. Most transition metals are insoluble under these conditions and were not detected. However, elements which can form oxyanionic complexes such as Mo (MoO_4^{-2}), Se (SeO_4^{-2}), As (AsO_4^{-3}) and V (VO_4^{-3}) were found in measurable and sometimes significant concentration (e.g. Mo reached maximum concentrations $>100 \text{ ppm}$ in several samples the first year).

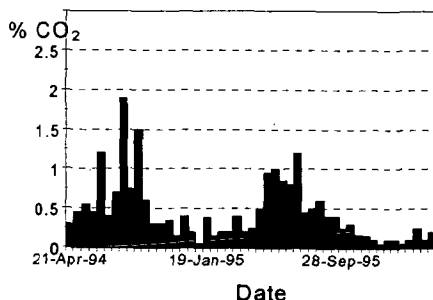
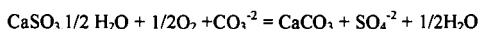


Figure 2. CO_2 Concentration in soil gas from 24 cm depth of lysimeter 1.

Carbon dioxide concentrations in the soil gases of the lysimeters were monitored in the second and third year of the study. In general, the highest CO₂ concentrations were reached during the summer and the lowest during mid-winter, as a function of respiration (Figure 2). The highest concentration recorded was 3.2% (32,000 ppm), well above that of atmospheric concentration (~350 ppm). Soil gas profiles gave clear and conclusive evidence of the highly reactive nature of the Coolside materials with respect to CO₂. At pH's above ~10 CO₂ reacts directly with hydroxide and forms carbonate ion,



The thermodynamic analysis of the chemical composition of the leachates indicated that they are all supersaturated with respect to calcite and undersaturated with respect to gypsum and hannebachite. This, combined with direct mineralogical evidence, indicates that minerals are both dissolving and precipitating. The most important long term weather reactions include the precipitation of calcium carbonate and the dissolution of sulfites and sulfates, primarily hannebachite in this case, summarized as follows:



Both the mineralogical and thermodynamic data indicate that ettringite will also break down over time. However this does not appear to proceed until the sulfate is largely exhausted. Thus, in effect, the sulfate acts as a buffer to extend the stability of the ettringite.

Elements of environmental concern which were found in concentrations exceeding RCRA limits included Se (RCRA limit 1 ppm) and As (RCRA limit 5 ppm). Some of the leachates from the L3 lysimeter reached concentrations as high as 19 ppm As during the first year of the study. The average concentration of Se for all of the leachates from the Coolside materials for the first year of study exceeded the 1 ppm limit.

References.

1. Ball, J.W., and D.K. Nordstrom, 99, WATEQ4F with Revised Thermodynamic Data Base and Test Cases for Calculating Speciation of Major, Trace, and Redox Elements in Natural Waters. USGS Open File Report 91-183.
2. Yoon, H., F.W. Theodore, F.P. Burke, B.J. Koch, 1986, Low Capital Cost, Retrofit SO₂ Control Technologies for High Sulfur Coal Applications. Reprint, Air Pollution Control Association, 79th Annual Meeting, Paper No. 86-47.5, 21 p.
3. Kanary, D.A., R.M. Statnick, H. Yoon, D.C. McCoy, J.A. Withum and G.A. Kudlac, 1990, Coolside Process Demonstration at the Ohio Edison Company Edgewater Plant Unit 4 - Boiler 13. *Proceedings, 1990 SO₂ Control Symposium*, EPRI and U.S. EPA, Session 7A, V 3, New Orleans, LA, 19p.

Acknowledgments

This work was funded by the United States Department of Energy, Contract No. DE-AC21-90MC2862 and the support of Peter Botros of that organization is gratefully acknowledged. We would like to thank our colleagues at the CAER Gerald Thomas, William Schram, William Atkins and Darrell Taulbee of the CAER and Tommy Hopkins and Tony Beckham of the University of Kentucky Transportation Research program for their help and support in this project.

A METHOD TO MEASURE BENZENE PRODUCTION DURING PYROLYSIS; RESULTS FROM TESTING OF CARBONACEOUS ADDITIVES IN FOUNDRY SANDS

Taulbee, D.N.¹, LaFay, V.², Dempsey, T.², and Neltner, S.²

¹Univ. of Kentucky-Center for Applied Energy Research
3572 Iron Works Pike, Lexington, KY 40511
(606) 257-0238-ph, (606) 257-0302-fax

²Hill and Griffith Co.
1262 State Avenue, Cincinnati, OH

Keywords: benzene emissions, foundry, pyrolysis

ABSTRACT

Carbonaceous additives that are blended with clays in foundry sands and sand cores are recognized as a source of benzene emissions in the foundry industry. Impending legislation will possibly mandate substantial reductions in benzene emissions in this sector despite the fact that, with current technology, carbonaceous additives are essential for the production of quality castings. However, it may be possible to identify substitutes that provide acceptable casting performance while generating less benzene. As a first step, a method has been developed to measure the production of benzene during pyrolysis of carbonaceous materials. The method entails pyrolysis of carbonaceous samples in a thermogravimetric analyzer, absorption of the pyrolysis products onto activated charcoal, extraction of the charcoal with CS₂ containing p-cymene, and gas chromatographic quantitation of benzene. Results are presented for several potential sand-mold additives including a series of coals of varying rank, gilsonite, asphaltic suspensions, and metallurgical coke.

INTRODUCTION

It has been estimated that about 90% of all durable goods produced in the U.S. contain at least some metal castings.¹ During 1994, over 13 million metric tons of metal, ~85% of which were iron or steel, were processed by ~3,100 foundries in the U.S.² In 1996, the number of persons directly employed in the U.S. foundry industry numbered just over 220,000³ which does not include the estimated hundreds of thousands of others that supply products to or sell finished goods from this sector. It is, therefore, clear that the foundry industry is a critical segment of the overall domestic economy, one that cannot be substantially curtailed without severe economic repercussions.

From 1971-1991, the domestic foundry industry declined by 32%, due in part to the implementation of increasingly stringent environmental protection regulations including the Clean Air Act (1970) and the Clean Air Act Amendments (1977 and 1990).⁴ The most recent amendment calls for development and implementation of maximum achievable control technology (MACT) standards for the iron foundry categories by November, 2000. Meanwhile, some states are planning to implement their own regulations which set limits separate from those federally mandated. In Wisconsin, for example, sites that exceed such limits must either demonstrate emission controls that provide the lowest achievable emission rates (LAER) through technological advances or other options or show why they should be granted a variance.⁵ In an effort to address the mandates of BACT and/or LAER, one of the options being examined by the foundry industry in that state is reformulation of the molding sand.

Though the carbonaceous materials added to sand molds and cores are believed partially responsible for unwanted emissions, they are essential in providing a reducing atmosphere during pouring which suppresses reaction between the casting sand and metal surfaces.⁶ They also seal the voids between the sand grains thereby suppressing penetration of the molten metal into the sand mold.⁷ The material most widely used to alleviate such casting defects is bituminous coal, commonly referred to in the foundry industry as seacoal. However, when subjected to high temperatures in a reducing atmosphere, i.e., pyrolysis, such coals generate one- and two-ring aromatics, both directly and via secondary reactions.⁸ Of the aromatic components, benzene is of greatest concern due to its relatively high production and proven carcinogenicity. Numerous materials including petroleum resins, cellulosic flours, rosin and petroleum pitch, asphaltic emulsions, asphaltene chips, graphite, fuel oil, gilsonite, coal tar, and even sugar, starch, and molasses were developed as replacements for seacoal.⁹ However, total displacement of seacoal by these additives was not realized for various reasons including uncertainties in availability and inferior performance. Today, the use of these replacements has either been discontinued or they are used as seacoal supplements, typically comprising 20-40 wt% of the carbonaceous additive. This latter trend of blending carbonaceous materials is believed to hold the most promise for reducing the release of hazardous pollutants. Accordingly, the work reported here represents an initial effort aimed at identifying potential additives that emit less benzene during casting yet meet the commercial criteria of low cost, acceptable performance, and availability.

EXPERIMENTAL

Briefly, measurement of the benzene-emitting potential entailed pyrolysis of carbonaceous additives by TGA, collection of evolved volatiles on activated charcoal, extraction of the charcoal with CS_2 , and chromatographic quantitation of benzene. With the exception of the pyrolysis step, the method was modified from OSHA protocols for the measurement of benzene vapors in the workplace.¹⁰

Study Samples. A listing of the samples examined along with a brief description is given in Table I. All samples were solid materials with the exception of two proprietary aqueous asphaltic suspensions (AE-1 and AE-2). Several of these materials are currently used in commercially prepared green-sand blends including the bituminous coals, gilsonite, lignite, and the asphaltic emulsions. The solids were pulverized to the particle range as utilized in molding sands ranging from ~75% pass 40 mesh for the lignite to >90% pass 100 mesh for the gilsonite.

Pyrolysis. 20-90 mg samples were pyrolyzed in triplicate in a TA model 2950 thermo-gravimetric analyzer (TGA) under flowing Argon (60 mL/min). Following a 1 minute equilibration, the furnace was ramped from ambient to 800 °C at 100 °C/min and held for 5 minute. A fast heating rate was selected to more closely simulate the conditions within a sand mold during casting. The heating profile used for the aqueous emulsions was similar except that a 3-minute hold at 100 °C was substituted for the initial 1-minute hold. This modification was necessitated by the high water content of these samples which otherwise resulted in sample *splattering* from the pan. Weight loss from room temperature to ~200 °C was assigned to H_2O while losses above ~200 °C assigned to volatile matter.

Collection of volatiles. Glass tubes (~100 x 5 mm-i.d.) containing 20/40 mesh activated coconut charcoal (ORBO™-32) were used to collect the volatile matter generated during each TGA run. These tubes were partitioned into two in-series chambers; a primary containing 400 mg and secondary containing 200 mg of charcoal. The primary chamber, positioned nearest to the furnace exit, served to absorb the volatile matter as it evolved (including benzene) during the TGA run. The secondary chamber was used to ensure that benzene did not saturate and break through the primary. One end of the tube was loosely connected to the TGA-furnace exit while the other was connected to house vacuum. The vacuum was regulated such that roughly 200 cm³/min gas flow was pulled through the tube. Thus, all carrier and pyrolysis gases exiting the TGA furnace were pulled into the charcoal tube without significantly affecting the furnace pressure.

Benzene quantitation. Prior to the extraction, benzene that is present in commercial-grade CS_2 was removed by passing the CS_2 through molecular sieve 13x, refluxing overnight with $\text{H}_2\text{SO}_4/\text{HNO}_3$ then again passing through molecular sieve. Chromatographic analysis of the processed CS_2 indicated complete removal of the benzene contaminants.

The charcoal from the primary chamber of each absorbent tube was transferred to a 4-mL, teflon-capped vial to which 2.00 mL of CS_2 spiked with *p*-cymene (10.24 ppm) was added. The vial was capped, shaken, and allowed to equilibrate at least 30 min at room temperature prior to analysis. Duplicate 1-2 μL injections of the extract were made into a HP5990 gas chromatograph equipped with a FID, a 10'x1/8" 20% SP2100/0.1% CW1500 column, and a HP-3390A integrator. Benzene was quantitated by comparison of the benzene/cymene ratios from the sample extract to a similar ratios from benzene/cymene standards, also prepared in CS_2 . Due to interference with the cymene internal standard, benzene quantitation for gilsonite was achieved via an external standard technique.

RESULTS

Volatile Release Profile. TGA plots for the lignite, gilsonite, anthracite, and one of the bituminous coals (D4) are shown in Figure 1. Bituminous coal provides beneficial volatile matter release characteristics as evidenced by its common commercial usage in green-sand blends. The volatile release curve for gilsonite, also often used in commercial blends, is similar in that volatiles evolve over a relatively narrow temperature range, typically from 450-500 °C. This is in contrast to the weight loss curves for lignite and anthracite which are broader and occur at lower and/or higher temperatures. The weight loss curves for the asphaltic emulsions were reasonably similar to the D4 plot whereas weight loss for metallurgical coke was more similar to that from the anthracite.

It must be noted that the presence of carbonaceous materials in the sand mold is not of itself sufficient to assure good castings. Rather, it is the volatile component released during pyrolysis that plays the most significant role in creating a reducing atmosphere thereby minimizing oxidation.¹¹ Further, it has been shown that both the composition and temperature of release of the volatile matter governs the amount of *lustrous* or pyrolytic carbon formed (coke deposited onto the molten metal and adjacent sand).¹² Compelling evidence has also shown that only additives that are prone to lustrous carbon formation are of benefit in preventing burn-on.¹³ Thus, the difference in volatile release profiles exhibited by the various materials in Figure 1 is likely an indicator of casting performance.

Method Reproducibility. Various aspects of the reproducibility of the method are shown by the data in Table II, obtained from replicate runs with the Birmingham seacoal. Columns 3 and 4 indicate the scatter in the moisture and volatile matter values from TGA was <5% rsd (σ -1) for this particular set of runs. Likewise, columns 6 and 7 indicate the range in peak integration reproducibility from duplicate injections was typically <10% relative to the mean. Finally, the last two columns indicate the overall reproducibility of the method was just over 1% rsd (σ -1) for this sample. This level of reproducibility was the best of the samples examined. However, the relative standard deviation was less than 5% rsd for most samples and less than 10% (Table III) for all samples with the exception of the anthracite and metallurgical coke from which benzene generation was very low.

Relative benzene generation. Benzene production, moisture content, and volatile matter release are shown for all samples in Table III. Benzene production ranged approximately two orders of magnitude from a low of <0.02 mg/g coal for the anthracite to approximately 2 mg/g for gilsonite. Benzene production is plotted versus volatile matter release in Figure 2. Not surprisingly, this plot shows that increased levels of volatile matter release results in a proportional increase in benzene generation. This implies that foundry-sand blends capable of generating the required levels of volatile matter during casting must obviously contain relatively greater quantities of those additives that generate less volatile matter (and less benzene) suggesting a near constant level of benzene production regardless of the additive. However, note that there are substantial differences in the ratio of benzene production to volatile matter release as shown in the last column of Table III. In general, those samples that generated less volatile matter during pyrolysis produced even less benzene on a relative basis. Thus, a 25 mg sample of lignite, for instance, would generate as much volatile matter on an absolute basis, as 10 mg of gilsonite while generating less than half as much benzene. The data in the final column of Figure 2 would, therefore, favor the use of anthracite, metallurgical coke, or lignite instead of bituminous coal or gilsonite in foundry sands. While this may well be true in terms of benzene generation, as discussed previously, suitable volatile release characteristics are critical for producing acceptable metal castings. In other words, it is not simply the quantity of volatile matter generated but the composition and temperature of release that are most important. In this respect, neither lignite nor metallurgical coke may be suitable as total replacements for bituminous coals (Figure 1) but may yet prove to be effective as partial replacements.

SUMMARY

A TGA pyrolysis/charcoal absorption method has been developed as a means to estimate the benzene-generating potential of carbonaceous additives in foundry sands. The method was shown to provide excellent reproducibility on samples ranging in size from 20 to 90 mg. Application of the method to a series of potential or currently used carbonaceous foundry-sand additives indicated substantial differences in the relative production of benzene during pyrolysis suggesting potentially fruitful areas for future work.

1. "Economic Analysis of Proposed Effluent Limitations and Standard for the Metal Molding and Casting (Foundry) Industry (Supplemental Analysis)"; Policy Planning & Evaluation, Inc.; Supplemental report submitted to the U.S. Environmental Protection Agency under Contract No. 68-01-6731; **1982**; 139 p.
2. "29th Census of World Casting Production-1994"; **1995**; Modern Casting; **85**; pp 24-25.
3. Employment and Earnings US Bureau of Labor, pub.; Washington, DC; March 1996.
4. Lassiter, M.J. "Foundries Prepare for Clean Air Act's Title V Showdown" **1994**, Editorial in Modern Casting, pp 58-59.
5. Personal communication with P. Kirsop, Plan Review Unit Supervisor, Compliance Section, Bureau of Air Management, Wisconsin Department of Natural Resources, Madison, WI.
6. Wang, C.; Heine, R.W.; Schumacher, J.S.; Green, R.A. "What's the Story on Seacoal Replacements in Foundry Sands?" **1961**, AFS Transactions, **73**, pp 496-503.
7. Lane, A.M.; Piwanka, T.S.; Stefanesev, D.M.; Giese, S.R. "Cast Iron Penetration in Sand Molds-Part I: Physics of Penetration Defects and Penetration Model" **1996**, AFS Research Report, CastExpo 96, April 1996.
8. Burnham, A.K.; and Happe, J.A. "On the Mechanism of Kerogen Pyrolysis" **1984**, Fuel, **63**, pp 1353-1356.
9. Dietert, H.W.; Doelman, R.L.; and Bennett, R.W.; "Mold Atmosphere Control"; **1944**; AFS Transactions; **52**; pp 1053-1077.

10. "OSHA Test Method No. 12 for Air Samples"; 1995 as taken from *Kentucky Occupational Safety and Health Standards for General Industry*; 29 CFR Part 1910; 1910.1028 Benzene; Promulgated by the Occupational Safety and Health Administration, U.S. Department of Labor; CCH Business Law Staff Pub., Chicago IL; 823 pp.
11. LaFay, V.S. and Neltner, S.L. "The Value of Seacoal and Seacoal Supplements in Today's Foundry Industry" 1987, *AFS Transactions*, 95, pp 133-137.
12. Bachmann, J. and Baier, D. "Some Aspects of Gas Evolution from Carbonaceous Materials Used in Foundry Molding Sands" 1974, *AFS Transactions*, 82, pp 465-471.
13. Stanbridge, R.P. "The Replacement of Seacoal in Iron Foundry Molding Sands" 1974, *AFS Transactions*, 82, pp 169-180.

ACKNOWLEDGEMENTS. The authors would like to thank Dr. J.C.Hower of the UK-CAER, for providing sample of anthracite.

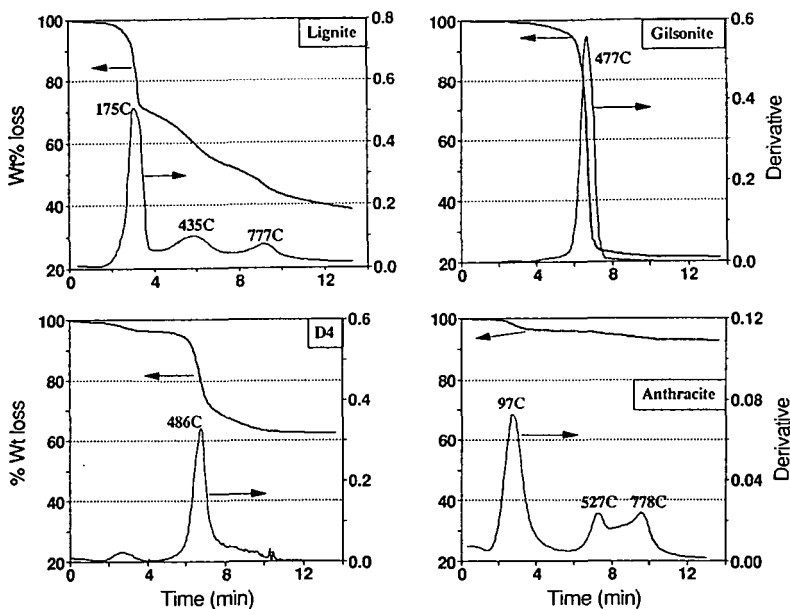


Figure 1. TGA plots showing weight loss and 1st derivative curves for lignite, Gilsonite, an asphaltic emulsion (AE-1), the D4 bituminous coal, and anthracite.

Table I. Listing and brief description of the samples examined.

Sample	Description
Anthracite	Mammoth coal bed, Schuylkill Co., PA
Met Coke	Commercial metallurgical coke
Lignite	Causticized lignite from North Dakota
Coal-Gran	Bituminous coal blended with 15% granulated sugar
D4 SC	Bituminous coal from West Virginia (washed)
Birm coal	Bituminous coal from West Virginia (washed)
Coal-liquid	Bituminous coal w/15% high fructose corn syrup
AE-1	asphaltic emulsion
AE-2	asphaltic emulsion
Gilsonite	gilsonite from Bonanza, Utah

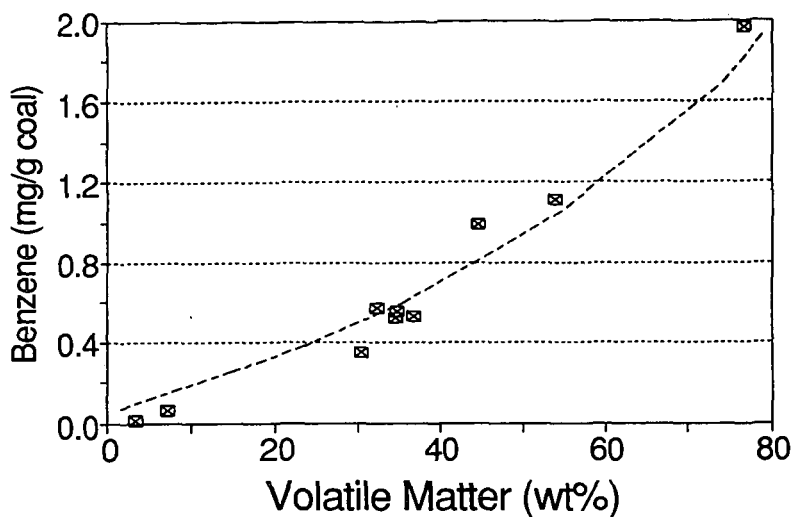


Figure 2. Benzene production as a function of volatile matter release during pyrolysis.

Table II. Method reproducibility as illustrated by replicate values from four TGA runs and duplicate GC injections (Birmingham coal sample).

TGA Run#	Sample Weight (mg)	Moisture by TGA (wt%)	Volatile matter (wt%)	GC Inj. #	Integrated Benz/cymene ratio	Total Benzene (ug)	Measured Benzene (mg/g coal)	Benzene Average (mg/g coal)
23	48.211	3.99	34.68	1st	1.408	26.26	0.545	0.549
				2nd	1.428	26.64	0.553	
24	42.883	3.90	35.46	1st	1.219	22.73	0.530	0.558
				2nd	1.349	25.16	0.587	
25	43.786	3.60	34.18	1st	1.302	24.29	0.555	0.553
				2nd	1.293	24.12	0.551	
26	34.140	3.73	34.47	1st	1.027	19.16	0.561	0.542
				2nd	0.958	17.86	0.523	
Mean		3.81	34.70				0.554	0.551
Std dev		0.151	0.475				0.016	0.007
rsd (%)		3.96	1.37				2.89	1.24

Table III. Benzene production (GC), moisture, and volatile matter (TGA) for all study samples.

Sample	# TGA runs	Moisture (wt%)	Vol matter (wt%)	Benzene (mg/g coal)	rsd (%) (sigma-1)	Benz/VM Ratio
Anthracite	4	3.88	3.45	0.019	22.5	0.006
Met Coke	4	0.92	7.32	0.065	35.2	0.009
Lignite	6	27.7	30.3	0.350	6.1	0.012
Coal-Gran	4	2.47	36.8	0.527	5.5	0.014
D4 SC	4	3.35	34.6	0.520	2.8	0.015
Birm coal	4	3.81	34.7	0.551	1.2	0.016
Coal-liquid	4	4.71	32.4	0.567	2.7	0.018
AE-1	5	35.8	53.9	1.117	8.9	0.021
AE-2	3	43.1	44.7	0.991	2.6	0.022
Gilsonite	3	0.88	76.6	1.972	2.9	0.026

IGNITION BEHAVIOR OF PULVERIZED COALS

John C. Chen,^{*} Subrahmanyam Musti,^{*} Vinayak Kabadi^{*}

Departments of ^{*}Mechanical and ^{*}Chemical Engineering

North Carolina A&T State University

Greensboro, NC 27411

KEYWORDS: Coal ignition, coal reactivity, modeling

INTRODUCTION

We present data from a laser-based experiment used to measure the ignitability of pulverized coals in a room-temperature gas environment. The absence of hot furnace walls surrounding the test section allowed for optical detection of the ignition process. The experimental parameters studied include the coal type, oxygen concentration and particle size. The results show clearly that ignition reactivity is strongly dependent on coal type, and that the ignition rate constants determined are consistent with published data for overall combustion reactivity. The data also show convincingly that particle-to-particle variations in physical and/or chemical property of the fuel must be accounted for in order to model the ignition data correctly, and to accurately describe their ignition reactivity. We present a distributed activation energy model which accomplishes this goal.

EXPERIMENT

The experiment is similar to one described in detail elsewhere,¹ so only a brief description is given here. Figure 1 presents a schematic of the laser ignition experiment; the inset shows the details around the test section. Sieve-sized particles were dropped through a tube into a laminar, upward-flow wind tunnel with a quartz test section (5 cm square cross-section). The gas was not preheated. The gas flow rate was set so that the particles emerged from the feeder tube, fell approximately 5 cm, then turned and traveled upward out of the tunnel. This ensured that the particles were moving slowly downward at the ignition point, chosen to be 2 cm below the feeder-tube exit. A single pulse from a Nd:YAG laser was focused through the test section, then defocused after exiting the test section, and two addition prisms folded the beam back through the ignition point. Heating the particles from two sides in this manner achieved more spatial uniformity and allowed for higher energy input than a single laser pass. For nearly every case, two to five particles were contained in the volume formed by the two intersecting beams, as determined by previous observation with high-speed video.²

The laser operated at 10 Hz and emitted a nearly collimated beam (6 mm diameter) in the near-infrared (1.06 μm wavelength). The laser pulse duration was $\sim 100 \mu\text{s}$ and the pulse energy was fixed at 830 mJ per pulse, with pulse-to-pulse energy fluctuations of less than 3%. The laser pulse energy delivered to the test section was varied by a polarizer placed outside of the laser head; variation from 150 to 750 mJ was achieved by rotating the polarizer. Increases in the laser pulse energy result in heating of the coal particles to higher temperatures. At the ignition point the beam diameter normal to its propagation direction was $\sim 3 \text{ mm}$ on each pass of the beam. An air-piston-driven laser gate (see Fig. 1) permitted the passage of a single pulse to the test section. The system allowed for control of the delay time between the firing of feeder and the passage of the laser pulse. Finally, ignition or nonignition was determined by examining the signal generated by a high-speed silicon photodiode connected to a digital oscilloscope, as described elsewhere.¹

We report here the ignition behavior of two coals: one medium-volatile bituminous, and one high-volatile bituminous. Both samples were obtained from the Penn State University Coal Sample Bank, and the reported proximate and ultimate analyses are shown in Table 1. The coals were sieve-sized using a Ro-Tap shaker to -120/+140 mesh (106-125 μm diameter), and dried at 70°C under vacuum for at least 12 hours prior to each day's experiment.

RESULTS

Each day's experiment was conducted as follows: After choosing the coal and oxygen concentration to examine, the coal was loaded into the batch-wise feeder. The delay time between the triggering of the feeder and the appearance of the coal batch at the feeder tube exit was measured by visual observation in conjunction with a stop watch; typical values were $\sim 2.9 \text{ s}$. The delay time was then programmed into the device which triggered the laser gate. The gas flow rate needed to achieve a drop distance of $\sim 5 \text{ cm}$ for the coal batch was also determined by visual observation. Finally, a laser pulse energy was chosen, and the experiment commenced. At each set of operating conditions (coal type and size, oxygen concentration, and laser energy), 20 attempts at ignition were made in order to measure the

ignition frequency, or probability, which is the parameter sought from these studies. Mapping this ignition frequency over a range of laser pulse energy produces an ignition-frequency distribution.

Such a frequency distribution is shown in Fig. 2 for the Pittsburgh #8 coal. It can be seen that at each oxygen concentration, ignition frequency increases monotonically over a range of increasing laser pulse energy. Below this range the ignition frequency is zero, and higher energies result in 100% ignition frequency. This behavior is due to the fact that, within any coal sample, there exists a variation of reactivity among the particles.³ Thus, in this experiment, in which a batch of perhaps several hundred particles of a sample is dropped into the test section but only a few are heated by the laser pulse, there is an increasing probability (or frequency) as the laser energy is increased that at least one of the heated particles is reactive enough to ignite under the given conditions.

The repeated distributions under 100% oxygen, measured on separate days, show the excellent repeatability of this experiment; the most important factor for reproducibility is the moisture content of the sample.

Figure 2 also shows the effect of oxygen concentration: As oxygen level is decreased from 100% to 75%, and then to 50%, the frequency distribution shifts to higher laser energies or, equivalently, higher particles temperatures, as expected. This is consistent with ignition theory since at decreased oxygen levels, higher temperatures are necessary to achieve the equality between heat generation by the particles (due to chemical reactions) and heat loss from the particles. This equality is the minimum requirement for ignition, and is termed 'critical ignition.' The shift in distribution can be viewed in two ways: First, for a fixed laser pulse energy, a decrease in oxygen level leads to a decrease in the ignition frequency, all else being the same; second, a decrease in oxygen implies that a higher laser pulse energy is needed, in order to achieve the same ignition frequency.

Finally, it should be noted that for the Pittsburgh #8, the decreases in oxygen concentration shift the distributions to higher laser energies in approximately equal increments (equal energy ranges), and with little or no effect on the slope of the distributions. This finding is in contrast to the results for the Sewell coal (Fig. 3).

Three major differences between the ignition behaviors of the Pittsburgh #8 and Sewell exist. First, decreasing oxygen concentrations has a stronger effect in shifting the distributions of the Sewell to higher laser pulse energies (or higher particle temperatures). Second, as oxygen level is decreased, the slope of the distribution is undoubtedly decreased for the Sewell, while little effect is observed for the Pittsburgh #8. Finally, a comparison of the distributions of the two coals under 100% oxygen shows that the Sewell reaches 100% ignition frequency in a significantly smaller range of laser energy (ΔE_{laser} of ~150 mJ versus ~250 mJ).

DISCUSSION

Over the past three decades, many experiments have examined the ignition of pulverized coals under conditions which simulate pulverized fuel-firing conditions.^{4,5,6,7,8,9} The common factor among these studies is the assumption of a single, average, kinetic rate-constant in describing the ignition reactivity of each coal. As we have shown previously,³ it is necessary to account for the variation in reactivity among the particles within a sample in order to model the ignition distribution observed in this and nearly all previous ignition studies. Once such a model is implemented, the parameters may then be adjusted to fit the data and produce the desired ignition rate constant and reaction order with respect to oxygen for each coal.

Our previous experience in modeling ignition distribution data³ provides some insight to explain the results described earlier. The model details will not be described here, but it is sufficient to note that the model accounts for particle-to-particle variations in reactivity by having a single preexponential factor and a Gaussian distribution of activation energies among the particles within a sample. The distribution is characterized by two parameters, an average activation energy (E_a) and a standard deviation (σ) in the activation energy.

In light of this model, the differences in the range of laser energies over which the various coals achieved 100% ignition frequency is a direct result of the breadth of the Gaussian distribution of activation energies: A narrow distribution (small standard deviation) leads to a small laser-energy range since most particles have similar activation energies and, thus, reactivities. Indeed, in the limit that the standard deviation is zero (all particles have the same activation energy), the ignition-frequency distribution would become a step function. Conversely, a broad distribution of reactivities (large σ) leads to a relatively larger range of

laser energy needed to achieve 100% frequency, as is the case for the Pittsburgh #8 compared to the Sewell. The effect of variations in the average value of the activation energy in the distribution is to shift the ignition-frequency plot; higher E_{av} means lower ignition reactivity for a particular coal, which would shift the ignition distribution to higher laser energies.

Finally, with regard to the effect of oxygen concentration on the slope and shift of the ignition-frequency distributions observed for the Pittsburgh #8 and Sewell coals, the model interprets such differences to be the result of the variation in the reaction order, n , with respect to oxygen concentration.

The model results for the Pittsburgh #8 coal are shown in Figs. 4, 5 and 6, for average particle sizes of 115 μm , 69 μm and 165 μm , respectively. The model parameters (E_{av} , σ , and n) were adjusted to produce the best fit at all oxygen concentrations for the 115 μm particles (Fig. 4). They were then left at these values to produce the results for other particle sizes (Figs. 5 and 6).

As can be seen, while the model captures salient features in the experimental data, the fit to the data is not ideal. This is attributed to a lack of knowledge of the particle temperature at ignition. Indeed the results shown relied on calculated temperatures as described previously.¹ We plan to improve the experiment by implementing a two-color pyrometry system to directly measure the ignition temperature in future studies.

ACKNOWLEDGEMENT

The support of this project by the U.S. Department of Energy through Grant DE-FG22-94MT94012 is gratefully acknowledged.

REFERENCES

- 1 Chen, J.C., Taniguchi, M., Narato, K., and Ito, K. "Laser Ignition of Pulverized Coal," *Combust. Flame* 97, 107 (1994).
- 2 Chen, J.C., Taniguchi, M., Ito, K. "Observation of Laser Ignition and Combustion of Pulverized Coals," *Fuel*, 74(3), 323 (1995).
- 3 Chen, J. C. "Distributed Activation Energy Model of Heterogeneous Coal Ignition," *Combust. Flame*, 107, 291 (1996).
- 4 Essenhigh, R.H., Mahendra, K.M., and Shaw, D.W. *Combust. Flame*, 77, 3 (1989).
- 5 Cassel, H.M. and Liebman, I. *Combust. Flame*, 3, 467 (1959).
- 6 Karcz, H., Kordylewski, W., and Rybak, W. *Fuel*, 59, 799 (1980).
- 7 Fu, W. and Zeng, T. *Combust. Flame*, 88, 413 (1992).
- 8 Zhang, D., Wall, T.F., Harrie, D.J., Smith, I.W., Chen, J., and Stanmore, B.R. *Fuel*, 71, 1239 (1992).
- 9 Boukara, R., Gadiou, R., Gilot, P., Delfosse, L., and Prado, G. *Twenty-Fourth Symposium (International) on Combustion*, The Combustion Institute, Pittsburgh, PA, 1993, pp. 1127-1133.

Coal Penn State ID	Rank	Prox. Analy. (dry wt%)		Ultimate Analysis (dry, ash-free wt%)				
		Vol. Matter	Ash	C	H	N	S	O (diff.)
Pittsburgh #8 (DECS 23)	low-volatile A bituminous	39.4	9.44	82.0	5.63	1.49	4.27	6.66
Sewell (DECS 13)	medium-volatile bituminous	25.0	4.22	88.2	4.95	1.50	0.65	4.71

Table 1: Ultimate and proximate analyses of coals used in this study.

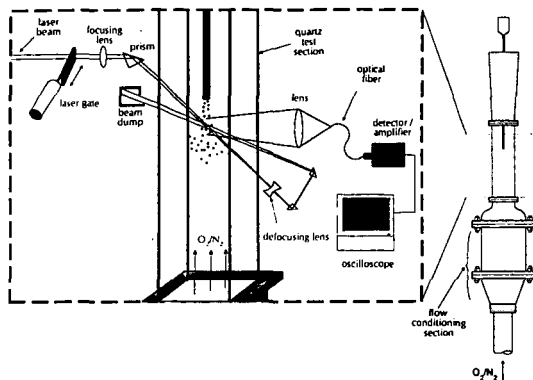


Fig. 1: Schematic of the laser ignition experiment.

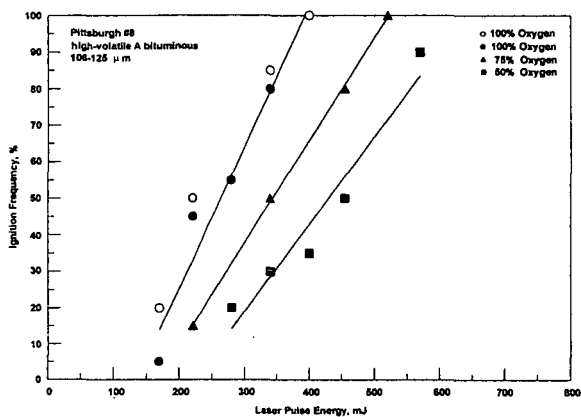


Fig. 2: Ignition-frequency distributions for the Pittsburgh #8 coal. Two data sets (open and filled circles) at 100% oxygen show reproducibility of experiment. Solid lines represent linear regressions of each data set.

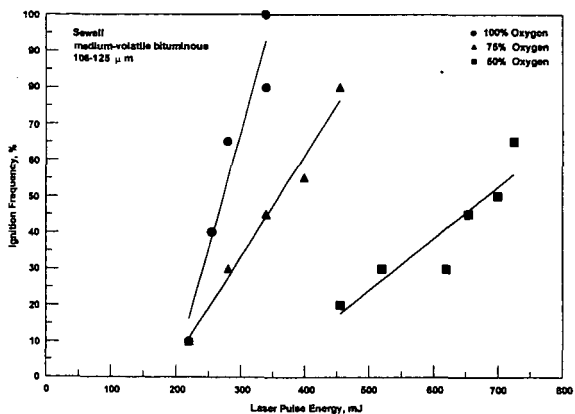


Fig. 3: Ignition-frequency distributions for the Sewell coal. Solid lines represent linear regressions of each data set.

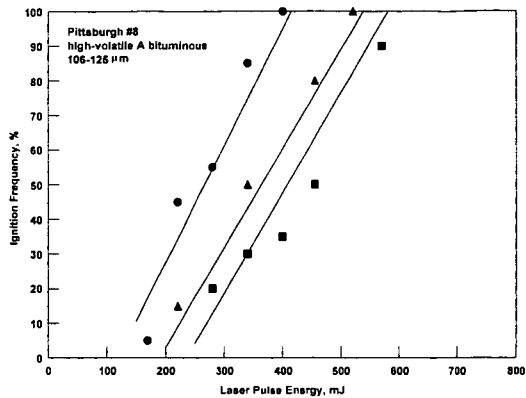


Fig. 4: Comparison of experimental data to model for 115 μm particles. Lines represent linear regressions of experimental data and symbols are from simulation.

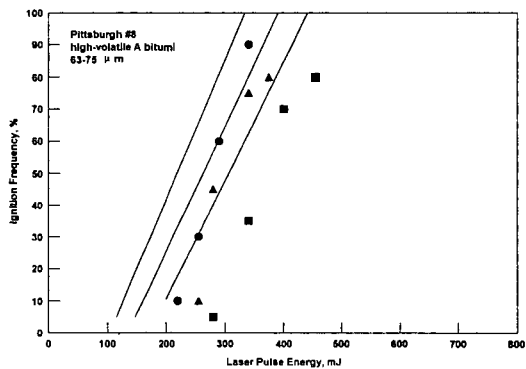


Fig. 5: Comparison of experimental data to model for 69 μm particles. Lines represent linear regressions of experimental data and symbols are from simulation.

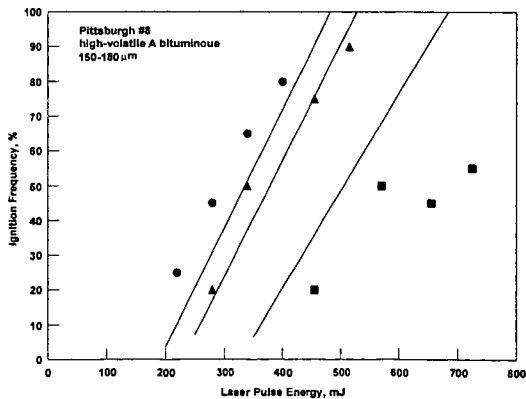


Fig. 6: Comparison of experimental data to model for 165 μm particles. Lines represent linear regressions of experimental data and symbols are from simulation.

STUDIES OF CHLORINE AND SULFUR BEHAVIOR DURING COAL COMBUSTION IN AN AFBC SYSTEM

Wei Xie, Wei-Lan Pan, David Shen, Wei-Ping Pan and John T. Riley
Materials Characterization Center and Department of Chemistry
Western Kentucky University
Bowling Green, KY 42101.

Keywords: combustion, sulfur, and chlorine

INTRODUCTION

The laboratory sized atmospheric bed combustor (AFBC) at Western Kentucky University was designed to serve as a flexible research and development facility to gain operating experience, evaluate combustion performance, and estimate the effects of flue gas emissions. The operating conditions for the AFBC system are similar to those used at the TVA 160-MW AFBC Pilot Plant located near Paducah, Kentucky. Fluidized bed combustion systems are particularly suited to waste fuels because of their ability to burn low grade and variable fuels as well as absorb sulfur oxides through the use of limestone.

It has been demonstrated that the following parameters have an effect on the amount of sulfur retained in the fluidized bed: the molar calcium-to-sulfur ratio, the sorbent particle size, the gas phase residence time, sorbent reactivity, bed temperature, feed mechanisms, and excess air level.¹ The amount of limestone sorbent needed in a fluidized-bed combustor is proportional to the sulfur contained in the fuel and inversely proportional to the amount of calcium contained in the limestone. Calcium in the limestone which can be reacted with sulfur oxides depends on factors specific to the limestone and to the operating conditions in the fluidized-bed combustor.

The chloride content of coal varies from just a few ppm to thousands of ppm. Emissions of chloride from coal-fired plants can range from 50 to several thousand parts per million by volume, depending on the original concentration in the coal, the type of combustor, and any pollution control equipment installed. It has been estimated that 94% of the chloride in coal is volatilized, generally being emitted as gaseous HCl.² In an AFBC system limestone may be able to capture the chlorine. Limestone degenerates to CaO, and CaO reacts with HCl to produce CaCl₂.³ In an AFBC system, capture of chloride by limestone in the combustion zone depends upon the temperature of the combustion zone and the ratio of calcium-to-sulfur. A study by Liang and others⁴ showed that chloride capture has a large variation with temperature moving from a low of 18% gaseous HCl at 700°C to 99% HCl at 950°C. The resulting product is almost entirely in the form of liquid CaCl₂. Munzner and Schilling⁵ studied the effect of limestone in a bench-scale AFBC system. The results showed that a greater recapture of chloride occurred with larger excesses of limestone, or when the Ca/S ratio was greater than 2.

To better understand the combustion behavior of sulfur and chlorine during coal combustion in an AFBC system, a comprehensive research project was performed at the Western Kentucky University on different aspects of emission reduction from fluidized beds during coal combustion. Some results of this study are reported in this paper.

EXPERIMENTAL

Two 1,000-hour burns were conducted with the 12-inch laboratory AFBC system at Western Kentucky University. Operating conditions similar to those at the 160-MW system at the TVA Shawnee Steam Plant located near Paducah, KY were used. A 1,000-hour burn was done with a low-chlorine (0.012% Cl and 3.0% S) western Kentucky # 9 coal (95011), which is the same type of coal as that supplied to the TVA plant during 1993. A second 1000-hour burn was conducted with high-chlorine (0.28% Cl and 2.4% S) Illinois # 6 coal (95031). Six moveable heat exchanger tubes are located within the bed area. Typical operation involves setting the correct coal/lime feeds and air flows and then using the moveable tubes to adjust the bed temperature to the desired setting. The combustor's operating parameters (air/water flow, coal/lime feed, bunker weight, temperatures and pressures) were controlled and logged to file with a Zenith 150 MHZ PC utilizing the LABTECH software version 3.0. During the combustion runs any needed changes in the parameters could easily be entered into the computer by accessing the correct control screen and making the necessary corrections on line. During combustion runs the flue gases at the heat exchanger region were analyzed continuously using on-line FTIR, GC, and IC instrumentation.

RESULTS AND DISCUSSION

The major operating parameters for the AFBC system were as follows: excess air level -- approximately 1.3; Ca/S ratio -- approximately 3; bed temperature -- 1144K, CO₂ level -- approximately -- 13%; oxygen in the flue gas -- 5-6%. Figure 1 shows the O₂ and CO₂ concentrations

in the flue gas at various positions above the fuel injection port. The influence of different process parameters on the emissions of SO_2 and HCl will be discussed.

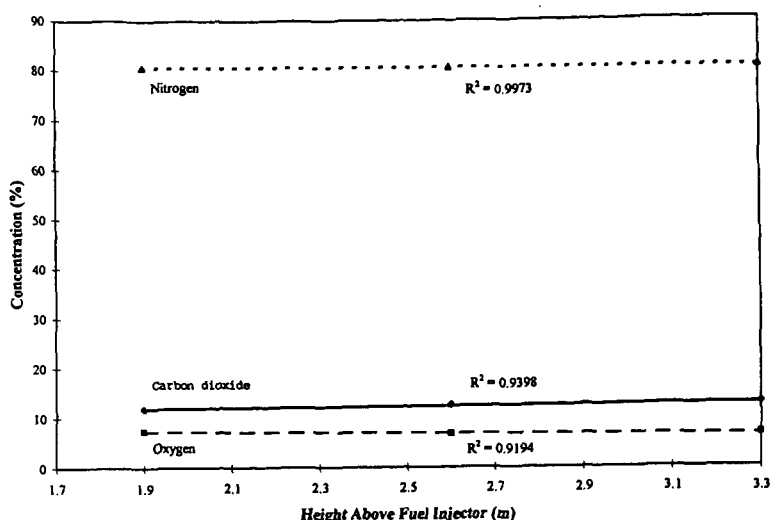


Figure 1. Flue gas composition in the center of the AFBC combustor at different heights above the fuel injection port.

The Effect of Bed Temperature. Figure 2 shows that the SO_2 emission increases as the bed temperature is increased. The optimal sulfur retention is obtained around 1120K. The sulfur retention reaches around 96% at this temperature. At higher temperatures (>1120K), the active internal surface of the limestone particles is decreased, which may be due to the effect of sintering of limestone particles. The thermal decomposition of the CaSO_4 under reducing conditions (such as in the presence of CO , hydrogen, or carbon) at the higher temperature may also contribute to the emission of SO_2 . The effect of temperature on the emission of chloride is shown on the Figure 3. More HCl is observed when the temperature was raised to the higher temperature. The capture of HCl by limestone is more difficult than the capture of SO_2 . Also, the reaction between HCl and CaO is more favorable at the lower temperature.⁴

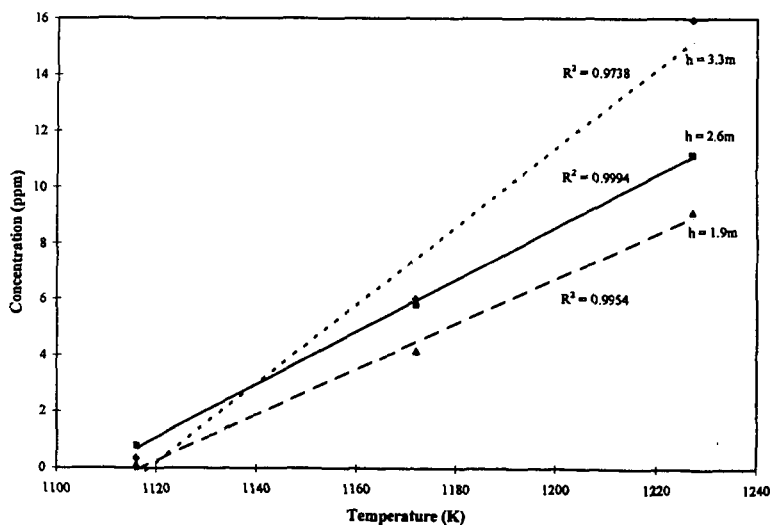


Figure 2. The effect of temperature on the emission of sulfur dioxide at different heights above the fuel injection port.

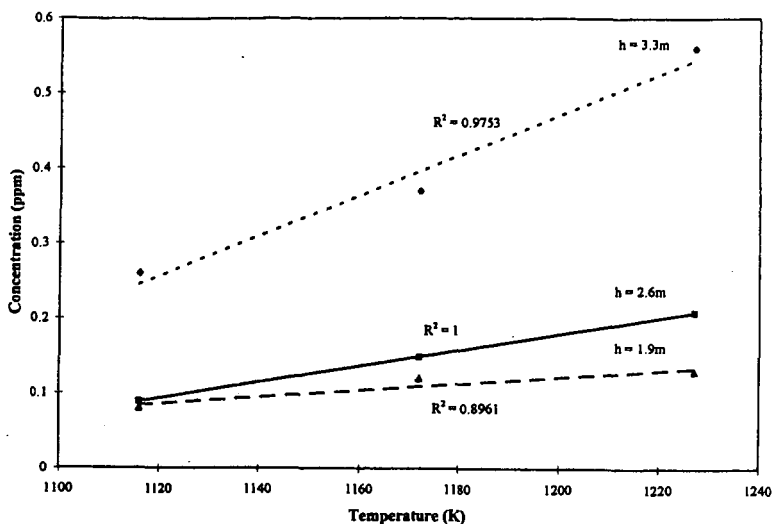


Figure 3. The effect of temperature on the emission of hydrogen chloride at different heights above the fuel injection port.

The Effect of Coal Type. Figure 4 shows the results of sulfur dioxide emission from tests with two different coals (95011 and 95031). It is clear that good sulfur capture is obtained between 1120K and 1170K for both coals. The higher sulfur oxide emission for coal 95011 observed at the higher temperature may be due to the effect of temperature and the higher sulfur content (3%). There is good agreement between the HCl emission and chloride content in the coal, as is illustrated in Figure 5. No chloride containing species were identified in a cold trap solution (methylene chloride with phenol).

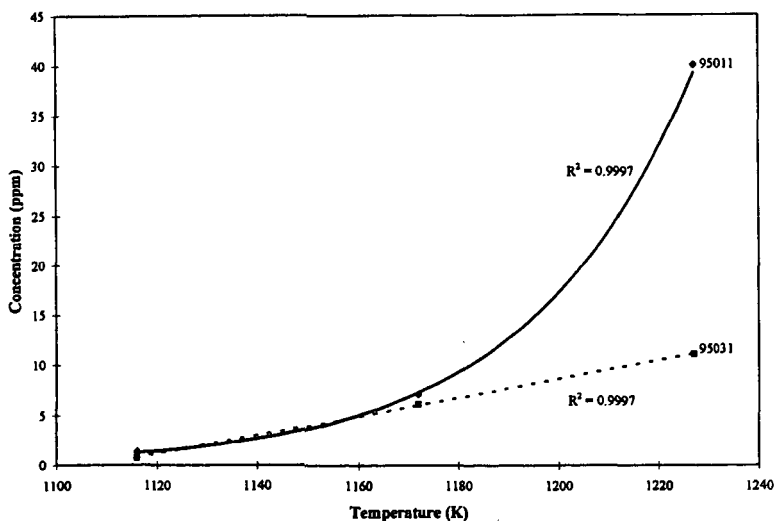


Figure 4. The effect of coal type on the emission of sulfur dioxide at different temperatures in the AFBC system.

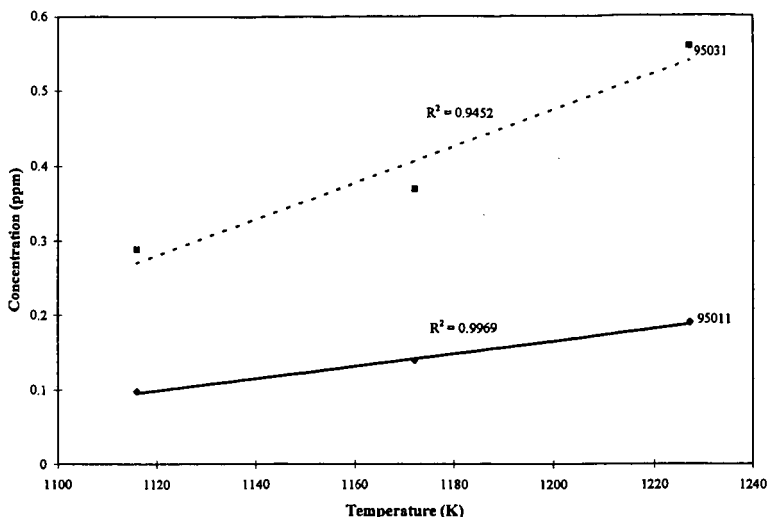


Figure 5. The effect of coal type on the emission of hydrogen chloride at different temperatures in the AFBC system.

The Effect of the Ca/S Ratio. In Figure 6 the measured SO_2 in the flue gas is plotted versus the calcium-to-sulfur molar ratio. The results indicate there is a significant improvement in the sulfur capture with the higher Ca/S ratio in the temperature between 1172 and 1227K. However, there is no effect at the optimal temperature (1116K). In the case of HCl emission, there is no significant difference on the emission of HCl between different Ca/S ratios, as is illustrated in Figure 7.

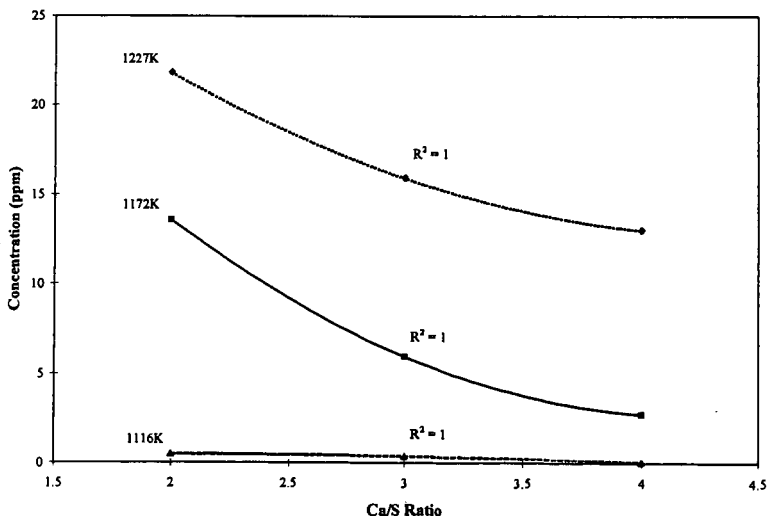


Figure 6. The effect of the Ca/S ratio on the emission of SO_2 different temperatures in the AFBC system.

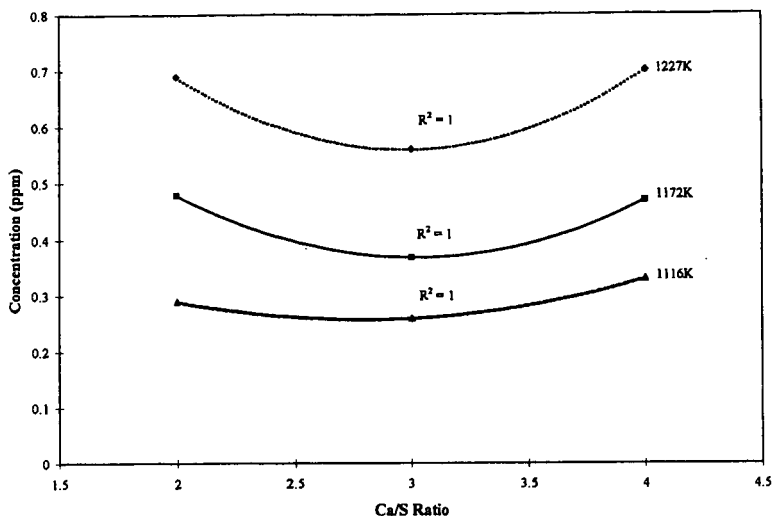


Figure 7. The effect of the Ca/S ratio on the emission of HCl at different temperatures in the AFBC system.

CONCLUSIONS

Based on the information presented in this paper summary statements that can be made include:

- The optimal sulfur retention is obtained around 1120K under our experimental conditions.
- The capture of HCl by limestone is more difficult than the capture of SO_2 .
- Molecular chlorine was not identified in any of the flue gases from the AFBC system.
- There is no significant change in the emission of HCl when the Ca/S ratio is varied.

ACKNOWLEDGMENTS

The financial support for this work received from the Electric Power Research Institute is gratefully acknowledged.

REFERENCES

1. Hartman, M.; Hejna, J.; and Beran, Z. *Chemical Engineering Science*, 1979, 34, 475.
2. Shao, T.; M.S. Thesis, Western Kentucky University, 1994.
3. Heidbrink, Jenny, M.S. Thesis, Western Kentucky University, 1996.
4. Liang, D.T.; Anthony, E.J.; Leowen, B.K.; Yates, D.J. *Proceedings of the 11th International Conference on FBC*, Montreal, Canada, April 21-24, 1991, Volume 2, pp. 917-22.
5. Munzner, H.; Schilling, D.H. *Proceedings of the 8th International Conference on FBC*, Volume III, Houston, March 18-21, 1985, pp. 1219-26.

THE EFFECT OF COAL CHLORINE AND SULFUR CONTENTS ON HIGH TEMPERATURE CORROSION IN AN AFBC SYSTEM

Wei Xie, Shi Su, Brian Sisk, Jeremy Bowles, Wei-Ping Pan and John T. Riley
Materials Characterization Center and Department of Chemistry
Western Kentucky University
Bowling Green, KY, 42101

Keywords: corrosion, combustion, chlorine, sulfur

INTRODUCTION

The occurrence of furnace wall and superheater corrosion in fluidized bed combustor systems has caused some operational and economic concerns.¹ It is generally accepted that chlorine and sulfur may play roles in this corrosion. In order to predict the performance of high chlorine or high sulfur coals in these combustion systems, it is necessary to have a better understanding of the different corrosion mechanisms in which chlorine and sulfur may be involved.² It is also important to evaluate the critical point of coal chlorine content which may cause initial corrosion.

TVA's Shawnee plant observed that the boiler tubes in the primary superheater region of the atmospheric fluidized bed combustion system had wastage/corrosion problems between 1992 and 1993. The boiler tubes were located in the bed area and the wastage was caused by both corrosion and erosion. It is difficult to isolate the factors (such as chlorine content, sulfur content, or erosion) causing this wastage. Also, the gas composition varies a great deal in the primary superheater region. However, the tube wastage problems were resolved after several modifications were made in the AFBC system. The modifications included (1) changing the type of coal to a low chlorine coal, and (2) elevation of the boiler tubes to a higher position in the unit.

Our study was designed to evaluate the role coal chloride may play in causing corrosion of boiler components. The Western Kentucky University AFBC system was configured to simulate the Shawnee Plant's system and especially the secondary superheater region in the TVA plant. This simulation excluded consideration of the erosion problems. Also, TVA did not observe any wastage in this location when they used low chloride content coal. The gas composition of this location is very consistent during constant operation.

EXPERIMENTAL

Two 1,000-hour burns were conducted with the 12-inch (0.3 m) laboratory AFBC system at Western Kentucky University. Operating conditions similar to those used at the 160-MW system at the TVA Shawnee Steam Plant located near Paducah, KY were used. A 1000-hour burn was done with a low-chlorine (0.012% Cl and 3.0% S) western Kentucky # 9 coal, which is the same type of coal as that supplied to the TVA plant during 1993. A second 1000-hour burn was conducted with high-chlorine (0.28% Cl and 2.4% S) Illinois # 6 coal. The limestone came from Kentucky Stone in Princeton, KY. This is the source of the limestone used by the Shawnee plant in their AFBC system during 1993. The major operating parameters were as follows: excess air level -- approximately 1.3; Ca/S ratio -- approximately 3; bed temperature -- approximately 1150 K; and temperature near metal coupons -- approximately 900 K. Four different metal alloys [carbon steel C1020 (0.18% C and 0.05% Cr), 304 SS (18.39% Cr and 8.11% Ni), 309 SS (23.28% Cr and 13.41% Ni), and 347 SS (18.03% Cr and 9.79% Ni)] were studied in this project. Each metal coupon had a 5.08 cm outside diameter, was 0.3175 cm thick, with 1.587 cm diameter hole in center. A set of metal coupons was placed at 3.35 m above the fuel injection port, which is 10 cm below the convective pass heat exchange tubes. Coupons were held in place by a machinable tungsten rod (powder metallurgically prepared) and separated by ceramic mounts. Two sets of each coupons (listed above) made a total of eight coupons for the run. Each specimen within a group was rotated as to position in an array every 250 hours during the test burn. The coupon was weighed before and after the run and examined using SEM. The SEM analysis was performed on a JEOL JSM-5400 SEM. Attached to the SEM for Energy Dispersive X-ray analysis (EDS) was a KEVEX Sigma 1 system with a Quantum detector for elemental analysis down to carbon. The following instrument operating parameters were used for the SEM/EDS analysis: electron beam energy -- 20 KeV; working distance -- 24 mm; sample tilt angle -- 0°.

RESULTS AND DISCUSSION

Only SEM/EDS results on different specimens will be presented in this paper. The results of corrosion with respect to the morphologies of the test coupons (cross section examination) will be reported in the near future.

The C1020 specimen was cracked after 250-hours of operation in both test runs. Figure 1 illustrates the weight change data for the alloys in the first 1000-hour burn with the low chloride coal. The type 347 specimen showed the highest weight gain among the other three samples. However, alloy 304 showed the most oxide scale on the surface and alloy 309 showed the least oxide scale on the surface. These observations are based on the color (reddish) and SEM studies. Also, slight scale failures were observed in all three samples. The degree of scale failure is in the following order: 304 > 347 > 309 (the least). This is the reason for the fluctuation of weight change shown for alloy 304. The weight gain is due to the oxidation and the weight loss is due to the scale failure. The two reactions compete with each other.

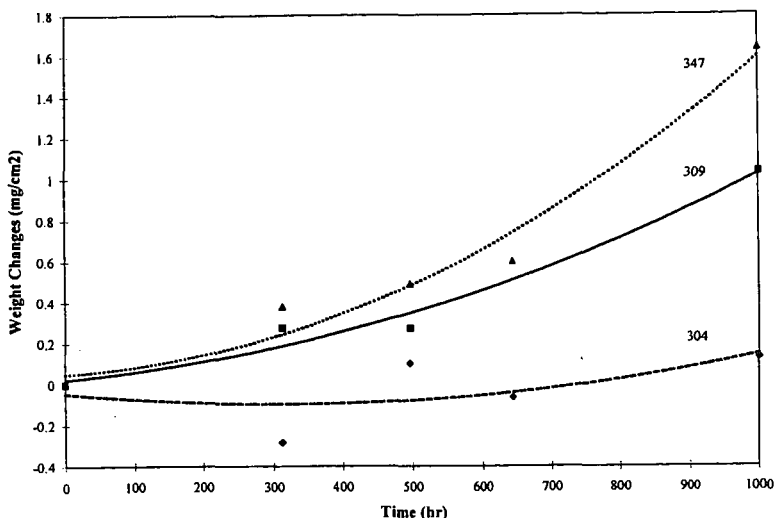


Figure 1. The effect of time of exposure to AFBC combustion gases on the weight of metal coupons.

The scale failure might be due to the sulfur attack and the effect of erosion. The EDS results indicated that the amount of sulfur, calcium and sodium on the surface increased with burning time, as is illustrated in Figures 2 and 3. A certain amount of fly ash passed through the specimens the entire time during the run. Thus, the effect of erosion should also be taken into consideration. The alloy 309 is the best (less oxide scale and scale failure) corrosion resistant material among the three samples under our experimental conditions. It may be due to the high amount of chromium in the compositions.

Figure 4 shows the weight change data for the alloy in the second 1000-hour burn with the higher chlorine coal (0.28% Cl). The weight gain was observed in the case of 309 and 347 before 500 hours. In the case of the 304 alloy, the weight almost remained constant in the first stages of the test burn. There is no chloride (EDS results) observed on the surface of coupons before 500 hours, as is illustrated in Figures 5 and 6. The small amount of scale failure was observed on all three samples, which is similar to the results obtained with the low chlorine coal in the first 1000-hour test. However, the weight loss was observed in all three coupons after 500 hours. The chloride also was identified on the surface of the coupons. Based on the mapping results, the chloride is evenly distributed on the surface of the coupons. There is no concentration of chloride on the spot of scale failure. There are more scale failures observed in this test run than was observed in the first test run. This suggests that chlorine may enhance attack on the metal coupons, but the data is not conclusive.

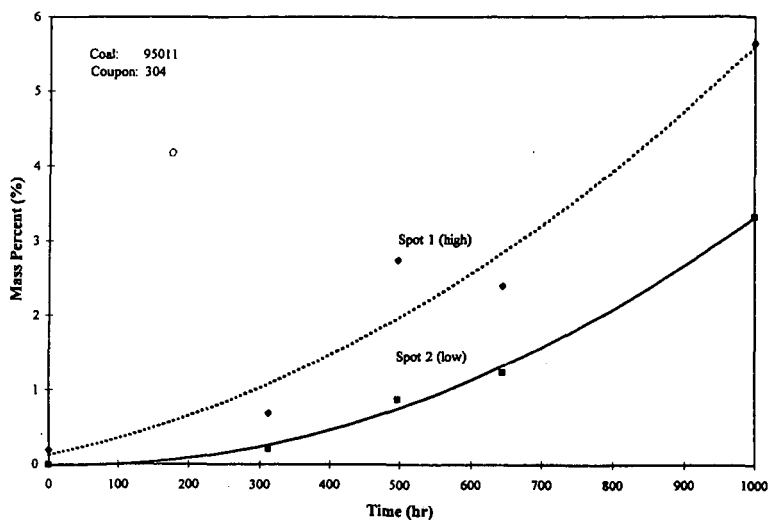


Figure 2. The effect of time of exposure to AFBC combustion gases on the sulfur concentration on metal coupons.

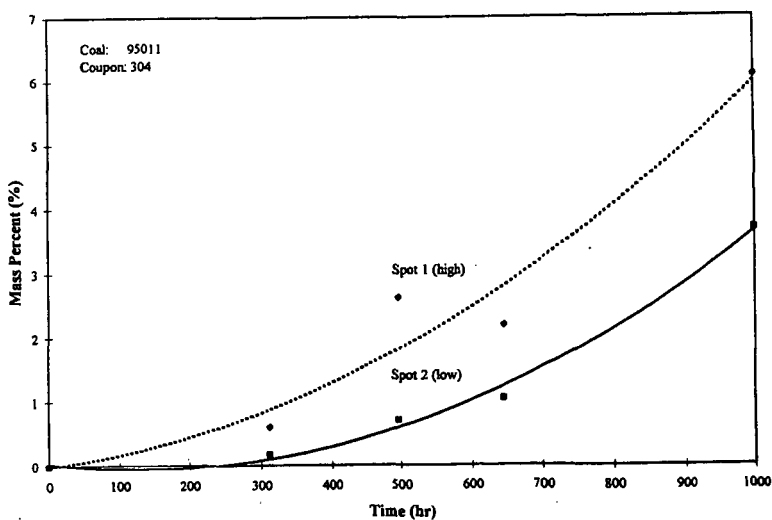


Figure 3. The effect of time of exposure to AFBC combustion gases on the calcium concentration on metal coupons.

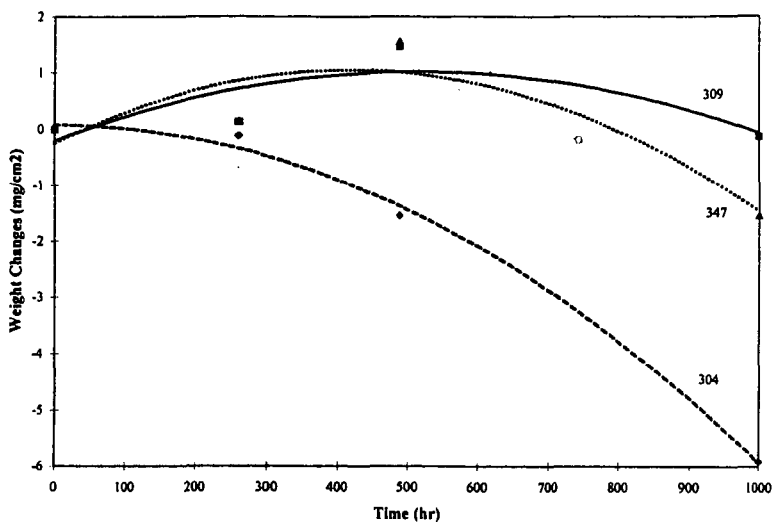


Figure 4. The effect of time of exposure to AFBC combustion gases on the weight changes of metal coupons.

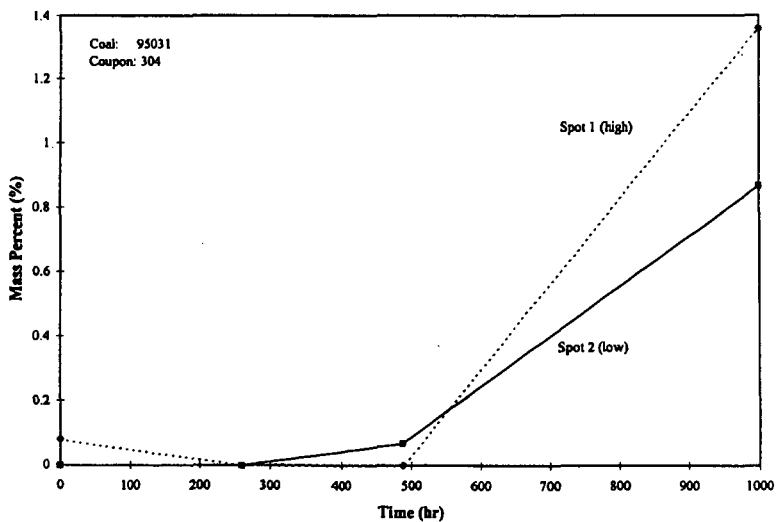


Figure 5. The effect of time of exposure to AFBC combustion gases on the chloride concentration on metal coupons.

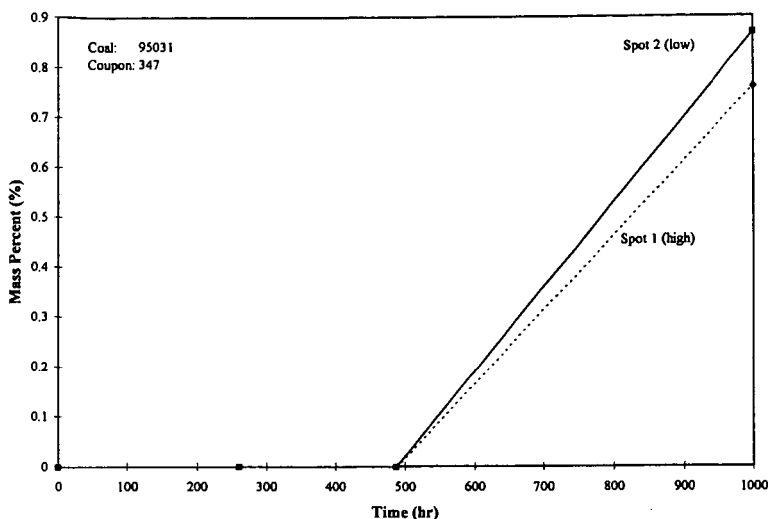


Figure 6. The effect of time of exposure to AFBC combustion gases on the chloride concentration on metal coupons.

CONCLUSIONS

Based on the data presented in this paper the following statements and observations can be made.

- High chromium (~ 23%) 309 alloy steels forming Cr_2O_3 on the surface possessed the greatest corrosion resistance of the four materials tested.
- Scale failure was observed in both 1000-hour test burns with low and high chlorine coals. The second test burn with the high chlorine coal showed more scale failure than that obtained with the first run with the low chlorine coal.
- Chlorine in the coal may enhance the scale failure but the evidence is not conclusive.

ACKNOWLEDGMENTS

The financial support for this work received from the Electric Power Research Institute is gratefully acknowledged.

REFERENCES

1. Minchener, A.J.; Lloyd, D. M.; Stringer J. "The Effect of Process Variables on High Temperature Corrosion in Coal-Fired Fluidized Bed Combustors," in *Corrosion Resistant Materials for Coal Conversion Systems*, (Ed. Meadowcroft, D.B. and Manning, M.I.) Chap. 15, Applied Science Publishers, New York, 1983, p. 299.
2. Mayer, P.; Manolescu, A. V.; Thorpe, S.J. "Influence of Hydrogen Chloride on Corrosion and Corrosion-Enhanced Cracking Susceptibility of Boiler Construction Steels in Synthetic Flue Gas at Elevated Temperature," in *Corrosion Resistant Materials for Coal Conversion Systems*, (Ed. Meadowcroft, D.B. and Manning, M.I.) Chap 5, Applied Science Publishers, New York, 1983, p. 87.